

A SPECTROSCOPIC INVESTIGATION OF THE  
HYDROGEN-DEFICIENT BINARY  $v$  SGR, AND  
RELATED OBJECTS

Richard E. Dudley

A Thesis Submitted for the Degree of PhD  
at the  
University of St Andrews



1992

Full metadata for this item is available in  
St Andrews Research Repository  
at:  
<http://research-repository.st-andrews.ac.uk/>

Please use this identifier to cite or link to this item:  
<http://hdl.handle.net/10023/14426>

This item is protected by original copyright

A Spectroscopic Investigation of the  
Hydrogen-Deficient Binary *v* Sgr,  
and Related Objects.

Richard E. Dudley

A Thesis presented for the Degree of Doctor of Philosophy in  
the University of St. Andrews.

17<sup>th</sup> April 1992



ProQuest Number: 10170984

All rights reserved

INFORMATION TO ALL USERS

The quality of this reproduction is dependent upon the quality of the copy submitted.

In the unlikely event that the author did not send a complete manuscript and there are missing pages, these will be noted. Also, if material had to be removed, a note will indicate the deletion.



ProQuest 10170984

Published by ProQuest LLC (2017). Copyright of the Dissertation is held by the Author.

All rights reserved.

This work is protected against unauthorized copying under Title 17, United States Code  
Microform Edition © ProQuest LLC.

ProQuest LLC.  
789 East Eisenhower Parkway  
P.O. Box 1346  
Ann Arbor, MI 48106 – 1346

TR B173

**To my Parents**

## Abstract

The bright hydrogen-deficient binary  $\nu$  Sgr has been studied in detail in the areas of radial velocities, flux distribution, temperature, surface gravity, composition and mass loss using the analysis of spectroscopic data.

From IUE high resolution spectra the primary radial velocity orbit has been confirmed ( $K_1 = 47.3 \pm 0.8 \text{ km s}^{-1}$ ) and the secondary radial velocity curve determined for the first time ( $K_2 = 29.7 \pm 1.7 \text{ km s}^{-1}$ ). The orbit has been constrained to an inclination of  $65 - 78^\circ$ . The masses of the primary and secondary are then  $3.0 \pm 0.3$  and  $4.8 \pm 0.5 M_\odot$  respectively, with an orbital separation of  $230 \pm 20 R_\odot$ . The primary is expected to fill its Roche Lobe at a radius of  $\sim 60 R_\odot$ .

Using all the available photometry and line-blanketed hydrogen-deficient model atmospheres the primary effective temperature has been determined to be  $11,800 \pm 500 \text{ K}$ . IUE spectra were used to determine an extinction of  $E_{B-V} = 0.20 \pm 0.05$  leading to a distance of  $\sim 1400 \text{ pc}$  and a luminosity of  $61,000^{+11,000}_{-5,000} L_\odot$ . The long standing problem of the flux distribution has been mostly solved and little of the UV flux shortward of  $1400 \text{ \AA}$  comes from a hot bright secondary.

The same model atmospheres and a high resolution CCD/echelle spectrum was used to confirm the temperature ( $T_{\text{eff}} = 11,750 \pm 750 \text{ K}$ ) and to obtain a surface gravity of  $\log g = 1.5 \pm 0.5$ .  $\nu$  Sgr is  $\sim 99.6\%$  helium,  $0.016\%$  H with CNO abundances indicative of advanced evolution and high main sequence mass.

From profile fitting of the UV resonance lines of C, N and Si the mass-loss rate from  $\nu$  Sgr is at least  $2.5 \times 10^{-10} M_\odot \text{ yr}^{-1}$ . The upper limit to the mass-loss rate is  $1.0 \times 10^{-5} M_\odot \text{ yr}^{-1}$  from the lack of observed changes in the orbital parameters.

The mass of the primary component and the low likely mass-loss rate indicate that the primary component will not be able to shed enough material before core collapse, an event that will be classed as a type Ib supernova. This is the first solid evidence that hydrogen-deficient binaries are progenitors of these objects although other candidates are not ruled out.

The other known hydrogen-deficient binaries (KS Per, LSS 1922 and LSS 4300) have had their temperatures ( $12,500 \pm 500 \text{ K}$ ,  $12,000 \pm 500 \text{ K}$ ,  $12,000 \pm 1,000 \text{ K}$ ) and interstellar extinctions ( $0.55 \pm 0.05$ ,  $0.80 \pm 0.05$ ,  $0.90 \pm 0.10$ ) re-determined from a flux distribution analysis.

Mass-loss rates from 6 O stars, 3 Extreme Helium stars and 2 sdO stars have also been determined. The O and EHe results broadly agree with the previous determinations. Results for the 2 sdO stars, BD +37° 1977 and BD +37° 442, are presented from profile fitting for the first time and indicate a mass-loss rate slightly higher than for the EHe stars.

## Declarations

1. I, Richard Ellis Dudley, hereby certify that this thesis has been composed by myself, that it is a record of my own work, and that it has not been accepted in partial or complete fulfilment of any other degree or professional qualification.

Signed

Date 1<sup>st</sup> June 1992

2. I was admitted to the Faculty of Science of the University of St. Andrews under Ordinance General No. 12 on 1<sup>st</sup> October 1989 and as a candidate for the degree of Ph.D. on 1<sup>st</sup> October 1990.

Signed

Date 1<sup>st</sup> June 1992

3. We hereby certify that the candidate has fulfilled the conditions of the Resolution and Regulations appropriate to the Degree of Ph.D.

Signed

Date 1.vi.92

Dr. C. S. Jeffery & Dr. P. W. Hill, Supervisors.

4. In submitting this thesis to the University of St. Andrews I understand that I am giving permission for it to be made available for use in accordance with the regulations of the University Library for the time being in force, subject to any copyright vested in the work not being affected thereby. I also understand that the title and abstract will be published, and that a copy of the work may be made and supplied to any *bona fide* library or research worker.

## Acknowledgements

I would like to thank the following people for their part in the production of this thesis.

Dr. C. Simon Jeffery, for supervising this project and, as Secretary of the SERC Collaborative Computational Project #7: The Analysis of Astronomical Spectra, providing access to a number of essential numerical codes. His knowledge of the area and extensive experience in many of the methods used here have allowed rapid, effective progress to be made from the outset.

Dr. Phil Hill for offering me the studentship, and for supervision in the first year.

Dr. Don Pollacco (St. Andrews) for generously obtaining the echelle spectrogram of  $\nu$  Sgr while at the Anglo-Australian Observatory.

Prof. Phillip Dufton (Belfast) for the use of the SPECTRUM line formation code.

Dr. Uli Heber (Kiel) for providing the hydrogen-deficient line-blanketed model atmospheres code STERNE essential for the fine analysis and flux distribution work.

Dr. Henny Lamers (Utrecht) for providing the wind line analysis code used, with modifications, in a substantial part of this work.

Dr. Raman Prinja (London) for providing an IUE spectrum of  $\zeta$  Puppis.

The Ministry of Defence (R.A.R.D.E.) for providing financial support during my undergraduate years, the use of which has extended into the time of this thesis and beyond.

The S.E.R.C. for partial financial support in the form of a postgraduate studentship.

Ernst & Young (Inverness) for, by offering me a career, allowing the completion of this thesis without the spectre of unemployment.

Those people who have read and commented on this work over the years; the members of the department, both staff and research students, past and present.

Those people, usually unconnected with my work, who have made my seven years at St. Andrews such an enjoyable and challenging time: Andy B., Penny, Janis, Anne-Marie, Martin, Fiona, John, Stuart, Nik, Catriona, Sandy and many others too numerable to mention. Thanks.

Above all I would like to thank my parents for their support, both financial and emotional, throughout the duration of this work. I could not have done it without them.

# Contents

<b>1</b>	<b>Introduction: Hydrogen-Deficient Binaries and Related Objects</b>	<b>1</b>
1.1	Single Stars . . . . .	1
1.2	Binary Stars . . . . .	2
1.3	Upsilon Sagittarii . . . . .	4
1.3.1	Radial velocities . . . . .	4
1.3.2	Spectral class . . . . .	4
1.3.3	Temperature . . . . .	6
1.3.4	Flux distribution . . . . .	6
1.3.5	Eclipses, light variability, and inclination . . . . .	8
1.3.6	Absolute magnitude and distance . . . . .	8
1.3.7	Interstellar extinction . . . . .	9
1.3.8	Spectral analyses . . . . .	9
1.3.9	Surface composition . . . . .	10
1.3.10	Mass loss . . . . .	12
1.3.11	The secondary component . . . . .	12
1.3.12	Models for the system . . . . .	13

1.3.13	The fate of $\nu$ Sgr? . . . . .	14
1.4	The Aims of this Thesis . . . . .	15
1.4.1	A note on Appendices . . . . .	16
1.5	References . . . . .	18
<b>2</b>	<b>The Mass of <math>\nu</math> Sgr From Ultraviolet Radial Velocities</b>	<b>22</b>
2.1	Improved Cross-Correlation Methods . . . . .	22
2.2	The Data . . . . .	23
2.3	Processing and Calibration . . . . .	23
2.4	Radial Velocity Determination . . . . .	29
2.5	Orbit Analysis . . . . .	35
2.6	Spectral Deconvolution . . . . .	39
2.6.1	Application to $\nu$ Sgr . . . . .	40
2.7	Discussion . . . . .	43
2.7.1	Masses and orbital radii . . . . .	43
2.7.2	Mass loss and transfer . . . . .	44
2.7.3	Orbital inclination . . . . .	44
2.7.4	Evolutionary status . . . . .	45
2.8	Addendum - The Radial Velocities of $\nu$ Sgr . . . . .	46
2.9	The Mass Ratio of KS Persei . . . . .	47
2.10	Summary . . . . .	50
2.11	References . . . . .	51
<b>3</b>	<b>The Wolf-Rayet Binary <math>\gamma^2</math> Velorum</b>	<b>53</b>

3.1	Introduction . . . . .	53
3.2	The Data . . . . .	56
3.3	Radial Velocity Determination . . . . .	58
3.4	Discussion . . . . .	59
3.5	Summary . . . . .	64
3.6	References . . . . .	65
<b>4</b>	<b>UV Wind Line Analysis</b>	<b>66</b>
4.1	Introduction . . . . .	66
4.2	The SEI Method . . . . .	68
4.2.1	Assumptions . . . . .	68
4.2.2	Theory . . . . .	68
4.3	The SEI Programs . . . . .	71
4.3.1	Solution method . . . . .	71
4.3.2	Radiative coupling . . . . .	71
4.3.3	Inputs . . . . .	71
4.4	"SEILS" - A Suite of Automated Profile Fitting Programs . . . . .	74
4.4.1	Major changes in SEILS over SEI . . . . .	74
4.4.2	Using SEILS . . . . .	75
4.5	Testing the Assumptions . . . . .	77
4.5.1	Photospheric velocity . . . . .	77
4.5.2	Turbulent profile . . . . .	78
4.5.3	Data point selection . . . . .	78

4.5.4	Continuum level . . . . .	78
4.5.5	Conclusions . . . . .	82
4.6	Photospheric Lines . . . . .	82
4.7	Correction for Lyman $\alpha$ - the NV Doublet . . . . .	85
4.8	Mass Loss . . . . .	86
4.9	Summary . . . . .	90
4.10	References . . . . .	91
<b>5</b>	<b>Mass Loss from O Stars</b>	<b>92</b>
5.1	Introduction . . . . .	92
5.2	The Data . . . . .	93
5.3	Analysis . . . . .	95
5.4	Results . . . . .	95
5.4.1	The line fits . . . . .	95
5.4.2	The singlet lines . . . . .	100
5.4.3	The doublet lines . . . . .	100
5.4.4	The photospheric lines . . . . .	100
5.4.5	Line parameters . . . . .	101
5.4.6	Errors . . . . .	102
5.5	Mass-Loss Rates and Ionisation Fractions . . . . .	103
5.5.1	Application of improved NLTE results . . . . .	105
5.5.2	Conclusions . . . . .	108
5.6	$\zeta$ Puppis and HD 14947: A Comparison of Different Studies. . . . .	108

5.7	Parameter Variation with Temperature . . . . .	110
5.8	Summary . . . . .	112
5.9	References . . . . .	113
<b>6</b>	<b>The Winds of the Extreme Helium Stars</b>	<b>115</b>
6.1	Introduction . . . . .	115
6.2	The Data . . . . .	116
6.3	Photospheric Lines . . . . .	118
6.4	The Line Profiles . . . . .	119
6.5	The Models . . . . .	119
6.5.1	The $\beta$ -dependent optical depth law . . . . .	120
6.5.2	The $\beta$ -independent optical depth law . . . . .	120
6.5.3	The $\beta = 1$ solution . . . . .	120
6.6	Results . . . . .	133
6.6.1	BD +10° 2179 . . . . .	133
6.6.2	BD -9° 4395 . . . . .	134
6.6.3	HD 160641 . . . . .	135
6.6.4	BD +37° 1977 . . . . .	137
6.6.5	BD +37° 442 . . . . .	138
6.6.6	Optical depth laws . . . . .	140
6.7	Mass Loss Rates . . . . .	140
6.7.1	Individual lines . . . . .	142
6.8	Discussion . . . . .	143

6.9	Summary . . . . .	150
6.10	References . . . . .	151
<b>7</b>	<b>Stellar Winds and Mass Loss from the <math>\nu</math> Sgr System</b>	<b>153</b>
7.1	Introduction . . . . .	153
7.2	Description of the UV Wind Profiles . . . . .	154
7.2.1	Phase dependency . . . . .	154
7.2.2	The summed profile . . . . .	154
7.3	Interstellar Extinction and Lyman $\alpha$ Correction . . . . .	156
7.4	Photospheric lines . . . . .	156
7.5	The Single Star Approximation . . . . .	160
7.6	A Model for the $\nu$ Sgr System . . . . .	165
7.7	Binary Models . . . . .	165
7.7.1	Modifying the velocity law . . . . .	166
7.7.2	Modifying the optical depth law . . . . .	166
7.7.3	Discussion . . . . .	167
7.8	The Modified Velocity Law Models . . . . .	167
7.8.1	The Inner Region profile . . . . .	167
7.8.2	The constant velocity approximation . . . . .	168
7.8.3	The variable velocity approximation . . . . .	170
7.8.4	The optical depth law . . . . .	170
7.8.5	The Inner Region profiles . . . . .	171
7.8.6	The final profiles . . . . .	171

7.9	The Modified Optical Depth Law Models . . . . .	181
7.9.1	Primary Model . . . . .	181
7.9.2	Secondary Model . . . . .	181
7.10	Discussion . . . . .	181
7.11	Mass Loss . . . . .	186
7.11.1	Wind line analysis . . . . .	186
7.11.2	Other methods . . . . .	187
7.11.3	Discussion . . . . .	190
7.12	Summary . . . . .	191
7.13	References . . . . .	192
<b>8</b>	<b>The Flux Distribution of <math>\nu</math> Sgr</b>	<b>194</b>
8.1	Introduction . . . . .	194
8.2	Photometry . . . . .	194
8.3	The Effectiveness of Hydrogen-deficient Line-blanketed Model Atmospheres . . . . .	195
8.3.1	Temperature and extinction determination . . . . .	195
8.3.2	Discussion . . . . .	197
8.4	Distance . . . . .	198
8.5	Luminosity . . . . .	199
8.6	The Flux Distribution of the Secondary Component . . . . .	199
8.6.1	Temperature and extinction determination . . . . .	199
8.6.2	Discussion . . . . .	202
8.7	Infrared Excess and Dust Component . . . . .	205

8.8	Summary . . . . .	208
8.9	References . . . . .	209
<b>9</b>	<b>The Flux Distributions of KS Per, LSS 1922 &amp; LSS 4300</b>	<b>211</b>
9.1	Fluxes . . . . .	211
9.2	KS Per . . . . .	212
9.2.1	Discussion . . . . .	214
9.3	LSS 1922 . . . . .	216
9.4	LSS 4300 . . . . .	217
9.5	IR Excess . . . . .	218
9.6	Discussion . . . . .	218
9.6.1	Temperatures . . . . .	218
9.6.2	Distances . . . . .	219
9.6.3	UV extinction and the 2,200 Å feature . . . . .	220
9.7	Summary . . . . .	224
9.8	References . . . . .	225
<b>10</b>	<b>High Resolution Optical Spectroscopy of <math>\nu</math> Sgr</b>	<b>226</b>
10.1	Introduction . . . . .	226
10.2	Observations . . . . .	226
10.3	Echelle Reduction . . . . .	227
10.4	Extraction . . . . .	228
10.5	Cosmic Rays . . . . .	228
10.6	Sky Subtraction . . . . .	229

10.7 Radial Velocity . . . . .	229
10.8 Line Identifications . . . . .	230
10.9 Summary . . . . .	247
10.10 References . . . . .	248
<b>11 A Spectroscopic Fine Analysis of <math>\nu</math> Sgr</b>	<b>249</b>
11.1 Introduction . . . . .	249
11.2 Equivalent Widths . . . . .	250
11.3 The Models . . . . .	254
11.4 Microturbulent and Rotational Velocities . . . . .	255
11.4.1 Microturbulent velocity . . . . .	255
11.4.2 Rotational velocity . . . . .	255
11.5 Temperature Determination . . . . .	257
11.5.1 Iron lines . . . . .	257
11.5.2 Nitrogen lines . . . . .	260
11.5.3 Titanium lines . . . . .	260
11.5.4 UV spectra . . . . .	260
11.6 Gravity Determination . . . . .	262
11.6.1 Helium lines . . . . .	262
11.6.2 Hydrogen lines . . . . .	264
11.7 The Final Model . . . . .	264
11.8 Final Abundances . . . . .	268
11.9 Discussion . . . . .	269

11.10 Summary . . . . .	271
11.11 References . . . . .	272
<b>12 Summary &amp; Conclusions</b>	<b>274</b>
12.1 Summary . . . . .	274
12.2 Conclusions . . . . .	276
12.3 Future Work . . . . .	279
12.4 References . . . . .	280
<b>A The Lucy Test</b>	<b>281</b>
A.1 The Test . . . . .	281
A.2 Example: $v$ Sgr . . . . .	282
A.3 References . . . . .	282
<b>B Non-Linear Least Squares Fit to an Arbitrary Function</b>	<b>283</b>
B.1 Introduction . . . . .	283
B.2 Linearisation of the Fitting Function . . . . .	284
B.3 Gradient Search . . . . .	286
B.4 Error Determination . . . . .	288
B.5 Weighting . . . . .	288
B.6 References . . . . .	289
<b>C SEILS - Parameters, Sample Input and Guide</b>	<b>290</b>
C.1 Input Files . . . . .	290
C.2 Output Files . . . . .	293

<b>D Checklist for Wind Line Analysis</b>	<b>296</b>
<b>E Echelle Reduction - A Worked Example</b>	<b>298</b>
<b>F Individual Line Fits for the O Stars, Extreme Helium Stars and <math>\nu</math> Sgr</b>	<b>306</b>
F.1 O Stars . . . . .	306
F.2 Extreme Helium Stars . . . . .	312
F.2.1 Notes on final parameter selection: $\beta$ -dependent . . . . .	312
F.2.2 Notes on final parameter selection: $\beta$ -independent . . . . .	316
F.2.3 Notes on final parameter selection: $\beta = 1.0$ . . . . .	321
F.3 $\nu$ Sgr . . . . .	321
<b>G The Principles of a Spectroscopic Fine Analysis</b>	<b>331</b>
<b>H Atomic Data and Multiplet Lists for <math>\nu</math> Sgr, 3980-4915 Å</b>	<b>334</b>
H.1 References . . . . .	342

# List of Figures

1.1	The position of the hydrogen deficient stars in the $\log T - \log g$ plane. . . . .	3
1.2	Modelling the flux distribution of $\nu$ Sgr - 1986. . . . .	7
1.3	Elemental abundances in the primary component of $\nu$ Sgr. . . . .	10
2.1	The $\lambda\lambda 1248 - 1308 \text{ \AA}$ region of the $\nu$ Sgr spectrum SWP1398 showing many interstellar lines. . . . .	25
2.2	A plot of interstellar line shifts against phase and J.D. for $\nu$ Sgr. . . . .	26
2.3	The IUE spectrum of $\nu$ Sgr from 1200 - 2800 $\text{\AA}$ . . . . .	27
2.4	CCFs for $\nu$ Sgr without template sharpening. . . . .	30
2.5	A preliminary orbit for $\nu$ Sgr from Fe II and C III lines. . . . .	31
2.6	An example of template construction for the primary component of $\nu$ Sgr. . . . .	32
2.7	CCFs and radial velocities after template sharpening on the primary component of $\nu$ Sgr. . . . .	33
2.8	CCFs for the secondary component of $\nu$ Sgr. . . . .	34
2.9	Radial velocity curves for $\nu$ Sgr. The IUE orbit. . . . .	38
2.10	A section of deconvolved spectra. $\nu$ Sgr, 1230-1270 $\text{\AA}$ . . . . .	41
2.11	A section of deconvolved spectra. $\nu$ Sgr, 1640-1670 $\text{\AA}$ . . . . .	42
3.1	The orbit of $\gamma^2$ Vel determined by Stickland & Lloyd from IUE spectra. . . . .	55

3.2	Spectra of $\gamma^2$ Vel showing some variability. . . . .	57
3.3	Three radial velocity curves for $\gamma^2$ Vel. . . . .	60
3.4	A section of the sharpened template of $\gamma^2$ Vel. . . . .	62
4.1	An IUE CIV wind line showing continuum and data points. . . . .	76
4.2	The effect of varying $w_0$ and IGMAX on line profiles. . . . .	79
4.3	The effect of data point selection on line profiles. . . . .	80
4.4	The effect of continuum level on line profiles. . . . .	81
4.5	The effect of photospheric line depths on line profiles. . . . .	84
4.6	Calculated LTE NV doublet profiles. . . . .	85
4.7	The Effect of $\beta$ on the mass-loss rate. . . . .	89
5.1	The final fits for the 6 O stars. . . . .	97
5.2	The variation of $\beta$ with effective temperature for O stars. . . . .	111
6.1	Final profiles for the EHe stars using the $\beta$ -dependent optical depth law. . . . .	122
6.2	Final profiles for the EHe stars using the $\beta$ -independent optical depth law. . . . .	126
6.3	Final profiles for the EHe stars using the $\beta$ -independent optical depth law and $\beta$ fixed at 1.0. . . . .	130
6.4	The SiIV line of BD -9° 4395. . . . .	147
6.5	The variation of the product of mass-loss rate and ionisation fraction with velocity for the EHe stars. . . . .	148
7.1	The variation of the CIV and SiIV profiles of $\nu$ Sgr with phase. . . . .	155
7.2	The six wind profiles of $\nu$ Sgr. . . . .	157
7.3	Extinction correction for $\nu$ Sgr. . . . .	158

7.4	Wind line profiles after treating $\nu$ Sgr as a single A star. . . . .	162
7.5	Wind line profiles after treating $\nu$ Sgr as a single B star. . . . .	163
7.6	Velocity profiles for the primary and secondary of $\nu$ Sgr . . . . .	169
7.7	Final profiles for $\nu$ Sgr using the variable velocity approximation. . . . .	173
7.8	Final profiles for $\nu$ Sgr using the constant velocity approximation. . . . .	177
7.9	Final wind line profiles for $\nu$ Sgr modelled as a binary star with the modified optical depth law. . . . .	182
7.9	<i>continued.</i> Primary approximation ( $x = 4$ ) with $\beta = 1$ . . . . .	183
7.9	<i>continued.</i> Secondary approximation ( $x = 80$ ) with $\beta$ free. . . . .	184
7.9	<i>continued.</i> Secondary approximation ( $x = 80$ ) with $\beta = 1$ . . . . .	185
8.1	The flux distribution of the primary component of $\nu$ Sgr, 1,000-7,000 Å . . . . .	197
8.2	The flux distribution of the primary component of $\nu$ Sgr, 800-3,000 Å. . . . .	198
8.3	The flux distribution for $\nu$ Sgr with model atmosphere fluxes superimposed. . . . .	200
8.4	Model atmosphere fluxes for the secondary of $\nu$ Sgr, 800-3000 Å. . . . .	203
8.5	Model atmosphere fluxes for the secondary of $\nu$ Sgr, 3000-7000 Å. . . . .	204
9.1	The flux distribution of KS Per. . . . .	215
9.2	The flux distribution of LSS 1922. . . . .	221
9.3	The flux distribution of LSS 4300. . . . .	222
9.4	IR excess for KS Per, LSS 1922 and LSS 4300. . . . .	223
10.1	The visual spectrum of $\nu$ Sgr from 3990-4050 Å. . . . .	231
10.2	The visual spectrum of $\nu$ Sgr from 4050-4110 Å. . . . .	232
10.3	The visual spectrum of $\nu$ Sgr from 4110-4170 Å. . . . .	233

10.4	The visual spectrum of $\nu$ Sgr from 4170-4230 Å. . . . .	234
10.5	The visual spectrum of $\nu$ Sgr from 4230-4290 Å. . . . .	235
10.6	The visual spectrum of $\nu$ Sgr from 4290-4350 Å. . . . .	236
10.7	The visual spectrum of $\nu$ Sgr from 4350-4410 Å. . . . .	237
10.8	The visual spectrum of $\nu$ Sgr from 4410-4470 Å. . . . .	238
10.9	The visual spectrum of $\nu$ Sgr from 4470-4530 Å. . . . .	239
10.10	The visual spectrum of $\nu$ Sgr from 4530-4590 Å. . . . .	240
10.11	The visual spectrum of $\nu$ Sgr from 4590-4650 Å. . . . .	241
10.12	The visual spectrum of $\nu$ Sgr from 4650-4710 Å. . . . .	242
10.13	The visual spectrum of $\nu$ Sgr from 4710-4770 Å. . . . .	243
10.14	The visual spectrum of $\nu$ Sgr from 4770-4830 Å. . . . .	244
10.15	The visual spectrum of $\nu$ Sgr from 4830-4890 Å. . . . .	245
10.16	The visual spectrum of $\nu$ Sgr from 4890-4915 Å. . . . .	246
11.1	Iron abundance vs. equivalent width for $\nu$ Sgr. . . . .	256
11.2	Rotational velocity of $\nu$ Sgr from the Fe II 4273 Å line. . . . .	258
11.3	Initial temperature determination for $\nu$ Sgr from a LTE <sub>S</sub> Fe curve of growth analysis.	259
11.4	Initial temperature determination for $\nu$ Sgr from a LTE <sub>S</sub> N curve of growth analysis.	261
11.5	Initial gravity determination for $\nu$ Sgr. . . . .	263
11.6	Profile fitting the He lines. . . . .	265
11.7	Modelling the hydrogen line profiles of $\nu$ Sgr. . . . .	266
11.8	Temperature and gravity determination for $\nu$ Sgr. . . . .	267
12.1	The evolution of a binary system with a 12 M <sub>⊙</sub> primary component. . . . .	277

B.1	Flowchart for a non-linear least squares algorithm. . . . .	287
C.1	A sample SEILS_DEFAULTS.DAT file. . . . .	291
C.2	A SEILS data file. . . . .	292
C.3	A sample .COM file for running SEILS in batch. . . . .	293
C.4	A sample output file from SEILS for a doublet line. . . . .	295
F.1	Initial profiles for the 6 O stars using the $\beta$ -independent optical depth law. . . . .	309
F.2	Initial profiles for the EHe stars using the $\beta$ -dependent optical depth law. . . . .	314
F.3	Initial profiles for the EHe stars using the $\beta$ -independent optical depth law. . . . .	318
F.4	Initial profiles for the EHe stars with $\beta$ fixed at 1.0. . . . .	323
F.5	Initial wind line profiles for $\nu$ Sgr modelled as a binary star with the modified optical depth law. . . . .	327
F.5	<i>continued.</i> Primary approximation ( $x = 4$ ) with $\beta = 1$ . . . . .	328
F.5	<i>continued.</i> Secondary approximation ( $x = 80$ ) with $\beta$ free. . . . .	329
F.5	<i>continued.</i> Secondary approximation ( $x = 80$ ) with $\beta = 1$ . . . . .	330
G.1	Schematic fine analysis results. . . . .	333

# List of Tables

1.1	Observational characteristics of the hydrogen-deficient binary stars. . . . .	5
1.2	Elemental abundances in the primary component of $\nu$ Sgr. . . . .	11
2.1	SWP and LWR/P IUE data for $\nu$ Sgr. . . . .	24
2.2	Interstellar lines removed from the IUE spectra of $\nu$ Sgr . . . . .	28
2.3	The IUE spectra and radial velocity data for $\nu$ Sgr. . . . .	36
2.4	Orbital solutions for $\nu$ Sgr. . . . .	37
2.5	Minimum masses and orbital radii for the $\nu$ Sgr system. . . . .	43
2.6	Independent radial velocity determination of $\nu$ Sgr. . . . .	48
3.1	IUE SWP spectral data for $\gamma^2$ Vel. . . . .	56
3.2	IUE LWR spectral data for $\gamma^2$ Vel. . . . .	58
3.3	Summary of results from SWP analysis of $\gamma^2$ Vel. . . . .	61
4.1	The inputs of SEIDOU3 and SEISING3. . . . .	72
5.1	Stellar data for the 6 O stars. . . . .	94
5.2	Atomic data for the wind lines. . . . .	94
5.3	Final fits for the 6 O stars. . . . .	96

5.4	A comparison of photospheric line profiles from parameter fitting and model atmospheres. . . . .	101
5.5	A comparison of O star wind line parameters. . . . .	102
5.6	The product of mass-loss rate and ionisation fraction for the 6 O stars. . . . .	104
5.7	Theoretical models for the 6 O stars. . . . .	105
5.8	Ionisation fractions for the O star analysis. . . . .	106
5.9	Mass-loss rates for the 6 O stars. . . . .	107
5.10	Mass loss determinations for HD14947 and $\zeta$ Puppis. . . . .	109
6.1	SWP IUE spectra for the EHe stars. . . . .	116
6.2	Physical data for the hydrogen-deficient stars. . . . .	117
6.3	Models used to determine the photospheric lines for the EHe stars. . . . .	118
6.4	Final fits for the EHe stars, using the $\beta$ -dependent form of the optical depth law. . . . .	121
6.5	Final fits for the EHe stars, using the $\beta$ -independent optical depth law. . . . .	125
6.6	Final fits for the EHe stars with $\beta = 1$ . . . . .	129
6.7	The product of ionisation and mass-loss rates for the EHe stars. . . . .	141
6.8	A comparison, for the EHe stars, of the results from SEILS and the co-moving frame method. . . . .	144
6.9	Minimum mass-loss rates for the EHe stars. . . . .	146
7.1	The low dispersion data available for $\nu$ Sgr. . . . .	159
7.2	Abundances and photospheric line parameters for $\nu$ Sgr. . . . .	160
7.3	The results of modelling $\nu$ Sgr as a single A star. . . . .	161
7.4	The results of modelling $\nu$ Sgr as a single B star. . . . .	161
7.5	Velocity profile parameters for two models of $\nu$ Sgr. . . . .	170

7.6	Final fits for $\nu$ Sgr using the modified optical depth law approximation . . . . .	186
7.7	The product of mass-loss rate and ionisation fraction for $\nu$ Sgr from the Inner Region profiles. . . . .	188
7.8	Minimum mass-loss rates for $\nu$ Sgr from the variable optical depth law approximation.	188
7.9	Mass-loss rates for $\nu$ Sgr from IR data. . . . .	189
8.1	Fluxes for $\nu$ Sgr . . . . .	206
8.2	Flux distribution analysis for the primary of $\nu$ Sgr. . . . .	207
8.3	Flux distribution analysis for $\nu$ Sgr. . . . .	207
9.1	Fluxes for KS Per, LSS 1922 & LSS 4300. . . . .	212
9.2	The flux distribution of KS Per. . . . .	213
9.3	The flux distribution of KS Per. . . . .	213
9.4	IUE low resolution data for KS Per. . . . .	214
9.5	The flux distribution of LSS 1922. . . . .	217
9.6	The flux distribution of LSS 4300. . . . .	217
10.1	A log of AAT observations for $\nu$ Sgr. . . . .	227
10.2	Measured radial velocity shifts for optical lines of $\nu$ Sgr. . . . .	229
11.1	EW's and atomic data for measured lines in $\nu$ Sgr. . . . .	251
11.2	The model grid for the fine analysis of $\nu$ Sgr. . . . .	254
11.3	Temperature determination from N and Fe lines. . . . .	260
11.4	Final abundances for $\nu$ Sgr. . . . .	268
B.1	Weighting and MODE of data. . . . .	289

C.1	"Standard inputs for a SEILS data file. . . . .	294
F.1	Individual fits for 6 O stars. . . . .	308
F.2	Individual fits for the EHe stars using the $\beta$ -dependent optical depth law. . . . .	313
F.3	Individual fits for the EHe stars using the $\beta$ -independent optical depth law. . . . .	317
F.4	Individual fits for the EHe stars with $\beta$ fixed at 1.0 . . . . .	322
F.5	Individual fits for $\nu$ Sgr using the modified optical depth law approximation . . . . .	326
H.1	Multiplet lists and Atomic data for $\nu$ Sgr, 3980-4915 Å. . . . .	334

# Chapter 1

## Introduction: Hydrogen-Deficient Binaries and Related Objects

There is a small class of stars that show hydrogen-deficiency and helium enrichment in their spectra. The whole area is reviewed in I.A.U. Colloquium #87 "Hydrogen-deficient Stars and Related Objects" (1986). It is useful to separate the hydrogen-deficient stars into those that are single (Drilling 1986) and those in binary systems (Plavec 1986).

### 1.1 Single Stars

The number of hydrogen-deficient single stars is relatively small (Drilling & Hill 1986), the largest single subclass being the R Coronae Borealis stars (RCB) with 24 members although there are a number of other candidate objects (*e.g.* Jones 1991).

The single stars may be sub-divided as follows.

1. **R Coronae Borealis stars** are cool giants that undergo random and sudden decreases in brightness of up 9 magnitudes in a few weeks probably due to pulsationally driven carbon ejection (Feast 1986), indicated by an infra-red (IR) excess. Three of these objects DY Cen, MV Sgr. and V348 Sgr. (Schönberner 1977; Heber, Heck, Houziaux, Manfroid & Schönberner 1984; Pollacco 1989) have higher temperatures more typical of the Extreme Helium stars. The RCB stars may be related to the hydrogen-deficient binaries (Whitney, Soker & Clayton 1991).
2. **Hydrogen-deficient Carbon stars** are spectroscopically identical to the RCB stars but

do not show the deep minima, nor do they have IR excesses (Bidelman 1953, Warner 1967, Jones 1991).

3. **Extreme Helium stars** are hot, low mass ( $< 1 M_{\odot}$ ) low gravity supergiant stars (Heber 1986, Jeffery & Heber 1992). All the EHe stars appear to be single (Jeffery, Drilling & Heber 1987) possibly due to their postulated formation from coalescing white dwarf binaries (Webbink 1984). A number of these objects have been the subject of spectroscopic fine analyses (Wolff, Pilachowski & Wolstencroft 1974; Schönberner & Wolf 1974; Kaufmann & Schönberner 1977; Schönberner 1978; Walker & Schönberner 1981 and Heber 1983).
4. **Intermediate Helium stars** are similar to normal B2 stars but with high helium to hydrogen line strengths (Walborn 1983). They are young massive Population I stars.
5. **Helium Rich Subluminous O stars** are similar to the EHe stars (Greenstein & Sargent 1974; Hunger 1975; Hunger, Gruschinske, Kudritzki & Simon 1981; Schönberner & Drilling 1984) but with a higher surface gravity.
6. **Other stars** such as Wolf-Rayet's and some central stars of planetary nebulae also show hydrogen depletion and helium enrichment.

These stars are shown in Figure 1.1.

## 1.2 Binary Stars

There are only four known binary stars with extreme hydrogen depletion, the hydrogen-deficient binary (HDB) stars, although all Algol-type stars should show mild hydrogen-deficiency (Plavec 1986). The HDBs are characterised by strong He I lines and weak hydrogen Balmer lines; they show narrow lines indicating low gravities. Their systemic radial velocities indicate circular orbits around the galactic centre and they are within 200pc of the galactic plane. They show enhanced N/C atmospheric abundance ratios and strong  $H\alpha$  emission. These objects are relatively young Population I stars.

The four known HDBs are all single-lined spectroscopic binaries (Jeffery, Drilling & Heber 1987) -  $\nu$  Sgr (Campbell 1899; Wilson 1914), KS Per (Danziger, Wallerstein & Böhm-Vitense 1967; Drilling & Schönberner 1982), LSS 4300 (Jeffery, Drilling & Heber 1987; Schönberner & Drilling 1984) and LSS 1922 (Drilling, Heber & Jeffery 1985).

All have relatively long orbital periods of between  $\sim 28$  days (LSS 4300) and nearly a year (KS Per, *e.g.* Margoni, Stagni & Mammano 1988). All four primary components are known to pulsate (Saio & Jeffery 1988), and consist of supergiant primaries ( $T \sim 10,000 - 14,000\text{K}$ ) that are very similar to the EHe stars but with an enhanced nitrogen to carbon ratio, the opposite to that

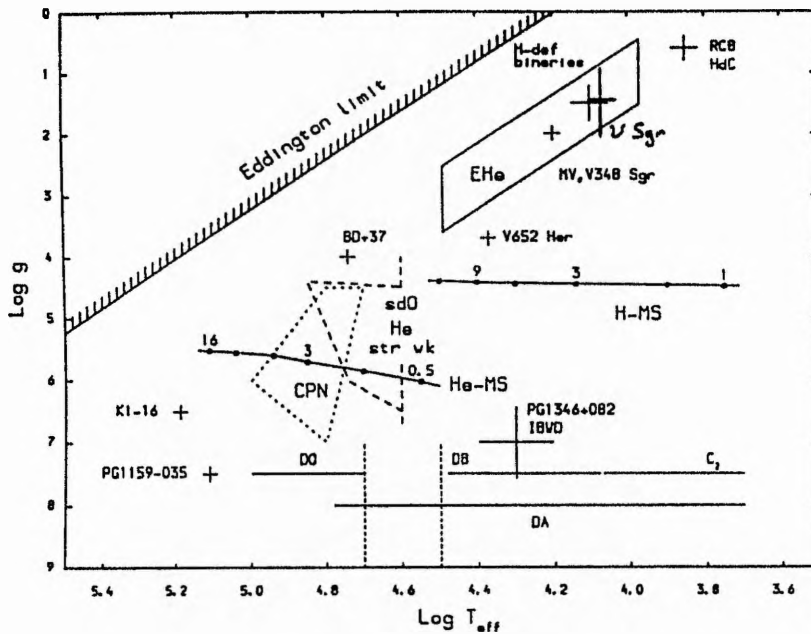


Figure 1.1: The position of the hydrogen deficient stars in the  $\log T - \log g$  plane. Shown are the location of the extreme helium (EHe) stars, the hydrogen-deficient binaries (HDB), the sub-dwarf O (sdO, including the two hot examples BD+37° 442 and BD+37° 1977), the central stars of planetary nebulae (CPN), single (DA, DB, DO), and interacting binary (IBWD) white dwarfs, the R Coronae Borealis (RCB) and hydrogen-deficient carbon (HdC) stars. The hydrogen and helium main sequences (H-MS, He-MS) are shown with masses ( $M_{\odot}$ ) indicated.  $\nu$  Sgr is plotted using the results from the fine analysis in Chapter 11. From Hill (1987).

found in the EHe stars. Almost nothing is known about the secondary components except they are expected to be hotter and there is tentative evidence of their detection in the UV (Duvigneau, Friedjung & Hack 1979; Rao & Venugopal 1985a,b). Three of the stars show an IR excess.

General data on the HDB stars is given in Table 1.1.

## 1.3 Upsilon Sagittarii

### 1.3.1 Radial velocities

$\upsilon$  Sgr was determined to be a binary by Campbell (1899), with the first orbital determination by Wilson (1914) using spectral radial velocities from the primary to determine the period (137.939 days), the primary velocity amplitude ( $48.15 \text{ km s}^{-1}$ ) and the mass function ( $1.582 M_{\odot}$ ). A small but non-zero eccentricity was found (0.087) although the radial velocities were subject to large residuals. Subsequent evidence for mass transfer within the system (Nariai 1967b) indicates that the use of hydrogen lines for some of Wilson's measurements may have lead to these uncertainties. The primary orbit of Wilson was confirmed by Seydel (1927). Eggen, Kron & Greenstein (1950) also found a non-zero eccentricity while further primary radial velocities were determined by Hack & Pasinetti (1963), Parthasarathy, Cornachin & Hack (1986) and Jeffery, Drilling & Heber (1987). Two further velocities by Jeffery are given in Dudley & Jeffery (1990). All of these radial velocities agree with the primary orbit determined by Wilson and Seydel.

The non-zero eccentricity is puzzling in the light of the obvious amount of mass transfer that has occurred in the system (see later) which should have circularised the orbit. However the eccentricity of KS Per (0.3, Margoni, Stagni & Mammano 1988) is indisputably non-zero, while a similar evolutionary scenario must be presumed to have occurred (but see Section 2.9 for a discussion).

### 1.3.2 Spectral class

Early researchers classified the primary component as B8p (Cannon 1912) and F0 (Plaskett 1928) although the latter was regarded as "uncertain" by Greenstein (1940).

Subsequent determination put the primary at A2Ia (Schönberner & Drilling 1983) consistent with the systemic velocity (Greenstein 1940) and the strength of the interstellar lines (McLaughlin 1939). The A2 classification is supported by Hack & Pasinetti (1963) but consider F0Ia also as a possibility.

Table 1.1: Observational characteristics of the hydrogen-deficient binary stars. "P" and "S" denote the primary and secondary components. For  $\nu$  Sgr, the most observed of the four systems, different investigators determine different results, indicated by the spread in the tabulated values. A value in parentheses indicates that the result is not obtained from a positive observation but from a non-result, a dubious model or speculation. Section 1.3 should be consulted for details. A number in square brackets indicates the power of ten to which the preceding number should be raised.

	$\nu$ Sgr	Ref.	KS Per	Ref.	LSS 1922	Ref.	LSS 4300	Ref.
Orbital period	137.839	2	362.6	20	63-81, <136	31		
$T_{\text{eff}}$ (P)	8,000-14,000	8,9,10,30	5,800-11,000	18,22,33	14,500	30	~14,600	26,30
$T_{\text{eff}}$ (S)	(20,000)	5	(30,000)	24				
$\log g$ (P)	1.6-2.0	10	1.0-2.0	22,25,33			1.4	26
$\log g$ (S)								
Pulsation period (P)	20	3	5-31	21,19,32	5-14	31		
Radial vel. (P)	48.18-49.1	2,7	48	20				
Radial vel. (S)	(<10)	5						
Mass function	1.58-1.67	2, 7	3.6-4.1	19,20				
Eccentricity	0.05	2,7	0.30	20				
Inclination ( $^{\circ}$ )	(33),(47),66-64,90	1,4,9,11,15,28						
$\omega$ ( $^{\circ}$ )	16-28	2,7	277	20				
Separation ( $R_{\odot}$ )	(110-320)	1,15,27,29	330, (390)	20,23				
Radius ( $R_{\odot}$ ) (P)	(30-120)	1,9,15,27,28						
Radius ( $R_{\odot}$ ) (S)	(3-60)	9,18,29						
Mass ( $M_{\odot}$ ) (P)	(1-13)	1,5,15,27,28,29	(2)	20				
Mass ( $M_{\odot}$ ) (S)	(3-11)	1,5,15,27,28,29	(4.4-6)	20,23				
Luminosity ( $L_{\odot}$ ) (P)	(1[4],5[4])	1,4						
Luminosity ( $L_{\odot}$ ) (S)	(200-1[4])	4,28						
$M_V$ (P)	(-3.0--7.6)	1,12, 16	(-3.2--6.3)	22,23			-4--5	26
$M_V$ (S)	(-2)	9						
$\frac{n(N)}{n(H)}$	20,10	8,17	1,000	18			20	26
$\frac{n(H)}{n(He)}$	2.5[-2],5[-4],5[-5]	8,16,17	1[-4]	18			0.003	26
$E_B - V$	0.0-0.30	1,4,5,6	0.35	22			0.9	26
Distance (pc)	350,2700	9,12	2,000				~2,000	26,30
Eclipsing?	(Yes)	1	No	32				
Detected secondary?	(Yes)	1,5,27	(Yes)	23				
IR excess?	Yes	13, 14	Yes	6			Yes	26

References: 1: Rao & Venugopal (1985a). 2: Wilson (1914). 3: Malcolm & Bell (1986). 4: Duvigneau, Friedjung & Hack (1979).

5: Parthasarathy, Cornachin & Hack (1986). 6: Drilling, Schönberner, Heber & Lynas-Gray (1986). 7: Seydel (1929). 8: Hack & Pasinetti (1963). 9: Hack, Flora & Santin (1980). 10: Leushin & Topil'skaya (1984). 11: Gaposkhin (1945). 12: Greenstein (1940). 13: Lee & Nariai (1967). 14: Humphreys & Ney (1974a,b). 15: Hellings, de Loore, Burger & Lamers (1981). 16: Drilling & Schönberner (1983). 17: Leushin & Topil'skaya (1988b). 18: Wallerstein, Greene & Tomley (1967). 19: Heard (1962). 20: Margoni, Stagni & Mammano (1988). 21: Morrison & Willingale (1987). 22: Danziger, Wallerstein & Böhm-Vitense (1967). 23: Schönberner & Drilling (1982). 24: Parthasarathy, Hack & Tektunali (1990). 25: Nariai (1967b). 26: Schönberner & Drilling (1984). 27: Schönberner & Drilling (1983). 28: Morrison (1986). 29: Plavec (1966). 30: Heber & Schönberner (1981). 31: Morrison, Drilling, Heber, Hill & Jeffery (1986). 32: Bakos (1962). 33: Nariai (1967a).

### 1.3.3 Temperature

10,500K was determined for the primary component from theoretical stellar atmospheres as early as 1940 (Greenstein 1940), although 7,000K had been previously found by spectrophotometric methods (Plaskett 1928). Hack and Pasinetti (1963) found that a two temperature model was needed with 8,000K and 12,800K regions to explain the observed visual spectrum. From IUE data Hack, Flora & Santin (1980) again determined that a two temperature model was needed with  $T=8,000\text{K}$  and  $T<11,000\text{K}$ . Leushin & Topil'skaya (1984) find a single temperature model will work but are undecided between a 13,500K low gravity one or a 14,000K model with a slightly higher gravity. However the early authors used either hydrogen rich model atmospheres or hydrogen poor ones where the hydrogen content can be lowered to only 5% or so. Leushin & Topil'skaya (1984) state that they used hydrogen-deficient model atmospheres ( $H \sim 0\%$ ).

### 1.3.4 Flux distribution

The flux distribution is one of the major long standing problems concerned with  $\nu$  Sgr. As detailed by Plavec (1986) the model atmospheres available at the time were not able to reproduce the observed flux distribution, especially around the Balmer decrement ( $\sim 3800\text{\AA}$ ) or shortward of  $\sim 2000\text{\AA}$ . This problem occurred whether hydrogen-rich or hydrogen-poor model atmospheres were used. This is illustrated in Figure 1.2 which shows a steep Balmer decrement in both the model atmospheres which is not observed in  $\nu$  Sgr. Both models also fail to account for the almost flat observed flux distribution in the 1200-3000  $\text{\AA}$  range.

This problem, well illustrated in the case of  $\nu$  Sgr, is symptomatic of the failure of hydrogen-poor model atmospheres to match observed fluxes. The main failure of these models is their inability to model very low hydrogen abundances; the hydrogen-poor model shown in Figure 1.2 still contains 6% hydrogen (Klinglesmith 1981). Leushin & Topil'skaya (1984) use some form of hydrogen-deficient model atmospheres but are still unable to model the flux distribution at all well in the UV.

As Plavec (1986) says

*"What is most urgently needed most of all is modern model stellar atmospheres, with line blocking taken into account, for stars with various degrees of helium depletion, all the way to pure helium stars."*

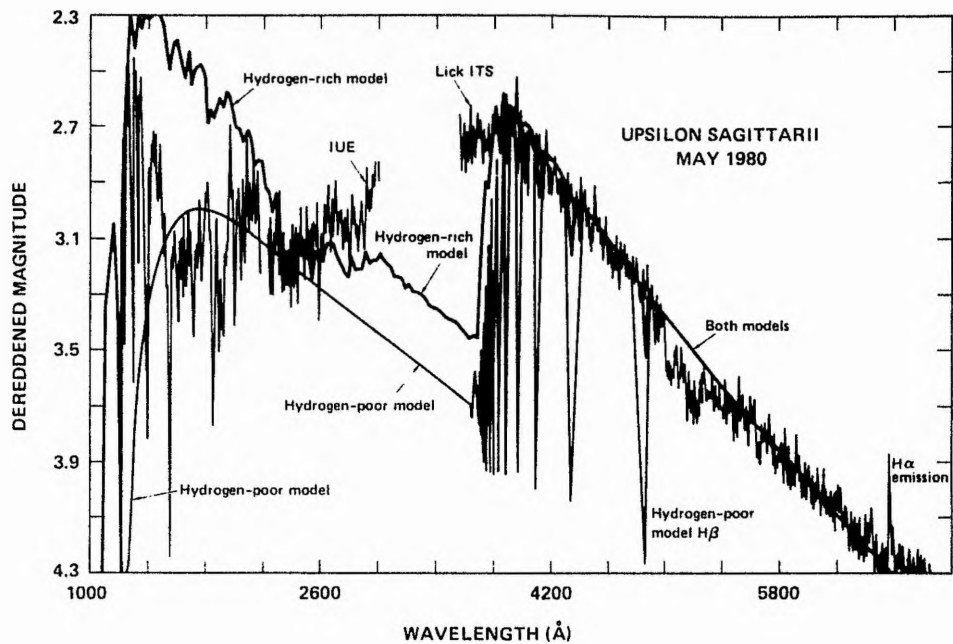


Figure 1.2: The flux distribution of  $\nu$  Sgr and two model atmospheres imposed. The hydrogen rich atmosphere is from Kurucz (1979) with  $T=11,000\text{K}$ . The hydrogen-poor model still contained 6% hydrogen and has  $T=10,000\text{K}$  (Klinglesmith 1981). Both models have  $\log g = 2.5$  and  $E_{B-V} = 0.25$ . From Plavec (1986).

### 1.3.5 Eclipses, light variability, and inclination

Gaposhkin (1945) ascertained that  $\nu$  Sgr had a variable light curve from photographic data although the minima were shallow,  $0.15^m$  for primary minima and  $0.08^m$  for the secondary minima. The light variations were exactly at the phases expected from the radial velocity curve for one component to be in front of the other. The primary is in front of the secondary at the deeper minimum and so the secondary must have a higher surface brightness (and thus temperature) than the primary. An inclination of  $47^\circ$  was determined on the assumption that the radii of both components were equal at  $150 R_\odot$  (and masses of  $15 M_\odot$  each). Such a tenuous determination of the inclination has been subsequently quoted without comment (*e.g.* Hack, Flora & Santin 1980).

Eggen, Kron & Greenstein (1950) observed  $\nu$  Sgr photoelectrically determining two minima with half the amplitudes of Gaposhkin's and with the time of primary minimum out by 7 days. These results then do not agree with the phases from radial velocity measurements which are beyond doubt, and indeed confirmed by Eggen *et al.* themselves. However, as pointed out by Malcolm & Bell (1986), half of the Eggen *et al.* observations used the variable star  $\rho^1$  Sgr as a comparison.

Malcolm & Bell (1986) determined UBV light curves and argued that incorrect rectification techniques used by Gaposhkin rendered his results "extremely doubtful". They determined a V curve amplitude of  $0.15^m$  but with a period of  $\sim 20$  days and conclude that the system does not show any of the attributes of a  $\beta$  Lyrae system as reported by Gaposhkin (1945). No signs of eclipses were detected but could not be ruled out on the basis of their data. They ascribed the light variations to pulsation (Saio & Jeffery 1988).

While the evidence for the detection of eclipses in the visual is negligible a number of authors report UV eclipses (Duvigneau, Friedjung & Hack 1979, Hack, Flora & Santin 1980, Rao & Venugopal 1985a). None of these reports are conclusive and the question of eclipses remains open.

### 1.3.6 Absolute magnitude and distance

$\nu$  Sgr has an apparent visual magnitude of 4.6 and a rough estimate of an absolute magnitude of -7 was made by McLaughlin (1939) based on the strengths of the interstellar K line. Greenstein (1940) determined  $M_v = -7.6$  and  $d = 2.7\text{kpc}$  from the assumption  $\nu$  Sgr takes part in simple galactic rotation. However as indicated by Danziger, Wallerstein & Böhm-Vitense (1967) when the spectral lines are greatly enhanced by low opacity the approximate spectral type cannot be used to infer the temperature or absolute magnitude with any accuracy. Rao & Venugopal (1985a,b) obtain  $M_v = -3.9 - -6.2$ , with a best fit value of  $-4.8 \pm 0.8$ . Hack, Flora & Santin (1980) expect

$\nu$  Sgr to be approximately the same distance away as  $\beta$  Lyrae from the strength of the interstellar lines, a distance of 350pc (Plavec, Weiland & Dobias 1982). There appears to be little agreement on either the distance or the absolute magnitude of  $\nu$  Sgr.

### 1.3.7 Interstellar extinction

As the galactic latitude for  $\nu$  Sgr is high Greenstein (1940) reasoned that the interstellar extinction would be small, seemingly confirmed by the value of  $E_{B-V} < 0.1$  determined from the MgII interstellar doublet (Duvigneau, Friedjung & Hack 1979). Nekeš (1967) finds such a low extinction in the direction of  $\nu$  Sgr only at distances less than 250pc; too close for  $\nu$  Sgr given the orbital dimensions and the adopted temperature and absolute luminosity. Confirmatory results of a value between 0.0 and 0.15 have been reported (Parthasarathy, Cornachin & Hack 1986). From the removal of the 2200 Å feature. Duvigneau, Friedjung & Hack (1979) determine 0.20 with a upper limit of 0.30. The same analysis by Drilling, Schönberner, Heber & Lynas-Gray (1984) yields 0.12, a value described as "not compatible" by Rao & Venugopal (1985a) with their observations from the ANS satellite which yield 0.12 to 0.20. Such conflicting results preclude any conclusions as to the extinction towards  $\nu$  Sgr.

### 1.3.8 Spectral analyses

Early analyses of the visual spectrum were carried out by Campbell (1899), Plaskett (1927), Morgan (1934, 1935) and Greenstein (1940). The latter noted the unusually high nitrogen abundance and the strength of the helium and iron lines. Hydrogen lines were weak but  $H\alpha$  showed emission as did  $H\beta$  (Fleming 1912). Ca and [Ca] emission was also detected (Merill 1943, Weaver 1943)

The  $H\alpha$  line is often displaced towards the blue by some  $300 \text{ km s}^{-1}$ ; this has been attributed to material flowing between the two components (Nariai 1967b, 1970). The duration of the absorption is  $\sim 40$  days but is not always present.

Lee & Nariai (1967) undertook photometry of  $\nu$  Sgr in the IR and found that at wavelengths of greater than  $1 \mu\text{m}$  there was IR excess assumed to come from circumstellar material (Nariai 1967b).

UV analyses (Greenstein 1940; Greenstein & Adams 1947; Duvigneau, Friedjung & Hack 1979; Hellings, de Loore, Burger & Lamers 1981; Hack, Flora & Santin 1980; Parthasarathy, Cornachin & Hack 1986) determined similar line strengths and abundances as earlier work on other spectral regions.

Rao & Venugopal (1985a,b) observed  $\nu$  Sgr in the 2 and 6cm radio region.

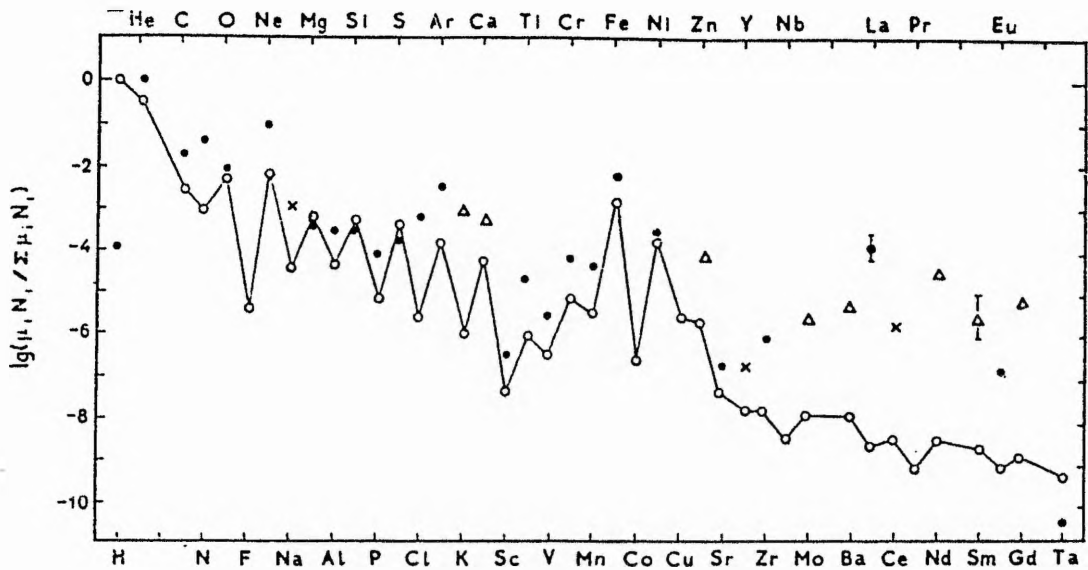


Figure 1.3: Elemental abundances in the primary component of  $\nu$  Sgr in the form of mass fractions with the solar values (open circles, continuous line) for comparison. For  $\nu$  Sgr crosses are upper limits, triangles are results based on a single line and filled circles are values based on several lines. From Leushin & Topil'skaya (1988b).

### 1.3.9 Surface composition

A detailed abundance analysis using photographic spectra and curve of growth analysis determined a surface composition for  $\nu$  Sgr but had to postulate a two temperature model (Hack & Pasinetti 1963). They determined a hydrogen to helium ratio of 0.025 but this has been disputed by Schönberner & Drilling (1983) who conclude a ratio of  $<0.0005$  from a reinterpretation of Hack & Pasinetti's results.

In a series of papers Leushin & Topil'skaya (1984, 1987, 1988a,b) discuss models and compositions for the primary component of  $\nu$  Sgr. Photographic spectra were again used with the addition of model atmospheres. These models did not include line blanketing. Two "best fit" models were determined, one with 5% metals and the other with 30%. Both were helium rich with hydrogen as a trace element. Their determined abundances, from the 5% metals model, are given in Table 1.2 and Figure 1.3.

Table 1.2: Elemental abundances in the primary component of  $\nu$  Sgr relative to the Sun. Both number fractions (left) and mass fractions are shown. From Leushin & Topil'skaya (1988b).

№	Element	$-\lg(N_{\text{el}}/\Sigma N)$		$-\lg(\mu_i N_i/\Sigma \mu_i N_i)$	
		$\odot$	$\nu$ Sgr	$\odot$	$\nu$ Sgr
1	H	0.05	3.3	-0.07	3.93
2	He	1.00	0.02	0.52	0.04
6	C	3.50	$2.27 \pm 0.13$	2.54	1.85
7	N	4.12	$1.87 \pm 0.07$	3.07	1.38
8	O	3.28	2.7	2.21	2.15
10	Ne	3.50	1.7	2.08	1.05
12	Mg	4.57	$4.07 \pm 0.07$	3.24	3.34
13	Al	5.65	$4.75 \pm 0.25$	4.34	3.48
14	Si	4.50	$4.13 \pm 0.07$	3.17	3.34
15	P	6.62	$4.90 \pm 0.20$	5.25	4.07
16	S	4.84	$4.54 \pm 0.04$	3.41	3.69
17	Cl	6.60	4.1	5.71	3.21
18	Ar	5.30	$3.58 \pm 0.09$	3.82	2.64
19	K	7.00	4.0	6.07	3.07
20	Ca	5.72	4.3	4.24	3.36
21	Sc	9.01	$7.35 \pm 0.15$	7.48	6.36
22	Ti	7.55	$5.66 \pm 0.07$	5.94	4.64
23	V	8.13	$6.70 \pm 0.10$	6.51	5.65
24	Cr	6.58	$5.16 \pm 0.05$	5.00	4.10
25	Mn	7.17	$5.55 \pm 0.05$	5.55	4.47
26	Fe	4.50	$3.33 \pm 0.10$	2.87	2.24
28	Ni	5.42	$4.78 \pm 0.09$	3.77	3.67
30	Zn	7.63	5.6	5.69	4.42
38	Sr	9.23	8.0	7.41	6.72
39	Y	9.60	8.1	7.77	6.81
40	Zr	9.60	$7.50 \pm 0.14$	7.76	6.20
42	Mo	10.00	7.3	7.90	5.98
56	Ba	10.15	7.0	7.89	5.52
57	La	10.60	$5.35 \pm 0.25$	8.58	3.87
58	Ce	10.40	$7.27 \pm 0.07$	8.37	5.81
60	Nd	10.50	6.0	8.46	4.50
62	Sm	11.00	7.0	8.70	5.48
63	Eu	11.30	8.3	9.00	6.78
64	Gd	10.90	6.6	8.82	5.06
71	Ta	11.70	12.2	9.32	10.60

### 1.3.10 Mass loss

The presence of the  $H\alpha$  emission indicates mass flowing between the two components (Nariai 1967b, 1970) while the IR excess (Lee & Nariai 1967) indicates matter has left the system. Sahade & Albano (1970) discuss the evidence for an envelope around  $\nu$  Sgr which is deduced to contain graphite (Woolf 1973) and observe an  $11\mu\text{m}$  peak due to silicates. This is disputed by Humphreys & Ney (1974a,b) who argue that it is due to a distant third body of  $T=2,500\text{K}$  with a mass of  $10\text{-}15 M_{\odot}$ , a radius of  $860 R_{\odot}$  and an orbital period of 4 years. The evidence for this object is limited.

With the advent of UV observations and, especially, the International Ultraviolet Explorer (IUE) satellite mass loss from  $\nu$  Sgr was obvious from the strong wind line profiles from a number of highly ionised species, including CIV, SiIV and NV (*e.g.* Hack, Flora & Santin 1980; Parthasarathy, Cornachin & Hack 1986). Although a number of the EHe stars have had their wind lines modelled using profile fitting techniques this has never been applied to  $\nu$  Sgr. Rao & Venugopal (1985a,b) did determine a mass-loss rate of  $5.4 \times 10^{-7} M_{\odot} \text{yr}^{-1}$  from radio observations.

### 1.3.11 The secondary component

There is no reliable data on the secondary component of  $\nu$  Sgr.

Undoubtedly the spectrum of  $\nu$  Sgr is unlike any other star and current (usually hydrogen-rich) model atmospheres fail to model the flat flux distribution in the UV. This has lead many investigators to assume that a substantial portion of the UV flux must come from the secondary. On this basis it has been classified as O9V (Hack, Flora & Santin 1980), a classification accepted by Hellings, de Loore, Burger & Lamers (1981). The latter authors also determined a secondary temperature of  $20,000\text{K}$  from hydrogen-rich model atmospheres. Duvigneau, Friedjung & Hack (1979) determine a spectral class for the secondary of B0-B3 from the single N III line at  $1183.7 \text{\AA}$ . Rao & Venugopal (1985a) determine a spectral type of B3 for the secondary with the unusual flux distribution due to the presence of an accretion disc with a colour similar to a B8-B9 star.

What other information that has been "determined" for the secondary has often come from models of the system that make some large and unjustified assumptions especially about the masses of the two components.

### 1.3.12 Models for the system

The very low hydrogen abundance of the primary is not in question (Hack & Pasinetti 1963, Leushin & Topil'skaya 1984) and the only way this can be achieved is through case BB mass transfer (*e.g.* Delgado & Thomas 1981). Here the primary fills its Roche lobe during the red giant phase before (and possibly during) core helium ignition. This causes material to be lost from the primary, some of which may well end up on the secondary. Upon helium ignition the star contracts to within its Roche lobe and mass transfer/loss stops. This is case B mass transfer and can only reduce the atmospheric hydrogen abundance to  $\sim 20\%$  (Lauterborn 1970). Case BB assumes that the primary again fills its Roche lobe as it ascends the giant branch for the second time (asymptotic giant branch evolution). This will allow the hydrogen content to fall to almost zero. Upon core carbon ignition mass transfer will again be reduced as the primary withdraws from the Roche lobe.

To put the details of this model onto a sure footing the masses of the two components need to be determined.

Duvigneau, Friedjung & Hack (1979) determine that the secondary must be less than half the mass of the primary from a non-measurement of UV spectral lines in Copernicus and S2/68 data. They also assert that eclipses were found although the data are poor.

Hellings, de Loore, Burger & Lamers (1981) look at a number of mass combinations for the components and conclude that the primary has a mass of  $13 M_{\odot}$  and the secondary  $10 M_{\odot}$ , a separation of  $320 R_{\odot}$  and an orbital inclination of  $74^{\circ}$ . These results were based on the assertion that the primary radius is  $120 R_{\odot}$  and the secondary radius  $3 R_{\odot}$  from the flux distribution modelling of Hack, Flora & Santin (1980). Again eclipses are assumed to occur to help tie down the orbital parameters.

Schönberner & Drilling (1983) determine a model for  $\nu$  Sgr based on the assumptions that  $M_v = -7$  and that eclipses occur. They propose that the secondary is a B2Ib star from the UV flux distribution, but is 3-5 magnitudes fainter than its spectral type indicates, to be consistent with the non-detection of the star in optical spectra. This problem is conveniently circumnavigated by postulating that the secondary is low mass (and thus low luminosity) but the spectrum is generated as the star "is not in thermal equilibrium" due to mass transfer from the primary. While there appears to be no evidence for a large mass transfer rate at the moment its presence may lead to the formation of an accretion disc. Such a disc has been postulated to explain the UV flux distribution (Rao & Venugopal 1985a) without modelling the distribution itself. There is no direct observational evidence for such a disc.

All the models presented until now have been speculative and based on insufficient evidence. To model the  $\nu$  Sgr system what is needed more than anything is a definite determination of the

masses of the two components from radial velocities. As the flux distribution has not been modelled by line-blanketed hydrogen-deficient model atmospheres it is not possible to say what portion of the flux comes from the secondary and so cannot be used to "determine" the mass. A mass-loss rate is required to determine if  $\nu$  Sgr is in a low mass loss phase indicative of core carbon burning. This can be confirmed by an abundance analysis of the products of carbon burning.

### 1.3.13 The fate of $\nu$ Sgr?

The question of what are the progenitors of type Ib supernovae has been contested since the first one was detected (Bertola & Sussi 1965). Uomoto (1986) reviews what criteria are needed for a SN to be classed as type Ib. There are three possible progenitors

1. Wolf-Rayet Stars.
2. Accreting white dwarfs.
3. Hydrogen deficient binaries.

The Wolf-Rayet candidates have been proposed by Begelman & Sarazin (1986) and supported by Schaefer, Cassé & Cahen (1987). Uomoto (1986) argues there are problems with a core collapsed WR star fitting the observed light curve and Ensman & Woosley (1988) rule out WR progenitors on this basis.

Branch & Nomoto (1986) propose that SN type Ia and Ib are similar with, in the case of the Ib event, a CO white dwarf accreting mass from a helium-enriched red giant in a binary system. When the base of the accreted layer ignites the resulting detonation will fit the observed properties of Ib events well. Harkness *et al.* (1987) doubt if the match to the light curve will be as good as claimed and, significantly, point out that it is difficult to reconcile this model with the association of SN Ib events to H II regions and consequent indication of youth.

The HDB model of SN Ib events postulates that the primary component undergoes core collapse in a mechanism that is the same as a SN II event, an assertion strengthened by the observations of Filippenko (1988). However the lack of hydrogen in the primary due to mass transfer explains the lack of hydrogen in the observed SN spectra while the shock wave interacting with the circumstellar material previously lost in the mass transfer/loss explains the radio emission. The evolutionary scenario proposed for HDB's explains their relative youth. Delgado & Thomas (1981) model case BB evolution and determine that the primary component ends its life as a CO white dwarf that undergoes core collapse after core iron exhaustion. The only problem with applying this model to the HDB's is that the primary component needs to be about  $3 M_{\odot}$  at the onset of carbon core ignition (the stage at which  $\nu$  Sgr is now expected to be at). As Delgado &

Thomas did not include mass loss from the system (rather than mass transfer) in their calculations it is not possible to determine whether  $\nu$  Sgr will end its life this way unless accurate masses and, if necessary, mass-loss rates are determined for  $\nu$  Sgr.

## 1.4 The Aims of this Thesis

The aims of this thesis are

1. To determine the current state of the  $\nu$  Sgr system using modern techniques, numerical codes and atomic data to determine, for each component where appropriate:
  - (a) Velocity semi-amplitude.
  - (b) Mass.
  - (c) Orbital separation.
  - (d) Orbital inclination.
  - (e) Orbital eccentricity.
  - (f) Radius.
  - (g) Effective temperature.
  - (h) Surface gravity.
  - (i) Luminosity.
  - (j) Surface composition.
  - (k) Mass-loss rate.
  - (l) Interstellar extinction.
  - (m) Distance.
  - (n) Origin.
  - (o) Future evolution.
2. To apply the improved techniques and codes developed for  $\nu$  Sgr to related objects of interest. These include the Wolf-Rayet binary  $\gamma^2$  Vel, the other HDBs (KS Per, LSS 1922 and LSS 4300) and a number of O, EHe and sdO stars.

As so little has been positively determined about the  $\nu$  Sgr system there are a large number of areas that required detailed investigation. Chapter 2 covers the key problem of determining the radial velocities for the secondary component using improved cross-correlation techniques. Using the determined masses and orbital separations it is possible to constrain the inclination of the orbit from the non-detection of eclipses and the presence of  $H\alpha$  emission. From the knowledge of

the inclination the absolute masses and separation of the components are determined. Spectral deconvolution can be used to check the determined values of the radial velocities and to separate spectral features from the two components. Given some assumptions on the state of the two components their radii can also be deduced. The luminosity ratio of the two components in the UV is determined from the shape of the cross-correlation functions.

In Chapter 3 the same techniques are applied to the Wolf-Rayet binary  $\gamma^2$  Vel in an attempt to determine the secondary radial velocities. Results were poor due to the nature of the spectral lines for such stars.

Chapters 4 to 7 cover UV wind line profile fitting to determine the mass-loss rates of 6 O stars (Chapter 5) as a means of testing the SEI code and its improved least squares implementation (Chapter 4). Then the code is applied to the winds of 3 EHe and 2 sdO stars. The sdO stars have never been analysed before using profile fitting techniques and an accurate determination of their mass loss rates is important. Chapter 7 covers the UV wind line analysis of  $\nu$  Sgr using a variety of assumptions not only to determine the mass-loss rate but to see how the binary nature of the system affects the mass loss from the system. From the analysis independent determinations of the interstellar extinction towards  $\nu$  Sgr are obtained to complement those from the flux distribution analysis.

The long standing problem of the flux distribution is solved in Chapter 8 using the latest line-blanketed, hydrogen-deficient model atmosphere codes. Similar modeling of the other three known HDBs is undertaken in Chapter 9.

The reduction of a CCD echelle spectrum of  $\nu$  Sgr is given in Chapter 10 along with the final spectrum and line identifications.

Chapter 11 uses this spectrum for an atmospheric fine analysis using the latest model atmospheres and LTE (with scattering) line formation codes together with improved atomic data.

Chapter 12 gives a summary of the results determined from this thesis and the conclusions that may be drawn including a discussion of the future evolution of the  $\nu$  Sgr system. Finally an indication of the future work that needs to be done to improve our knowledge of the HDB class of stars is given.

#### **1.4.1 A note on Appendices**

A number of appendices are included at the end of this thesis for details that were not warranted in the main body of the text due, mainly, to reasons of length. Here are line lists, details of preliminary analyses required for the work in the body of the thesis and a user guide for some analytical code.

As well as these results there are also appendices on useful methods that are not described in such detail elsewhere. There is one appendix on CCD echelle reduction and another on conducting a fine analysis. Both are in principle easy if the methods are known, but the methods are not widely reported in such detail that the student can actually duplicate them. The appendices are intended as a useful reference for methods, instructions and general data while the main body of the thesis contains the details of specific analyses of various objects.

## 1.5 References

- Bakos, G.A., 1962. *Reported in Heard (1962)*.
- Begelman, M.C. & Sarazin, C.L., 1986. *Astrophys. J.*, **302**, L59.
- Bertola, F. & Sussi, M.G., 1965. *Cont. Oss. Astr. Univ. Padova*, **176**, 1.
- Bidelman, W.P., 1953. *Astrophys. J.*, **117**, 25.
- Branch, D. & Nomoto, K., 1986. *Astr. Astrophys.*, **164**, L13.
- Campbell, W.W., 1899. *Astrophys. J.*, **10**, 241.
- Cannon, A.J., 1912. *Havard Ann.*, **56**, 108.
- Danziger, I.J., Wallerstein, G., & Böhm-Vitense, E., 1967. *Astrophys. J.*, **150**, 239.
- Delgado, A.J. & Thomas, H.-C., 1981. *Astr. Astrophys.*, **96**, 142.
- Drilling, J.S., 1986. In: *Hydrogen-Deficient Stars & Related Objects*, IAU Coll. No. 87, p.9, eds. K. Hunger, D. Schönberner & N.K. Rao, Reidel, Dordrecht, Holland.
- Drilling, J.S. & Hill, P.W., 1986. In: *Hydrogen-Deficient Stars & Related Objects*, IAU Coll. No. 87, p.499, eds. K. Hunger, D. Schönberner & N.K. Rao, Reidel, Dordrecht, Holland.
- Drilling, J.S. & Schönberner, D., 1982. *Astr. Astrophys.*, **113**, L22.
- Drilling, J.S., Schönberner, D., Heber, U, & Lynas-Gray, A.E., 1984. *Astrophys. J.*, **278**, 224.
- Drilling, J.S., Heber, U. & Jeffery, C.S., 1985. *IAU Circ. No. 4086*.
- Dudley, R.E. & Jeffery, C.S., 1990. *Mon. Not. R. astr. Soc.*, **247**, 400.
- Duvigneau, H., Friedjung, M. & Hack, M., 1979. *Astr. Astrophys.*, **71**, 310.
- Eggen, O.J., Kron, G.E. & Greenstein, J.L., 1950. *Publs astr. Soc. Pacif.*, **62**, 171.
- Ensman, L.M. & Woosley, S.E., 1988. *Astrophys. J.*, **333**, 754.
- Feast, M.W., 1986. In: *Hydrogen-Deficient Stars & Related Objects*, IAU Coll. No. 87, p.151, eds. K. Hunger, D. Schönberner & N.K. Rao, Reidel, Dordrecht, Holland.
- Filippenko, A.V., 1988. *Astr. J.*, **96**, 1941.
- Fleming, W.P., 1912. *Havard Ann.*, **56**, 108.
- Gaposhkin, S., 1945. *Astr. J.*, **51**, 109.
- Greenstein, J.L., 1940. *Astrophys. J.*, **91**, 438.
- Greenstein, J.L. & Adams, W.S., 1947. *Astrophys. J.*, **106**, 339.
- Greenstein, J.L. & Sargent, A.I., 1974. *Astr. J. Suppl.*, **28**, 157.

- Hack, M., Flora, U. & Santin, P., 1980. In: *Close Binary Stars*, IAU Symp. No. 88, p.271, eds. M. Plavec, D.M. Popper & R.K. Ulrich, Reidel, Dordrecht, Holland.
- Hack, M. & Pasinetti, L., 1963. *Contr. Oss. astr. Milano-Merate*, 215, 1.
- Halstead, B., 1987. *Bull. Brit. Phys. Soc.*, 40, 99.
- Harkness, R.P., Wheeler, J.C., Margon, B., Downes, R.A., Kirshner, P., Uomoto, A., Barker, E.S., Cochran, A.L., Dinerstein, H.L., Garnett, D.R. & Levreault, R.M., 1987. *Astrophys. J.*, 317, 355.
- Heard, J.F., 1962. *Publ. David Dunlap Obs.*, 2, 269.
- Heber, U., 1983. *Astr. Astrophys.*, 118, 39.
- Heber, U., 1986. In: *Hydrogen Deficient Stars and Related Objects*, I.A.U. Colloquium No. 87, p.33, eds. K. Hunger, D. Schönberner, & N.K. Rao, Reidel.
- Heber, U., Heck, A., Houziaux, L., Manfroid, J. & Schönberner, D., 1984. *Proc. Fourth European IUE Conference*, ESA.
- Heber, U. & Schönberner, D., 1981. *Astr. Astrophys.*, 102, 73.
- Hellings, P., de Loore, C., Burger, M. & Lamers, H.J.G.L.M., 1981. *Astr. Astrophys.*, 101, 161.
- Hill, P.W., 1987. *Quart. J. R. astr. Soc.*, 28, 225.
- Humphreys, R.M. & Ney, E.P., 1974a. *Astrophys. J.*, 187, L75.
- Humphreys, R.M. & Ney, E.P., 1974b. *Astrophys. J.*, 190, 339.
- Hunger, K., 1975. In: *Problems in Stellar Atmospheres and Envelopes*, p.57, eds. B. Baschek, W.H. Kegel & G. Traving, Springer-Verlag.
- Hunger, K., Gruschinske, J., Kudritzki, R.P. & Simon, K.P., 1981. *Astr. Astrophys.*, 95, 244.
- Jeffery, C.S., Drilling, J.S. & Heber, U., 1987. *Mon. Not. R. astr. Soc.*, 226, 317.
- Jeffery, C.S. & Heber, U., 1992. *Astr. Astrophys.*, in press.
- Jones, K.N., 1991. *Ph.D. Thesis*, University of St. Andrews.
- Kaufmann, J.P. & Schönberner, D., 1977. *Astr. Astrophys.*, 57, 169.
- Klinglesmith, D.A., 1981. *Hydrogen Line Blanketed Model Stellar Atmospheres*, NASA, SP-3065.
- Kurucz, R.L., 1979. *Astrophys. J. Suppl.*, 40, 1.
- Lauterborn, D., 1970. *Astr. Astrophys.*, 7, 150.
- Lee, T.A. & Nariai, K., 1967. *Astrophys. J.*, 149, L93.
- Leushin, V.V. & Topil'skaya, G.P., 1984. *Astrophysics*, 22, 74.

- Leushin, V.V. & Topil'skaya, G.P., 1987. *Astrophysics*, **26**, 117.
- Leushin, V.V. & Topil'skaya, G.P., 1988a. *Astrophysics*, **28**, 213.
- Leushin, V.V. & Topil'skaya, G.P., 1988b. *Astrophysics*, **28**, 329.
- Malcolm, G. & Bell, S.A., 1986. *Mon. Not. R. astr. Soc.*, **222**, 543.
- Margoni, R., Stagni, R. & Mammano, A., 1988. *Astr. Astrophys. Suppl.*, **75**, 157.
- McLaughlin, D.P., 1939. *Publs. Amer. astr. Soc.*, **9**, 224.
- Merill, P.W., 1943. *Publs astr. Soc. Pacif.*, **55**, 242.
- Morgan, W.W., 1934. *Astrophys. J.*, **79**, 513.
- Morgan, W.W., 1935. *Publs. Yerkes Obs.*, **7**, Part III.
- Morrison, K., 1988. *Mon. Not. R. astr. Soc.*, **233**, 621.
- Morrison, K., Drilling, J.S., Heber, U., Hill, P.W. & Jeffery, C.S., 1986. In: *Hydrogen-Deficient Stars & Related Objects*, IAU Coll. No. 87, p.245, eds. K. Hunger, D. Schönberner & N.K. Rao, Reidel, Dordrecht, Holland.
- Morrison, K. & Willingale, G.P.M., 1987. *Mon. Not. R. astr. Soc.*, **228**, 819.
- Nariai, K., 1967a. *Publs astr. Soc. Japan*, **19**, 63.
- Nariai, K., 1967b. *Publs astr. Soc. Japan*, **19**, 564.
- Nariai, K., 1970. *Publs astr. Soc. Japan*, **22**, 559.
- Nekel, Th., 1967. *Veröff. Heidelberg Königstuhl*, **19**, .
- Parthasarathy, M., Cornachin, M. & Hack, M., 1986. *Astr. Astrophys.*, **166**, 237.
- Parthasarathy, M., Hack, M. & Tektunali, G., 1990. *Astr. Astrophys.*, **230**, 136.
- Phillips, E.M. & Pugh, D.S., 1987. *How To Get a Ph.D.*, Open University Press.
- Plaskett, J.S., 1927. *Publs Dom. astrophys. Obs.*, **4**, 1.
- Plaskett, J.S., 1928. *Publs Dom. astrophys. Obs.*, **4**, 103.
- Plavec, M.J., 1986. In: *Hydrogen-Deficient Stars & Related Objects*, IAU Colloquium No. 87, p.231, eds. K. Hunger, D. Schönberner & N.K. Rao, Reidel, Dordrecht, Holland.
- Plavec, M.J., Weiland, J.L. & Dobias, J., 1982. In: *Advances in Ultraviolet Astronomy*, p.550, eds. Y. Kondo, Mead & Chapman.
- Pollacco, D.L., 1989. *Ph.D. Thesis*, University of St. Andrews.
- Rao, N.K. & Venugopal, V.R., 1985a. *J. Astrophys astr.*, **6**, 101.

- Rao, N.K. & Venugopal, V.R., 1985b. *J. Astrophys astr.*, **6**, 153.
- Saio, H. & Jeffery, C.S., 1988. *Astrophys. J.*, **328**, 714.
- Sahade, J. & Albano, J., 1970. *Astrophys. J.*, **162**, 505.
- Schaefer, R., Cassé, M. & Cahen, S., 1987. *Astrophys. J.*, **316**, L31.
- Schönberner, D., 1977. *Astr. Astrophys.*, **57**, 437.
- Schönberner, D., 1978. *Mitt. Astron. Gesellschaft*, **43**, 266.
- Schönberner, D. & Drilling, J.S., 1983. *Astrophys. J.*, **268**, 225.
- Schönberner, D. & Drilling, J.S., 1984. *Astrophys. J.*, **276**, 229.
- Schönberner, D. & Wolf, R.E.A., 1974. *Astr. Astrophys.*, **37**, 87.
- Seydel, F.L., 1929. *Publs. Amer. astr. Soc.*, **6**, 278.
- Uomoto, A., 1986. *Astrophys. J.*, **310**, L35.
- Walborn, N.R., 1983. *Astrophys. J.*, **268**, 195.
- Walker, H.J. & Schönberner, D., 1981. *Astr. Astrophys.*, **97**, 291.
- Wallerstein, G., Greene, T.F. & Tomley, L.J., 1967. *Astrophys. J.*, **150**, 245.
- Warner, B., 1967. *Mon. Not. R. astr. Soc.*, **137**, 119.
- Weaver, H.F., 1943. *Astrophys. J.*, **98**, 130.
- Webbink, R.F., 1984. *Astrophys. J.*, **277**, 355.
- Whitney, B.A., Soker, N. & Clayton, G.C., 1991. *Astr. J.*, **102**, 284.
- Wilson, R.E., 1914. *Lick Obs. Bull.*, **8**, 132.
- Wolf, N.J., 1973. *Astrophys. J.*, **185**, 229.
- Wolff, S.C., Pilachowski, C.A. & Wolstencroft, R.D., 1974. *Astrophys. J.*, **194**, L83.

## Chapter 2

# The Mass of $\nu$ Sgr From Ultraviolet Radial Velocities

Upsilon Sagittarii has its orbital period and phasing (as well as other parameters) well determined from the work of Wilson (1914) and others (*e.g.* Eggen, Kron & Greenstein 1950). In the orbit the only parameters that are unknown are the inclination and the semi-amplitude of the secondary,  $K_2$ , with reports in the literature (*e.g.* Duvigneau, Friedjung & Hack 1979; Parthasarathy, Cornachin & Hack 1986) suggesting a value of less than  $10 \text{ km s}^{-1}$  as being most the likely.

A number of authors have tried to determine the orbit of the secondary component using both direct (*e.g.* Duvigneau *et al.*; Parthasarathy *et al.*) and indirect methods (*e.g.* Hellings, de Loore, Burger & Lamers 1979; Schönberner & Drilling 1983) but with no success.

The secondary radial velocity curve is of vital importance as its determination give the minimum masses of the two components in absolute units. These are required to put the whole discussion about  $\nu$  Sgr, and by extension the other HDB's, onto a secure footing. This will allow an objective judgement of the validity of the large number of speculative models that have been discussed for  $\nu$  Sgr.

### 2.1 Improved Cross-Correlation Methods

The problem is to determine the velocity of the secondary component with respect to that of the primary. The simplest way is to look for spectral lines of both components in a wavelength region where the secondary is visible. This region is expected to be in the UV; the secondary, being hotter than the primary, will have the greatest flux in this region. However the secondary is very faint,

even in this wavelength range, and no lines have been conclusively determined to come from the secondary. Parthasarathy, Cornachin & Hack (1986) expect the secondary radial velocities to be less than  $10 \text{ km s}^{-1}$  based on the non-detection of secondary lines.

With a low relative luminosity and small relative velocity the problem becomes extracting secondary radial velocities from spectral lines dominated by the primary but with some small secondary contribution. The method chosen was the standard technique of cross-correlation (CC) where one spectrum is compared with another to determine the shift between the two. This is unlikely to work with  $\nu$  Sgr as the primary component dominates and the detected shifts will be due to the differing primary radial velocities on the two spectra.

The refinement used here is template sharpening whereby all the spectra are shifted by the *expected* velocity of the secondary and co-added. This strengthens the secondary signal while smearing the primary contribution. Cross correlating each spectrum against this template should give a small sharp signal from the secondary superimposed on a broad (smeared) signal from the primary. The determined secondary radial velocities can then be used to determine a better template. This procedure of cross-correlation with template sharpening (CCTS) is repeated until convergence of the secondary radial velocities occurs.

## 2.2 The Data

The UV data were retrieved from the IUE archive in the PHOT and GPHOT formats supplied by the IUE project. There are 17 SWP and 15 LWR/LWR frames available, obtained between 1978 and 1985 of which one frame (SWP7165) was unuseable. These data are given in Table 2.1.

The data were further reduced using the STARLINK package IUEDR (Rees & Giddings 1989). The ripple corrections for the SWP spectra were calculated using a modified version of Barker's (1984) method; overlapping regions of the spectrum were merged with weights proportional to the inverse ripple correction factors.

## 2.3 Processing and Calibration

Since the wavelength calibration of IUE is not absolute, the wavelength scale was adjusted to tie known interstellar features to their laboratory (vacuum) wavelengths. Here each spectrum is shifted so the interstellar features coincide with those of a chosen spectrum (SWP1398). They are then summed to form a rough template and the individual spectra cross-correlated against this template over the wavelength range  $\lambda\lambda 1248\text{-}1308 \text{ \AA}$  where there are many strong interstellar lines

Table 2.1: SWP and LWR/P IUE data for  $\nu$  Sgr.

Spectrum	J.D. (-2440000)	dd/mm/yy	ddd/yy	Type	Aperture	Exposure (seconds)	ITFMAX	THDA
SWP1398	3621	22/04/78	112/78	PHOT	SAP	3600	19632	-
SWP1544	3643	14/05/78	134/78	GPHOT	LAP	600	19632	-
SWP1592	3650	21/05/78	141/78	PHOT	SAP	3600	19632	-
SWP1691	3662	02/06/78	153/78	GPHOT	SAP	960	19632	-
SWP1856	3685	25/06/78	176/78	GPHOT	SAP	3600	19632	-
SWP2136	3718	28/07/78	209/78	PHOT	SAP	3600	19632	-
SWP2137	3719	29/07/78	210/78	PHOT	SAP	4500	19632	-
SWP2219	3727	07/08/78	218/78	GPHOT	LAP	900	19632	-
SWP2492	3757	05/09/78	248/78	GPHOT	SAP	960	19632	-
SWP8473	4035	10/06/79	161/79	GPHOT	SAP	1500	19632	-
SWP8299	4318	19/03/80	079/80	GPHOT	LAP	1328	19632	-
SWP9110	4385	28/05/80	146/80	GPHOT	LAP	2100	19632	-
SWP9118	4388	28/05/80	146/80	GPHOT	LAP	1900	19632	-
SWP26096	6222	05/06/85	156/85	PHOT	LAP	540	19632	10.81
SWP26103	6223	06/06/85	157/85	PHOT	LAP	900	19632	10.18
SWP26881	6345	06/10/85	279/85	PHOT	LAP	2400	19632	-
LWR1494	3643	14/05/78	135/78	GPHOT	LAP	480	27220	-
LWR1505	3645	16/05/78	137/78	GPHOT	LAP	600	27220	-
LWR1828	3650	21/05/78	142/78	GPHOT	SAP	800	20000	-
LWR1595	3662	02/06/78	153/78	GPHOT	SAP	1020	27220	-
LWR1618	3664	04/06/78	155/78	GPHOT	SAP	400	27220	-
LWR1909	3718	28/07/78	209/78	GPHOT	SAP	600	27220	-
LWR1910	3719	29/07/78	210/78	GPHOT	SAP	1200	27220	-
LWR1994	3727	06/08/78	218/78	GPHOT	LAP	465	27220	-
LWR2276	3557	05/09/78	248/78	GPHOT	SAP	600	27220	-
LWR4749	4035	10/06/79	161/79	GPHOT	SAP	900	27220	-
LWR4754	4035	10/06/79	161/79	GPHOT	SAP	840	27220	-
LWP6127	6221	04/06/85	155/85	PHOT	LAP	300	27220	10.51
LWP6133	6222	05/06/85	156/85	PHOT	LAP	240	27220	10.51
LWP6150	6223	06/06/85	157/85	PHOT	LAP	210	27220	10.18
LWP6859	6345	06/10/85	279/85	PHOT	LAP	240	27220	8.17

(Figure 2.1).

The new velocities from the cross-correlation are used to form a better template with the interstellar lines at vacuum wavelengths. These shifts were checked to see if they showed any phase dependency that would indicate that the lines used originated in circumstellar/stellar material. Figure 2.2 shows a plot of the interstellar line shifts against phase (from Eggen *et al.* 1950) and against date.

Three sets of radial velocities were determined for  $\nu$  Sgr - the secondary from short wavelength SWP data and the primary from both longer wavelength SWP data and LWR/LWP data.

The UV spectrum of  $\nu$  Sgr contains absorption lines from primary and secondary components, from a stellar wind, and from the interstellar medium. Figure 2.3 shows the spectrum in the range 1200 - 2800 Å after de-reddening by  $E_{B-V} = 0.20$  (Chapter 7 and Figure 7.3). To maximise the orbital information obtained by correlation requires that unwanted spectral information be minimised. The major interstellar lines were replaced by interpolated continuum values and the stellar continuum was subtracted. In this study, care was taken to preserve the wavelength information in the interpolated regions so that the software used did not undersample the cross-correlation functions (CCF's). Strong wind-lines were excluded from the correlation by using only selected regions of spectrum in the CCF measurements, a device which also helped to minimize computational effort. The interstellar lines removed are given in Table 2.2.

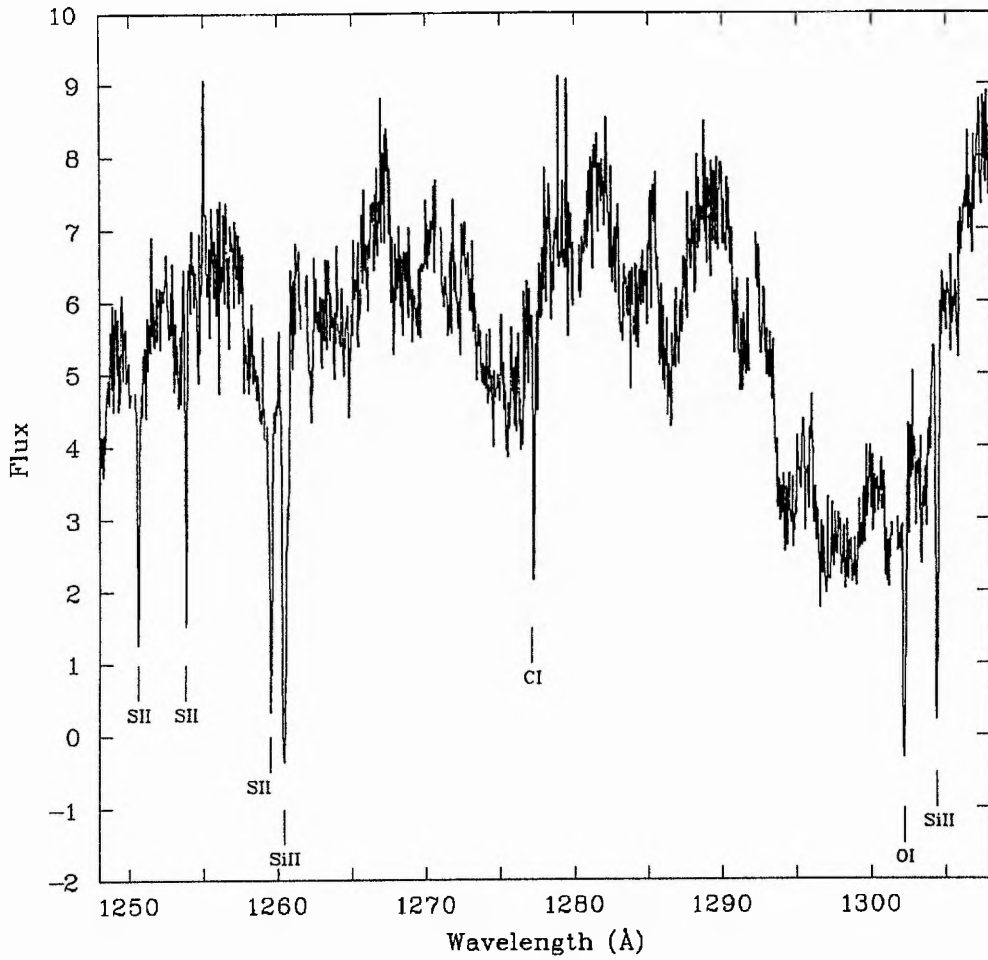
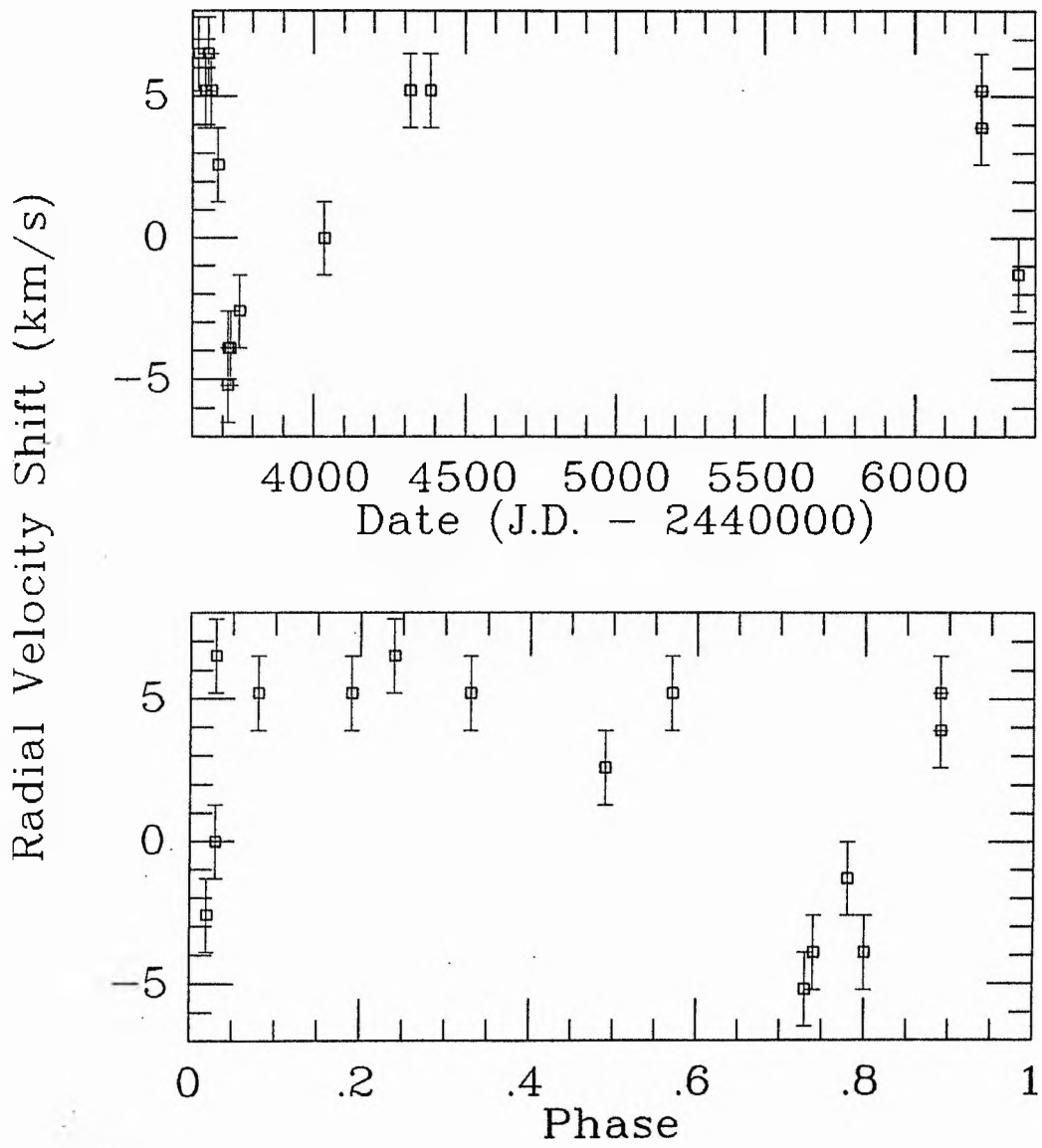


Figure 2.1: A region of SWP spectrum rich in sharp interstellar lines ( $\lambda\lambda$  1248 - 1308 Å). The spectrum shown is that of SWP1398.



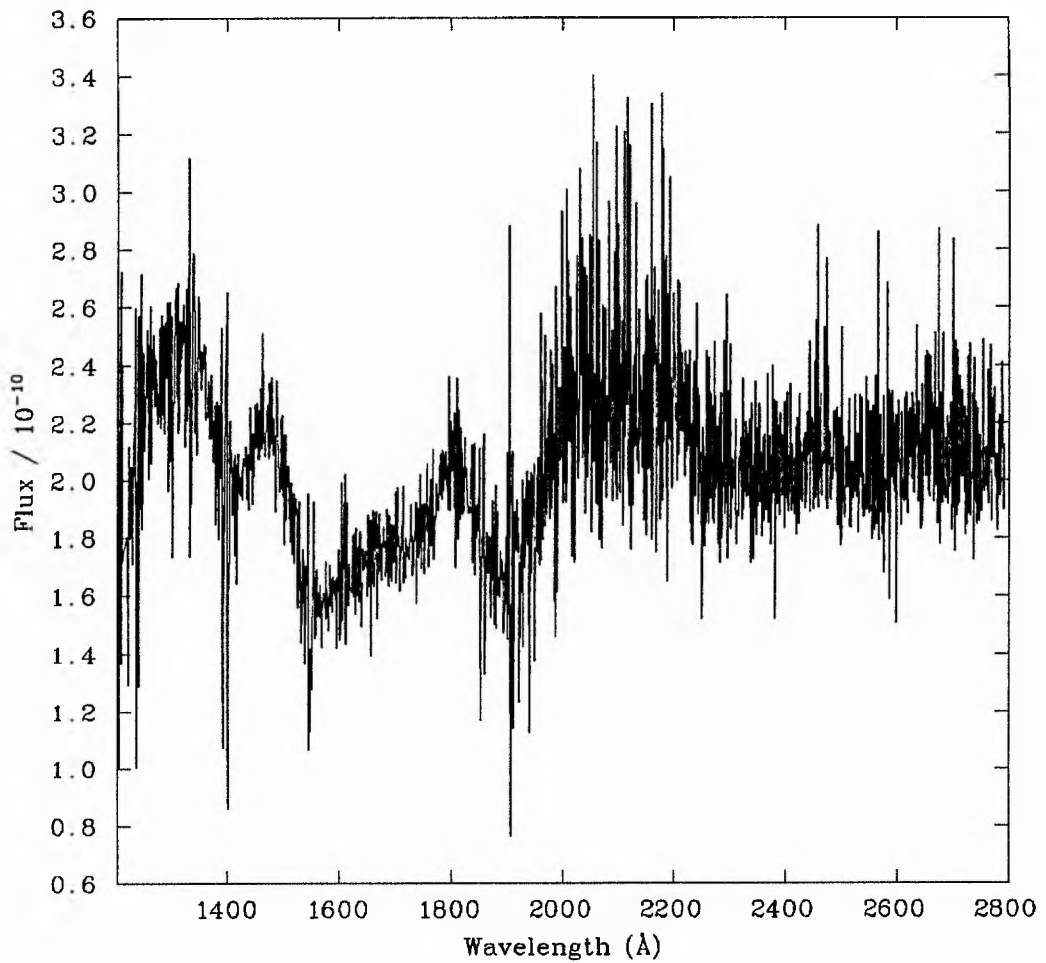


Figure 2.3: The IUE spectrum of  $\nu$  Sgr from 1200 - 2800 Å. The spectrum is the sum of 16 individual spectra after template sharpening. The flux is in absolute units ( $\text{erg s}^{-1} \text{cm}^{-2} \text{Å}^{-1}$ ) as the continuum-removed high resolution data was mapped onto the low resolution (flux calibrated) spectra. The spectrum has been de-reddened by  $E_{B-V} = 0.20$ .

**Table 2.2:** The interstellar lines removed from the sections of spectra used for the cross-correlation analysis.

Wavelength Range (Å)	Wavelengths Removed (Å)	Identification
1230 - 1380	1250.1 - 1251.5	S II
	1253.4 - 1254.3	S II
	1259.3 - 1260.8	Si II
	1276.0 - 1277.9	Cl
	1279.8 - 1280.7	Cl
	1301.9 - 1302.9	O I
	1303.8 - 1305.0	Si II
	1316.7 - 1317.9	Ni II
	1328.6 - 1329.6	Cl
	1334.1 - 1336.5	C II
	1346.7 - 1347.9	Cl
	1358.4 - 1359.1	Cl
	1369.8 - 1370.5	Ni II
1562 - 1700	1607.8 - 1608.9	Fe II
	1656.1 - 1658.6	Cl
	1669.9 - 1671.4	Al II
	1691.7 - 1693.2	Ni III
2300 - 2450	2342.5 - 2344.5	Fe II
	2372.0 - 2375.0	Fe II
	2381.0 - 2382.0	Fe II

The selected regions were  $\lambda\lambda 1230\text{-}1380 \text{ \AA}$  (SWP) for the secondary and  $\lambda\lambda 1562\text{-}1700 \text{ \AA}$  (SWP) and  $\lambda\lambda 2300\text{-}2450 \text{ \AA}$  (LWR/LWP) for the primary. Finally, all wavelengths were transformed to a logarithmic scale. The spectral manipulation and cross-correlation described in this section was carried out almost entirely with the STARLINK package DIPSO (Howarth and Murray, 1991).

## 2.4 Radial Velocity Determination

Initially the spectra were cross-correlated against a single spectrum. Phase-binning was then tried whereby spectra with a similar phase were co-added (no shifts). The results for the primary were in both cases reasonable, but very poor for the secondary even in the short wavelength range where the secondary was expected to be detected. See Figure 2.4. The individual spectra were then cross-correlated against the spectrum of the sub-dwarf O star HD 128220 which was expected to have a similar spectral type to that of the secondary. The results were poor, a sample CCF also being given in Figure 2.4.

Template sharpening was then applied to find both the primary and the secondary orbits. Initial velocity shifts and the phasing for the primary template sharpening (both SWP and LW spectra) were obtained from an circular orbit determined from eight FeII lines visible on all SWP spectra. The known optical orbit could have been used, but the procedure adopted provided a check for internal consistency. Initial velocities for the secondary orbit were based on a circular orbit with a semi-amplitude of  $10 \text{ km s}^{-1}$ , as indicated by the preliminary results from the CIII  $\lambda 1247 \text{ \AA}$  measurements in the phase binned spectra. The radial velocities determined from the FeII and CIII lines are given in Figure 2.5. The results of template sharpening are illustrated in Figure 2.6 for the case of the primary spectrum, the secondary spectrum is still too weak to be identified after sharpening except by correlation.

Determining the radial velocities for the primary from both SWP and LWP/LWR data was straightforward, once an initial velocity was determined, as the CCF's were sharp and single-peaked, Figure 2.7.

The CCF measurements for the secondary were more difficult because the primary spectrum still contributes much of the power in the broad correlation peak. The weak secondary spectrum is registered as a sharp feature superimposed on this peak; its strength is variable and cannot always be distinguished from the broader feature. See Figure 2.8(a).

The velocities were determined by fitting a parabola to the peak of the CCF. When fitting the secondary peak the presence of the primary peak did not in most cases seriously affect the measurement of the secondary velocity. Using the derived velocities to redetermine the secondary orbit,

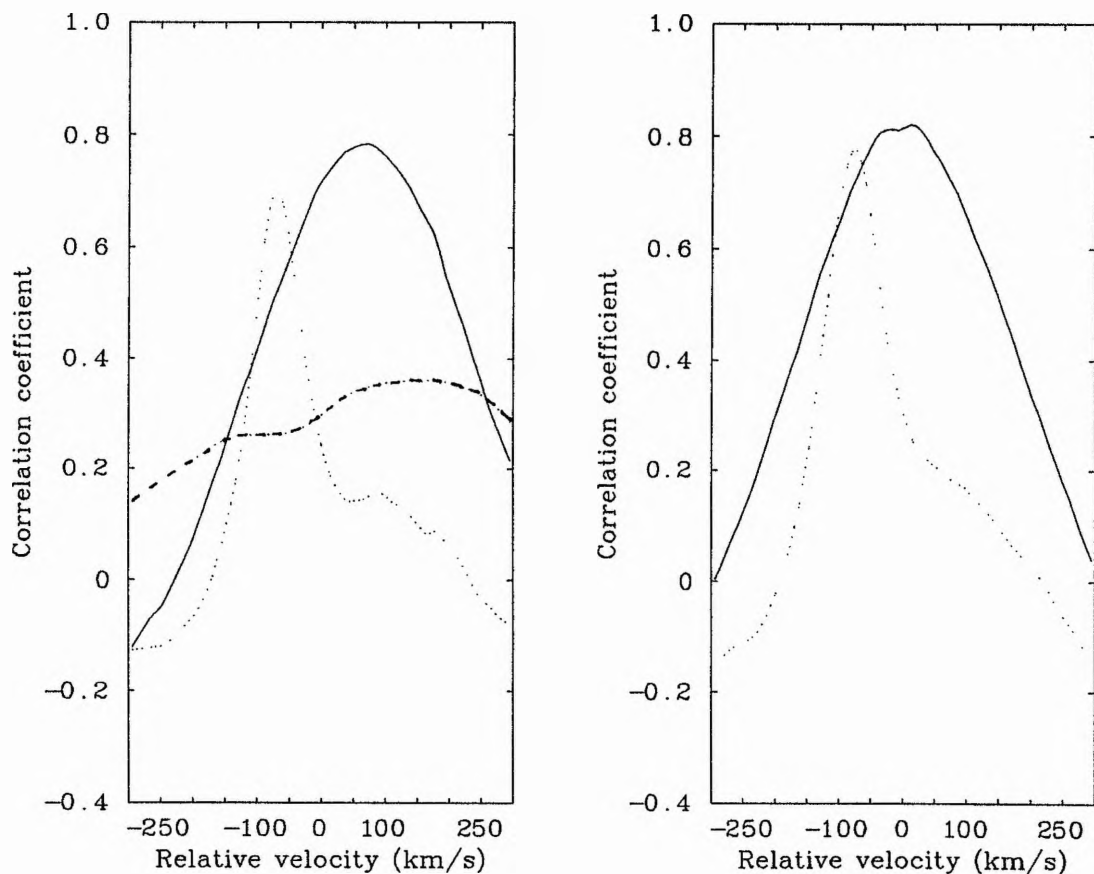


Figure 2.4: Left: CCFs from two individual spectra (SWP1398 and SWP9110) cross-correlated against each other in the wavelength region 1230-1380 Å (solid) and 1562-1700 Å (dotted). The dashed line is the cross-correlation of SWP1398 against a single spectrum from the sdO star HD 128220. Right: CCFs from cross-correlating two phase-binned spectra, each consisting of three co-added spectra, in the wavelength ranges 1230-1380 Å (solid) and 1562-1700 Å (dotted).

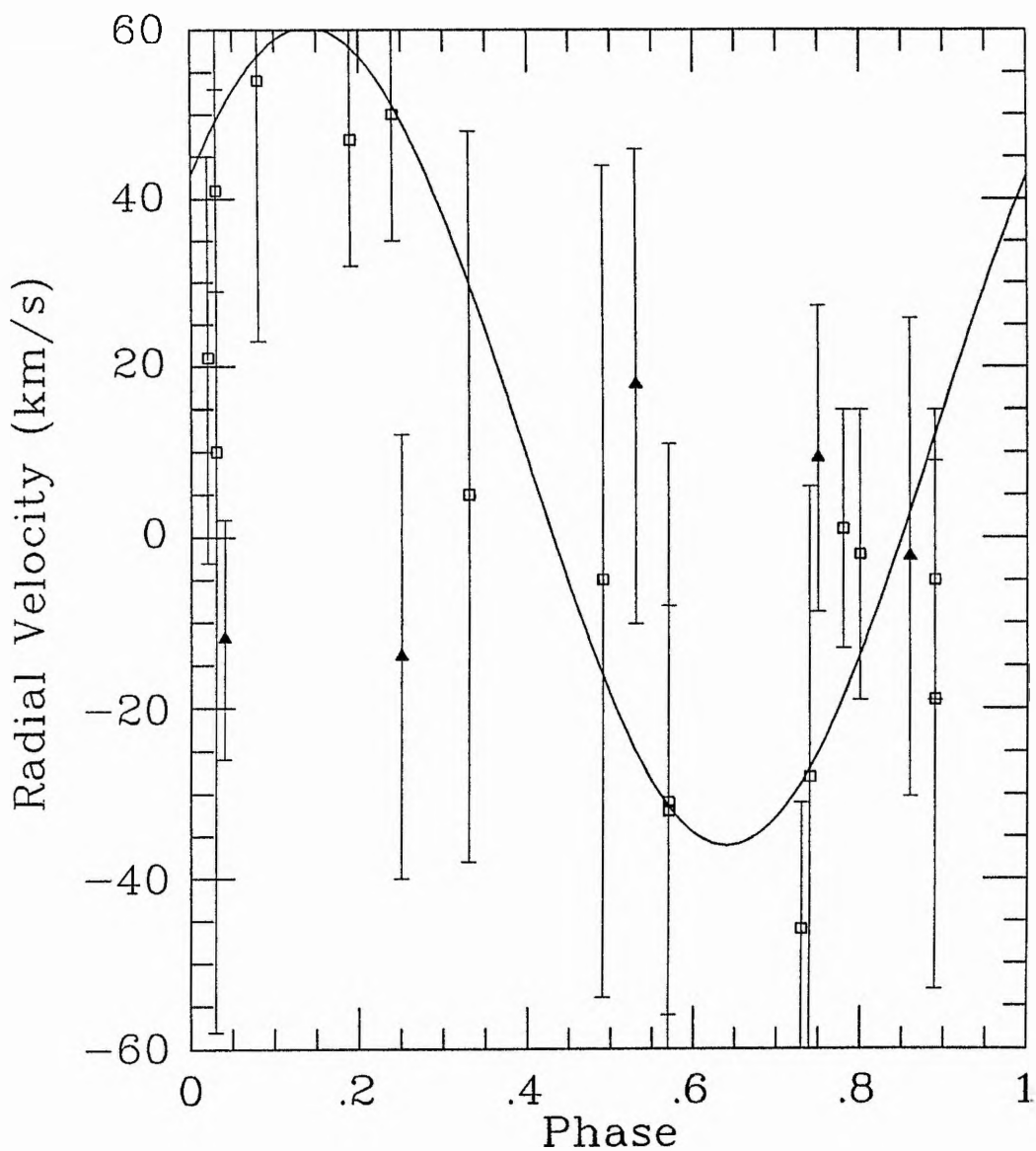


Figure 2.5: The data from the 8 FeII lines (open squares) and the C III  $\lambda 1248 \text{ \AA}$  line (filled triangles). A semi-amplitude of  $\sim 45 \text{ km s}^{-1}$  is indicated for the primary and  $\sim 17 \text{ km s}^{-1}$  for the secondary. Note the very large error bars characteristic of orbits determined from line measurements. Only five secondary velocity points are given as phase-binned spectra were used. The phasing is from Wilson's (1914) orbit with phase zero being time of periastron passage; his orbit is shown by the solid line.

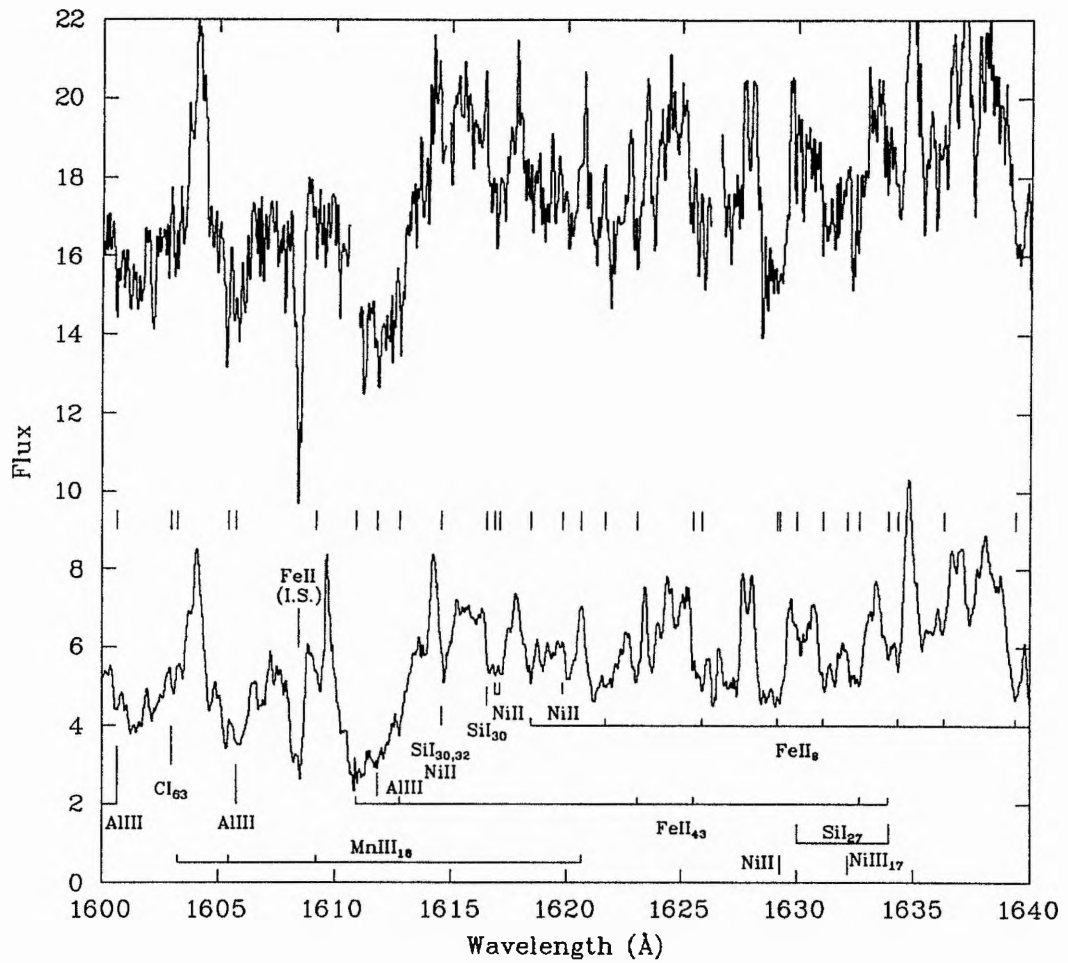


Figure 2.6: A demonstration of template construction for the primary spectrum. A single spectrum (SWP26096) is compared with the sum of 16 spectra after template sharpening (lower). The line identifications and multiplet numbers are from Moore (1950, 1952), Wiese, Smith & Glennon (1966) and Wiese, Smith & Miles (1969). Identifications for the most highly ionised lines may be uncertain.

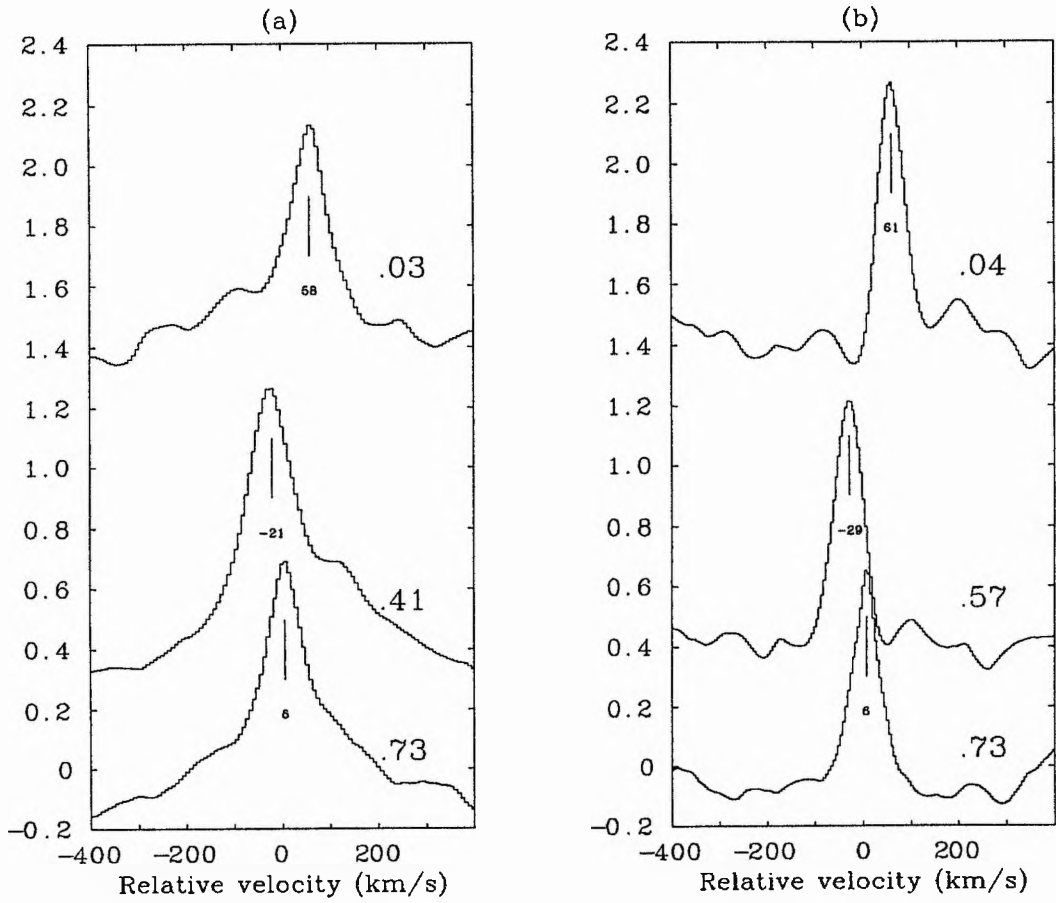
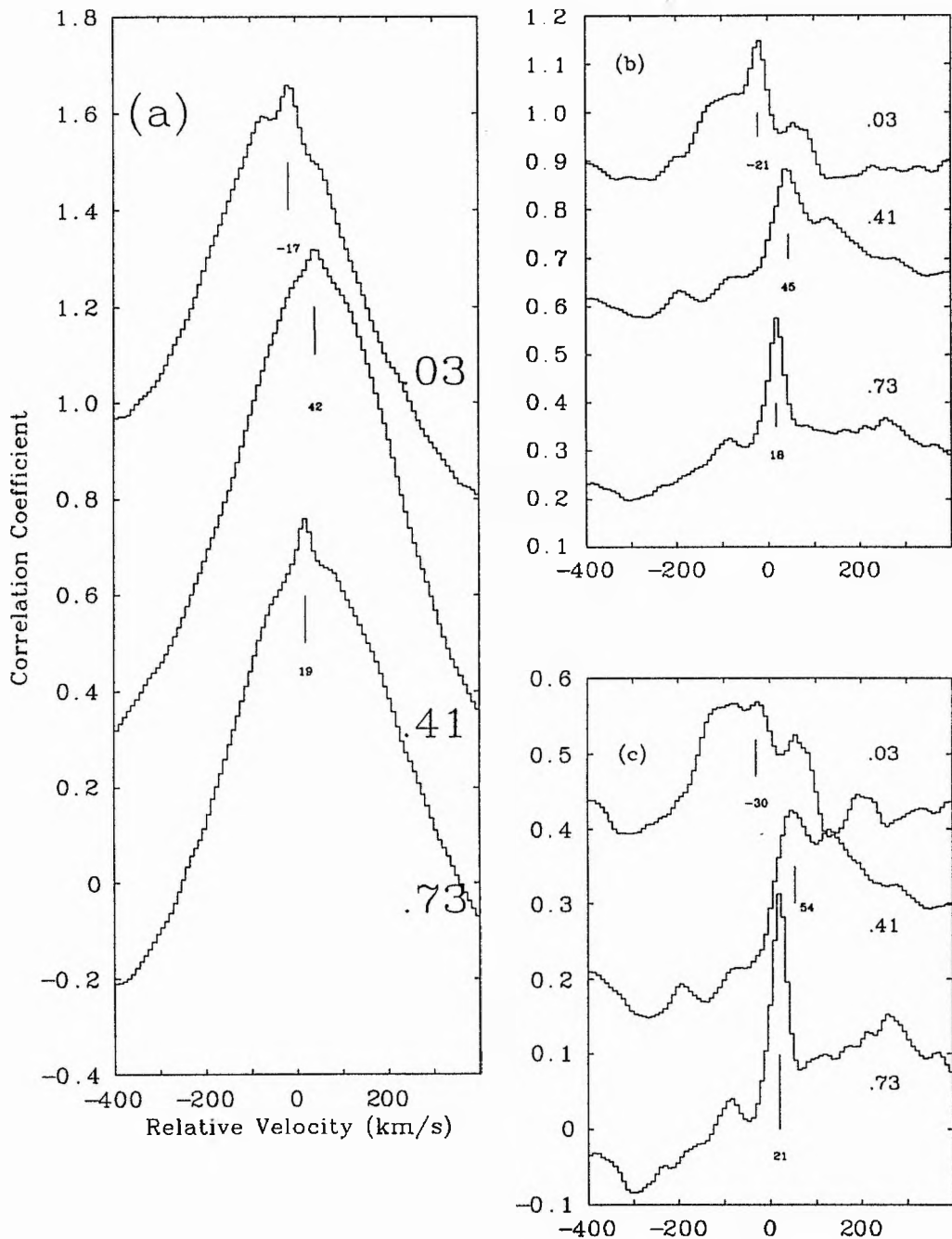


Figure 2.7: CCFs and radial velocities after template sharpening on the primary component. (a) from SWP spectra, (b) from LWR/LWP spectra. The phases are marked on the right, as is the measured radial velocity. The zero points of the CCF's are 0.0, 0.5 and 1.5.



**Figure 2.8:** CCFs for the secondary at three phases (marked on the right-hand side). (a) shows the CCF's used to determine the velocities given in Table 2.3. (b) shows the CCF's after deconvolution of the secondary spectra. The differences are within the measurement error ( $\pm 5 \text{ km s}^{-1}$ ). (c) shows the CCF's after deconvolution, where the template spectrum does *not* include the spectrum being cross-correlated against it. See Section 2.8

the template sharpening and velocity measurements were repeated five times until convergence, at which point the individual measurements were inspected.

In view of the variable strength of the secondary component in the CCF's, a weighting procedure based on the CCF shape was adopted in which a measurement from a 'good' CCF was weighted 1.0, 'fair' 0.7 and 'poor' 0.3. Five measurements of the secondary velocity with residuals greater than three times the standard deviation were discarded. Two of these lay a long way from either primary or secondary velocity curves while one point lay exactly on the radial velocity curve for the primary, probably indicating a null contribution from the secondary to the CCF. Another two were close to the systemic velocity, indicating possible interference by a residual interstellar spectrum. The five discarded velocities were all measured from CCF's rated 'poor', whilst nine of the remaining eleven were rated 'fair' or 'good'. The velocity measurement and template sharpening iteration was repeated using the eleven retained spectra. The reduction in template spectrum S/N ratio was not critical since the discarded spectra showed the lowest S/N ratios.

The final radial velocities measured relative to the interstellar lines are shown in Table 2.3, along with details of the image numbers and dates of observation.

## 2.5 Orbit Analysis

The preliminary orbits for the UV template sharpening and the analyses of the final orbit have been carried out using the program RVORBIT by Dr G.Hill (1987, private communication).

The first step in the analysis of the final orbit was to determine the primary orbit from the 31 IUE radial velocities. This fixes the frame of reference of the IUE velocity system which, so far, is tied to the interstellar lines and provides basic data for the calculation of the secondary orbit. Fixing the period at 137.939 days (Wilson 1914) and the eccentricity to be zero, the primary orbit was solved for  $\gamma$ ,  $K_1$ , and  $T_{max}$  (time of maximum positive velocity). The semi-amplitude  $K_1=45.6 \text{ km s}^{-1}$  is satisfactorily close to Wilson's original value of  $48.2 \text{ km s}^{-1}$  given the phase distribution of the IUE observations. A small eccentricity in the IUE orbit had previously been shown to be spurious after application of the Lucy (1989) version of the first Bassett (1978) test (see Appendix A).

Retaining  $K_1$ ,  $\gamma$ , and  $T_{max}$  from the primary orbit,  $K_2$  was determined from the IUE velocities for the secondary to be  $29.7 \text{ km s}^{-1}$ . The IUE orbital elements are listed in Table 2.4, where parentheses denote that  $\gamma$  is relative to the interstellar lines. The orbits and IUE radial velocities are shown in Figure 2.9. Also shown is the radial velocity determined from the high resolution visual spectrum analysed in Chapter 10. This data point was not used when determining

Table 2.3: The IUE spectra and radial velocity data for  $\nu$  Sgr.

Spectrum	J.D. (-2440000)	Primary			Secondary		
		R.V. ( $\text{km s}^{-1}$ )	O-C	Phase	R.V. ( $\text{km s}^{-1}$ )	O-C	Quality
SWP1398	3621	41	-4	0.87	-11	-5	Fair
SWP1544	3643	58	0	0.03	-17	-2	Good
SWP1592	3650	57	4	0.08	-13	-2	Fair
SWP1691	3662	36	-1	0.17	4	4	Poor
SWP1856	3685	-8	0	0.33	29	-1	Poor
SWP2136	3718	-27	-2	0.57	(-0.4)	-	Discarded
SWP2137	3719	-29	-5	0.58	(4.0)	-	Discarded
SWP2219	3727	-5	9	0.64	29	-6	Good
SWP2492	3757	41	-1	0.86	3	6	Fair
SWP5473	4035	51	6	0.87	(-99.0)	-	Discarded
SWP8299	4318	50	-4	0.92	(38.0)	-	Discarded
SWP9110	4385	-25	-2	0.41	40	0	Fair
SWP9118	4385	-21	2	0.41	42	3	Good
SWP26096	6222	6	-2	0.73	19	-1	Good
SWP26103	6223	7	-3	0.73	17	-1	Good
SWP26881	6345	-15	3	0.62	(-14.0)	-	Discarded
LWR1494	3643	61	1	0.02			
LWR1505	3645	61	2	0.04			
LWR1528	3650	65	10	0.08			
LWR1595	3662	36	-3	0.16			
LWR1616	3664	34	-1	0.18			
LWR1909	3718	-29	-2	0.57			
LWR1910	3719	-27	-2	0.58			
LWR1994	3727	-10	6	0.63			
LWR2276	3557	32	-10	0.85			
LWR4749	4035	48	2	0.87			
LWR4754	4035	51	5	0.87			
LWP6127	6221	8	3	0.71			
LWP6133	6222	4	-4	0.72			
LWP6150	6223	6	-3	0.73			
LWP6859	6345	-22	-3	0.61			

Note: The phases were determined by the ephemeris  $T = 2447916.16 + 137.943n$ .

Table 2.4: Orbital solutions for  $\nu$  Sgr.

Source	Period (days)	$K_1$ (km/s)	$e$	$\omega$ (degrees)	$\gamma$ (km/s)	$f(M)$ ( $M_\odot$ )	$K_2$ (km/s)	$T_{max}$ (-2447900)
IUE data	137.939 (fixed)	45.6 $\pm 1.1$	0.0 -	-	(14.8) (0.6)	1.36 .10	29.7 1.7	15.6 0.6
Wilson's solution	137.939 $\pm .017$	46.2 -	0.087 .016	28.6 2.8	12.1 -	1.58 -	-	17.0 1.2
Wilson's data - new solution	137.945 $\pm .030$	47.4 1.1	0.0 -	-	7.9 .8	1.61 .09	-	14.4 5.1
All optical data	137.952 $\pm .005$	48.9 1.0	0.0 0.0	35.4 16.3	7.4 .7	1.61 .11	-	17.9 0.9
IUE + optical data (adopted)	137.944 $\pm .004$	47.3 .8	0.0 -	-	7.4 (fixed)	1.52 .08	29.7 1.7	16.2 0.5

the final orbital solution.

In addition to the radial velocities obtained from IUE, previous optical measurements of the primary radial velocity have been used in a complete re-analysis of the orbit, including a re-derivation of the orbital period. These data consists of 36 measurements by Wilson (1914), eleven by Hack & Pasinetti (1963), six by Jeffery, Drilling & Heber (1987) and two by Jeffery (reported in Dudley & Jeffery 1990). To check for consistency, Wilson's data alone were first re-analysed using RVORBIT. The comparison is made in the second and third entries in Table 2.4. The eccentricity demonstrated by Wilson's data alone appears to be spurious following the application of the Lucy test. The eccentricity in the orbit determined after inclusion of more recent optical data (fourth entry) also is consistent, according to the Lucy test, with a circular orbit. This is also indicated by the IUE data alone. A spurious eccentricity may have been introduced into Wilson's analysis by his reliance on hydrogen lines for some velocity measurements, and the concentration of most measurements in a single orbit. Gas streams indicated by hydrogen emission (Nariai 1967), and pulsations indicated from photometry (Malcolm & Bell 1986) could both have disturbed the original orbital measurement.

Until now the IUE radial velocities are tied to the motion of the interstellar medium as the interstellar lines are at their laboratory wavelengths. Thus the radial velocities need to be adjusted for their heliocentric radial velocity. Initially this velocity is unknown but can be eliminated by equating  $\gamma$  for the IUE primary orbit to  $\gamma$  from the new optical orbit, the IUE radial velocities are transformed to a heliocentric system. The optical data and IUE data were combined in a further determination of the primary orbit (entry 5 in Table 2.4) which, along with  $K_2$  from the IUE velocities, is adopted as the final set of orbital elements for  $\nu$  Sgr.

Using the orbit thus determined it was possible to deconvolve the primary and secondary spectra (next section). The deconvolved secondary spectrum was used as a template and cross-correlated with the original spectra, and also with the deconvolved individual spectra of the secondary. A good CCF was obtained in about one third of the cases and the velocities determined were close to those determined previously. Fig 2.8 (b) shows three CCFs for the cross-correlation

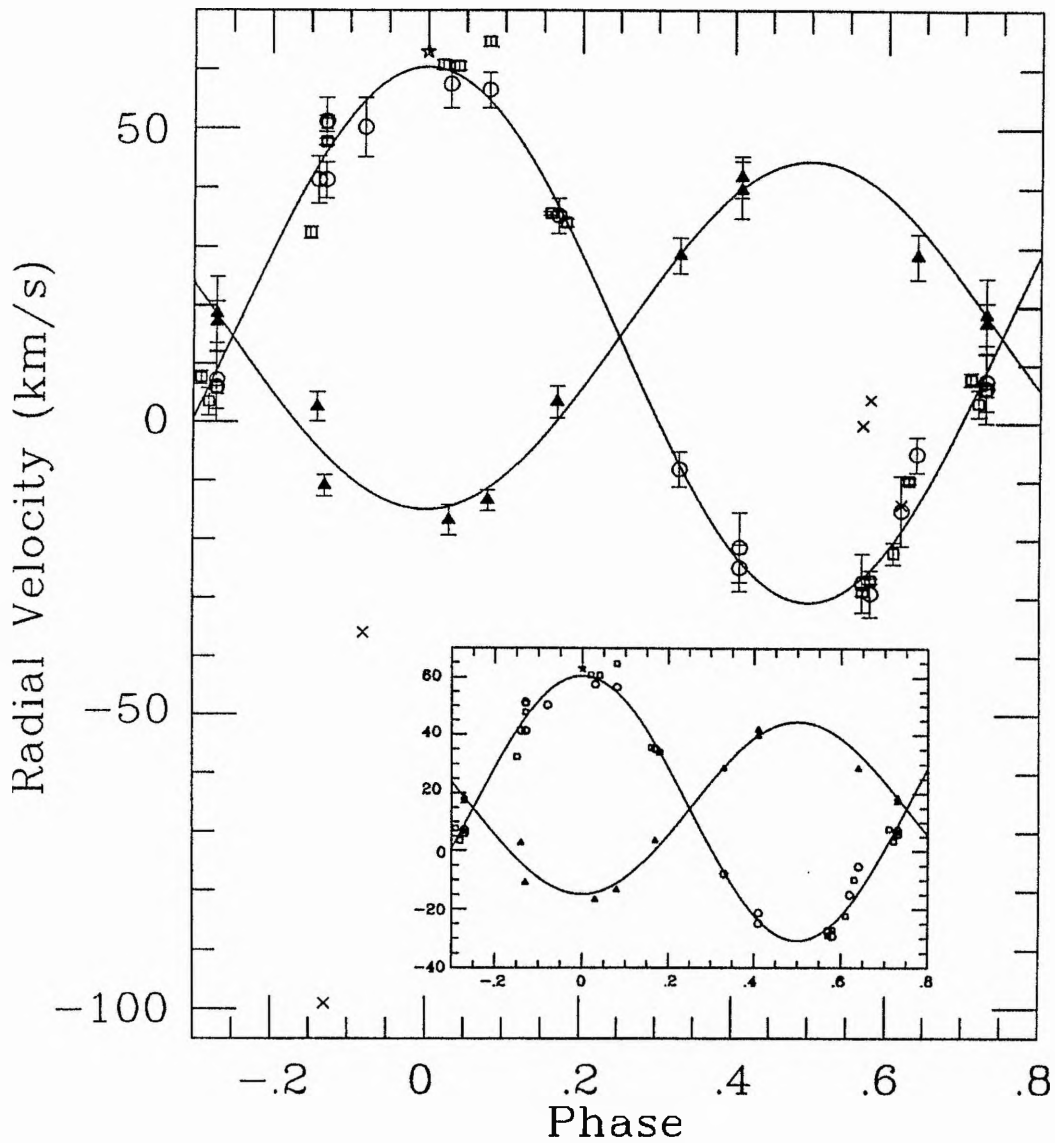


Figure 2.9: The primary and secondary radial velocity curves determined from IUE data. Triangles: secondary velocities (SWP), circles: primary velocities (SWP), squares: primary velocities (LWR/LWP), crosses: discarded secondary velocity points not used in the orbit determination. The error bars are the errors in fitting a parabola to the CCF peak and do not necessarily equal the error in the CCF. The open star shows the primary radial velocity from the high resolution optical spectrum analysed in Chapter 10. This velocity point was not used in the determination of the final orbital parameters. Inset: A clearer view of the orbit.

of the secondary template against individual secondary spectra. While the results seem to confirm the validity of the velocities determined initially it must be remembered that the deconvolution process requires a pre-determined orbit and thus re-determining the orbit from the deconvolved spectra is not an independent check of the orbit. However the CCFs from the deconvolved spectra were sharp and thus indicated that the radial velocities so determined were correct.

## 2.6 Spectral Deconvolution

Once an orbit has been determined for both components of a binary system it should, in principle, be possible to deconvolve the composite spectrum into the individual spectra.

The full spectrum of an object is given by  $F_i(\lambda)$  where the index  $i$  runs from 1 to  $n$ , where  $n$  is the number of individual spectra available. Each of these spectra consists of the sum of a spectral component from the primary and one from the secondary (ignoring any interstellar component), *i.e.*

$$F_i(\lambda) = s_i(\lambda) + p_i(\lambda) \quad (2.1)$$

If the spectra are in turn shifted to the expected velocity of the primary and also the secondary then we obtain two sets of spectra:

$$P_i(\lambda) = F_i(\lambda + \delta\lambda_{p,i}) \quad (2.2)$$

$$S_i(\lambda) = F_i(\lambda + \delta\lambda_{s,i}) \quad (2.3)$$

where the sign of the  $\delta\lambda$  terms are chosen to bring the radial velocity to zero with respect to the frame defined by the interstellar lines.

These sets of spectra are then summed to form two templates: one sharpened on the primary component ( $T_p$ ) and the other on the secondary component ( $T_s$ ).

$$T_p = \frac{1}{n} \sum_{i=1}^n P_i(\lambda) \quad (2.4)$$

$$T_s = \frac{1}{n} \sum_{i=1}^n S_i(\lambda) \quad (2.5)$$

This primary (secondary) template is then subtracted from the individual shifted primary (secondary) spectra to form a set of deconvolved secondary (primary) spectra  $S'_i(\lambda)$  ( $P'_i(\lambda)$ ), where

$$S'_i(\lambda) = P_i(\lambda) - T_p(\lambda) \quad (2.6)$$

$$P'_i(\lambda) = S_i(\lambda) - T_s(\lambda) \quad (2.7)$$

These deconvolved primary (secondary) spectra are then shifted to the expected velocity of the primary (secondary) and summed to form a sharpened deconvolved template  $X_p(\lambda)$  ( $X_s(\lambda)$ ).

$$X_p(\lambda) = \frac{1}{n} \sum_{i=1}^n S'_i(\lambda - \delta\lambda_{p,i} + \delta\lambda_{s,i}) \quad (2.8)$$

$$X_s(\lambda) = \frac{1}{n} \sum_{i=1}^n P'_i(\lambda - \delta\lambda_{s,i} + \delta\lambda_{p,i}) \quad (2.9)$$

Note that because of the way they are constructed the mean value of the deconvolved spectra after summation over the wavelength range is zero. The continuum has been removed in the deconvolution process leaving spectral features distributed around the zero flux level. Wind features will also be mainly removed.

Spectral features should be distinguishable in the spectra but the interstellar lines will persist in both spectra. Their strength will depend on the relative velocities of the primary and secondary components and the distribution in phase of the spectra. Generally the interstellar lines profiles will be distorted with the central wavelength on the deconvolved spectra not agreeing with the vacuum wavelength.

### 2.6.1 Application to $v$ Sgr

Sections of the deconvolved primary and secondary spectra are shown in Figures 2.10 and 2.11. Both Figures show the primary deconvolved spectrum at the top and the secondary deconvolved spectrum at the bottom. The middle spectrum is the original template spectrum (*i.e.* with all the interstellar lines coincident) that has been smoothed and vertically scaled for ease of comparison. As smoothing and scaling has been done the relative strengths of the lines cannot be directly compared. Figure 2.10 shows a section of spectra in the wavelength region where the secondary may be expected to have a significant contribution. As can be seen the deconvolved primary spectrum consists mainly of weak metal lines with a few interstellar lines. The secondary spectrum however seems to show a number of features (notably the NV doublet and the C III line) that are not present in the primary. The reverse is true for Figure 2.11 where the deconvolved primary lines are strong but the secondary lines weak. Note, however, that there are still features in the secondary spectrum that are not in the primary (the 1668 Å line for example).

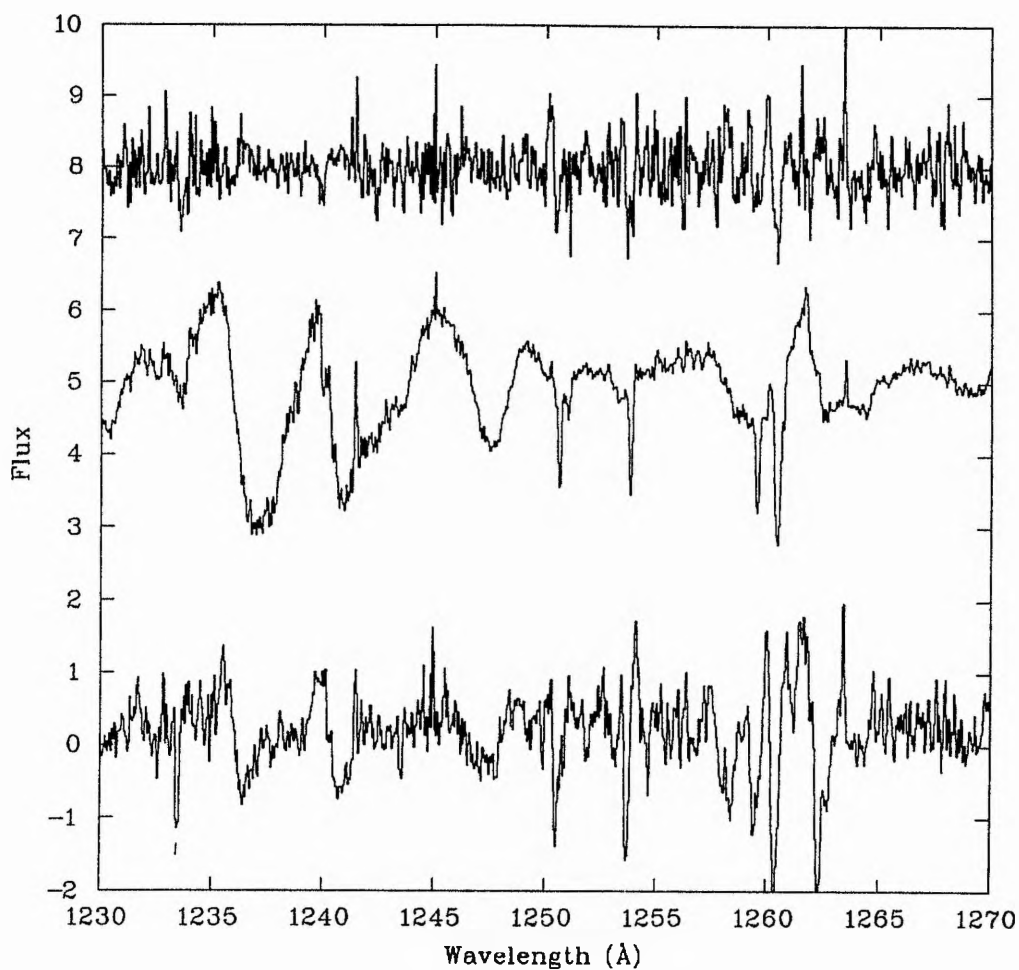


Figure 2.10: A section of both the deconvolved spectrum of the primary (upper) and secondary (lower), 1230-1270 Å. The continuum component has been removed from both spectra during the deconvolution. The middle spectrum shows the template spectrum after smoothing and a vertical scale multiplication of 2 for ease of comparison. A vertical offset of 0, 4 and 8 has been applied to the spectra.

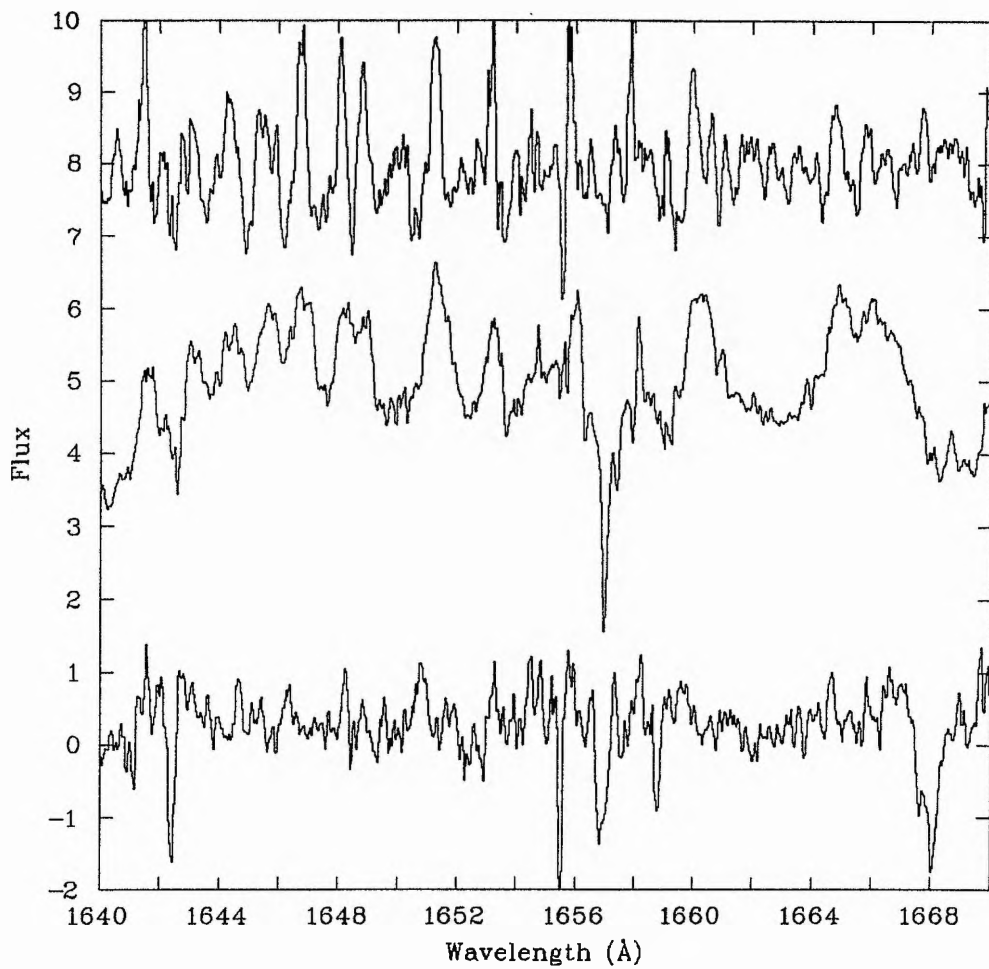


Figure 2.11: As for Figure 2.10 except the template spectrum has a vertical scale multiplier of 5 and a wavelength range 1640-1670 Å.

Table 2.5: The minimum masses and orbital radii of the  $\nu$  Sgr system.

	IUE	All
$q = (M_p/M_s)$	$0.65 \pm 0.04$	$0.63 \pm 0.01$
$M_p \sin^3 i (M_\odot)$	$2.41 \pm 0.18$	$2.52 \pm 0.05$
$M_s \sin^3 i (M_\odot)$	$3.69 \pm 0.17$	$4.02 \pm 0.10$
$a_p \sin i (R_\odot)$	$124 \pm 3$	$129 \pm 2$
$a_s \sin i (R_\odot)$	$80.9 \pm 4.7$	$80.9 \pm 4.7$

## 2.7 Discussion

### 2.7.1 Masses and orbital radii

The most significant result of this investigation is the first direct measurement of the orbit of the secondary component in  $\nu$  Sgr and hence of the mass ratio of the system. It is also the first mass determination of any of the known hydrogen-deficient binaries. The mass ratio, minimum masses and orbital radii are shown for the IUE and final orbits in Table 2.5.

Hack & Pasinetti (1963) found that 4 spectral lines were of a doublet nature at a certain phase (only) with a velocity separation of  $\sim 30 \text{ km s}^{-1}$  between them. The phase of their observation was 0.89 on the ephemeris determined here where the expected velocity of the secondary with respect to the primary would be  $\sim 60 \text{ km s}^{-1}$ . It seems unlikely that this effect could be due to the secondary component; it was attributed to the gas jet between the two components by the authors.

It is notable that the mass ratio is twice that for the 'consensus' model of Schönberner & Drilling (1983) and other authors, and is inconsistent with any other proposed models (*e.g.* Hellings, de Loore, Burger & Lamers 1981, Morrison 1988).

Even with no knowledge of the inclination of the orbit ( $i$ ), the IUE results alone provide a minimum mass for the primary of  $2.4 M_\odot$ , although the adopted value of  $2.5 M_\odot$  is more probable.

## 2.7.2 Mass loss and transfer

Wilson's original period and time of maximum positive velocity are confirmed (within error bounds) using the IUE data and the substantially longer baseline, thus providing no evidence of a secular period change in the orbit.

Using  $\dot{P}/P < 10^{-6} \text{yr}^{-1}$  (as the maximum period change is 0.030 days in the interval 1912 to 1985, taking into account the errors in the values of the period determination), we can obtain the maximum mass-loss rates supported by this data using the relationships:

$$\frac{\dot{P}}{P} = 3\dot{M}_1 \left[ \frac{M_1 - M_2}{M_1 M_2} \right] \quad (2.10)$$

if the mass transfer is fully conservative and

$$\frac{\dot{P}}{P} = \frac{-2\dot{M}_1}{(M_1 + M_2)} \quad (2.11)$$

if the mass loss is fully non-conservative.

This gives a mass-loss rate of  $\dot{M}_1 < 1.9 \times 10^{-5} M_{\odot} \text{yr}^{-1}$  (non-conservative) or  $\dot{M}_1 < 8.4 \times 10^{-6} M_{\odot} \text{yr}^{-1}$  (conservative). This result only weakly constrains the mass-loss rate as Rao and Venugopal (1985) find an upper limit of  $5 \times 10^{-7} M_{\odot} \text{yr}^{-1}$  from 2cm and 6cm radio observations. However the circularity of the orbit resolves the conflict between Wilson's moderately eccentric orbit, and the tendency for tidal force to circularise the orbits of binary systems such as  $\nu$  Sgr which have already undergone substantial mass transfer. See Chapter 7 for details of mass loss determination from UV wind line analysis for  $\nu$  Sgr.

## 2.7.3 Orbital inclination

Some relief from the orbital inclination uncertainty is available since Nariai (1967) documents substantial observations of a displaced H $\alpha$  absorption component visible for the part of the orbit when the primary is most distant. Nariai attributes these to line absorption by material ejected from the surface of the primary into the Roche lobe surrounding the secondary.

For a circular orbit to produce the 40 day H $\alpha$  eclipse would require the material flowing through the inner Lagrangian point to exit as a nozzle with a projected angular extent of 140°. However for the Roche geometry of a system such as  $\nu$  Sgr the angular width of the Roche lobe at the inner Lagrangian point is 114° (Kopal 1959).

The relationship between the Roche Lobe opening semi-angle  $\beta$ , the projected Roche Lobe opening semi-angle,  $\alpha$ , as viewed from  $\gamma^\circ$  ( $\equiv 90^\circ - i$ ) above the plane of the orbit is

$$\tan^2 \gamma = \tan^2 \beta - \frac{\tan^2 \alpha}{\cos^2 \gamma} \quad (2.12)$$

Then for  $\nu$  Sgr where  $\beta = 57^\circ$ ,  $\alpha = \frac{\text{H}\alpha \text{ duration}}{\text{orbital period}} \times 180^\circ (=52^\circ)$  the inclination of the orbit would be  $63^\circ$ . This assumes that the jet of material lies along the line of centres of the stars and completely fills the space inside the secondary Roche lobe adjacent to the  $L_1$  point. For a smaller filling factor the inclination would be greater. Although Equation 2.12 is sensitive to the duration of the H $\alpha$  eclipse, a duration of between 38 and 42 days would still constrain the inclination to be at least  $56^\circ$  and thus  $\sin i$  to be at least 0.83.

However conventional jet models (*e.g.* Lubow & Shu 1975) predict that the jet of material flowing from the primary is more tightly focussed and that the material does not fill the Roche lobe on the secondary's side adjacent to  $L_1$  but forms an accretion disc. Thus conventional theory fails to predict the duration of the observed eclipses.

At phase 0.75 the primary should eclipse the secondary if the orbital inclination is large. No spectra are available for this phase but two are available for  $\phi = 0.73$ . Deconvolved secondary spectra were obtained and the presence of a visible secondary was proven by the fact that subsequent cross correlation of this spectrum with the template yielded a very definite confirmation of the secondary's radial velocity. One of these CCF's is shown in Figure 2.8(b).

Given a primary radius of  $60 R_\odot$ , a secondary radius of  $3 R_\odot$  (see next subsection) and a separation of  $210 R_\odot$  then the primary will totally eclipse the secondary if  $i \geq 75^\circ$ . (A partial eclipse will occur for  $i \geq 74^\circ$ .) From the CCF analysis the secondary is fully visible at  $\phi = 0.73$ , some 4 days before conjunction. From this it follows that  $i \leq 78^\circ$ . From the rotational velocity, determined in Chapter 11, of  $25 \pm 5 \text{ km s}^{-1}$  and a primary radius of  $60 R_\odot$  then assuming synchronous rotation the inclination is further constrained to  $i > 65^\circ$ . Thus  $i$  must be between  $65^\circ$  and  $78^\circ$  and so  $\sin i$  is between 0.91 and 0.98. Thus the mass of the primary component of  $\nu$  Sgr must be  $3.0 \pm 0.3 M_\odot$  and the secondary  $4.8 \pm 0.5 M_\odot$ .

## 2.7.4 Evolutionary status

Since  $\nu$  Sgr is an H-deficient supergiant, its high luminosity is most probably provided by a helium-burning shell around a carbon-oxygen core. With a total mass exceeding the Chandrasekhar mass-limit for CO white dwarfs, its future evolution depends critically on the mass of the CO core and, if this is less than  $\sim 1.4 M_\odot$ , the ability of the system to remove mass from the primary. Delgado & Thomas (1981) have already proposed that if  $M_p > 2 - 3 M_\odot$ , a type II supernova would occur. In the case of an H-deficient progenitor, there would be no H-lines in the supernova spectrum, which would then be classified type Ib. Uomoto (1986) has also proposed that sufficiently massive HDB's would be potential SNIb progenitors, but evidence available to him indicated that the four known HDB primaries were of too low mass ( $\sim 1.2 M_\odot$ ) to be candidates. The minimum mass determined above increases the likelihood that  $\nu$  Sgr will explode as a type Ib supernova. Given a luminosity

of  $\log L_p/L_\odot \sim 4.6$  (see below) and a helium envelope mass of  $\sim 2 M_\odot$ , the nuclear timescale of the primary is  $\sim 4 \times 10^5$  yrs. A mass transfer rate substantially greater than the observed upper limit would be required for  $\nu$  Sgr to avoid a SN explosion. See Chapter 7 for a determination of the mass-loss rate of  $\nu$  Sgr.

These results could be carried further if evidence for eclipses could be used to constrain the orbital inclination angle. Unfortunately there is no evidence for eclipses at optical wavelengths (Malcolm & Bell 1986), and the UV data is at best ambiguous (Duvigneau, Friedjung & Hack 1979, Rao & Venugopal 1985). However by assuming a high inclination angle and supposing the secondary to be a normal main-sequence star, an interesting consequence is obtained. With  $M \sim 5 M_\odot$ , a zero-age main-sequence star (Hejlesen 1980, C02 model) would be of spectral type B4-B5, with  $T_{\text{eff}}$ ,  $\sim 18,000\text{K}$ ,  $\log L_s/L_\odot \sim 2.60$  and  $R_s \sim 3.2 R_\odot$ . Given a separation of  $210 R_\odot$  and  $q=0.63$ , then the radius of the Roche-lobe filling primary becomes  $R_p \sim 60 R_\odot$  and the luminosity ratio of the two components becomes  $L_p/L_s \sim 65$  since  $T_{\text{eff},p} \sim 11,800\text{K}$  (Chapters 8 and 11). With  $M_p=2.5 M_\odot$ , the surface gravity of the primary becomes  $\log g_p \sim 1.28$ . These values are limits assuming the primary fills its Roche lobe. If it does not then the luminosity ratio will be lower and the surface gravity higher. (The corresponding values for a Terminal Age Main Sequence (TAMS)  $5 M_\odot$  star are spectral type B6,  $T_{\text{eff}}$ ,  $\sim 14,500\text{K}$ ,  $\log L_s/L_\odot \sim 2.8$ ,  $R_s \sim 5.7 R_\odot$  and  $L_p/L_s \sim 50$ ; again limiting values.) Given the relative radii of the stars and their orbital separation, an eclipse will occur for orbital inclinations greater than  $72^\circ$ .

## 2.8 Addendum - The Radial Velocities of $\nu$ Sgr

With the exception of the C III 1247 Å line used to determine the approximate velocity semi-amplitude of the secondary no spectral lines within the composite spectrum have been identified as coming from the secondary. The velocity determinations rely heavily on picking up a weak signal from the secondary component within spectral lines via cross-correlation. Deconvolution was used to confirm the radial velocities but as the template also includes the spectrum cross-correlated against it there is a possibility that *auto-correlation* affected both the original and deconvolved radial velocities. Such a contribution would have been small as the secondary radial velocity semi-amplitude did not converge on the initial value of  $10 \text{ km s}^{-1}$  but on the much larger value of  $29.7 \text{ km s}^{-1}$ . The primary radial velocities would not be affected due to the much stronger correlation.

Two independent checks on the radial velocities were applied. Firstly for both the deconvolved secondary spectra and the composite spectra a template was constructed, one for each spectrum, that did not contain the spectrum that was cross-correlated against it. The previously determined radial velocities were used.

For the deconvolved spectra some sample CCFs are shown in Figure 2.8c). The original peaks in Figures 2.8b) are mainly due to auto-correlation but smaller peaks do appear in roughly the correct positions. The exception is phase 0.73 where a strong peak is found due to the fact that two spectra were available at  $\phi = 0.73$  taken in the same orbit. The spectra are almost identical giving rise to the sharp *quasi*-auto-correlation peak. For the composite spectra the original velocities were recovered.

Secondly a velocity semi-amplitude was assumed and no iterative scheme was used to determine the secondary radial velocities. After template construction and cross-correlation the velocities were inspected to see if the velocities from the original study had been recovered. The assumed semi-amplitudes were from  $0\text{--}70\text{ km s}^{-1}$  in steps of  $10\text{ km s}^{-1}$ . The results are given in Table 2.6. The measurement errors in the results are  $\sim 10\text{ km s}^{-1}$  larger than the errors in the original study due to the smaller peaks caused by the lack of an auto-correlation component. RVORBIT was again used to fit the velocities. From Table 2.6 the original radial velocities are recovered irrespective of which semi-amplitude was assumed. A secondary radial velocity semi-amplitude of  $\sim 27\text{ km s}^{-1}$  is indicated with a systemic velocity of  $\sim 12\text{ km s}^{-1}$  (not tied to the interstellar lines).

These results confirm the validity of the results in the original study.

## 2.9 The Mass Ratio of KS Persei

Unlike  $v\text{ Sgr}$ , which has been well observed at high resolution by IUE, KS Per has only one high resolution spectrum available for it (SWP32200). The primary orbit has been well determined using data over a number of decades (Margoni, Stagni & Mammano 1988). Previous investigators failed to find lines that could be identified with the secondary (Heard 1962) although Drilling & Schönberner (1982) did detect excess UV flux which they attributed to the secondary component (see Chapter 9), in IUE low resolution data. No eclipses have been detected but violet shifted  $H\alpha$  absorption occurs when the primary is behind the secondary (Nariai 1972). This behaviour, similar to that for  $v\text{ Sgr}$ , indicates that the inclination is not far from  $90^\circ$ .

The salient features of the primary's radial velocity curve is a period of  $\sim 360$  days (although a period of half that is also plausible, Margoni *et al.*), with a definite, and large, eccentricity of 0.3. The primary velocity semi-amplitude is  $48\text{ km s}^{-1}$ , the separation  $a \sin i = 330 R_\odot$ , and the mass function  $q = 3.6$ . Both Margoni, Mamanno & Stagni (1988) and Drilling & Schönberner (1982) use this mass ratio to suggest a  $2 M_\odot$  hydrogen-deficient supergiant primary and the secondary as a  $6 M_\odot$  B star.

The KS Per system is different from  $v\text{ Sgr}$  as the eccentricity is non-zero at 0.30. Such an elliptical orbit is at odds with the substantial mass loss / transfer that must have occurred in

Table 2.6: Independent radial velocity determination of  $\nu$  Sgr. For each secondary velocity semi-amplitude used the determined secondary velocity is given, for each of the 16 spectra. The second column gives the results obtained in the original study; those in brackets indicating that the data point was discarded in the original study. The bottom two rows give the systemic velocity and the determined velocity semi-amplitude (both  $\text{km s}^{-1}$ ) after the radial velocities had been analysed with RVORBIT. Errors are in small type.

Spectrum (SWP)	Prev. Vel.	Secondary velocity semi-amplitude used ( $\text{km s}^{-1}$ )							
		0	10	20	30	40	50	60	70
1398	-11	-17	-17	-17	-19	-17	-17	-18	-20
1544	-17	-37	-32	-30	-28	-25	-23	-21	-23
1592	-13	-25	-23	-18	-19	-25	-30	-32	-32
1691	4	8	9	9	11	11	11	14	18
1856	29	-19	-26	-30	-22	-19	-19	-22	-25
2136	(0)	-15	-15	-11	-5	-4	-3	-2	-22
2137	(4)	-10	-8	-5	-6	-9	-10	-12	-13
2219	29	17	17	25	34	38	41	29	24
2492	3	20	22	28	29	28	25	22	8
5473	(-99)	-143	-134	-115	-120	-120	-130	-143	-145
8299	(38)	-62	-61	-61	-63	-69	-70	-70	-70
9110	40	30	34	38	38	36	41	45	41
9118	42	44	42	38	37	35	40	46	47
26096	19	19	20	13	47	47	43	40	33
26103	17	8	5	5	5	7	12	17	15
26881	(-14)	-33	-31	-34	-40	-46	-51	-50	-50
$\gamma_0$		-14	-13	-11	-8	-9	-9	-10	-14
$K_2$		28	26	24	26	26	29	30	28
		13	12	11	13	13	14	15	14

the system and which would have circularised the orbit and have lead to the hydrogen-deficiency observed in the primary (Wallerstein, Greene & Tomley 1967).

The 1230-1380 Å section of SWP32200 was cross-correlated against both the composite and deconvolved secondary template spectra of  $\nu$  Sgr. The results were poor and no secondary radial velocity could be determined.

One explanation that could accommodate both the orbital eccentricity and the hydrogen depletion is to assume that the system is highly evolved. Here what is now the secondary (initially more massive) undergoes Case BB RLOF depositing matter on (what is now) the primary and becomes less massive in the process (*i.e.* becomes like  $\nu$  Sgr is currently). Then the secondary detonates as a type Ib supernova, leaving behind a compact remnant, and disrupting the orbit. The primary star continues to evolve until it leaves the main sequence, and begins to undergo Case B RLOF itself. This is then the current position, with a low mass primary just beginning to lose/transfer mass in a non-circular disrupted orbit. The primary is hydrogen-deficient in its surface layers due to the helium rich material deposited on it during mass transfer when the secondary was a red supergiant. Although this scenario is a logical extension of the HDB evolutionary scenario, and does explain all the main observational points it requires a supernova to have occurred in the system and that a compact object is the secondary. As the secondary has a mass of  $> 3.6 M_{\odot}$  then it must be a black hole, and its progenitor must have been very massive when on the main sequence. This would mean the supernova would occur relatively early in the history of the binary star (10 million years for a  $15 M_{\odot}$  star). 600 million years would pass before the  $\sim 2 M_{\odot}$  star began to evolve up the giant branch. The interval is sufficient to have removed all evidence for the original supernova explosion except for the black hole remnant. Interestingly KS Per has been previously suggested as having a black hole companion (Zeldovich & Guseinov 1965; Guseinov & Novruzova 1973). It was these investigations that prompted Margoni *et al.* to look further at KS Per although they subsequently accepted Drilling & Schönberner's model. If a black hole were present then an X-ray flux should be present although the large separation of components ( $\sim 1.5$  A.U.) would limit it.

## 2.10 Summary

*Using an improved cross-correlation technique and high resolution IUE spectra radial velocities for the secondary component of  $v$  Sgr have been determined and the primary radial velocities confirmed. The primary has a velocity semi-amplitude of  $47 \text{ km s}^{-1}$  and the secondary  $30 \text{ km s}^{-1}$ . From the radial velocity orbit the revised ephemeris is  $T = 2447916.16 + 137.954n$ .*

*From these data an orbit was determined which fixes the minimum masses of the components at  $2.5$  and  $4.0 M_{\odot}$  respectively (mass ratio  $0.63$ ), and a minimum separation of  $210 R_{\odot}$ .*

*These results constitute the first positive detection of the secondary, the first determination of the secondary radial velocity curve and by extension the first mass determinations for  $v$  Sgr and thus the first for any HDB.*

*The system does not show eclipses up to 4 days before conjunction but the long standing problem of whether eclipses occur at all cannot be answered by this study.*

*The inclination has been shown to lie in the range  $78^{\circ} \leq i \leq 65^{\circ}$  from the geometry of the mass transfer between the two components. The masses of the two components are then  $3.0 \pm 0.3 M_{\odot}$  and  $4.8 \pm 0.5 M_{\odot}$  for the primary and secondary respectively.*

*This determination of the absolute masses and sizes of the system puts  $v$  Sgr on a real observational footing and allows detailed modelling of the system in terms of past and future evolution, especially the problem of the final state of  $v$  Sgr - a SN Ib or not?*

## 2.11 References

- Barker, P., 1984. *Astr. J.*, **89**, 899.
- Bassett, E.E., 1978. *Observatory*, **98**, 123.
- Delgado, A.J. & Thomas, H.-C., 1981. *Astr. Astrophys.*, **96**, 142.
- Drilling, J.S. & Schönberner, D., 1982. *Astr. Astrophys.*, **113**, L22.
- Dudley, R.E. & Jeffery, C.S., 1990. *Mon. Not. R. astr. Soc.*, **247**, 400.
- Duvigneau, H., Friedjung, M. & Hack, M., 1979. *Astr. Astrophys.*, **71**, 310.
- Eggen, O.J., Kron, G.E. & Greenstein, J.L., 1950. *Publs astr. Soc. Pacif.*, **62**, 171.
- Guseinov, O.H. & Novruzova, H.I., 1971. *Astrofizika*, **7**, 5.
- Heard, J.F., 1962. *Publ. David Dunlap Obs.*, **2**, 269.
- Hack, M. & Pasinetti, L., 1963. *Contr. Oss. astr. Milano-Merate*, **215**, 1.
- Hejlesen, P.M., 1980. *Astr. Astrophys. Suppl.*, **39**, 347.
- Hellings, P., de Loore, C., Burger, M. & Lamers, H.J.G.L.M., 1981. *Astr. Astrophys.*, **101**, 161.
- Howarth, I.D. & Murray, J., 1991. *STARLINK User Note 50.13*.
- Jeffery, C.S., Drilling, J.S. & Heber, U., 1987. *Mon. Not. R. astr. Soc.*, **226**, 317.
- Kopal, Z., 1959. *Close Binary Systems*, Chapman & Hall, London.
- Leushin, V.V. & Topil'skaya, G.P., 1984. *Astrophysics*, **22**, 74.
- Lubow, S.H. & Shu, F.H., 1975. *Astrophys. J.*, **198**, 383.
- Lucy, L.B., 1989. *Observatory*, **109**, 100.
- Malcolm, G. & Bell, S.A., 1986. *Mon. Not. R. astr. Soc.*, **222**, 543.
- Margoni, R., Stagni, R. & Mammano, A., 1988. *Astr. Astrophys. Suppl.*, **75**, 157.
- Moore, C.E., 1950. *Circular of the NBS*, **488**, Section 1.
- Moore, C.E., 1952. *Circular of the NBS*, **488**, Section 2.
- Morrison, K., 1988. *Mon. Not. R. astr. Soc.*, **233**, 621.
- Nariai, K., 1967. *Publs astr. Soc. Japan*, **19**, 564.
- Nariai, K., 1972. *Publs astr. Soc. Japan*, **24**, 495.
- Parthasarathy, M., Cornachin, M. & Hack, M., 1986. *Astr. Astrophys.*, **166**, 237.
- Rao, N.K. & Venugopal, V.R., 1985. *J. Astrophys astr.*, **6**, 101.

- Rees, P. & Giddings, J., 1989. *STARLINK User Note 37.7*.
- Schönberner, D. & Drilling, J.S., 1983. *Astrophys. J.*, **268**, 225.
- Uomoto, A., 1986. *Astrophys. J.*, **310**, L35.
- Wallerstein, G., Greene, T.F. & Tomley, L.J., 1967. *Astrophys. J.*, **150**, 245.
- Wiese, W.L., Smith, M.W. & Glennon, B.M., 1966. *Atomic Transition Probabilities*, NBS, Washington.
- Wiese, W.L., Smith, M.W. & Miles, B.M., 1969. *Atomic Transition Probabilities*, NBS, Washington.
- Wilson, R.E., 1914. *Lick Obs. Bull.*, **8**, 132.
- Zeldovich, Ya.B. & Guseinov, O.H., 1965. *Astrophys. J.*, **144**, 841.

## Chapter 3

# The Wolf-Rayet Binary $\gamma^2$ Velorum

### 3.1 Introduction

$\gamma^2$  Vel is a double-lined binary consisting of a WC8 Wolf-Rayet (WR) primary of  $\sim 6 M_{\odot}$  orbiting a  $\sim 18 M_{\odot}$  O9I supergiant (Stickland & Lloyd 1990).

Wolf-Rayet stars are massive evolved objects<sup>1</sup> whose evolution is thought to consist of phases of mass transfer within the binary system and mass loss from the system (binary stars) or massive stellar winds alone (single stars). The rapid mass loss is indicated by strong P Cygni profiles in the UV. (See Hillier (1990) for a discussion of WR emission line formation.) They are hydrogen poor and helium rich and show overabundances of carbon or nitrogen (the WC and WN classifications respectively). They are young, Population I, objects many, if not most, of which are now found in binary systems in orbit around a OB star (Cherepashchuk 1991). See Abbott & Conti (1987) and I.A.U. Symposium No. 143 (van der Hucht & Hidayat 1991) for reviews of WR stars.

Wolf-Rayet stars have been extensively studied over the years as there are still many unanswered questions about their past, and subsequent, evolution including:

- What are their masses? Accurate determinations of masses have so far been few as radial velocities are difficult to determine.
- Mass-loss rates need to be determined to help determine the evolutionary status. (Section V

---

<sup>1</sup>Not everyone holds this view. Some evidence has been presented that WR stars are pre-Main Sequence objects of solar composition that have low mass-loss rates. See Underhill (1991).

in van der Hucht & Hidayat 1991).

- The evolutionary history of these objects needs to be refined (Section VII in van der Hucht & Hidayat 1991). Are the WC and WN series connected to main sequence stars by the sequence  $O \Rightarrow WN \Rightarrow WC$ ? Are Wolf-Rayet stars connected with high mass X-ray binaries and how does mass loss and the binary nature of these stars affect the evolution of the individual components and the system as a whole?
- Are they possible progenitors of Type Ib supernovae (Nomoto 1991; Filippenko 1991).

The most fundamental of these problems is the lack of accurately determined masses. Good WR masses are needed to put other observations and theory (especially evolutionary calculations) on a sounder footing. As an offshoot, the analysis of WR systems should also lead to more accurate masses of OB stars, poorly known at present, further refining general evolutionary calculations.

In many ways WR-OB binary systems appear to be more massive counterparts to the HDBs, in that mass transfer seems to account for the peculiar spectra in both systems. However, everything in the WR-OB systems is more extreme than in the HDBs and mass transfer may have exposed processed CNO material (WN stars) or, at a later stage,  $3\alpha$  material (WC stars). Just as HDBs have been postulated as Type Ib supernova progenitors (Uomoto 1986) so have WR stars (*e.g.* Begelman & Sarazin 1986; Schaefer, Cassé & Cahen 1987). Although some authors (Ensmann & Woosley 1988) categorically rule out this possibility the question still appears to be open (Filippenko 1991).

It is difficult to determine radial velocities for WR stars because the absorption lines are difficult to find, being shallow and broad. Thus the prominent emission lines are often used to trace the orbital motion of the WR component. However it is not certain where in the massive stellar wind or extended photosphere the emission lines are formed or how they may be affected by the binary nature of the system.

Also, in the case of  $\gamma^2$  Vel at least (Baade, Schmutz & Kerkwijk 1990), the primary is a non-radial pulsator leading to periodic line profile variations. However some WR spectra show similar variations that have not been attributed to any cause, further hampering accurate radial velocity determinations. (See van der Hucht & Hidayat 1991, Section III and especially Moffat & Robert 1991.)  $\gamma^2$  Vel is the brightest WR in the sky and has thus been well studied, the orbit first being determined in 1968 (Ganesh & Bappu) with further investigations by Willis (1975); Niemela & Sahade (1980); Pike, Stickland & Willis (1983); Moffat, Vogt, Paquin, Lamontagne & Barrera (1986), and Stickland & Lloyd (1990).

The most recent orbital determination, by Stickland & Lloyd, used data from the IUE archive and absorption lines from both objects to determine an orbit. Their results are in approximate

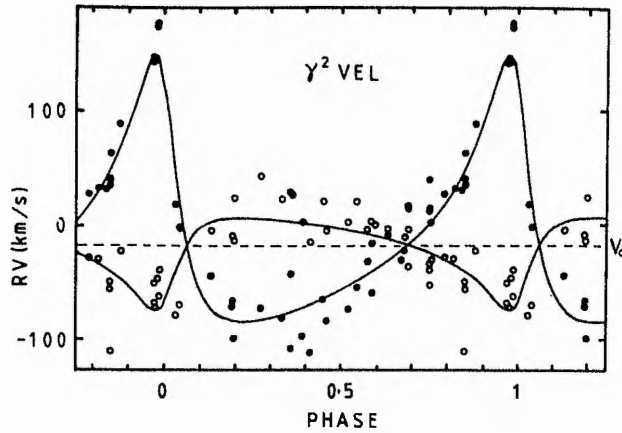


Figure 3.1: The orbit of  $\gamma^2$  Vel determined by Stickland & Lloyd (1990) from IUE spectra. Filled circles are the WR star, open circles the O supergiant. Error bars are typically  $25 \text{ km s}^{-1}$ .

agreement with the previous orbits although they must still suffer from the line profile variability problem.

Stickland & Lloyd get a good spread of possible orbits just using their data depending on whether they chose to solve for a single or double-lined orbit. Eventually they fix the period and eccentricity to obtain a final orbit. This orbit is shown in Figure 3.1, and shows considerable scatter in the data.

The largest problem with their analysis was that only 6 lines were used to determine the orbit of the O star and 10 more for the WR component. Considering the line profile variation and the low number of lines it was to be expected that the derived radial velocities had large errors.

A further radial velocity study of  $\gamma^2$  Vel to try to determine more accurate masses was deemed appropriate, using the techniques developed for  $\nu$  Sgr for a number of reasons.

- Masses of WR and O stars are so important that any new means of investigation should be employed.
- To test the template sharpening and cross-correlation (TS-CC) method on data that had already been analysed to determine radial velocities using a different, and more conventional, technique.
- To confirm or reject Stickland & Lloyd's results and by comparison to determine the validity of using emission lines to obtain orbital radial velocities in a binary system.
- The  $\gamma^2$  Vel IUE data was readily available, was plentiful and had good signal-to-noise. The system also fulfilled the requirements that the period and phasing of the orbit is well known

Table 3.1: IUE SWP spectral data for  $\gamma^2$  Vel.

Spectrum	J.D. (-2440000)	dd/mm/yy	ddd/yy	Type	Aperture	Exposure (seconds)	ITFMAX	THDA
SWP1358	3613	14/04/78	104/78	GPHOT	SAP	3	19983	-
SWP1359	3613	14/04/78	104/78	GPHOT	SAP	6	19983	-
SWP1413	3624	25/04/78	115/78	GPHOT	SAP	5	19983	-
SWP1425	3626	27/04/78	117/78	GPHOT	SAP	5	19983	-
SWP1545	3645	15/05/78	136/78	GPHOT	SAP	5	19983	-
SWP1546	3645	15/05/78	136/78	GPHOT	SAP	6	19983	-
SWP1605	3653	23/05/78	144/78	GPHOT	SAP	5	19983	-
SWP1606	3653	23/05/78	144/78	GPHOT	SAP	5	19983	-
SWP1717	3664	04/06/78	155/78	GPHOT	SAP	1	19632	-
SWP1718	3664	04/06/78	155/78	GPHOT	SAP	3	19632	-
SWP1719	3664	04/06/78	155/78	GPHOT	SAP	5	19632	-
SWP1811	3679	19/06/78	170/78	GPHOT	SAP	5	19632	-
SWP2070	3711	21/07/78	202/78	GPHOT	SAP	4	19632	-
SWP2290	3735	14/08/78	226/78	GPHOT	SAP	5	19632	-
SWP2291	3735	14/08/78	226/78	GPHOT	SAP	2	19632	-
SWP2295	3735	14/08/78	226/78	GPHOT	SAP	2	19632	-
SWP2388	3745	24/08/78	236/78	PHOT	SAP	6	19632	-
SWP2389	3745	24/08/78	236/78	GPHOT	SAP	12	19632	-
SWP2504	3758	06/09/78	249/78	GPHOT	SAP	6	19632	-
SWP2514	3759	07/09/78	250/78	GPHOT	SAP	5	19632	-
SWP2683	3770	16/09/78	261/87	GPHOT	SAP	6	19632	-
SWP2817	3783	01/10/78	274/78	GPHOT	SAP	6	19632	-
SWP2964	3795	13/10/78	286/78	GPHOT	SAP	4	19632	-
SWP3139	3807	25/10/78	298/78	GPHOT	SAP	4	19632	-
SWP3271	3821	08/11/78	312/78	GPHOT	SAP	6	19632	-
SWP3377	3831	18/11/78	322/78	GPHOT	SAP	3	19632	-
SWP3378	3831	18/11/78	322/78	GPHOT	SAP	3	19632	-
SWP3379	3831	18/11/78	322/78	GPHOT	SAP	4	19632	-
SWP3386	3832	19/11/78	323/78	GPHOT	SAP	3	19632	-
SWP3498	3844	01/12/78	335/78	GPHOT	SAP	3	19632	-
SWP3572	3855	12/12/78	346/78	GPHOT	SAP	3	19632	-
SWP3677	3866	23/12/78	357/78	GPHOT	SAP	3	19632	-
SWP3935	3892	18/01/79	018/79	GPHOT	SAP	3	19632	-
SWP4636	3948	15/03/79	074/79	GPHOT	SAP	3	19632	-
SWP4719	3954	21/03/78	080/79	GPHOT	SAP	3	19632	-
SWP6480	4035	10/06/79	161/79	GPHOT	SAP	5	19632	-
SWP6175	4099	13/08/79	225/79	GPHOT	SAP	2	19632	-
SWP6351	4118	01/09/79	244/79	GPHOT	SAP	5	19632	-
SWP6532	4133	16/09/79	259/79	GPHOT	SAP	3	19632	-
SWP6672	4146	29/09/79	272/79	GPHOT	SAP	6	19632	-
SWP6673	4146	29/09/79	272/79	GPHOT	SAP	6	19632	-
SWP6674	4146	29/09/79	272/79	GPHOT	SAP	6	19632	-
SWP6675	4146	29/09/79	272/79	GPHOT	SAP	6	19632	5.81
SWP6676	4146	29/09/79	272/79	GPHOT	SAP	6	19632	5.81
SWP7200	4200	22/11/79	326/79	GPHOT	SAP	3	19632	-
SWP7980	4288	18/02/80	049/80	GPHOT	SAP	3	19632	-

so that that the template sharpening method should have a reasonable chance of success.

### 3.2 The Data

The high resolution IUE data for  $\gamma^2$  Vel consists of 47 SWP spectra and 36 LWP ones of which 46 and 33 respectively were available from the Rutherford Appleton Laboratory (RAL) at the time of analysis. The unobtainable spectra were LWR1691, LWR2511, LWR2512 and SWP1761. Data for both the LWR and SWP spectra are given in Tables 3.1 and 3.2. The frames were processed in exactly the same way as was described for  $\nu$  Sgr.

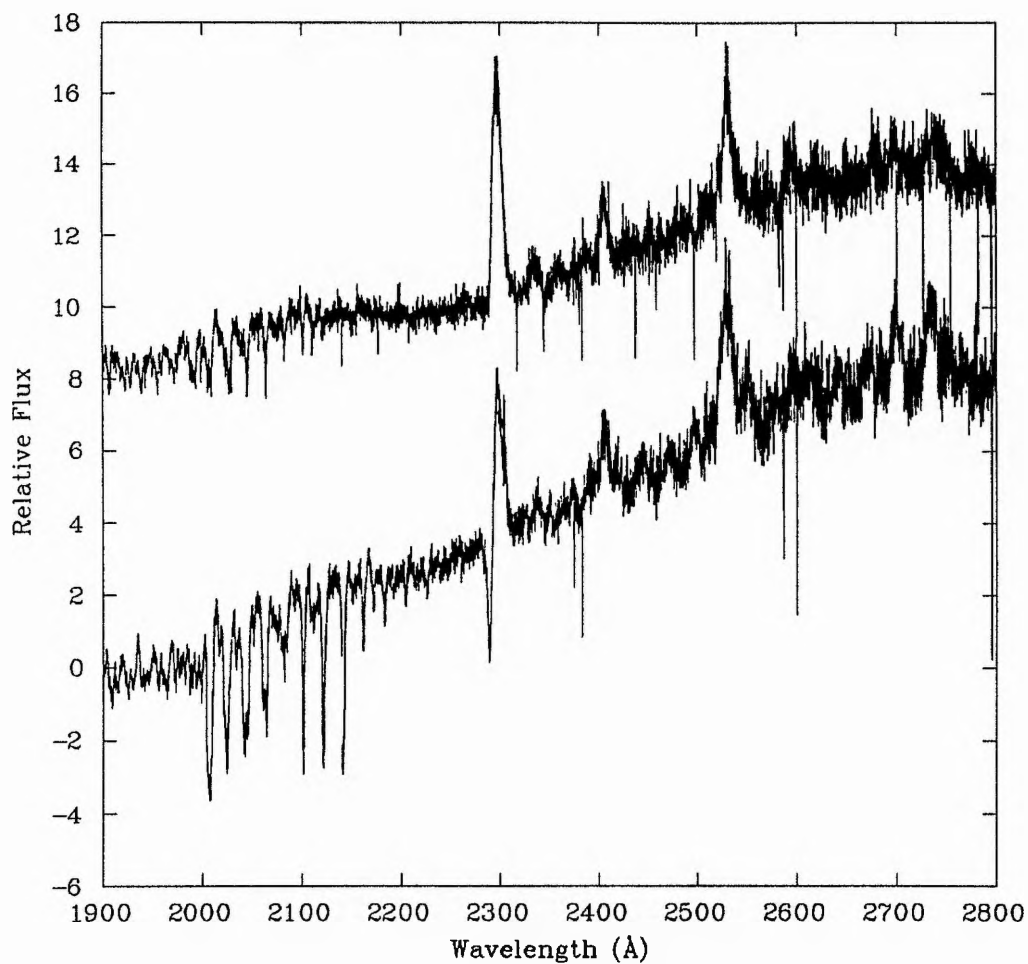


Figure 3.2: Two sections of LWR IUE spectra of  $\gamma^2$  Vel. Lower - LWR1315 showing a P Cygni profile at  $\sim 2300 \text{\AA}$ . Upper - LWR1497 showing only an emission peak. A vertical offset of 8 units has been applied to the upper spectrum.

Table 3.2: IUE LWR spectral data for  $\gamma^2$  Vel.

Spectrum	J.D. (-2440000)	dd/mm/yy	ddd/yy	Type	Aperture	Exposure (seconds)	ITPMAX	THDA
LWR1315	3613	14/04/78	104/78	GPHOT	SAP	5	20000	-
LWR1316	3613	14/04/78	104/78	GPHOT	SAP	8	20000	-
LWR1396	3626	27/04/78	117/78	GPHOT	SAP	7	20000	-
LWR1497	3645	15/05/78	136/78	GPHOT	SAP	7	27220	-
LWR1498	3645	15/05/78	136/78	GPHOT	SAP	8	27220	-
LWR1543	3653	23/05/78	114/78	GPHOT	SAP	7	20000	-
LWR1619	3666	06/06/78	187/78	GPHOT	SAP	4	27220	-
LWR1681	3670	10/06/78	161/78	GPHOT	SAP	7	20000	-
LWR1869	3711	21/07/78	202/78	GPHOT	SAP	4	27220	-
LWR2073	3735	14/08/78	226/78	GPHOT	SAP	12	27220	-
LWR2074	3735	14/08/78	226/78	GPHOT	SAP	4	27220	-
LWR2076	3735	14/08/78	226/78	GPHOT	SAP	5	27220	-
LWR2167	3743	24/08/78	236/78	GPHOT	SAP	3	27220	-
LWR2296	3759	07/09/78	250/78	GPHOT	SAP	4	27220	-
LWR2596	3796	14/10/78	287/78	GPHOT	SAP	3	27220	-
LWR2708	3808	25/10/78	298/78	GPHOT	SAP	3	27220	-
LWR2882	3822	08/11/78	312/78	GPHOT	SAP	3	27220	-
LWR2963	3831	18/11/78	322/78	GPHOT	SAP	3	27220	-
LWR2964	3831	18/11/78	322/78	GPHOT	SAP	4	27220	-
LWR2973	3832	19/11/78	323/78	GPHOT	SAP	3	27220	-
LWR3075	3844	21/11/78	325/78	GPHOT	SAP	3	27220	-
LWR3145	3855	12/12/78	346/78	GPHOT	SAP	3	27220	-
LWR3240	3866	23/12/78	357/78	GPHOT	SAP	3	27220	-
LWR3510	3892	18/01/79	018/79	GPHOT	SAP	3	27220	-
LWR4026	3948	15/05/79	074/79	GPHOT	SAP	3	27220	-
LWR4084	3954	21/05/79	080/79	GPHOT	SAP	3	27220	-
LWR4753	4035	10/06/79	161/79	GPHOT	SAP	4	27220	-
LWR5340	4099	13/08/79	228/79	GPHOT	SAP	3	27220	-
LWR5486	4118	01/09/79	244/79	GPHOT	SAP	3	27220	-
LWR5601	4133	16/09/79	259/79	GPHOT	SAP	3	27220	-
LWR5717	4146	29/09/79	272/79	GPHOT	SAP	4	27220	-
LWR6210	4200	22/11/79	326/79	GPHOT	SAP	3	27220	-
LWR6952	4288	18/02/80	049/80	GPHOT	SAP	3	27220	-

### 3.3 Radial Velocity Determination

A number of subsets of the available data were used for the TS-CC and are catalogued below. In general all features that were not photospheric absorption lines were removed and the continuum subtracted just as in the analysis of  $\nu$  Sgr. Figure 3.2 shows two spectra of  $\gamma^2$  Vel. The P Cygni profiles characteristic of rapid mass loss in WR stars are evident in one spectrum but only an emission peak is visible in the other.

1. SWP 1248-1308 Å, direct summation of all the images to form the initial template. Results poor, getting poorer on TS-CC.
2. SWP 1248-1308 Å, initial template constructed by shifting to published (Stickland & Lloyd 1990) WR velocities. Results reasonable but  $K_{WR}$  smaller than the published value,  $e$  in agreement with their single-lined WR solution (0.59), but not their final double-lined solution.
3. SWP 1248-1308 Å, direct summation of 9 spectra having approximately the same phase (SWP3377-3379, SWP6672-6676) to overcome the possibility the the period was not the  $\sim 78$  days reported. Results promising but after TS-CC  $e$  drops to 0.1 and  $K_{wr} = 29 \text{ kms}^{-1}$ . All CCF's are "poor", possibly due to the reduced S/N in the template (formed from only 9 spectra). After removing all velocity points that were clustered around the systemic velocity,

$$e = 0.64 \text{ and } K_{WR} = 35 \text{ km s}^{-1}.$$

4. SWP 1248-1308 Å, phase binning the spectra into 11 groups having a similar phase, a mean phase being calculated for each group by weighting the phases of the individual spectra by the length of their exposure. A reasonable orbit resulted.
5. LWR 2543-2580 Å, direct summation of all data. Results poor.
6. LWR 2543-2580 Å, initial template from sharpening on the published (Stickland & Lloyd 1990) velocities of the O star. Results poor.
7. LWR 2543-2580 Å, as above, sharpening on the WR published orbit. Results poor.
8. LWR 2543-2580 Å, using a single spectrum (LWR1497) as a template. Results poor.
9. LWR 2600-2660 Å, initial template sharpened on published O star orbit. Results poor.

From the analysis nothing could be obtained from the LWR data except that the TS-CC results did not reproduce Stickland & Lloyd's results for either component.

The SWP analysis produced better results, although each analysis produced a significantly different orbit. These results are shown in Table 3.3 and three of the determined radial velocity curves (1,2 and 4 in the above list) are shown in Figure 3.3.

### 3.4 Discussion

Template sharpening and cross-correlation gave quite poor results in the case of  $\gamma^2$  Vel. The reason for this is that once the wind, interstellar and emission lines have been removed there were very few features left from which to determine an orbit. The lines that were there were shallow and broad and thus sharp CCF peak are not recorded; all the peaks were broad and thus all the velocities are subject to large error. Together with the line profile variability which also distorts the CCF the low quality of the results is perhaps not surprising. A section of sharpened template is shown in Figure 3.4; however as no orbit could be said to be the definitive one the sharpened template also cannot be taken to be exactly correct. As can be seen the photospheric lines that appear to be present are weak and broad.

A number of points arise from this analysis. Firstly when sharpening on the velocities determined by Stickland & Lloyd (1990) their results were not reproduced exactly. However the eccentricity found was almost the same as quoted by them for their single-lined WR solution which suggests that the TS-CC technique was picking up the WR star with little difficulty. However the velocity semi-amplitude determined is much less than they quoted. The results presented here are too poor to say that Stickland & Lloyd's orbit is incorrect only that the results are not consistent

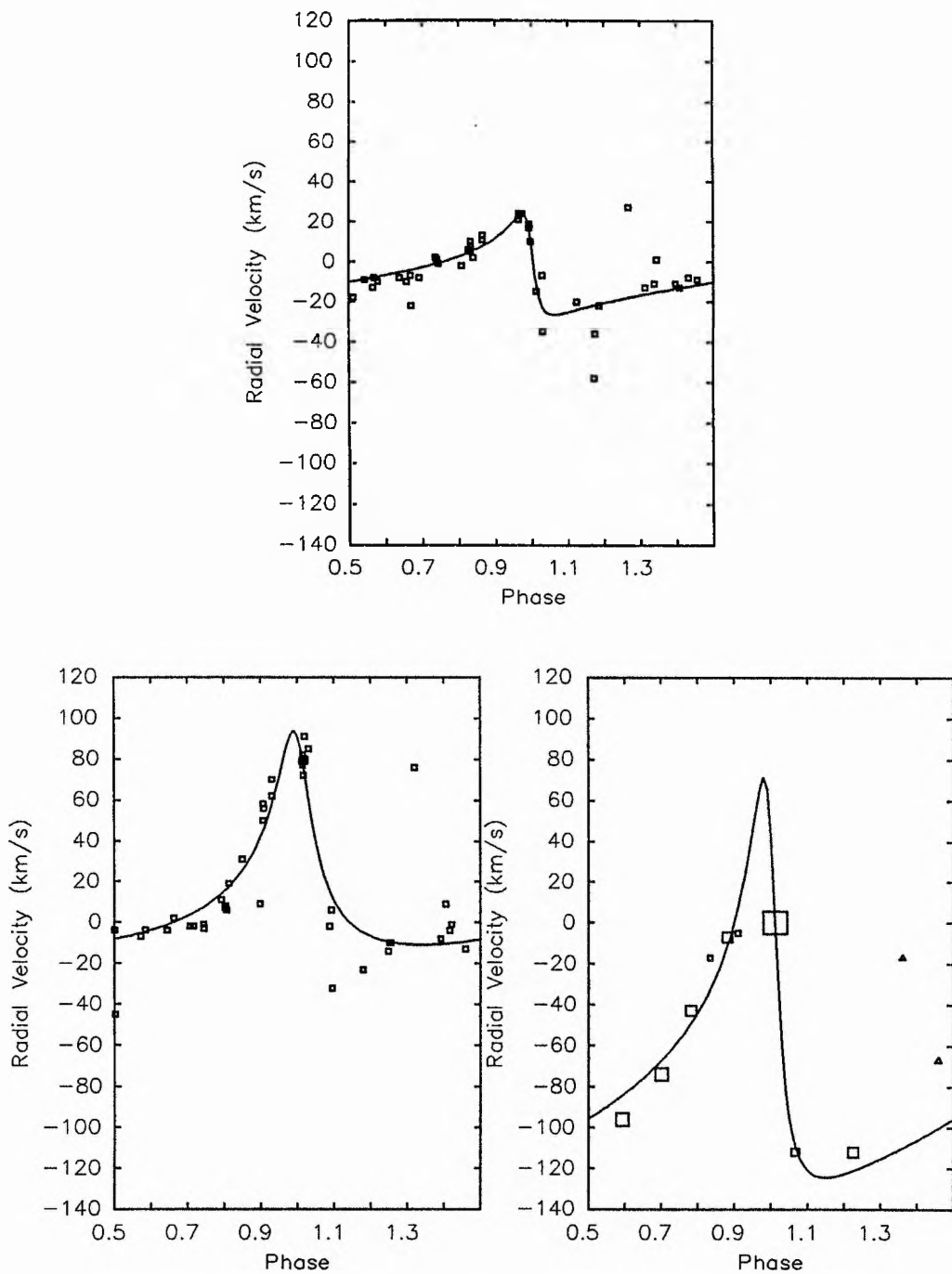


**Figure 3.3:** Three radial velocity curves for  $\gamma^2$  Vel, all using the SWP spectra in the region 1248-1308 Å only. Upper - The template constructed from a direct summation of all the spectra. Lower left - The template constructed by shifting all the spectra to Stickland & Lloyd's published WR velocities. Lower right - The spectra binned into 11 groups each containing spectra of approximately the same phase. The size of the symbols is indicative of the number of spectra in the group. For the final orbit two data points (triangles) were discarded and the other data points were weighted according to the number of spectra they contained.

Table 3.3: Summary of results from SWP analysis of  $\gamma^2$  Vel. The final orbit and single-lined WR solutions from Stickland & Lloyd are given for comparison.

Ref.	$K_{WR}$	$K_O$	$P$	$V_0$	$\omega$	$e$	$T_{max}$
(1)	118.6	40.8	<i>78.519</i>	-18	221	0.53	597.5
	5.2	5.1		2.7	6	0.03	0.8
(2)	121.1	-	<i>78.519</i>	-18	43	0.59	597.6
	5.5			3.7	7	0.03	0.8
(3)	25.4	-	78.160	-7.9	249	0.74	629.1
	4.3		0.218	1.7	12	0.08	9.5
(4)	52.3	-	78.843	11.36	17	0.60	597.3
	16.9		0.268	3.3	13	0.12	10.2
(5)	29.0	-	<i>78.519</i>	-46	145	0.16	577.8
	9.7			6.4	114	0.23	24.6
(6)	46.5	-	<i>78.519</i>	50.6	243	0.10	570.4
	5.1			3.9	70	0.10	14.5
(7)	97.9	-	<i>78.519</i>	-73.7	45	0.68	570.4
	26.7			4.7	11	0.10	0.7

Notes

- (1) - Stickland & Lloyd's final double-lined orbit.
- (2) - Stickland & Lloyd's single-lined WR orbit.
- (3) - Template from direct summation (#1 in list above).
- (4) - Sharpening on Stickland & Lloyd's published WR orbit (#2).
- (5) - 9 co-added spectra of similar phase, first pass (#3).
- (6) - 9 co-added spectra of similar phase, later pass after removing systemic velocity points (#3).
- (7) - Phase binned orbit (#4).

Small figures are errors.

Italics denote an adopted (not derived) value.

$T_{max}$  is days after J.D. 2443000.

The systemic velocities ( $V_0$ ) have no absolute significance.

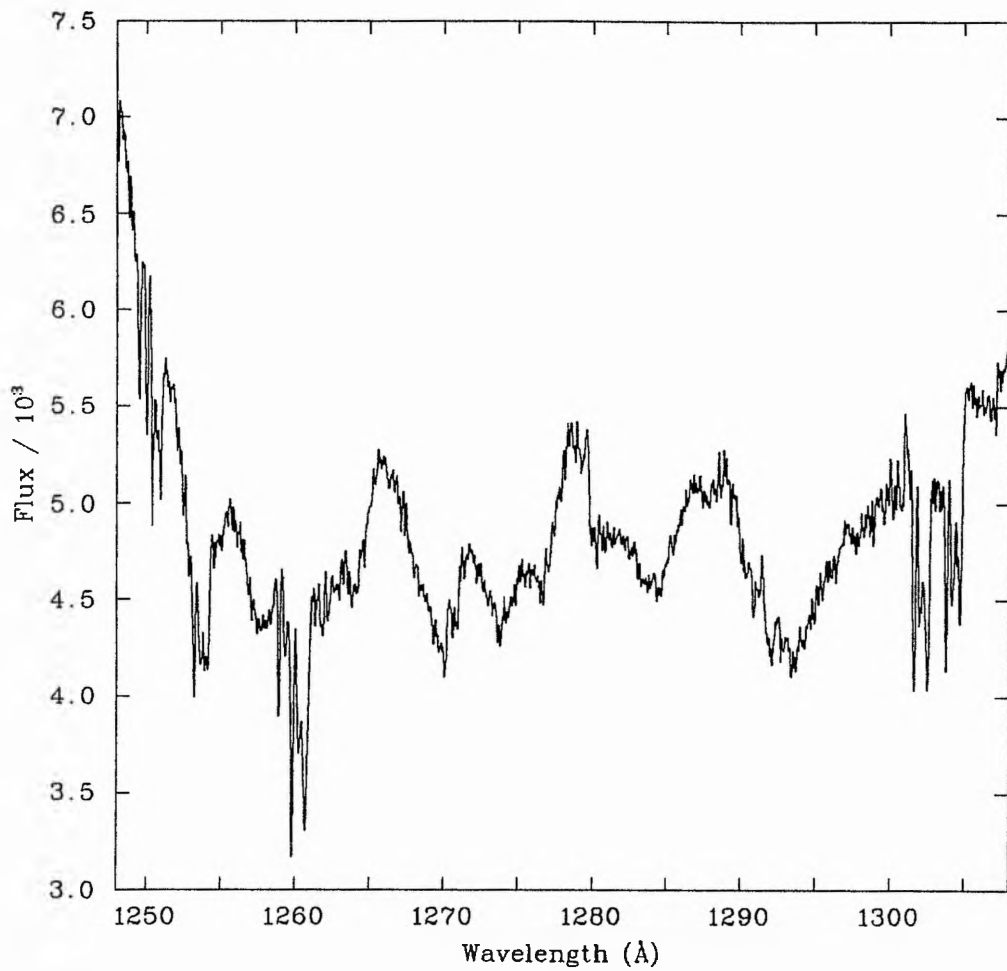


Figure 3.4: A section of the sharpened spectrum of  $\gamma^2$  Vel showing the shallow broad lines.

with theirs. The results are not of sufficient quality to replace theirs - they only weakly indicate that they may be wrong.

As the lines in the spectra of both stars will be weak and broad there will be a tendency for the lines of one star to "pull" the lines of the other towards it (as far as TS-CC is concerned) simply due to the merging of the two lines. This is especially true for stars with similar temperatures and chemical compositions where most lines will have a component from both stars. This is true of  $\gamma^2$  Vel and thus it may be expected that the velocity semi-amplitudes determined from the template sharpening and cross-correlation method will be too small. This seems to be the case; although whether this is the whole explanation for the discrepancy between the results here and Stickland & Lloyd's is still an open question.

### 3.5 Summary

*The cross-correlation with template sharpening technique described in Chapter 2 have been applied with less success to the Wolf-Rayet binary  $\gamma^2$  Vel.*

*The results are poor for both the analysis in the SWP and LWR regions of spectra despite the large amount of good quality data. The results do not confirm or reject previous orbits published for  $\gamma^2$  Vel.*

*Despite failing in this application, the analysis of  $\gamma^2$  Vel has allowed some of the limitations of the template sharpening and cross-correlation method to be brought to light. Principally that sharp lined objects or those with very high relative radial velocities are required.*

### 3.6 References

- Abbott, D.C. & Conti, P.S., 1987. *Ann. Rev. Astr. Astrophys.*, **25**, 113.
- Baade, D., Schmutz, W. & Kerkwijk, M. van., 1990. *Astr. Astrophys.*, **240**, 105.
- Begelman, M.C. & Sarazin, C.L., 1986. *Astrophys. J.*, **302**, L59.
- Cherepashchuk, A.M., 1991. In: *Wolf-Rayet Stars and Interrelations with other Massive Stars in Galaxies*, I.A.U. Symposium No. 143, p.187, eds. van der Hucht, K.A. & Hidayat, B., Kluwer.
- Ensmann, L.M. & Woosley, S.E., 1988. *Astrophys. J.*, **333**, 754.
- Filippenko, A.V., 1991. In: *Wolf-Rayet Stars and Interrelations with other Massive Stars in Galaxies*, I.A.U. Symposium No. 143, p.529, eds. van der Hucht, K.A. & Hidayat, B., Kluwer.
- Ganesh, K.S. & Bappu, M.K.V., 1968. *Kodiakanal Obs. Bull., Ser. A*, **183**, 177.
- Hillier, D.J., 1990. In: *Properties of Hot Luminous Stars*, *Astron. Soc. Pacific Conf. Series*, vol. 7, p.340, eds. Garmany, C.D., .
- Moffat, A.F.J. & Robert, C., 1991. In: *Wolf-Rayet Stars and Interrelations with other Massive Stars in Galaxies*, I.A.U. Symposium No. 143, p.109, eds. van der Hucht, K.A. & Hidayat, B., Kluwer.
- Moffat, A.F.J., Vogt, N., Paquin, G., Lamontagne, R. & Barrera, L.H., 1986. *Astr. J.*, **91**, 1386.
- Niemela, V.S. & Sahade, J., 1980. *Astrophys. J.*, **238**, 44.
- Nomoto, K., 1991. In: *Wolf-Rayet Stars and Interrelations with other Massive Stars in Galaxies*, I.A.U. Symposium No. 143, p.515, eds. van der Hucht, K.A. & Hidayat, B., Kluwer.
- Pike, C.D., Stickland, D.J. & Willis, A.J., 1983. *Observatory*, **103**, 154.
- Schaefer, R., Cassé, M. & Cahen, S., 1987. *Astrophys. J.*, **316**, L31.
- Stickland, D.J. & Lloyd, C., 1990. *Observatory*, **110**, 1.
- Underhill, A.B., 1991. In: *Wolf-Rayet Stars and Interrelations with other Massive Stars in Galaxies*, I.A.U. Symposium No. 143, p.53, eds. van der Hucht, K.A. & Hidayat, B., Kluwer.
- Uomoto, A., 1986. *Astrophys. J.*, **310**, L35.
- van der Hucht, K.A. & Hidayat, B. (eds.), 1991. *Wolf-Rayet Stars and Interrelations with other Massive Stars in Galaxies*, I.A.U. Symposium No. 143, Kluwer.
- Willis, A.J., 1975. *Ph.D. Thesis, University College London*.

## Chapter 4

# UV Wind Line Analysis

### 4.1 Introduction

Many hot stars show the effects of stellar winds and mass loss in the UV part of the spectrum (*e.g.* Pauldrach, Kudritzki, Puls & Butler 1990, hereafter PKPB). The types of profiles include:

- Emission line profiles. (Wolf-Rayet stars.)
- P Cygni profiles. (OB supergiants.)
- Absorption lines with extended violet wings. (OB main sequence stars.)

The analysis of wind line profiles can lead to an accurate determination of the structure of the wind, including the composition, velocity, temperature, ionisation, and density.

These results can then be used, in principle, to estimate the mass loss from the star. However the results are usually for a single ion of a single element. To get details of the mass loss, density *etc* for a given element requires the ionisation fraction of the element to be known. To determine the ionisation fraction requires NLTE codes and a knowledge of the temperature structure of the wind. Current indications are that the “superionised” winds once invoked to explain the ionisation structure in winds (*e.g.* Hamann, Schönberner & Heber 1982) are no longer required if the NLTE analysis is sufficiently detailed; a “cool wind” model will then explain the very high ionisation states (see Kudritzki 1988 for a review and PKPB).

There are three methods available for modelling wind line profiles, all of which have their advantages and disadvantages. They are the co-moving frame method, the Sobolev approximation and the improved NLTE method. See Kudritzki (1988) for a review of all these methods.

The Sobolev method (Sobolev 1947, 1957; Rybicki & Hummer 1978; Olson 1982 and Lamers, Cerruti-Sola & Perinotto 1987) uses the Sobolev approximation to enable the solution of the radiative transfer and scattering equations to be computed more simply. The Sobolev approximation is that the photons from the atmosphere interact with the wind over a very small interaction region over which the wind parameters (density, temperature, radiation intensity *etc*) vary little. Thus large velocity gradients in the wind are required to keep the interaction region small. This method begins to break down at the line centers and where the turbulent velocity in the wind is greater than  $\sim 5\%$  of the terminal velocity.

The co-moving frame method (Mihalas, Kunasz & Hummer 1975; Hamann 1980, 1981) has the advantage that it is very accurate and can be used for stellar atmospheres with small velocity gradients, overcoming the problems with the Sobolev approximation. It avoids the large number of lines of sight and frequency points associated with determining the intensity at the observer. The co-moving frame method solves the equation of transfer, not in the observers (fixed) frame of reference, but in the frame of reference seen by a moving volume element in the wind. For a choice between the co-moving frame and Sobolev methods the co-moving frame method is clearly indicated.

However, Lamers, Cerruti-Sola & Perinotto (1987) extended the Sobolev method by solving the scattering integral using the Sobolev approximation and using a two level atom source function in the wind, followed by the exact integration of the radiative transfer equation. Like the other investigators they calculated the source function by using the escape probability method (*e.g.* Olson 1982). Their improved method was named "SEI" for "Sobolev with Exact Integration". Compared with the co-moving frame method the improved Sobolev method has the advantages of being very fast and has only small differences between it and the co-moving frame method itself (Lamers *et al.*, Hamann 1980, 1981, Pauldrach, Puls & Kudritzki 1986).

The third method of determining wind line profiles is not to fit empirical profiles to the observed profiles by determining such parameters as the optical depth and velocity laws by trial and error but to use improved NLTE atmosphere codes to generate the profiles, requiring only basic stellar parameters as input. They are based on the Castor, Abbott & Klein (1975) theory of radiatively driven winds, as modified by Abbott (1982) incorporating the crucial "finite cone angle correction" (Pauldrach, Puls & Kudritzki 1986) and using complex multi-level atoms with over 100,000 lines being accounted for. Currently these methods still use the core-halo approach of wind line analysis (*e.g.* PKPB) whereby the emergent flux from the stellar atmosphere is determined and then used as a lower boundary condition to the flux in the wind. Thus there is no coupling between the wind and the atmosphere. This may be an adequate (although obviously not physical) approximation for optically thin winds but for optically thick winds (*e.g.* in Wolf-Rayet stars) the coupling between the wind and the atmosphere will be significant. So far the improved NLTE methods have been used with the co-moving frame method to determine stellar wind parameters

and to solve a number of outstanding problems. The "Unified Model Atmospheres" approach has been developed (Gabler, Gabler, Kudritzki, Puls & Pauldrach 1989), principally at Munich, and is the most accurate method for modelling hot star winds as it is self-consistent, using only stellar parameters (mass, luminosity *etc*), rather than the variety of free parameters that are used currently (Kudritzki 1988).

The primary objective here is to analyse the stellar wind of  $\nu$  Sgr. For this purpose the SEI program is adapted and automated. This chapter discusses some numerical procedures, subsequently applied to six O stars already studied by Groenewegen & Lamers (1989) (GL89), to a number of EHe and sdO stars, and finally to  $\nu$  Sgr. A User Guide to the SEILS codes described in this Chapter are given in Appendix C with a checklist for wind line analysis in Appendix D.

## 4.2 The SEI Method

### 4.2.1 Assumptions

SEI uses the Sobolev approximation to the source function and integrates the equation of transfer exactly. The Sobolev approximation is that the natural velocity width for absorption in a line is small compared to the velocity gradient. Put simply, this means that a given transition occurs at a single frequency only.

SEI makes a number of other assumptions:

1. Wind line formation occurs in a spherically symmetric expanding stellar wind.
2. All non-smooth velocity variations (thermal effects, shocks *etc*) are approximated by a "turbulent" velocity in the wind.
3. The turbulent profile is isotropic and Gaussian in shape.
4. A velocity law (of the form given in Equation 4.3) is assumed.
5. An optical depth law (of the form given in Equation 4.4) is assumed.
6. The underlying photospheric lines, if present, are Gaussian in shape.

### 4.2.2 Theory

Full details of the method (including full details of the solution schemes) are given in Lamers *et al.* (1987); only a brief resumé of the important equations needed to understand subsequent sections is given here.

In all cases velocities are normalised to the terminal velocity of the wind,  $v_\infty$ , *i.e.*

$$w(r) = \frac{v(r)}{v_\infty} \quad (4.1)$$

and distances,  $r$ , are normalised to the photospheric radius of the star,  $R_*$

$$x = \frac{r}{R_*} \quad (4.2)$$

A velocity law for the wind is adopted of the form

$$w(x) = w_0 + (1 - w_0) \left(1 - \frac{1}{x}\right)^\beta \quad (4.3)$$

where  $w_0$  is the normalised photospheric velocity and  $\beta$  (also known as  $\gamma$ ) is a constant (for a given star) that describes the gradient of the velocity law.

The optical depth law is given by:<sup>1</sup>

$$\tau(w) = \left(\frac{T}{I}\right) \left(\frac{w}{w_1}\right)^{\alpha_1} \left\{1 - \left(\frac{w}{w_1}\right)^{\frac{1}{\beta}}\right\}^{\alpha_2} \quad w \leq w_1 \quad (4.4)$$

$$\tau(w) = 0 \quad w > w_1 \quad (4.5)$$

Here  $w_1$  is the extent of the blue wing of the wind profile (normalised to  $v_\infty$ ), and

$$I = \int_{w_0}^{w_1} \left(\frac{w}{w_1}\right)^{\alpha_1} \left\{1 - \left(\frac{w}{w_1}\right)^{\frac{1}{\beta}}\right\}^{\alpha_2} dw \quad (4.6)$$

$$T = \int_{w_0}^1 \tau(w) dw \quad (4.7)$$

The source function of a two level atom is given by

$$S_\nu(x) = \frac{[\beta_c(x) I_\nu^* + \epsilon' B_\nu(x)]}{(\beta + \epsilon')} \quad (4.8)$$

For other atoms, an equivalent two level atom approximation can be used to yield the source function

$$S_\nu(x) = \frac{[\beta_c(x) I_\nu^* + (\epsilon' + \theta) B_\nu(x)]}{(1 + \eta + \epsilon')} \quad (4.9)$$

---

<sup>1</sup>This is the formulation given by GL89 in the paper. However when using SEI to model the winds of the O stars they used a slightly different formulation of the optical depth law - the same as given in Equations 4.4 and 4.6 but without the  $\frac{1}{\beta}$  term. For the work reported in this thesis the formulation given here will be used unless specifically stated otherwise. The O star analysis (Chapter 5) uses the formulation without the  $\frac{1}{\beta}$  term while Chapter 6 on the winds of the EHe stars uses both formulations. The analysis of the winds of  $\nu$  Sgr (Chapter 7) also only uses the formulation without the  $\frac{1}{\beta}$  term.

where  $\eta$  and  $\theta$  allow for coupling to other levels (see Mihalas 1978). In Equations 4.8 and 4.9  $\beta$  and  $\beta_c$  are escape probabilities and

$$\epsilon' = \frac{C_{ul}}{A_{ul}} \quad (4.10)$$

is the ratio of collisional to radiative de-excitation (*i.e.* transitions from the upper ( $u$ ) to the lower ( $l$ ) level of a two level, or equivalent two level, atom).  $I_\nu$  is the continuum intensity and  $B_\nu$  the Planck Function of the wind and is parameterised by

$$\frac{B_\nu}{I_c} = \left( \frac{B_\nu}{I_c} \right)_0 e^{(-a_T (w-w_0))} \quad (4.11)$$

where the subscript "0" denotes the value at  $x = 1$  and  $w = w_0$ .

$a_T$  parameterises the form of the Planck Function in the wind:

$a_T < 0$	$B_\nu$ increases outward in the wind.
$a_T = 0$	$B_\nu$ is constant; isothermal wind.
$a_T > 0$	$B_\nu$ decreases outward in the wind.

The equation of transfer is then solved exactly with the photosphere acting as the lower boundary condition. The photospheric spectrum is a continuum with the option of a photospheric absorption line at the rest frequency.

For singlet lines the underlying photospheric intensity is given by

$$I = e^{-A_{\text{phot}} \epsilon} - \left( \frac{w}{w_{\text{phot}}} \right)^2 \quad (4.12)$$

while for doublet lines the intensity is

$$I = e^{-A_{\text{phot}B} \epsilon} - \left( \frac{w}{w_{\text{phot}B}} \right)^2 - A_{\text{phot}R} \epsilon - \left( \frac{w-\delta}{w_{\text{phot}R}} \right)^2 \quad (4.13)$$

where  $\delta$  is the doublet separation in velocity units normalised to the terminal velocity, given by

$$\delta = \frac{c}{v_\infty} \left( \frac{\lambda_R - \lambda_B}{\lambda_R} \right) \quad (4.14)$$

Limb-darkening is not accounted for as the effect is small (Castor & Lamers 1979). The effects described by GL89 are spurious, being accounted for by an error in programming (Lamers, private communication 1991; and Groenewegen & Lamers 1991).

It should be noted that the coefficients  $\beta$  (from the velocity law, Equation 4.3),  $v_\infty$  and  $w_g$  are the same for all the wind lines of a given star.

## 4.3 The SEI Programs

Two programs SEIDOUN3 and SEISING3, obtained from Dr. Henny Lamers *via* CCP7, were used for modelling doublet and singlet lines respectively. Details of SEIDOUN3 are presented here as it was mainly resonance doublets that were of interest in this study. Some analyses of singlet lines were undertaken and differences between SEISING3 and SEIDOUN3 are indicated.

### 4.3.1 Solution method

SEIDOUN3 proceeds as follows:

1. Calculate a pre-specified distance grid and a pre-specified grid of impact parameters for the lines of sight along which the equation of transfer is to be solved, also pre-specified.
2. Calculate the Gaussian turbulent profile, and its integral (the "error function") at pre-specified wavelength points.
3. Calculate the blue component of the source function directly from escape probabilities, in the pre-specified distance grid.
4. Calculate the red component of the source function taking into account radiatively coupled points.
5. Solve the equation of transfer for each wavelength point along each line of sight.
6. Calculate the emergent flux from the contributions along the different lines of sight.

### 4.3.2 Radiative coupling

Radiative coupling is whereby a photon scattered or emitted by one component may subsequently, at another point in the wind, be absorbed by the other component. For the given symmetry and velocity law (Equation 4.3) this means that a photon emitted or scattered by the blue component can subsequently be absorbed elsewhere in the wind by the red component if the relative velocities of the emitter and absorber correspond to the doublet wavelength separation. Note that red photons cannot subsequently be absorbed by the blue component.

### 4.3.3 Inputs

Table 4.1: The inputs of SEIDOU3 and SEISING3. Those inputs not required for SEISING3 are indicated by a †.

Variable	Function / Description
$\beta$	Gradient of the velocity law, Equation (4.3).
$T_B$	Optical depth of the blue component.
$T_R$ †	Optical depth of the red component.
$\alpha_1$	Parameter of the optical depth law, Equation (4.4).
$\alpha_2$	Parameter of the optical depth law, Equation (4.4).
$w_g$	Turbulent velocity as a fraction of $v_\infty$ .
$w_0$	Normalised photospheric velocity, Equation (4.3).
$\delta$ †	Doublet separation, Equation (4.14).
$w_1$	Extent of violet wings, in terms of $v_\infty$ .
$\epsilon_B$	Collisional parameter, Equation (4.10).
$\epsilon_R$ †	Collisional parameter, Equation (4.10).
$\left(\frac{B_\nu}{T_c}\right)_0$	Planck Function in the wind, Equation (4.11).
$a_T$	Parameter governing the radial behaviour of $B_\nu$ .
$A_{photB}$	Optical depth of the blue photospheric line.
$w_{photB}$	FWHM of the blue photospheric line.
$A_{photR}$ †	Optical depth of the red photospheric line.
$w_{photR}$ †	FWHM of the red photospheric line.
IGMAX	Number of points in the turbulent profile used in the integration of the source function.
PRSTART	Starting wavelength of profile in terms of $v_\infty$ .
PREND	Finishing wavelength of profile in terms of $v_\infty$ .
PRSTEP	Wavelength interval in terms of $v_\infty$ .

The required input to SEIDOUN3 and SEISING3 are given in Table 4.1. Not all of these parameters are of equal importance and a number, once fixed, does not affect the shape of the profile.

PRSTART, PREND, PRSTEP are initially fixed to values reflecting the required wavelength coverage and the resolution of the wavelength grid. IGMAX is initially fixed at 15 (Lamers *et al.* 1987) and  $w_0$  is fixed, usually at 0.01. Varying these does not change the resultant profiles significantly (but see Sections 4.5.1 and 4.5.2).

Also, when dealing with singlets and resonance doublets the following can be assumed, except in the case of wind-line profiles in Wolf-Rayet stars.

$$\begin{aligned}
 \left(\frac{B_\nu}{I_c}\right)_0 &= 1 && \text{Photospheric continuum is the Planck Function.} \\
 a_T &= 0 && \text{Isothermal wind.} \\
 \epsilon_B, \epsilon_R &= 0 && \text{Collisional de-excitation is unimportant.} \\
 w_1 &= 1 && \text{Violet wings reach } v_\infty. \\
 T_R &= \frac{T_B}{2} && \text{For resonance doublets.}
 \end{aligned}$$

For strong lines (*e.g.* resonance doublets) the equivalent widths of the underlying photospheric lines are small in comparison to the equivalent widths of the wind lines; however they cannot be ignored (set to zero) for the purposes of profile fitting as they play an important role and can alter the determined parameters significantly if good approximations are not used. See Section 4.6 for details of initial photospheric line determination.

Thus only six parameters are actually "free" and require determination:  $\beta$ ,  $T_B$ ,  $\alpha_1$ ,  $\alpha_2$ ,  $w_g$  and  $v_\infty$ .

Then for resonance doublets in stars other than Wolf-Rayets the problem of wind-line fitting with SEIDOUN3 and SEISING3 reduces to a problem with six free parameters.

In broad terms  $\beta$  governs the position of the emission peak, if present, with a higher  $\beta$  moving the emission peak further redwards. The turbulent velocity,  $w_g$  determines the steepness of the blueward edge of the profile and can push the blue edge to shorter wavelengths than would be expected from  $v_\infty$  itself. Conversely, ignoring  $w_g$  leads to an overestimate of  $v_\infty$ . The lower the turbulent velocity the steeper the blue edge. The optical depth law parameters  $\alpha_1$  and  $\alpha_2$  govern the shape of the profile while the optical depth  $T_B$  governs the depth of the profile. However all these parameters are interlinked and depending on the values of the other parameters, altering one may not have the expected, or desired, effect.

## 4.4 “SEILS” - A Suite of Automated Profile Fitting Programs

Initially it was thought that wind-line profile fitting would be a simple interactive task. However the six free parameters affect the profile in subtle and unpredictable ways. Thus once a profile is obtained it was not obvious which parameters needed to be changed to improve the fit to the observed data. Test profiles were interactively fitted to the CIV 1548 Å doublet in the composite high resolution IUE spectra of  $\nu$  Sgr. Over 100 interactive profiles were generated and the “final” profile was no more than “reasonable” and poorer than the quality of fits published (for other objects) by GL89. The greatest problem was that the same quality of results could be achieved with widely different sets of input parameters.

It was necessary to develop an automatic routine that would produce a good profile that was (hopefully) a singular solution. A least squares procedure was adopted as being the most suitable. Full details of the algorithms and the error analysis are given in Appendix B. A similar method was adopted by GL89 for finding initial profiles, but their code was not released.

The program SEILS - SEI fitting by Least Squares, was not intended to be a “black box” producing perfect profiles but a method of producing a good profile that could be fine-tuned by hand if necessary. Three versions of SEILS were written altogether, the one described here is SEILS1 for fitting single star profiles. SEILS2 and SEILS3 for fitting wind profiles from binary stars are discussed in Chapter 7 on the winds of  $\nu$  Sgr. Differences between the program inputs and their use are in Appendix C. SEILS is the generic name for all three programs.

### 4.4.1 Major changes in SEILS over SEI

1. SEILS determines the best fit parameters, within the SEI implementation, using a non-linear least squares algorithm (Appendix B). It allows any, or all, of the six parameters to be fixed.
2. Singlet and doublet lines are all solved within a single code.
3. The fit can be constrained between upper and lower velocity limits without altering the photospheric velocity. This is very useful for modelling only part of a given profile, something that is needed for modelling binary star winds.
4. SEILS allows photospheric lines to be Gaussian, as in SEI, or to read in a file containing an arbitrary photospheric profile. This allows non-Gaussian photospheric lines to be used if a reliable way of generating them is available.
5. Non-resonance doublets can be modelled, *e.g.* the C II doublet that has  $T_B = \frac{T_R}{2}$  rather than  $T_R = \frac{T_B}{2}$ .

6. It allows the optical depth laws both with and without the  $\frac{1}{\beta}$  term to be used, without modification of the code.
7. The determined fits are converted into DIPS0 format for immediate display.

#### 4.4.2 Using SEILS

SEILS is a batch program taking its input from two data files containing all the necessary information. Appendix C gives a sample data file to indicate the structure and includes information on the default values of those parameters that are fixed before execution.

To analyse a wind line profile a number of steps must be executed:

1. Continuum subtraction. For some lines the continuum slopes greatly in the vicinity of the line. This general trend must first be removed to obtain a flat continuum. For the NV doublet the contribution from interstellar Lyman- $\alpha$  must also be removed.
2. Continuum level determination. The level of the continuum must be set to 1; when determining the continuum level only the flux very close to (within a few  $\text{\AA}$  of) the wind line should be considered as it is this flux that goes into the line, the behaviour of the continuum further away is of no importance. Generally the the continuum level was set to be at 90 - 95% of the level of the the top of the peaks in the surrounding IUE high-resolution spectrum.
3. Re-binning. If the spectra shows much noise (as in a single IUE spectrum for example) then re-binning allows a much more accurate determination of the flux levels. In all wind line studies reported here the high-resolution IUE data was re-binned from 0.04  $\text{\AA}$  onto a 0.2  $\text{\AA}$  grid. Re-binning rather than smoothing was used so as to preserve the independence of the data.
4. Data point selection. SEILS does not fit the calculated profile to the whole of the observed profile as this would have far too many points and would take too long. Also it is the gross, rather than fine, structure for which modelling is attempted. To this end a number of data points are selected, by hand, across the profile; it is these flux-wavelength pairs that are fitted by SEILS. As can be seen from Appendix C, each data pair can be given a weight which affects the fitting depending on which mode of weighting is selected (see Appendix B for details of the weighting schemes possible). In this study uniform weighting was used with the weighting of different parts of the profile being achieved by selecting more data points in the critical parts of the profile (*e.g.* the blue edge). In the analysis presented here some 25 - 35 data points were usually chosen for doublet lines and 15 - 20 for singlets.
5. Input file preparation. Having selected the data points, starting values for the six free parameters are chosen. Also specified is a value,  $\Delta a$ , that controls how far away from the

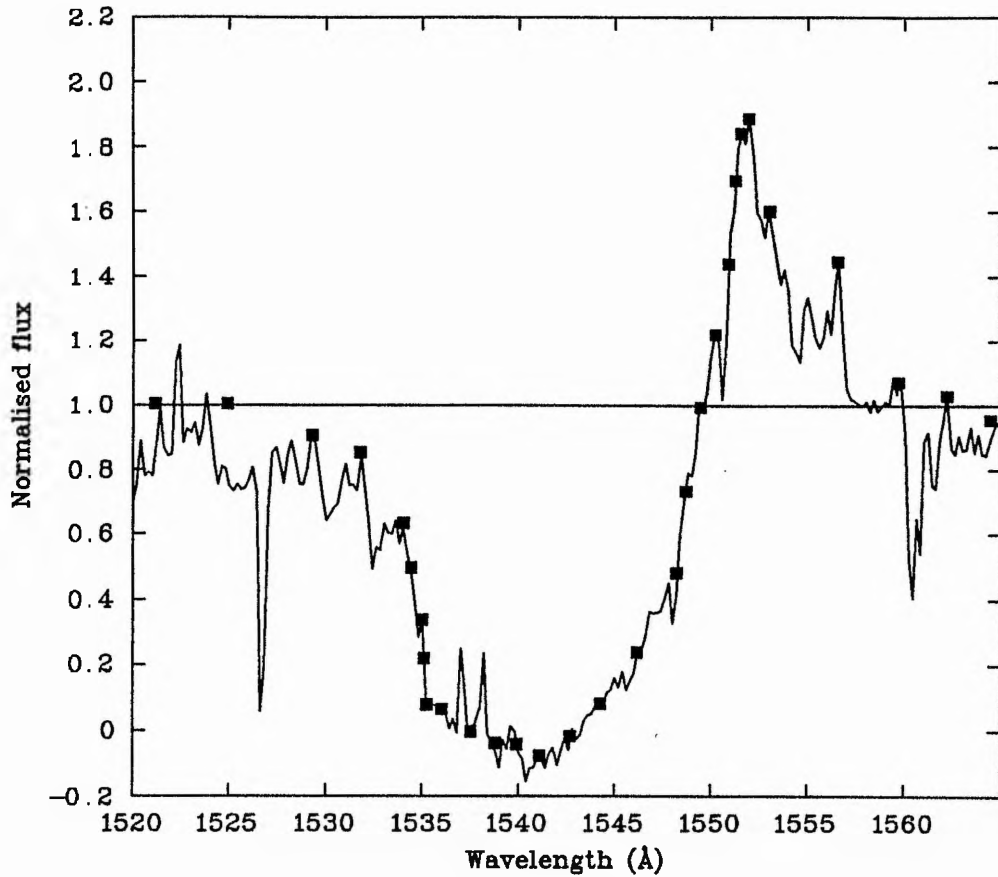


Figure 4.1: An IUE CIV wind line profile showing the adopted continuum level and representative data points.

parameter value,  $a$ , the program looks when searching for the global minimum for  $\chi^2$ . (This value only determines the initial baseline over which the gradient of  $\chi^2$  is determined with respect to the parameter; it does not stop the final value of the parameter being further away from the initial value than  $\Delta a$ .)

Figure 4.1 shows a CIV line with the continuum indicated as well as a representative choice of data points to illustrate the principles involved.

As the six free parameters are treated as numerical (rather than physical) parameters it is possible that SEILS will determine that the best fit profile will include one or more parameters that are unphysical (*e.g.* a negative optical depth, or a negative  $\beta$  which would allow the velocity in the wind to be greater than the terminal velocity). To avoid this, if the parameters  $T_B$ ,  $v_\infty$ ,  $w_g$  or  $\beta$  become negative then the value of  $\chi^2$  is set very large (5) to ensure that the fit is forced back into an area of parameter space that is physical.

## 4.5 Testing the Assumptions

In Sobolev theory, the interpretation of Lamers, Cerruti-Sola & Perinotto (1987) in coding it in the form of SEI, and in the development of SEILS, a number of assumptions have been made about some of the input parameters. Also a number of the steps in SEILS require subjective evaluation. It is important to determine just what effect these assumptions and judgements, of which four have been tested, have on the final profiles.

1. The wind line profiles are not greatly affected when the value of the photospheric velocity,  $w_0$ , is varied around its assumed value of 0.01 (normalised to  $v_\infty$  as usual).  $w_0 = 0.01$  corresponds to  $\sim 10 \text{ km s}^{-1}$ , the sonic velocity at the photosphere.
2. Setting the number of points within the Gaussian turbulent profile (IGMAX) to more than 15 does not affect the profile unless  $w_g$  is large.
3. The wind line profile parameters are not dependent on small changes in the choice of continuum level.
4. The wind line profile parameters are not changed greatly when different sets of data points are chosen.

### 4.5.1 Photospheric velocity

GL89 assert that the value of  $w_0 = 0.01$  is "representative" and tested it with a value of 0.001 and 0.03 but did not publish their profiles. To find the extent of the errors involved profiles were generated for 4 values of  $w_0$ , namely 0.001, 0.01, 0.03 and 0.05.  $w_0$ , being the lower boundary condition of the integration of the equation of transfer, will affect the shape of the profile most greatly when the majority of absorbing material is in the lower reaches of the atmosphere. From the optical depth law (Equation 4.4) this condition will occur most greatly when  $\alpha_1$  is large and negative.  $\alpha_2$  plays a much smaller rôle close to the stellar surface, but will also have the greatest effect when large and negative. Thus for this test  $\alpha_1 = \alpha_2 = -2$  and the optical depth was chosen to be large ( $T_B = 10$ ) to accentuate any effect. The results are shown in the upper diagram of Figure 4.2.

As can be seen the photospheric velocity is a very important parameter when  $\alpha_1$  is large and negative. A similar test was done with  $\alpha_1 = \alpha_2 = -3$  where the results were more extreme; the flux reaching to over 55 for  $w_0 = 0.001$ . For  $\alpha_1 = \alpha_2 = 0$  the results showed only an imperceptible difference between profiles.

Thus the photospheric velocity is an important parameter but only when the emission peaks

are very large (*e.g.* in Wolf-Rayet stars). When fitting profiles to wind lines without large emission profiles then the photospheric velocity is not important.

#### 4.5.2 Turbulent profile

Lamers & Jeffery (1991) state that a value of the number of wavelength points within the Gaussian turbulent profile, IGMAX, should be set to 15 for good results as long as  $w_g < 0.3$ . Figure 4.2 shows the results, on a typical CIV profile, of having IGMAX take the values 9, 15, 19 and 25. The differences are very minor, but a larger value of ITMAX should be used, as a precaution, if  $w_g$  is, or is expected to be, large.

#### 4.5.3 Data point selection

To see if the subjective choice of data points had any major bearing on the fitted profile when using SEILS (an effect that would also affect the results of GL89) three sets of data points were chosen. The three data sets were selected so that they had roughly the same number of points and that the distribution of the points within the profile were roughly similar. The results are shown in Figure 4.3, along with the associated parameter values.

From the profiles it is seen that the choice of data points makes little difference to the goodness of fit of the profile to the data and has little effect on the determined values of the six free parameters.

#### 4.5.4 Continuum level

One of the most problematic of the subjective judgements facing GL89 in their study, and also when using SEILS, is the selection of the continuum level.

Using SEILS and a standard input file, profile fitting was done on a wind line using a continuum level set at 90%, 100% and 110% of the judged "best" value. The same wavelength-flux data pairs were used for each profile with only small modifications to the flux in some instances. The results are shown in Figure 4.4 and the corresponding parameters in the table. From this it can be seen that continuum selection can change the derived parameters and fits significantly, much more so than the selection of data points.

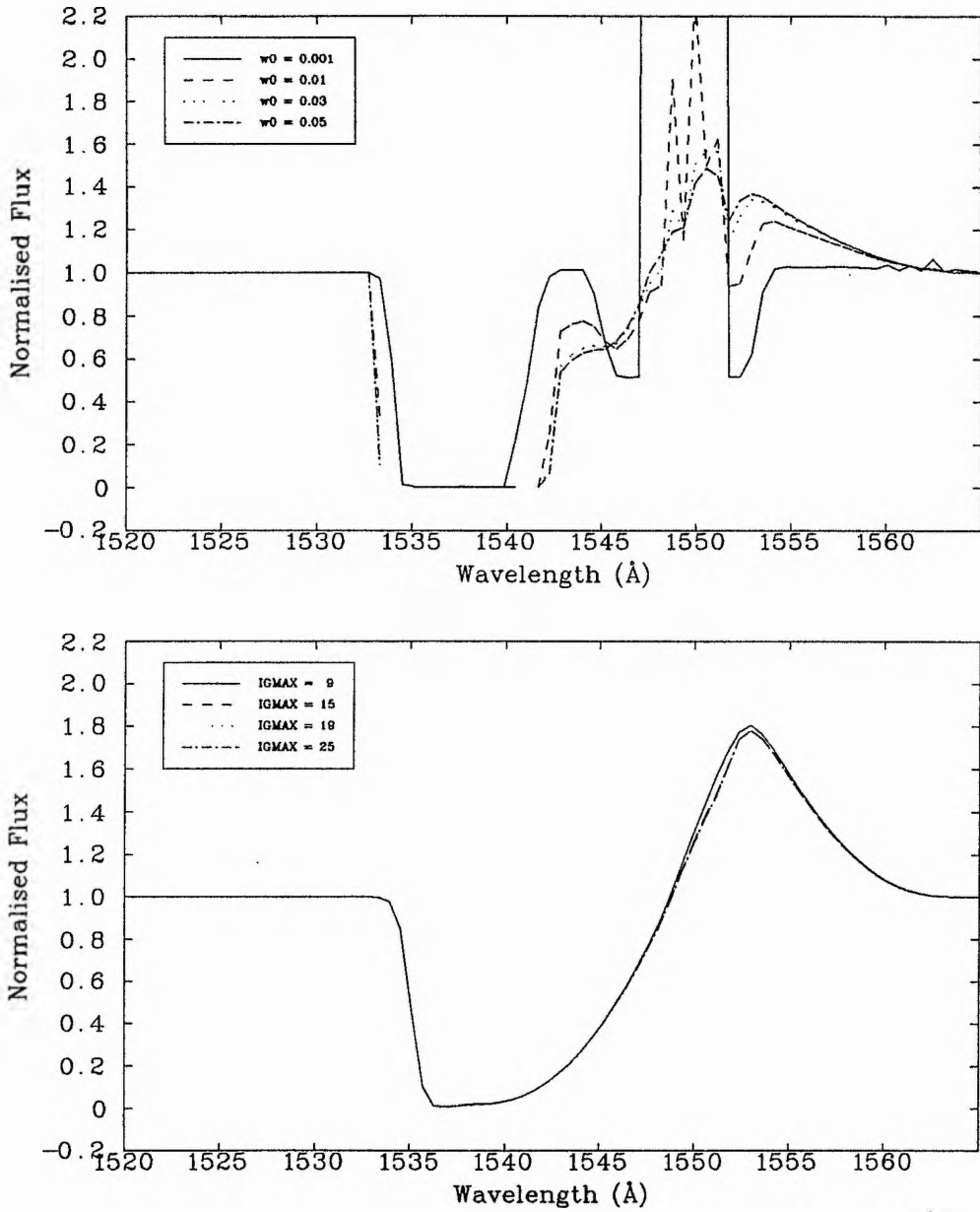
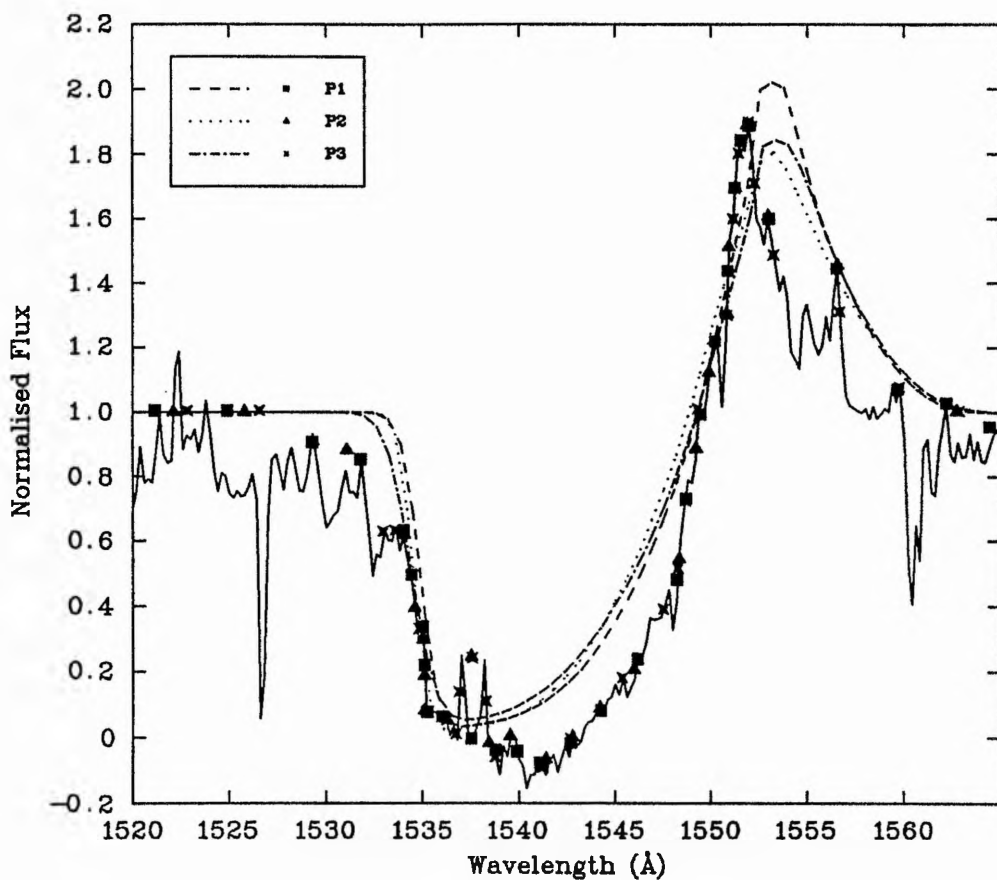
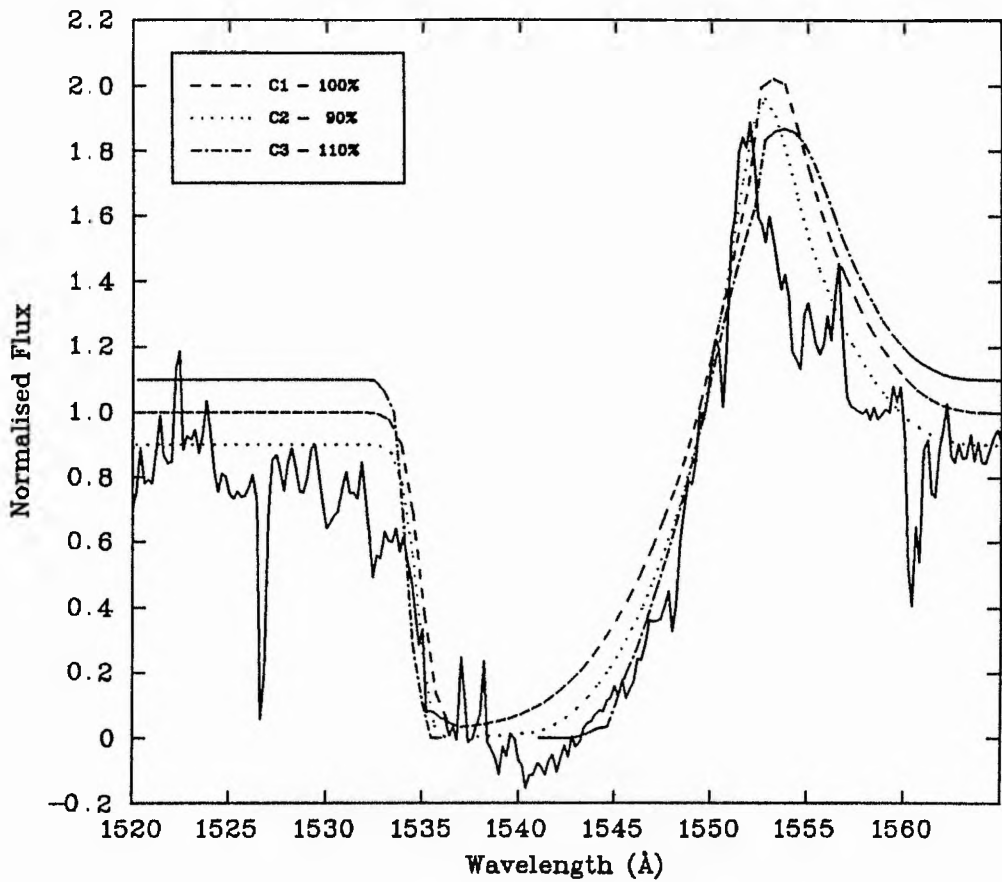


**Figure 4.2:** The effect of varying  $w_0$  (upper) and IGMAX (lower) on line profiles. The parameters used were  $\beta = 0.7$ ,  $T_B = 10$ ,  $w_g = 0.1$  and  $v_\infty = 2300 \text{ km s}^{-1}$  for both diagrams. For the upper diagram  $\alpha_1 = \alpha_2 = -2$ , while for the lower one  $\alpha_1 = \alpha_2 = 0$ . For  $w_0 = 0.001$  the emission peak reaches a flux value of 46.



Param.	P1		P2		P3	
	Value	$\sigma$	Value	$\sigma$	Value	$\sigma$
$\beta$	1.10	1.01	0.75	0.26	1.00	0.09
$T_B$	16.1	26.9	10.3	3.9	9.99	1.49
$\alpha_1$	-0.20	1.51	0.01	0.35	-0.27	0.02
$\alpha_2$	0.51	2.33	0.32	0.46	0.45	0.14
$w_g$	0.12	0.14	0.10	0.02	0.14	0.01
$v_{\infty}$	2410	430	2470	120	2510	50
$\chi^2$	0.86		0.70		0.93	

Figure 4.3: The effect of data point selection on line profiles is illustrated with 3 sets of data points P1, P2 and P3 and the fitted profiles. A standard input to SEILS was used. The table gives the derived parameters for the fits.



Param.	90%		100%		110%	
	Value	$\sigma$	Value	$\sigma$	Value	$\sigma$
$\beta$	0.69	0.66	1.10	1.01	1.15	0.65
$T_B$	27.1	26.9	16.1	26.9	10.9	6.9
$\alpha_1$	-0.36	0.10	-0.20	1.51	0.30	1.05
$\alpha_2$	-0.67	1.21	0.51	2.53	-0.15	1.07
$w_g$	0.19	0.04	0.12	0.14	0.14	0.05
$v_\infty$	1960	290	2410	430	2210	310
$\chi^2$	0.44		0.86		0.40	

Figure 4.4: The effect of continuum level on line profiles is illustrated with the continuum set at 100%, 110% and 90% of the judged "best" value. A standard input to SEILS was used. The table gives the derived parameters for the fits.

### 4.5.5 Conclusions

From the tests applied to SEILS a number of conclusions can be drawn.

1. SEILS and the SEI method should not be used on Wolf-Rayet wind line profiles or others that show large emission peaks.
2. For stars other than Wolf-Rayet's then a photospheric velocity of  $w_0 = 0.01$  is adequate.
3. IGMAX should be set at 15 unless  $w_g > 0.3$ .
4. Due to problems of data point selection and continuum placement, errors of at least 10% will occur on all parameters other than  $\alpha_1$  and  $\alpha_2$ . For these, an error of  $\pm 0.5$  at least should be attributed.
5. In general the best fit must be selected by eye from the possibilities generated. Using Figure 4.4 as an example, there are a number of points to bear in mind when selecting the best fit. The most problematic point concerns the continuum level and the emission peak. It is possible that line absorption across the whole spectral range under scrutiny will lower the continuum as a whole. This effect will be negated by selecting the continuum level at the level of flux going into the line (*i.e.* the 100% level given in Figure 4.4). If this is done then the fit to the emission peak should also take into account the underlying line absorptions and the fit to the peak should be equally good. This does not seem to be the case, the fit to the blueward edge of the peak being good, but the fit to the redward side being much poorer.
6. Good fits are non-singular when dealing with just a single line. However all the lines of a given star can be combined to determine more accurate values for the three parameters ( $\beta$ ,  $w_g$  and  $v_\infty$ ) that are the same for all wind lines of a given star.

## 4.6 Photospheric Lines

Within the SEI implementation the lower boundary condition for the solution of the transfer equation in the wind is a continuum with (optional) photospheric lines superimposed (the "core-halo" approach). The lines are described by the parameters  $A_{phot}$  and  $w_{phot}$  where the former is linked to the depth of the line ( $A_{phot} = -\ln(flux)$ ) and the later represents the FWHM of the line, which is modelled by a Gaussian (SEILS1, SEILS3) or by an arbitrary profile read in from an external data file (SEILS2).

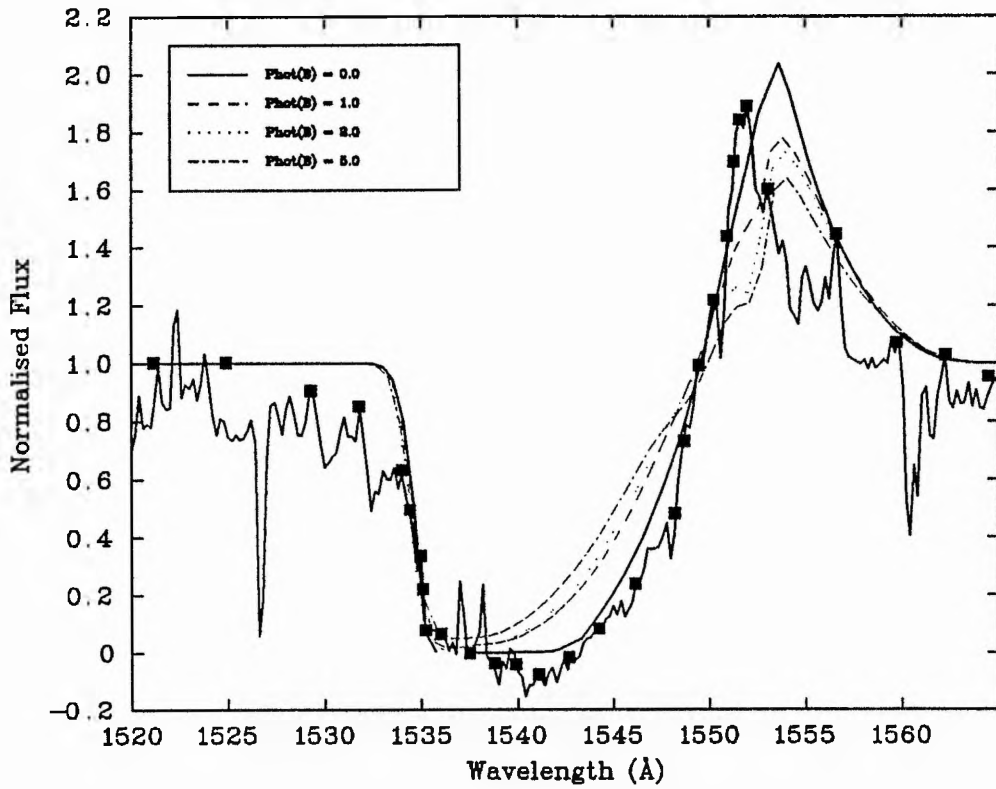
From a modeling standpoint it is important to know if good values of the photospheric line depths and widths need to be known before a solution is attempted or whether they can be omitted in the first instance and later added as fine tuning for an already good fit.

Figure 4.5 shows the effects of using SEILS with four sets of photospheric line depths. As can be seen the values of the parameters determined (especially  $\beta$ ) are quite different depending on the value of the photospheric depth used. The quality of the fits also varies enormously depending on the value of the photospheric lines. From viewing Figure 4.5 the fit with no photospheric line is much better than the other three even though all lines have been optimised with SEILS. Increasing the values of the wind optical depth has very little effect on the profile with a line photospheric depth of 5.0. Another very important point is that the effect of including a photospheric line can give counter-intuitive results. If a photospheric depth of 1.0 was used (dashed line) then it may be assumed that a greater line optical depth would depress the continuum on the redward side to give a better fit. However doing this results in an even poorer fit. Thus judging the photospheric depth required by eye is not a fool-proof method of obtaining a better fit. Contrary to the comments of GL89, photospheric lines cannot be ignored if the wind line profile is saturated as a photospheric line can still change the profile substantially.

Thus it is important to determine reasonably good values for the photospheric line depths and widths before determining an initial solution. These initial values can be determined in three ways:

1. Use published values.
2. Use a model atmosphere and line formation program to determine the photospheric lines. This procedure requires knowledge of
  - (a) Atomic data such as oscillator strengths, and electron damping constants and collisional cross-sections. These may only be poorly known for highly excited UV lines.
  - (b) The temperature and composition of the star needs to be known. In the current study of hydrogen-deficient stars these data may only be poorly known.
  - (c) NLTE model atmospheres may need to be used; these are not always available especially when combined with the study of highly excited lines in hydrogen-deficient stars.
3. From studies of similar objects take an estimate then after the initial solution be prepared to change the values quite considerably to obtain the best fit.

GL89 make the reasonable assumption that  $w_{phot_B} = w_{phot_R}$  while they use  $A_{phot_B} = 2 A_{phot_R}$  as the oscillator strengths differ by a factor of  $\sim 2$  between the lines of the doublet. The fact that this latter assumption is not justified is illustrated in Figure 4.6. Here the program SPECTRUM (written by Prof. P. Dufton, Belfast) was used to generate line profiles based on the line-blanketed LTE model atmospheres code STERNE developed at Kiel. The example is of a unsaturated NV doublet from a 30,000K,  $\log g = 3.5$  model with a microturbulent velocity of  $10 \text{ km s}^{-1}$  and an abundance ratio of  $\frac{N_V}{N_H} = 8.5 \times 10^{-5}$ . The profiles are nearly identical in both central depth and equivalent width despite the different oscillator strengths (which cause the two



Param.	0.0		1.0		2.0		5.0	
	Value	$\sigma$	Value	$\sigma$	Value	$\sigma$	Value	$\sigma$
$\beta$	1.03	0.07	0.99	0.27	0.97	0.04	0.68	0.23
$T_B$	19.8	2.6	16.1	6.7	16.5	0.6	12.2	1.5
$\alpha_1$	-0.52	0.10	-0.55	0.12	-0.75	0.01	-0.78	0.03
$\alpha_2$	-0.53	0.14	0.06	0.43	-0.06	0.05	0.05	0.14
$w_g$	0.149	0.005	0.105	0.023	0.094	0.003	0.096	0.010
$v_\infty$	2100	40	2420	120	2460	10	2510	30
$\chi^2$	0.442		0.917		1.149		1.738	

Figure 4.5: The effect of photospheric line depths on line profiles is illustrated with optical depths in the blue component of the doublet of 0.0, 1.0, 2.0 and 5.0. A standard input to SEILS was used. The table gives the derived parameters for the fits.

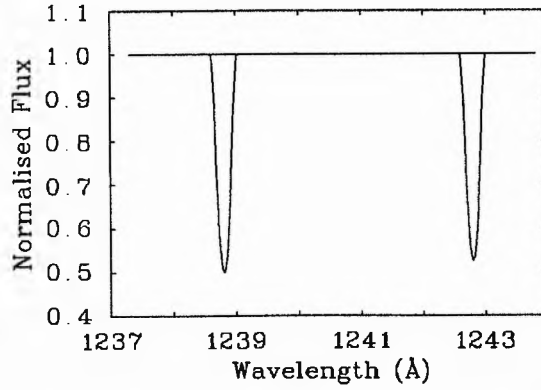


Figure 4.6: Calculated LTE N V doublet profiles. The model used was  $T_{eff} = 30000\text{K}$ ,  $\log g = 3.5$ ,  $\frac{N_N}{N_H} = 8.5 \times 10^{-5}$  and a micro-turbulent velocity of  $10 \text{ km s}^{-1}$ . The corresponding values for  $A_{phot_B}$  and  $A_{phot_R}$  are 0.88 and 0.82.

lines to be formed in different regions of the atmosphere). The corresponding values for  $A_{phot}$  are 0.88 and 0.82. This effect arises as both lines lie on the flat part of the curve of growth when this abundance is adopted. For very low or high abundances then the differences in the equivalent widths, and thus line depths, would be more apparent. Very high abundances could not be modelled with SPECTRUM as it does not include all the line broadening mechanisms, especially the important Stark broadening mechanism which cause line profiles to deviate substantially from a Gaussian profile. Neither SEI or SPECTRUM accounts for this so the differences cannot be judged<sup>2</sup>.

For a first approximation, the generation of photospheric line profiles using LTE model atmospheres can be used to obtain  $A_{phot}$  and  $w_{phot}$ . The approximation of  $w_{phot_B} = w_{phot_R}$  is a good one but also the approximation  $A_{phot_B} = A_{phot_R}$  should be used.

## 4.7 Correction for Lyman $\alpha$ - the N V Doublet

The analysis of the N V doublet requires correction for the lowering of the continuum by interstellar Lyman  $\alpha$ .

Due to the  $1215.67 \text{ \AA}$  line of interstellar Lyman  $\alpha$  the continuum in the region of the N V doublet ( $\lambda\lambda 1238.81, 1242.80 \text{ \AA}$ ) is depressed. Before modelling the wind line profile this interstellar contribution must be removed.

The variation of optical depth with wavelength from the center of the  $L\alpha$  profile is given by

$$\tau(\lambda) = 7.0562 \times 10^{-11} \frac{N_H}{1 + 1.6574 \times 10^9 (\Delta\lambda)^2} \quad (4.15)$$

where  $N_H$  is the column density of hydrogen ( $\text{cm}^{-2}$ ) in the direction of the object and  $\Delta\lambda$  ( $\text{\AA}$ ) is

<sup>2</sup>SELS2 can account for this but only if good Stark broadened profiles can be determined.

the wavelength difference between the wavelength under consideration and the wavelength of  $L\alpha$  (1215.67 Å).

After subtraction of the gross continuum each wavelength point in the spectrum is multiplied by  $e^{\tau(\lambda)}$  until the continuum at the blue side of the NV profile matches that at the red side. Similarly, after determination of the subsequent profiles, these profiles are multiplied by  $e^{-\tau(\lambda)}$  to allow plotting of the derived profiles on the original spectrum.

A checklist for the analysis of a NV doublet is as follows

1. Remove the continuum through  $\sim 200$  Å around the NV doublet, setting the level of the residual continuum on the redward side of the doublet to 90 – 95% of the height of the peaks in the continuum.
2. Remove the  $L\alpha$  contribution by selection of an appropriate column density until the continuum at the blueward side of the doublet matched the redward side as far as is possible.
3. Select data points on the *original* spectrum (*i.e.* that determined after step 1.)
4. Correct these data points for the  $L\alpha$  contribution. Small flux errors in the selection of data points on the blueward side of the doublet may become very large errors after the correction for the  $L\alpha$  contribution, so set any blueward flux values that are greater than 1 to 1.
5. Determine a solution using SEILS.
6. Correct the resultant theoretical profiles for the  $L\alpha$  contribution.

## 4.8 Mass Loss

If stellar parameters are known then it is possible to determine mass-loss rates (MLR) from the parameters of the theoretical wind line profiles.

The radial optical depth is defined by

$$\tau(v) = \left( \frac{\pi e^2}{m c} \right) (gf)_{lu} \lambda_0 \left( \frac{n_l}{g_l} - \frac{n_u}{g_u} \right) \frac{dr}{dv} \quad (4.16)$$

where  $\lambda_0$  is the rest wavelength of the transition from the lower ( $l$ ) to the upper ( $u$ ) level of a two level, or equivalent two level, atom.  $g$  is the statistical weight of the level,  $f$  the oscillator strength and  $n$  the number density of the ion.  $m$  is the electron mass,  $c$  the speed of light and  $e$  the electronic charge.

For a symmetrical wind with steady mass loss then in time  $dt$  a shell of radius  $r$  expands by an amount  $dr$  giving an increase in shell volume of  $4\pi r^2 dr$ . The mass within this shell is then just  $\dot{M} dt$  where  $\dot{M}$  is the total MLR for the star. The density of the material in the wind is then

$$\rho = \frac{\dot{M}}{4\pi r^2} \frac{dt}{dr} \stackrel{dt \rightarrow 0}{=} \frac{\dot{M}}{4\pi r^2 v} \quad (4.17)$$

Using this expression for density the mass continuity equation can be written

$$n_i = \left( \frac{n_i}{n_E} \right) \left( \frac{n_E}{n_H} \right) \left( \frac{n_H}{\rho} \right) \frac{\dot{M}}{4\pi r^2 v} \quad (4.18)$$

Here  $n_i/n_E$  ( $\equiv q_i$ ) is the ionisation fraction of ion  $i$  of element  $E$ .  $n_E/n_H$  ( $\equiv A_E$ ) is the abundance relative to hydrogen and  $n_H/\rho$  is the number of hydrogen atoms per gram of material in the wind of the star under consideration.

For a resonance transition where  $n_u \ll n_l$  Equation (4.16) becomes

$$\tau(v) = \frac{\pi e^2}{mc} f \lambda_0 n_i \frac{dr}{dv} \quad (4.19)$$

Now, from Equations (4.1) and (4.2) we have

$$\frac{dr}{dv} = \frac{dw}{dr} v_\infty \quad (4.20)$$

and

$$\frac{dw}{dr} = \frac{dw}{dx} \frac{dx}{dr} \equiv \frac{dw}{dx} \frac{1}{R_*} \quad (4.21)$$

Making these substitutions to obtain

$$\dot{M} q_i(w) = \frac{mc}{\pi e^2} (f \lambda_0)^{-1} 4\pi x^2 R_* w \frac{dw}{dx} \tau(w) \frac{\rho}{n_H A_E} \quad (4.22)$$

Now, noting

$$\frac{\rho}{n_E} = \left( Y_E \frac{N_0}{m_E} \right)^{-1} \equiv \frac{m_E m_H}{Y_E} \quad (4.23)$$

where  $N_0$  is Avagadro's Number,  $m_E$  the atomic mass number (in a.m.u.) of element  $E$  and  $m_H$  is the atomic mass of hydrogen (in grams).  $Y_E$  is the fractional abundance of helium by mass.

Thus obtaining the MLR in the form

$$\dot{M} q_i(w) = \underbrace{\frac{4mc}{e^2} m_H}_{(1)} \underbrace{m_E (f \lambda_0)^{-1}}_{(2)} \underbrace{\frac{R_*}{Y_E}}_{(3)} \underbrace{v_\infty^2 \frac{dw}{dx} x^2 w \tau(w)}_{(4)} \quad (4.24)$$

where (1) is a constant, (2) depends on the line being modelled, (3) depends on the physical parameters of the star, while (4) depends on the determined line fit parameters and where in the wind the product of MLR and ionisation fraction is being calculated.

With  $\dot{M}$  in  $M_{\odot} \text{ yr}^{-1}$ ,  $R_*$  in  $R_{\odot}$ ,  $v_{\infty}$  in  $\text{km s}^{-1}$  and  $\lambda_0$  in  $\text{\AA}$ , (4.24) becomes

$$\dot{M}q_i(w) = 8.70 \times 10^{-19} \frac{m_E}{\lambda_0 f} \frac{R_*}{Y_E} v_{\infty}^2 \frac{dw}{dx} x^2 w \tau(w) \quad (4.25)$$

and since by definition  $\frac{m_E}{Y_E} = \frac{1}{A_E X}$ ,

$$\dot{M}q_i(w) = \frac{8.70 \times 10^{-19}}{X} R_* v_{\infty}^2 (f A_E \lambda_0)^{-1} \frac{dw}{dx} x^2 w \tau(w) \quad (4.26)$$

where  $X$  is the mass fraction of hydrogen.

Equations (4.25) and (4.26) are general for all stars no matter what the surface composition. (4.25) requires the mass fractions of the elements while (4.26) requires number densities relative to hydrogen and the mass fraction of hydrogen. In general the formulation in Equation (4.25) will be the most appropriate. For a Population I mixture,  $X = 0.78$  and the constant in (4.26) becomes  $1.115 \times 10^{-18}$ , the small difference between this and the GL89 constant lies in the different values of the numerical constants used.

For hydrogen-deficient stars where  $X$  and  $A_E$  may be poorly known or have large errors the formulation in (4.25) is more accurate.

For non-resonance transitions the the left hand sides of both (4.25) and (4.26) are multiplied by  $E_i$ , the excitation fraction of ion  $i$ .

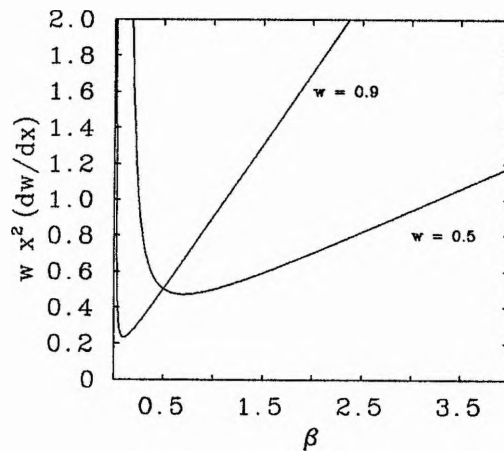
Thus the product of MLR and ionisation fraction can be determined at any point in the wind. The centre of the velocity profile, at  $w = 0.5$ , is an appropriate place to measure the MLR. To determine  $\tau(w)$  in those equations a 50 point numerical integration was performed to obtain  $I$  (in Equation (4.6)). The value of  $T$  used is  $T_B$ , giving an integration constant of  $\frac{T_B}{I}$ .

To determine the MLR requires a knowledge of the ionisation fraction; this is not usually available with any accuracy. However as mass is conserved then the maximum value for the product of MLR and ionisation fraction (which may occur anywhere in the wind depending on the optical depth law) will be a minimum value for the MLR. Where only one ion is available for a given element, and this ion is a highly ionised species (*e.g.* NV) then the minimum mass loss determined may be a very low estimate. However if many ionisation stages of a given element are available (*e.g.* CII, CIII, CIV) then the minimum mass loss may give a good approximation, as at some point in the wind a sizeable fraction of that element may be in a given ionisation stage.

The value of  $\beta$  has a dramatic effect on the shape on the wind-line profiles although the effect on the MLR is much less. For the  $\beta$ -independent optical depth law the factor  $x^2 w \frac{dw}{dx}$  in Equations (4.25) and (4.26) is the only one to depend on  $\beta$ . As shown in Figure 4.7 this factor has an almost constant value of  $\sim 0.5$  for  $0.5 \leq \beta \leq 1$ , increasing slowly for larger  $\beta$ . However for  $\beta \leq 0.5$ , and especially  $\beta \leq 0.15$ , the effect is substantially larger and thus small errors in  $\beta$  can lead to large errors in the MLR.

Of the stars analysed in this study only BD +10° 2179 had a very low value of  $\beta$ . Here the MLR cannot be evaluated at  $w = 0.5$  as the low value of  $\beta$  confines much of the velocity profile to the surface of the star where  $x = 1$  and the MLR formula breaks down. In such cases the MLR is evaluated further out in the wind (e.g.  $w = 0.9$ ) where  $\frac{dw}{dx}$  is smaller.

Figure 4.7: The effect of  $\beta$  on the mass-loss rate. The variation of  $x^2 w \frac{dw}{dx}$  with  $\beta$  is shown at two different values of  $w$ ; namely 0.5 and 0.9.



## 4.9 Summary

*The improved Sobolev method incorporated into SEI has been described and tested. An automated wind-line fitting suite of programs, SEILS, has been developed and its operation described and a number of tests applied to determine the accuracy of the solutions. The importance, and validity, of some of the underlying assumptions has also been investigated. Equations and methods of determining the mass-loss rates from the determined parameters have been given*

*SEILS, given the inherent limitations of the improved Sobolev method, should be a powerful tool for fast and accurate determinations of minimum mass loss rates. This, coupled with the anticipated publication of ionisation fractions for stellar winds from the improved NLTE, and possibly Unified Model Atmospheres, methods, should allow very accurate determinations of the actual MLR without the need to invoke "superionisation".*

## 4.10 References

- Abbott, D.C., 1982. *Astrophys. J.*, **259**, 893.
- Castor, J.I., Abbott, D.C. & Klein, R., 1975. *Astrophys. J.*, **195**, 157.
- Castor, J.I. & Lamers, H.J.G.L.M., 1979. *Astrophys. J. Suppl.*, **39**, 481.
- Gabler, R., Gabler, A., Kudritzki, R.P., Puls, J. & Pauldrach, A., 1989. *Astr. Astrophys.*, **226**, 162.
- Groenewegen, M.A.T. & Lamers, H.J.G.L.M., 1989. *Astr. Astrophys. Suppl.*, **79**, 359.
- Groenewegen, M.A.T. & Lamers, H.J.G.L.M., 1991. *Astr. Astrophys. Suppl.*, **88**, 625.
- Hamann, W.-R., 1980. *Astr. Astrophys.*, **84**, 342.
- Hamann, W.-R., 1981. *Astr. Astrophys.*, **93**, 353.
- Hamann, W.-R., Schönberner, D. & Heber, U., 1982. *Astr. Astrophys.*, **116**, 273.
- Kudritzki, R.P., 1988. In: *Radiation in Gaseous Moving Media, Eighteenth "Saas-Fee" Conference*, p.1, eds. W. Chmielewski & T. Lanz, Geneva Observatory.
- Lamers, H.J.G.L.M., Cerruti-Sola, M. & Perinotto, M., 1987. *Astrophys. J.*, **314**, 726.
- Lamers, H.J.G.L.M. & Jeffery, C.S., 1991. *C.C.P.7 Newsletter*, **15**, 51.
- Mihalas, D., 1978. *Stellar Atmospheres*, Freeman.
- Mihalas, D., Kunasz, P.B. & Hummer, D.G., 1975. *Astrophys. J.*, **202**, 465.
- Olson, G.L., 1982. *Astrophys. J.*, **255**, 267.
- Pauldrach, A.W.A., Kudritzki, R.P., Puls, J. & Butler, K., 1990. *Astr. Astrophys.*, **228**, 154.
- Pauldrach, A., Puls, J. & Kudritzki, R.P., 1986. *Astr. Astrophys.*, **164**, 86.
- Rybicki, G.B & Hummer, D.G., 1978. *Astrophys. J.*, **219**, 654.
- Sobolev, V.V., 1947. *Moving Envelopes of Stars*, Havard University Press, translated 1960.
- Sobolev, V.V., 1957. *Astr. J.*, **1**, 678.

## Chapter 5

# Mass Loss from O Stars

### 5.1 Introduction

O stars undergo substantial mass loss, shown most prominently in the line profiles of strong resonance lines, found mainly in the UV. Although P Cygni profiles, indicating high mass-loss rates, were detected in the UV from early rocket experiments (Morton 1967) and by Copernicus (*e.g.* Snow & Morton 1976), it was the launch of IUE that enabled systematic investigations of mass loss for early type stars (*e.g.* Kondo 1987).

UV spectra provide a useful means of mass-loss rate determination, procedures using visual (*e.g.* Hutchings 1976, Conti & Frost 1977, Klein & Castor 1978, Olson & Ebbets 1981), IR (*e.g.* Barlow & Cohen 1977) and radio data (*e.g.* Abbott, Biegging, Churchwell & Cassinelli 1980) have all complemented the UV results. There are often discrepancies amongst the results from these different methods, especially the radio data, (*e.g.* Abbott *et al.* 1980).

The line radiation driven wind theory of Castor, Abbott & Klein (CAK) (1975) has been used to explain the mass loss and the dependence of mass-loss rate on luminosity, although this latter result has been modified somewhat with new NLTE models (Pauldrach, Kudritzki, Puls & Butler 1990, hereafter PKPB). A major prediction of the CAK theory, after refinement by Friend & Castor (1983) and Friend & Abbott (1986), is that  $\beta$ , the gradient of the velocity law (Equation 4.3), should be approximately constant at  $\sim 0.8$ . Most early investigators fixed this gradient at 0.5, 1.0 or other convenient value. Recently investigators have tried to determine  $\beta$  from UV data (*e.g.* Groenewegen & Lamers 1989, hereafter GL89) although similar work has been done in the IR (Bertout, Leitherer, Stahl & Wolf 1985). These two sets of results differ in that the IR data seem to show that  $\beta$  increases with decreasing  $T_{\text{eff}}$  while the UV results do not, thus supporting the CAK theory.

A problem with determining mass-loss rates is the lack of knowledge of ionisation fractions. Some authors have tried to determine these and thus minimum values of the actual mass-loss rate by means of a "superionised" wind and the "corona" or "warm wind" models (*e.g.* Hamann 1980; Hamann, Schönberner & Heber 1982). Recently, work done at Munich (see Kudritzki 1988 for a review and PKPB) using improved NLTE model atmospheres have shown that "superionisation" is not required if the physics of the winds are modelled in sufficient detail. Some authors, noting the deficiency of the "superionised" wind models, simply quote the product of ionisation fraction and mass-loss rate (*e.g.* GL89). This is of little use, except as a lower limit, to the study of actual mass loss rates. Using the new NLTE code PKPB have published grids of theoretical models for O stars and their associated ionisation fractions. These allow the study of O star winds using less sophisticated methods to be taken a step further.

Before using the Sobolev approximation, in the form of SEILS, on objects that have not had their wind lines analysed and mass-loss rates determined it is necessary to test the code, the reduction and analysis procedures and to gain familiarity with their use. O stars provide a good basis for these tests as they show signs of high mass loss, distinctly non-photospheric absorption profiles and have the advantage that much previous work has been done on them. There are many O star mass-loss rate determinations in the literature against which the results using SEILS can be compared (*e.g.* Howarth & Prinja 1989). An additional advantage is that many O stars have been analysed with the SEI method itself, although using a different least squares procedure (GL89), allowing direct comparisons to be made. Success at this stage will allow greater confidence in the results when SEILS is applied to those objects that have not been analysed using the improved Sobolev approximation *i.e.* the EHe and HDB stars.

## 5.2 The Data

A sample of 6 O stars of differing spectral subtypes and luminosity classes were chosen to give a wide range of profiles to model. They include HD 14947 and  $\zeta$  Puppis (HD 66811) that have had their mass-loss rates analysed with some of the other techniques available (Section 5.6) and so provide good comparisons for the results determined here. The stellar data for the 6 chosen stars are given in Table 5.1 and are the same values as used by GL89.

The atomic data for the lines analysed here and in objects described in following chapters are given in Table 5.2 (from Snow & Morton 1976 and Danckwort & Treffitz 1978).

Table 5.1: Stellar data for the 6 O stars. (HD 66811 is  $\zeta$  Puppis.) The data are those used by GL89. The hydrogen column depth is given where required.

Star HD	Sp. Type	SWP #	$E_{B-V}$	$T_{\text{eff}}$ (K)	$\log L$ ( $L_{\odot}$ )	R ( $R_{\odot}$ )	M ( $M_{\odot}$ )	$\log g$ (c.g.s.)	$\log N_{\text{H}}$ (c.g.s.)
14947	O5 If+	10724	0.76	40,000	5.85	17.4	55	3.70	-
24912	O7.5 IIIInf	20606	0.35	37,000	5.32	11.0	32	3.86	21.08
30614	O9.5 Ia	2542	0.28	31,000	5.95	33.1	51	3.11	21.04
37043	O9 III	26567	0.06	34,000	5.58	17.8	39	3.53	20.18
46150	O5 Vf	10758	0.46	44,000	5.72	12.3	52	3.98	21.32
66811	O4 Inf	36151	0.03	42,000	5.87	15.8	59	3.81	-

Table 5.2: Atomic data for the wind lines.  $\lambda_0$  is the rest wavelength ( $\text{\AA}$ ),  $g_{\text{lower}}$  is the statistical weight of the lower level of the transition and  $f$  the oscillator strength.  $\chi_{\text{exc}}$  is the excitation potential of the lower level of the transition above the ground level. The final column give the abundance ratios for a Population I gas. Data from Snow & Morton (1976) except the CII data (from Danckwort & Treffitz 1978; tabulated in Heber 1983).

Ion	$\lambda_0$ ( $\text{\AA}$ )	$g_{\text{lower}}$	$f$	$\chi_{\text{exc}}$ (eV)	$\left(\frac{N_X}{N_{\text{H}}}\right)_{\text{Pop I}}$
C IV	1548.19	2	0.194	0.00	$3.2 \times 10^{-4}$
	1550.76	2	0.097	0.00	
N V	1238.81	2	0.152	0.00	$7.9 \times 10^{-5}$
	1242.80	2	0.076	0.00	
Si IV	1393.76	2	0.528	0.00	$4.0 \times 10^{-5}$
	1402.77	2	0.262	0.00	
C III	1175.66	9	0.257	6.50	$3.2 \times 10^{-4}$
C II	1334.53	6	0.043	0.00	$3.2 \times 10^{-4}$
	1335.71	6	0.077	0.01	
N IV	1718.55	3	0.179	16.21	$7.9 \times 10^{-5}$

## 5.3 Analysis

To allow a good comparison with the results of GL89, the spectra were reduced as described in Chapter 4. The NV doublet was corrected for the Lyman- $\alpha$  absorption, if necessary, using the same column densities as GL89, without re-determination. One exception was  $\zeta$  Puppis where a normalised spectrum was obtained from Dr. R.K. Prinja (Imperial College, London). Here the Lyman- $\alpha$  contribution had already been removed from the spectrum.

The photospheric lines profiles used were those of GL89 where for a doublet line the optical depth of the red component ( $A_{photR}$ ) was half that of the blue component ( $A_{photB}$ ). This has been shown to be incorrect in Chapter 4 but has been retained to allow direct comparison with the GL89 results. The same optical depth law ( $\beta$ -independent) was used and  $w_1 = 1$  for all lines analysed here. GL89 adopted a procedure of lowering  $w_1$  for a few of the singlet lines to obtain a better fit; only one of these appears in this study (the NIV line of HD 41650). In this analysis  $w_1 = 1$  was used as the fit was poor and did not influence the final mass-loss rates.

Data points were selected and initial input files generated for each line before submission to SEILS. The line parameters for each star were combined to fix the values of  $\beta$ ,  $w_g$  and  $v_\infty$  before generating the final profiles. These final parameters are given in Table 5.3 and shown in Figure 5.1. Appendix F contains the profiles and the line fitting parameters for the individual line fits.

## 5.4 Results

### 5.4.1 The line fits

From the fits given in Figure 5.1 the agreement between the theoretical profiles and observation is in most cases very good. It is not possible to give a direct comparison between the fits from this study and the ones given in GL89 due to a number of causes:

1. GL89 used an incorrectly programmed limb-darkening correction in most of their profiles which can give rise to significant changes in the profiles. See Figure 1 of GL89, and Groenewegen & Lamers (1991).
2. GL89 used the IUESIPS data extraction and ripple correction programs while this study used the more accurate IUEDR (Rees & Giddings 1989) program to re-extract the data. The differences in the extraction can lead to subtle differences in the determined spectra and thus the profile to be fitted.

Table 5.3: Final fits for the 6 O stars.

Star	Ion	$\beta$	$v_{\infty}$	$w_g$	$\alpha_1$	$\alpha_2$	$T_B$	$A_{photB}$	$w_{photB}$
HD14947 O5 If+	CIV	1.1	2100	0.13	0.2	-0.7	13.0	3.6	0.04
		0.2	100	0.02	1.0	1.0	2		
	SiIV	1.1	2100	0.13	-1.2	-0.7	4.7	0.0	0.00
		0.2	200	0.02	0.8	0.8	3		
HD24912 O7.5 IIIaf	CIV	0.9	2200	0.25	0.2	-0.1	5.5	0.0	0.00
		0.1	100	0.02	0.5	0.5	2		
	NV	0.9	2200	0.25	0.5	0.1	6.2	0.0	0.00
		0.4	200	0.03	0.7	0.7	4		
	NIV	0.9	2200	0.25	-0.5	1.0	0.36	0.9	0.04
		0.4	500	0.10	4.7	3.3	1.2		
HD30614 O9.5 Ia	CIV	1.8	1400	0.18	-0.7	-0.7	13.3	0.0	0.00
		0.5	100	0.05	0.5	0.5	2		
	NV	1.8	1400	0.18	-1.5	-1.2	6.6	0.0	0.00
		1.0	500	0.16	1.0	1.0	5		
	SiIV	1.8	1400	0.18	-1.5	-0.9	8.8	0.0	0.00
		0.5	100	0.05	0.5	0.5	2		
HD37043 O9 III	CIV	1.2	2500	0.01	0.1	0.7	2.3	2.0	0.15
		0.5	200	0.05	0.5	0.5	1		
	NV	1.2	2500	0.01	-1.5	0.2	12.6	0.8	0.08
		0.5	500	0.05	0.5	0.5	6		
	CIII	1.2	2500	0.01	-1.7	3.3	9.9	3.5	0.09
		0.5	500	0.05	0.5	0.5	6		
HD41650 O5 Vif	CIV	0.75	3100	0.035	-0.6	0.0	2.9	2.0	0.07
		0.1	200	0.01	0.5	0.5	1		
	NV	0.75	3100	0.035	-1.4	-0.8	8.7	2.0	0.03
		0.1	200	0.10	0.5	0.5	1		
	NIV	0.75	3100	0.035	-1.0	-0.9	0.2	0.8	0.04
		0.1	200	0.01	0.5	0.5	1		
HD66811 C Puppis O4 Iaf	CIV	0.9	2300	0.1	-0.7	-0.8	13.7	0.0	0.00
		0.2	250	0.02	0.5	0.5	5.0		
	NV	0.9	2300	0.1	-0.3	-0.4	13.9	0.7	0.10
		0.2	250	0.02	0.5	0.5	1.0		
	NIV	0.9	2300	0.1	-1.0	0.8	3.9	0.0	0.00
		0.2	300	0.02	0.5	0.5	2.0		
	SiIV	0.9	2300	0.1	-0.7	-0.3	2.6	1.0	0.10
		0.2	200	0.02	0.5	0.5	1.0		

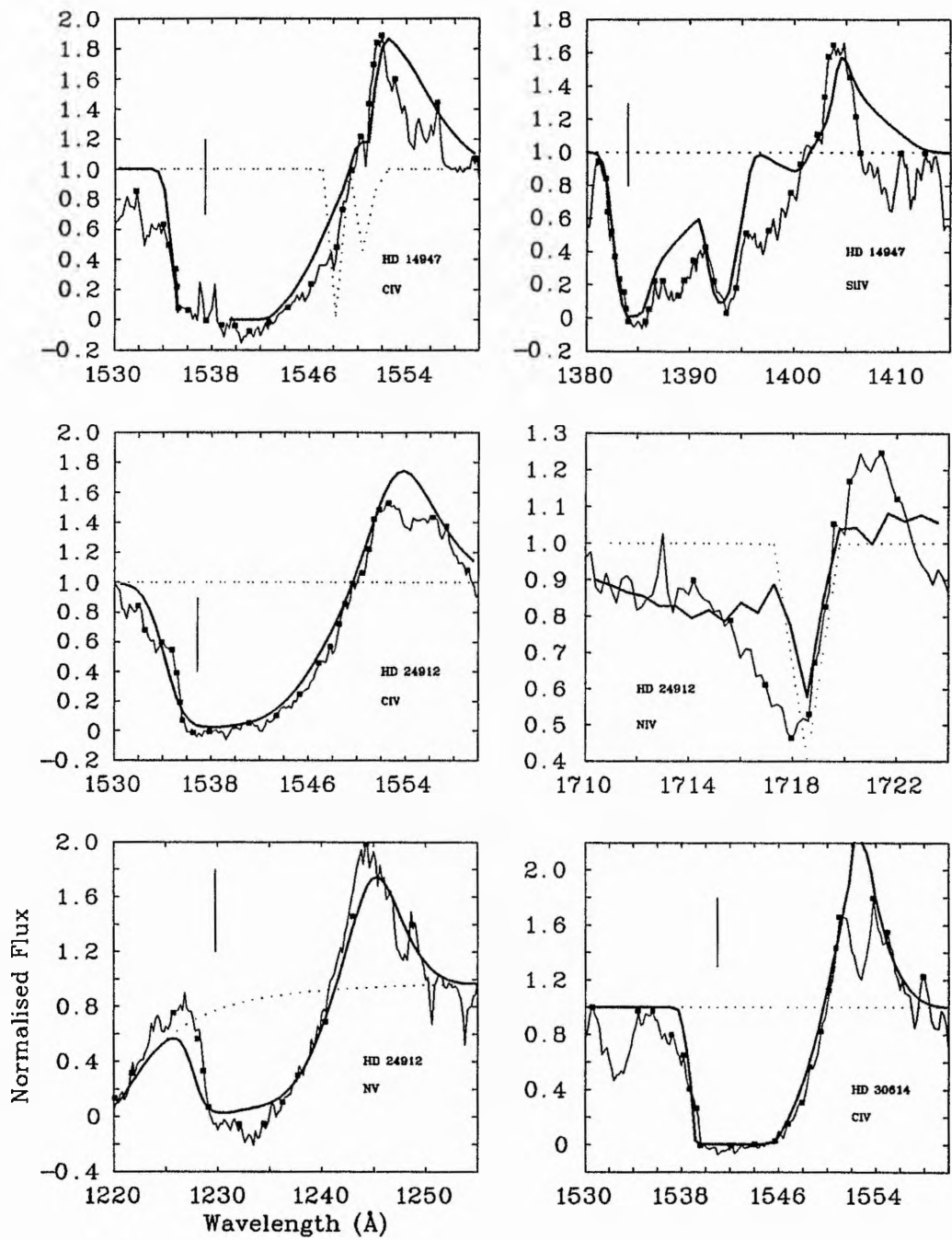


Figure 5.1: The final fits for the 6 O stars. The terminal velocity, relative to the blue component, is marked with a vertical line. The underlying photospheric profiles are shown by the dashed lines.

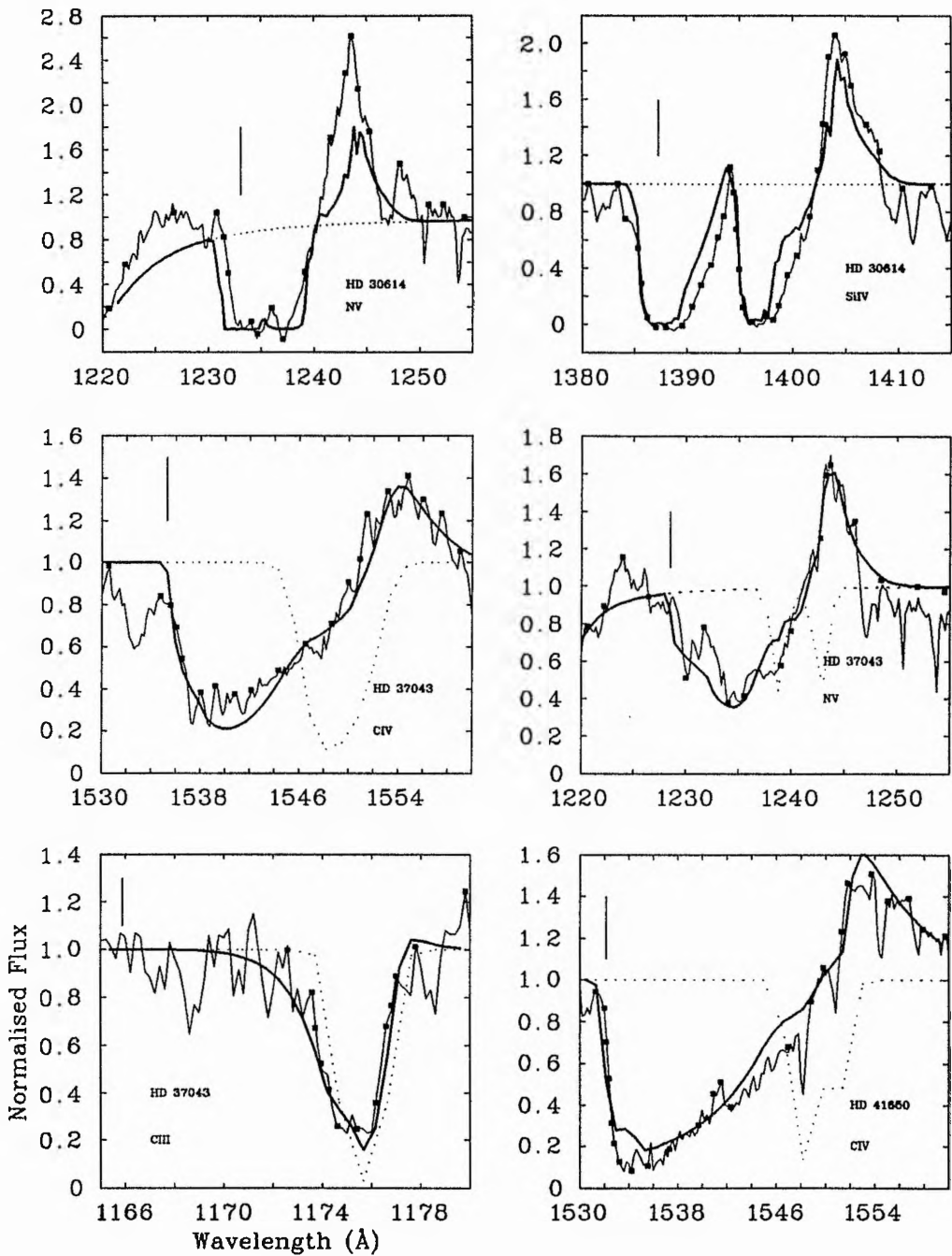


Figure 5.1: *continued*

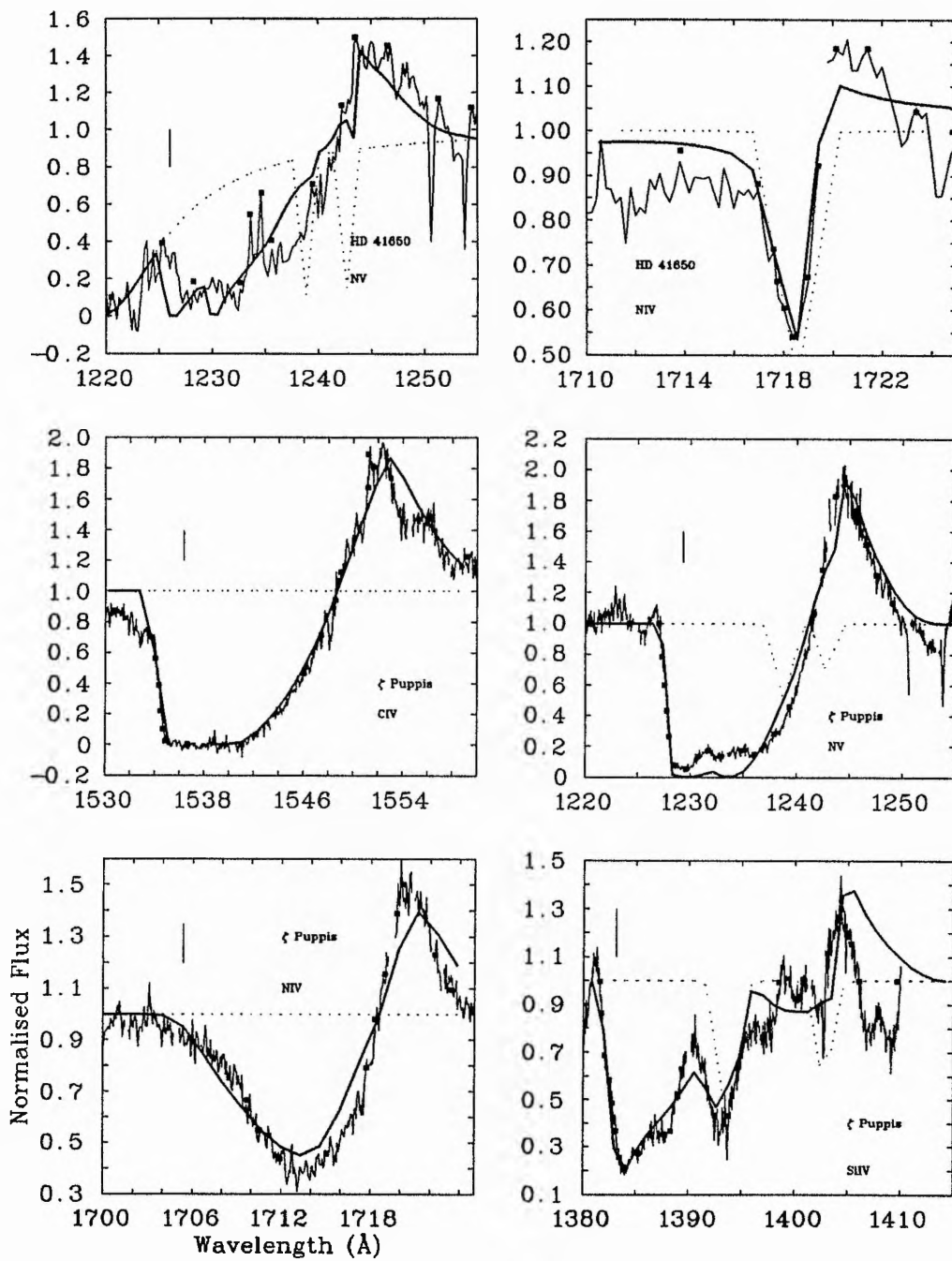


Figure 5.1: *continued*

3. GL89 did not give details of their continuum selection procedure in sufficient detail to allow duplication.

### 5.4.2 The singlet lines

The singlet lines show little deviation from a photospheric profile and thus do not strongly indicate a particular value of  $\beta$ ,  $w_g$  or  $v_\infty$ . Uncertainties in the adopted photospheric profiles lead to substantial uncertainties in these values. Specifically the absence of an appreciable emission peak leads to a poorly determined value of  $\beta$  and the lack of a steep blue edge an uncertain value of  $v_\infty$ .

### 5.4.3 The doublet lines

The CIV theoretical profiles provide very good fits to the observed wind line profiles. The steep blue edges, unaffected by blends with other lines, give a good indication of  $v_\infty$  (from its position) and  $w_g$  (from its gradient). The presence of a strong emission peak helps to constrain  $\beta$ .

The fits to the SiIV lines are good although the presence of blends and the fact that the observed profiles have a more photospheric-like profile leads to larger uncertainties in the determination of the three fixed parameters.

NV is especially poor for the determination of these fixed parameters. The poorer response of the IUE detector at this wavelength leads to a smaller signal to noise ratio. The presence of the  $L\alpha$  wing and numerous weak blending lines weakens the actual NV profile hampering the modelling and reducing the value of the results determined from this line.

### 5.4.4 The photospheric lines

The photospheric lines used in the final fit determination were the ones used by GL89. They used these parameters as another way of improving the fit and made no attempt at a scientific determination of the line depths. As the analysis of the O stars was primarily for testing the methods used, rather than for obtaining better parameters for the stars themselves, the values were not changed for this study.

A comparison of the depths and widths of photospheric lines given by GL89 and those determined from LTE model atmospheres for two stars is given in Table 5.4. Note that GL89 used no photospheric line when the wind line was deemed to be saturated. Elsewhere their lines are  $\sim 3$  times broader than determined from SPECTRUM but increasing the FWHM of a Gaussian profile is one approximate way of modelling a Stark-broadened profile.

Table 5.4: A comparison of photospheric line profiles from parameter fitting and model atmospheres.

		HD30614				HD37043			
		SPECTRUM		GL89		SPECTRUM		GL89	
Ion	$\lambda$ (Å)	$A_{phot}$	$w_{phot}$	$A_{phot}$	$w_{phot}$	$A_{phot}$	$w_{phot}$	$A_{phot}$	$w_{phot}$
C IV	1548.19	2.2	0.06	0.0	0.00	2.0	0.04	2.0	0.15
	1550.76	2.2	0.06	0.0	0.00	2.0	0.04	1.0	0.15
C III	1175.66	-	-	-	-	2.8	0.03	3.5	0.09
N V	1238.81	0.7	0.04	0.0	0.00	0.9	0.03	0.8	0.08
	1242.80	0.6	0.04	0.0	0.00	0.8	0.03	0.4	0.08
Si IV	1393.76	2.4	0.05	0.0	0.00				
	1402.77	2.4	0.05	0.0	0.00				

From Figure 5.1 it can be seen, especially in the C IV lines of HD 14947 and HD 41650, that the underlying photospheric lines are still visible in the observed profiles.

#### 5.4.5 Line parameters

In determining the final parameters for each star the results from the C IV line were given greater weighting than the other lines. The singlet and N V lines were given very little weight. Full details are given in Appendix F.

For the 6 stars analysed the line parameters determined with SEILS and those determined from a similar method by GL89 are in good agreement; Table 5.5.

The results for the terminal velocities are very good; agreement is in all cases within the error bounds and the results from SEILS do not seem to systematically differ from those of GL89.

The results for  $\beta$  are not in such good agreement even after 0.2 is added to the published values to take into account the effects of the limb-darkening error in the GL89 analysis (Groenewegen & Lamers 1991). In all cases except HD 41650 and HD 66811 the values of  $\beta$  determined with this study are greater than those published although for all but one of the stars the results just agree within the error bounds. The exception is HD 30614, the coolest of the five stars analysed, where the determined value of 1.8 is substantially above the published (and corrected) value of 0.9. However the associated uncertainty is large at 0.5.

The turbulent velocity is the most difficult parameter to determine accurately and uncertainties of  $\pm 100 \text{ km s}^{-1}$  on both the SEILS and published results are typical. For four of the six stars the results agree within error bounds, for the other 2 the discrepancy is much larger. HD 24912

Table 5.5: A comparison of the derived parameters for the wind lines of the O stars from SEILS and Groenewegen & Lamers (GL89). To allow meaningful comparison the turbulent velocity ( $v_g$ ) is given in  $\text{kms}^{-1}$  after multiplication by the terminal velocity. The published values of  $\beta$  have been corrected for the limb-darkening error (Groenewegen & Lamers 1991). The errors shown for SEILS are the smallest values of the error for the quantity, determined for individual lines, in Table 5.3

Star	$\beta$		$v_\infty$		$v_g$	
	SEILS	GL89	SEILS	GL89	SEILS	GL89
HD 14947	1.1	0.9	2100	2300	270	230
	$\pm 0.2$	$\pm 0.1$	$\pm 100$	$\pm 70$	$\pm 40$	$\pm 100$
HD 24912	0.9	0.7	2200	2400	550	290
	$\pm 0.1$	$\pm 0.15$	$\pm 100$	$\pm 100$	$\pm 45$	$\pm 120$
HD 30614	1.8	0.9	1400	1550	250	190
	$\pm 0.3$	$\pm 0.1$	$\pm 100$	$\pm 60$	$\pm 70$	$\pm 60$
HD 37043	1.2	0.8	2500	2450	25	370
	$\pm 0.1$	$\pm 0.1$	$\pm 200$	$\pm 150$	$\pm 125$	$\pm 70$
HD 41650	0.75	0.9	3100	2900	110	200
	$\pm 0.1$	$\pm 0.1$	$\pm 200$	$\pm 200$	$\pm 30$	$\pm 90$
HD 66811	0.9	0.9	2300	2200	230	290
	$\pm 0.2$	$\pm 0.1$	$\pm 200$	$\pm 60$	$\pm 45$	$\pm 70$

has twice the published turbulent velocity while HD30743 has a turbulence less than one tenth the published value; although with the largest error this discrepancy would be a factor of two.

In general these results are very encouraging; the agreement for  $v_\infty$  is excellent and that for  $\beta$  very good. The rather poorer results for  $v_g$  ( $\equiv w_g v_\infty$ ), for some stars is due to the difficulty in determining this parameter in line profiles that suffer from blending, especially at the blue edge. It is the hardest of the three main parameters to determine accurately.

#### 5.4.6 Errors

The individual fits are, in some cases, poor and do not agree well with other lines of the same star, although some of these discrepancies are numerical rather than physical in origin. When choosing values of  $\beta$ ,  $w_g$  and  $v_\infty$ , the spread of possible values amongst the individual fits is sometimes large and so the final adopted values must have large associated errors. C IV gives the best results for the determination of  $v_\infty$  and  $w_g$ , but if it is saturated then  $T_B$  is only a lower limit and the determined mass-loss rate also loses some accuracy. The errors given for the final fits (Table 5.3) are not formally derived but are estimates based on the quality of the individual fits and of the spread of values between the individual line fits. They are thus only guidelines to the quality of

the stated parameter. The errors given in the table are much larger than the errors quoted by GL89 for their final fits because to determine an error on a parameter they took the original fit and perturbed a single parameter until the fit became noticeably poorer. A much more accurate way would be to alter one parameter and then minimise the fit by altering the other parameters using a least squares method. This would give much larger errors as a large change in one parameter may be compensated (to some degree) by changing others. It was not possible to implement this method due to the large amounts of time that would be required.

## 5.5 Mass-Loss Rates and Ionisation Fractions

From the final line-fitting parameters given in Table 5.3, and from Equations 4.26 and 4.25 the mass-loss rates can be determined and are given in Table 5.6 along with the results of GL89 and the difference between the two. To give results that could be compared with those of GL89 the product of mass loss rate and ionisation fraction was evaluated at  $w = 0.5$ .

The uncertainties given in Table 5.6 were calculated as follows. First the formal errors were determined by varying each parameter by the error given in the final fit (Table 5.3) and calculating the change in the mass-loss rate. This generally gives low errors. Then the change of the product of the ionisation fraction and mass-loss rate through the wind was taken into account. The mass-loss rate is constant throughout the wind but the ionisation fraction will change due to the radial change of temperature and electron density in the wind. This factor, in general, produces larger errors and it is these that are quoted in Table 5.6. The error bounds were determined at  $w = 0.2$  and  $w = 0.8$  to eliminate "end effects" due to the parameterisation of the optical depth law used in the SEI method. The run of optical depth with velocity was also checked by eye to avoid errors where the difference between the values of ionisation fraction and mass-loss rate was small at  $w = 0.2, 0.5, 0.8$  but significant deviations occurred between these values.

The products of mass-loss rate and ionisation fraction determined by this study and the corrected values of GL89 are in good agreement. 10 out of the 18 lines agree with the GL89 results to within the errors given and most of the other lines have differences that are a factor of 3 (0.5 dex) or less. Only one line differs from the GL89 value by a factor of 10 or more. There appears to be no systematic difference between the GL89 and SEILS results; 10 lines have positive differences and 8 have zero or negative differences.

There are a number of sources of error, both inherent in the fitting process (*e.g.* continuum selection) and also in the way that GL89 chose to do their analysis (*e.g.* variable  $w_1$  and limb darkening). The values and associated errors of the GL89 mass-loss rates may be questioned. The errors on the results determined from this study are more realistic but are also, in some cases, quite large. The adoption of the GL89 photospheric line profiles cast some doubt on the accuracy of the

Table 5.6: The product of mass-loss rate and ionisation fraction for the 6 stars, determined at  $w = 0.5$ . The errors from the results of this study are determined by varying each of the 6 free parameters by the errors given in Table 5.3 to get the error in the mass-loss rate. This formal error is then compared with the range of mass loss rates with velocity in the range  $w = 0.2$  to 0.8 and the larger value used. The GL89 results have been corrected for the limb-darkening error (Groenewegen & Lamers 1991).

Star	Ion	SEILS		GL89		Difference
		$\dot{M}q_i$	Error	$\dot{M}q_i$	Error	SEILS - GL89
HD14947	CIV	-8.4	$^{+0.5}_{-0.7}$	> -8.4		< 0.0 $^{+0.5}_{-0.7}$
	SiIV	-8.3	$\pm 0.2$	-7.4	$\pm 0.2$	-0.9 $\pm 0.3$
HD24912	CIV	-8.7	$^{+0.3}_{-0.5}$	> -8.0		< -0.7 $^{+0.3}_{-0.5}$
	NV	-7.6	$^{+0.2}_{-0.5}$	> 7.0	$\pm 0.4$	< -0.6 $^{+0.4}_{-0.6}$
	NIV <sup>†</sup>	-9.3	$^{+0.1}_{-0.4}$	-9.6	$\pm 0.1$	0.3 $^{+0.1}_{-0.4}$
HD30614	CIV	-8.3	$^{+0.4}_{-0.5}$	> -8.3		< 0.0 $^{+0.4}_{-0.5}$
	NV	-8.8	$^{+0.4}_{-0.3}$	-7.7	$\pm 0.2$	-1.1 $\pm 0.4$
	SiIV	-8.2	$^{+0.3}_{-0.2}$	> -7.3		< -0.9 $^{+0.3}_{-0.2}$
HD37043	CIV	-8.7	$^{+0.1}_{-0.3}$	-8.5	$\pm 0.2$	0.2 $^{+0.2}_{-0.4}$
	NV	-8.0	$\pm 0.2$	-8.2	$\pm 0.1$	0.2 $\pm 0.2$
	CIII <sup>†</sup>	-10.2	$^{+1.0}_{-1.4}$	-9.9	$\pm 0.1$	-0.3 $^{+1.0}_{-1.4}$
HD41650	CIV	-8.8	$\pm 0.1$	-9.2	$\pm 0.1$	0.4 $\pm 0.1$
	NV	-7.8	$^{+0.0}_{-0.2}$	-8.0	$\pm 0.1$	0.2 $^{+0.1}_{-0.2}$
	NIV <sup>†</sup>	-9.4	$^{+0.3}_{-0.1}$	-10.2	$\pm 0.1$	0.8 $^{+0.3}_{-0.1}$
HD66811	CIV	-8.4	$\pm 0.3$	> -8.5		< 0.1 $\pm 0.3$
	NV	-7.2	$\pm 0.3$	> -7.8		< 0.6 $\pm 0.3$
	NIV	-8.5	$^{+0.2}_{-0.4}$	-8.7	$\pm 0.1$	0.2 $^{+0.3}_{-0.5}$
	SiIV	-8.2	$\pm 0.3$	-8.5	$\pm 0.1$	0.3 $\pm 0.4$

<sup>†</sup> For non-resonance lines the value given is for  $\log \dot{M}q_i E_i$ , where  $E_i$  is the excitation fraction of ion  $i$ .

Table 5.7: Theoretical models for the 6 O stars. Theoretical values of the stellar parameters can be compared with the observed values in Table 5.1. The models and theoretical data are from Pauldrach, Kudritzki, Puls & Butler (1990). The observed  $\dot{M}q$  values are from the SEILS analysis of this Chapter, the mass-loss rates are then determined from the ionisation fractions (see text and Table 5.9). A “C” model is for  $60 M_{\odot}$ , a “D” model is  $40 M_{\odot}$ . The arabic numerals give the stage of evolution with 1 being the ZAMS. Terminal velocities are in  $\text{kms}^{-1}$ , mass-loss rates in  $M_{\odot} \text{yr}^{-1}$ .

Observed				Theoretical Model					
Star	$v_{\infty}$	$\log \dot{M}q$	$\log \dot{M}$	Model	$T_{eff}$	R ( $R_{\odot}$ )	$\log(L/L_{\odot})$	$v_{\infty}$	$\log \dot{M}$
HD 14947	2100	-8.4	$-4.6 \pm 0.2$	C5	38,000	22.7	6.0	2120	-5.4
HD 24912	2200	-7.6	$-6.1^{+0.2}_{-0.5}$	C5	38,000	22.7	6.0	2120	-5.4
HD 30614	1400	-8.2	$-4.8^{+0.3}_{-0.2}$	C6	35,000	27.6	6.0	1420	-5.4
HD 37043	2500	-8.0	$-7.0 \pm 1.0$	C3	35,000	23.9	5.9	2650	-5.8
HD 46150	3100	-7.8	$-5.5 \pm 0.1$	D1	41,000	11.2	5.5	3650	-6.3
HD 66811	2300	-8.3	$-5.8 \pm 1.0$	C5	38,000	22.7	6.0	2120	-5.4

results presented here but with large (and realistic) errors the extra uncertainty introduced from the photospheric lines is likely to be small. From a similar study using SEI on the central stars of planetary nebulae, Perinotto, Cerruti-Sola & Lamers (1989) conclude that errors in the mass-loss rate determination of up to one dex can arise by using either different methods or different values of stellar parameters, which are often only poorly known. From this study, where the method and the stellar parameters are the same as used by GL89, it seems as if errors of a factor of 3 or so can be expected solely from a different interpretation of the “best fit”.

### 5.5.1 Application of improved NLTE results

It is only possible to determine true mass-loss rates if the ionisation fractions are known. From the previous discussion, the methods of LTE analysis or superionised winds (*e.g.* Hamann, Schönberner & Heber 1982) are not valid and only unified model atmospheres will give the correct results. Such codes have not been released and so such ionisation ratios cannot be generated to fit the stars analysed here. However PKPB use an improved NLTE wind line formation code to determine the wind lines and ionisation ratios for O stars of masses 40, 60, 85 and  $120 M_{\odot}$ . For these stars they calculated wind line profiles, ionisation ratios, mass-loss rates and terminal velocities, at different stages of the stars evolution.

For the 6 O stars it is not possible to tie the nearest model used with those stars analysed here by looking at the usual stellar parameters (*i.e.* mass, temperature, luminosity) as these are only poorly known for the observed stars; large errors in the data in Table 5.1 are very likely. However the terminal velocity of the stars in this sample can be determined without the need for such stellar parameters. These can be compared with the theoretical values given by PKPB. The closest matches between theory and observation are given in Table 5.7.

Table 5.8: Ionisation fractions for ions used in the O star analysis, taken from PKPB. Values greater than 1.00 are due to the slightly different number fractions used by PKPB and those given in Table 5.2. These values were reduced by 23% before application to Table 5.9.

Ion	Model				
	C1	C3	C5	C6	D1
CIII	$<3.0 \times 10^{-6}$	$4.4 \times 10^{-5}$	$1.3 \times 10^{-4}$	$2.8 \times 10^{-4}$	$<3.0 \times 10^{-6}$
CIV	$1.6 \times 10^{-3}$	0.95	0.88	1.15	0.001
NIV	0.013	1.15	1.14	1.23	0.14
NV	1.14	0.080	0.042	0.014	1.10
SiIV	$<2.5 \times 10^{-5}$	$1.5 \times 10^{-4}$	$2.8 \times 10^{-4}$	$5.0 \times 10^{-4}$	$<2.5 \times 10^{-5}$

Due to the fact that there are only two theoretical models in the required mass range and that for the  $40 M_{\odot}$  star there is only one model published (a main sequence model, "D1") means that the models given in Table 5.7 can only be approximations to the observed stars. Also in the sequence of 7 stars of  $60 M_{\odot}$  ("C1" to "C7") the terminal velocity does not decrease monotonically with increasing age but starts high ("C1"), falls ("C3") and then rises again ("C4") before falling away. Thus for a given terminal velocity two theoretical models may be applicable. In these cases (HD 37043 and HD 46150) the observationally determined luminosity classes were compared with the theoretical ones to determine the better option. For HD 46150 the "D1" model was preferred due to the high temperature and terminal velocity (model "C1" may also be applicable). For  $\zeta$  Puppis only a rough approximation was available in the form of the "C5" model. This model accounts for the star's high mass and moderate terminal velocity and supergiant classification but predicts a radius twice that given by GL89.

Using the published ionisation ratios relative to hydrogen (PKPB) and the elemental abundances (Table 5.2) the ionisation fractions in the wind were determined for the models used, Table 5.8.

From these ionisation fractions the actual mass-loss rates can be determined. The fact that some ionisation fractions are greater than one is due to the different values of the elemental abundances given in PKPB and in Table 5.2. As PKPB do not give the abundances used we assume that the largest tabulated ionisation fraction (1.23 for NIV) actually correspond to full ionisation and furthermore that as well as the nitrogen ionisation fractions being 23% too high the carbon and silicon abundances are too high by the same factor. This correction is made to the ionisation fractions before calculating the mass-loss rates given in Table 5.9.

The mass-loss rates for all ions should be the same; however a number of complications confound the agreement. Firstly some lines have better fits and thus smaller errors than other lines. More importantly some lines (notably CIV) are saturated and thus only a minimum mass-loss rate can be determined (due to the lower limit placed on the optical depth) even when the

Table 5.9: Mass-loss rates for the 6 O stars in  $\log \dot{M}$  ( $M_{\odot} \text{ yr}^{-1}$ ). Where two figures are given the first is for the "C1" model, the second for the "D1" model. The final mass loss rates are echoed in Table 5.6

Star	Ion	$\log \dot{M}$	
		Ion	Final
HD 14947	CIV	-8.1	$-4.6 \pm 0.2$
	SiIV	-4.6	
HD 24912	CIV	-8.5	$-6.1^{+0.2}_{-0.5}$
	NIV	-9.4	
	NV	-6.1	
HD 30614	CIV	-8.3	$-4.8^{+0.3}_{-0.2}$
	NV	-6.8	
	SiIV	-4.8	
HD 37043	CIII	-5.7	$-7.0 \pm 1.0$
	CIV	-8.6	
	NV	-6.7	
HD 41650	CIV	-5.6, -5.4	$-5.6 \pm 0.1, -5.4 \pm 0.1$
	NIV	-7.4, -8.4	
	NV	-7.7, -7.7	
$\zeta$ Puppis	CIV	-5.6	$-5.8 \pm 0.5$
	NV	-7.2	
	NIV	-6.6	
	SiIV	-3.6	

ionisation fraction is known. SiIV appears to be the best line for determining mass loss rates for O stars as it has a good wind line profile but is not saturated. For stars with a SiIV wind line the final adopted mass-loss rate is that given by the SiIV ion. For those three stars that do not have a SiIV wind line profile other lines must be used with caution. For HD 46150 the CIV line gives the largest mass-loss rates; this line is only just saturated at the terminal velocity and thus should give a good mass-loss rate. For HD 37043 none of the three lines are saturated and thus all lines should give the same result to within the errors quoted. There appears to be nothing to choose between the three lines and thus a mean value of -7.0 has been quoted, with a large uncertainty. For HD 24912 the NV line gives the highest mass-loss rate. The CIV line is saturated and the NIV line has a very poor fit of the theoretical to the observed profile; thus the value from the NV line is used. For  $\zeta$  Puppis the SiIV line is present but the fit is not excellent; the CIV line gives a much better fit although the theoretical profile has a greater optical depth than is indicated by the observed profile. The final mass-loss rate for this star is thus the mean values of the SiIV and CIV values with a correspondingly large uncertainty.

### 5.5.2 Conclusions

The agreement between the theoretical results and those from SEILS appear to be reasonable although the difference in mass-loss rates is greater than the errors on them. There are a number of reasons for this. Firstly the errors given assume that the SEI method works exactly and that the errors are solely determined from the accuracy in which the SEI method fits the observed profiles. Of course there will be errors in the SEI method itself, in the assumed physics and especially the parameterisation of the optical depth and velocity laws. Secondly the poor agreement between the theoretical models and the observed stars means that direct comparisons of mass-loss rates is not applicable. Specifically most of the observed stars are of lower mass than the theoretical models; thus the mass-loss rates for the observed stars would be expected to be lower than predicted for the higher mass theoretical models. Additionally, these theoretical mass-loss rates may not be correct, may not be applicable to all stars and have (unknown) errors associated with them. Indeed Howarth & Prinja (1989) find that for a given luminosity a scatter of 1 dex in observed mass-loss rates are found. If this level of error is applicable in this study then the observed and theoretical mass-loss rates are in good agreement. There seems to be no systematic variation between the theoretical mass-loss rates of PKPB and those found in this study.

## 5.6 $\zeta$ Puppis and HD 14947: A Comparison of Different Studies.

Of the 6 stars used in this program two, HD14947 and HD66811 ( $\zeta$  Puppis) have been analysed by a number of workers, in addition to this study. The results from these studies are given in Table 5.10, although note that not all are truly independent and some use poor data or *a priori* assumptions that may not be valid.

Those methods that determine the mass-loss rate directly give consistent results in general. In general UV wind line analyses only provide the product of mass-loss rate and ionisation fraction reliably. Determination of an accurate ionisation fraction is not possible without the use of improved NLTE or unified model atmospheres. The ionisation fractions used from the models of PKPB can only be approximate for the actual stars under investigation here. However, mass-loss rates of  $\log \dot{M} = -4.6$  and  $-5.8$  ( $M_{\odot} \text{ yr}^{-1}$ ) are obtained for HD 14947 and  $\zeta$  Puppis respectively. These results are a factor of 3 (0.5 dex) too high (HD 14947) or too low ( $\zeta$  Puppis). The associated errors on all the values in the table will amount to  $\pm 0.2$  dex or more. However a number of these published results use poor data (*e.g.* Abbott, Biegging, Churchwell & Cassinelli 1980) or techniques that appear to be wrong (*e.g.* the "warm wind model" of Hamann, 1980) At best the actual errors on the published results will be substantially higher.

Table 5.10: Mass loss determinations for HD14947 and  $\zeta$  Puppis from the literature. The method of determination is indicated.

Technique	log $\dot{M}$		Reference
	HD14947	$\zeta$ Puppis	
H $\alpha$	-5.08	-5.04	(1)
H $\alpha$	-5.04	-5.05	(2)
H $\alpha$	-5.11		(3)
H $\alpha$		-5.22	(4)
H $\gamma$	-5.22	-5.30	(5)
IR	-5.62	-5.46	(6)
Radio	< -4.62 <sup>‡</sup>	-5.46	(7)
UV	$\geq$ -5.24	$\geq$ -5.7	(8)
UV <sup>†</sup>	< -7.4	-7.8	(9)
UV <sup>¶</sup>		-5.23	(10)
UV	-5.5	-5.3	(11)
UV <sup>§</sup>		-5.4	(12)
UV		-5.14	(13)
UV + NLTE	< -4.6	-5.8	This study

References: (1): Conti & Frost 1977. (2): Klein & Castor 1978. (3): Peppel 1984. (4): Olson & Ebbets 1981. (5): Hutchings 1976. (6): Barlow & Cohen 1977. (7): Abbott, Biegling, Churchwell & Cassinelli 1980. (8): Garmany, Olson, Conti & Van Steenberg 1981. (9): Groenewegen & Lamers 1989. (10): Hamann 1980. (11): Howarth & Prinja 1989. (12): Puls 1987. (13): Lamers & Morton 1976.

Notes:

<sup>‡</sup> To determine this value an erroneously high terminal velocity of 3500 km s<sup>-1</sup> was used (determined from low resolution IUE spectra).

<sup>†</sup> These values are the product of the mass-loss rate and the ionisation fraction of the Si IV line - the one that gives the highest value. Without knowledge of the ionisation fractions these values cannot be compared with the others in the table.

<sup>¶</sup> The ionisation fractions used were determined from the incorrect "warm wind model".

<sup>§</sup> Some a priori assumptions were made about the mass loss so this is not a totally independent determination.

H $\alpha$ , H $\gamma$ : Mass loss determination from the measurement of the equivalent widths of H $\alpha$  and H $\gamma$ .

IR: From the measurement of infra-red excesses.

Radio: From radio emission.

UV: From the analysis of UV profiles using SEI or the co-moving frame method.

UV + NLTE: As above but using ionisation fractions from improved NLTE wind line formation codes to determine actual mass-loss rates.

The results of this study have large associated errors as the mass-loss rates from the individual lines do not agree well with each other. Although there are good reasons for accepting one value over another, the errors in the final mass-loss rates from this study must amount to at least one dex. The use of the NLTE ionisation fractions can only be regarded as an approximation due to the differences between the NLTE stellar models parameters and those of the study sample.

A final agreement within a factor of three for the mass-loss rates can be regarded as very good.

## 5.7 Parameter Variation with Temperature

One major unsolved problem in stellar wind analysis is whether the value of the gradient of the velocity law,  $\beta$ , is temperature dependent. Bertout, Leitherer, Stahl & Wolf (1985) found from looking at mass-loss rates in the infra-red determined from the continuum flux that there is a variation with  $\beta$  with temperature and that  $\beta$  is greater for lower temperatures. GL89 could find no such variation in their analysis.

The results presented in this study, although consisting of only 6 points, do seem to indicate that Bertout *et al.* may be correct with a higher value of  $\beta$  being indicated for stars with lower effective temperatures. However this conclusion can only be tentative as the result relies on the high  $\beta$  of the coolest star; the only point that deviates significantly from  $\beta \sim 0.8$ . From the profiles in Figure 5.1, the results for this star (HD 36014) are seen to be fair, with a spread of  $\beta$  values in the individual fits (Appendix F). The presence of the blend in the CIV emission peak and the less than perfect fit for the SiIV emission peak also make the values of  $\beta$  uncertain for this star.

The apparent systematic shift of  $\Delta\beta = 0.5$  between the values presented here and those of Bertout *et al.* for the higher temperature stars may not be significant due to the completely different methods of determining  $\beta$  (IR flux distribution and detailed UV wind line modelling). However with only a test sample of 6 stars it is not possible to conclude with any certainty; especially as  $\beta$  is a parameter that has large errors. Figure 5.2 shows the data of GL89 and Bertout *et al.* with the results of this study superimposed.

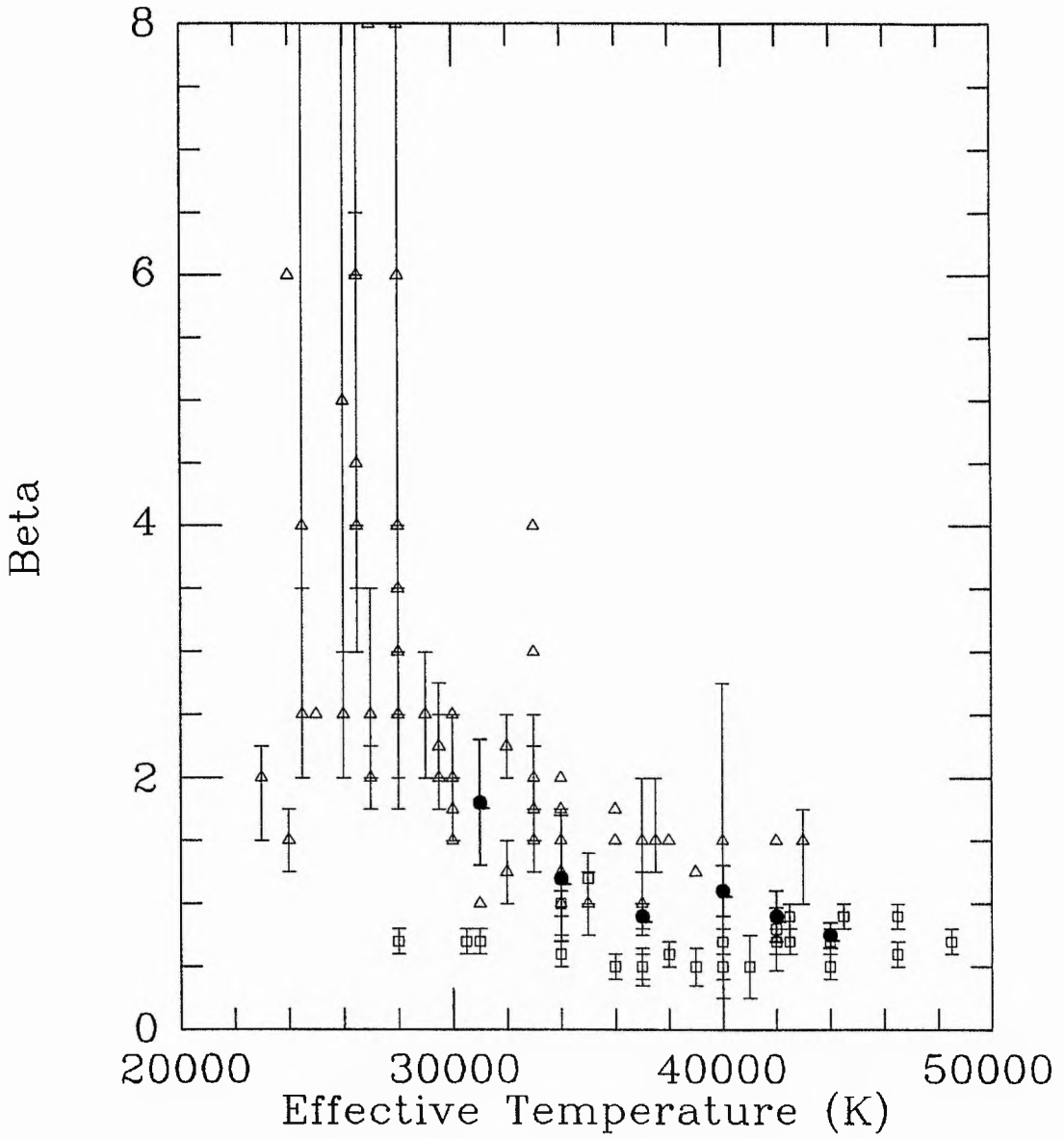


Figure 5.2: The variation of  $\beta$  with effective temperature for O stars. The results of Groenewegen & Lamers (1989) (open squares) and Bertout *et al.* (1985) (open triangles) are shown with those of this study superimposed (solid circles). Points with no error bars are upper limits.

## 5.8 Summary

*Results from a SEILS analysis of six O stars are very encouraging, in that the parameters determined in this study lead to theoretical profiles which fit the observed profiles as well as those published previously.*

*From the fits performed for each star  $v_{\infty}$  and  $w_g$  seem to be consistent in each individual fit while the values of  $\beta$  show more scatter. However the values of  $\beta$  obtained do seem to show tentative agreement with those values determined by Bertout et al. (1985) lending some support to these results and indicating that  $\beta$  may increase with decreasing temperature. Further studies need to be implemented to solve the problem conclusively.*

*The determined products of mass-loss rate and ionisation fraction are in good agreement with those published by GL89. Using ionisation fractions from accurate improved NLTE codes the actual mass-loss rates have been determined for the stars. These are in good agreement with previously published results.*

*The purpose of the O star study - to gain familiarity with the method and to test the results of GL89 - has been fully successful. The extensive testing and analysis undertaken gives good reason to believe that a wind line analysis of the EHe and sdO stars as well as the hydrogen-deficient binary  $\nu$  Sgr can be undertaken and the results given considerable weight.*

## 5.9 References

- Abbott, D.C., Biegging, J.H., Churchwell, E. & Cassinelli, J.P., 1980. *Astrophys. J.*, **238**, 196.
- Barlow, M.J. & Cohen, M., 1977. *Astrophys. J.*, **213**, 737.
- Bertout, C., Leitherer, C., Stahl, O. & Wolf, B., 1985. *Astr. Astrophys.*, **144**, 87.
- Castor, J.I., Abbott, D.C. & Klein, R., 1975. *Astrophys. J.*, **195**, 157.
- Conti, P.S. & Frost, S.A., 1977. *Astrophys. J.*, **212**, 728.
- Danckwort, W. & Treffitz, E., 1978. *Astr. Astrophys.*, **65**, 93.
- Friend, D.B. & Abbott, D.C., 1986. *Astrophys. J.*, **311**, 701.
- Friend, D.B. & Castor, J.I., 1983. *Astrophys. J.*, **272**, 259.
- Garmany, C.D., Olson, G.L., Conti, P.S. & Van Steenberg, M.E., 1981. *Astrophys. J.*, **250**, 660.
- Groenewegen, M.A.T. & Lamers, H.J.G.L.M., 1989. *Astr. Astrophys. Suppl.*, **79**, 359.
- Groenewegen, M.A.T. & Lamers, H.J.G.L.M., 1991. *Astr. Astrophys. Suppl.*, **88**, 625.
- Hamann, W.-R., 1980. *Astr. Astrophys.*, **84**, 342.
- Hamann, W.-R., Schönberner, D. & Heber, U., 1982. *Astr. Astrophys.*, **116**, 273.
- Heber, U., 1983. *Astr. Astrophys.*, **118**, 39.
- Howarth, I.D. & Prinja, R.K., 1989. *Astrophys. J. Suppl.*, **69**, 527.
- Hutchings, J.B., 1976. *Astrophys. J.*, **203**, 438.
- Klein, R.I. & Castor, J.I., 1978. *Astrophys. J.*, **220**, 902.
- Kondo, Y., 1987. *Exploring the Universe with the IUE Satellite*, Reidel.
- Kudritzki, R.P., 1988. In: *Radiation in Gaseous Moving Media, Eighteenth "Saas-Fee" Conference*, p.1, eds. W. Chmielewski & T. Lanz, Geneva Observatory.
- Lamers, H.J.G.L.M., Cerruti-Sola, M. & Perinotto, M., 1987. *Astrophys. J.*, **314**, 726.
- Lamers, H.J.G.L.M. & Morton, D.C., 1976. *Astrophys. J. Suppl.*, **32**, 715.
- Morton, D.C., 1967. *Astrophys. J.*, **147**, 1017.
- Olson, G.L. & Ebbets, D., 1981. *Astrophys. J.*, **248**, 1021.
- Pauldrach, A.W.A., Kudritzki, R.P., Puls, J. & Butler, K., 1990. *Astr. Astrophys.*, **228**, 154.
- Peppel, U., 1984. *Astr. Astrophys. Suppl.*, **57**, 107.
- Perinotto, M., Cerruti-Sola, M. & Lamers, H.J.G.L.M., 1989. *Astrophys. J.*, **337**, 398.

Puls, J., 1987. *Astr. Astrophys.*, **184**, 227.

Rees, P. & Giddings, J., 1989. *STARLINK User Note* 37.7.

Snow, T.P. & Morton, D.C., 1976. *Astrophys. J. Suppl.*, **32**, 429.

## Chapter 6

# The Winds of the Extreme Helium Stars

### 6.1 Introduction

Mass loss from O stars is well documented, but mass loss from the much smaller and less massive sdO stars has not been investigated in such depth. The EHe stars also show signs of mass loss but with much lower terminal velocities than the sdO stars. Accurate mass-loss rates (MLR) from these stars are necessary to determine how their future evolution will proceed and to determine the mechanism for the mass loss and whether their peculiar chemical composition and late stage of evolution affects the MLR.

The SEILS code was applied to all EHe stars that have high resolution IUE SWP spectra available for them. Of the 27 stars catalogued as EHe or possible EHe stars by Drilling & Hill (1986) there are 7 that are EHe stars or related objects (Landolt 1986) and have the required spectra available. The true EHe stars are HD 168476, HD 160641, BD +10° 2179 and BD -9° 4395. The other 3 stars (BD +37° 442, BD +37° 1977 and BD +13° 3224) appear to be in some ways between the EHe stars and the related sdO stars. See Figure 1.1, page 3.

Little previous analysis has been done on the winds of the EHe stars; and none with the SEI method. However three of these objects (HD 160641, BD -9° 4395 and BD +10° 2179) have already had their wind lines analysed with the co-moving frame method (Hamann, Schönberner & Heber 1982, hereafter HSH). With this method the final results for the MLR still have errors of between 30% and 100%. Their continuum determinations (especially in the case of BD -9° 4395) are open to question and so their final wind line parameters can also be questioned. Their final MLR appear

Table 6.1: SWP IUE spectra for EHe stars.

Star	Spectrum	J.D. (-2440000)	dd/mm/yy	ddd/yy	Type	Ap.	Exp. (sec.)	ITFMAX
HD 168476	SWP5767	4066	11/07/79	192/79	GPHOT	LAP	18180	19632
BD +10° 2179	SWP7678	4256	17/01/80	017/80	GPHOT	LAP	8700	
BD -9° 4395	SWP13626	4723	12/04/81	118/81	GPHOT	LAP	39800	
	SWP30797	4903	17/04/87	107/87	GPHOT	LAP	40400	
	SWP30808	4905	19/04/87	109/87	GPHOT	LAP	39200	
	SWP30814	4906	20/04/87	110/87	GPHOT	LAP	34100	
BD +13° 3224	SWP19841	5453	26/04/83	118/83	GPHOT	LAP	21000	
	SWP19968	5468	12/05/83	133/83	GPHOT	LAP	26000	
HD 160641	SWP9742	4460	08/08/80	221/80	GPHOT	LAP	14400	
BD +37° 1977	SWP7248†	7859	28/11/89	332/89	GPHOT	LAP	2643	
BD +37° 442	SWP6768	4152	06/10/79	276/79	GPHOT	LAP	3600	

† SWP7248 would not re-extract so the spectra extracted using IUESIPS, provided by the IUE project, was used.

to be invalid due to the use of the apparently incorrect “warm wind” model (Pauldrach, Kudritzki, Puls & Butler 1990).

It is appropriate to analyse the winds of all suitably observed EHe stars using the SEILS method, including the EHe/sdO stars BD +37°1977 and BD +37°442 which have not been fully analysed before, and to compare the results with those from the co-moving frame method, which may be more appropriate for the low terminal velocity EHe stars where the Sobolev approximation may break down. The results of Lamers, Cerruti-Sola & Perinotto (1987) indicate that the improved Sobolev method (incorporated in SEILS) give comparable results to those from the co-moving frame method for high terminal velocity stars. If the Sobolev method will also give comparable results for these lower terminal velocity stars then SEILS will be a powerful tool for the determination of MLR from all stars rather than just those with high terminal velocities.

## 6.2 The Data

The IUE spectra analysed are listed in Table 6.1 along with dates, exposure times and ancillary data. In all but one case the spectra were re-extracted using IUEDR (Rees & Giddings 1989) and Barker’s (1984) ripple correction method. Where a number of spectra were available these were co-added, with weights proportional to exposure time, to form a higher signal to noise template. The spectra were then corrected for the heliocentric radial velocities of the stars to bring all the stellar lines to their laboratory wavelengths. Radial velocity and other physical data for the stars are given in Table 6.2.

The spectra were normalised, correction for Lyman- $\alpha$  made if necessary and the data points selected. Photospheric line profiles were determined and an initial solution obtained using a standard input file. Full details of the procedures for each individual star are given in Section 6.6, along with a discussion of the results.

Table 6.2: Physical data for the hydrogen-deficient stars. The abundances are logarithms of mass fractions, which have been extracted from number fractions or values relative to the Sun, taken from the references. The luminosities,  $L$ , are relative to BD +13° 3224. Typical masses of  $0.8 M_{\odot}$  are assumed (Hamann, Schönberner & Heber 1982) for all stars to obtain the radii,  $R$ , and luminosities.

Star	Abundances				
	C	N	Si	H	He
HD 168476	-1.7 <sup>(6)</sup>	-2.1 <sup>(6)</sup>	-3.0 <sup>(6)</sup>	<-4.4 <sup>(6)</sup>	-0.1 <sup>(6)</sup>
BD +10° 2179	-1.5 <sup>(6)</sup>	-2.9 <sup>(6)</sup>	-3.4 <sup>(6)</sup>	-3.7 <sup>(6)</sup>	-0.1 <sup>(6)</sup>
BD -9° 4395	-1.9 <sup>(5)</sup>	-2.9 <sup>(5)</sup>	-2.8 <sup>(5)</sup>	-4.0 <sup>(5)</sup>	-0.1 <sup>(5)</sup>
BD +13° 3224		-1.4 <sup>(3)</sup>	-2.3 <sup>(3)</sup>	-1.3 <sup>(3)</sup>	-0.1 <sup>(3)</sup>
HD 160641	-2.4 <sup>(4)</sup>	-3.0 <sup>(4)</sup>	-3.2 <sup>(4)</sup>		
BD +37° 1977	-1.6	-2.5			
BD +37° 442	-1.6 <sup>(12)</sup>	-2.5 <sup>(12)</sup>			

Star	Rad. Vel. ( $\text{km s}^{-1}$ )	$T_{\text{eff}}$ (K)	$\log g$ ( $\text{cm s}^{-1}$ )	$L$	$R$ ( $R_{\odot}$ )
HD 168476	-172 <sup>(11)</sup>	12400 <sup>(7)</sup>	1.3 <sup>(7)</sup>	9.5	33.0
BD +10° 2179	+155 <sup>(8)</sup>	16800 <sup>(4)</sup>	2.6 <sup>(4)</sup>	1.6	7.4
BD -9° 4395	-59 <sup>(4)</sup>	24000 <sup>(5)</sup>	2.4 <sup>(5)</sup>	6.7	9.3
BD +13° 3224	+3 <sup>(10)</sup>	28000 <sup>(3)</sup>	3.7 <sup>(3)</sup>	1.0	2.1
HD 160641	+78 <sup>(11)</sup>	35000 <sup>(4)</sup>	3.5 <sup>(4)</sup>	6.8	2.6
BD +37° 1977	-59 <sup>(2)</sup>	50000 <sup>(1)</sup>	4.0	37.0	1.5
BD +37° 442	-94 <sup>(9)</sup>	60000 <sup>(12)</sup>	4.0 <sup>(12)</sup>	54.1	1.5

References: (Unreferenced values are estimates.)

- (1): Darius, Giddings & Wilson (1979). (2): Wolff, Pilachowski & Wolstencroft (1974). (3): Jeffery, Heber & Hill (1986). (4): Hamann, Schönberner & Heber (1982). (5): Jeffery & Heber (1992). (6): Heber (1986). (7): Walker & Schönberner (1981). (8): Klemola (1961). (9): Drilling & Heber (1989). (10): Jeffery & Hill (1986). (11): Drilling & Heber (1986). (12): Husfeld (1989).

Table 6.3: Models used to determine the photospheric lines for the EHe stars. Where no model is given there was no model available and so estimates had to be used. The models are shown in the format “TttGggXxxyy” where tt is the effective temperature in thousands of Kelvin, gg is ten times the logarithm of the surface gravity (cgs) . xx is the percentage abundance of hydrogen and yy that of helium (by number). (Thus a model T24G40X0099 represents a star with an effective temperature of 24,000K, a logarithm of surface gravity 4.0 and a zero hydrogen abundance and 99% helium by number.)

Star	Model
HD 168476	T14G15X0099
BD +10° 2179	T16G25X0099
BD -9° 4395	T24G25X0099
BD +13° 3224	T28G35X0099
HD 160641	T28G35X0099
BD +37° 1977	Estimated
BD +37° 442	Estimated

### 6.3 Photospheric Lines

The underlying photospheric lines for the stars were calculated from hydrogen-deficient model atmospheres (without line-blanketing) using the SPECTRUM line synthesis code together with the abundances given in Table 6.2. SPECTRUM does not include all broadening mechanisms and so the synthetic line profiles are only an initial approximation.

The derived photospheric depths were retained, with the same depth being used for both components of a doublet. The widths were initially calculated with SPECTRUM using a rough estimate of the terminal velocity to obtain  $w_{phot}$ . The widths obtained were then broadened by a factor of roughly three based on the experience with O star wind lines (Chapter 5) and comparison with Stark broadened line profiles calculated in HSH for BD -9° 4395 and HD 160641. These, non-Gaussian, profiles were then matched as far as possible with Gaussian photospheric profiles within SEILS. The final photospheric profiles adopted are shown in Table 6.4. The photospheric line parameters were used in part as free parameters to improve the fit, being adjusted as necessary and did not always correspond to those determined by SPECTRUM and then broadened.

The model atmosphere used for each star was the closest model that was available at the time; given in Table 6.3. No models were available for BD +37° 442 and BD +37° 1977 as these stars are much hotter than the hottest model available and for such stars an LTE model atmosphere would not be appropriate (Kudritzki 1988) even though they are high gravity objects.

## 6.4 The Line Profiles

Of the seven stars that fulfil the criteria for SEILS analysis two of them (HD 168476 and BD +13° 3224) do not show sufficiently large line profile asymmetries to allow wind line modelling given the uncertainty in the photospheric line profiles. If such small asymmetries are indicative of a low terminal velocity then the Sobolev approximation would break down and SEILS could not be used to model these lines.

For HD 168476, despite being quite luminous, it is too cool ( $T_{\text{eff}} = 12,400\text{K}$ ) for resonance wind lines in the UV; none were found in an inspection of the spectrum. No modelling of this star was undertaken although in principle lower limits to the MLR could be determined if accurate Stark broadened photospheric line profiles were available.

## 6.5 The Models

From the analysis of the 6 O stars (Chapter 5) and from a discussion of the theory of wind lines as well as the mechanics of the numerical solution it is uncertain whether the  $\beta$ -independent or  $\beta$ -dependent optical depth laws should be used. The  $\beta$ -dependent optical depth law was recommended by Groenewegen & Lamers (1989) from assumptions made about the behaviour of the ionisation fraction within the wind.

The results with the  $\beta$ -independent optical depth law on O stars (Chapter 5) were very good indicating that the  $\beta$ -independent form may be the more applicable. It also has the advantage that the parameters  $\beta$  and  $\alpha_2$  are fully independent of each other and this form of the optical depth law should be favoured from the stand point of a numerical solution.

Furthermore, there is the question of whether a fixed value of  $\beta=1$  will give similar results to those when  $\beta$  is allowed to be free. This is important to determine whether  $\beta \sim 1$ , as predicted by the Castor, Abbott & Klein (1975) wind line theory, is consistent with the observed wind line profiles.

When analysing the winds of the EHe stars both the  $\beta$ -dependent and the  $\beta$ -independent optical depth laws were used to enable comparisons to be made and to determine which law gives the most accurate results. Following these analyses the wind-line profiles were re-determined with  $\beta = 1$  to allow further comparisons. Each analysis is discussed separately below.

The errors shown in the tables of initial line fit parameters are those errors generated by SEILS. The errors in the tables of final line fit parameters are a combination of the errors. For the three main parameters ( $\beta$ ,  $w_g$  and  $v_\infty$ ) the errors determined by SEILS are modified by taking into

account the spread of values between the different lines of a given star determined in the initial fits. For  $\alpha_1$  and  $\alpha_2$  the errors from SEILS are used unless these are less than 0.5, in which case a value of 0.5 is given to take into account inherent uncertainties in the fitting (Section 4.5.5).

The same photospheric profiles were used in all the solutions and full discussions of all the results are given in Section 6.8. The parameters and profile fits for the initial fitting of the lines for all three analyses are grouped together in Appendix F.

### **6.5.1 The $\beta$ -dependent optical depth law**

The results from the initial fitting of the wind line profiles are given in Table F.2 with the profiles themselves in Figure F.2. The final results are in Table 6.4 and the final profiles are shown in Figure 6.1.

### **6.5.2 The $\beta$ -independent optical depth law**

The initial and final fit parameters are tabulated in Tables F.3 and 6.5 respectively with the initial and final profiles shown in Figures F.3 and 6.2.

### **6.5.3 The $\beta = 1$ solution**

The initial and final results are tabulated in Tables F.4 and 6.6 respectively with the initial and final profiles shown in Figure F.4 and 6.3.

Table 6.4: Final fits for the EHe stars, using the  $\beta$ -dependent form of the optical depth law. Errors are in small type.

Star	Ion	$\beta$	$v_\infty$	$w_g$	$\alpha_1$	$\alpha_2$	$T_B$	$A_{phot}$	$w_{phot}$
BD +10° 2179	CIV	0.10	350	0.39	-0.3	-0.3	1.8	0.85	0.05
		0.03	70	0.03	0.5	0.5	0.22		
BD -9° 4395	CII	1.0	400	0.40	9.4	6.4	2.6	1.29	0.30
		0.4	50	0.1	3.0	2.0	1.0		
	CIV	1.0	400	0.40	2.9	0.1	11.2	1.62	0.30
		0.4	100	0.2	2.0	0.3	4.0		
SiIV	1.0	400	0.40	-1.0	0.1	23.1	1.09	0.60	
	+3.0 -0.7	80	0.1	2.0	2.0	20			
HD 160641	CII	3.5	600	0.2	1.7	8.9	5.5	1.40	0.05
		0.3	200	0.02	1.0	2.0	1.0		
	CIV	3.5	600	0.2	1.6	-0.4	63	1.43	0.25
		+2.0 -0.3	100	0.05	2.0	2.0	50		
	NV	3.5	600	0.2	3.5	0.6	1.0	0.07	0.30
		+2.0 -0.5	200	0.05	0.5	0.5	0.5		
SiIV	3.5	600	0.2	0.6	0.0	12.5	1.11	0.40	
	+4.0 -0.5	150	0.05	0.5	2.0	5			
BD +37° 1977	CIV	0.17	1930	0.06	2.7	5.6	143	1.0	0.10
		0.02	200	0.01	10	10	100		
	NIV	0.17	1930	0.06	-1.9	-0.4	0.1	0.50	0.02
		0.08	400	0.04	2.0	4.0	+0.3 -0.05		
NV	0.17	1930	0.06	1.0	3.7	51	1.0	0.12	
	0.03	300	0.03	2.0	2.0	40			
BD +37° 442	CIV	1.0	2200	0.03	2.0	2.4	11.8	1.0	0.1
		0.3	100	+0.20 -0.02	0.5	0.5	3.0		
	NIV	1.0	2200	0.03	-0.9	3.0	0.4	0.60	0.01
		0.6	400	+0.10 -0.01	4.0	5.0	+1.0 -0.3		
	NV	1.0	2200	0.03	0.4	1.4	2.0	2.0	0.1
		0.8	400	+0.20 -0.02	2.0	2.0	+4.0 -1.5		

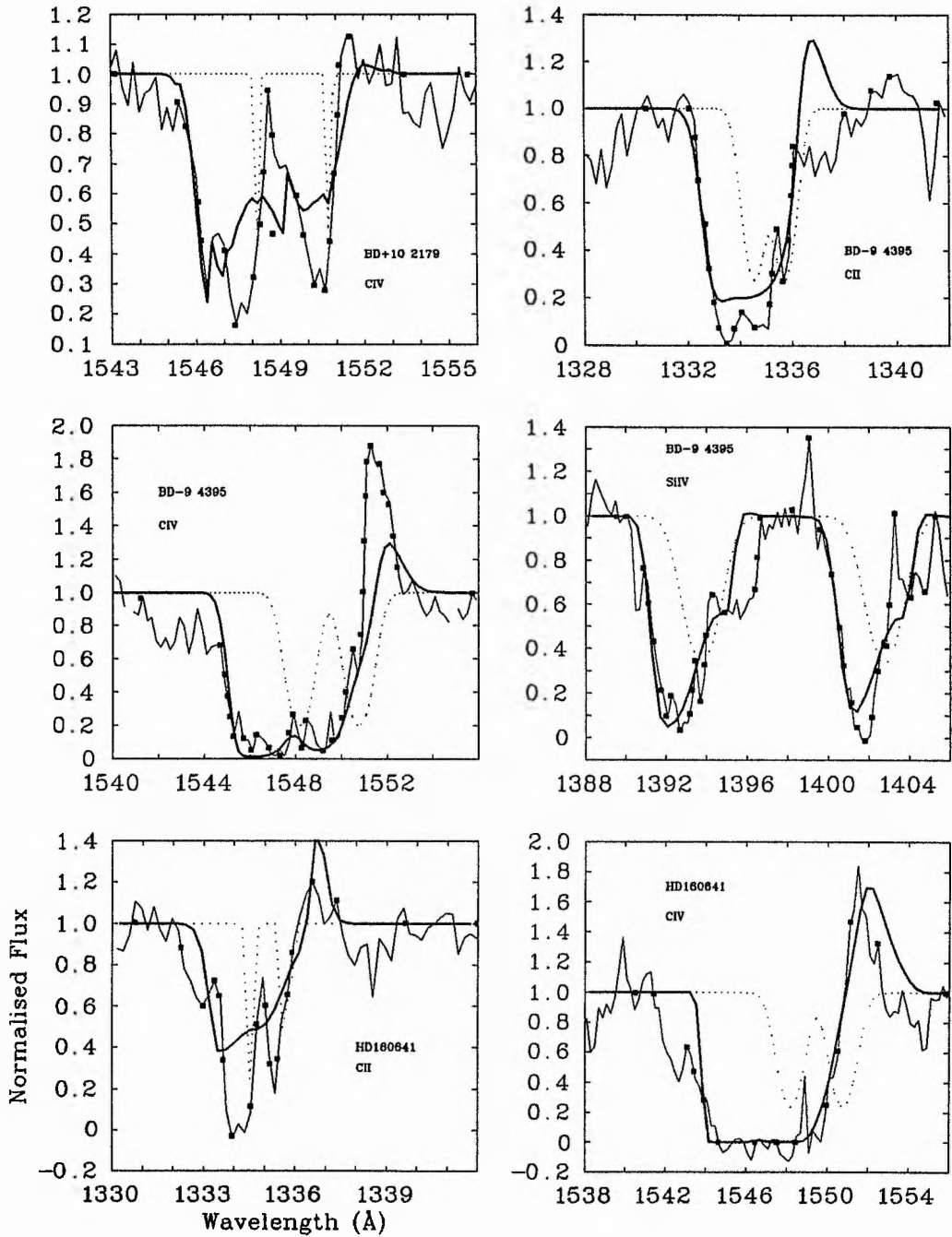


Figure 6.1: Final profiles for the EHe stars using the  $\beta$ -dependent optical depth law. The heavy lines are the final profiles, the dotted lines the photospheric profiles.

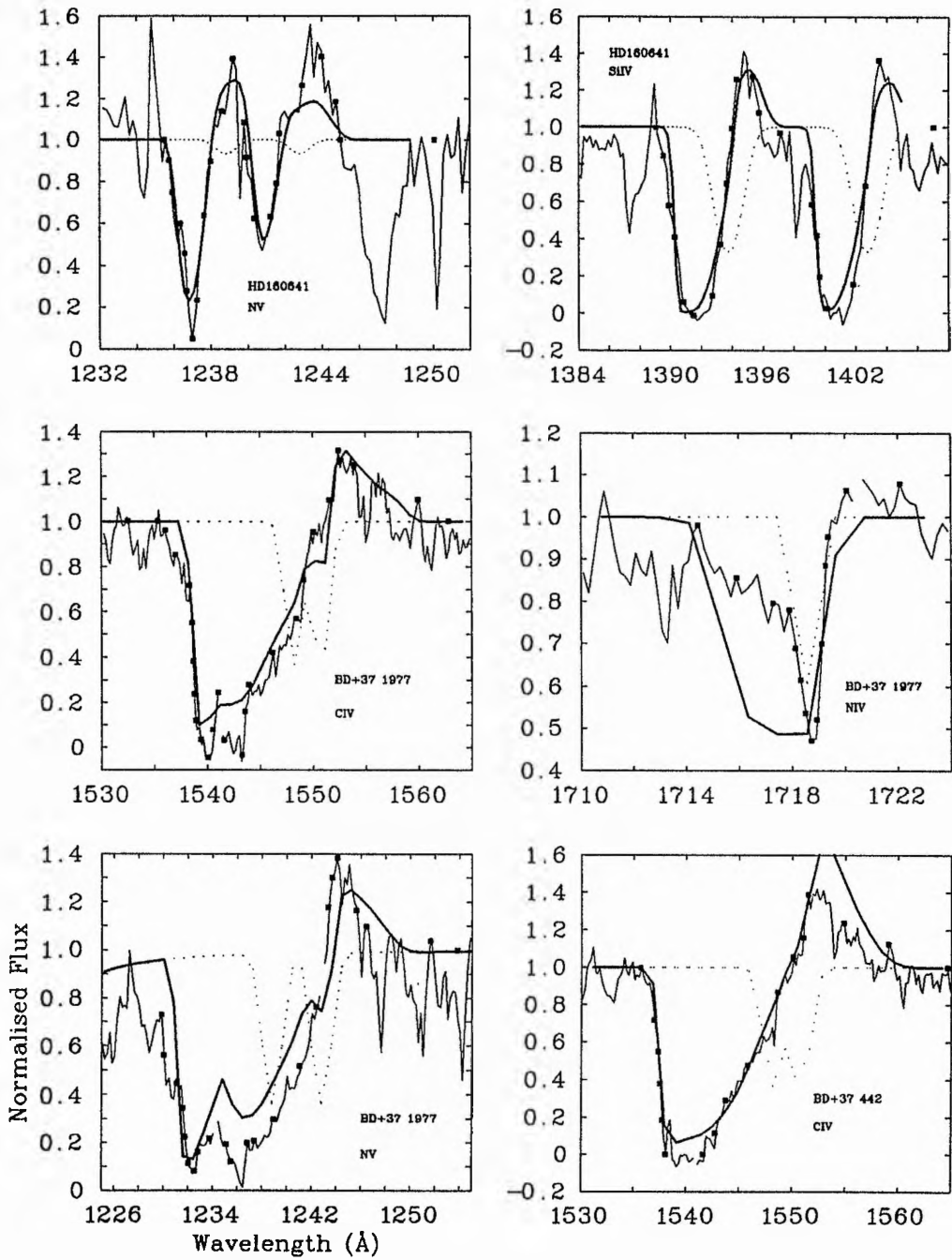


Figure 6.1: *continued.*

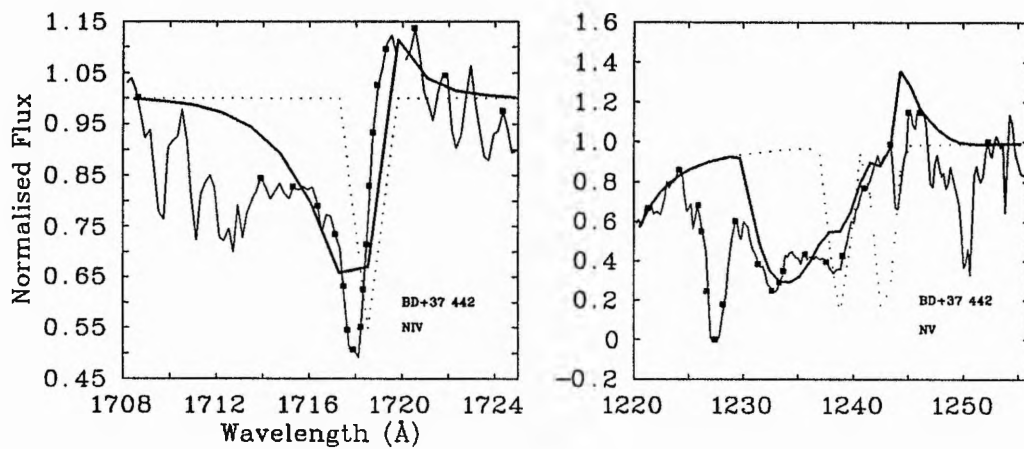
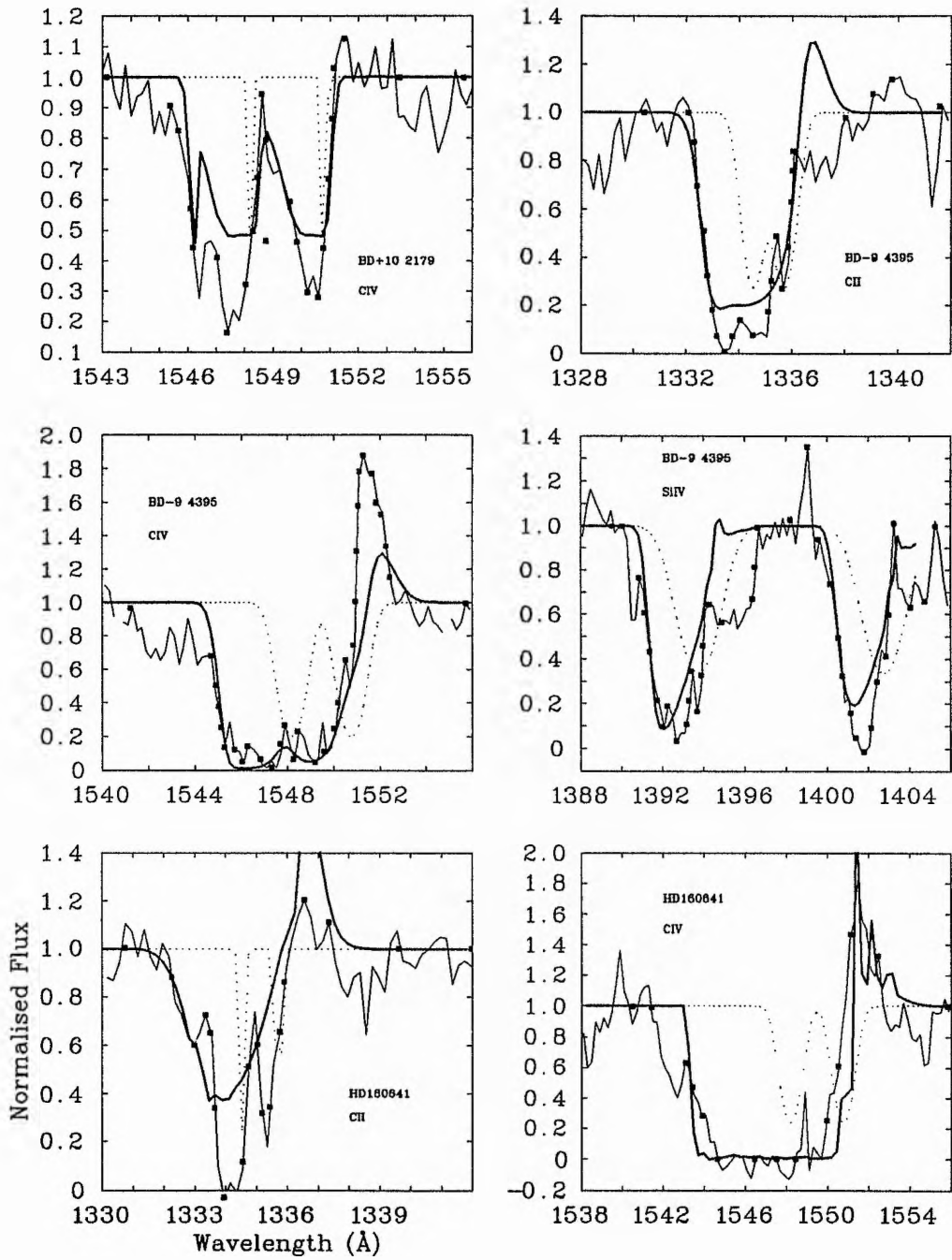


Figure 6.1: *continued.*

Table 6.5: Final fits for the EHe stars, using the  $\beta$ -independent optical depth law. Errors are in small type.

Star	Ion	$\beta$	$v_{\infty}$	$w_g$	$\alpha_1$	$\alpha_2$	$T_B$	$A_{phot}$	$w_{phot}$
BD +10° 2179	CIV	0.004	380	0.133	-1.1	-0.7	0.7	0.85	0.05
		<small>+0.030 -0.063</small>	70	0.05	0.5	0.5	0.2		
BD -9° 4395	CII	10.0	450	0.25	-1.0	-0.1	3.8	1.29	0.30
		<small>+7.0 -3.0</small>	150	0.15	0.5	1.0	0.5		
	CIV	10.0	450	0.25	-0.8	-1.1	1.9	1.62	0.30
		<small>+7.0 -3.0</small>	150	0.10	0.5	0.5	0.5		
SiIV	10.0	450	0.25	-0.7	0.0	8.1	1.09	0.60	
		<small>+7.0 -3.0</small>	200	0.15	0.5	0.5	0.5		
HD 160641	CII	4.0	480	0.35	-1.0	0.5	5.4	1.40	0.05
		2.0	150	0.05	0.5	0.5	0.5		
	CIV	4.0	480	0.35	-3.7	-3.1	6.4	1.43	0.25
		2.0	50	0.05	0.5	0.5	0.5		
	NV	4.0	480	0.35	-0.9	-1.0	0.3	0.07	0.30
		2.0	100	0.05	0.05	0.05	0.07		
SiIV	4.0	480	0.35	-2.0	-1.8	0.9	1.11	0.40	
	2.0	50	0.05	0.5	0.5	0.2			
BD +37° 1977	CIV	0.10	1700	0.06	0.6	-0.5	10.9	1.00	0.10
		0.02	200	0.01	2.4	1.0	26		
	NIV	0.10	1700	0.06	-1.3	-0.6	0.03	0.50	0.003
		<small>+0.50 -0.05</small>	1000	0.02	0.5	0.5	0.00		
NV	0.10	1700	0.06	0.7	0.1	67.4	1.00	0.12	
	0.02	500	0.04	3.0	1.1	150			
BD +37° 442	CIV	1.0	2240	0.02	0.2	1.9	37.3	1.00	0.10
		0.2	100	0.005	2.5	3.0	<small>+30.0 -15.0</small>		
	NIV	1.0	2240	0.02	-0.7	5.2	0.3	0.60	0.002
		0.1	300	0.005	1.5	5.0	0.03		
	NV	1.0	2240	0.02	0.0	1.2	2.6	2.00	0.10
0.1		100	0.10	2.5	1.7	<small>+12.0 -3.0</small>			



**Figure 6.2:** Final profiles for the EHe stars using the  $\beta$ -independent optical depth law. The heavy lines are the final profiles, the dotted lines the photospheric profiles.

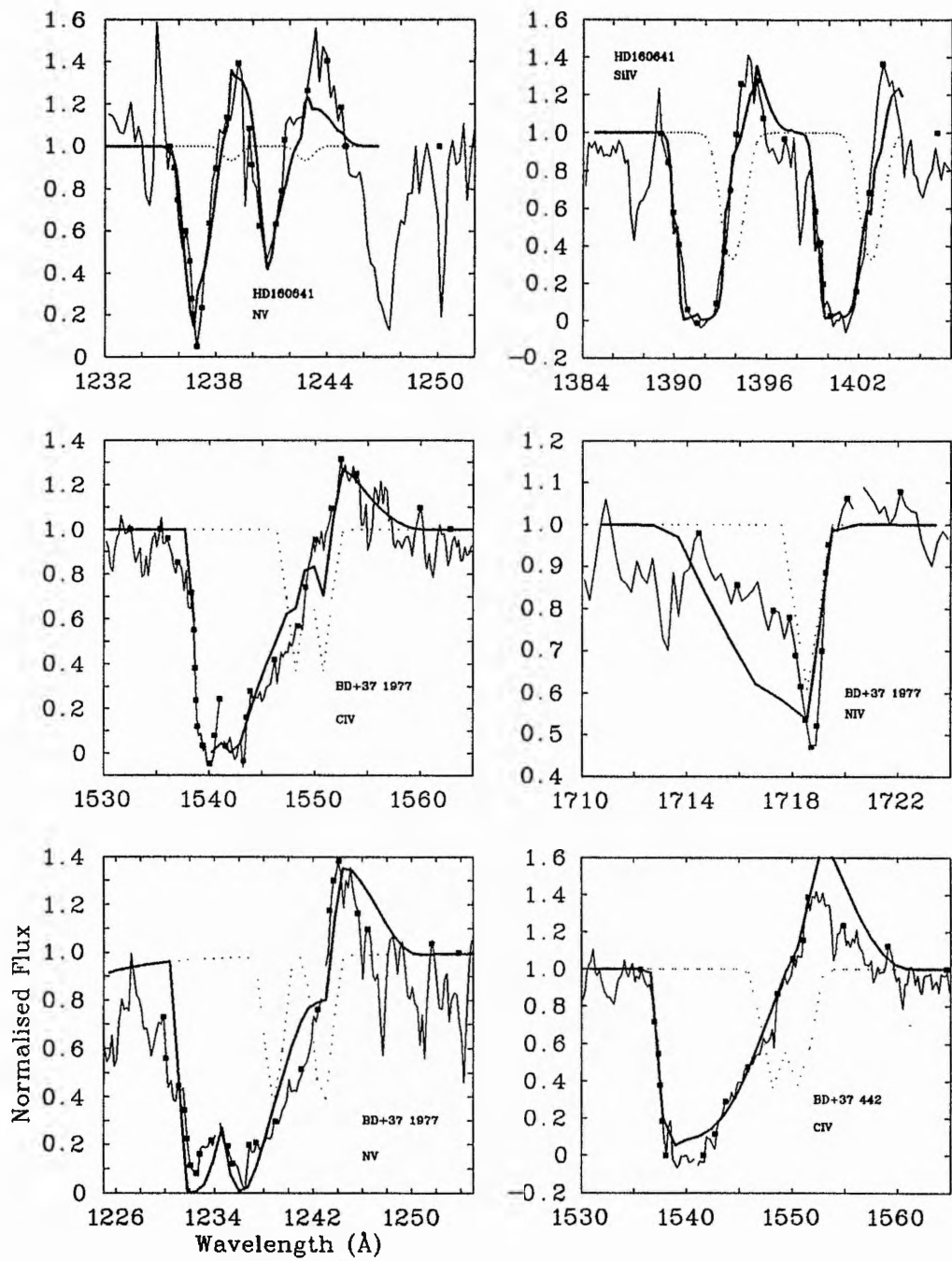


Figure 6.2: *continued.*

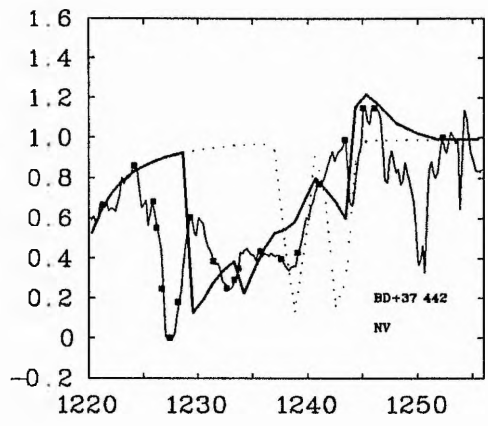
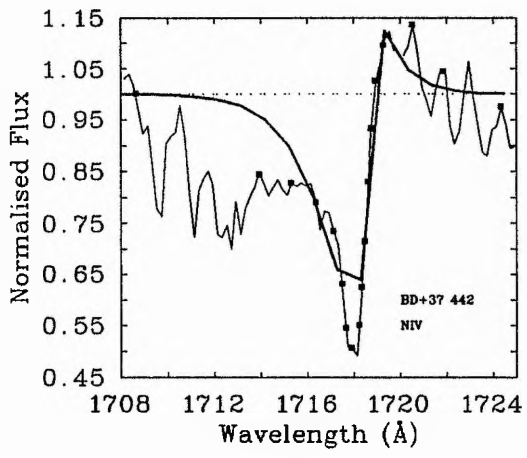
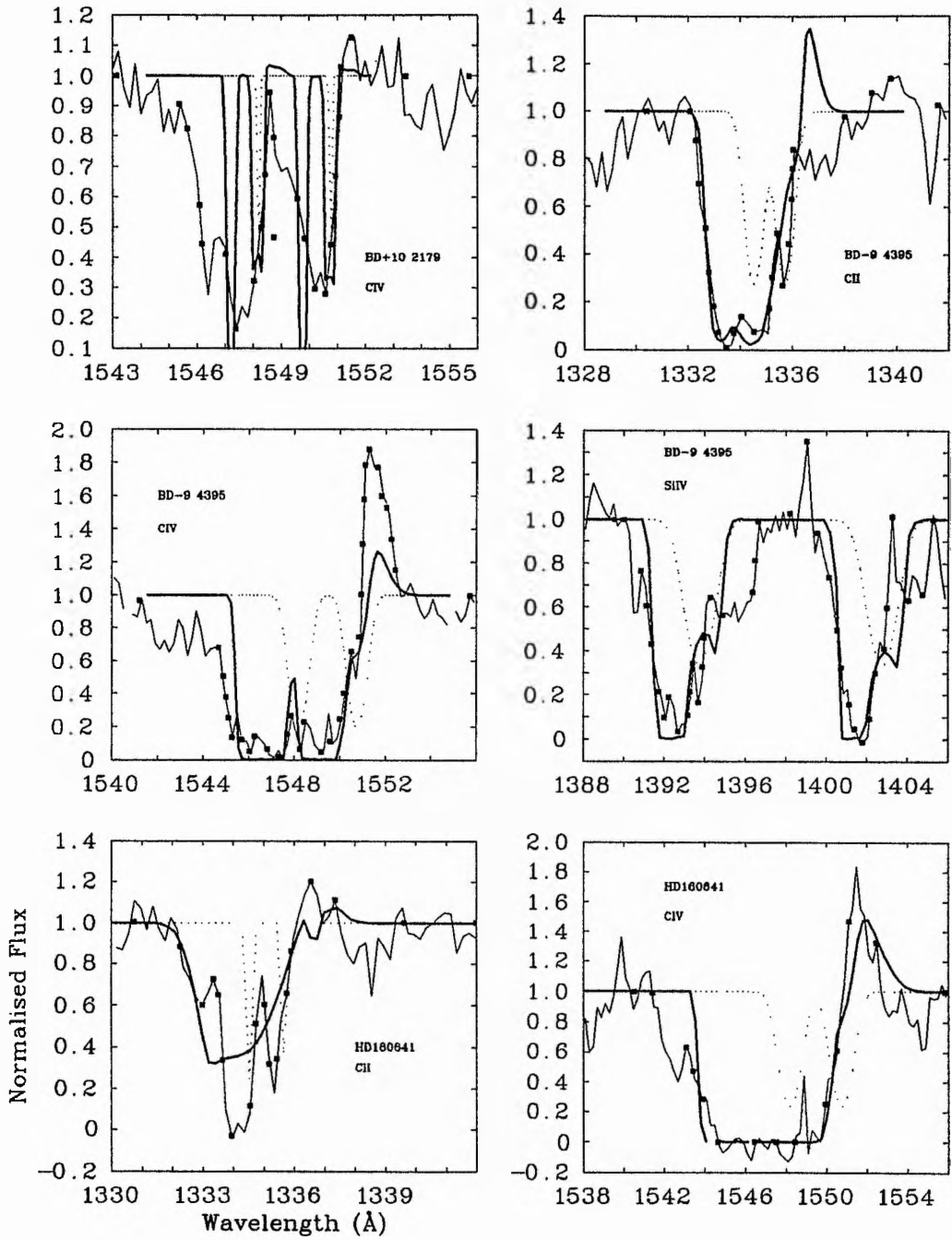


Figure 6.2: *continued.*

Table 6.6: Final fits for the EHe stars, using the  $\beta$ -independent optical depth law and  $\beta = 1$ .  
 Errors are in small type.

Star	Ion	$\beta$	$v_{\infty}$	$w_g$	$\alpha_1$	$\alpha_2$	$T_B$	$A_{phot}$	$w_{phot}$
BD +10° 2179	CIV	1.0	190	0.105	-2.9	-1.8	8.4	0.85	0.05
			10	0.01	0.5	0.5	1.4		
BD -9° 4395	CII	1.0	320	0.30	-0.4	-0.2	7.7	1.29	0.30
	CIV	1.0	20	0.1	0.5	0.5	3.7	1.62	0.30
			40	0.1	0.5	0.5	0.1		
	SiIV	1.0	320	0.30	-2.2	-1.4	37.1	1.09	0.60
60	0.1	1.0	0.5	37.0					
HD 160641	CII	1.0	500	0.30	-0.8	1.9	7.4	1.40	0.05
	CIV	1.0	200	0.3	0.5	5.0	0.5	1.43	0.25
			50	0.2	1.4	0.5			
	NV	1.0	500	0.30	2.4	-0.4	0.7	0.07	0.30
20	0.05	5.4	1.5	1.1					
SiIV	1.0	500	0.30	1.4	-0.5	8.7	1.11	0.40	
			30	0.1	5.9	1.6	17.2		
BD +37° 1977	CIV	1.0	1700	0.20	-1.0	0.1	25.0	1.00	0.10
			200	0.1	1.6	1.9	26		
	NIV	1.0	1700	0.20	-2.0	-1.1	0.12	0.50	0.003
	300	0.1	3.0	1.7	0.00				
NV	1.0	1700	0.20	-0.5	-0.2	4.2	1.00	0.12	
			300	0.1	0.6	0.5	150		
BD +37° 442	CIV	1.0	2300	0.010	1.6	2.8	23.7	1.00	0.100
			50	0.002	13.0	5.1	209		
	NIV	1.0	2300	0.010	-1.1	4.6	0.4	0.60	0.002
	300	0.010	6.7	47.3	2.2				
NV	1.0	2300	0.010	-1.5	0.0	12.4	2.00	0.10	
			200	0.005	3.5	1.2	73		



**Figure 6.3:** Final profiles for the EHe stars using the  $\beta$ -independent optical depth law with  $\beta$  fixed at 1.0. The heavy lines are the final profiles, the dotted lines the photospheric profiles.

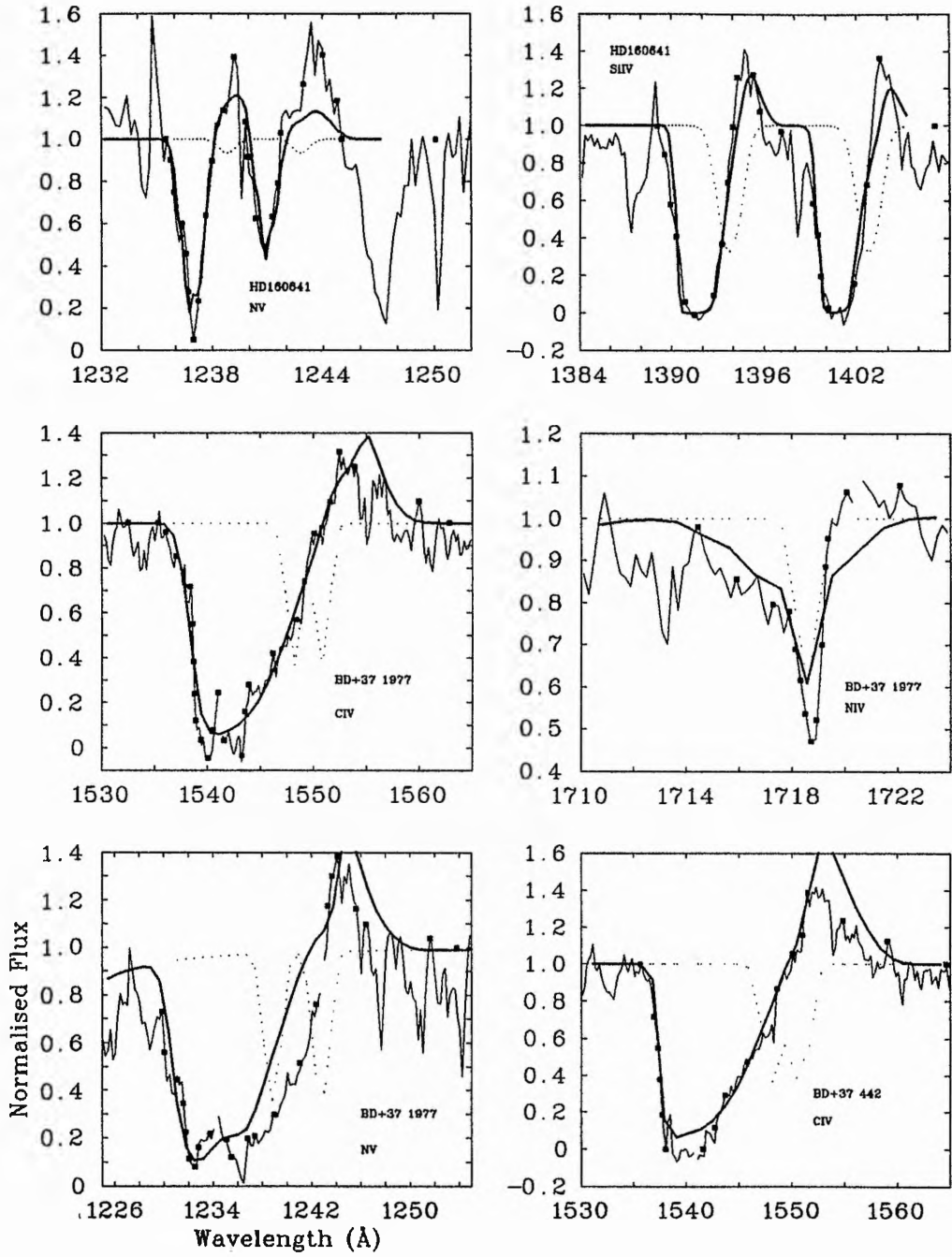


Figure 6.3: *continued.*

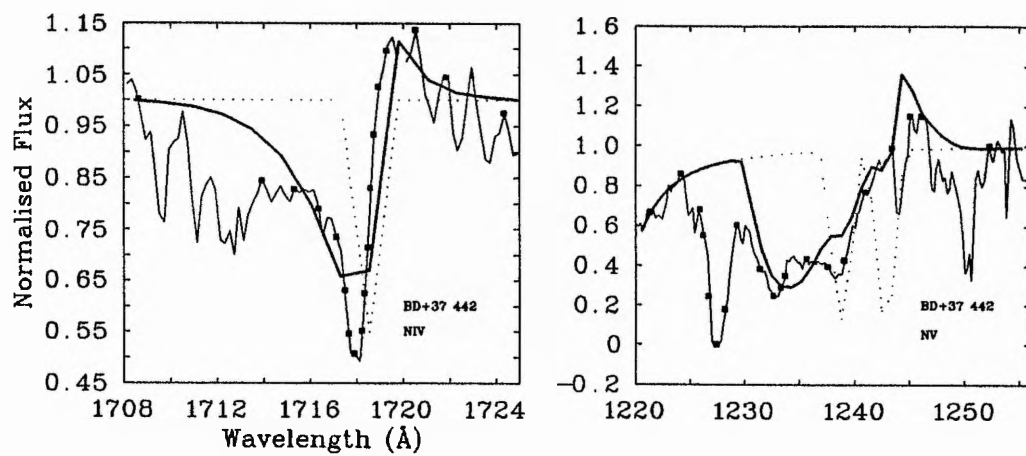


Figure 6.3: *continued.*

## 6.6 Results

### 6.6.1 BD +10° 2179

Only CIV is present as a wind line profile in BD +10° 2179. A small emission peak may be present depending on the adopted continuum level. Unusually, the CIV profile shows a true doublet structure indicating that  $v_\infty$  may be low or that most of the absorbing material is close to the star. A steep blue edge is noticeable along with a terminal dip at  $\sim 1546 \text{ \AA}$ ; the blue edge of this dip is not sharply inclined and may indicate a high turbulence. The line is not saturated. As only one line is available to model it is not possible to determine consensus values for the three main wind line parameters; thus they have large uncertainties associated with them.

#### 6.6.1.1 $\beta$ -dependent optical depth law

Using the  $\beta$ -dependent optical depth law the initial fit for the line, using a standard input file, was poor ( $\chi^2 = 2.13^1$ ). A high  $\beta$  (1.25) and  $v_\infty$  ( $760 \text{ km s}^{-1}$ ) were indicated along with a low turbulence ( $w_g = 0.06$ ).

As a check, the values published by HSH ( $\beta = 1.0$ ,  $w_g = 0.15$  and  $v_\infty = 400 \text{ km s}^{-1}$ ) were fixed and SEILS run to maximise the fit. The results were still poor ( $\chi^2 = 1.5$ ), but better than the original fit<sup>2</sup>.

The photospheric lines were increased in depth from those of SPECTRUM ( $A_{phot} = 0.35$ ) after comparison with those shown by HSH ( $A_{phot} = 0.85$ ) but the fit did not improve when fixing the three main parameters at HSH's values.

The deeper photospheric lines were then used for an all parameters free fit, using an input file with HSH's results as starting values. A better fit ( $\chi^2 = 0.6$ ) was obtained.  $\beta$  and  $v_\infty$  were now small ( $0.05$  and  $290 \text{ km s}^{-1}$  respectively) and the turbulence was high ( $w_g = 0.41$ ) The fit still looked poor however with the blue edge not fitted well (*i.e.*  $v_\infty$  too small) and the lower absorption features not filled. The terminal velocity was increased to  $350 \text{ km s}^{-1}$ , fixed, and the other parameters left free. This resulted in a slightly poorer fit ( $\chi^2 = 0.8$ ) but with the profile looking better than the others. This profile was adopted as the final profile but it must be recognised that with such a poor fit most of the parameters must be regarded as undefined. It should be noted that *when using the parameterisation of Groenewegen & Lamers' (1989) optical depth law* it is possible to get results

<sup>1</sup>These values of  $\chi^2$  can only be compared to other values from the same line of the same star. Inter-line and inter-star comparisons are not valid.

<sup>2</sup>This highlights the fact that SEILS does not always find the very best solution but the best solution in the neighbourhood of the starting solution. Thus SEILS output was never taken as the answer before the profiles had been displayed and checked.

three times better than using HSH's parameters. The results still seem to be poorer than those obtained by HSH using the co-moving frame method.

#### 6.6.1.2 $\beta$ -independent optical depth law

With the  $\beta$ -independent optical depth law the fit was much better ( $\chi^2 = 0.3$ ) with a good fit to the blue and red edges and the central "peak" between the two absorption dips. However although the profile was good in these regions it did not fit the depth of the profile well; worse even than the  $\beta$ -dependent results in this aspect even though better in the others.

#### 6.6.1.3 $\beta = 1.0$

A very poor fit with no parts of the observed profile being well fitted. The theoretical profile consists of 4 narrow discrete absorption profiles. Although the redward edge of the profile is well fitted the blue edge is not; the theoretical profile coming nowhere near the edge.

#### 6.6.1.4 Conclusions

Both the  $\beta$ -independent and the  $\beta$ -dependent fits are of a similar "fair" quality. The  $\beta=1.0$  fit is very poor; it seems certain that  $\beta \neq 1$  for this star. The best result is given by the  $\beta$ -independent law, marginally.

### 6.6.2 BD -9° 4395

BD -9° 4395 has three lines that show mass loss. The C II line shows only absorption while the C IV line has a substantial emission peak. The Si IV line may have a small residual emission peak between the two absorption components.

#### 6.6.2.1 $\beta$ -dependent optical depth law

Using the  $\beta$ -dependent optical depth law, the initial fits with all parameters free gave a large scatter in  $\beta$  but with reasonable agreement for  $v_{\infty}$  and  $w_g$ . The latter two values were then fixed from the values determined from the C IV fit and SEILS re-run to determine the values of  $\beta$  for each line. The results were again poor. The fit to Si IV was just as good with  $\beta = 1$ . as it was with the determined value of 0.4. The same was true for C IV whether 1.0 was used or the determined value of 25. Thus  $\beta$  must be regarded as undefined for this star. After looking at the initial fits and

those with  $v_\infty$  and  $w_g$  fixed,  $\beta$  was fixed at 1.0 and  $v_\infty$  and  $w_g$  at  $400 \text{ km s}^{-1}$  and 0.4 respectively. The final fits are shown in Figure 6.1. The final profiles show good fits to the position and slope of the blue edge and are generally very good. A small, unobserved, emission peak is predicted for the C II doublet while the fit to the C IV emission peak is very poor indeed.

It should be noted that when fitting the Si IV profiles using narrow photospheric lines and a large turbulence the results are excellent, including the fitting of the shoulder absorption dips. This is shown in Figure 6.4. However narrow photospheric lines are not justified by comparison with those determined by HSH.

#### 6.6.2.2 $\beta$ -independent optical depth law

The analysis with the  $\beta$ -independent optical depth law gives a large scatter in  $\beta$  and  $v_\infty$ . Final values for  $\beta$ ,  $v_\infty$  and  $w_g$  were fixed at 10,  $450 \text{ km s}^{-1}$  and 0.25 respectively with only the terminal velocity being regarded as secure. The resultant profiles are very similar to those determined with the  $\beta$ -dependent optical depth law. Again the C IV emission peak is not fitted at all well and a small emission peak is predicted for the C II line. The Si IV line fit is slightly poorer than with the other optical depth law but still adequate.

#### 6.6.2.3 $\beta = 1.0$

An excellent fit to the C II profile with reasonable fits to C IV and Si IV although the emission peak of C IV is not fitted well. The C IV line is saturated in this fit, which is not what is observed in the actual profile. The emission peak is fitted better as regards position, and of similar quality in intensity. The Si IV fit is good with the shoulder "humps" not fitted but getting a good fit to the redward edge of the red profile - something also achieved with the  $\beta$ -independent law but not with the  $\beta$ -dependent one.

#### 6.6.2.4 Conclusions

All the profiles from the three methods are similar but the  $\beta$ -independent law gives slightly better results, but the other two laws are not discounted.

### 6.6.3 HD 160641

For HD 160641 there are 4 lines that show wind line features. The N V doublet was not corrected for the Lyman- $\alpha$  contribution as the N V lines did not extend far enough towards  $\text{L}\alpha$  to be affected.

Broadened photospheric lines from SPECTRUM were used initially.

### 6.6.3.1 $\beta$ -dependent optical depth law

The initial results, using the  $\beta$ -dependent optical depth law, were good for all 4 lines, although a large scatter was found in  $\beta$  and  $w_g$ , with the terminal velocity around  $800 \text{ km s}^{-1}$ .

The CIV profile is the most accurate and a set of profiles was run for all lines with the three main parameters fixed close to the CIV values ( $\beta = 3.5$ ,  $v_\infty = 800 \text{ km s}^{-1}$  and  $w_g = 0.14$ ). The results were very good, especially for SiIV and NV although in the former case the redward part of the two absorptions were not filled completely. CII and CIV were adequate, but the CIV emission was not modelled well at all. The blue edges were all fitted well indicating that the terminal velocity and turbulent velocity were almost correct.

However, the photospheric lines were compared to those given by HSH and altered. The lines were re-analysed. These results are given in Table F.2. SiIV was fitted better as was CIV except the emission peak was too redward. NV converged on a slightly different (and worse) solution due to a slightly different input file, even though the photospheric lines were not changed. (The previous, better solution, is the one given in Table F.2.)

In an attempt to model the emission peak of the CIV doublet the value of  $\beta$  was reduced to 1, the terminal velocity to  $600 \text{ km s}^{-1}$  and the turbulence to 0.12. The values were fixed and final profiles run. The CIV emission was fitted well, but the blue edge was too steep (increasing the turbulence had no effect). SiIV was modelled very well while CII and NV were poor. These results were adopted as the final results, and are given in Table 6.4 and Figure 6.1. However they are not very good, and it must be concluded that fitting HD 160641 using SEI is not possible with great accuracy.

HSH's results were also used ( $\beta = 0.5$ ,  $v_\infty = 550 \text{ km s}^{-1}$  and  $w_g = 0.18$ ) but the fits were no better than found in the previous trial. HSH's results when using the co-moving frame method were not very good, especially the fit to the blue edge of the CIV doublet. To model the CII doublet they had to fine tune their optical depth law (which is not possible in SEI) and use a different turbulence to that used to fit the other lines. Also when a wind line was saturated they then ignored the underlying photospheric line; fine for the center of the line but grossly wrong for the wings of the photospheric line where the wind line is not saturated.

The final profiles are of variable quality. The CII doublet is very poorly fitted except for the small emission peak. The depth of the CIV line is well fitted and the emission peak, although slightly displaced, is well fitted. However the blue edge is only poorly fitted, especially in the slope. This is partly due to a line at  $1543 \text{ \AA}$  that distorts the blue edge. The NV profile is well fitted in

all respects except that the sharp absorptions are slightly displaced to the blue. The Si IV doublet is fitted excellently including the small emission peaks.

#### 6.6.3.2 $\beta$ -independent optical depth law

Using the  $\beta$ -independent optical depth law the initial fits gave excellent agreement on the turbulent velocity and good agreement on the terminal velocity. There was some scatter on the value of  $\beta$ , but a high value was indicated. The final profiles were very good especially the Si IV doublet that was fitted as well as with the other optical depth law. The NV fit was much improved with the theoretical absorptions fitting the observed ones perfectly. Both the C II and CIV profiles were quite poor; the C,II being poorer than the previous fit and the CIV being slightly different, still poor, but with the emission peak fitted more accurately.

#### 6.6.3.3 $\beta = 1.0$

Poor fits to the C II line where the structure of the observed profile is not matched by that of the theoretical one. However the emission peak is well fitted. The CIV fit is good, very similar in profile to the  $\beta$ -independent result, while the NV and Si IV fits are almost perfect.

#### 6.6.3.4 Conclusions

Good fits to Si IV and NV for all three methods; poorer fits to the other lines. No one method seems better than the others.

### 6.6.4 BD +37° 1977

By removing the lowering of the continuum in the region of the NV doublet due to the absorption of  $L\alpha$  a neutral hydrogen column depth of  $\log N_H = 20.3 \pm 0.3$  was determined although this value was not critical as the lowering of the continuum around NV was small.

The profiles of the photospheric lines for BD +37° 1977 had to be guessed. However the terminal velocity of the wind is so large that the photospheric profiles only affect a small region of the wind line profile and so the actual shape of the photospheric line is not crucial.

#### 6.6.4.1 $\beta$ -dependent optical depth law

Initial fits (given in Table F.2), using the  $\beta$ -dependent optical depth law were quite good; especially for the CIV doublet. In all three cases  $\beta$  was very low, some agreement between the terminal velocities was found for NIV and NV however the quality of the CIV was so good that its values were fixed for the final solution. Slight adjustments to the photospheric lines were made before the final fits were run. The final results are given in Table 6.4 and shown in Figure 6.1. The final CIV profile was excellent with even the small emission peak being fitted exactly. The NIV line was mainly photospheric with only a small wind feature; this was not fitted well at all due to the low value of  $\beta$ . The NV profile gave a good fit especially to the blue edge. The red edge and the emission peak were fitted well if not perfectly.

#### 6.6.4.2 $\beta$ -independent optical depth law

Using the  $\beta$ -independent optical depth law again a low value of  $\beta$  was found. The fits were very similar to those determined previously with an excellent fit to the CIV doublet. However both the NIV and NV fits were improved with this optical depth law. The improvement was only slight for the NIV singlet but was significant for the NV doublet, with an improvement in the fit to both the red edge and the emission peak.

#### 6.6.4.3 $\beta = 1.0$

The CIV line has an excellent fit but the NV fit is poor. The blue edge is well fitted but the redward edge is not; possibly indicating that larger photospheric lines are required. The NIV line is good considering the difficulties found in fitting singlet lines.

#### 6.6.4.4 Conclusions

Similar quality of fits for all three methods, none being preferable over the others.

#### 6.6.5 BD +37° 442

By removing the lowering of the continuum in the region of the NV doublet due to the absorption of  $L\alpha$  a neutral hydrogen column depth of  $\log N_H = 20.5 \pm 0.5$  was determined.

The profiles of the photospheric lines for BD +37° 442 had to be guessed as no SPECTRUM model was available to model them. However the terminal velocity of the wind is so large that the

photospheric profiles only affect a small region of the wind line profile and so the actual shape of the photospheric line is not crucial.

The profiles show quite a similarity to those of the other hot star, BD +37° 1977 except there is a broad line at 1228 Å which is not present in the other star. It appears to be far too broad to be an interstellar line and yet if it were a photospheric line it could be expected to be found in BD +37° 1977. The logical conclusion is that it is part of the wind line profile<sup>3</sup>. Similar, large, terminal dips have been found when modelling other stars (*e.g.* the  $v_{\infty} = 760 \text{ km s}^{-1}$  model of BD +10° 2179 showed the same thing; the fit was discarded as the observed profile did not have such a dip.). However for this to occur in this star the wind line would have to extend to  $\sim 1226 \text{ Å}$  which would imply a terminal velocity of  $4000 \text{ km s}^{-1}$  or so. This is twice the value determined for the CIV doublet which gives an excellent fit to the blue edge.

#### 6.6.5.1 $\beta$ -dependent optical depth law

With the  $\beta$ -dependent optical depth law the initial fits were very good, especially for the CIV line. The NV solution did not fit the 1228 Å dip, even though the (high) terminal velocity of  $3000 \text{ km s}^{-1}$  was found. As the 1228 Å dip was not fitted in the individual fits the 5 points which lie in the dip were weighted one tenth of that of the other points for the final fit. Here  $\beta$ ,  $v_{\infty}$  and  $w_g$  were taken from the initial CIV profile fit (*i.e.* 1.0,  $2200 \text{ km s}^{-1}$  and 0.03 respectively), as this fit was excellent. The final fits were very good; given in Table 6.4 and shown in Figure 6.1. The CIV line gives an excellent fit to the blue edge and only slightly overestimates the emission peak. Likewise the NV fit, always one of the poorer fits due to low signal and the removal of the Lyman- $\alpha$  contribution, gives a good final profile that well models the small emission peak. Due to the 1228 Å dip most of the expected blue edge is not present. However the profile fits the lower part of the profile, and the blue edge, reasonably well. The fit to the NIV singlet is adequate given that most of the profile is photospheric in origin.

#### 6.6.5.2 $\beta$ -independent optical depth law

With the  $\beta$ -independent optical depth law, the initial fit of the CIV line was again excellent, and with good agreement between the terminal velocities from the NV and CIV lines. Both NV and NIV indicated a value of  $\beta$  around 0.3 but the fits were not exceptional. The final values of the three major parameters were those found from the CIV line; the fit being so much better than the others. The final profiles for the CIV and NIV are almost identical to those found from the  $\beta$ -dependent optical depth law. The NV profile has changed significantly with the emission peak

<sup>3</sup> Another possibility is that it is an error in the image due to microphonics. When the image was displayed there do appear to be some faults in the image at the short wavelength end, presumably due to microphonics or other problems. It was not possible to determine if any of these faults lay at 1228 Å but it was certainly possible.

being fitted better, but a poorer fit to the blue edge (with the 1228 Å dip ignored). Overall the quality of the fits between the two optical depth laws is similar.

#### 6.6.5.3 $\beta = 1.0$

A good CIV fit with the emission peak only slightly overestimated by the theoretical profile. Both NV and NIV are good.

#### 6.6.5.4 Conclusions

As  $\beta=1$  is determined for both the  $\beta$ -independent and  $\beta$ -dependent laws and is a pre-requisite for the  $\beta=1$  solution it is not surprising that all the methods give a similar quality of fit.

Although the CIV profiles of both BD +37 stars are similar, and the fits equally good, the values of  $\beta$  determined are different with 1.0 in the case of BD +37° 442 but 0.17 for BD +37° 1977. This results in a good fit to the CIV emission peak in the case of BD +37° 1977 but a slightly higher peak for BD +37° 442. However lowering  $\beta$  for BD +37° 442 results in an emission peak that is of a more appropriate height, but is displaced to the redward side significantly. Also the whole of the redward side of the absorption profile is fitted less accurately; although the fit could still be described as "good".

#### 6.6.6 Optical depth laws

From this study there is little to choose between the three optical depth laws under test except to say that for BD +10°2179 the  $\beta=1$  fit is very poor. The  $\beta$ -independent optical depth law is favoured from numerical considerations.

### 6.7 Mass Loss Rates

Mass-loss rates were determined using the method given in Section 4.8 and equations 4.25 and 4.26. The results are given in Table 6.7 for the  $\beta$ -dependent,  $\beta$ -independent and  $\beta = 1.0$  optical depth laws.

The MLR are determined at the  $w = 0.5$  point and then formal errors determined by varying each parameter by the error given in the tables of final parameters (6.4, 6.5 and 6.6). In many cases these formal errors at the  $w = 0.5$  point were smaller than the corresponding variation of the MLR.

Table 6.7: The product of ionisation and mass loss rates for the EHe stars compared with those of Hamann, Schönberner & Heber (1982). Results for the  $\beta$ -dependent,  $\beta$ -independent and  $\beta=1$  optical depth laws are given, in  $\log M_{\odot} \text{ yr}^{-1}$ . For the non-resonance lines (CII, NIV) the value given is the product of ionisation fraction, MLR and excitation fraction. An error of +? indicates the value is a lower limit. In any case the values are all lower limits to the true MLR.

Star	Ion	SEILS			HSH
		$\beta$ -dep	$\beta$ -indep	$\beta=1$	HSH
BD+10° 2179	CIV	$-10.5^{+0.8}_{-0.2}$	$-10.5^{\dagger} \pm 2.0$	$-14.4^{+0.4}_{-0.3}$	$-11.4^{+0.4}_{-0.3}$
BD -9° 4395	CII	$-10.4^{+0.5}_{-0.2}$	$-10.2 \pm 0.2$	$-10.6^{+0.2}_{-0.3}$	$-10.6 \pm 0.5$
	CIV	$-10.9 \pm 0.2$	$-10.9 \pm 0.2$	$-11.6 \pm 0.9$	$-10.5 \pm 0.3$
	SiIV	$-9.9^{+0.3}_{-0.5}$	$-9.3^{+0.2}_{-0.1}$	$-10.9^{+0.3}_{-0.0}$	$-9.9 \pm 0.5$
HD 160641	CII	$-14.4^{+1.4}_{-3.4}$	$-10.5 \pm 0.2$	$-10.8^{+0.3}_{-0.7}$	$-10.6 \pm 1.0$
	CIV	$-9.3^{+0.8}_{-1.5}$	$-13.8^{+0.4}_{-0.2}$	$-10.8^{+0.8}_{-1.0}$	$-9.7^{+?}_{-0.8}$
	NV	$-10.6^{+0.8}_{-1.9}$	$-11.2^{+0.1}_{-0.2}$	$-11.2^{+0.8}_{-1.5}$	$-10.0 \pm 0.3$
	SiIV	$-9.2^{+0.7}_{-0.9}$	$-11.7 \pm 0.2$	$-10.1^{+0.7}_{-1.1}$	$-9.4^{+?}_{-0.3}$
BD +37° 1977	CIV	$-6.7^{+0.9}_{-0.3}$	$-8.9^{+0.5}_{-0.4}$	$-10.5^{+0.0}_{-0.1}$	
	NIV	$-12.2^{+1.1}_{-0.4}$	$-10.9^{+2.4}_{-0.4}$	$-12.8^{+0.3}_{-0.0}$	
	NV	$-9.7^{+0.6}_{-0.3}$	$-6.7^{+0.3}_{-0.5}$	$-9.8^{+0.1}_{-0.3}$	
BD +37° 442	CIV	$-10.1 \pm 0.1$	$-10.0 \pm 0.2$	$-9.7^{+0.0}_{-0.4}$	
	NIV	$-11.7^{+1.0}_{-0.4}$	$-12.2^{+0.9}_{-0.2}$	$-12.3^{+0.9}_{-1.9}$	
	NV	$-9.5^{+1.5}_{-0.2}$	$-9.7^{+0.5}_{-0.2}$	$-9.8^{+0.2}_{-0.1}$	

$\dagger$  Evaluated at  $w = 0.97$ , see text.

evaluated at  $w = 0.3$  or  $w = 0.7$ . In these cases the final errors (shown in the tables) were taken from this variation of MLR around the  $w = 0.5$  point. Alternatively an integral method could have been used to determine the mean MLR over a given range of velocity (Perinotto, Cerruti-Sola & Lamers 1989). The MLR are determined at a given velocity rather than at a given radius from the star as the velocity translates well onto the final profile in a way that looking at radial distance does not.  $w = 0.0$  corresponds to the stellar surface and the red edge of the profile while  $w = 1.0$  roughly corresponds to the blue edge of the profile (actually slightly redward of the blue edge as turbulence extends the blue edge). The fractional velocity  $w = 0.5$  corresponds to the middle of the profile, and as most profiles are doublets the point  $w = 0.5$  occurs twice in the profile, once for each component. Measuring the MLR at  $w = 0.5$  should, if the profiles are fitted well, give accurate values for the MLR. Plots of the optical depth laws (and thus MLR) are given in Figure 6.5 for both optical depth laws and for  $\beta$  fixed at 1.0.

### 6.7.1 Individual lines

Although there is little to choose between the final theoretical profiles, the variation of optical depth with velocity is very different for the different optical depth laws. Very rarely do optical depths for a given line agree for both laws. Due to the parameterisation used, the values close to  $w = 0.0$  and  $w = 1.0$  are often unphysical, but the effect of turbulence will reduce this effect somewhat. The important part of the run of optical depth with velocity is from  $w = 0.2$  to  $w = 0.8$ . Even ignoring these "edge effects" the match between the two optical depth laws for most lines is very poor. This lack of agreement leads to different MLR as shown in Table 6.7.

The results for BD+10° 2179 agree well for the  $\beta$ -independent and  $\beta$ -dependent laws but not for  $\beta=1$ . The errors from the  $\beta$ -independent optical depth law are huge due to the rapid fall-off of the optical depth with velocity. Due to the very low value of  $\beta$  determined for this star with the  $\beta$ -independent optical depth law no values of mass loss can be determined at velocities below  $w = 0.94$  as all these velocities correspond to the surface of the star where the MLR formula breaks down. The mass loss variation with velocity for both optical depth laws (shown in Figure 6.5) show a very similar trend; a rapid falling of the optical depth with increasing velocity. However there is a large velocity shift between them.

The BD -9° 4395 results show very good agreement between the MLR of the two optical depth formulae. The run of optical depth with velocity for the 3 lines for all the optical depth formulae show fair agreement. The  $\beta=1$  results systematically show slightly decreased mass loss rates.

For HD160641 the MLR from the three laws show little agreement although the run of optical depth with velocity show similar trends, at least in the important region around  $w = 0.5$ .

For BD +37° 1977 the MLR do not agree well at all with a huge mass loss indicated from the NV line and a small value from the CIV line, with the  $\beta$ -dependent, and  $\beta=1$ , optical depth laws. With the  $\beta$ -independent optical depth law the situation is reversed. The run of MLR with velocity shows some agreement in terms of the trends of the profiles.

BD +37° 442 shows very good agreement with MLR between all three formulations and an exceptionally good agreement between the run of optical depth with velocity. However this is just what would be expected as with  $\beta = 1.0$  in the  $\beta$ -dependent optical depth law all formulations of the optical depth law become equivalent.

## 6.8 Discussion

The final profiles indicate that there is little to choose between the three optical depth laws as far as the quality of the theoretical fits to the observed data is concerned. However the  $\beta$ -independent law is preferred on the basis of the good results obtained from modelling O star winds. Also the de-coupling of  $\beta$  and  $\alpha_2$  leads to more independent results for the final profiles and their associated parameters.

Of the three main parameters,  $v_\infty$  gives very good agreement, to within the quoted uncertainty, between the three optical depth laws for all stars.

For the  $\beta$ -independent optical depth law there is a much greater spread in the final values of  $\beta$  between the stars. For the  $\beta$ -dependent law the values of  $\beta$  range from 0.1 to 1.0 but for the  $\beta$ -independent law the spread is 0.004 to 10.0. The coupling of the velocity law to the optical depth law forces more moderate values of  $\beta$  (i.e. towards  $\beta = 1.0$ ). When the velocity and optical depth laws are de-coupled  $\beta$  can take more extreme values without directly affecting the optical depth law, and thus the profile. For the two stars that have  $\beta = 1.0$  for the  $\beta$ -dependent optical depth law it may be expected that very similar results would be obtained from both optical depth laws. This is the case with BD +37° 442 where excellent agreement is achieved for all of the parameters of all the lines with the exception of  $T_B$  for the CIV line. Even here the uncertainty on  $T_B$  is large enough to overlap the value determined from the  $\beta$ -independent solution. For HD 160641 very different values for all parameters are determined from both optical depth laws even though a final value of  $\beta = 1.0$  was found for the  $\beta$ -dependent law. This discrepancy is due to the way the parameters for the final fit are selected. Each line has its parameters determined individually, resulting in  $\beta \neq 1.0$  for most lines. A compromise between the values of the parameters for all the lines in a given star is then found, fixing values of  $\beta$  and  $v_\infty$  and  $w_g$ . Thus the final values of  $w_g$  and  $v_\infty$  used are a compromise of values that were determined from individual line fits that did not have, in most cases,  $\beta = 1.0$ . If  $\beta$  were fixed at 1.0 and then individual solutions determined for  $v_\infty$  and  $w_g$  and compromise values fixed and then solutions determined for the other parameters the discrepancy would then disappear. This subtle effect, plus the similarity of the final profiles, indicates that the  $\beta$ -dependent optical depth law probably should not be used.

$w_g$  shows substantial variation between the same stars using the two optical depth laws. This parameter has little overall effect on the shape of the final profile except for a small change in the determined terminal velocity and the slope of the blue edge of the profile. Apart from insofar as it affects the other parameters in the fit  $w_g$  is not involved in the determination of MLR. Being the hardest parameter to determine, its relative unimportance, and since the values of  $v_\infty$  give good agreement between the two optical depth laws even when  $w_g$  varies significantly, this parameter can be regarded as essentially undefined. Profile fitting is not a good method of determining  $w_g$ . Except for obviously extreme cases it appears that  $w_g$  could be fixed between  $\sim 60 - 200 \text{ km s}^{-1}$

Table 6.8: A comparison, for the EHe stars, of the results from SEILS and the co-moving frame method (from Hamann, Schönberner & Heber 1982). Three values are given in the SEILS column the lefthand number is for the  $\beta$ -dependent law, the centre for the  $\beta$ -independent and the righthand one for the  $\beta=1$  optical depth law. To allow direct comparison the turbulent velocity is given in  $\text{km s}^{-1}$  ( $v_g = w_g \times v_\infty$ ). For BD+10°2179 the  $\beta=1$  results are not given as the fit was so poor.

Star	$v_\infty$			$\beta$				$v_g$				
	seils		HSH	seils		HSH	seils		HSH			
BD +10° 2179	350	380	-	400	0.1	0.004	-	1.0	140	50	-	60
BD -9° 4395	400	450	330	600	1.0	10.0	1.0	"Tailored"	160	110	100	60
HD 160641	600	480	500	550	1.0	4.0	1.0	0.5	70	170	150	60-100

without a noticeable degradation of accuracy.

The results from SEILS agree reasonably well with those from the co-moving frame analysis (Hamann, Schönberner & Heber 1982); a comparison of resulting parameters is given in Table 6.8, with the comparison of MLR in Table 6.7.

The final profiles of HSH are slightly better than those from SEILS. For BD +10° 2179 the co-moving profiles fit the full depth of the absorption troughs while the SEILS profile does not get the correct depth. For BD -9° 4395 the SEILS profiles give a much better fit to the observations for the C II line, a slightly poorer fit for the Si IV line and a substantially worse fit for the CIV line where SEILS fails to fit the observed emission peak at all, although the rest of the profile is a good fit to observations. To obtain such good results HSH used a "tailored" velocity field rather than using the power law field. This was not possible with SEILS. However the results seem comparable for the two stars that didn't use the tailored velocity field. For HD 160641 neither SEILS nor the co-moving frame method fit the C II profile well; both are unable to match the depth of the observed profile. For the CIV line both fits are also quite poor with neither SEILS nor the co-moving frame method fitting the blue edge well, due possibly to the presence of a strong blending line. The NV and Si IV doublets are almost identical in both methods, the fits being very good.

As far as the determined products of MLR and ionisation fractions are concerned the agreements between the co-moving frame method and SEILS are very good. Interestingly the agreement appears better for the  $\beta$ -dependent optical depth law where the differences are smaller and 5 out of the 8 lines agree to within the uncertainty limits. For the  $\beta$ -independent optical depth law the differences are larger, but so are the uncertainties. Here there is agreement within uncertainty bounds for four out of eight lines. For BD +10° 2179 and BD -9° 4395 the differences in minimum MLR between the two optical depth laws are minor. For HD 160641 the differences are substantial; a difference of 5.2 dex in the minimum MLR from the CIV line is the most extreme example. With the  $\beta$ -dependent optical depth law, the CIV and Si IV lines give consistent results of about 1 dex higher MLR than the co-moving frame results. For the  $\beta$ -independent law the minimum MLR are between 2 and 4 dex lower than the co-moving frame values. The  $\beta=1.0$  solutions had MLR that were about 1 dex from the HSH results and were the poorest of the three methods on this criteria.

For all methods the fit of theoretical to observed profiles was fairly good; this seems to show that for final profiles, as far as MLR are concerned, the solutions may be non-singular.

For the two sdO stars in this study there has been little previous wind line analysis. A lower limit to the MLR for these stars was determined by Darius, Giddings & Wilson (1979) of  $6 \times 10^{-9} M_{\odot} \text{ yr}^{-1}$ . However this MLR can only be a poor reflection of the true value as only a single line was used for the mass loss determination; photospheric lines and turbulence were ignored. Radiative coupling between the two components was also ignored and solar abundances were assumed. The SEILS results show that the MLR for these two stars are very high, with some agreement between the optical depth laws. The CIV profiles, especially, are very good for both stars; the NV results are poorer and the NIV profiles bear little resemblance to the observed profiles. From the CIV lines and the  $\beta$ -independent optical depth law the determined product of MLR and ionisation fraction are given in Table 6.9. The errors given for BD +37 1977 are larger than given in Table 6.7 due to the discrepancy between the results from the three optical depth laws.

No NLTE ionisation fractions are available to determine the true MLR from these stars and the "warm wind" model invoked by HSH to determine the minimum ionisation fractions has been shown to be unjustified (*e.g.* Kudritzki 1988).

Similarly the use of other techniques to determine the ionisation balance will also give results that cannot be trusted. These include a simple LTE Saha treatment, the use of radiative and dielectric recombination together with photoionisation and collisional ionisation for either the optically thin approximation (*e.g.* Hamann 1980, 1981, Lamers & Morton 1976, Abbott & Lucy 1985) or the optically thick approximation (*e.g.* Abbott 1982, Pauldrach, Puls & Kudritzki 1986, Kudritzki, Pauldrach & Puls 1987). A number of authors have tabulated ionisation fractions against temperature using the ionisation and recombination processes listed above (*e.g.* Shull & Van Steenberg 1982, Arnauld & Rothenflug 1985), however they all assume a low density where the density-dependent effects are small (*i.e.*  $n_e \leq 10^{11} \text{ cm}^{-3}$ ) (Jordan 1969). Use of these tables is also not justified as the ionisation fractions depart very significantly from the standard LTE or NLTE ratios and yet do not require a super-heated wind.

Only the product of MLR and ionisation fraction can be determined from this study; the final adopted values taken from the CIV and SiIV minimum MLR are given in Table 6.9.

From the study of O stars in the previous Chapter the ionisation fraction of CIV for stars with an effective temperature of 30,000 to 40,000 K was about 1.0 for the models used. For the sdO stars with temperatures closer to 60,000 K the ionisation fraction of CIV would be substantially less than 1.0. Similarly for the much cooler EHe stars the ionisation fraction of CIV will also be much smaller. Complications arise from the different chemical compositions of the stars in this study and the O stars for which the ionisation fractions are published. Because the sdO stars are

Table 6.9: Minimum mass-loss rates (mass-loss rate times ionisation fraction) for the EHe stars. The  $\beta$ -independent results are quoted here with errors that take into account the spread of results between the three optical depth laws.

Star	$\log \dot{M} q$	Error
BD +10° 2179	-10.5	$\pm 2.0$
BD -9° 4395	-10.0	$\pm 1.0$
HD 160641	-11.0	$\pm 1.5$
BD +37° 1977	-9.0	$\pm 2.0$
BD +37° 442	-10.0	$\pm 1.0$

so much hotter than the O stars the ionisation fraction of CIV is likely to be low, say 0.001 or less as the “A1” model of Pauldrach, Kudritzki, Puls & Butler (1990) ( $120 M_{\odot}$ ,  $T_{eff} = 51,000$  K) has a CIV ionisation fraction of 0.001.

Similarly it may be expected that the EHe stars will have ionisation fractions of the same order. Thus it seems likely that the true MLR of the EHe and sdO stars analysed in this study have MLR of some 2 or 3 dex greater than those given in Table 6.9. This would give MLR for all the stars of about  $10^{-8} M_{\odot} \text{ yr}^{-1}$ .

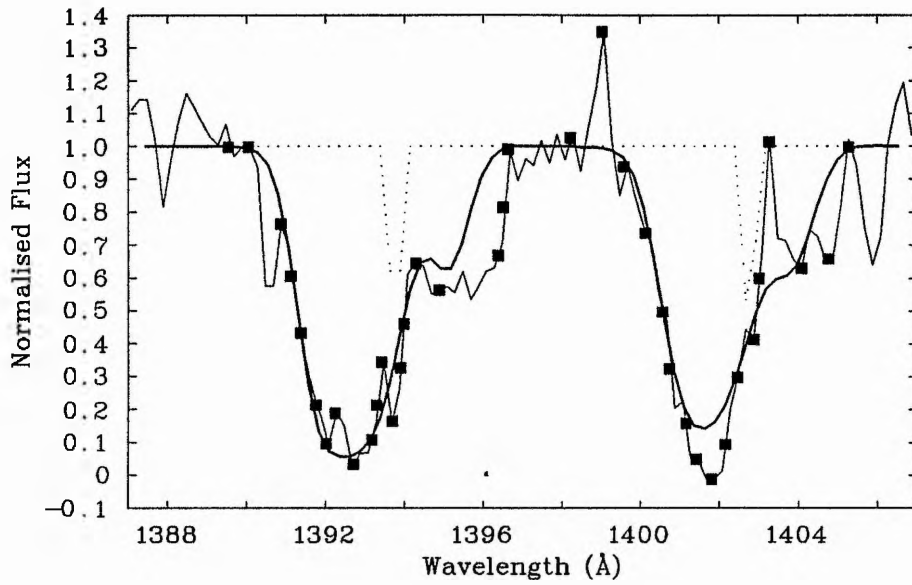


Figure 6.4: The Si IV line of BD -9° 4395 showing a very good fit to the profile, including the two “shoulder” absorptions. Narrow photospheric lines were used ( $w_{phot} = 0.11$ ) together with a large turbulence ( $w_g = 0.81$ ). The values for  $\beta$ ,  $v_{\infty}$ ,  $\alpha_1$  and  $\alpha_2$  were 0.99,  $280 \text{ km s}^{-1}$ , -1.2 and -0.6 respectively. The  $\beta$ -dependent optical depth law was used.

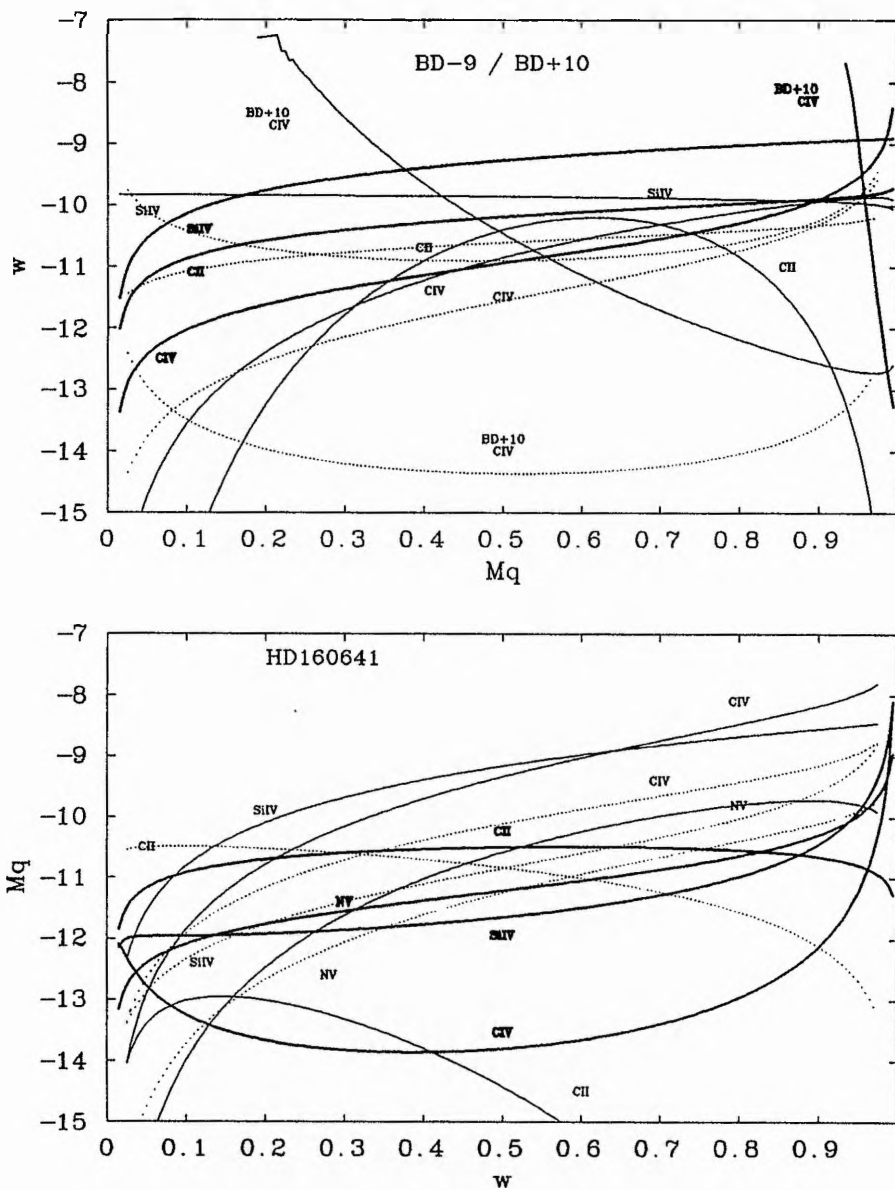


Figure 6.5: The variation of the product of mass-loss rate and ionisation fraction with velocity for the  $\beta$ -independent (heavy line) and  $\beta$ -dependent (light line) optical depth laws together with the  $\beta = 1.0$  analysis (dotted line).

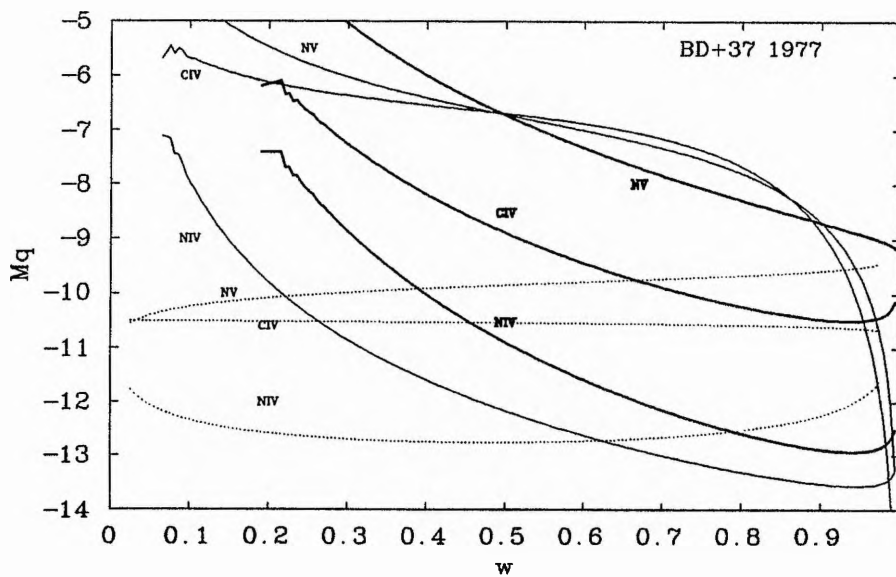
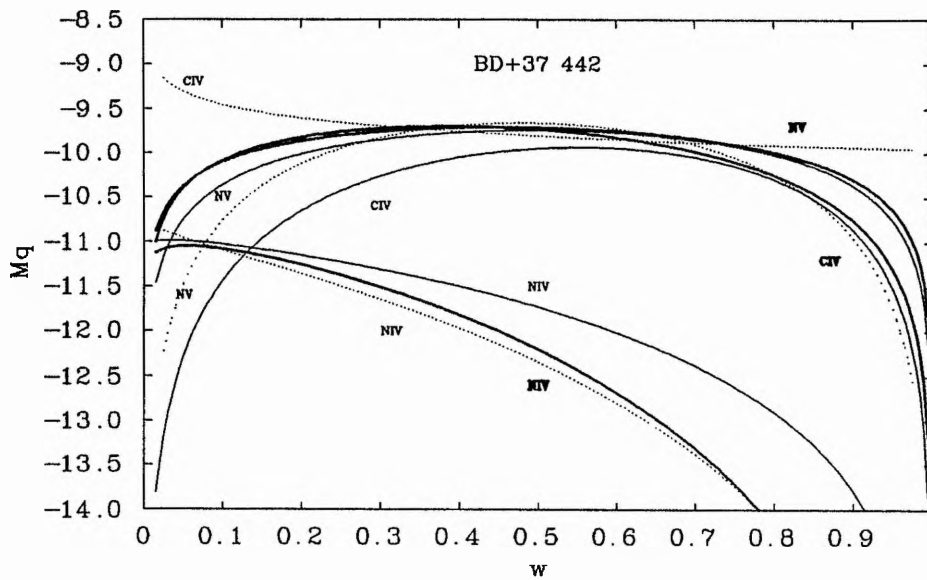


Figure 6.5: *continued.*

## 6.9 Summary

*The improved Sobolev method in the form of SEILS has been used to model the wind lines of the three EHe stars that show substantial mass loss and of two stars hydrogen-deficient sdO stars.*

*Three optical depth laws were used; all giving approximately equivalent results, with BD +10° 2179 being shown to have a value of  $\beta$ , the gradient of the velocity law, substantially less than one. For the other stars the results are consistent with the CAK luminosity driven wind theory.*

*Minimum MLR are determined from the wind line profiles and an indication of true MLR are obtained by adopting approximate improved NLTE ionisation fractions. The minimum MLR and profiles agree well with the results from the co-moving frame method.*

*The hydrogen-deficient sdO stars have high MLR of  $\sim 10^{-8} M_{\odot} \text{ yr}^{-1}$ , as may be expected from luminous stars with high terminal velocities and deep absorption profiles. The EHe stars show a similar MLR, despite much lower terminal velocities.*

*The results presented here represent the most accurate determinations of MLR for the EHe stars available and the only thorough results for the two hydrogen-deficient sdO stars, BD +37° 1977 and BD +37° 442.*

## 6.10 References

- Abbott, D.C., 1982. *Astrophys. J.*, **259**, 282.
- Abbott, D.C. & Lucy, L.B., 1985. *Astrophys. J.*, **288**, 679.
- Arnauld, M. & Rothenflug, R., 1985. *Astr. Astrophys. Suppl.*, **60**, 425.
- Barker, P., 1984. *Astr. J.*, **89**, 899.
- Castor, J.I., Abbott, D.C. & Klein, R., 1975. *Astrophys. J.*, **195**, 157.
- Darius, J., Giddings, J.P. & Wilson, R., 1979. *First Year of IUE Symposium*, .
- Drilling, J.S. & Heber, U., 1986. In: *Hydrogen Deficient Stars and Related Objects, I.A.U. Colloquium No. 87*, p.23, eds. K. Hunger, D. Schönberner & N.K. Rao, Reidel.
- Drilling, J.S. & Heber, U., 1989. In: *The Second Conference on Faint Blue Stars, I.A.U. Colloquium No. 95*, p.603, eds. A.G. Philip, D.S. Hayes & J.W. Liebert, L. Davis Press Inc.
- Drilling, J.S. & Hill, P.W., 1986. In: *Hydrogen Deficient Stars and Related Objects, I.A.U. Colloquium No. 87*, p.499, eds. K. Hunger, D. Schönberner & N.K. Rao, Reidel.
- Groenewegen, M.A.T. & Lamers, H.J.G.L.M., 1989. *Astr. Astrophys. Suppl.*, **79**, 359.
- Hamann, W.-R., 1980. *Astr. Astrophys.*, **84**, 342.
- Hamann, W.-R., 1981. *Astr. Astrophys.*, **93**, 353.
- Hamann, W.-R., Schönberner, D. & Heber, U., 1982. *Astr. Astrophys.*, **116**, 273.
- Heber, U., 1986. In: *Hydrogen Deficient Stars and Related Objects, I.A.U. Colloquium No. 87*, p.33, eds. K. Hunger, D. Schönberner & N.K. Rao, Reidel.
- Husfeld, D., 1989. In: *The Second Conference on Faint Blue Stars, I.A.U. Colloquium No. 95*, p.237, eds. A.G. Philip, D.S. Hayes & J.W. Liebert, L. Davis Press Inc.
- Jeffery, C.S. & Heber, U., 1992. *Mon. Not. R. astr. Soc.*, in press.
- Jeffery, C.S. & Hill, P.W., 1986. *Mon. Not. R. astr. Soc.*, **221**, 975.
- Jeffery, C.S., Heber, U. & Hill, P.W., 1986. In: *Hydrogen Deficient Stars and Related Objects, I.A.U. Colloquium No. 87*, p.101, eds. K. Hunger, D. Schönberner & N.K. Rao, Reidel.
- Jordan, C., 1969. *Mon. Not. R. astr. Soc.*, **142**, 501.
- Klemola, A.R., 1961. *Astrophys. J.*, **134**, 1961.
- Kudritzki, R.P., 1988. In: *Radiation in Gaseous Moving Media, Eighteenth "Saas-Fee" Conference*, p.1, eds. W. Chmielewski & T. Lanz, Geneva Observatory.
- Kudritzki, R.P., Pauldrach, A. & Puls, J., 1987. *Astr. Astrophys.*, **173**, 293.

- Lamers, H.J.G.L.M., Cerruti-Sola, M. & Perinotto, M., 1987. *Astrophys. J.*, **314**, 726.
- Lamers, H.J.G.L.M. & Morton, D.C., 1976. *Astrophys. J. Suppl.*, **32**, 715.
- Landolt, A.U., 1986. In: *Hydrogen Deficient Stars and Related Objects*, I.A.U. Colloquium No. 87, p.51, eds. K. Hunger, D. Schönberner & N.K. Rao, Reidel.
- Lynas-Gray, A.E., Schönberner, D., Hill, P.W. & Heber, U., 1984. *Mon. Not. R. astr. Soc.*, **209**, 387.
- Pauldrach, A., Puls, J. & Kudritzki, R.P., 1986. *Astr. Astrophys.*, **164**, 86.
- Pauldrach, A.W.A., Kudritzki, R.P., Puls, J. & Butler, K., 1990. *Astr. Astrophys.*, **228**, 154.
- Perinotto, M., Cerruti-Sola, M. & Lamers, H.J.G.L.M., 1989. *Astrophys. J.*, **337**, 398.
- Rees, P. & Giddings, J., 1989. *STARLINK User Note 37.7*.
- Shull, J.M. & Van Steenberg, M.E., 1982. *Astrophys. J. Suppl.*, **48**, 95.
- Walker, H.J. & Schönberner, D., 1981. *Astr. Astrophys.*, **97**, 291.
- Wolff, S.C., Pilachowski, C.A. & Wolstencroft, R.D., 1974. *Astrophys. J.*, **194**, L83.

## Chapter 7

# Stellar Winds and Mass Loss from the $\nu$ Sgr System

### 7.1 Introduction

$\nu$  Sgr shows many signs of mass loss in the UV; the most notable being the resonance lines of CIV, SiIV and NV, which show strong wind profiles, and the non-resonance lines of Si III, C II, C III and others (Parthasarathy, Cornachin & Hack 1986).

Violet-shifted H $\alpha$  absorptions documented by Nariai (1967) when the secondary is in front of the primary indicate that a jet of material is passing from the primary towards the secondary, through the Inner Lagrangian point, L<sub>1</sub>. This indicates a jet of material leaving the system while the IR excess (Chapter 8 and *e.g.* Lee & Nariai 1967; Woolf 1973; Humphreys & Ney 1974a,b) and the fact that the primary is a supergiant filling its Roche Lobe also indicate that there is radial outflow of mass from the system, driven by the primary.

Modelling of these wind lines has not been undertaken before and is complicated by the binary nature of the system. However from the lack of observed period changes in the orbit an upper limit of  $1.9 \times 10^{-5} M_{\odot} \text{yr}^{-1}$  was determined (Chapter 2). This result only determines the upper limits for mass-loss rate (MLR) while a detailed analysis of the individual wind line profiles of  $\nu$  Sgr should allow the determination of the MLR with much greater accuracy; thus helping to answer the crucial question on the future evolution of the system - whether  $\nu$  Sgr can avoid becoming a Type Ib supernova.

Some work on binary star winds has been done by Drew and co-workers (Drew 1986, 1987; Drew, Hoare & Woods 1991). Their work details mass loss within a cataclysmic binary system,

consisting of a supergiant primary, a white dwarf secondary and a hot accretion disc. Although the model has some refinements, such as deviations from spherical outflow and flux infilling by the UV from the disk, it is still a crude model by the standards of SEILS. No account is made of photospheric lines, radiative coupling or turbulence. A linear velocity law is used where the velocity is proportional to the distance from the star. SEILS appears to be the best available code for modelling the wind lines of  $\nu$  Sgr.

Chiosi & Maeder (1986) provide an overview of mass loss from an observational viewpoint and Kudritzki (1988) from a theoretical one.

## 7.2 Description of the UV Wind Profiles

### 7.2.1 Phase dependency

One of the most significant assumptions when modelling winds with SEILS is that of spherical symmetry. This does not hold exactly for  $\nu$  Sgr due to the binary nature of the system; shown in Figure 7.1 are the wind line profiles for the CIV and SiIV doublets at 5 different phases (upper diagrams) while the lower diagrams shows two such profiles taken one day apart. The spectra show some degree of variability (or, possibly, noise - the major areas are highlighted) but mainly in the spectral lines that do not show wind profiles. There does not appear to be any *phase dependent* variability of the wind line profiles themselves except that the blue edge of the phase 0.33<sup>1</sup> seems to show a blueward shift relative to the others but only in the CIV profiles. The shape of the profiles appear remarkably constant over all phases with the blue edge being at an almost constant velocity.

To a reasonable approximation it appears that the main wind forming region is phase independent.

### 7.2.2 The summed profile

Due to the phase-independence of the resonance wind lines the merged spectrum consisting of the 16 available IUE SWP frames was used to obtain the profiles that were to be fitted with SEILS. (See Chapter 2 for details of the IUE spectra.) As the mass flow might be expected to originate from the primary and the ionising radiation from the secondary the template sharpened on the interstellar lines was used. The small ( $< 10 \text{ km s}^{-1}$ ) correction for the systemic velocity was ignored.

<sup>1</sup>Phase 0.25 is the secondary in front of the primary and phase 0.0 the maximum approaching velocity of the secondary.

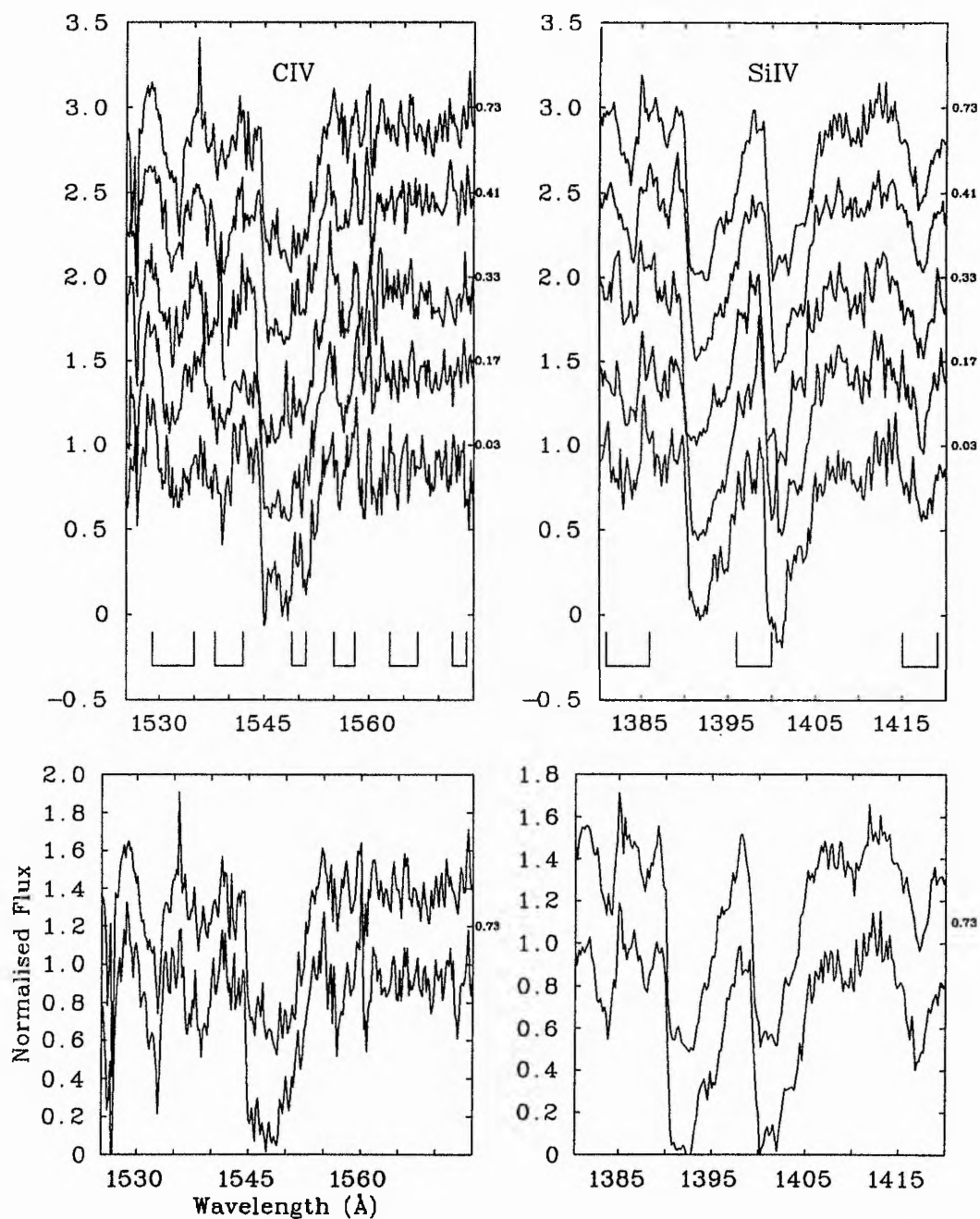


Figure 7.1: Upper - the variation of the CIV (left) and SiIV (right) profiles of  $v$  Sgr with phase. Lower - the variations of the profiles over the space of less than 1 day. Phases are marked on the right hand side; areas of marked variability are also indicated.

The 6 most prominent wind line profiles are shown in Figure 7.2. The most notable feature of the doublet line profiles is the lack of an emission peak, especially in the CIV profile where one might be expected. Parthasarathy *et al.* dismiss the lack of the emission peak by reduction due to underlying photospheric FeIII and P II lines. However calculations using model atmospheres show that these lines are weak and could not remove a sizeable emission peak, which in any case should be visible as the continuum level is set to the average level after the lowering by weak lines is accounted for. It appears that the lack of an emission peak is a definite attribute of the CIV, and other, wind profiles in  $\nu$  Sgr.

### 7.3 Interstellar Extinction and Lyman $\alpha$ Correction

Removal of the Lyman- $\alpha$  contribution is required to determine the correct profiles of the NV and Si III lines before modelling. To determine this the column density is required; using the technique given in Chapter 4 a value of  $\log N_H = 21.0 \pm 0.3$  was determined.

Using flux-calibrated low resolution IUE data obtained from the Uniform Low Dispersion Archive (ULDA) and using Seaton's UV de-reddening law (1979) the 2200 Å feature was removed and a value for the extinction of  $E_{B-V} = 0.20 \pm 0.05$  determined. The large error is due to the fact that in  $\nu$  Sgr the continuum around 2200 Å is not smooth; containing many lines and blends. The ULDA data for  $\nu$  Sgr is given in Table 7.1 while the de-reddened spectra for various values of  $E_{B-V}$  are shown in Figure 7.3. This value for the extinction has been independently confirmed by the modelling of the flux distribution of the primary component given in Chapter 8.

From the extinction-column density relationship of Bohlin, Savage & Drake (1978)

$$E_{B-V} = \frac{N_H}{4.8 \times 10^{21}} \quad (7.1)$$

the column density gives rise to an extinction of  $E_{(B-V)} = 0.17^{+0.24}_{-0.07}$ , giving confirmation within a wide margin of uncertainty. These results are higher than the previous estimates of Schönberner & Drilling (1984) (0.10), Rao & Venugopal (1985) (0.00 to 0.12) and Parthasarathy *et al.* (0.12 to 0.20).

The NV and SiIII profiles were corrected using  $\log N_H = 21.0$ , although the NV profile was hardly affected due to the low terminal velocity of the wind.

### 7.4 Photospheric lines

It was expected that the mass outflow from the system would come from the primary as stellar winds are luminosity driven. The UV radiation would also mainly come from the primary; an

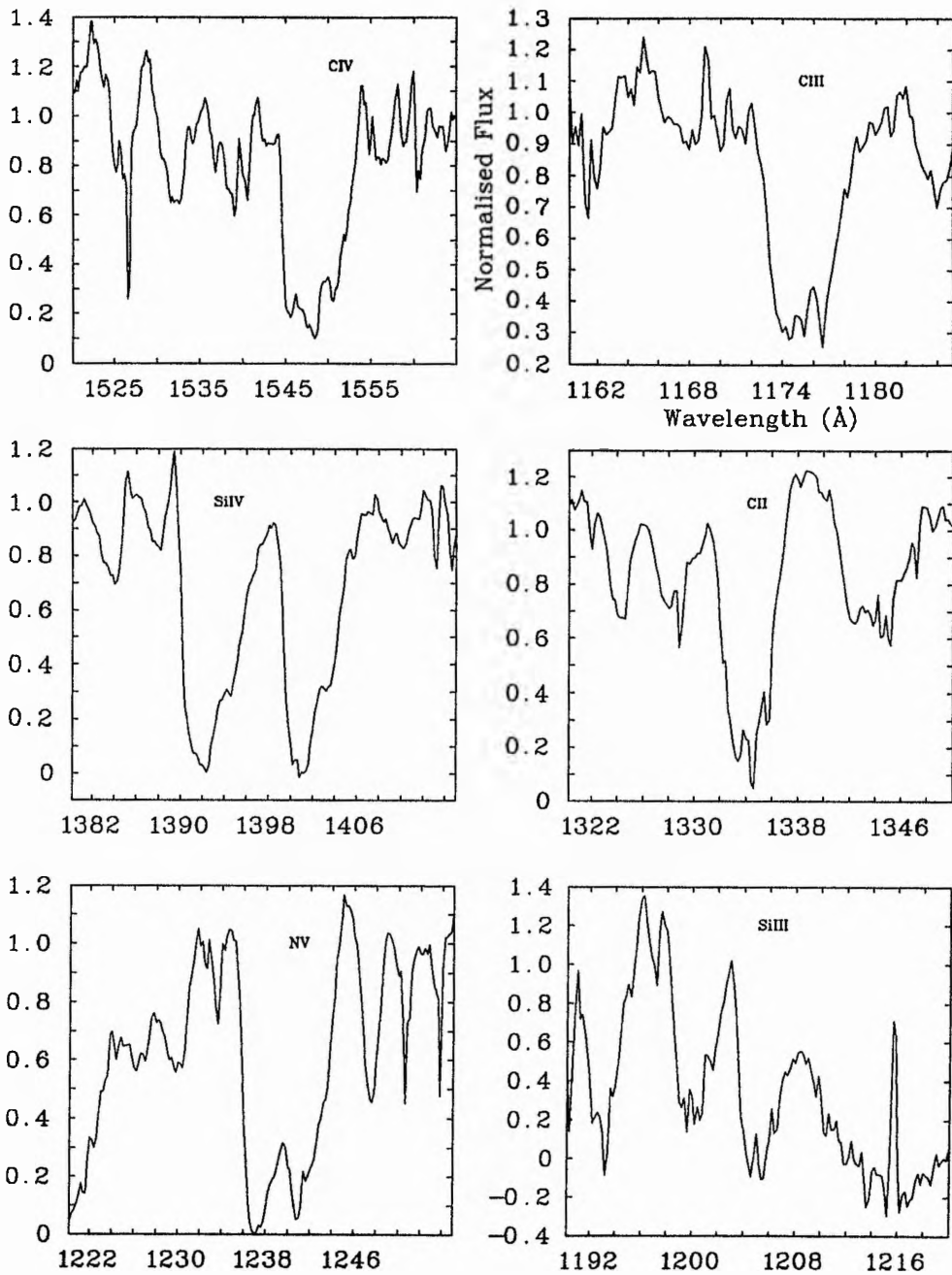
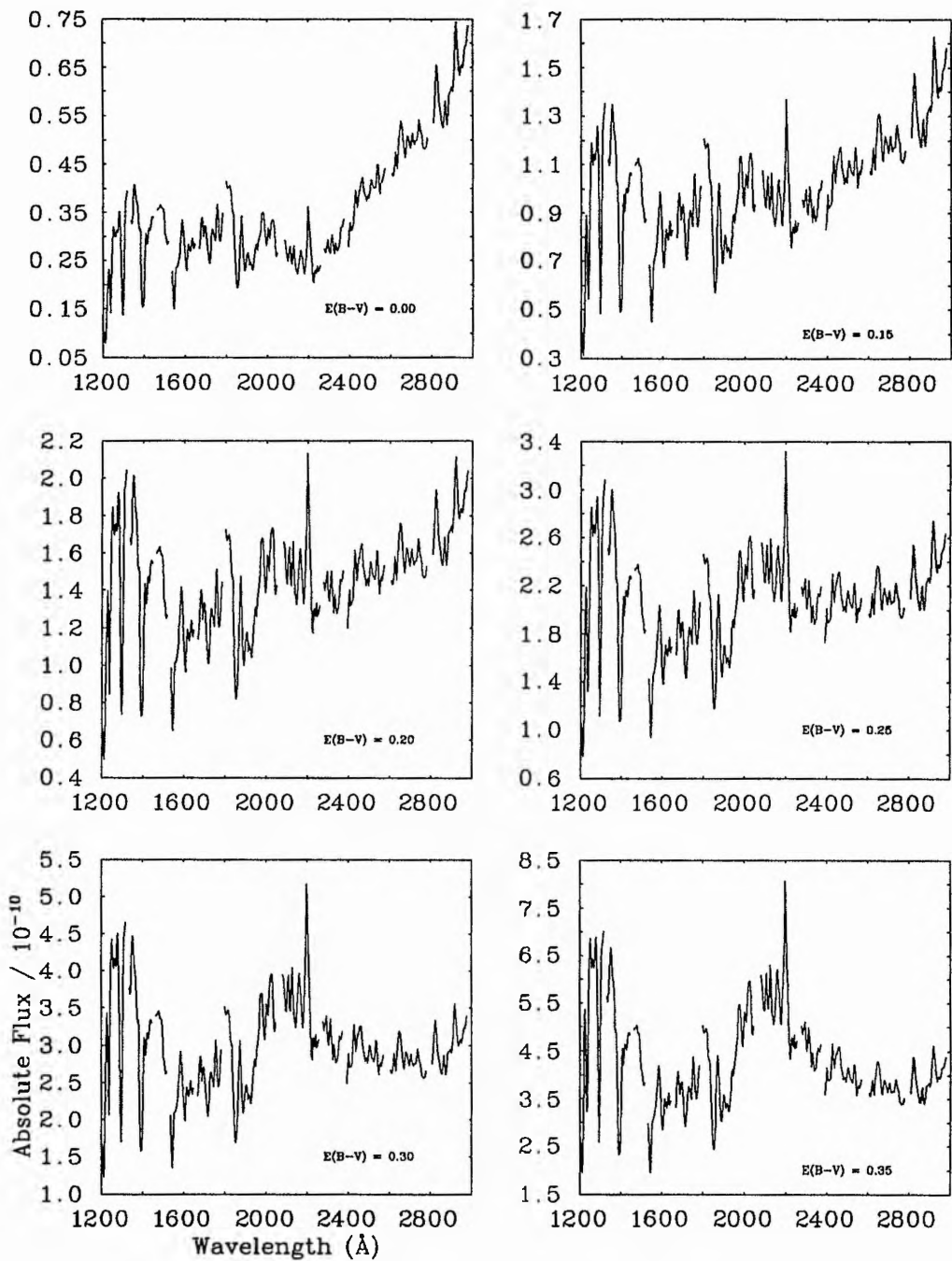


Figure 7.2: The six wind profiles of  $\nu$  Sgr. The three doublets are shown on the left, the three singlets on the right.



**Figure 7.3:** Extinction correction for  $\nu$  Sgr. IUE ULDA spectra are shown after de-reddening with the values of  $E_{B-V}$  indicated. The fluxes are in units of  $\text{ergs cm}^{-2} \text{s}^{-1} \text{\AA}^{-1}$ . The spectrum used is that of SWP8297 merged with LWR7245. The data have been smoothed for clarity; an extinction of  $E_{B-V} = 0.20 \pm 0.05$  gives the best removal of the 2200  $\text{\AA}$  feature.

Table 7.1: The low dispersion data available for  $\nu$  Sgr. The phase is determined from the ephemeris given in Dudley & Jeffery (1990) and Chapter 2, p.36. Only the spectra taken through the large (LAP) aperture are accurately flux calibrated, and thus useful for this study. An asterisk indicates that a spectrum was unuseable; usually due to many bad data points within the spectrum.

Spectrum	Aperture	Date	J.D. (-2440000)	Exposure (seconds)	Phase
SWP26090*	L	04/06/85	6221	600	0.71
SWP1554*	L	15/05/78	3644	11.8	0.03
SWP5784	S	13/07/79	4068	24.9	0.10
SWP5784	L	13/07/79	4068	27.7	0.10
SWP8297	L	19/03/80	4318	11.7	0.92
SWP8298	L	19/03/80	4318	60.0	0.92
SWP9109	L	25/05/80	4385	26.5	0.40
LWR5028*	L	13/07/79	4068	25.7	0.10
LWR5028	S	13/07/79	4068	8.5	0.10
LWR7243*	L	19/03/80	4318	140	0.92
LWR7244*	L	19/03/80	4318	58.8	0.92
LWR7245	L	19/03/80	4318	12.0	0.92
LWR7848	L	25/05/80	4385	8.5	0.40

expectation reinforced by the determination of a high UV luminosity ratio (primary/secondary) from the CCF analysis (Chapter 2) and the analysis of the primary flux distribution (Chapter 8).

This being the case there will be no underlying photospheric profiles as the primary is cool ( $\sim 11,800\text{K}$ , Chapters 8 and 11). However photospheric line profiles do appear strongly in the deconvolved secondary spectrum (Chapter 2) and indicate that the secondary may have a role in driving the wind. If the secondary is a normal  $5 M_{\odot}$  B star then its effective temperature of  $\sim 18,000\text{K}$ . A secondary temperature of  $24,000\text{K}$  was assumed for the purposes of photospheric line determination with, possibly, the high temperature due to infalling material. Secondary photospheric profiles were determined with SPECTRUM and a T24G40X0099 model. The widths of these profiles were then modified after comparison with Stark broadened profiles for BD -9° 4395 (Hamann, Schönberner & Heber 1982). With a surface gravity of  $\log g = 2.4$ , BD -9° 4395 will have sharper lines than that for the secondary of  $\nu$  Sgr and thus the published line widths for BD -9° 4395 provide lower limits to the line widths of the secondary component.

The assumed abundances (logarithm of number fractions) and the line parameters are given in Table 7.2. As usual, for a doublet both lines are assigned the same profile.

Table 7.2: Abundances (log of mass fractions) and photospheric line parameters for  $\nu$  Sgr. The line parameters were calculated with a T24G40X0099 SPECTRUM model and a terminal velocity of  $600 \text{ km s}^{-1}$  was assumed for the determination of the widths. The values given for  $w_{phot}$  are those after modification (see text) while those for  $A_{phot}$  are those determined by SPECTRUM alone.

Ion	Wavelength ( $\text{\AA}$ )	Element Abundance	$A_{phot}$ (SPECTRUM)	$w_{phot}$
C II	1335.70	-2.7	1.85	0.20
C III	1175.67		1.08	0.15
C IV	1548.19		1.54	0.20
Si III	1206.51	-3.9	1.08	0.25
Si IV	1393.76		1.78	0.35
N V	1238.81	-2.9	0.00	0.00

## 7.5 The Single Star Approximation

It was possible that the winds of  $\nu$  Sgr could be modelled satisfactorily as a single star in the usual way. The primary drives the wind so it would be expected that the velocity law determined would be that of the primary. However it is not clear whether any photospheric lines should be used. The primary, which still contributes most of the flux in the UV region will have none of the photospheric lines being investigated as it is too cool. The secondary will have the lines but there is the possibility that they would be infilled by the flux from the primary. Thus the wind lines of  $\nu$  Sgr were first modelled by SEILS with no photospheric lines - the single A star approximation. Both forms of the optical depth law were used. The results are given in Table 7.3 and shown for the  $\beta$ -independent optical depth law in Figure 7.4.

The results for the A star approximation are quite poor in the case of all the lines except, perhaps, the C II doublet. The blue edges of the C II, NV and Si IV lines are fitted very well but with terminal velocities between  $490$  and  $730 \text{ km s}^{-1}$  and turbulent velocities of  $\sim 0.25 v_{\infty}$ . For all the lines, except C III and NV, the calculated absorption does not fit the observed absorption, this being most notable in the two silicon lines. The most obvious result is that the gradient of the velocity law,  $\beta$ , is strongly clustered about zero. While the largest value is 0.7, 11 out of the 12 fits have  $\beta$  less than 0.052.

To determine whether the assumption that the secondary photospheric profiles were infilled by the primary flux the wind lines of  $\nu$  Sgr were also modelled as a single B star using the photospheric lines determined above. The results given in Table 7.4 and are shown for the  $\beta$ -independent optical depth law in Figure 7.5.

The results were better, in some cases, but with the lower parts of the profiles not being

Table 7.3: The wind line profile results of modelling the  $\nu$  Sgr system as a single A star. Shown are the results obtained when the  $\frac{1}{\beta}$  term was (upper) and was not (lower) included in the optical depth law. No photospheric lines were used. The values shown are those determined from using SEILS on each line individually.

Ion	$\beta$	$v_\infty$	$w_g$	$\alpha_1$	$\alpha_2$	$T_B$
C II	0.008	520	0.30	0.4	0.1	6.0
C III	0.007	490	0.73	-1.8	0.0	0.7
C IV	0.004	770	0.35	0.2	0.4	8.0
Si III	0.023	940	0.19	-1.9	11.1	74.2
Si IV	0.052	730	0.28	-2.4	-1.1	3.2
N V	0.002	490	0.24	-1.3	-0.8	12.0
C II	0.025	540	0.12	-0.7	-0.4	7.4
C III	0.001	290	0.52	-1.3	0.7	4.5
C IV	0.008	580	0.24	-0.5	-0.6	3.3
Si III	0.721	430	0.28	-2.6	-2.8	0.2
Si IV	0.001	600	0.27	-2.9	-1.6	9.9
N V	0.024	540	0.19	-2.2	-1.4	16.3

Table 7.4: The wind line profile results of modelling the  $\nu$  Sgr system as a single B star. Shown are the results obtained when the  $\frac{1}{\beta}$  term was (upper) and was not (lower) included in the optical depth law. The values shown are those determined from using SEILS on each line individually.

Ion	$\beta$	$v_\infty$	$w_g$	$\alpha_1$	$\alpha_2$	$T_B$	$A_{phot}$	$w_{phot}$
C II	0.719	310	1.11	1.3	0.2	2.6	1.85	0.20
C III	0.003	490	0.49	-3.5	0.5	5.2	1.08	0.15
C IV	0.130	730	0.25	-0.2	18.0	62.9	1.54	0.20
Si III	0.001	430	0.27	-0.6	-0.7	143.3	1.08	0.25
Si IV	0.051	720	0.13	-0.2	-0.1	4.8	1.78	0.35
N V	0.007	520	0.23	-1.6	-0.8	26.8	0.00	0.00
C II	0.659	520	0.34	-0.3	-0.6	0.6	1.85	0.20
C III	0.005	580	0.14	-0.8	-0.5	2.9	1.08	0.15
C IV	0.004	610	0.20	-0.2	-0.5	2.9	1.54	0.20
Si III	1.572	590	0.15	-1.8	-1.3	2.8	1.08	0.25
Si IV	0.992	600	0.30	-3.5	-2.0	6.4	1.78	0.35
N V	0.024	540	0.19	-2.2	-1.4	16.3	0.00	0.00

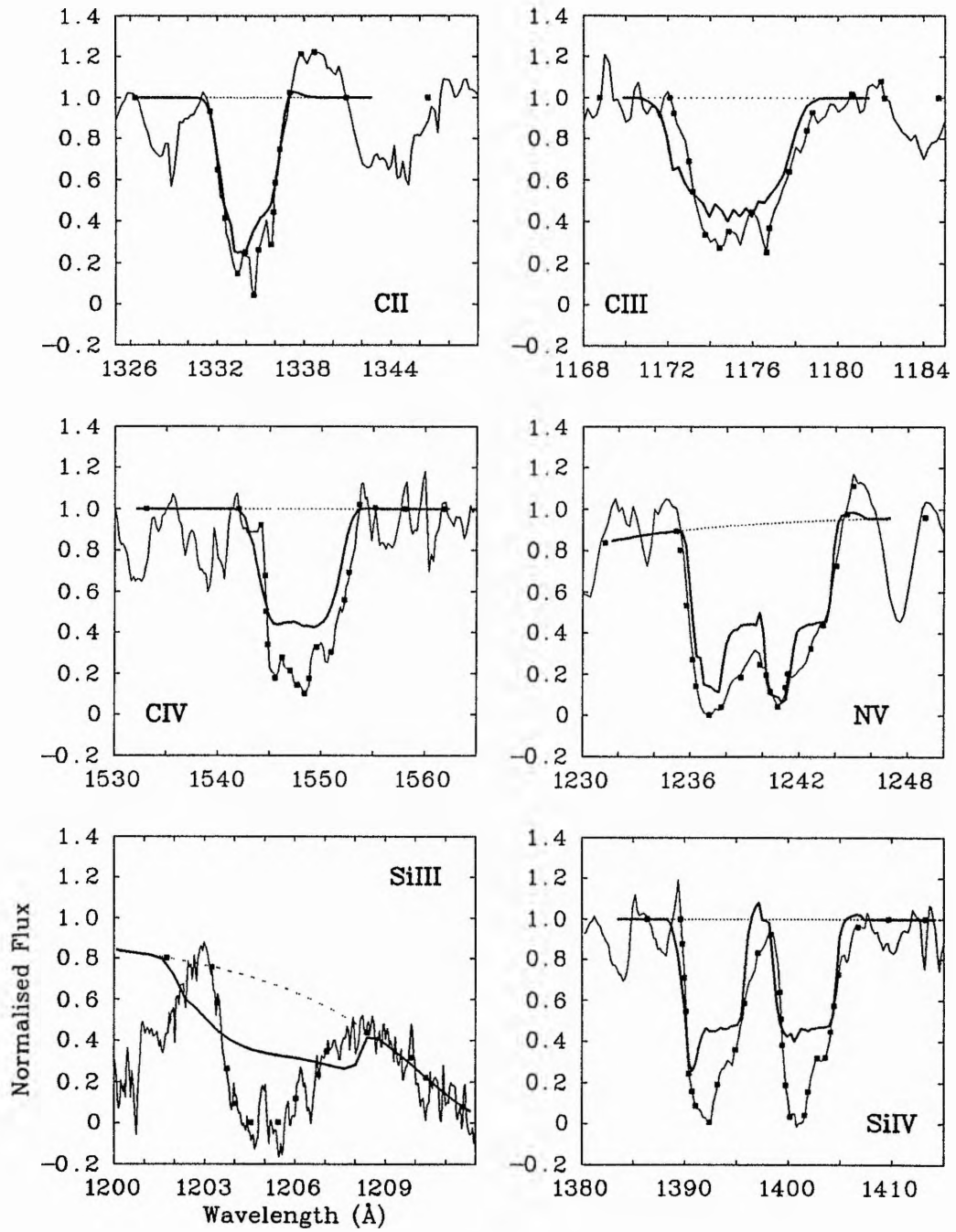


Figure 7.4: The wind line profiles of  $\nu$  Sgr treated as a single A star. Shown are the profiles determined with the  $\beta$ -independent optical depth law. Dotted lines are photospheric profiles. Different values of  $\beta$ ,  $w_g$  and  $v_\infty$  are used for each line (see Table 7.3).

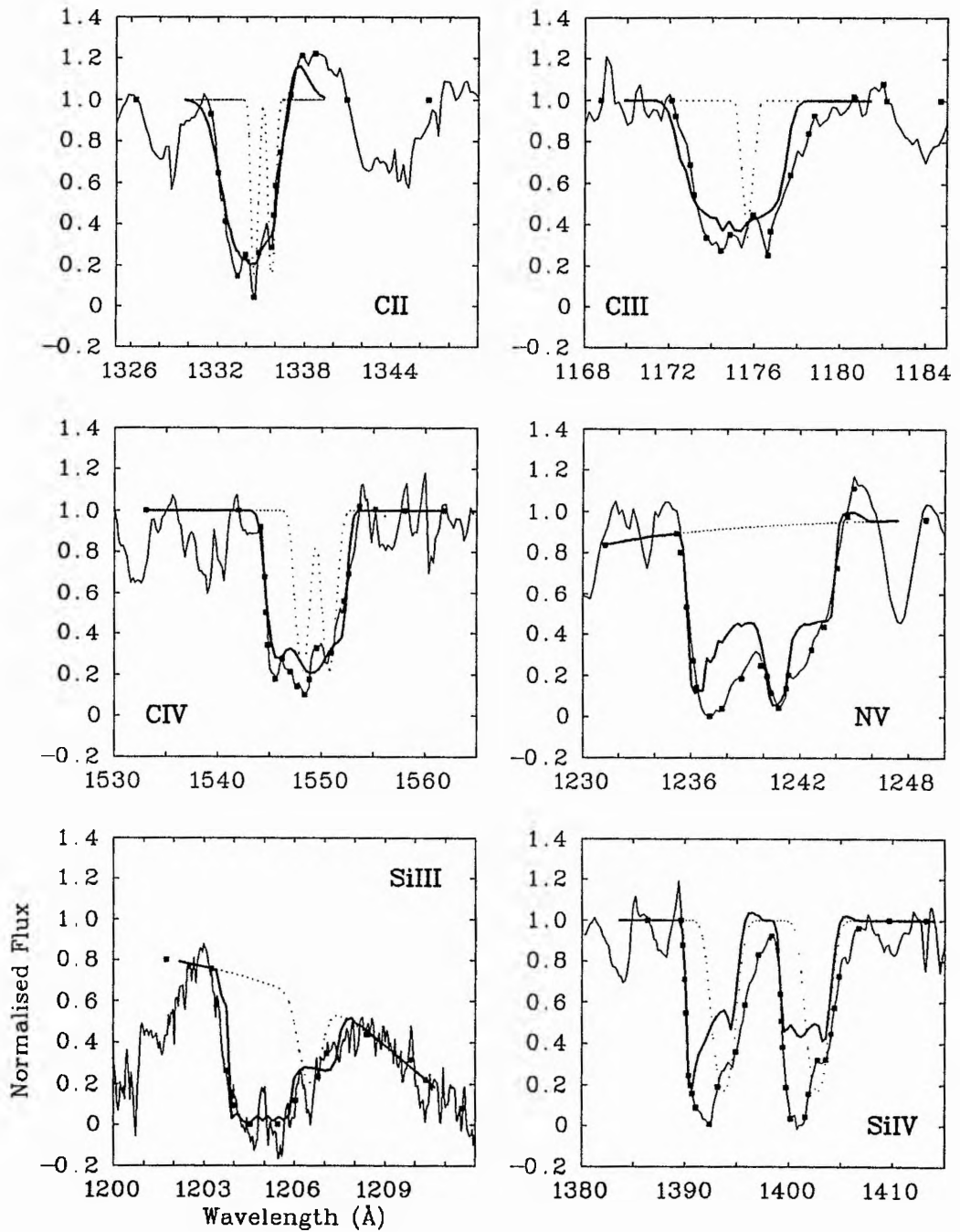


Figure 7.5: The wind line profiles of  $\nu$  Sgr treated as a single B star. Shown are the profiles determined with the  $\beta$ -independent optical depth law. Dotted lines are photospheric profiles. Different values of  $\beta$ ,  $w_g$  and  $v_\infty$  are used for each line (see Table 7.4).

filled by the theoretical profiles. Increasing the optical depth only worsened the fit; the profile did not get significantly deeper and the fit to the blue edge became poorer. This was especially true of the Si IV line, the fit being similar to those found for the A star approximation and indicate that the inclusion of photospheric line in these cases had no effect. (Indeed the parameters determined from both approximations are very close with the exception that the turbulences from the B star approximation were half that from the A star approximation.) The NV line had no photospheric component in either approximation and still the fit was quite poor<sup>2</sup>.

Again, significantly, the values for  $\beta$  were generally low but with a number of exceptions, these being the poorer singlet lines (especially C II). The Si IV with the  $\beta$ -independent optical depth law and C IV with the  $\beta$ -dependent optical depth law had  $\beta$  greater than 0.1. As for the A star approximation the spread of values for the terminal and turbulent velocities was large.

The C II line appears to show that the photospheric lines of the secondary are visible and are not infilled by the flux from the primary; however this is not so obvious in the other lines.

The fits from the B star approximation are better than those from the A star approximation; most of the line fits being fairly good; the only exceptions being NV and Si IV. However the fits shown in Figures 7.4 and 7.5 have different sets of parameters for each line. The results do show that *for each line individually* it is possible to get better fits with the B star approximation than the A star approximation.

A final fit, by fixing  $\beta$ ,  $w_g$  and  $v_\infty$ , was not attempted as a value of  $\beta = 0$  would be the most appropriate. However, using  $\beta = 0$  and the published form of the optical depth law (Equation 4.4) the velocity of the wind at all distances would be the terminal velocity (*c.f.* Equation 4.3). Then the optical depth is just given by a constant and  $\alpha_1$  and  $\alpha_2$  are redundant. This final solution would have little meaning for a single B star, but does provide a pointer to the plausability of other models, discussed later.

These results seem to indicate that the  $\nu$  Sgr system cannot be modelled satisfactorily as a single star of either spectral type A or B. However they do strongly indicate that a large part of the wind has constant velocity ( $\beta = 0$ ) and, as slightly better fits are determined with the B star approximation than the A star approximation, there may be some photospheric line contribution to the observed profiles.

---

<sup>2</sup>The small differences in the parameter values for the A and B star approximations, in the  $\beta$ -dependent case, is due to the slightly different starting values for the parameters in the two fits.

## 7.6 A Model for the $\nu$ Sgr System

Using the dimensions of the system given in Table 2.4 and the fact that the major part of the wind profiles are phase independent, a simplified model for the system can be constructed to aid wind line modelling.

It is assumed that the reasoning in Chapter 2 is correct and that the primary is a A-type supergiant with a radius of  $\sim 60 R_{\odot}$ , constrained by its Roche Lobe.

The  $\nu$  Sgr system, as viewed from the secondary component, can be divided into three zones:

1. A turbulent Inner Region with a radius of at least  $240 R_{\odot}$  (the separation of the components plus the radius of the primary).
2. An Outer Region mainly consisting of the material lost radially from the primary.
3. A jet of material escaping radially from the system, presumably through or near the  $L_3$  point.

With an edge velocity of  $\sim 750 \text{ km s}^{-1}$ , estimated from the blue edges of the resonance doublets the jet will travel  $\sim 12,000 R_{\odot}$  in the course of one revolution of the system. The jet can be ignored for the purposes of wind line studies as the jet material will be very tenuous when this far from the system and yet when close to the system only shows itself in the  $H\alpha$  profile.

## 7.7 Binary Models

With the failure of the single star models to accurately represent the wind lines it was necessary to change SEILS to allow the code, in some way, to model a binary system. Two options were available - to modify the velocity law or the optical depth law.

To keep the number of models that must be calculated down to a manageable number and to reduce the number of free parameters in the numerical fit as far as possible the  $\beta$ -independent optical depth law was used for all the binary models.

When changing both the velocity and the optical depth laws the changeover point was at the Inner/ Outer Region boundary ( $r = 240 R_{\odot}$ ). Inside this point one optical depth law (or velocity law) was used while outwards from this point a different law was used.

### 7.7.1 Modifying the velocity law

In section 7.8 are details of the models run using a different velocity law.

Two options were modelled:

1. A single (modified) velocity law operated in both the Inner and Outer regions (the "variable velocity approximation").
2. The velocity profile in the Inner Region was generated using the standard velocity law but in the Outer region the wind was at a constant velocity corresponding to  $\beta = 0$  in the Outer region (the "constant velocity approximation").

As the primary drives the wind four values of  $\beta$  were used (0.7, 1.0, 2.0 and 4.0) rather than allowing a freely floating value of  $\beta$ . This makes the solutions faster and easier by confining, but not fixing, one of the free parameters.

In this approximation the secondary was assumed to provide the UV radiation that ionises the wind and thus the mass flow from the primary must be modelled in SEILS as if it came from the secondary. A velocity law must be used that imitates this. A primary driven wind can be modelled as it is seen by the secondary if the 4 values of  $\beta$  for the primary are replaced by values of  $\beta$  for the secondary of 15, 25, 40 and 80. Figure 7.6 shows that the different values of  $\beta$  for the two stars produce velocity law profiles that are very similar.

### 7.7.2 Modifying the optical depth law

Alternatively the optical depth law can be changed. The form of the law is the same as in Equation 4.4 (without the  $\frac{1}{\beta}$  term) but with the two parameters  $\alpha_1$  and  $\alpha_2$  for the Inner region replaced by two different ones ( $\alpha_3$  and  $\alpha_4$ ) in the Outer Region.

Again two sets of models were run:

1. Assuming the primary drives and powers the wind. Then the I/O Region boundary is at  $x = 4$  (the boundary at  $240 R_{\odot}$  as seen from a star of radius  $60 R_{\odot}$ ).
2. Assuming the secondary drives and powers the wind, so  $x = 80$  (as the secondary is expected to have a radius of  $3 R_{\odot}$ ).

### 7.7.3 Discussion

The modified velocity law models should indicate if the assumption of the primary driving the wind with the secondary providing the ionising radiation is true. The constant velocity approximation will also indicate if the  $\beta \sim 0$  values found in the single star approximations are correct; at least in the Outer region.

The two models in the modified optical depth law approximation correspond to the single A and B star approximations but with a modified optical depth law to account for the possible different wind structure in the Inner and Outer regions.

Together these four sets of models provide a broad range of tests for the  $\nu$  Sgr wind system. Good results for one over the others will allow much to be said about the validity of the assumptions made and thus, by extension, the possible state of the stellar wind of  $\nu$  Sgr.

## 7.8 The Modified Velocity Law Models

The wind is assumed to come from the A2I primary as the secondary does not have enough radiation pressure to drive a wind, nor does it have enough radiation pressure to alter the flow significantly although gravitational interaction of the secondary with the wind may lead to some distortion of the wind from a radial outflow.

A velocity profile for the primary must be chosen; as the value of  $\beta$  for a A2 star is not known and there is the possibility that  $\beta$  increases for stars later than O type (Chapter 5), 4 values of  $\beta$  that may be appropriate for the primary were chosen; the corresponding velocity profiles are shown in Figure 7.6. The x-axis of Figure 7.6 is given in  $R_{\odot}$  so that primary and secondary velocity profiles can be shown together.

As viewed from the secondary the velocity profile seen by it in the Outer Region (*i.e.* outwards from  $240 R_{\odot}$ ) is given by the profiles in Figure 7.6 to the right of the right hand vertical line. It is this part of the profile that needs to be modelled by a stellar wind while the profile from the Inner Region (to the left of the vertical line) must be modelled in other ways.

### 7.8.1 The Inner Region profile

The Inner Region of the  $\nu$  Sgr model can only be treated approximately. As the system shows no phase-dependent wind line profiles, one possibility is that the Outer Region dominates the formation of the wind line profiles and the Inner Region is unimportant and may or may not show

phase dependency (if it could be studied independently). From the studies of the O stars and EHe stars it seems that the region close to the stars is important as the density of material will be the highest. Thus the Inner Region is probably important in the case of  $\nu$  Sgr and will contribute a large part to the total wind line profile. If this is the case then the Inner Region profile must be essentially phase independent. Modelling this Inner Region profile provides the largest problems with the modelling of the system. Two possibilities are available:

1. Assume the Inner Region profile can be modelled by a wide Gaussian profile, the FWHM of which corresponds to the wind velocity at the boundary between the Inner and Outer Regions (*i.e.* the  $240 R_{\odot}$  point).
2. Determine photospheric lines for the secondary, from SPECTRUM. Fix the Inner/Outer Region boundary velocity as an upper limit and fix the terminal velocity. Then for each value of  $\beta$ , determine the best fit profile. As the cut-off excludes the blue edge from the fit then SEILS is determining the best fit for the redward absorption edge and the depth of the absorption. The redward edge fitting is crucially dependent on the photospheric widths although these have only been poorly determined as the temperature and surface gravity of the secondary can only be estimated at this point.

The first option has the drawbacks that the determined Inner Region profile is symmetrical with no emission possible and is Gaussian in shape. There is no way of determining, *a priori*, the shape of the Inner Region profile, and trial and error must be used to determine the best fit. A number of sample profiles were determined and it was found that the Gaussian approximation was not justified.

The second is the more accurate as it allows non-symmetrical profiles including emission, something that SEILS can achieve.

It is not possible to fix the shape of the profile and still allow the fit to the Outer Region to have the terminal velocity as a free parameter. The turbulence was allowed as a free parameter as it was expected that within the turbulent motion in the Inner Region that different areas of the Inner Region would have different turbulent velocities. As the different ions are predominant in different areas it was plausible that different turbulent velocities would occur for different ions. As the turbulent velocity plays only a small part in the overall shape of the profile this is a minor assumption.

### 7.8.2 The constant velocity approximation

For whichever value of  $\beta_p$  is chosen a constant velocity profile out from  $240 R_{\odot}$  is assumed; this profile will have  $\beta = 0$  (cf. Equation 4.3) and the value of the velocity used will be some large

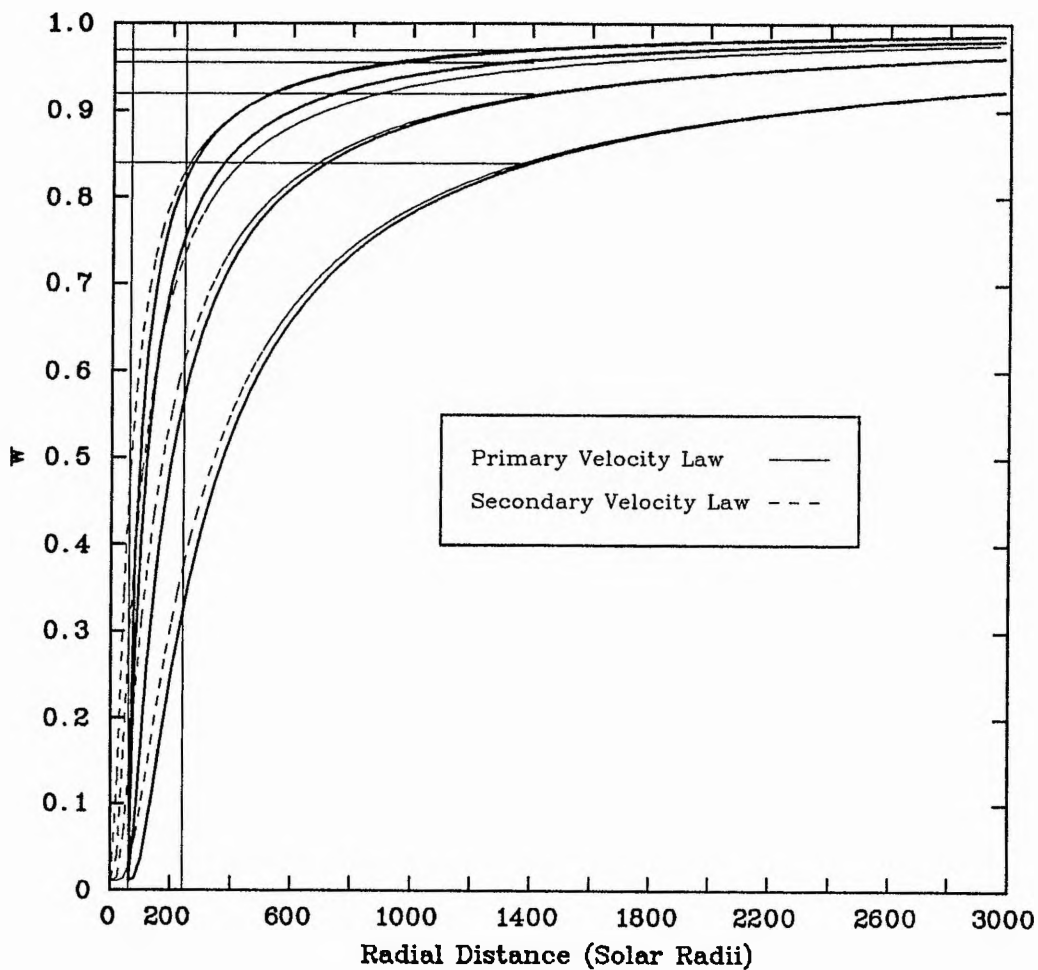


Figure 7.6: Velocity profiles for the primary (solid lines, 4 values of  $\beta_p$  indicated) and the secondary. The Inner/Outer Region boundary is shown by the righthand vertical line. The lefthand vertical line corresponds to the surface of the primary. Models for the secondary velocity profiles are shown dotted; the horizontal ones for the constant velocity approximation, the curved ones for the variable velocity approximation. Parameter values for these fits are given in Table 7.5.

Table 7.5: The fractional values of  $v_{\infty}$  used to model the primary velocity profile out from  $240 R_{\odot}$  for the constant velocity approximation are given ( $w_{fraction}$ , with the actual velocity,  $v_{fraction}$ , assuming a terminal velocity of  $570 \text{ km s}^{-1}$ ) along with the values of  $w_{OR}$  (the Inner/Outer Region boundary velocity) for the variable velocity approximation. The values for 4 different values of  $\beta_p$  are given together with the values of  $\beta_s$  that approximate them.

$\beta_p$	$w_{fraction}$	$v_{fraction}$	$w_{OR}$	$\beta_s$
0.7	0.97	550	0.82	15
1.0	0.96	550	0.75	25
2.0	0.92	520	0.57	40
4.0	0.84	480	0.32	80

fraction of the terminal velocity (indeed the terminal velocity will be set as this new value.) The fraction of the measured terminal velocity as used for each value of  $\beta_p$  is given in Table 7.5. These values are shown in Figure 7.6. As the secondary is assumed to be ionising the wind then, in the SEI implementation, the wind is modelled out to  $1000 R_{*}$  (*i.e.*  $3,000 R_{\odot}$  in this case). However as the geometrical dilution will rapidly reduce the optical depth of the material at large distances from the star, the value of the velocity used is that given at the arbitrary distance of  $1400 R_{\odot}$ .

### 7.8.3 The variable velocity approximation

Rather than approximating the velocity profile outwards from the Inner Region by a constant velocity another velocity profile can be chosen that gives a good fit to it.

As the wind is driven by the primary then the velocity-distance relationship that the secondary sees is defined by the primary. When modelling wind lines with the ionising radiation coming from the secondary, the velocity law used must match that given by the primary. However the same values for  $\beta$  (*i.e.* 0.7, 1.0, 2.0 and 4.0) cannot be used for the secondary as the secondary has a radius some 20 times smaller than the primary and thus the gradient of the velocity law ( $\beta_s$ ) required by the secondary to match the velocity-distance law of the primary is about 20 times larger. The values for  $\beta_s$  used for each values of  $\beta_p$  assumed are given in Table 7.5 and the match between the two sets of velocity laws are shown in Figure 7.6.

### 7.8.4 The optical depth law

From the two models discussed above a number of other considerations are apparent when looking at the optical depth law *for the parameterisation given within SEI*.<sup>3</sup>

<sup>3</sup>To change the parameterisation significantly would require the whole SEI code to be re-written; this would not be justified.

It is not possible to use the  $\beta$ -dependent optical depth law for the constant velocity model as  $\beta = 0$  and  $w = w_1 = 1$  (always) and thus  $\alpha_1$  and  $\alpha_2$  are redundant and an optical depth law of the form  $\tau(w) = \text{constant}$  is obtained. For the variable velocity approximation with  $\beta_s$  between 15 and 80 the same optical depth law can be used except that inwards of  $240 R_\odot$  the optical depth is zero (the Inner Region optical depth being incorporated into the lower boundary condition, “photospheric”, profile). Here, as  $\frac{1}{\beta_s}$  is very small the optical depth law breaks down to  $\tau(w) = 0$  for all but the smallest values of  $w$ .

### 7.8.5 The Inner Region profiles

As a non-Gaussian Inner Region profile was determined the terminal velocity had to be fixed before analysis could begin. Measuring the blue edge of the CIV profile lead to an edge velocity of  $750 \text{ km s}^{-1}$ . Using the relationship between edge velocity and terminal velocity given in Groenewegen & Lamers (1989) and borne out by previous modelling experience (*i.e.*  $v_\infty = 0.68 v_{\text{edge}}$ ), a terminal velocity of  $570 \text{ km s}^{-1}$  was fixed for  $v \text{ Sgr}$ . As the Outer Region was to be modelled with the  $\beta$ -independent optical depth law this formulation was also used in the modelling of the Inner Region profiles.

For each of the 4 doublet lines being modelled the Inner Region profile is calculated.

The results are shown as “photospheric” profiles in the final results. The results are tabulated and the profiles drawn in Figures 7.7 and 7.8.

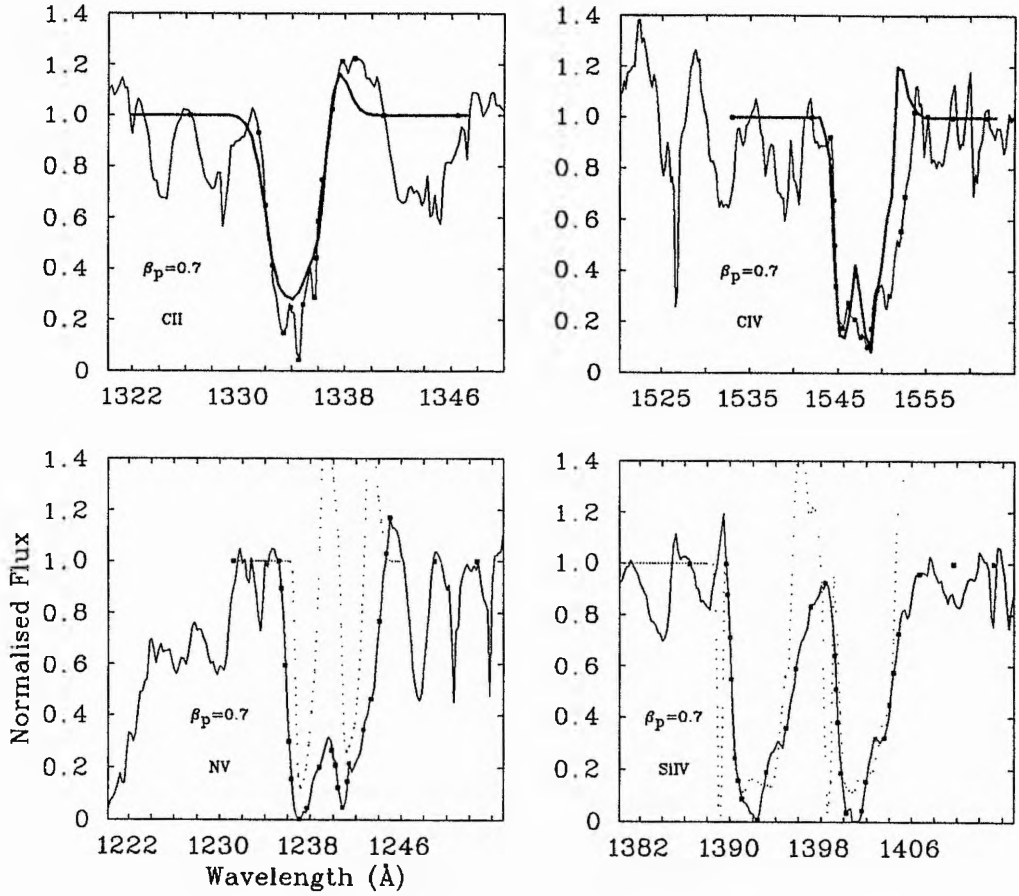
### 7.8.6 The final profiles

The final profiles are determined by inputting the results from the Inner Region profiles (that includes the B star true photospheric lines) into SEILS2 to determine the theoretical wind line profiles.

The variable velocity approximation gave the poorer results. Convergence was not possible for some lines, especially for the lower values of  $\beta_p$ . For the four values of  $\beta_p$  the results were quite similar. C II was in general fitted well and CIV adequately. However Si IV and NV showed a number of problems with the depth of the absorption trough, spurious emission peaks or poor fits to the redward edge.

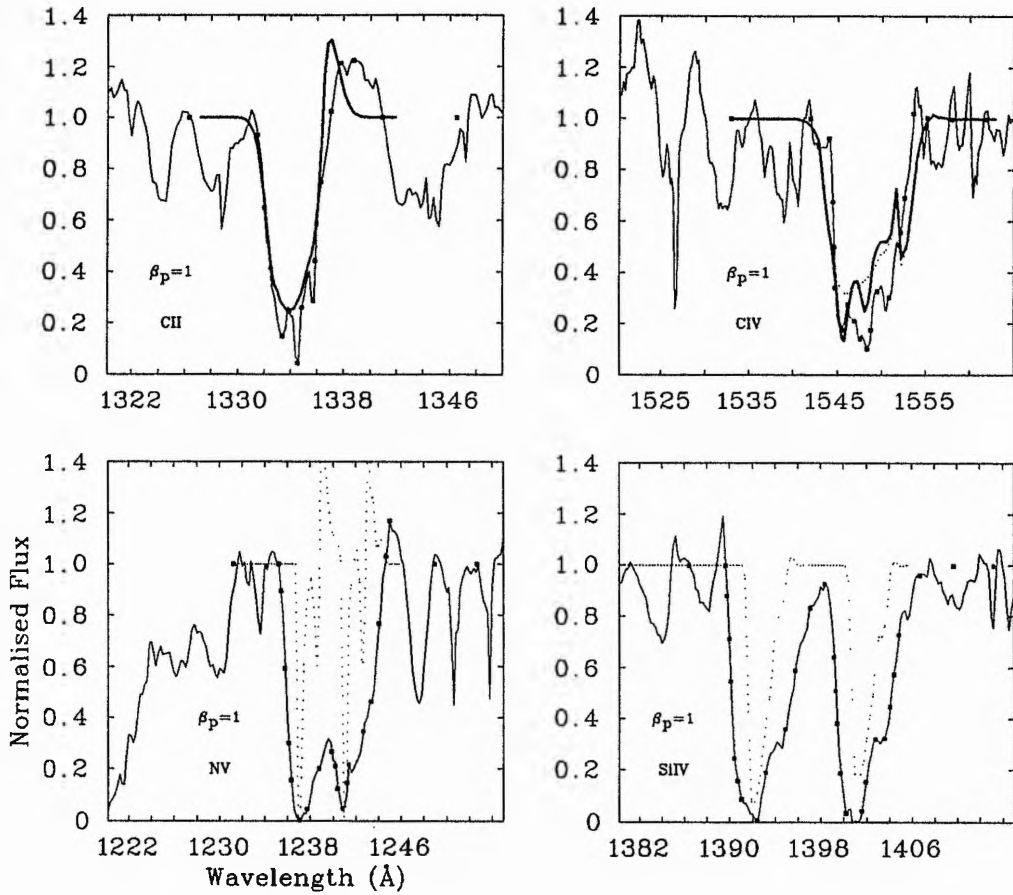
The constant velocity approximation profiles were much better with no convergence problems. There were no problems with spurious emission peaks and the fits to the redward edge and the depth of the absorption trough.

Of the four values of  $\beta_p$  used the results are all quite similar for the constant velocity approximation. NV gives almost exactly similar profiles for all values of  $\beta_p$ ; CII seems to favour lower values of  $\beta_p$  while the best fit for SiIV is obtained with  $\beta_p = 4.0$ . CIV profiles are also marginally better with a higher value of  $\beta_p$ .



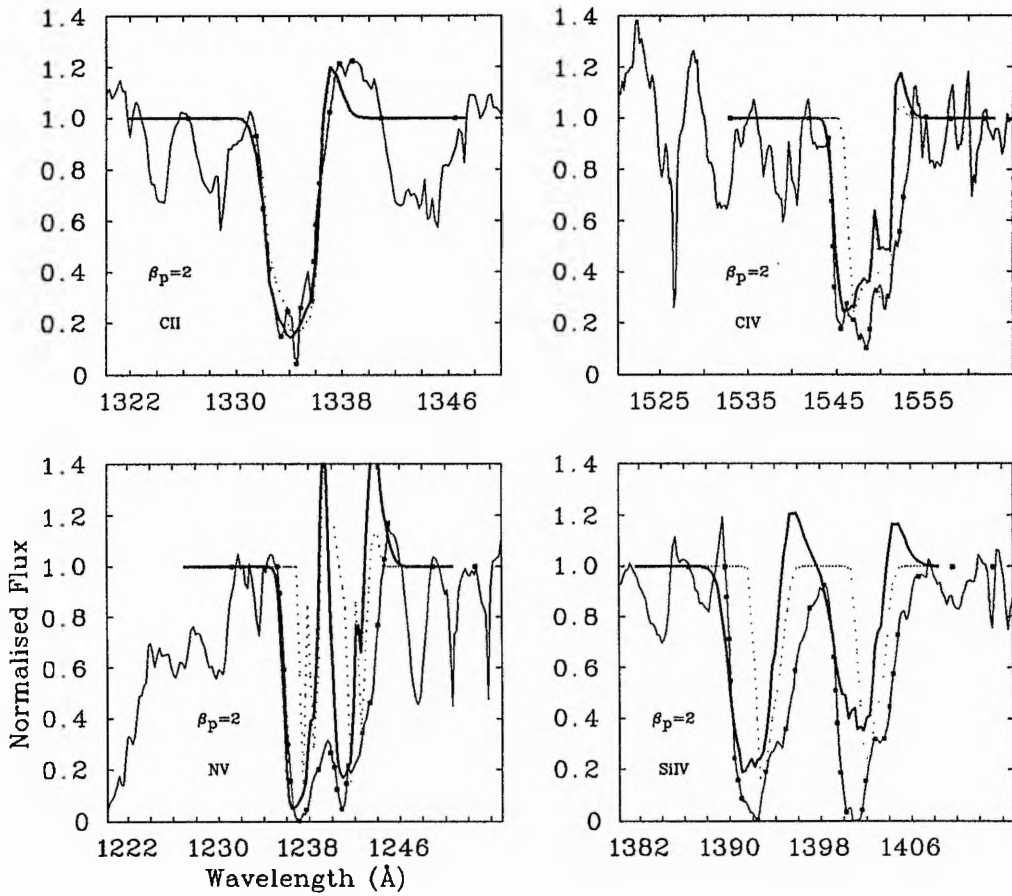
Line	Photospheric		"Inner Region"				Full Profile			
	$A_{phot_B}$	$w_{phot}$	$w_g$	$\alpha_1$	$\alpha_2$	$T_B$	$w_g$	$\alpha_1$	$\alpha_2$	$T_B$
CII	1.85	0.20	0.57	-0.27	0.13	2.06	0.16	-2.57	0.95	5.36
CIV	1.54	0.20	0.26	-2.50	-1.47	1.33	0.16	-0.15	0.33	7.05
NV	0.00	0.00	0.11	-0.96	-0.12	6.31	Non-convergent			
SiIV	1.78	0.35	0.62	-1.37	-1.02	0.55	Non-convergent			
Inner/Outer Region Boundary = 0.82, $\beta_s = 15$ , $\beta_p = 0.7$ , $v_\infty = 570 \text{ km s}^{-1}$										

Figure 7.7: Final profiles for  $\nu$  Sgr using the variable velocity approximation. The spectra and data point selection are drawn along with the "Inner Region" profile (dotted line) and the final, full, profile (heavy line). If only a dotted line is shown then no final convergent solution was possible. If only a heavy line is shown then the "Inner Region" profile is identical. Fit parameters are given in the table at the bottom.



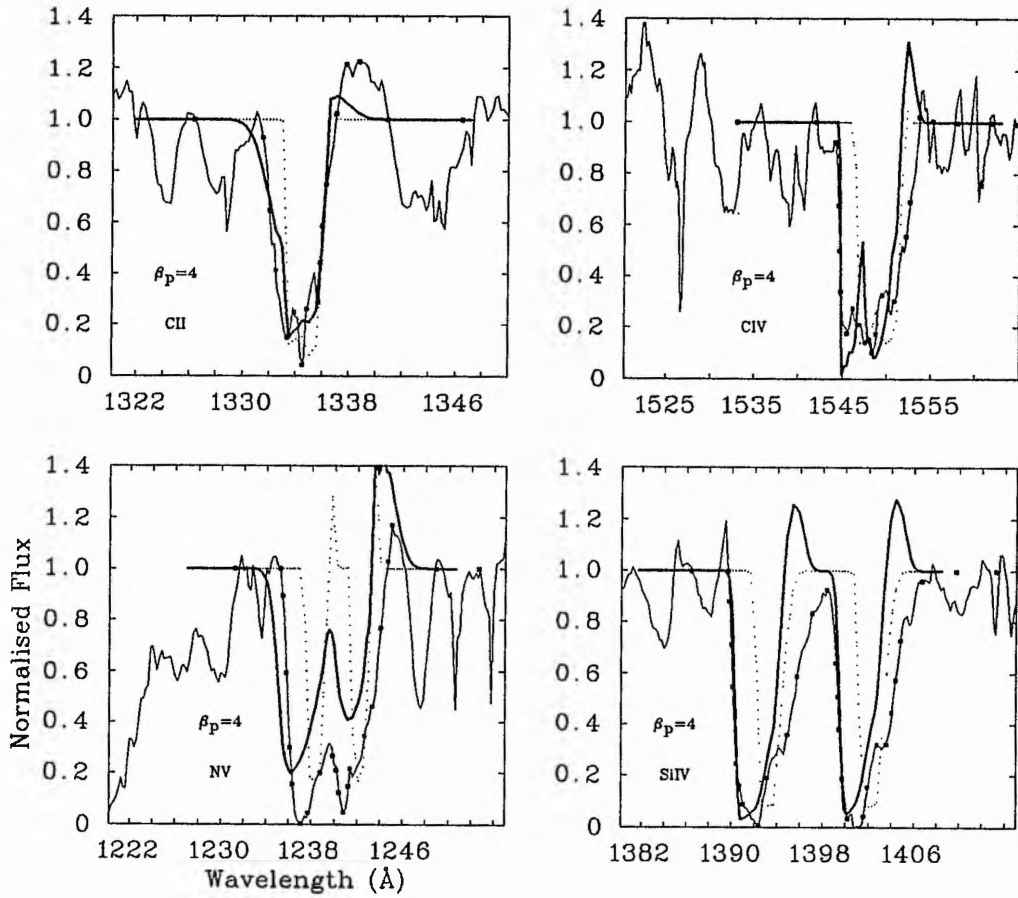
Line	Photospheric		"Inner Region"				Full Profile			
	$A_{photB}$	$w_{phot}$	$w_g$	$\alpha_1$	$\alpha_2$	$T_B$	$w_g$	$\alpha_1$	$\alpha_2$	$T_B$
CII	1.85	0.20	0.43	0.46	0.10	1.68	0.16	-2.69	0.93	1.24
CIV	1.54	0.20	0.84	-0.84	0.74	68.1	0.16	-0.15	0.33	7.07
NV	0.00	0.00	0.04	-3.31	-1.92	0.43	Non-convergent			
SiIV	1.78	0.35	0.01	1.23	1.07	5.32	Non-convergent			
Inner/Outer Region Boundary = 0.75, $\beta_s = 25$ , $\beta_p = 1.0$ , $v_\infty = 570 \text{ km s}^{-1}$										

Figure 7.7: continued.



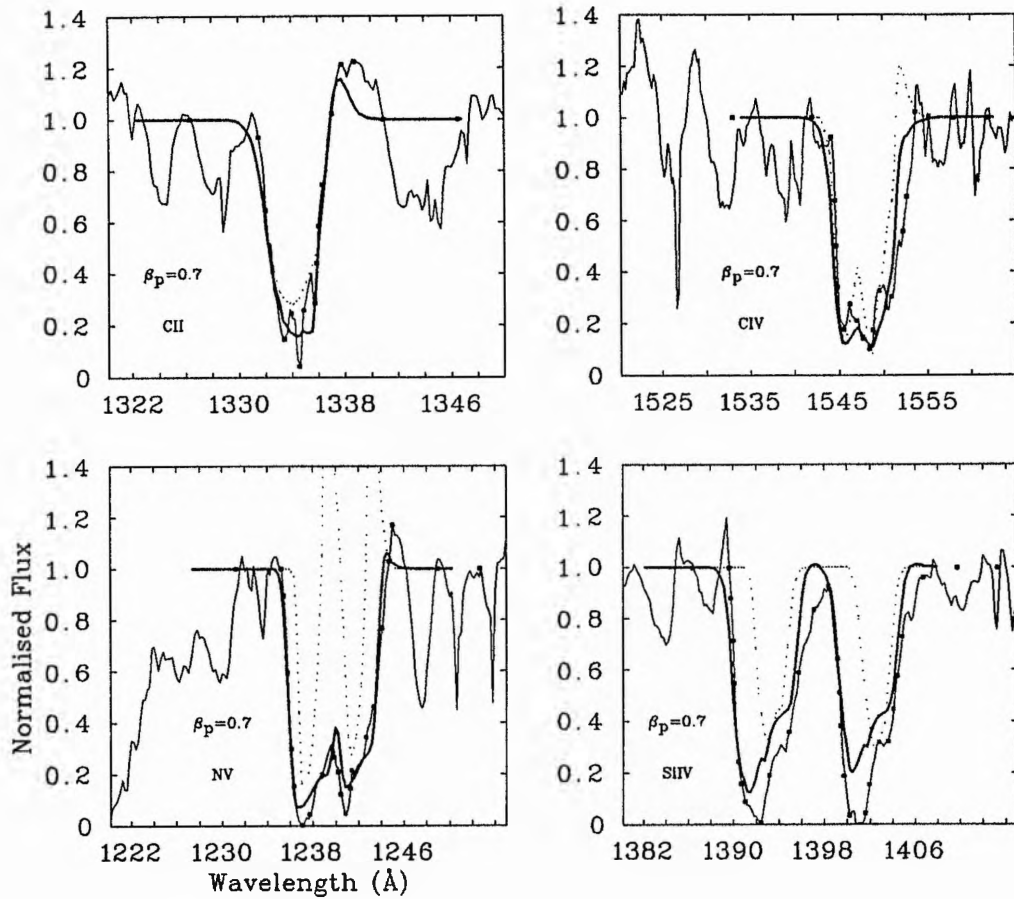
Line	Photospheric		"Inner Region"				Full Profile			
	$A_{photB}$	$w_{phot}$	$w_g$	$\alpha_1$	$\alpha_2$	$T_B$	$w_g$	$\alpha_1$	$\alpha_2$	$T_B$
CII	1.85	0.20	0.48	2.73	0.10	1.46	0.33	-0.50	0.68	14.75
CIV	1.54	0.20	0.21	-2.69	-0.88	2.73	0.35	-0.42	-0.01	4.01
NV	0.00	0.00	0.06	-5.67	-2.38	27.6	0.33	-1.03	-0.22	15.2
SiIV	1.78	0.35	0.06	0.05	0.27	3.88	0.55	-0.83	-0.18	7.02
Inner/Outer Region Boundary = 0.57, $\beta_s = 40$ , $\beta_p = 2.0$ , $v_\infty = 570 \text{ km s}^{-1}$										

Figure 7.7: *continued.*



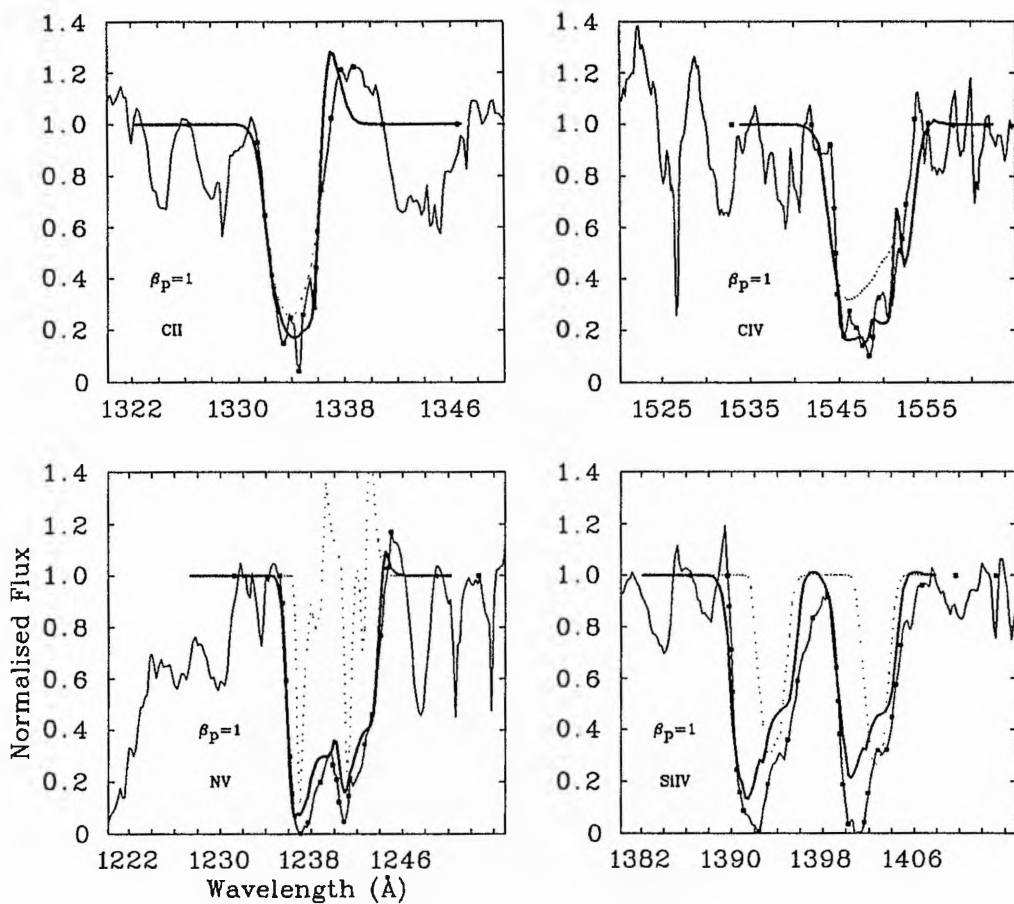
Line	Photospheric		"Inner Region"				Full Profile			
	$A_{photB}$	$w_{phot}$	$w_g$	$\alpha_1$	$\alpha_2$	$T_B$	$w_g$	$\alpha_1$	$\alpha_2$	$T_B$
CII	1.85	0.20	0.11	4.83	0.11	5.61	0.62	0.39	0.31	2.39
CIV	1.54	0.20	0.46	-0.26	-0.14	11.7	0.11	-1.23	-1.56	1.05
NV	0.00	0.00	0.15	-2.39	-1.08	0.52	0.60	-1.88	-0.71	10.30
SiIV	1.78	0.35	0.14	0.15	-0.61	2.82	0.26	-1.06	-0.42	13.1
Inner/Outer Region Boundary = 0.32, $\beta_s = 80$ , $\beta_p = 4.0$ , $v_\infty = 570 \text{ km s}^{-1}$										

Figure 7.7: *continued.*



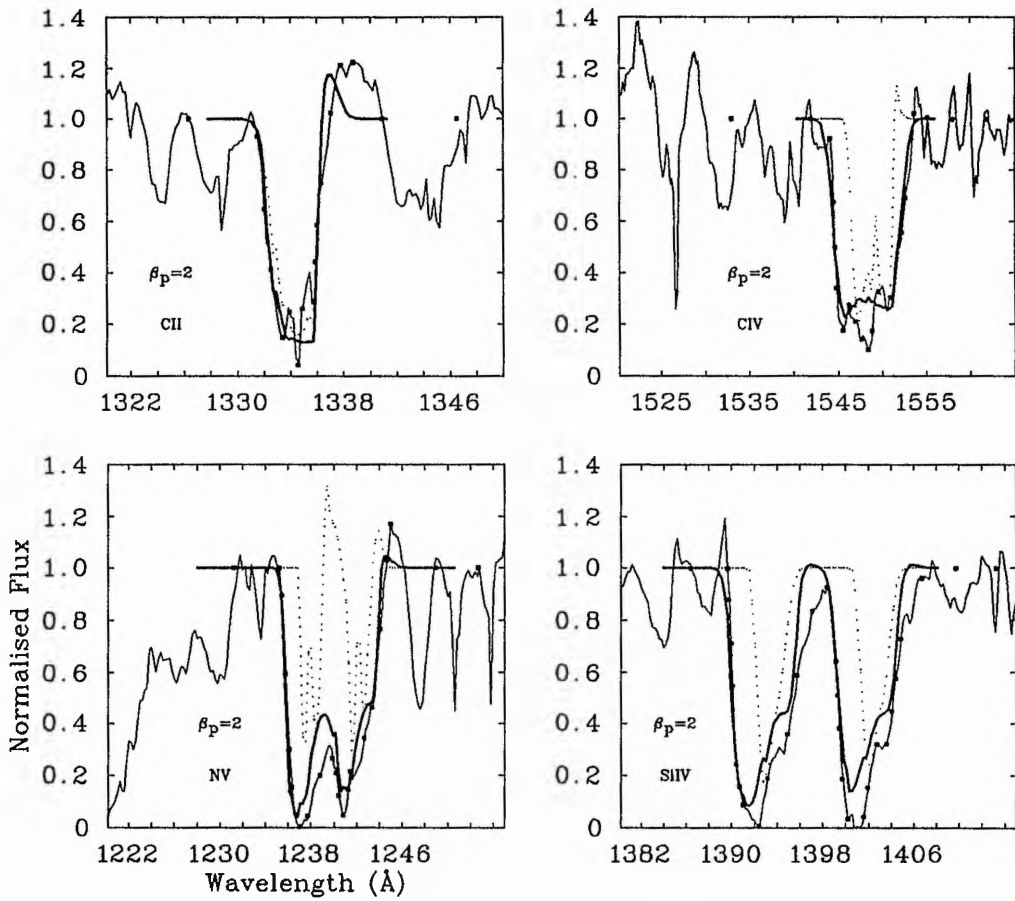
Line	Photospheric		"Inner Region"				Full Profile	
	$A_{photB}$	$w_{phot}$	$w_g$	$\alpha_1$	$\alpha_2$	$T_B$	$w_g$	$T_B$
CII	1.85	0.20	0.57	-0.27	0.05	0.10	0.05	0.56
CIV	1.54	0.20	0.26	-2.50	-1.47	1.33	0.81	1.58
NV	0.00	0.00	0.11	-0.96	-0.12	6.31	0.36	22.71
SiIV	1.78	0.35	0.62	-1.37	-1.03	0.55	0.49	23.34
I/O Region Boundary = 0.82, $\beta_s = 15$ , $\beta_p = 0.7$ , $v_\infty = 550 \text{ km s}^{-1}$								

Figure 7.8: Final profiles for  $v$  Sgr using the constant velocity approximation. The spectra and data point selection are drawn along with the "Inner Region" profile (dotted line) and the final, full, profile (heavy line). If only a dotted line is shown then no final convergent solution was possible. If only a heavy line is shown then the "Inner Region" profile is identical. Fit parameters are given in the table at the bottom.



Line	Photospheric		"Inner Region"				Full Profile	
	$A_{photB}$	$w_{phot}$	$w_g$	$\alpha_1$	$\alpha_2$	$T_B$	$w_g$	$T_B$
CII	1.85	0.20	0.43	0.46	0.10	1.68	0.11	0.37
CIV	1.54	0.20	0.84	-0.84	0.74	68.1	0.12	6.49
NV	0.00	0.00	0.04	-3.31	-1.92	0.43	0.34	32.62
SiIV	1.78	0.35	0.01	1.23	1.07	5.32	0.49	23.98
I/R Boundary = 0.75, $\beta_s = 25$ , $\beta_p = 1.0$ , $v_\infty = 550 \text{ km s}^{-1}$								

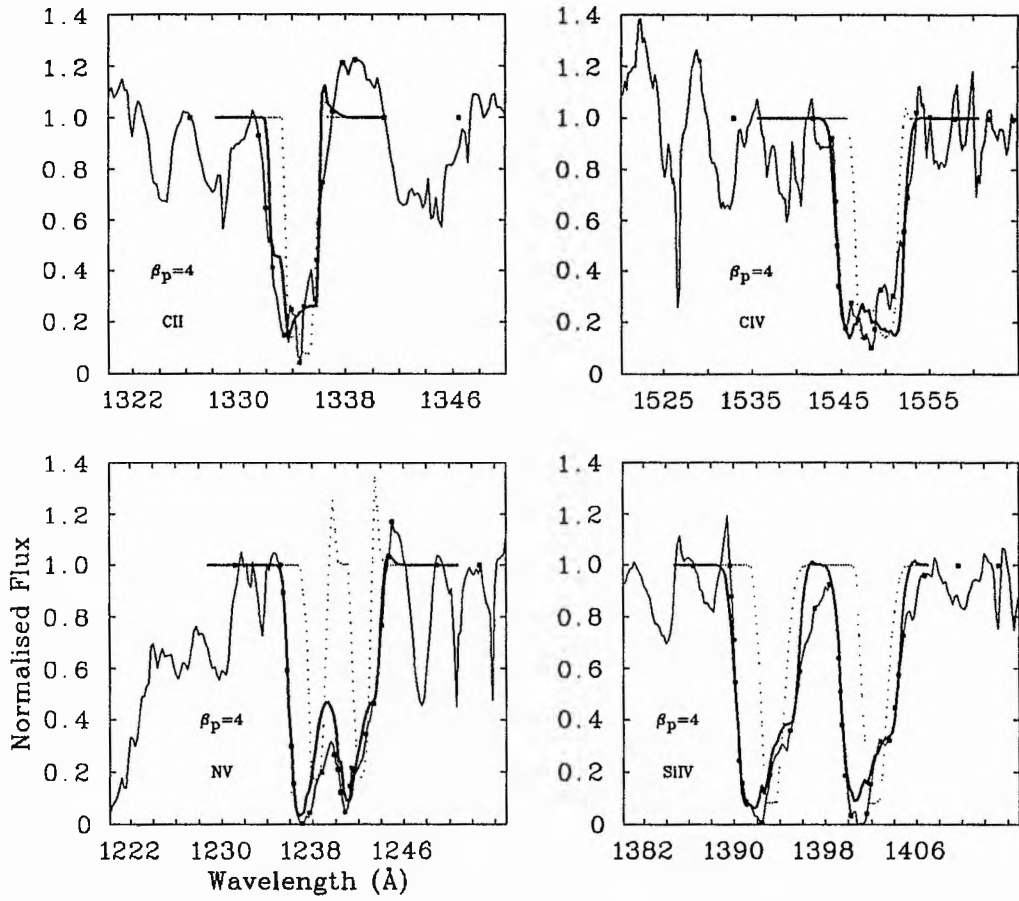
Figure 7.8: *continued.*



Line	Photospheric		"Inner Region"				Full Profile	
	$A_{photB}$	$w_{phot}$	$w_g$	$\alpha_1$	$\alpha_2$	$T_B$	$w_g$	$T_B$
CII	1.85	0.20	0.48	2.73	0.10	1.46	0.01	2.46
CIV	1.54	0.20	0.21	-2.69	-0.88	2.73	0.51	10.77
NV	0.00	0.00	0.06	-5.67	-2.38	27.6	0.34	59.29
SiIV	1.78	0.35	0.06	0.05	0.27	3.88	0.50	17.29

I/O Region Boundary = 0.57,  $\beta_e = 40$ ,  $\beta_p = 2.0$ ,  $v_\infty = 520 \text{ km s}^{-1}$

Figure 7.8: *continued.*



Line	Photospheric		"Inner Region"				Full Profile	
	$A_{photB}$	$w_{phot}$	$w_g$	$\alpha_1$	$\alpha_2$	$T_B$	$w_g$	$T_B$
CII	1.85	0.20	0.11	4.83	0.11	5.61	0.06	8.12
CIV	1.54	0.20	0.46	-0.26	-0.14	11.7	0.48	21.93
NV	0.00	0.00	0.15	-2.39	-1.08	0.52	0.37	78.36
SiIV	1.78	0.35	0.14	0.15	-0.61	2.82	0.51	54.53
I/O Region Boundary = 0.32, $\beta_s = 80$ , $\beta_p = 4.0$ , $v_\infty = 480 \text{ km s}^{-1}$								

Figure 7.8: continued.

## 7.9 The Modified Optical Depth Law Models

For these models  $\beta$  was allowed to vary freely to determine the validity of the  $\beta = 0$  results of the single star approximations. A set of profiles was also run with  $\beta = 1$  to test if this gave similar quality results. The  $\beta$ -independent optical depth law was used for all the models.

Limits of  $\pm 10$  were placed on each of the variables  $\alpha_1$ ,  $\alpha_2$ ,  $\alpha_3$  and  $\alpha_4$  to avoid computational problems when an unimportant parameter took on an unrealistically low or high value.

As with the O and EHe stars only the final parameters and profiles are given here to save space. The initial parameters and profiles are given in Appendix F (Table F.5 and Figure F.5).

### 7.9.1 Primary Model

Assuming that the primary both powers and drives the wind then the I/O Region boundary is at  $x = 4$  where  $x$ , the radial distance coordinate, is measured in units of the primary star radius, *i.e.*  $60 R_{\odot}$ . The final results are given in Table 7.6 and Figure 7.9 along with the results from the secondary model.

### 7.9.2 Secondary Model

Here the secondary star was assumed to power and drive the wind; then the I/O region boundary is at ( $x = 80$ ). The final results are given in Table 7.6 and Figure 7.9.

## 7.10 Discussion

For the variable velocity law approximation the profiles for the models are all very poor for all values of  $\beta_p$  with convergence not always being achieved. For the constant velocity models, the profiles are better but the observed line depths are not matched in the lower  $\beta_p$  models; the fits are adequate in the  $\beta_p = 4$  model.

With the variable optical depth approximation the final profiles with the primary model and  $\beta$  fixed are very poor while with a free  $\beta$  the results are substantially better with good fits in all cases except to the redward edge of the absorption profiles. Both sets of results for the secondary model are very good with the  $\beta = 1$  (fixed) model giving the best results.

From the shapes of the profiles alone it appears that the model with the secondary generating

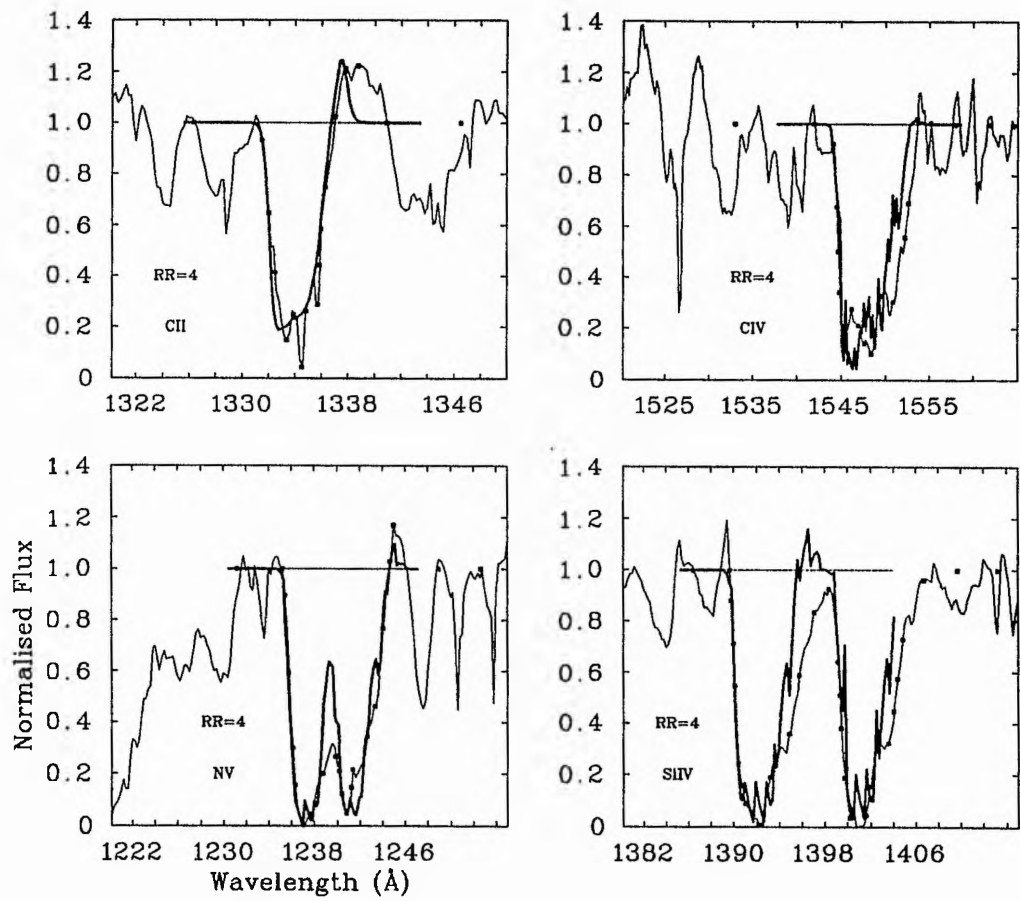


Figure 7.9: Final wind line profiles for  $\nu$  Sgr modelled as a binary star with the modified optical depth law. The heavy lines are the final profiles, the dotted lines the photospheric profiles. This page: Primary approximation ( $x = 4$ ) with  $\beta$  free.

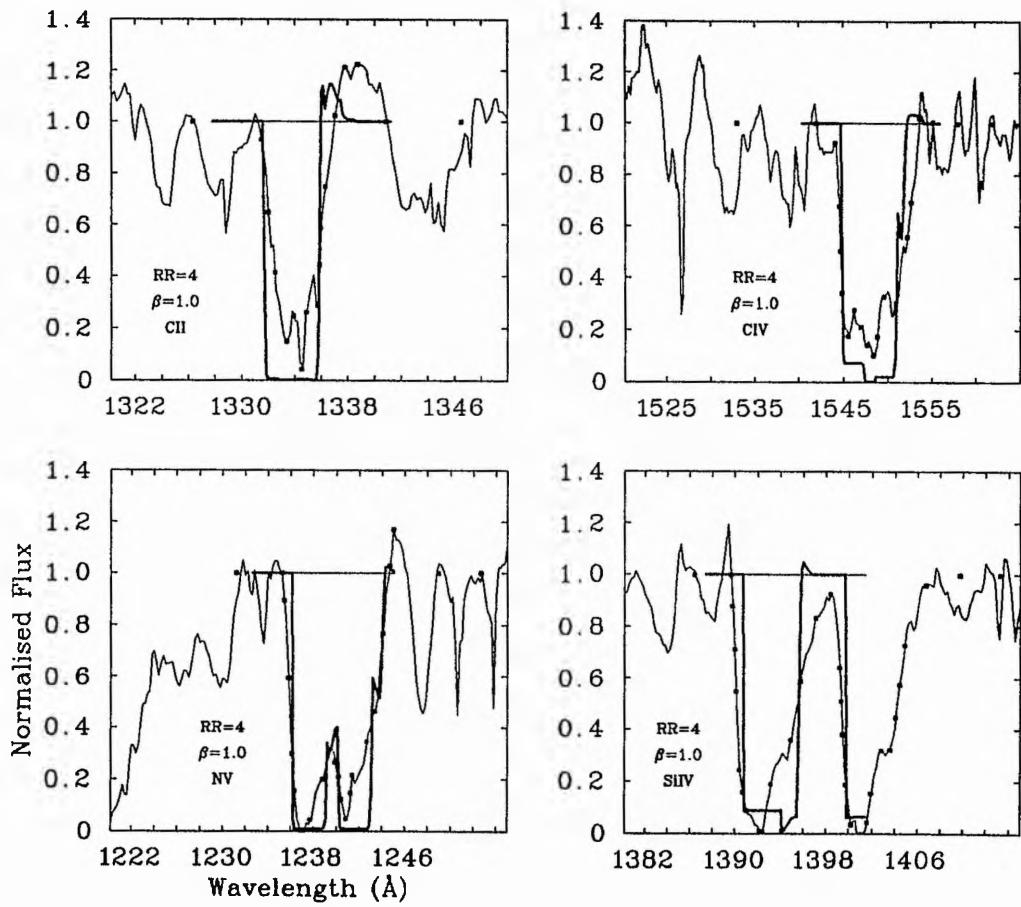


Figure 7.9: *continued*. Primary approximation ( $x = 4$ ) with  $\beta = 1$ .

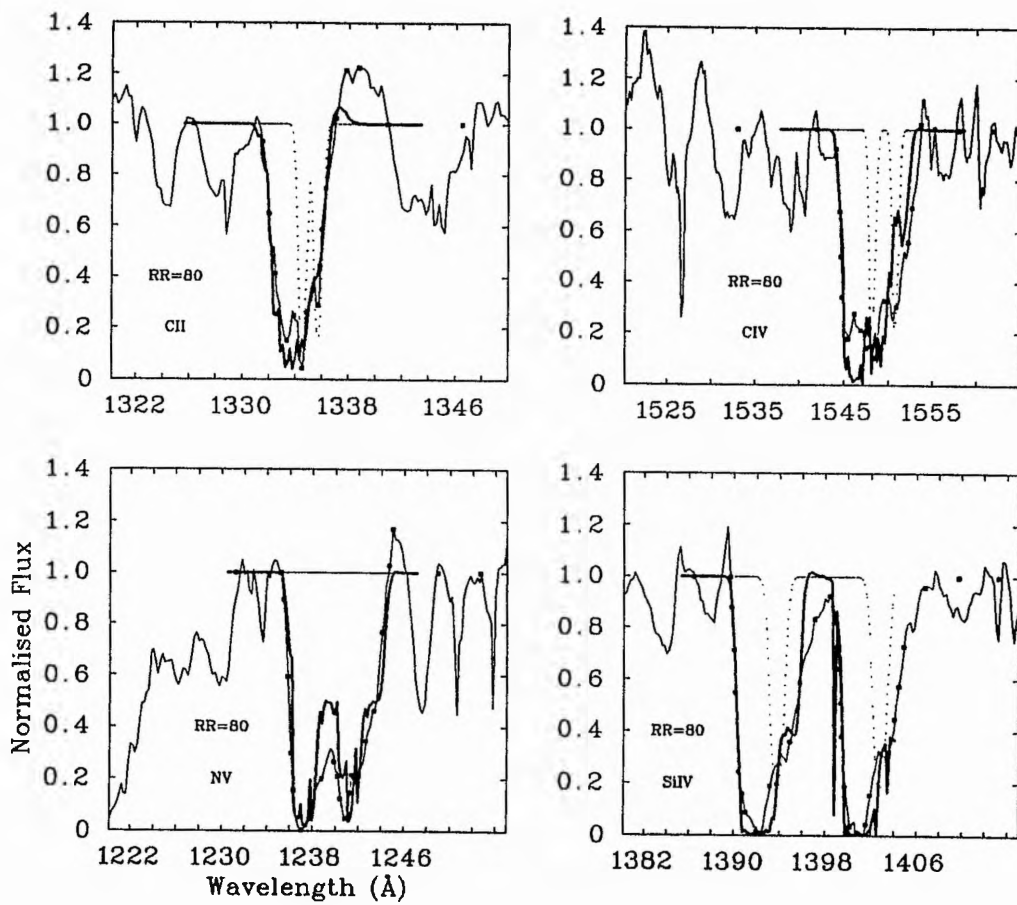


Figure 7.9: *continued*. Secondary approximation ( $x = 80$ ) with  $\beta$  free.

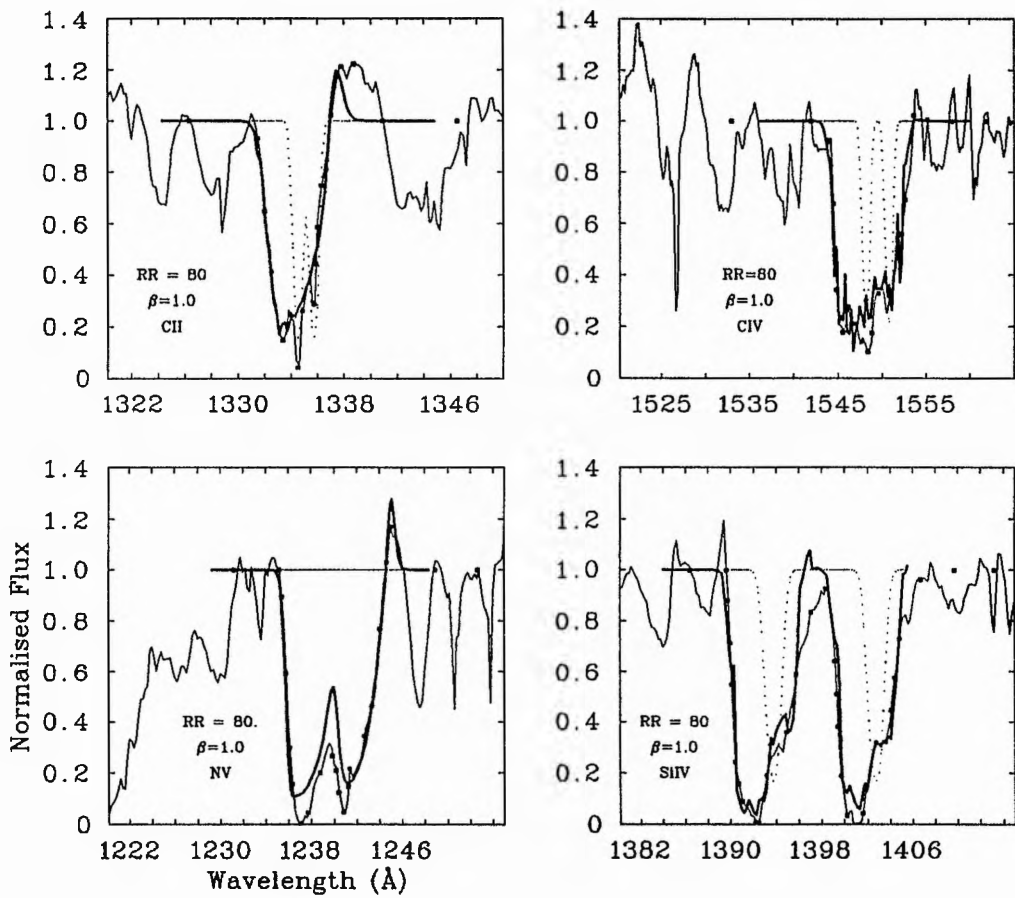


Figure 7.9: *continued.* Secondary approximation ( $x = 80$ ) with  $\beta = 1$ .

Table 7.6: Final fits for  $\nu$  Sgr using the modified optical depth law approximation with  $\beta$  both free and fixed at 1.0. The  $\beta$ -dependent optical depth law was used and results are shown for both the primary ( $x = 4$ ) and the secondary ( $x = 80$ ) models. Errors are in small type.

Model	Ion	$\beta$	$v_\infty$	$w_g$	$\alpha_1$	$\alpha_2$	$\alpha_3$	$\alpha_4$	$T_B$	
Primary ( $x = 4$ ) $\beta$ free	C II	0.4	400	0.50	0.1	1.7	10.0	10.0	20.2	
		0.3	200	0.10	1.8	2.9	9.0	9.0	34	
	C IV	0.4	400	0.50	-0.5	10.0	10.0	-0.5	4.4	
		1.0	200	0.10	0.8	9.0	9.0	0.8	4.7	
	N V	0.4	400	0.50	-2.9	-9.2	-10.0	-1.9	6.4	
		0.05	50	0.10	0.5	1.5	9.0	0.5	3.2	
	Si IV	0.4	400	0.50	-6.0	-10.0	-10.0	-4.3	0.8	
		0.3	100	0.05	0.7	9.0	9.0	0.5	0.3	
	Primary ( $x = 4$ ) $\beta = 1$	C II	1.0	300	0.40	-1.0	6.2	2.5	-2.0	5.1
			100	0.50	0.5	44	4.0	0.5	0.9	
C IV		1.0	300	0.40	-5.0	-10.0	10.0	-4.2	4.1	
		100	0.10	0.9	9.0	9.0	0.5	3.6		
N V		1.0	300	0.40	-2.8	2.3	10.0	-2.2	184	
		200	0.20	1.3	94.0	9.0	0.8	221		
Si IV		1.0	300	0.40	-7.6	-10.0	-10.0	-6.0	34.0	
		100	0.10	5.0	9.0	9.0	0.5	62.6		
Secondary ( $x = 80$ ) $\beta$ free		C II	0.1	400	0.5	0.4	-0.1	10.0	-0.3	3.0
			0.3	50	0.30	2.1	3.0	9.0	1.5	10.5
	C IV	0.1	400	0.5	-0.6	-1.5	3.4	-0.6	4.9	
		0.1	50	0.3	0.5	0.5	1904	0.5	0.6	
	N V	0.1	400	0.5	-2.2	-3.5	-10.0	-1.4	1.8	
		0.05	50	0.05	1.1	0.5	9.0	0.6	2.7	
	Si IV	0.1	400	0.5	-1.6	-4.1	-10.0	-1.1	17.0	
		0.05	50	0.05	0.5	0.8	9.0	0.5	6.6	
	Secondary ( $x = 80$ ) $\beta = 1$	C II	1.0	460	0.5	0.4	1.5	-10.0	0.3	3.9
			100	0.3	5.8	9.1	9.0	6.4	14.2	
C IV		1.0	460	0.5	-2.2	-2.3	-10.0	-1.4	2.1	
		50	0.1	1.4	1.5	9.0	0.8	1.9		
N V		1.0	460	0.5	0.3	3.5	-10.0	10.0	316	
		50	0.2	4.9	11.6	-9.0	9.0	104		
Si IV		1.0	460	0.5	-1.2	0.7	10.0	-0.6	12.2	
		200	0.2	0.6	3.1	9.0	0.5	11.1		

and powering the wind with a modified optical depth law is the most appropriate. However there will no doubt also be a contribution from the primary.

## 7.11 Mass Loss

### 7.11.1 Wind line analysis

For the modified velocity law models the MLR were determined at  $w = 0.5, 0.5, 0.4$  and  $0.2$  for  $\beta_p = 0.7, 1.0, 2.0$  and  $4.0$  respectively. This allows the mass loss determination to be made in the middle of velocity space for the Inner Region for the value of  $\beta_p$  under consideration. The results

for each individual line for each value of  $\beta_p$  in the form of MLR times ionisation fraction are given in Table 7.7; the bottom line gives the final values.

In Table 7.8 are the MLR for the modified optical depth law approximation. The MLR were determined at  $w = 0.5$  which for all 4 models lies well within the Inner Region (*i.e.* covered by  $\alpha_1$  and  $\alpha_2$  in the optical depth law).

When determining these final values the results from the CIV, NV and SiIV doublets are given equal weight, not as in the O star analysis in Chapter 5. This is because all three of these observed profiles show good unblended profiles with very good signal to noise due to the number of co-added spectra. Additionally the theoretical fits to the observed profiles are excellent for all lines and the CIV profile, although deep, is not saturated and so is as good an indicator of mass loss as the SiIV line in this case. It is possible that the different minimum MLR for the different ions are correct and reflect the (unknown) differences in the ionisation fractions. However mean values for the MLR from the doublet lines are quoted as the final adopted values as the spread of results is more likely to be explained by the quality of the fits, the validity of the Sobolev approximation in this case and errors introduced by data point, continuum and photospheric line selection.

From the modified velocity law approximation the product of MLR and ionisation fraction for  $\nu$  Sgr lies between -8.5 and -10.2 depending on the value of  $\beta_p$  adopted although  $\beta_p = 0.7$  seems unlikely from the shape of the profiles.

For the variable optical depth law approximation the MLR is between -9.4 and -12.4. The  $\beta = 1$  results for the secondary are better than the free  $\beta$  ones but the  $\beta = 1$  primary profiles are very poor. The product of MLR and ionisation fraction of between -9.4 and -10.3 is indicated irrespective of whether the primary or secondary is modelled.

Both sets of results are consistent and a final minimum MLR for  $\nu$  Sgr is  $-9.6 \pm 0.8$  determined from both methods. SEI appears to be a code whereby good profiles can be generated with a number of different assumptions all of which give rise to similar MLR. The agreement on the numerical results is encouraging although it is difficult to choose between the different assumptions being modelled.

### 7.11.2 Other methods

As indicated in Section 5.6 there are a number of ways of determining mass loss rates without using wind line analysis. These methods include H $\alpha$  equivalent width measurements, IR fluxes and radio observations and give direct MLR without the need for ionisation fractions although other poorly known quantities (*e.g.* distance or luminosity) are often required. These methods can be applied to  $\nu$  Sgr to give extra weight to the MLR determined from the wind line analysis.

Table 7.7: The product of mass-loss rate and ionisation fraction (and excitation fraction in the case of CII) for  $\nu$  Sgr from the Inner Region profiles, in  $\log M_{\odot} \text{ yr}^{-1}$  using the variable velocity law approximation. Errors are determined from the variation of optical depth with velocity with the central values are determined at  $w = 0.5, 0.5, 0.4$  and  $0.2$  for  $\beta_p = 0.7, 1.0, 2.0$  and  $4.0$  respectively. The bottom row gives the final values of the product of MLR and ionisation fraction determined from the mean of the doublet profiles.

Line	$\beta_p$			
	0.7	1.0	2.0	4.0
CII	-9.5 $\pm 0.5$	-8.0 $\pm 0.8$	-8.6 $\begin{smallmatrix} +0.5 \\ -1.0 \end{smallmatrix}$	-10.5 $\pm 2.0$
CIV	-10.7 $\begin{smallmatrix} +0.5 \\ -0.1 \end{smallmatrix}$	-7.3 $\begin{smallmatrix} +0.1 \\ -0.5 \end{smallmatrix}$	-10.5 $\pm 0.2$	-8.1 $\pm 0.5$
NV	-8.0 $\pm 0.5$	-11.7 $\begin{smallmatrix} +0.7 \\ -0.1 \end{smallmatrix}$	-13.4 $\pm 0.5$	-10.0 $\pm 0.2$
SiIV	-8.6 $\pm 0.5$	-6.6 $\begin{smallmatrix} +0.2 \\ -1.0 \end{smallmatrix}$	-6.7 $\pm 0.5$	-7.8 $\pm 1.0$
Final	-9.1 $\pm 0.5$	-8.5 $\begin{smallmatrix} +0.2 \\ -1.0 \end{smallmatrix}$	-10.2 $\pm 0.5$	-8.6 $\pm 1.0$

Table 7.8: Minimum mass-loss rates for  $\nu$  Sgr from the variable optical depth law approximation. P stands for Primary and S for secondary. A non-convergent solution is indicated by a \*.

Model	CII	CIV	NV	SiIV	Mean
P, $\beta$ free	-8.3 $\begin{smallmatrix} +0.3 \\ -0.5 \end{smallmatrix}$	-10.2 $\begin{smallmatrix} +1.2 \\ -3.1 \end{smallmatrix}$	-10.8 $\begin{smallmatrix} +1.9 \\ -0.0 \end{smallmatrix}$	-16.8 $\begin{smallmatrix} +1.9 \\ -0.0 \end{smallmatrix}$ *	-9.8 $\pm 1.0$
P, $\beta = 1$	-12.7 $\begin{smallmatrix} +3.9 \\ -0.0 \end{smallmatrix}$	-13.3 $\begin{smallmatrix} +0.0 \\ -2.3 \end{smallmatrix}$	-10.7 $\begin{smallmatrix} +1.2 \\ -0.0 \end{smallmatrix}$	-16.0 $\begin{smallmatrix} +0.5 \\ -0.0 \end{smallmatrix}$ *	-12.4 $\pm 1.5$
S, $\beta$ free	-8.8 $\begin{smallmatrix} +2.9 \\ -1.5 \end{smallmatrix}$	-9.3 $\begin{smallmatrix} +3.2 \\ -1.7 \end{smallmatrix}$	-10.4 $\begin{smallmatrix} +4.0 \\ -2.0 \end{smallmatrix}$	-9.0 $\begin{smallmatrix} +3.7 \\ -1.8 \end{smallmatrix}$	-9.4 $\pm 0.7$
S, $\beta = 1$	-10.2 $\begin{smallmatrix} +0.3 \\ -0.0 \end{smallmatrix}$	-12.5 $\begin{smallmatrix} +0.7 \\ -0.0 \end{smallmatrix}$	-8.1 $\begin{smallmatrix} +1.2 \\ -0.2 \end{smallmatrix}$	-10.2 $\begin{smallmatrix} +0.2 \\ -0.3 \end{smallmatrix}$	-10.3 $\pm 2.0$

IR excess measurements can yield MLR by assuming that the IR emission comes from free-free transitions in the outer wind, where the velocity is constant. Barlow & Cohen (1977) quote the formula of Wright & Barlow (1975) as a means of determining MLR. Although this formula may give results that are a factor of 5 too high in the case of some early O stars (Barlow & Cohen 1977) it should give better results for later type stars and will give an indication of whether the MLR for  $\nu$  Sgr determined earlier is supported by IR measurements. Barlow & Cohen refined the procedure by using model atmospheres to fit the MLR to the observed IR flux using the velocity law they determined for P Cygni. Such a complex procedure is not justified in this case.

IRAS measurements of IR fluxes in 4 wavelength bands for  $\nu$  Sgr are obtainable from the IRAS point source catalogue. The colour corrected fluxes are tabulated in Trams, Waters, Lamers, Waelkens, Geballe & Thé (1991) and given in Table 7.9. Interstellar extinction is negligible at these

wavelengths (see Chapter 8) so no de-reddening corrections are applied. The formula of Wright & Barlow is

$$\dot{M} = 0.095 \frac{\mu v_{\infty} S_{\nu}^{0.75} D^{1.5}}{Z \gamma^{0.5} g^{0.5} \nu^{0.5}} M_{\odot} \text{ yr}^{-1} \quad (7.2)$$

where  $\mu$  is the mean atomic weight,  $Z$  the mean atomic charge,  $\gamma$  the mean number of electrons per ion and  $g$  the Gaunt factor (*e.g.* see Kargas & Latter 1961, Howarth & Prinja 1989).  $D$  is the distance to the star in kpc and  $S_{\nu}$  the free-free flux (in Janskys) at the frequency  $\nu$  (Hz).  $v_{\infty}$  is the terminal velocity in  $\text{kms}^{-1}$ .  $550 \text{ kms}^{-1}$  was used as this is an average Outer Region velocity for the constant velocity approximation.

For  $\nu$  Sgr we have  $\mu \simeq 4$ ,  $Z \simeq 1.5$ ,  $\gamma \simeq 1.5$ ,  $g \simeq 1$  and  $D \simeq 1.4$  kpc. This latter value is from the results of the flux distribution analysis in Chapter 8. The determined MLR are given in Table 7.9.

Table 7.9: Mass-loss rates for  $\nu$  Sgr from IR data.

Wavelength ( $\mu\text{m}$ )	Frequency $\nu$ (Hz)	Flux (Jy)	$\frac{\dot{M}}{v_{\infty}}$ ( $M_{\odot} \text{ yr}^{-1} \text{ s km}^{-1}$ )	$\log \dot{M}$ ( $\log M_{\odot} \text{ yr}^{-1}$ )
12	$2.5 \times 10^{13}$	99.54	$8.1 \times 10^{-7}$	-2.9
25	$1.2 \times 10^{13}$	32.73	$5.1 \times 10^{-7}$	-3.0
60	$5.0 \times 10^{12}$	6.14	$2.3 \times 10^{-7}$	-3.4
100	$3.0 \times 10^{11}$	2.38	$4.9 \times 10^{-7}$	-3.1

The MLR from the IR data are even higher than from the UV wind line analysis. MLR of -2.9 to -3.4 dex can be ruled out as they would give rise to measurable changes in the orbital period and time of maximum velocity. The assumption that all the IR flux comes from the cooler outer parts of the wind is false as is shown by the 950K IR excess from dust (Chapter 8).

A number of authors have determined empirical relationships between MLR and luminosity (*e.g.* Barlow & Cohen 1977; Abbott, Biegging & Churchwell 1981; de Loore (1984), Garmany, Olson, Conti & Van Steenberg 1981; Garmany & Conti 1984).

The Barlow & Cohen (1977) relationship between MLR and luminosity for A and B supergiants is

$$\dot{M} = 5.0 \times 10^{-13} \left( \frac{L}{L_{\odot}} \right)^{1.20 \pm 0.08} M_{\odot} \text{ yr}^{-1} \quad (7.3)$$

From the primary flux distribution and the extinction the luminosity of  $\nu$  Sgr is determined as  $61,000^{+11,000}_{-5,000} L_{\odot}$ .

Using this luminosity the MLR is then  $(2.8^{+3.9}_{-1.7}) \times 10^{-7} M_{\odot} \text{ yr}^{-1}$  (-6.6 $^{+0.4}_{-0.2}$  dex). The uncertainty in the exponent in Equation 7.3 leads to much larger uncertainties in the MLR than the considerable uncertainty in the luminosity.

### 7.11.3 Discussion

An upper limit to the MLR can be determined from the lack of observed changes in the period and time of maximum positive velocity of the orbit. Assuming a MLR of  $10^{-5} M_{\odot} \text{ yr}^{-1}$  then over the baseline 1912-85 the orbital period would have changed by  $\sim 0.03$  days and  $T_{\text{max}}$  by about 1 day. Deviations in the orbital parameters of this magnitude cannot be ruled out from the data given in Table 2.4 (page 37), mainly due to the errors in the orbital parameters of Wilson's (1914) original orbit. These results do however determine an upper limit to the MLR. The empirical relationship for single AB supergiants gives a MLR some 300 times that of the the UV results. A mean ionisation fraction of 0.3% for CIV, SiIV and NV does not seem implausible although the primary of  $\nu$  Sgr, filling its Roche lobe and thus with a lower effective surface gravity, will possibly have a higher MLR than the single star formula predicts.

## 7.12 Summary

*v Sgr currently has a mass-loss rate of  $-5.0 \geq \log \dot{M} \geq -9.6 M_{\odot} \text{yr}^{-1}$  with the limits coming from the lack of observed changes in the orbital parameters and the UV wind line analysis.*

*After demonstrating that the wind of v Sgr system cannot be modelled by a single star (of either the spectral type of the primary or the secondary), SEILS has been used to model the winds of the v Sgr system using a simplified binary star model consisting of an Inner Region of turbulent material driven by the primary and a laminar flow in an Outer Region beyond  $240 R_{\odot}$ .*

*Four varied models were used to determine whether the primary or secondary provided the ionising radiation and whether different optical and velocity laws in the Inner and Outer Regions were justified.*

*The quality of the results was similar for all the approximations showing that the method gives results that are independent of the assumptions used. While this strengthens the determined mass-loss rates it does not allow discrimination between the various models.*

*Due to the problems of not having access to improved NLTE model atmospheres for the wind line analysis, the ionisation fractions cannot be determined with any accuracy which prevents actual limits to the mass-loss rate being determined. The products of mass loss and ionisation fraction that have been determined indicate that the v Sgr system is losing mass at a rate of at least  $2.5 \times 10^{-10} M_{\odot} \text{yr}^{-1}$  although the uncertainty in this value is in the region of an order of magnitude. Ionisation fractions have then to be taken into account.*

*Depending on the approximation used this rate of mass loss is equal to or slightly greater than the single EHe stars and comparable to the mass-loss rate from the two hydrogen-deficient sdO stars, BD +37° 442 and BD +37° 1977.*

## 7.13 References

- Abbott, D.C., Biegging, J.H. & Churchwell, E.B., 1981. *Astrophys. J.*, **250**, 645.
- Barlow, M.J. & Cohen, M., 1977. *Astrophys. J.*, **213**, 737.
- Bohlin, R.C., Savage, B.D. & Drake, J.F., 1978. *Astrophys. J.*, **224**, 131.
- Chiosi, C. & Maeder, A., 1986. *Ann. Rev. Astr. Astrophys.*, **24**, 329.
- de Loore, C., 1984. *Phys. Scr.*, **T7**, 25.
- Drew, J.E., 1986. *Mon. Not. R. astr. Soc.*, **218**, 41p.
- Drew, J.E., 1987. *Mon. Not. R. astr. Soc.*, **224**, 595.
- Drew, J.E., Hoare, M.G. & Woods, J.A., 1991. *Mon. Not. R. astr. Soc.*, **250**, 144.
- Dudley, R.E. & Jeffery, C.S., 1990. *Mon. Not. R. astr. Soc.*, **247**, 400.
- Garmany, C.D. & Conti, P.S., 1984. *Astrophys. J.*, **284**, 705.
- Garmany, C.D., Olson, G.L., Conti, P.S. & Van Steenberg, M.E., 1981. *Astrophys. J.*, **250**, 660.
- Groenewegen, M.A.T. & Lamers, H.J.G.L.M., 1989. *Astr. Astrophys. Suppl.*, **79**, 359.
- Hamann, W.-R., Schönberner, D. & Heber, U., 1982. *Astr. Astrophys.*, **116**, 273.
- Howarth, I.D. & Prinja, R.K., 1989. *Astrophys. J. Suppl.*, **69**, 527.
- Humphreys, R.M. & Ney, E.P., 1974a. *Astrophys. J.*, **187**, L75.
- Humphreys, R.M. & Ney, E.P., 1974b. *Astrophys. J.*, **190**, 339.
- Kargas, T.A. & Latter, R., 1961. *Astrophys. J. Suppl.*, **6**, 167.
- Kudritzki, R.P., 1988. In: *Radiation in Gaseous Moving Media, Eighteenth "Saas-Fee" Conference*, p.1, eds. W. Chmielewski & T. Lanz, Geneva Observatory.
- Lee, T.A. & Nariai, K., 1967. *Astrophys. J.*, **149**, L93.
- Nariai, K., 1967. *Publs astr. Soc. Japan*, **19**, 564.
- Parthasarathy, M., Cornachin, M. & Hack, M., 1986. *Astr. Astrophys.*, **166**, 237.
- Rao, N.K. & Venugopal, V.R., 1985. *J. Astrophys astr.*, **6**, 101.
- Schönberner, D., & Drilling, J.S., 1984. *Astrophys. J.*, **276**, 229.
- Seaton, M.J., 1979. *Mon. Not. R. astr. Soc.*, **187**, 75p.
- Trams, N.R., Waters, L.B.F.M., Lamers, H.J.G.L.M., Waelkens, C., Geballe, T.R. & Thé, P.S., 1991. *Astr. Astrophys. Suppl.*, **87**, 361.

Wilson, R.E., 1914. *Lick Obs. Bull.*, 8, 132.

Wright, A.E. & Barlow, M.J., 1975. *Mon. Not. R. astr. Soc.*, 170, 41.

Woolf, N.J., 1973. *Astrophys. J.*, 185, 229.

## Chapter 8

# The Flux Distribution of $\nu$ Sgr

### 8.1 Introduction

The flux distribution of  $\nu$  Sgr is a long standing problem, covered in detail by Plavec (1986). At that time neither hydrogen-rich nor hydrogen-poor models were able to match the flux distribution well, especially shortward of 2800 Å (Figure 1.2). This problem, well illustrated by  $\nu$  Sgr, is symptomatic of the failure of hydrogen-poor model atmospheres to match observed fluxes, Plavec (1986).

With the new line-blanketed version of the Kiel model atmospheres code STERNE (Möller 1990) it is now possible to do this modelling for  $\nu$  Sgr and to determine how well model atmospheres have improved since 1985. If the models are good then the effective temperature of the primary and, possibly, the secondary can be determined from the flux distribution alone without recourse to a fine analysis. Modelling of the flux distribution is the most accurate way to determine the effective temperature and also enables an independent determination of the interstellar reddening to complement those from the removal of the 2200 Å and Lyman- $\alpha$  features.

### 8.2 Photometry

$\nu$  Sgr has been observed photometrically from 1550 Å to 100  $\mu$ m. All photometric measurements and fluxes have been collected by Trams, Waters, Lamers, Waelkens, Geballe & Thé (1991) and are given in Table 8.1.

$\nu$  Sgr also has a number of observations using the low resolution mode of both the long and short wavelength cameras onboard IUE (Table 7.1). These data (unlike the high resolution spectra) has been flux calibrated and so can be used alongside the photometric data, as can the

Voyager space probe photometry from 900 to 1650 Å (observations made by Polidan, reported in Plavec 1986).

All the fluxes for  $\nu$  Sgr are shown in Figure 8.3 with the Voyager and IUE ULDA fluxes merged, with the ULDA data weighted four times that of Voyager data as the latter is of much poorer quality.

## 8.3 The Effectiveness of Hydrogen-deficient Line-blanketed Model Atmospheres

To try to solve the long standing problem of the UV flux distribution of  $\nu$  Sgr all the flux was assumed to come from the primary component so that the results could be compared directly with the hydrogen-rich and hydrogen-poor model atmospheres used by Plavec (1986) and shown in Figure 1.2. The secondary was assumed not to contribute any flux for the purposes of this analysis.

### 8.3.1 Temperature and extinction determination

The effective temperature is defined as the temperature at which a black body of the same radius as the star in question would have an equivalent bolometric luminosity. Thus for a given observed flux distribution there is a unique effective temperature associated with it.

To determine the temperature of the primary component the observed flux, de-reddened, over a given wavelength region is normalised to a model atmosphere flux over the same region. For  $\nu$  Sgr the whole observed wavelength range cannot be used due to contamination by the dust component at longer wavelengths. The short wavelength regions are the most important as the flux here is very sensitive to temperature changes. For  $\nu$  Sgr a wavelength range of 1500-16,000 Å was used.

The model atmospheres used had a composition of 99.6% He, 0.1% H and 0.14% C and 0.3% N. Although these are not the final adopted abundances (see Chapter 11) they are close enough for the purposes of flux determination.

Following Underhill (1982) a quantity  $G$  can be defined as the ratio of the total model flux to the model flux in the normalisation region ( $\lambda_1, \lambda_2$ ).

$$G = \frac{\int_0^{\infty} F_{\lambda} d\lambda}{\int_{\lambda_1}^{\lambda_2} F_{\lambda} d\lambda} \quad (8.1)$$

where  $F_\lambda$  is the model flux at wavelength  $\lambda$  and is an astrophysical flux.

To determine the radius of the star the model and observed fluxes are normalised at a single wavelength. The radius of the star at this wavelength,  $\theta_\lambda$ , is then

$$\theta_\lambda = \left[ \frac{f_\lambda}{\pi F_\lambda} \right]^{0.5} \quad (8.2)$$

where  $f_\lambda$  is the observed flux (de-reddened) at wavelength  $\lambda$ .

The effective temperature,  $T_{\text{eff}}$ , is then given by

$$\sigma T_{\text{eff}}^4 = \frac{4G}{\theta^2} \int_{\lambda_1}^{\lambda_2} f_\lambda d\lambda \quad (8.3)$$

where  $\sigma$  is the Stefan-Boltzmann constant.

For the determination of  $\theta$  and  $T_{\text{eff}}$  four wavelengths were used - 2365 (S/68 photometry), 3600, 5500 and 7000 Å (U, V and R band photometry). Six values of  $E_{B-V}$  were also evaluated, 0.05 to 0.30 in steps of 0.05.

For each model, four temperatures, one for each wavelength, were determined for each of the six values of the extinction. To determine the adopted temperature and extinction for a given theoretical model the spread in the four temperature values was taken into account for each of the six values of extinction, leading to a mean effective temperature and a standard deviation. The value of  $E_{B-V}$  that lead to the lowest spread in temperatures was adopted along with the mean temperature as the best value for that model. This procedure was repeated for all the models used, the results shown in Table 8.2. The adopted surface gravity has very little influence on the results (Figure 8.2) and so low gravity models ( $\log g = 1.3 - 1.7$  depending on the model temperature) were used for this analysis on the basis of the surface gravity determined from both the orbital analysis (Chapter 2) and the fine analysis (Chapter 11).

From the best result for each model the final temperature and extinction can be determined. To determine the extinction the criterion used is not just that the standard deviation of the temperature is smallest but that the temperature determined from normalising to the 2365 Å photometry point agrees well with the mean temperature. This is because the UV photometry is affected the most by changes in the extinction; for the correct extinction the temperature from the UV flux will agree with the others assuming that the theoretical models are correct.

From the table the 10,000K and 15,000K models can be rejected outright due to the large standard deviation in the mean temperature and the lack of agreement of the 2365 Å temperature

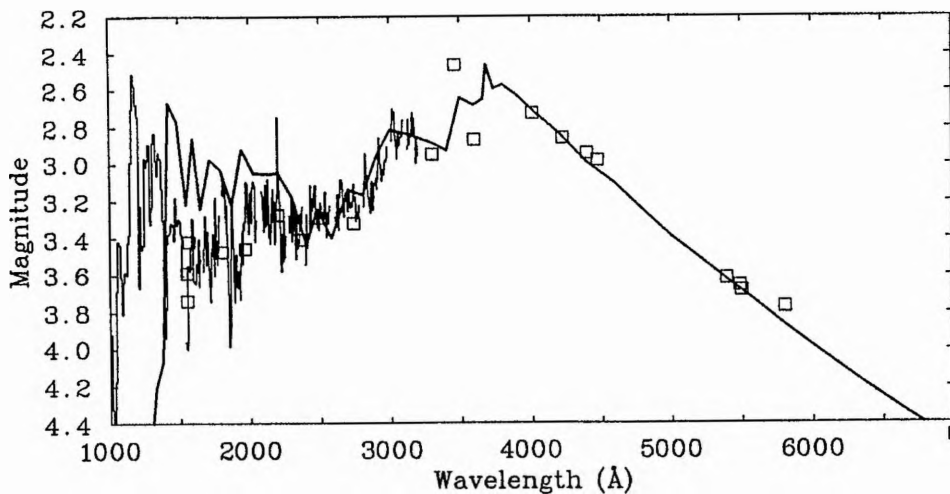


Figure 8.1: The flux distribution of the primary of  $\nu$  Sgr, 1,000-7,000 Å compared with the observed ULDA (histogram) fluxes and photometry (open squares). The heavy line is for a 11,800K hydrogen-deficient line-blanketed model atmosphere. These results should be compared to Figure 1.2, page 7. The observational data has been de-reddened by  $E_{B-V} = 0.20$ .

with the mean.

The adopted model for  $\nu$  Sgr is then the 11,800K one which has the second lowest standard deviation in the temperature but has a 2365 Å temperature that agrees extremely well with the mean. The extinction is then determined to be 0.20 but due to the good quality of the fits of the 11,500K and 12,000K models an uncertainty of  $\pm 0.05$  must be assigned. From the adopted model the uncertainty in the temperature is about 300K; accounting for the uncertainty in the extinction this rises to 500K. This is the most accurate temperature determination of the primary to date and totally independent of the fine analysis (Chapter 11). This adopted model is shown in Figure 8.1 and should be compared with the models of Plavec (1986) in Figure 1.2. An expanded version showing just the region 800 - 3000 Å is shown in Figure 8.2 with a 11,800K,  $\log g = 3.0$  model superimposed to show that the surface gravity is fairly unimportant compared to the temperature for purposes of modelling flux distributions.

### 8.3.2 Discussion

Comparing Figure 8.1 with 1.2 it is obvious that the new hydrogen-deficient line-blanketed model atmospheres are a significant improvement over the model atmospheres available to Plavec (1986). The most significant improvement is the lack of a Balmer decrement so obvious in the other models. The fit of the 11,800K model to the observed fluxes is excellent down to  $\sim 2200$  Å below which the

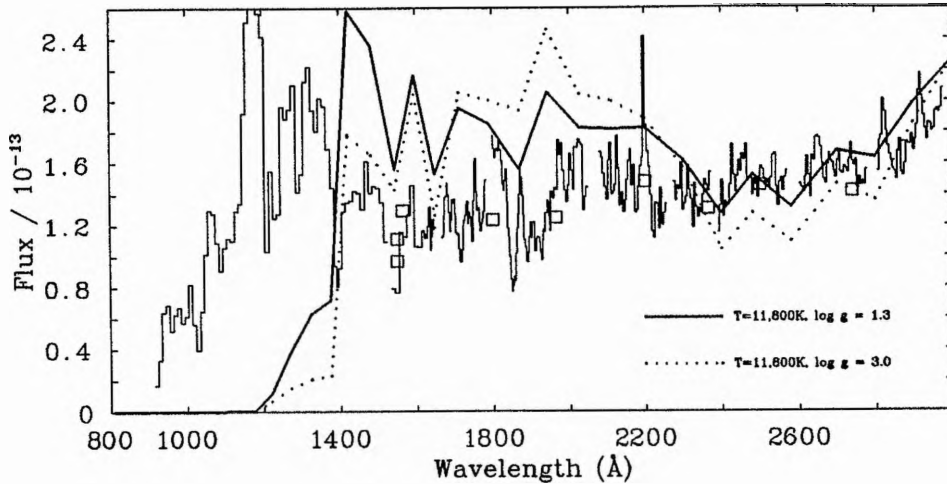


Figure 8.2: The flux distribution of the primary of  $\nu$  Sgr, 800-3,000 Å, with a 11,800K model with  $\log g = 1.3$  and 3.0. Symbols as Figure 8.1,  $E_{B-V} = 0.20$

model flux is up to 50% greater than the observed flux. However, as in Plavec's hydrogen-deficient model, the theoretical model flux falls steeply at wavelengths less than 1400 Å. This model flux is in agreement with the orbital analysis where there was no sign of the secondary component at 1562-1700 Å and 2300-2450 Å. Even in the range 1230-1380 Å the contribution from the secondary was very weak indicating that the primary was still the dominant source of flux at these wavelengths. It is clear that while the new model atmospheres resolve the major discrepancy in previous model atmospheres, the Balmer decrement, there are still a number of problems in modelling the short wavelength flux distribution in  $\nu$  Sgr.

There is a carbon absorption edge at around 1,400 Å which may account for the steep drop in flux at this point. The excess flux at 1,500-2,000 Å would possibly indicate that the model continuous opacity at  $\lambda \leq 1400$  Å is too high resulting in too little model flux at shorter wavelengths with this flux being redistributed into the longer UV region. To test this hypothesis, an 11,800K model was run with the carbon abundance reduced by 4 dex. No change was noticeable in the resulting flux distribution. If the discrepancy in the flux distribution is caused by the incorrect continuous opacity then carbon is not the cause.

## 8.4 Distance

From the adopted model an angular radius of  $9.5 \pm 0.5 \times 10^{-10}$  radians is determined. Assuming that the radius of the primary component of  $\nu$  Sgr is  $60 R_{\odot}$  as indicated from the orbital analysis

(Chapter 2) the distance becomes  $1440 \pm 60$  pc. If the uncertainty in the extinction and temperature of the model are accounted for as well as the uncertainty in the radius of the primary then the uncertainty in the distance rises to 300pc.

At this distance the two components will have an angular separation of  $0.7 \times 10^{-3}$  arc-seconds. This value is sufficiently large to allow independent confirmation from interferometric techniques (*e.g.* Halbwachs 1981).

## 8.5 Luminosity

If the primary is filling its Roche lobe with a radius of  $60 R_{\odot}$  then its luminosity is  $61,000^{+11,000}_{-5,000} L_{\odot}$  with the uncertainty coming from the uncertainty in the temperature of the primary. The absolute bolometric magnitude is then  $-7.2^{+0.1}_{-0.2}$ .

These results are fully consistent with the primary component being a supergiant with a temperature of 11,800K and thus a spectral type of A0 or A1 (Schönberner & Drilling 1983). From this the expected absolute bolometric magnitude would be -7 (Allen 1973) as derived.

With these values  $\nu$  Sgr has been plotted on Figure 1.1, given in Chapter 1, page 3.

## 8.6 The Flux Distribution of the Secondary Component

As the primary model atmosphere does not model the flux between 1230 Å and 1400 Å well it is necessary to model the observed flux in terms of a primary and secondary model. This will determine if any of the observed flux shortward of  $\sim 1,400$  Å could come from the secondary. With the inclusion of a secondary flux source the primary has to be modelled anew.

### 8.6.1 Temperature and extinction determination

The same procedure as before was used to determine the primary temperature and the extinction. Only 3 wavelengths were used with the 2365 Å point being dropped because of possible secondary contamination at this wavelength. The Voyager data was also considered as, despite its poor quality, it gives vital information on the flux distribution in a wavelength region that is expected to be dominated by the secondary. The results are given in Table 8.3.

The 13,000K and 15,000K models can be discounted due to the large scatter in their determined temperatures.

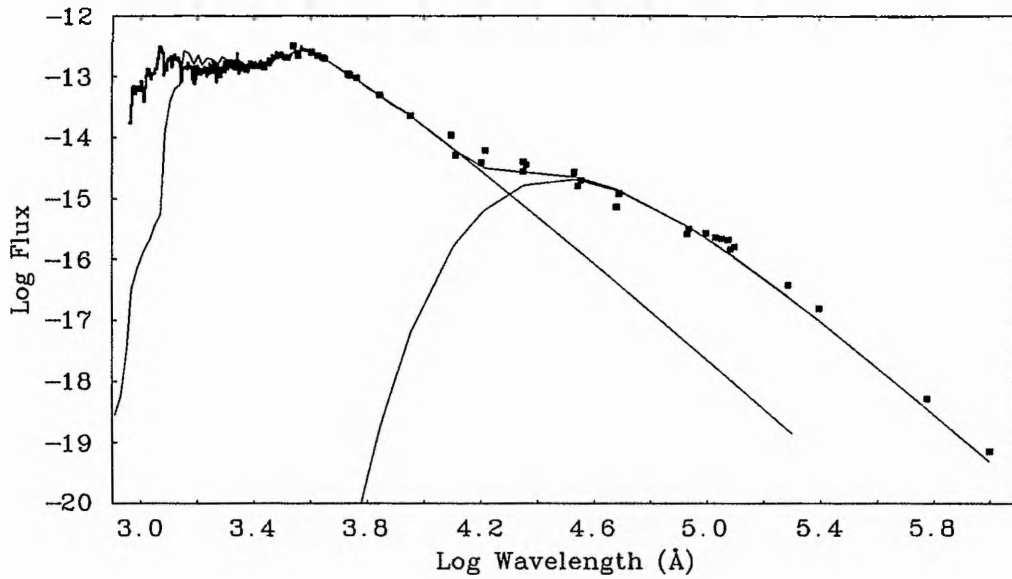


Figure 8.3: The flux distribution of  $\nu$  Sgr with model atmosphere fluxes superimposed. Filled squares are photometry while light lines are the ULDA and Voyager spectra. Heavy lines are the 11,800K model for the primary and the 950K dust component. The observed fluxes have been de-reddened by  $E_{B-V} = 0.20$ . The Voyager and ULDA data have been merged for clarity with the ULDA data being weighted 4 times that of the Voyager data. No flux is detected at wavelengths less than  $\sim 950 \text{ \AA}$  because of interstellar extinction.

There is little to choose between the other models. All the candidate models were examined but none matched the flat flux distribution between 1400 and 2800 Å well. On this basis the 11,000K model with  $E_{B-V}=0.20$  was chosen. Here the primary flux falls short of the observed flux in most of the ULDA region which, when combined with the secondary flux, provides a reasonable fit to the observed flux.

To determine the approximate secondary temperature the flux distribution at  $\leq 1400$  Å must be used. This is predominantly Voyager data and thus is subject to errors of up to 50%. Within the Voyager flux distribution is a small depression at  $\sim 1215$  Å due to the Lyman- $\alpha$  transition. If the flux at this wavelength is predominantly from the secondary then the shallowness of this feature may indicate either a very high temperature for the secondary or a low hydrogen abundance. The de-reddening procedure does not remove the interstellar  $L\alpha$  and so the stellar  $L\alpha$  absorption must be less than observed. As nothing is known about the secondary, hydrogen-rich and hydrogen-poor models were calculated.

Figure 8.4 shows model atmosphere fluxes for the secondary component in the range 800-3000 Å. All the models have been normalised at 1340 Å to a flux of  $1.45 \times 10^{-13} \text{ W m}^{-2} \text{ Å}^{-1}$ . At this wavelength the models are normalised at halfway between the observed and primary model fluxes to ensure that the sum of the primary and secondary fluxes at around  $\sim 1400$  Å is equal to the observed fluxes. The surface gravity has little effect on the gross flux distribution when compared to the temperature; the gravities used for the models varied from 2.0 (lower temperatures) to 4.0 (very high temperatures).

The hydrogen-rich model atmospheres are ATLAS models (Kurucz 1979) and a model of  $22,000 \pm 2,000$ K fits the Voyager observations the best. Here the flux falls away very rapidly, as observed, in the region of  $\sim 950$  Å and falls to almost zero except in the case of the very hottest models.

Also shown are hydrogen-deficient model atmospheres from STERNE. They show a more shallow depression in the region of  $\sim 1200$  Å but, except for the 16,000K model, show substantial flux at  $\leq 950$  Å. The best fit model would be  $18,000 \pm 2,000$ K in agreement with the  $5 M_{\odot}$  secondary component from the orbital analysis.

There is little to choose between the two candidate models from the flux distribution in this wavelength region. Neither explains the high flux at 1200 Å. However the ULDA data ends at 1200 Å with no sign of an emission peak. The Voyager data shows, apart from an absorption at  $\sim 1230$  Å, a constant flux between 1150 and 1350 Å. The ULDA data do not show such high flux in the region 1200-1350 Å so upon merging the data the higher weight of the ULDA data lower the flux in the region 1200-1350 Å but the flux remains high in the region 1150-1200 Å as only Voyager data exist here. Thus the peak can be regarded as spurious, an indication of the poor quality of the Voyager data.

From Figure 8.4 the 11,000K primary model fits the observed fluxes very well up  $\sim 3000 \text{ \AA}$  whereupon the model flux at shorter wavelengths is too low compared to observations. This leaves room for the secondary flux but no secondary will be able to fill the dip between 2400 and 2800  $\text{\AA}$  without being the dominant source of flux at shorter wavelengths and increasing the flux at those short wavelengths to much greater than that observed. The orbital analysis showed that at  $\sim 2400 \text{ \AA}$  the primary was the dominant source of flux.

Figure 8.5 shows the same data as in Figure 8.4 except in the wavelength region from 3000-9000  $\text{\AA}$ . Here there are much greater differences in the spectra with there being a large Balmer discontinuity in the hydrogen rich models with much greater flux in the visual region. If the secondary were a 22,000K hydrogen rich star then some 10% of the observed visual flux would be from the secondary. This would be detected in the optical spectrum, which it is not (Chapter 11). However for the 18,000K helium rich model only some 2-3% of the visual flux is contributed by the secondary; this is negligible and would not expect to be detected.

The flux shortward of  $\sim 1,500 \text{ \AA}$  can be modelled by a hydrogen deficient secondary component with a temperature of  $18,000 \pm 2,000 \text{ K}$ , corresponding to a B6 type star, although a later spectral type and lower temperature are indicated if there is excess UV flux from infalling matter on to the secondary. The secondary can also be modelled satisfactorily by a slightly hotter (22,000K) hydrogen-rich star. At wavelengths of less than 3000  $\text{\AA}$  a hydrogen-rich secondary is ruled out by the flux distribution in the optical region. Both these models require the secondary to contribute a substantial amount of flux within the IUE wavelength range. This is certainly not observed and confirms that the excess UV flux at  $< 1500 \text{ \AA}$  cannot be explained by a stellar model.

### 8.6.2 Discussion

The crucial observational fact that the primary dominates the UV flux distribution down to, at least, 1300  $\text{\AA}$  introduces some uncertainty as to the validity of the theoretical models at this wavelength although it is expected that the discrepancy in this region is due to incorrect continuous opacity.

If the secondary is a normal main sequence star with a mass of  $5 M_{\odot}$  then it is spectral type B5, with  $T_{\text{eff}}$ ,  $\sim 18,000 \text{ K}$ ,  $\log L_s/L_{\odot} \sim 2.6$ ,  $R_s \sim 3.2 R_{\odot}$  and  $L_p/L_s \sim 65$ . With such a low luminosity ratio and an effective temperature only slightly higher than the primary it is fully consistent with being invisible at all wavelengths except the very shortest and then, as in Chapter 2, only barely detectable. Unfortunately, although this evidence is consistent with such a secondary component there is no positive data on the star except for its mass.

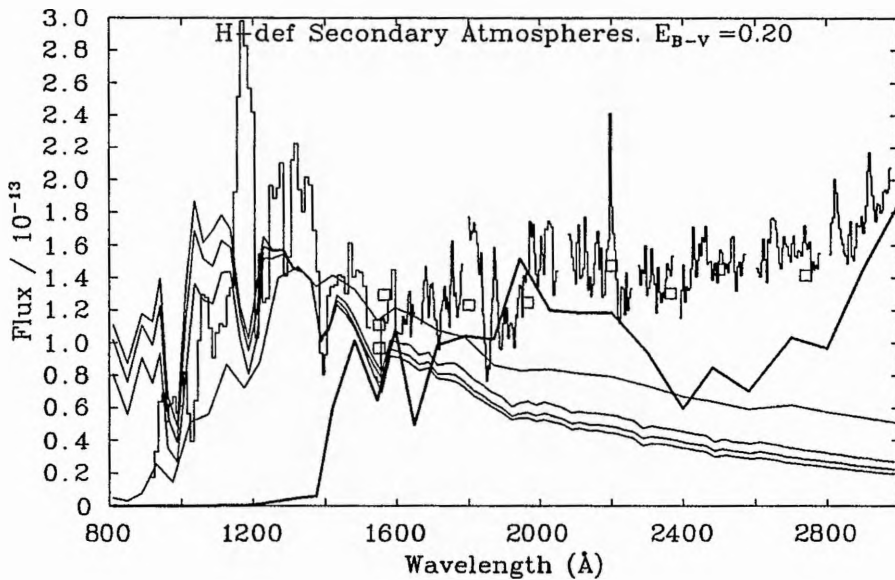
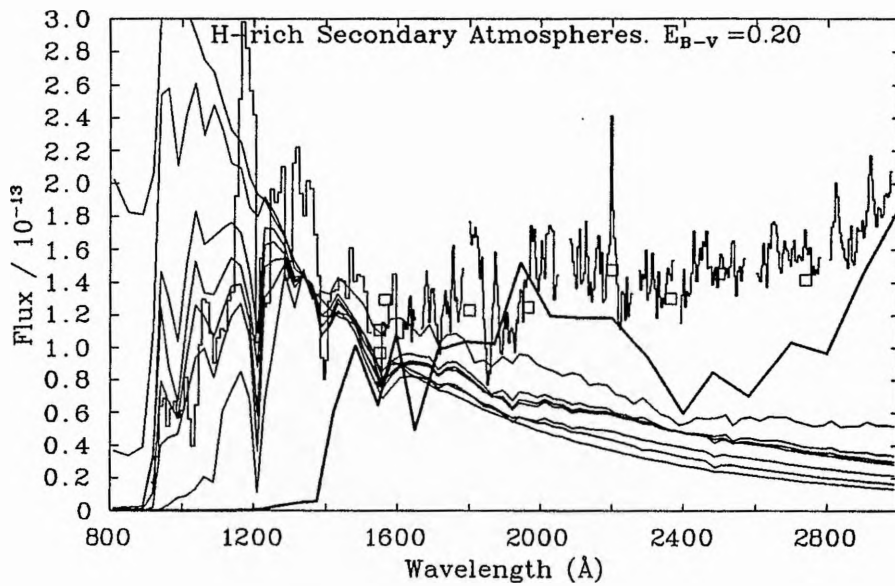


Figure 8.4: Model atmosphere fluxes for the secondary of  $\nu$  Sgr, 800-3000 Å. The upper diagram shows hydrogen-rich model atmospheres with temperatures of 40,000K (upper, left hand side and lower, righthand side), 30,000K, 22,500K, 20,000K, 18,000K, 16,000K and 12,000K (lower, lefthand side and upper righthand side). The lower diagram shows hydrogen-deficient models with 26,000K (upper left, lower right), 24,000K, 22,000K and 16,000K (lower left, upper right). The open squares are photometry points, the light histogram the observed ULDA and Voyager fluxes and the heavy line the 11,000K primary model. The other light lines are the models normalised to  $1.45 \times 10^{-13}$   $\text{W m}^{-2} \text{Å}^{-1}$  at 1340 Å.

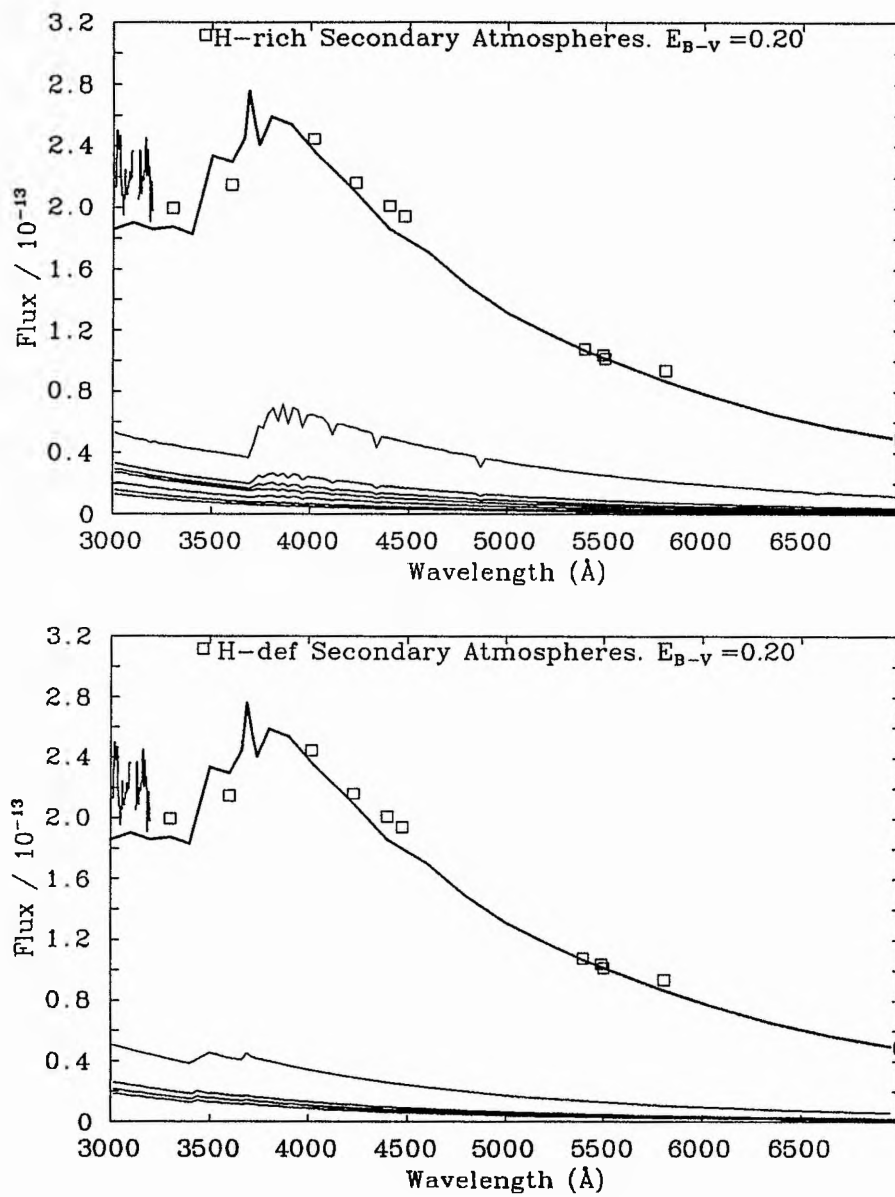


Figure 8.5: Model atmosphere fluxes for the secondary of  $\nu$  Sgr, 3000-7000  $\text{\AA}$ . Details as Figure 8.4.

## 8.7 Infrared Excess and Dust Component

As shown in Figure 8.3 the adopted primary model atmosphere does not fit the observed long wavelength flux distribution well. It is obvious that  $\nu$  Sgr has excess flux at wavelengths greater than  $2.5\mu\text{m}$  and that, while the visual flux and UV flux are well represented by the 11,800K primary model, the IR excess can be matched by a black body of  $950\text{K} \pm 100\text{K}$ . This dust temperature agrees well with the simple analysis of Walker (1985, 1986)<sup>1</sup> ( $T = 1000\text{K}$ ) and is lower than the value of 1060K (Giesel 1970) determined from the K-N colour. These results rule out the higher temperature ( $T=2,500\text{K}$ ) proposed by Humphreys & Ney (1974) for a "third body" in the system. This excess flux arises from the cloud of ejected material that surrounds the  $\nu$  Sgr system (*e.g.* Sahade & Albano 1970). The temperature is less than the maximum of  $\sim 1000\text{K}$  above which dust grains have difficulty in forming (Gilman 1969) and, together with the observed  $11\mu\text{m}$  peak (Woolf 1973, Humphreys & Ney 1974) indicating the presence of silicates, these observations strongly point to dust formation within the ejected material. These silicates are possibly in the form of silicon nitride ( $\text{Si}_3\text{N}_4$ ) rather than silicon carbide (SiC) due to the enhanced nitrogen content of the atmosphere and the lower carbon abundance; the  $11\mu\text{m}$  peak is missing in carbon stars (*e.g.* Stein, Gaustad, Gillett & Knacke 1969).

The observed flux at  $3.6\mu\text{m}$  is used with the model flux at the same wavelength for a 950K black body to determine the angular radius for the dust shell as was done for the primary. The measured radius of  $9.5 \times 10^{-10}$  radians corresponds to a shell radius of  $2960 R_\odot$  at a distance of 1400pc. This represents a mean distance. Assuming a mean wind velocity over these distances of  $500 \text{ km s}^{-1}$  the material will take about 50 days to reach  $3000 R_\odot$ .

Walker (1986) determines the angular extent at which the radiation from the dust "shell" is above the background level using an IRAS scan across the object. The Full Width at Zero Intensity (FWZI) varies from 4 arcmin at  $12\mu\text{m}$  to 9 arcmin at  $100\mu\text{m}$ . Only one measurement was made and no profiles were published. These observations indicate a cooler component with a substantially greater angular radius.

---

<sup>1</sup>The  $12\mu\text{m}$  flux quoted by Walker is in fact not, as is stated, a colour corrected flux (see Beichman, Neugebauer, Habing, Clegg & Chester 1984). The corrected flux seems to have been used for her analysis and so her conclusions stand.

Table 8.1: Fluxes for  $\nu$  Sgr from Trams, Waters, Lamers, Waelkens, Geballe & Thé (1991). The magnitude is given (reference, column 5) with the log of the observed flux,  $F_{obs}$  ( $\text{erg s}^{-1} \text{cm}^{-2} \text{Hz}^{-1}$ ) using the calibrations indicated (column 7). These fluxes are then converted into units of  $\text{W m}^{-2} \text{Å}^{-1}$  (column 8) by multiplying by  $\frac{3 \times 10^{15}}{\lambda^2}$  with  $\lambda$  in Å. These fluxes are then de-reddened (column 9) using  $E_{B-V} = 0.20$  and the laws of Seaton (1979) and Howarth (1983).

Type	Band	Wavelength	Mag	Ref.	$\log F_{obs}$	ref	Flux	Flux
UV	15N	1550	5.553		-22.75		-13.65	-13.02
ANS	15W	1550	5.386		-22.69		-13.59	-13.96
	18	1800	5.219		-22.50		-13.53	-12.91
	22	2200	5.397		-22.39		-13.60	-12.83
	25	2500	4.945		-22.09		-13.41	-12.84
	33	3300	4.143		-21.54		-13.10	-12.70
UV S2/68		1565	29.83 <sup>1</sup>	1	-22.61		-13.52	-12.89
		1965	26.37 <sup>1</sup>	1	-22.47		-13.58	-12.90
		2365	28.46 <sup>1</sup>	1	-22.27		-13.54	-12.88
		2740	45.85 <sup>1</sup>	1	-21.94		-13.34	-12.85
Visual Johnson	U	3600	4.18	2	-21.40	3	-13.04	-12.67
	B	4400	4.71	2	-21.21	3	-13.02	-12.70
	V	5500	4.61	2	-21.24	3	-13.24	-12.99
	R	7000	3.63	2	-21.28	3	-13.49	-13.31
	I	9000	4.21	2	-21.33	3	-13.76	-13.64
Visual Geneva	U	3464	4.37	4	-21.29	5	-12.89	-12.51
	B <sub>1</sub>	4015	4.49	4	-21.23	5	-12.96	-12.61
	B	4227	3.65	4	-21.23	5	-13.00	-12.67
	B <sub>2</sub>	4476	5.18	4	-21.21	5	-13.03	-12.71
	V <sub>1</sub>	5395	5.23	4	-21.23	5	-13.22	-12.97
	V	5488	4.51	4	-21.23	5	-13.23	-12.98
	G	5807	5.60	4	-21.21	5	-13.26	-13.03
IR	J	12500	3.89	2	-21.31	3	-14.03	-13.96
		13000	4.38	6	-21.60	7	-14.35	-14.29
		16000	3.72	6	-21.52	7	-14.45	-14.41
		16500	3.31	2	-21.29	3	-14.25	-14.21
	K	22500	2.48	2	-21.19	3	-14.42	-14.40
		22500	2.68	6	-21.35	9	-14.58	-14.56
	L	23000	2.49	8	-21.22	8	-14.47	-14.45
		34000	1.20	2	-20.99	3	-14.58	-14.57
		35000	1.64	6	-21.19	9	-14.80	-14.79
	M	36000	1.28	8	-21.07	8	-14.71	-14.70
		48000	1.20	6	-21.25	9	-15.14	-15.14
		49000	0.55	8	-21.02	8	-14.92	-14.92
		86000	-0.10	6	-21.19	9	-15.58	-15.58
		87000	-0.42	8	-21.10	8	-15.50	-15.50
	N	100000	-0.84	8	-21.05	8	-15.57	-15.57
		N <sub>2</sub>	108000	-0.91	6	-21.05	9	-15.64
	P	114000	-1.19	8	-21.02	8	-15.66	-15.66
		122000	-0.86	6	-21.14	9	-15.84	-15.84
		126000	-1.26	8	-21.08	8	-15.80	-15.80
		195000	-1.45	8	-21.33	8	-16.43	-16.43
IRAS		120000	99.54 <sup>2</sup>		-21.00		-15.68	-15.68
		250000	32.73 <sup>2</sup>		-21.49		-16.81	-16.81
		600000	6.14 <sup>2</sup>		-22.21		-18.29	-18.29
		1000000	2.38 <sup>2</sup>		-22.62		-19.14	-19.14

References: (1) Thomson, Nandy, Jamar, Mosfle, Houziaux, Carnochan & Wilson (1978); (2) Lee & Nariel (1967); (3) Landolt-Börnstein (1962); (4) Rufener (1966); (5) Rufener & Nicolet (1966); (6) Humphreys & Ney (1974); (7) Strecker & Ney (1974); (8) Gerha, Hackwell & Jones (1974); (9) Ney, Strecker & Gerha (1973).

Notes 1: Flux in  $10^{-12} \text{ erg s}^{-1} \text{ cm}^{-2} \text{ Å}^{-1}$ ; 2: Colour corrected fluxes in Janskys.

Table 8.2: Flux distribution analysis for the primary of  $\nu$  Sgr. For a given model the extinction is given (column 3) that gives rise to the mean temperature with the lowest scatter (column 4) from the individual temperatures determined from the fluxes at the four wavelengths used. The temperature determined from the 2365 Å flux is shown separately (column 5, see text) as well as the derived angular radius of the primary component (column 6).

Model		$E_{B-V}$	$T_{\text{eff}}$		Angular Radius ( $\times 10^{-10}$ ) rad
Temp.	Log g		(mean)	(2365 Å)	
10,000	1.5	0.10	10,280 $\pm$ 1230	8,440	10.7 $\pm$ 0.5
11,000	1.5	0.10	11,600 $\pm$ 440	11,230	8.8 $\pm$ 0.7
11,500	1.3	0.15	11,540 $\pm$ 350	11,620	8.8 $\pm$ 0.6
11,800	1.3	0.20	11,820 $\pm$ 290	11,790	9.5 $\pm$ 0.5
12,000	1.5	0.25	12,040 $\pm$ 270	11,760	10.1 $\pm$ 0.5
13,000	1.5	0.30	13,000 $\pm$ 300	13,290	9.9 $\pm$ 0.5
15,000	1.7	0.30	14,670 $\pm$ 1460	16,760	8.3 $\pm$ 0.2

Table 8.3: Flux distribution analysis for  $\nu$  Sgr. For a given model the extinction is given (column 3) that gives rise to the mean temperature with the lowest scatter (column 4) from the individual temperatures determined from the fluxes at the three wavelengths used. The temperature determined from the 3600 Å flux is shown separately (column 5, see text) as well as the derived angular radius of the primary component (column 6).

Model		$E_{B-V}$	$T_{\text{eff}}$		Angular Radius ( $\times 10^{-10}$ ) rad
Temp.	Log g		(mean)	(3600 Å)	
10,000	1.5	0.10	10,000 $\pm$ 60	10,025	10.0 $\pm$ 0.1
11,000	1.5	0.20	11,030 $\pm$ 70	11,150	10.1 $\pm$ 0.3
11,500	1.3	0.25	11,490 $\pm$ 90	11,600	10.5 $\pm$ 0.2
11,800	1.3	0.30	11,810 $\pm$ 90	11,810	11.0 $\pm$ 0.2
12,000	1.5	0.30	12,020 $\pm$ 90	12,160	10.7 $\pm$ 0.2
13,000	1.5	0.30	12,950 $\pm$ 280	13,270	10.0 $\pm$ 0.4
15,000	1.7	0.30	15,020 $\pm$ 980	16,210	8.7 $\pm$ 1.1

## 8.8 Summary

*Using line-blanketed hydrogen-deficient model atmospheres to model the flux distribution of the primary component of  $\nu$  Sgr a temperature of  $11,800 \pm 500 K$ , with  $E_{B-V} = 0.20 \pm 0.05$ , have been determined. These results confirm other determinations within this thesis.*

*With an assumed radius of  $60 R_{\odot}$  the primary has a luminosity of  $61,000^{+11,000}_{-5,000} L_{\odot}$  corresponding to an absolute magnitude of  $-7.2^{+0.1}_{-0.2}$  at the derived distance of  $1440 \pm 300 pc$ .*

*The long standing problem, noted by Plavec (1986), that model atmospheres failed to model the observed flux of  $\nu$  Sgr has been mostly solved by new models. There remains excess model flux at  $\sim 1500 \text{ \AA}$  and too little at  $< 1400 \text{ \AA}$ , probably due to inadequate atomic data.*

*The IR excess can be successfully modelled by a  $950 \pm 100 K$  blackbody corresponding to a dust shell with a radius of  $\sim 3000 R_{\odot}$ . This result shows that some of the material is relatively close to the star and is indicative of the mass loss, and subsequent dust formation, that is taking place within the  $\nu$  Sgr system. A cool distant third body can be excluded.*

*These determinations of temperature, extinction, distance, luminosity and absolute magnitude are by far the most accurate ever determined for the  $\nu$  Sgr system and in the case of the latter three values are the only available values based on measurement rather than speculation.*

## 8.9 References

- Allen, C.W., 1973. *Astrophysical Quantities*, Third Edition, Athlone Press.
- Gerhz, R.D., Hackwell, J.A. & Jones, T.W., 1974. *Astrophys. J.*, **191**, 675.
- Giesel, S.C., 1970. *Astrophys. J.*, **161**, L105.
- Gilman, R.C., 1969. *Astrophys. J.*, **155**, L185.
- Halbwachs, J.L., 1981. *Astr. Astrophys. Suppl.*, **44**, 47.
- Howarth, I.D., 1983. *Mon. Not. R. astr. Soc.*, **203**, 301.
- Humphreys, R.M. & Ney, E.P., 1974. *Astrophys. J.*, **190**, 339.
- Kurucz, R.L., 1979. *Astrophys. J. Suppl.*, **40**, 1.
- Landolt-Börnstein, 1982. *Numerical Data and Functional Relationships in Science and Technology, New Series, Group VI, Vol. 2b.*, Springer-Verlag.
- Lee, T.A. & Nariai, K., 1967. *Astrophys. J.*, **149**, L93.
- Möller, R.U., 1990. *Diplom. Thesis*, Kiel University.
- Ney, E.P., Streker, D.W. & Gerhz, R.D., 1973. *Astrophys. J.*, **180**, 809.
- Plavec, M.J., 1986. In: *Hydrogen-Deficient Stars & Related Objects*, IAU Colloquium No. 87, p.231, eds. K. Hunger, D. Schönberner & N.K. Rao, Reidel, Dordrecht, Holland.
- Rufener, F., 1988. *Catalogue of Stars Measured in the Geneva Photometric System, Fourth Edition.*, Obs. de Geneve.
- Rufener, F. & Nicolet, B., 1988. *Astr. Astrophys.*, **206**, 357.
- Sahade, J. & Albano, J., 1970. *Astrophys. J.*, **162**, 905.
- Schönberner, D. & Drilling, J.S., 1983. *Astrophys. J.*, **268**, 225.
- Seaton, M.J., 1979. *Mon. Not. R. astr. Soc.*, **187**, 75p.
- Stein, W.A., Gaustad, J.A., Gillett, F.C. & Knacke, R.F., 1969. *Astrophys. J.*, **155**, L3.
- Streker, D.W. & Ney, E.P., 1974. *Astr. J.*, **79**, 797.
- Thomson, G.I., Nandy, K., Jamar, C., Monfils, A., Houziaux, L., Carnochan, D.J. & Wilson, R., 1978. *Catalogue of Stellar Ultraviolet Fluxes*, .
- Trams, N.R., Waters, L.B.F.M., Lamers, H.J.G.L.M., Waelkens, C., Geballe, T.R. & Thé, P.S., 1991. *Astr. Astrophys. Suppl.*, **87**, 361.
- Underhill, A.B., 1982. *Astrophys. J.*, **263**, 741.

Walker, H.J., 1985. *Astr. Astrophys.*, **152**, 58.

Walker, H.J., 1986. In: *Hydrogen-Deficient Stars & Related Objects*, IAU Colloquium No. 87, p.407, eds. K. Hunger, D. Schönberner & N.K. Rao, Reidel, Dordrecht, Holland.

Woolf, N.J., 1973. *Astrophys. J.*, **185**, 229.

## Chapter 9

# The Flux Distributions of KS Per, LSS 1922 & LSS 4300

The other three known hydrogen-deficient binaries (KS Per, LSS 1922 & LSS 4300) have not been studied in the same depth as  $\nu$  Sgr due to their fainter nature (all three) and their recent discovery (LSS 1922 & LSS 4300) as members of this class of objects (Schönberner & Drilling 1984; Jeffery, Drilling & Heber 1987; Morrison, Drilling, Heber, Hill & Jeffery 1986).

Little is known about the temperatures or extinctions of these objects and new determinations with different methods and /or new data are required. Modelling the flux distribution in the way that was done for  $\nu$  Sgr should allow more accurate temperatures and extinctions to be determined, while IR excesses as indications of mass loss or transfer can be identified.

Exactly the same methods of flux distribution modeling as described in Chapter 8 are used for these three stars.

### 9.1 Fluxes

Table 9.1 lists the available photometric observations for the three stars. In addition, all three objects have IUE low resolution spectra available for them.

Table 9.1: Fluxes for KS Per, LSS 1922 & LSS 4300. Data from Trams, Waters, Lamers, Waelkens, Geballe & Thé (1991) (KS Per) and Drilling, Landolt & Schönberner (1984) (LSS 1922, LSS 4300). The magnitudes are converted into fluxes with units of  $\text{W m}^{-2} \text{Å}^{-1}$  using the calibrations in Landolt-Börnstein (1982). Logarithmic fluxes are tabulated.

Type	Band	Wavelength	KS Per		LSS 1922		LSS 4300	
			Mag.	Flux	Mag.	Flux	Mag.	Flux
UV	15N	1550	9.662	-15.30				
ANS	15W	1550	9.528	-15.25				
	18	1800	9.662	-15.30				
	22	2200	10.87	-16.79				
	25	2500	9.507	-15.25				
	33	3300	8.272	-14.75				
Visual Johnson	U	3600	8.13	-14.62	10.99	-15.77	10.44	-15.55
	B	4400	8.31	-14.47	11.15	-15.65	10.57	-15.42
	V	5500	7.84	-14.54	10.44	-15.60	9.75	-15.33
	R	7000	7.28	-14.66	9.87	-15.71	9.14	-15.41
	I	9000	6.90	-14.84	9.27	-15.78	8.49	-15.47
IR	J	12500	6.48	-15.06	8.41	-15.87	7.50	-15.51
	H	16500	6.27	-15.44	8.12	-16.16	6.78	-15.63
	K	22500	6.03	-15.84	7.94	-16.58	5.88	-15.76
	L	34000	5.55	-16.31	7.64	-17.20	4.50	-15.95
IRAS		120000	1.16 <sup>1</sup>	-17.62			6.78 <sup>1</sup>	-16.85
		250000	0.40 <sup>1</sup>	-18.72			3.07 <sup>1</sup>	-17.83

Note 1: Colour corrected fluxes in Janskys.

## 9.2 KS Per

As there is no 2365 Å photometry point available for KS Per, as there was for  $\nu$  Sgr, the 2500 Å ANS point was used instead. The other wavelengths were retained (3600, 5500 and 7000 Å).

The results are shown in Table 9.2 where for each model is quoted the mean temperature that has the lowest standard deviation.

As can be seen the results are quite poor compared to those from  $\nu$  Sgr and do not well tie down the the temperature and extinction.

Using the low resolution IUE spectra it is difficult to determine the reddening but the value of 0.90 in the table can be ruled out. Here the low standard deviation is not to be trusted.

Table 9.3 shows the results from determining which model has the closest average determined temperature to the model temperature.

From these results a model temperature of  $\sim 12,000\text{K}$  and  $E_{B-V} \sim 0.50$  would give the best results. From Table 9.2 a higher temperature and extinction (13,000K, 0.70 respectively) give the best results which, when combined with the others, gives a best fit model of  $12,500 \pm 500\text{K}$  and  $E_{B-V} = 0.55 \pm 0.10$ .

Table 9.2: The flux distribution of KS Per. For each model the extinction that gives rise to the lowest scatter in the determined temperature from the four wavelength points is quoted along with the temperature from the 2500 Å point. The standard deviation from the four temperature measurements is also shown.

Model		$E_{B-V}$	$T_{\text{eff}}$		Angular Radius ( $\times 10^{-10}$ ) rad
Temp.	Log g		(mean)	(2500 Å)	
10,000	1.5	0.20	9,890±850	9,430	2.6±0.4
11,000	1.5	0.30	10,770±710	11,410	3.0±0.3
12,000	1.5	0.60	11,650±550	11,090	3.7±0.3
13,000	1.5	0.70	12,640±450	12,180	4.0±0.2
15,000	1.7	0.80	14,860±600	14,700	4.0±0.3
16,000	1.7	0.90	15,650±350	15,220	4.6±0.2

Table 9.3: The flux distribution of KS Per. For each model the extinction that gives rise to the closest mean value of the four temperatures to the model temperature is quoted along with the standard deviation from the four temperature measurements.

Model		$E_{B-V}$	$T_{\text{eff}}$	Angular Radius
Temp.	Log g		(mean)	( $\times 10^{-10}$ ) rad
10,000	1.5	0.20	9,890±850	2.6±0.4
11,000	1.5	0.30	11,080±960	2.5±0.4
12,000	1.5	0.50	11,910±700	3.1±0.3
13,000	1.5	0.60	12,890±640	3.3±0.3
15,000	1.7	0.80	14,860±600	4.0±0.3
16,000	1.7	0.70	15,860±560	3.8±0.2

Table 9.4: IUE low resolution data used for KS Per. The images with the same phase were merged with weights equal to their exposure times. The two merged spectra were themselves merged to form a higher signal to noise template.

Spectrum	Aperture	Date	Exposure (s)
LWR6252	L	28/11/79	136
SWP7249	L	28/11/79	636
LWR6351	L	10/12/79	137
SWP7358	L	10/12/79	727

Drilling & Schönberner (1982) determine a value of the extinction of 0.35 with an uncertainty of  $\pm 0.1$  at least. Examining the available low resolution spectra shows that any extinction in the range  $\sim 0.25 - 0.70$  is reasonably acceptable. The uncertainty arises from the low signal to noise of the data and the structure around the 2,200 Å region.

Figure 9.1 shows the final adopted model and the observed data. The IUE data consists of two sets of data (one long wavelength, one short wavelength at the same phase, merged with weights equal to their exposures) merged to form a higher signal to noise spectrum. The data is given in Table 9.4, and has been slightly smoothed for clarity in Figure 9.1.

The lower part of the Figure 9.1 shows the effect of modelling the observed data with the parameters quoted by Drilling & Schönberner (10,000K,  $E_{B-V} = 0.35$ ).

### 9.2.1 Discussion

From Figure 9.1 it is clear that the effective temperature favoured by Drilling & Schönberner (1982) fails to match the observed fluxes well. The UBV photometry is not matched by the fluxes except at the 5,500 Å point where the model was normalised to the photometry. In the UV the model only matches the observed fluxes at  $\sim 2,000$  Å, elsewhere the flux is either not matched or dominated by a hot secondary component. Although Drilling & Schönberner claim to have detected some evidence for a hot secondary component the evidence is not so strong as to suggest that 80-100% of the flux in the IUE UV wavelength region comes from this hot component. No secondary component would have a flux distribution that would match the deficiencies in the primary flux caused by this model.

The 12,500K,  $E_{B-V} = 0.55$  model determined here provides a much better fit to the observations especially in the UV, although like the other model it overestimates the flux at 3-4,000 Å. Significantly the fit to the UBV data is much more satisfactory than the other model. Note that the models have a bump in the theoretical flux at 2,200 Å, while flattening this flux, by a de-reddening law, to determine the extinction will underestimate its value. Thus Drilling & Schönberner's value

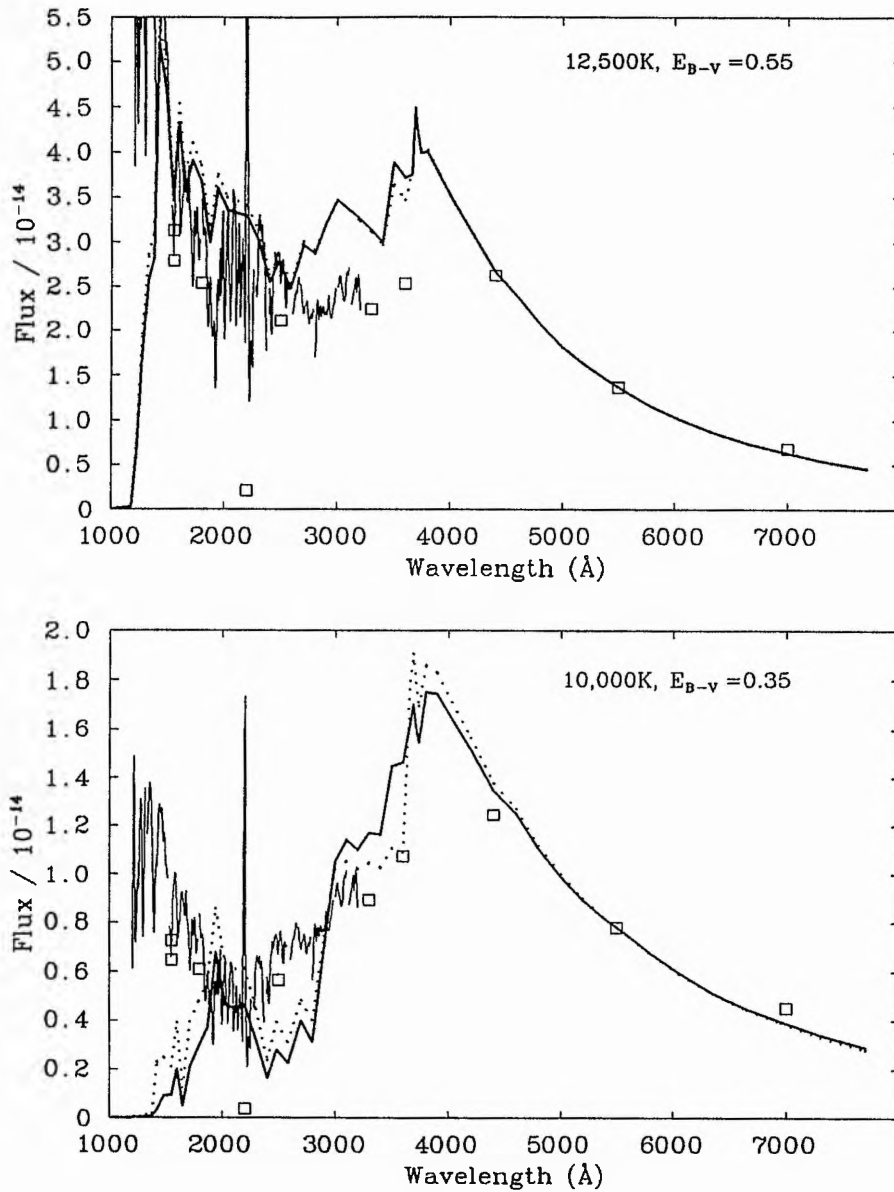


Figure 9.1: The flux distribution of KS Per with a 12,500K model and  $E_{B-v} = 0.55$  (top) and using the results quoted by Drilling & Schönberner (1982), 10,000K and 0.35 (bottom). All models are normalised to the 5,500 Å photometry point. Note the different vertical scales. The solid lines are for models with 0.016% hydrogen and the dotted lines for 1% hydrogen. The fluxes are in units of  $\text{W m}^{-2} \text{\AA}^{-1}$ .

of the extinction is too low.

Wallerstein, Greene & Tomley (1967) determine a hydrogen abundance of 0.01%, similar to that of  $\nu$  Sgr (0.016%) used in these models. By increasing the hydrogen content of the models by a factor of 60 to 1% it is possible that the Balmer decrement would lower the model flux around  $\sim 3,500 \text{ \AA}$  and would increase the short wavelength UV flux to match the observed values for a lower model temperature (*c.f.* Figure 8.4). Models were run with 1% hydrogen and temperatures of 12,500K and 10,000K, the results are shown in Figure 9.1. For the hotter model the difference is negligible and indicate that as long as hydrogen is a trace element the actual abundance make very little difference to the emergent flux. For the 10,000K model the difference is more pronounced, especially the lowering of the flux in the 3,000-4,000  $\text{\AA}$  region. However the fit to UBV photometry is still poor; the fit to the B point even poorer than with the previous model. The fit to the UV flux, although slightly better, is still poor. It is likely that a model with, perhaps, 2-3% hydrogen and a temperature and extinction between the two sets of values here would fit the observation best although it is perhaps a little dangerous to determine temperature, extinction and hydrogen content from photometry alone. A modern, reliable atmospheric fine analysis is required on KS Per to tie down the hydrogen abundance.

### 9.3 LSS 1922

There is little published photometry on LSS 1922 (Table 9.1) and only one low resolution IUE spectrum (SWP26410L) available. No long wavelength spectra covering the 2200  $\text{\AA}$  region are available.

Table 9.5 shows the results of the flux distribution analysis. As the photometry covers the region 1,200 - 34,000  $\text{\AA}$  the flux normalisation region was 1,500-16,000  $\text{\AA}$  and four wavelength points were used, 1,900, 3,600, 5,500 and 7,000  $\text{\AA}$ . The 1900  $\text{\AA}$  photometry point was taken from the ULDA data with a flux of  $1.57\text{E-}17 \text{ W m}^{-2} \text{ \AA}^{-1}$ .

The determined temperature and extinction are  $12,000 \pm 500\text{K}$  and  $0.80 \pm 0.05$  as this model has the closest mean temperature to the model temperature, the lowest standard deviation in the temperature and the closest value of the 1,900  $\text{\AA}$  temperature to the model temperature.

Heber & Schönberner (1981) find  $T=14,400\text{K}$  from un-blanketed model atmospheres although they do not determine an extinction. As extinction of 0.90 is assumed and both models are shown in Figure 9.2. The Heber & Schönberner result is not consistent with the data.

Table 9.5: The flux distribution of LSS 1922. For each model the extinction that gives rise to the closest mean value of the four temperatures to the model temperature is quoted along with the standard deviation from the four temperature measurements. The temperature from the 1,900 Å point is also given.

Model		$E_{B-V}$	$T_{\text{eff}}$		Angular Radius ( $\times 10^{-10}$ ) rad
Temp.	Log g		(mean)	1,900 Å	
8,000	1.5	0.30	7,920 $\pm$ 840	6,600	1.4 $\pm$ 0.3
10,000	1.5	0.70	10,480 $\pm$ 680	11,350	1.1 $\pm$ 0.1
11,000	1.5	0.70	11,270 $\pm$ 240	11,240	1.3 $\pm$ 0.0
12,000	1.5	0.80	12,230 $\pm$ 190	12,180	1.4 $\pm$ 0.0
13,000	1.5	0.90	13,210 $\pm$ 240	13,080	1.5 $\pm$ 0.1
15,000	1.7	1.00	15,340 $\pm$ 440	15,530	1.5 $\pm$ 0.1

Table 9.6: The flux distribution of LSS 4300. For each model the extinction that gives rise to the closest mean value of the four temperatures to the model temperature is quoted along with the standard deviation from the four temperature measurements. The temperature from the 1,900 Å point is also given.

Model		$E_{B-V}$	$T_{\text{eff}}$		Angular Radius ( $\times 10^{-10}$ ) rad
Temp.	Log g		(mean)	1,900 Å	
8,000	1.5	0.30	8,150 $\pm$ 390	7,750	1.8 $\pm$ 0.2
10,000	1.5	0.70	10,360 $\pm$ 260	10,710	2.0 $\pm$ 0.1
11,000	1.5	0.80	11,330 $\pm$ 310	11,690	2.0 $\pm$ 0.1
12,000	1.5	0.90	12,270 $\pm$ 280	12,630	2.2 $\pm$ 0.1
13,000	1.5	1.00	13,260 $\pm$ 300	13,531	2.4 $\pm$ 0.1
15,000	1.7	1.10	15,350 $\pm$ 630	16,060	2.4 $\pm$ 0.1

## 9.4 LSS 4300

As with LSS 1922 there is little published photometry on LSS 4300 (Table 9.1). There are 5 low dispersion IUE spectra available of which only two have an acceptable signal to noise ratio. These two spectra (LWR11395L and SWP14802) were merged with weights equal to their exposure times.

Table 9.6 shows the results of the flux distribution analysis. As the photometry covers the region 1,200 - 34,000 Å the flux normalisation region was 1,500-16,000 Å and four wavelength points were used, 1,900, 3,300, 5,500 and 7,000 Å.

From these results a temperature of 12,000 $\pm$ 1,000K with an extinction of  $E_{B-V} = 0.90\pm 0.10$  is indicated. Displaying the results shows that this is the case. These results along with a 14,400K,  $E_{B-V} = 0.90$  model from Schönberner & Drilling (1984) and Heber & Schönberner (1981) are

shown in Figure 9.3. The hotter model provides a poorer fit to the observations than the cooler one.

Schönberner & Drilling (1984) fit a 14,400K,  $\log g = 1.4$  He I 4471 Å line profile to their undersampled observed data obtaining excellent results. The determined EW of the He lines is very temperature and gravity sensitive in this region. However these results do not contradict those presented here as, in the case of  $\nu$  Sgr, it is expected that the determined temperature from the helium lines disagrees with that determined from other methods. A full spectral fine analysis is required for LSS 4300 to determine if the helium lines show the same sort of discrepancy as in  $\nu$  Sgr and to determine the temperature from a curve of growth analysis.

## 9.5 IR Excess

Using the temperatures and the extinctions determined here the long wavelength photometry can be analysed to determine the existence of a IR excess and to determine its temperature if present.

Figure 9.4 shows the models for the three stars with the photometry up to  $3.4\mu\text{m}$  (LSS 1922) and  $100\mu\text{m}$  (KS Per and LSS 4300).

It is clear that KS Per has an IR excess very similar to that from  $\nu$  Sgr and can be modeled with a black body with a temperature of  $1,100\pm 200\text{K}$ .

LSS 1922 has a slight IR excess from a nearby star, Drilling, Landolt, Schönberner & Heber (1984), with a temperature of  $3,500\pm 500\text{K}$ . If there is a contribution from dust it is very weak. LSS 4300 can also have its IR excess modelled by a cool dust shell with  $T_{\text{eff}} = 720 \pm 50\text{K}$ .

## 9.6 Discussion

### 9.6.1 Temperatures

The results presented here are an improvement of those of previous authors. The determined temperature for KS Per of  $12,500\pm 500\text{K}$  is greater than those of Wallerstein, Greene & Tomley (1967) and Nariai (1967) of  $\sim 9,000\text{K}$  and  $\sim 10,000\text{K}$  respectively. The results of this study are to be preferred as more sophisticated methods and codes have been used.

The temperatures of LSS 1922 and LSS 4300 are less, at  $12,000\pm 500\text{K}$  and  $12,000\pm 1000\text{K}$  respectively, than those determined by Heber & Schönberner (1981) ( $\sim 14,500\text{K}$ ). The tempera-

tures determined by Heber & Schönberner (1981) use the observed value of the reddening-free  $Q$  parameter and a theoretical evolutionary track for single EHe stars in the  $Q$ - $\theta_{\text{eff}}$  plane<sup>1</sup> to obtain  $\theta_{\text{eff}}$  ( $\equiv 5040\text{K}/T_{\text{eff}}$ ) and thus  $T_{\text{eff}}$ . However LSS 1922 and LSS 4300 both have values of  $Q$  ( $Q = -0.660$  and  $-0.670$  respectively). Drilling, private communication, reported in Heber & Schönberner) that each give rise to two values of  $\theta_{\text{eff}}$  on the  $Q$ - $\theta_{\text{eff}}$  plane, namely  $0.36$  ( $T_{\text{eff}} \sim 14,000\text{K}$ ) and  $0.42$  ( $T_{\text{eff}} \sim 12,000\text{K}$ ). Only the former value was reported. They do not account for line-blanketing in the temperature but do report that when 400 UV lines were included the temperature drops by  $\sim 500\text{K}$ . The effect is likely to be greater when many more lines are accounted for, as in the line-blanketed models used here. Thus the higher temperature determined from  $Q$ - $\theta_{\text{eff}}$  analysis may not be using the correct value of the pair of values determined and the use of a EHe evolutionary track for HDBs will also give rise to substantial uncertainties in the temperatures.

Also, for LSS 4300 the temperature from the He I line cannot be trusted as it may show the same effect as in  $\nu$  Sgr where the temperature from the He lines do not agree with other determinations.

### 9.6.2 Distances

All three stars analysed here have smaller angular radii than  $\nu$  Sgr indicating that either they are further away or they have smaller primary radii. If the assumption is made that all three have primaries filling a Roche lobe of a radius of  $60 R_{\odot}$  as is probably true for  $\nu$  Sgr then the determined distances for the three objects are 4230, 9660 and 6280 for KS Per, LSS 1922 and LSS 4300 respectively. These distances may be uncertain by up to 50%.

Heber & Schönberner (1981) determined a distance of 1,700pc for LSS 4300 from their unblanketed model atmospheres after assuming  $\log(L/L_{\odot}) = 4.1$ . This luminosity is a mean from the values of the single EHe stars and is not appropriate for the HDBs. (With their model temperature of 14,500K, which itself has been shown to be unreliable, they determine an absolute magnitude of  $-4.1$ , some three magnitudes less than for  $\nu$  Sgr.)

Although the radii of these three objects are not known it is likely that KS Per, with an orbital period twice that of  $\nu$  Sgr, will have a larger Roche lobe than  $\nu$  Sgr (and therefore be more luminous) and thus will be further away than the distance indicated above. Conversely both LSS 1922 and LSS 4300 have shorter periods than  $\nu$  Sgr and will have smaller Roche lobes and will be closer than the distances indicated above. However the exact sizes of the Roche lobes will depend on the masses of the components as well as the separations. The radii of the primary components will depend on the size of the Roche lobe and whether the component fills it; it is expected that they will due to the IR excesses and hydrogen emission observed.

<sup>1</sup>Neither LSS 1922 nor LSS 4300 were known to be HDBs at that time.

### 9.6.3 UV extinction and the 2,200 Å feature

An important result from this analysis is the realisation, shown in Figure 9.1, that hydrogen-deficient models show a pronounced "bump" at  $\sim 2,200$  Å due to less opacity in this region, probably caused by an absorption edge. This effect is only small for a 12,500K model but is substantial for a 10,000K model. *If* the model atmospheres used here model the flux in the region 1,500 - 3,000 Å accurately then the removal of the 2,200 Å feature to determine the reddening will lead to the extinction always being underestimated.

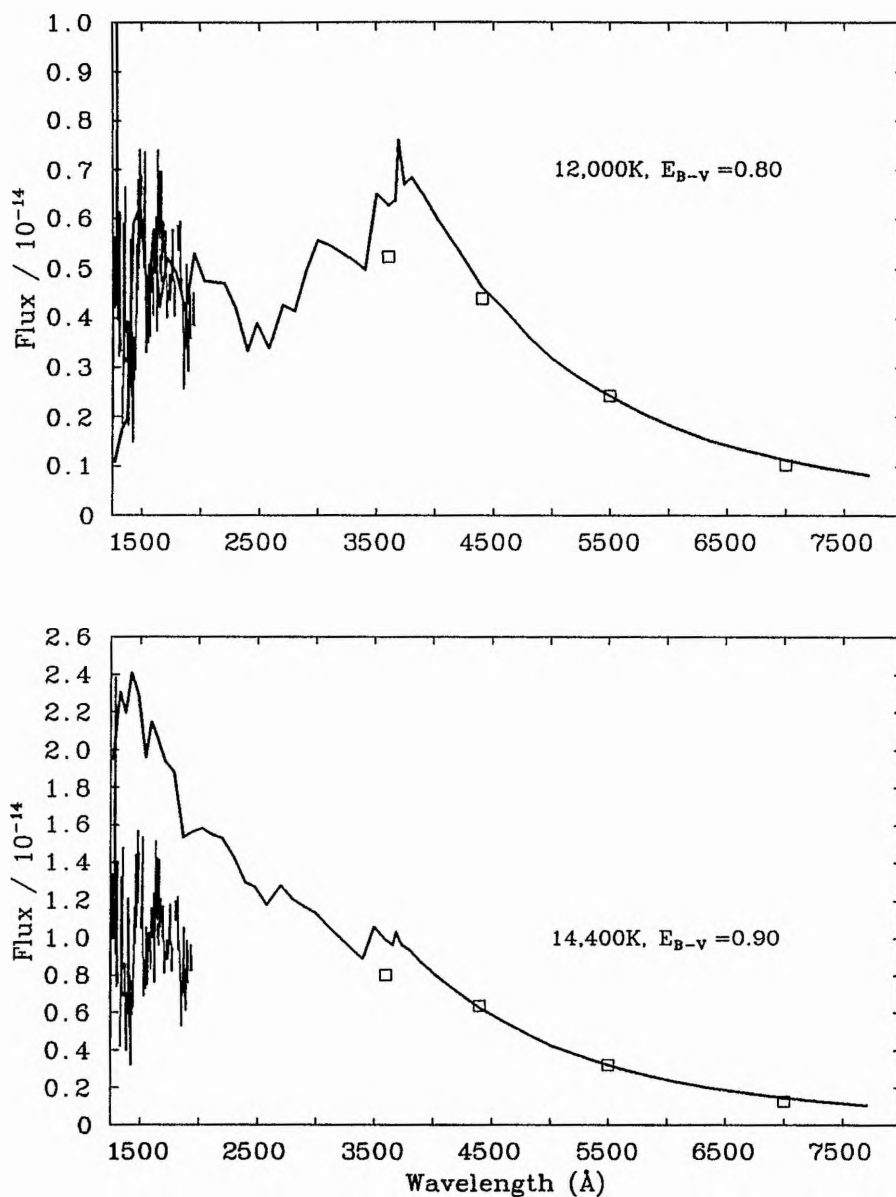


Figure 9.2: The flux distribution of LSS 1922 shown for two models. Shown are the 12,000K,  $E_{B-V} = 0.80$  model (top) and the model determined by Heber & Schönberner (1981) (14,400K,  $E_{B-V} = 0.90$ ) (bottom). The IUE data has been rebinned onto a 5 Å grid for clarity. The fluxes are in units of  $W m^{-2} \text{Å}^{-1}$ .

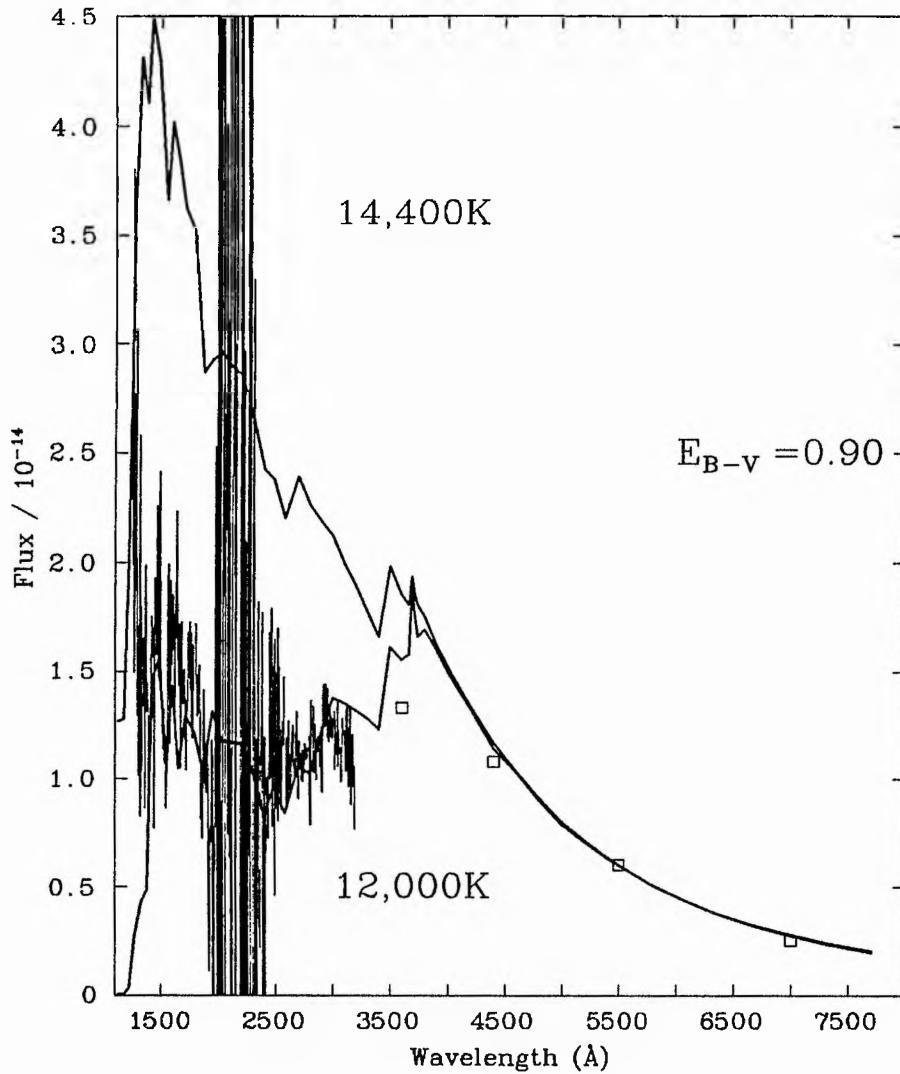


Figure 9.3: The flux distribution of LSS 4300 shown for two models. The best fit model from the temperature analysis (12,000K,  $E_{B-v} = 0.90$ , lower heavy line) and the model determined by Heber & Schönberner (1981) and Drilling & Schönberner (1984) (14,400K,  $E_{B-v} = 0.90$ , upper heavy line). The IUE data has been rebinned onto a 5 Å grid for clarity. The poor quality of the data around the 2,200 Å feature is clearly shown. The fluxes are in units of  $\text{W m}^{-2} \text{Å}^{-1}$ .

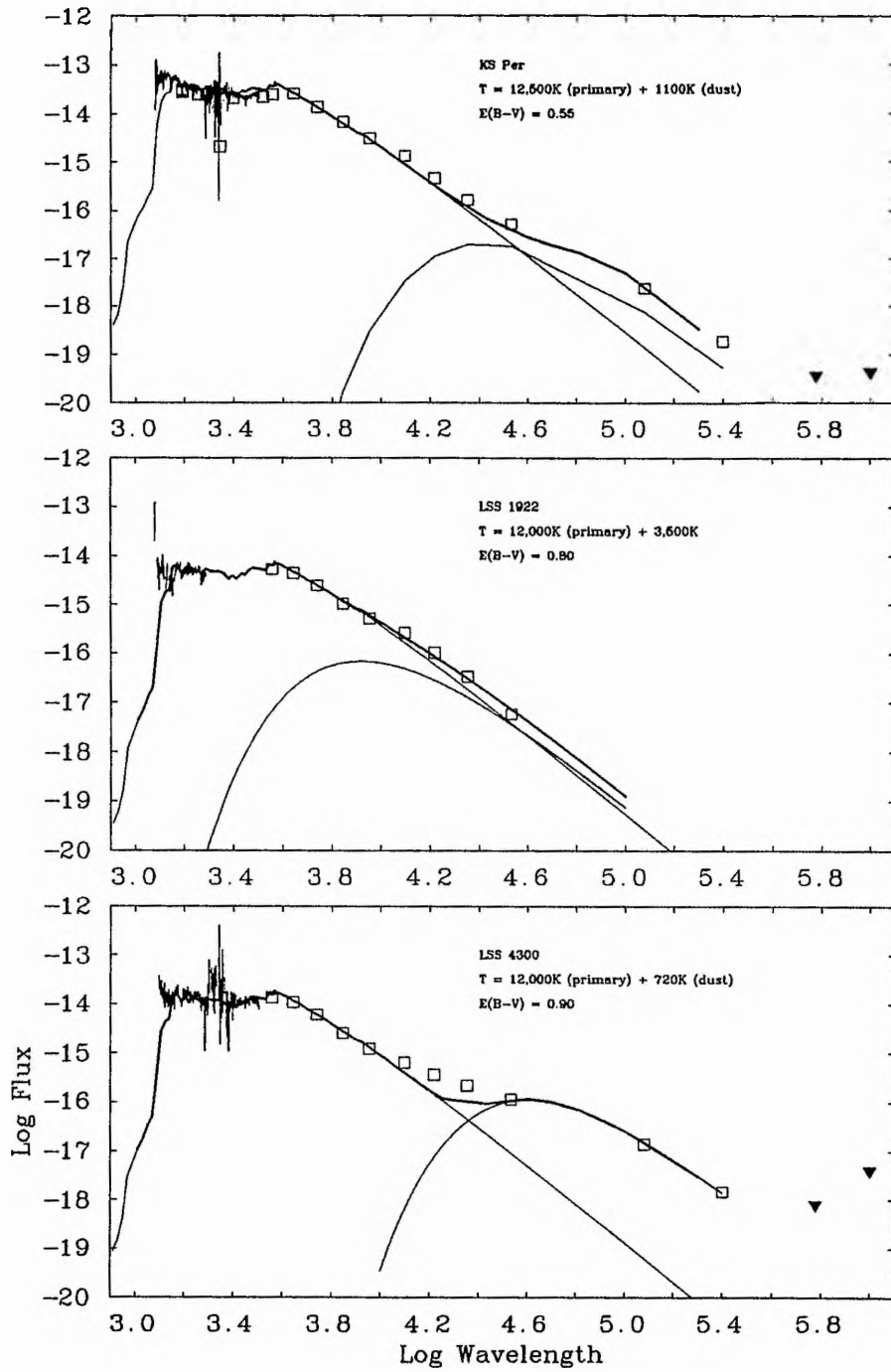


Figure 9.4: The long wavelength photometry for KS Per (upper), LSS 1922 (middle) and LSS 4300 (lower). Filled triangles are IRAS upper limits. The fluxes are in units of  $\log(\text{W m}^{-2} \text{\AA}^{-1})$ .

## 9.7 Summary

*The hydrogen-deficient binaries KS Per, LSS 1922 and LSS 4300 have had their available photometry analysed to determine their temperatures and the presence of an IR excess. The methods and codes used represent a substantial improvement over previous investigations.*

*KS Per is hotter than previously expected with a temperature of  $12,500 \pm 500K$  and an extinction of  $E_{B-V} = 0.55 \pm 0.10$  also higher than previously determined. An IR excess is observed with a temperature of  $\sim 900K$ , just as in  $\nu$  Sgr and is probably due to mass loss from the system and subsequent dust formation. A distance of  $\sim 4300pc$  is determined if the primary radius is  $60R_{\odot}$ .*

*LSS 1922 and LSS 4300 are cooler than previously thought at  $12,000 \pm 500K$  and  $12,000 \pm 1,000K$  respectively. while the extinctions at  $E_{B-V} = 0.80 \pm 0.05$  and  $0.90 \pm 0.10$  confirm previous estimates. LSS 4300 shows a substantial IR excess while LSS 1922 does not. The helium line problem encountered for  $\nu$  Sgr (Chapter 11) explains the high temperature determined from a helium line as opposed to the flux distribution. Experience from modeling  $\nu$  Sgr indicates that the temperature from the flux distribution will be more accurate than that from a helium line. If the primary components of both objects have radii of  $60R_{\odot}$  then the distances are  $\sim 9600pc$  and  $\sim 6280pc$  for LSS 1922 and LSS 4300 respectively. However uncertainties of up to 50% are expected.*

*This analysis indicates that all the HDB's have a temperature of  $\sim 12,000K$  and there is no indication of an orbital period - temperature relationship.*

*The hydrogen-deficient line-blanketed model atmospheres used here have been shown, for some temperatures, to give rise to a flux "bump" at  $\sim 2,200 \text{ \AA}$  which has previously not been accounted for when determining the reddening of hydrogen deficient stars. Further work is required in this area to determine if the model atmospheres are correct and, if so, what range of temperatures and compositions give rise to the effect.*

*Radial velocity curves for both components of LSS 1922 and LSS 4300 and a secondary radial velocity curve for KS Per are required to determine the masses of both components of these objects. This will allow the primary radii and distances to be determined.*

## 9.8 References

- Drilling, J.S. & Schönberner, D., 1982. *Astr. Astrophys.*, **113**, L22.
- Drilling, J.S., Landolt, A.U. & Schönberner, D., 1984. *Astrophys. J.*, **279**, 748.
- Heber, U. & Schönberner, D., 1981. *Astr. Astrophys.*, **102**, 73.
- Jeffery, C.S., Drilling, J.S. & Heber, U., 1987. *Mon. Not. R. astr. Soc.*, **226**, 317.
- Landolt-Börnstein, 1982. *Numerical Data and Functional Relationships in Science and Technology, New Series, Group VI, Vol. 2b.*, Springer-Verlag.
- Morrison, K., Drilling, J.S., Heber, U., Hill, P.W. & Jeffery, C.S., 1986. In: *Hydrogen-Deficient Stars & Related Objects, IAU Coll. No. 87*, p.245, eds. K. Hunger, D. Schönberner & N.K. Rao, Reidel, Dordrecht, Holland.
- Nariai, K., 1967. *Publs astr. Soc. Japan*, **19**, 63.
- Schönberner, D. & Drilling, J.S., 1984. *Astrophys. J.*, **276**, 229.
- Trams, N.R., Waters, L.B.F.M., Lamers, H.J.G.L.M., Waelkens, C., Geballe, T.R. & Thé, P.S., 1991. *Astr. Astrophys. Suppl.*, **87**, 361.
- Wallerstein, G., Greene, T.F. & Tomley, L.J., 1967. *Astrophys. J.*, **150**, 245.

## Chapter 10

# High Resolution Optical Spectroscopy of $\nu$ Sgr

### 10.1 Introduction

To enable accurate determination of the atmospheric composition of  $\nu$  Sgr it is necessary to have good spectra to analyse. The accuracy of the spectra determines upper limits to the accuracy with which the temperature, surface gravity and composition may be determined. Previous analyses of the surface composition have all relied on photographic spectra (Greenstein & Adams 1947; Hack & Pasinetti 1963; Leushin & Topil'skaya 1984), giving necessarily poor results.

$\nu$  Sgr is a bright object and so a high signal to noise ratio can be obtained with most detectors. For this study a Thompson CCD was used with the University College London Echelle Spectrograph (UCLES) on the Anglo-Australian Telescope. The CCD/Echelle combination allows good wavelength coverage and resolution with a high S/N ratio obtained over a short time interval. Being an electronic detector the analysis of the spectra is much simplified.

### 10.2 Observations

The observations were made on the Anglo-Australian Telescope with the UCLES/ Thompson CCD combination by Dr. D. Pollacco on the night of 30-31 July 1991. A log of the observations is given in Table 10.1.

The blue Thompson CCD was chosen because of its high quantum efficiency and its large

Table 10.1: A log of AAT observations for  $\nu$  Sgr.

Frame	HJD	Exposure (s)
1	2448468.488	5
2	2448468.497	100
3	2448468.502	300
4	2448468.598	600

size ( $1024 \times 1024$  pixels) that allowed the spectral range of  $3980 \text{ \AA} - 4915 \text{ \AA}$  to be covered in a single exposure.

As well as the exposures of  $\nu$  Sgr the usual bias (dark noise) and flat field (relative sensitivity calibration) frames were taken as well as a Thorium-Argon arc exposure for wavelength calibration purposes.

### 10.3 Echelle Reduction

Reduction of echelle spectra is a complicated and time-consuming task which has not been well documented. The available documentation, a FIGARO text file, is poor and inaccurate. A full worked example of the reduction used here is given in Appendix E with brief details here.

The reduction was done using a number of FIGARO routines (Shortridge 1986).

1. The bias frames, all with the same exposure, are median filtered to remove cosmic ray events. The same is done with the flat field exposures.
2. The median bias frame is then subtracted from each of the  $\nu$  Sgr frames and from the median flat field frame to remove the effect of thermal noise.
3. After discarding the 5 sec exposure of  $\nu$  Sgr the other three frames were then co-added. This is possible due to the extreme positional stability of the UCLES/CCD arrangement.
4. The median flat frame is divided into the summed  $\nu$  Sgr frame. As the light path for the flat field exposures passes through the echelle this should remove most of the blaze function of the echelle that causes the signal strength to be high at the center of an order but weak towards the edges.
5. The median  $\nu$  Sgr frame is then rotated  $90^\circ$  clockwise and flipped about the x-axis to put the frame in the required orientation for the subsequent FIGARO operations.
6. The position of the spectral orders on the CCD frame are identified and a "mask" made that outlines these orders. Problems arise in tracking orders with absorption lines in them and so

the orders are found from the flat field exposures. The orders are straight but not horizontal so a polynomial of order 1 was used to fit them.

7. The orders were extracted and each order collapsed so that it is only one pixel in vertical extent.
8. The image is wavelength calibrated using the Thorium-Argon arc. Three orders on the arc spectrum are chosen and lines identified manually. The lines in other orders are then fitted automatically. This wavelength calibration is then passed to the  $\nu$  Sgr data, again possible due to the extreme stability of the setup.
9. Each order is then extracted, displayed, and any residual blaze function removed by fitting a low order polynomial to the highest points in the spectrum. The orders are then merged to form the full spectrum. Some gaps are unavoidable as the orders do not always overlap.
10. The spectrum is re-binned to a uniform wavelength interval (0.02 Å per pixel) as the echelle data has a varying wavelength interval per pixel as the velocity interval per pixel is fixed in the raw echelle data.

Finally a normalised, re-binned spectrum of  $\nu$  Sgr is obtained.

## 10.4 Extraction

As the echelle orders are not straight on the CCD chip a mask is used to delineate the position of the orders. The mask has to be sufficiently wide to encompass the order but not so wide as to include adjacent orders. However the width of the orders varies over the chip and so the width of the mask is determined by the narrow closely-spaced, blue, orders. With the wider red orders some of the light within the order will fall outside the mask. This leads to slight discontinuities in the output spectrum with jumps of  $\sim 2 - 10\%$  in flux. This first happens at 4423 Å in the spectrum of  $\nu$  Sgr and leads to some extra uncertainty in the measured equivalent widths of spectral lines. This error will still be small in comparison with the uncertainties in the oscillator strengths of the lines. It can be very important when profile fitting and lines so affected should not be used for this purpose.

## 10.5 Cosmic Rays

Cosmic rays hitting the CCD produce a large spike in the image which can be a nuisance depending on their location. For  $\nu$  Sgr with such short exposures they were not considered a great problem but some precautions were taken.

Table 10.2: Measured radial velocity shifts for optical lines of  $\nu$  Sgr.

Line	Wavelength ( $\text{\AA}$ )		Velocity ( $\text{km s}^{-1}$ )
	Rest	Observed	
Ti II	4028.33	4029.36	76.71
Ni II	4067.05	4068.03	72.29
Fe II	4122.64	4123.65	73.50
Sc II	4246.83	4247.84	71.35
Mg II	4481.23	4482.25	68.28
Average = $72.42 \pm 2$			
Heliocentric R.V. correction = -9.21			
Radial Velocity = $63.21 \text{ km s}^{-1}$			

The bias and flat field frames were median filtered. This is possible if all the frames have the same exposure time, and thus approximately the same count per pixel. The median value of each pixel is then used as the final value for the pixel. This removes the spikes due to cosmic rays in a way that is not possible if the frames were just averaged.

A similar procedure is not possible with the  $\nu$  Sgr frames as the exposure times differ greatly. No attempt was made to remove the effects of cosmic ray events other than co-adding the frames to dilute the effect of a given event. Any absorption line affected by a cosmic ray event was not used in any future analysis.

## 10.6 Sky Subtraction

As well as recording light from  $\nu$  Sgr the CCD/UCLES combination records light from the night sky. As  $\nu$  Sgr is very bright with respect to the night sky the fractional contribution of night sky lines to the total signal will be insignificant. No attempt was made to remove this contribution.

## 10.7 Radial Velocity

Before beginning to identify the many lines in the  $\nu$  Sgr spectrum the spectrum has to be shifted to bring these lines to their rest wavelengths. This shift is due to the radial velocity of the  $\nu$  Sgr system as a whole with the orbital velocity of the primary component superimposed. For this purpose 5 prominent lines were identified and velocities determined, Table 10.2.

The mean radial velocity of  $72 \pm 2 \text{ km s}^{-1}$  was corrected for a heliocentric radial velocity of

$-9.21 \text{ km s}^{-1}$  determined using OBSDAT (Dr. P.W. Hill). The final radial velocity of  $63 \pm 2 \text{ km s}^{-1}$  agrees well with the radial velocity curve for  $\nu$  Sgr given in Figure 2.9. The observations are at phase 0.004 where the expected velocity would be  $60.4 \text{ km s}^{-1}$ .

The spectrum was shifted by  $72 \text{ km s}^{-1}$  to bring all the lines to their rest wavelengths.

## 10.8 Line Identifications

The spectrum of  $\nu$  Sgr with all the lines at their rest wavelengths is shown in Figures 10.1 to 10.16 with many lines identified.

The line identifications were primarily from Moore (1945), Wiese, Smith & Glennon (1966) and Wiese, Smith & Miles (1969). Additional multiplets and lines are from the NBS publications (for C,N,O,S). Line lists from previous analyses of  $\nu$  Sgr were used especially those of Hack & Pasinetti (1963) but also Leushin & Topil'skaya (1984) and Greenstein & Adams (1947). Gigas (1986) was used for additional identifications of Fe I and Fe II lines.

All the lines in a multiplet were checked and if the strong ones were all identified then *all* lines of that multiplet have been marked in Figures 10.1 to 10.16 even if the weak ones have not been individually identified in the spectrum.

Blending is a severe problem due to the number of lines and thus equivalent widths are difficult to measure for a lot of the lines. Appendix H gives a list, multiplet by multiplet, of the lines identified while Chapter 11 gives the measured equivalent widths and atomic data (Table 11.1).

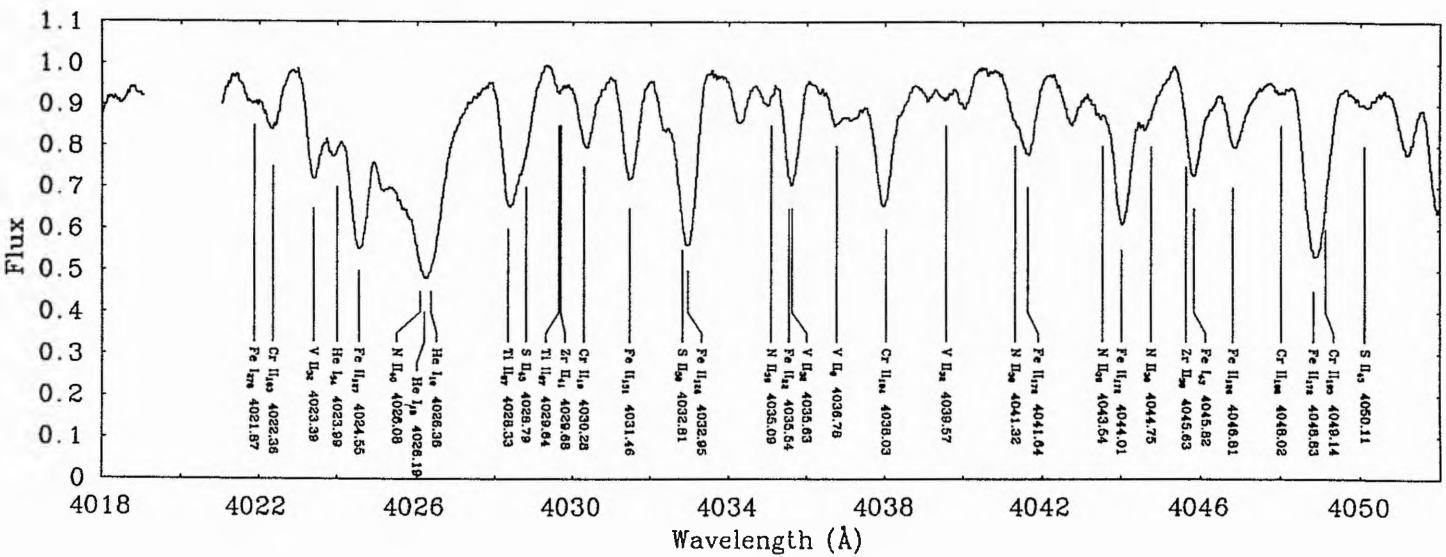
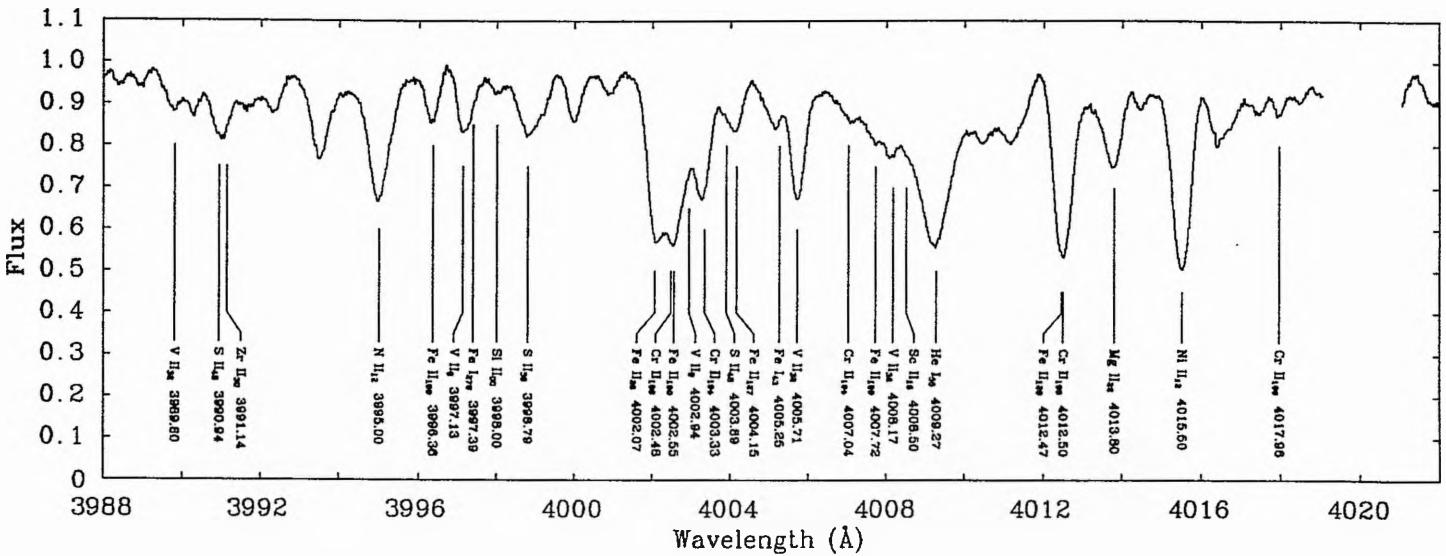


Figure 10.1: The visual spectrum of  $\nu$  Sgr from 3990-4050 Å.

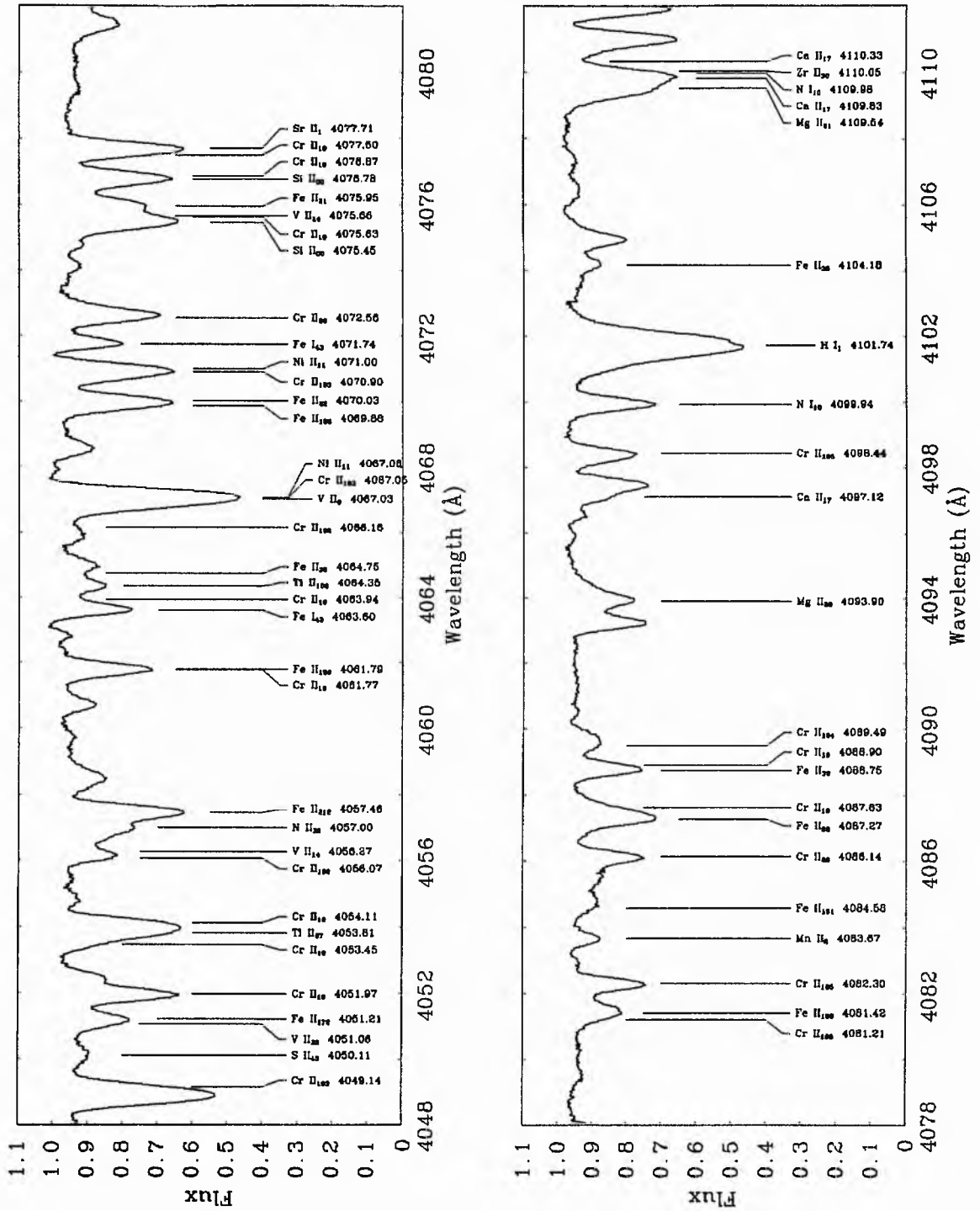


Figure 10.2: The visual spectrum of  $\nu$  Sgr from 4050-4110  $\text{\AA}$ .

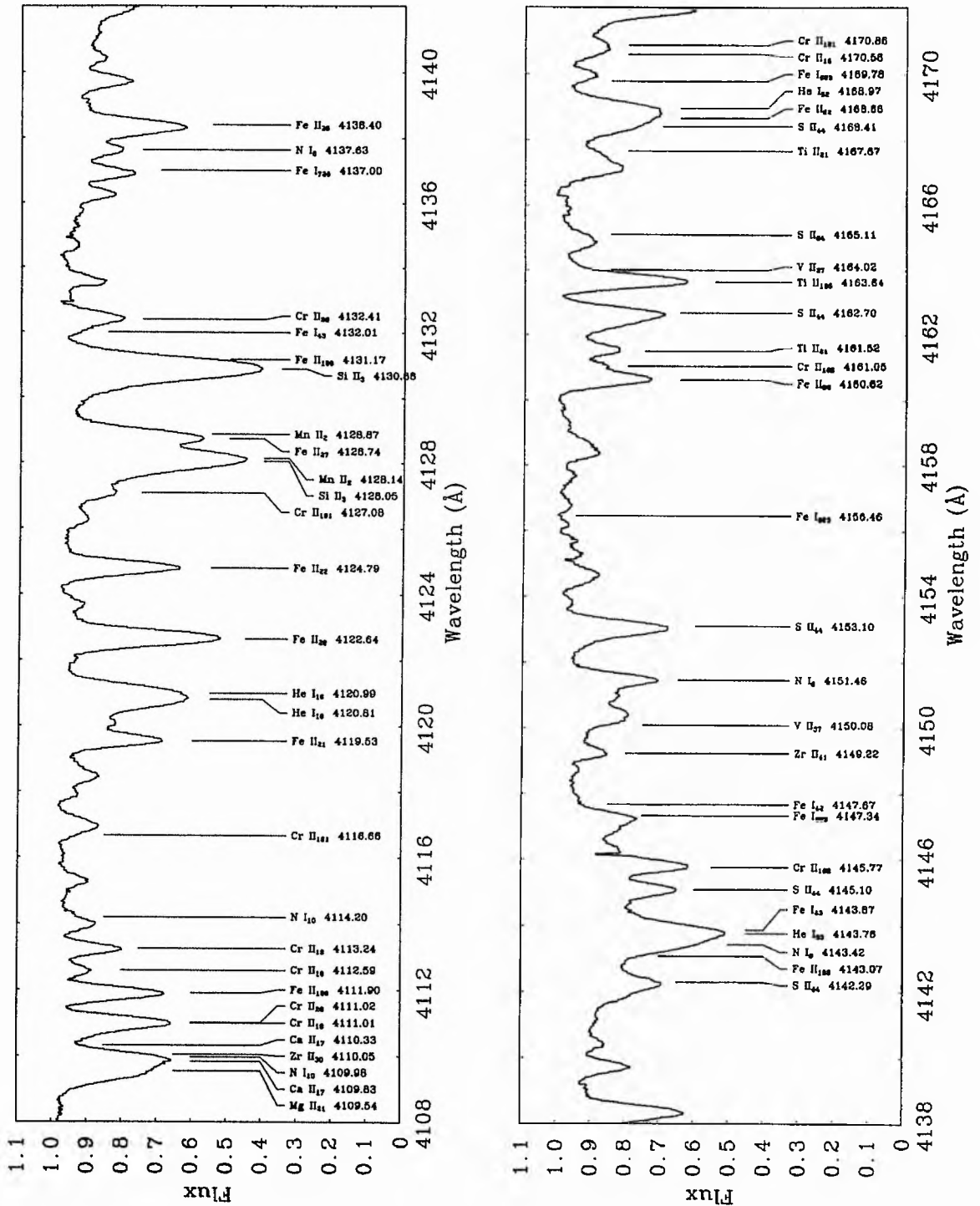


Figure 10.3: The visual spectrum of  $\nu$  Sgr from 4110-4170  $\text{\AA}$ .

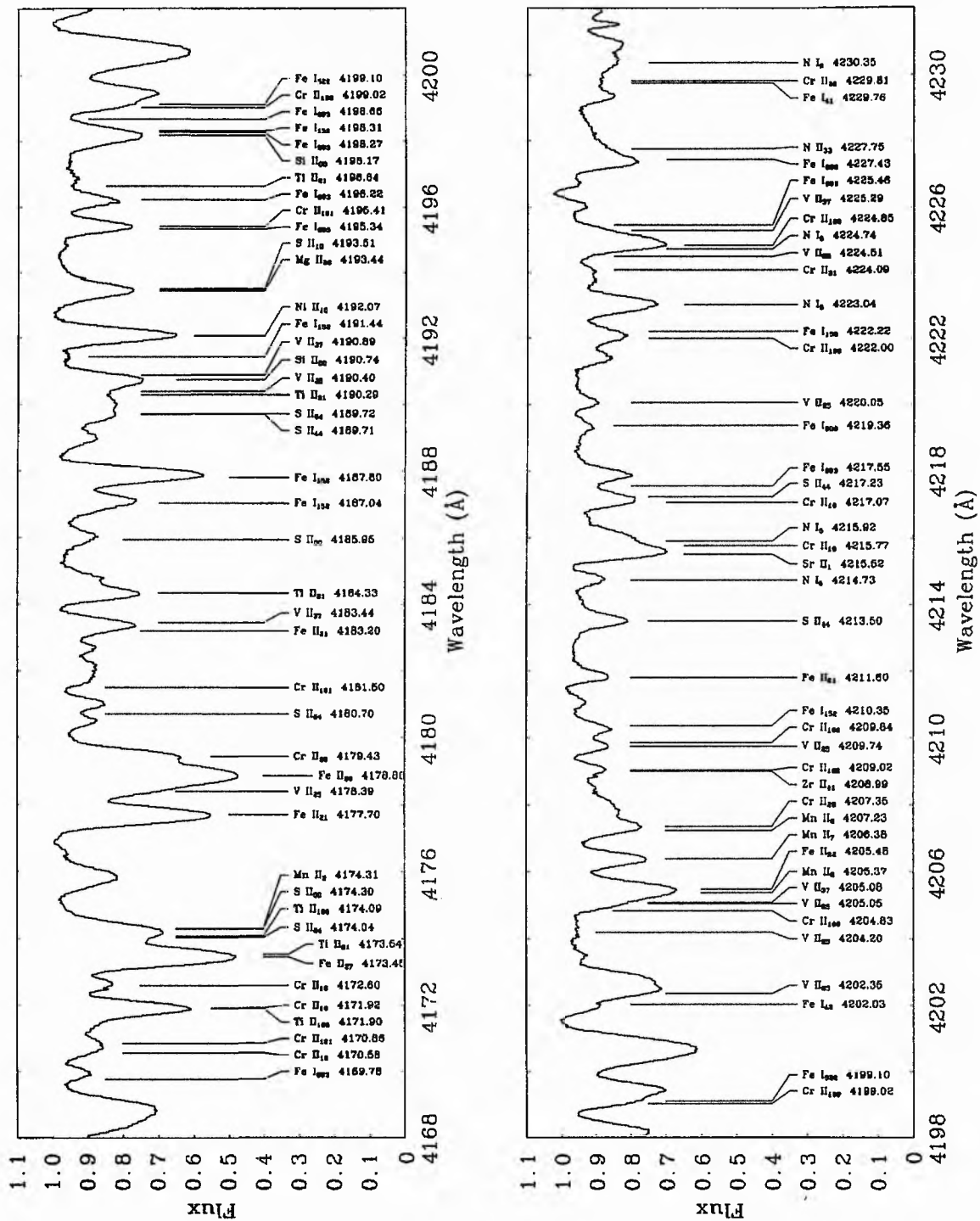


Figure 10.4: The visual spectrum of  $\nu$  Sgr from 4170-4230 Å.



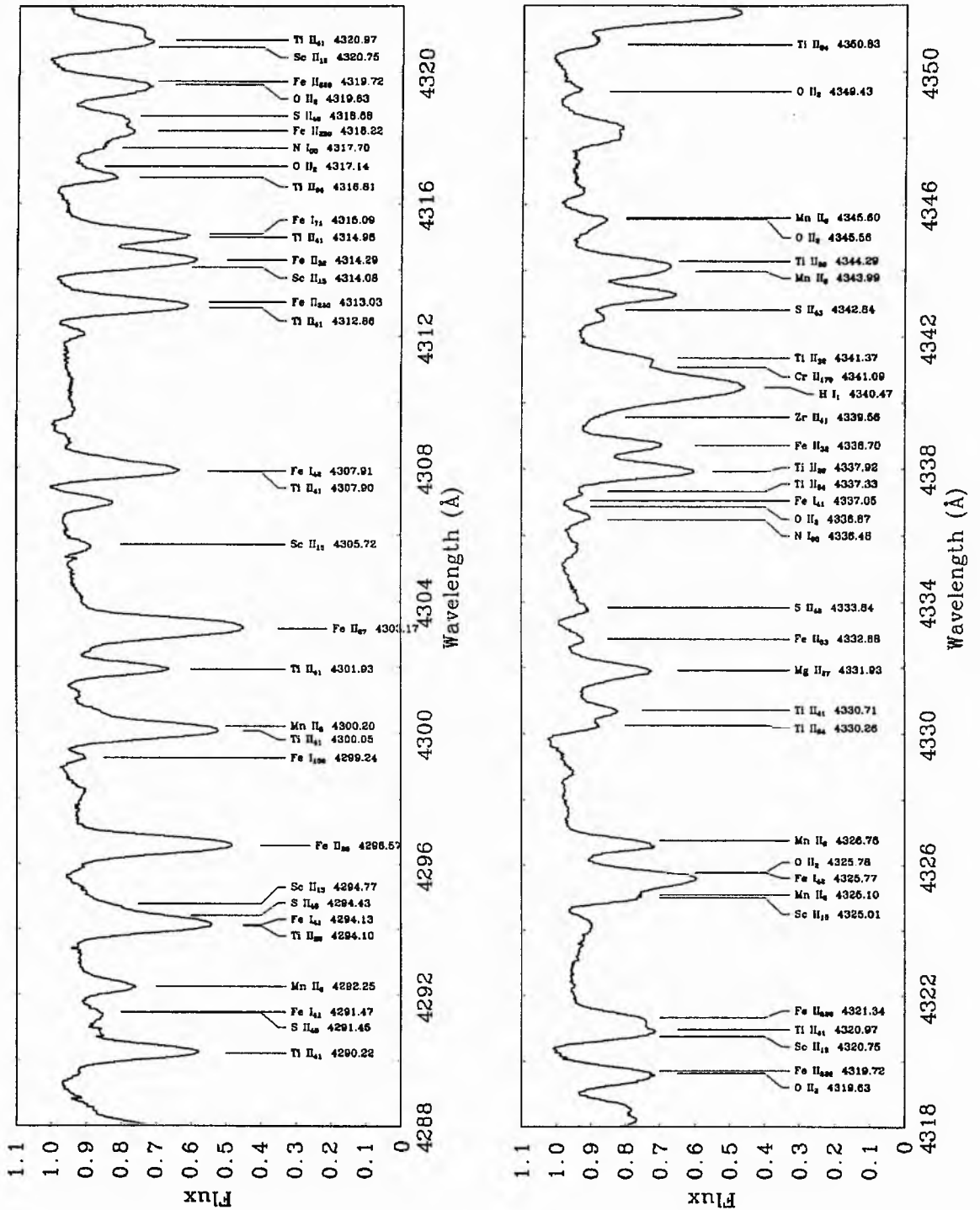


Figure 10.6: The visual spectrum of  $\nu$  Sgr from 4290-4350  $\text{\AA}$ .

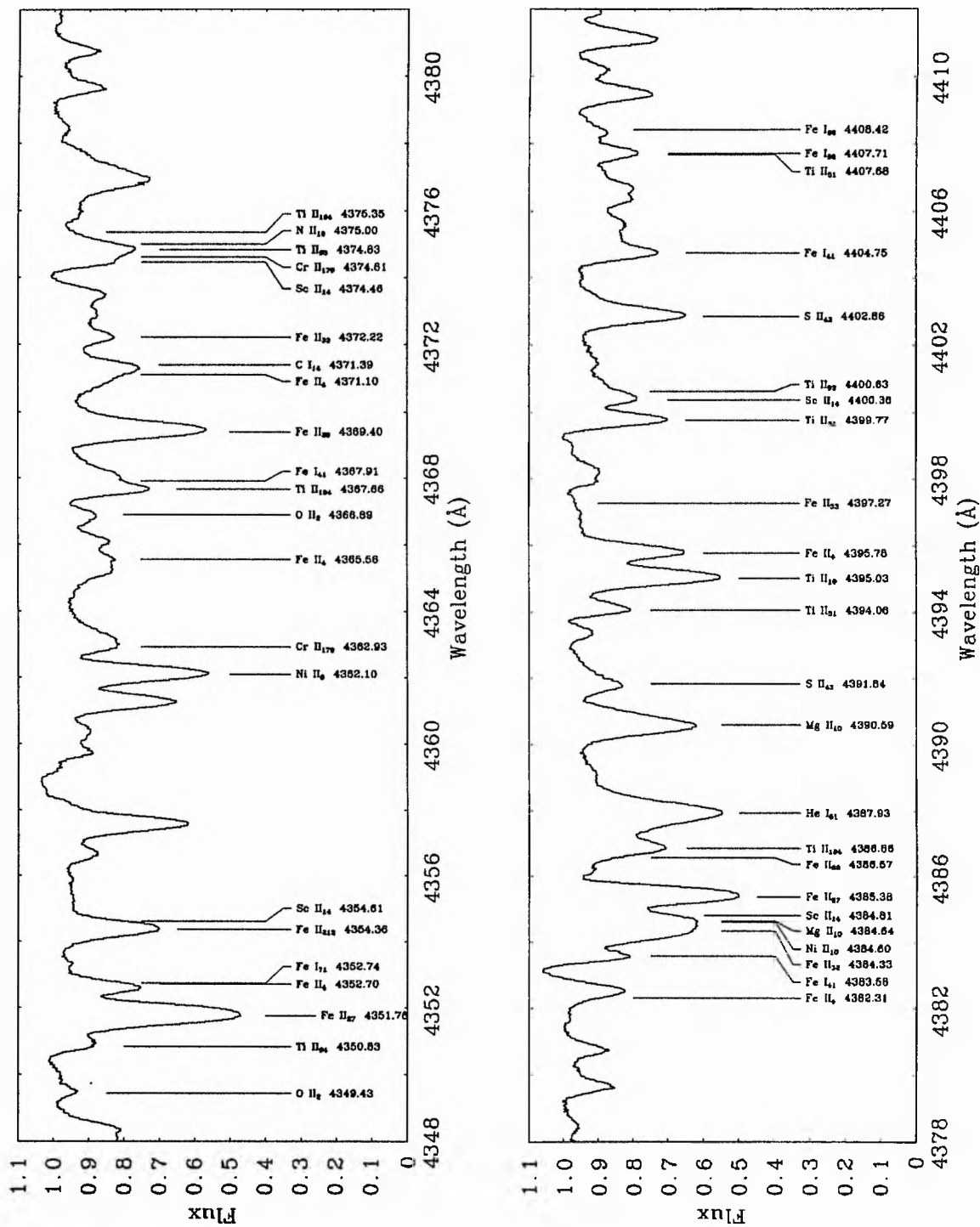


Figure 10.7: The visual spectrum of  $\nu$  Sgr from 4350-4410  $\text{\AA}$ .

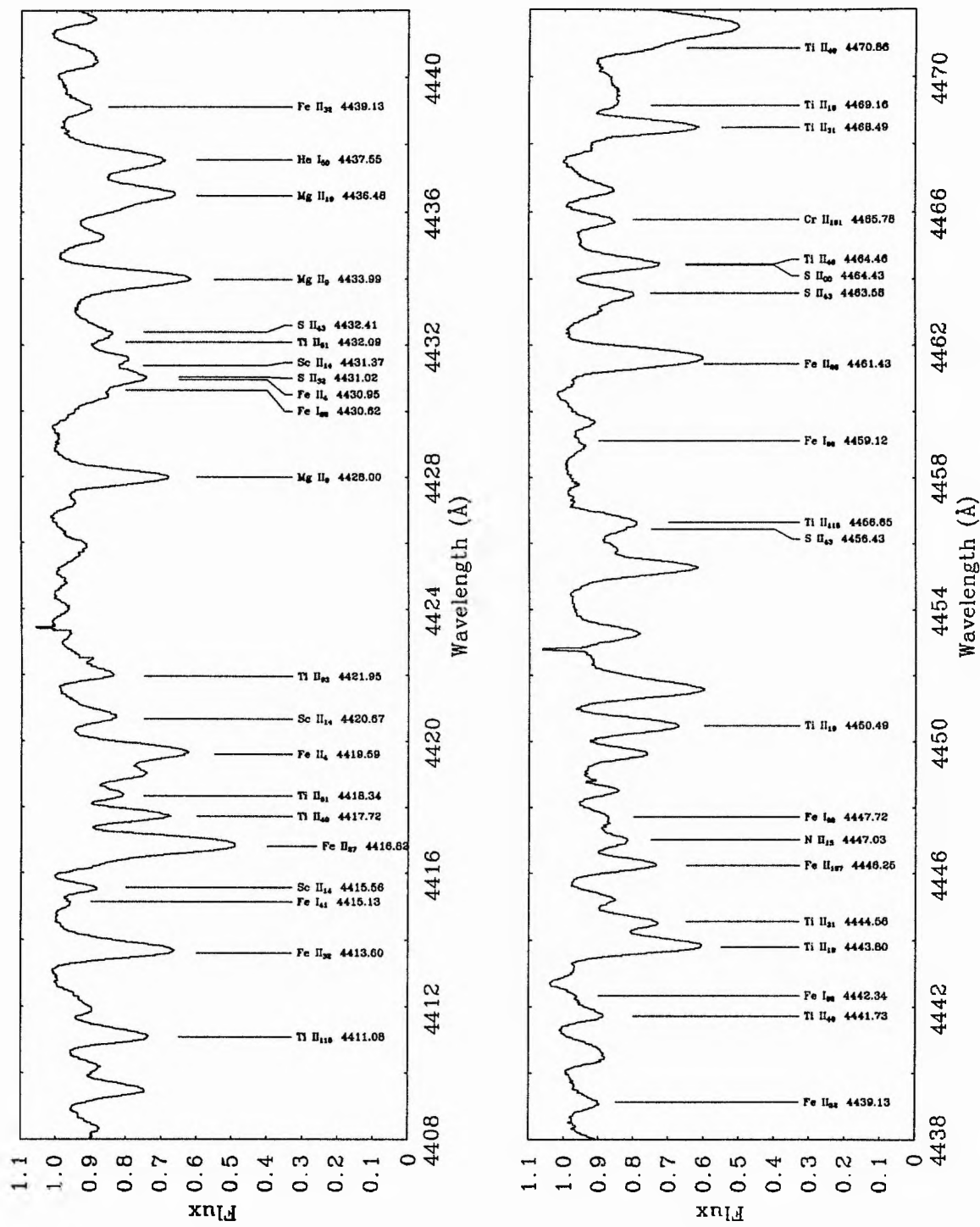


Figure 10.8: The visual spectrum of  $\nu$  Sgr from 4410-4470  $\text{\AA}$ .

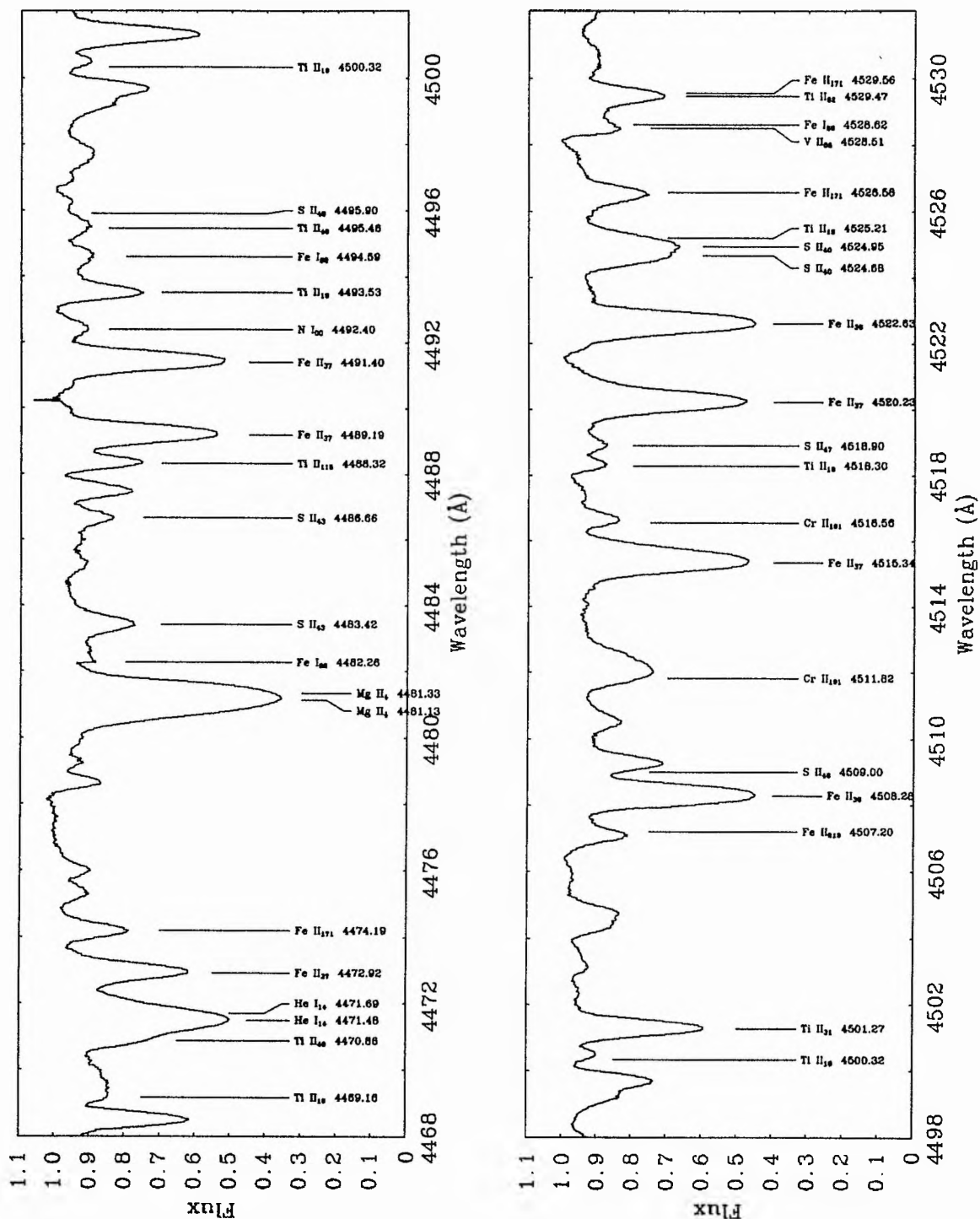


Figure 10.9: The visual spectrum of  $\nu$  Sgr from 4470-4530 Å.

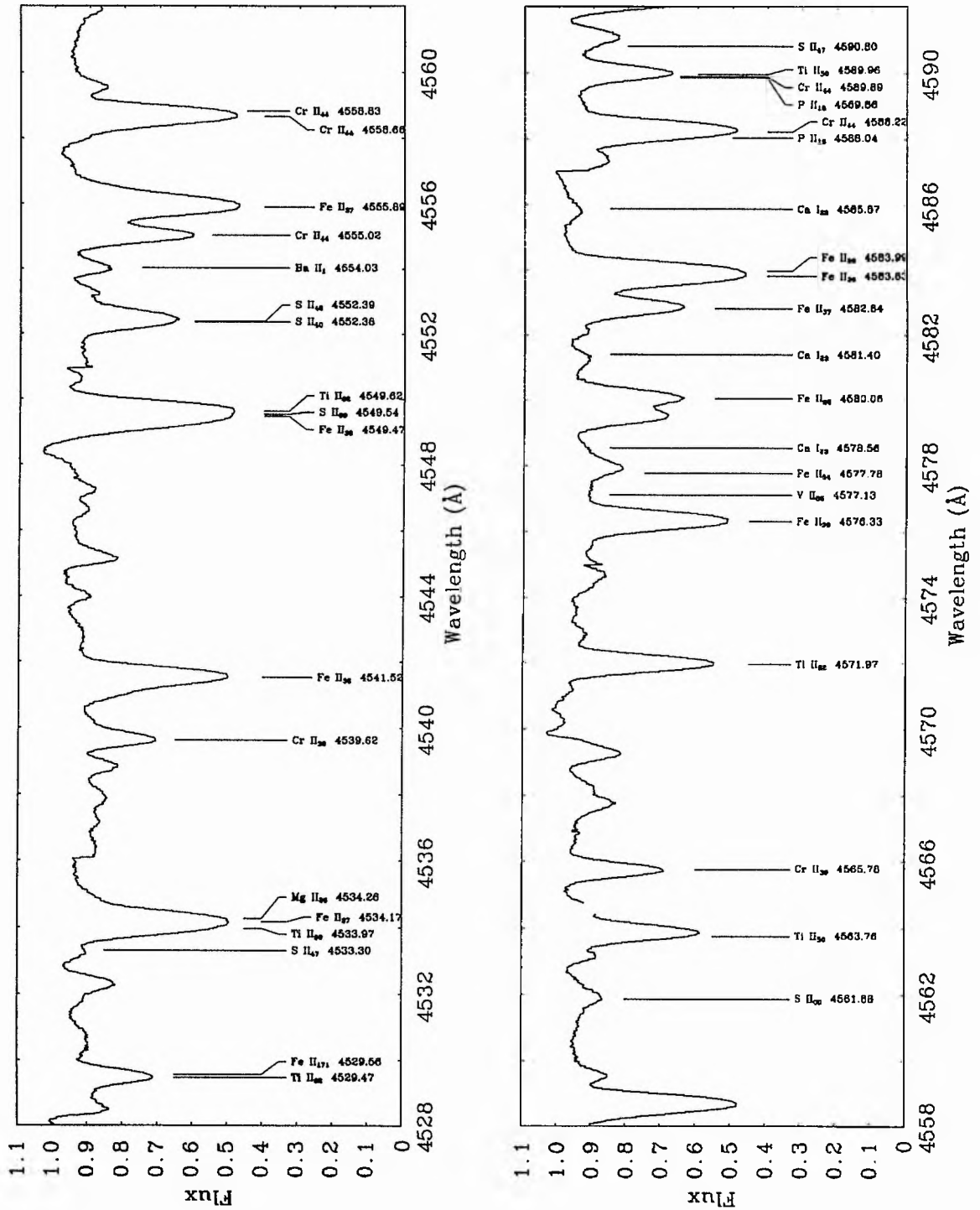


Figure 10.10: The visual spectrum of  $\nu$  Sgr from 4530-4590  $\text{\AA}$ .

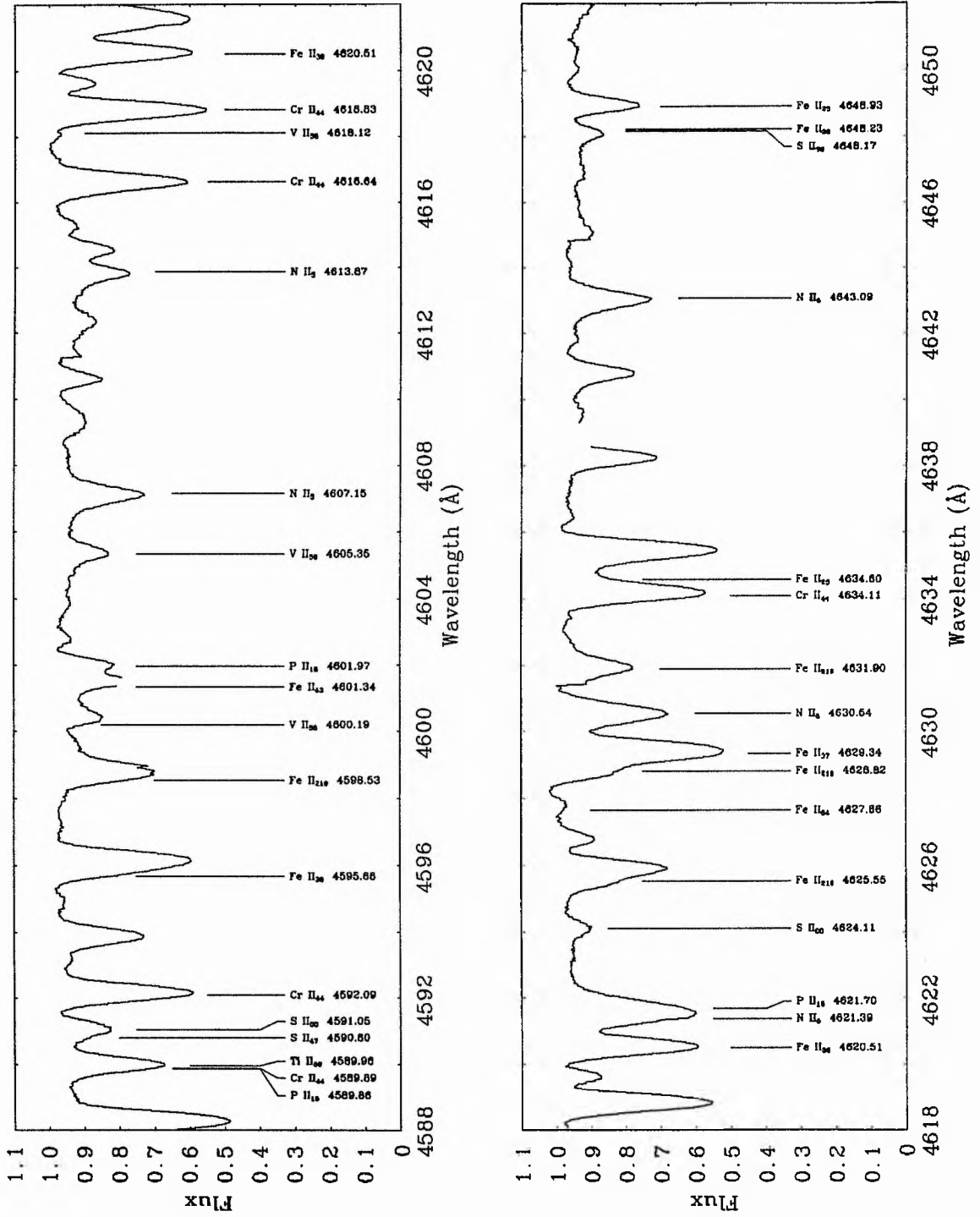


Figure 10.11: The visual spectrum of  $\nu$  Sgr from 4590-4650 Å.

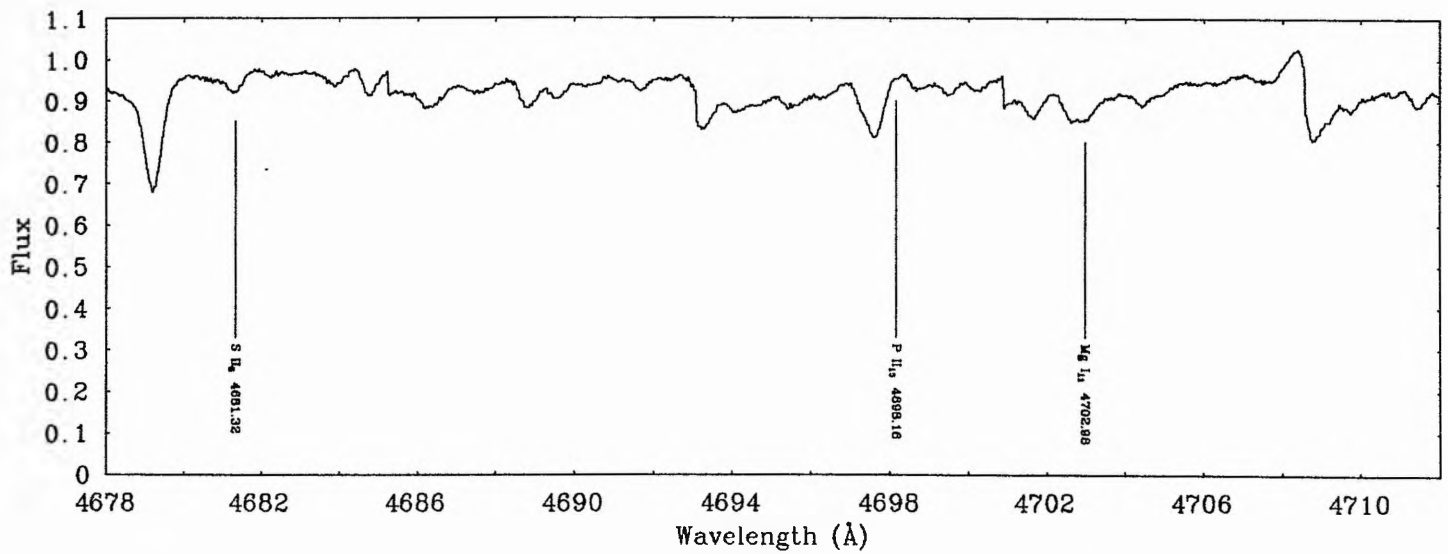
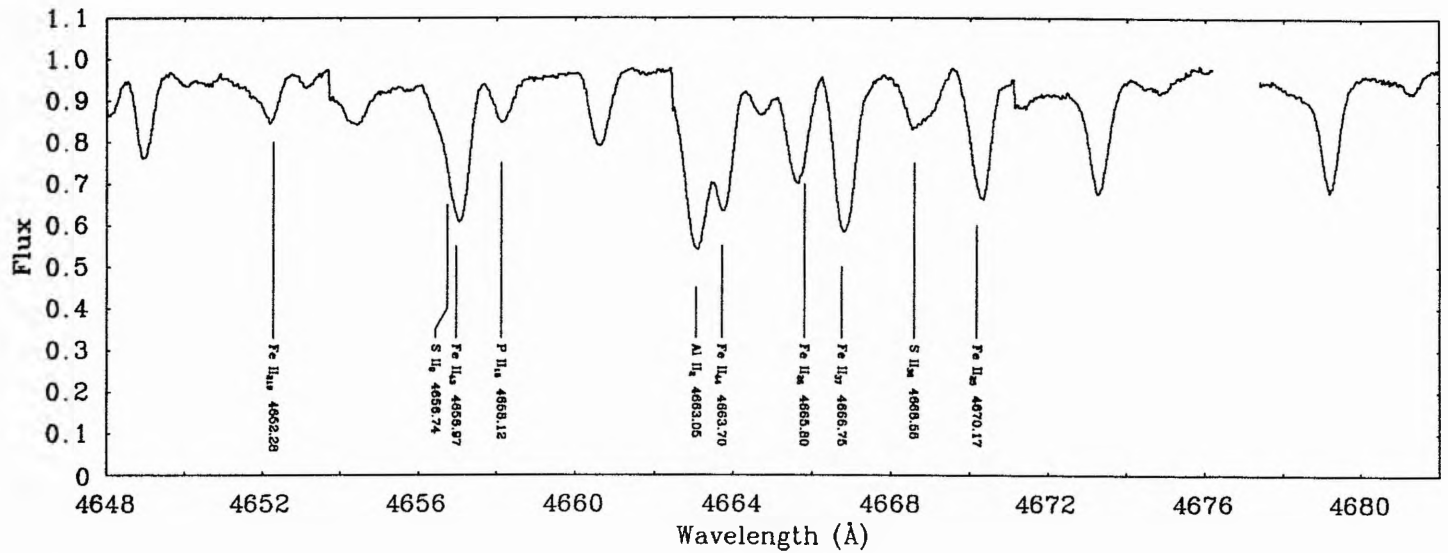


Figure 10.12: The visual spectrum of  $\nu$  Sgr from 4650-4710 Å.

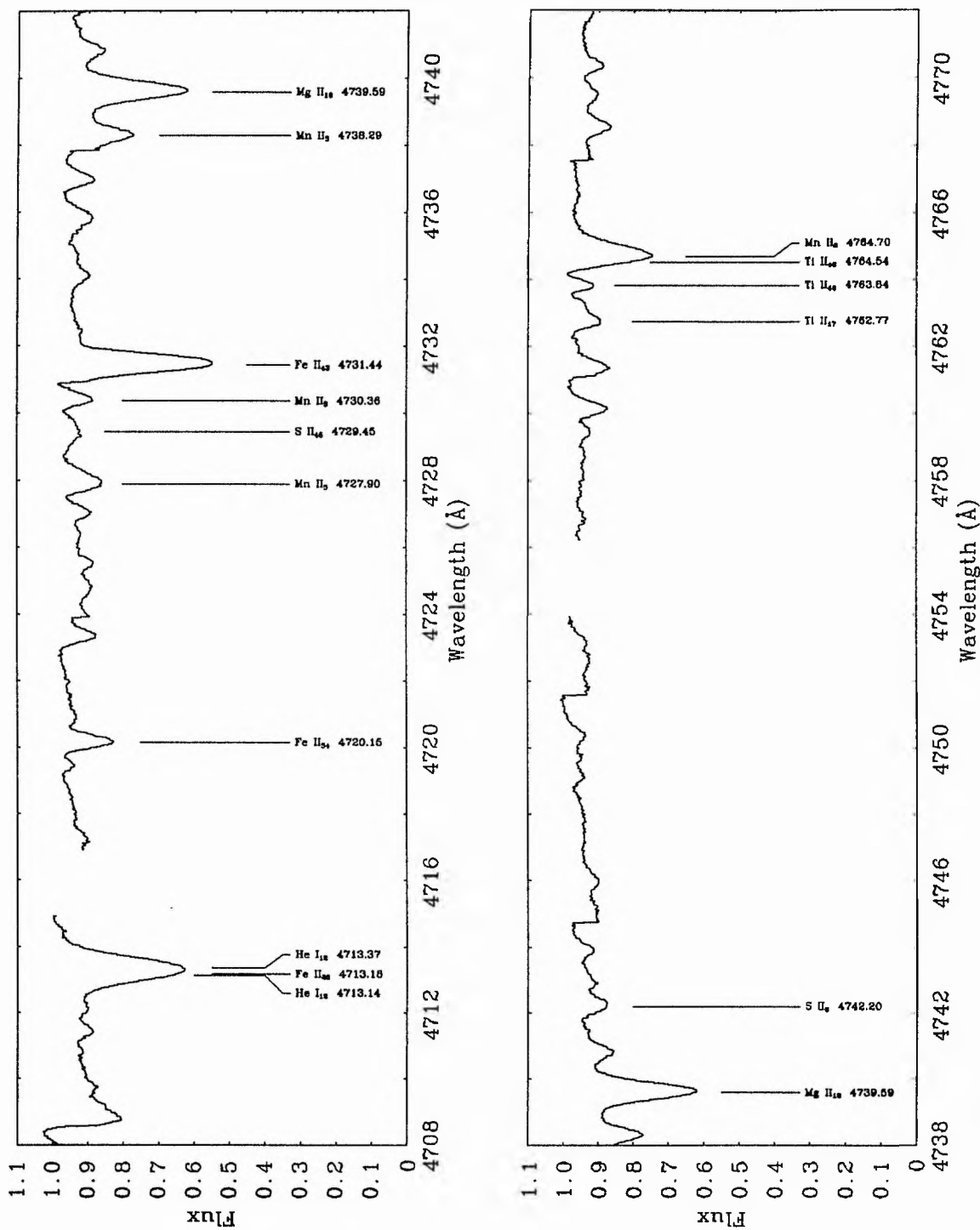


Figure 10.13: The visual spectrum of  $\nu$  Sgr from 4710-4770  $\text{\AA}$ .

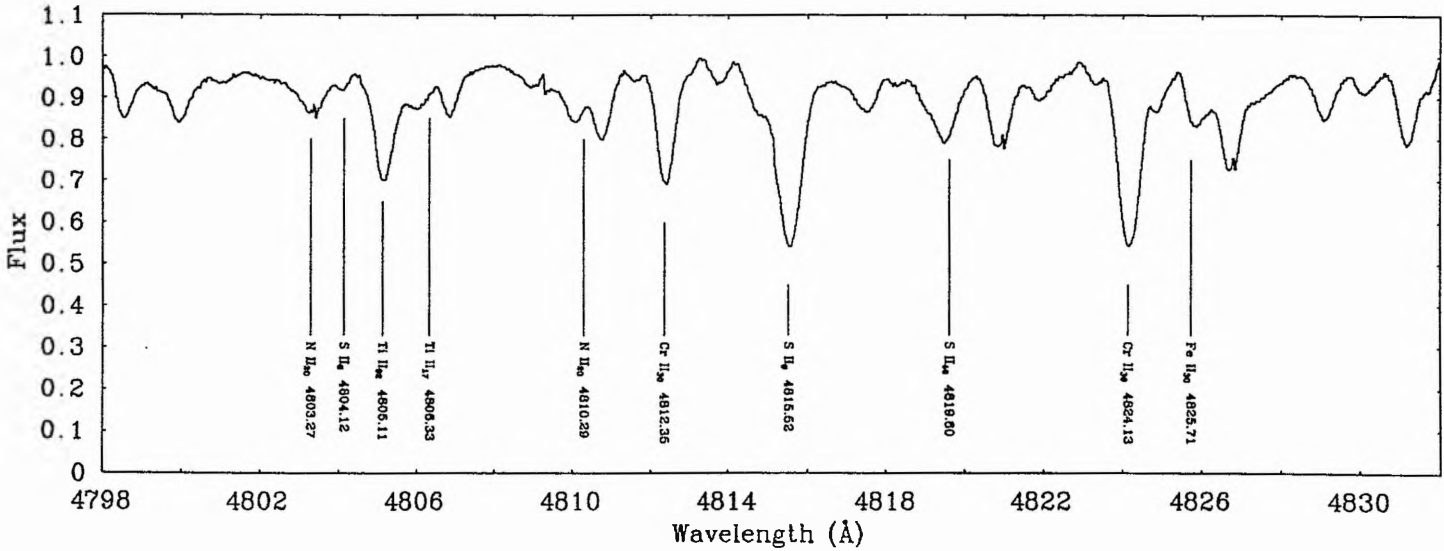
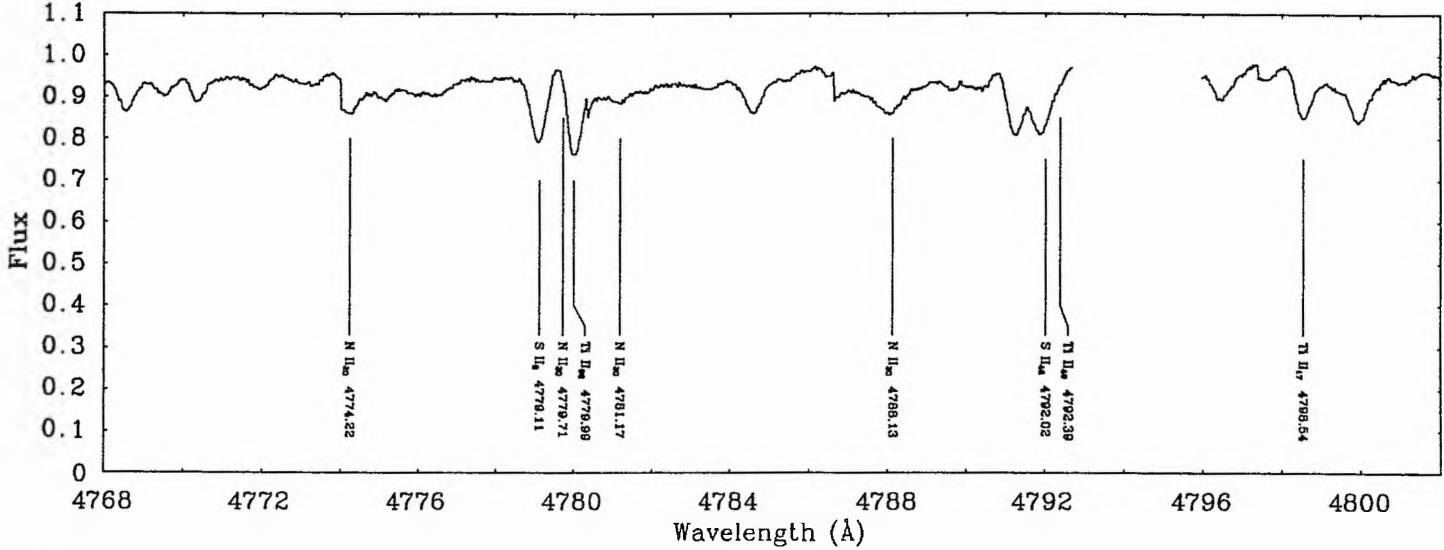


Figure 10.14: The visual spectrum of  $v$  Sgr from 4770-4830 Å.

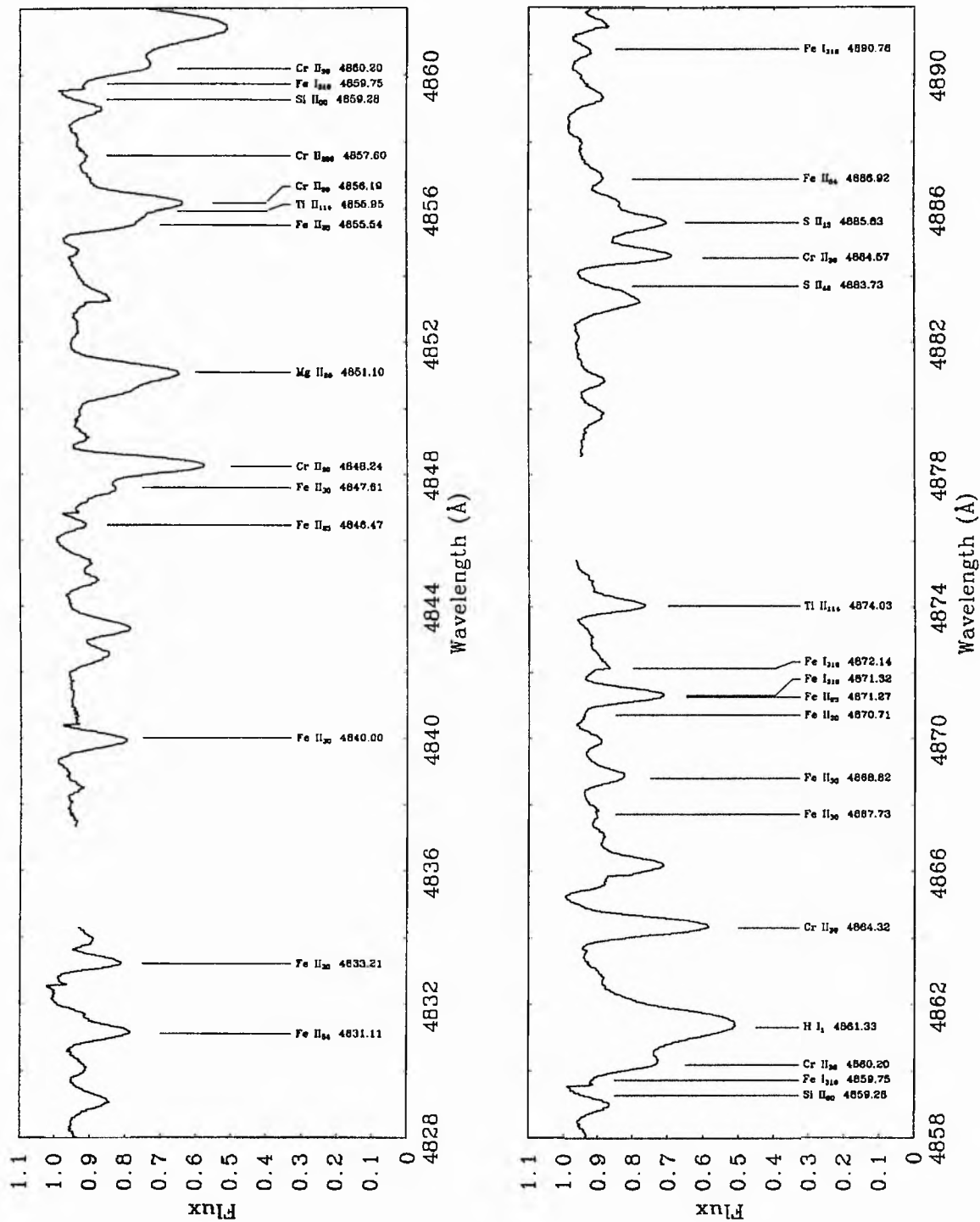


Figure 10.15: The visual spectrum of  $\nu$  Sgr from 4830-4890  $\text{\AA}$ .

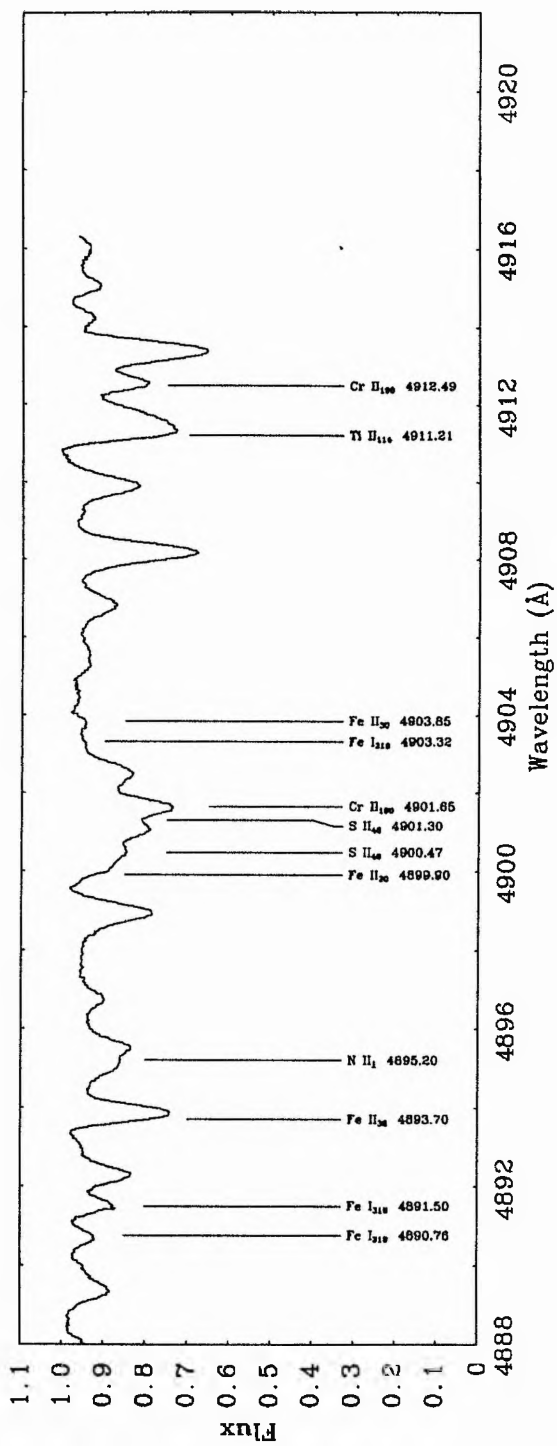


Figure 10.16: The visual spectrum of  $\nu$  Sgr from 4890-4915 Å.

## 10.9 Summary

*Exposures totalling 1000 seconds have been obtained on the Anglo-Australian Telescope using a Thompson CCD and UCLES echelle spectrograph. The resulting blue spectrum (3990-4915 Å) is the highest resolution, highest signal to noise ratio spectrum of  $\nu$  Sgr ever obtained. The quality of this data will allow the temperature, surface gravity and composition of the primary component to be determined with much greater accuracy than ever before.*

*A further radial velocity point for the primary was determined in good agreement with the previously determined orbit.*

*Over 500 line identifications have been made.*

## 10.10 References

Gigas, D., 1986. *Astr. Astrophys.*, **165**, 170.

Greenstein, J.L. & Adams, W.S., 1947. *Astrophys. J.*, **106**, 339.

Hack, M. & Pasinetti, L., 1963. *Contr. Oss. astr. Milano-Merate*, **215**, 1.

Howarth, I.D. & Murray, J., 1991. *STARLINK User Note 50.13*.

Leushin, V.V. & Topil'skaya, G.P., 1984. *Astrophysics*, **22**, 121.

Moore, C.E., 1945. *A Multiplet Table of Astrophysical Interest*, Princeton.

Shortridge, K., 1986. *FIGARO Users Guide*.

Wiese, W.L., Smith M.W. & Glennon, B.M., 1966. *Atomic Transition Probabilities*, NBS, Washington.

Wiese, W.L., Smith M.W. & Miles, B.M., 1969. *Atomic Transition Probabilities*, NBS, Washington.

## Chapter 11

# A Spectroscopic Fine Analysis of $\nu$ Sgr

### 11.1 Introduction

Atmospheric fine analyses have been carried out twice before on the primary component of  $\nu$  Sgr in a effort to determine the temperature, surface gravity and composition. Hack & Pasinetti (1963) determined that the atmosphere could be modelled in two layers one with  $T=8000\text{K}$  and the other  $T=12,800\text{K}$ , with different lines being formed in the different layers. Hydrogen deficiency by a factor of 200 was found while carbon and nitrogen were determined to be overabundant by factors of 4 and 60 respectively.

In a series of papers, Leushin & Topil'skaya (1984, 1987, 1988a,b) obtained a model for the primary of  $\nu$  Sgr and derived a surface composition. They determine that two models give the best fit to the observations; a  $13,500\text{K}$ ,  $\log g = 1.5$  model and a  $14,000\text{K}$   $\log g = 2.0$  model. The former has 95% He and 5% metals, the latter 70% He and 30% metals. Both models have 0.0001% hydrogen. For the abundance analysis the former model was used.

In view of these conflicting results it is necessary to undertake a fine analysis using high signal to noise CCD spectrograph data, rather than the photographic data used in the other two analyses, and to use line-blanketed hydrogen-deficient model atmospheres.

Although the temperature has been determined from the flux distribution (Chapter 8) and a minimum value of the surface gravity from the orbital analysis (Chapter 2) the fine analysis will allow independent determinations of these values as well as for the surface composition.

The basis of this analysis is the standard fine analysis technique, given in outline in Appendix H.

## 11.2 Equivalent Widths

The equivalent widths (EW) of unblended or slightly blended lines were measured with the Emission Line Fitting (ELF) package within DIPSO (Howarth & Murray 1991).

After the spectrum was normalised, a Gaussian profile was fitted to the line using a least squares procedure to find the best values for line center, width and depth. The equivalent width is then just the area enclosed by the Gaussian profile and the continuum level. For blended lines where the individual components could be distinguished, fitting with multiple Gaussians was used.

The equivalent widths and atomic data used are given in Table 11.1

Table 11.1: Measured equivalent widths and atomic data for lines in the spectrum of  $\nu$  Sgr. Errors are typically 20%.

Ion	Mult.	Wavelength	EW (m Å)	log gf	Ref.
AlII	2	4663.05	395	-0.30	Wie69
CII	6	4267.02	294	0.56	Yan87
CrII	18	4113.24	90	-2.74	MFW88
	30	4824.13	328	-1.22	MFW88
		4812.35	187	-1.80	MFW88
	39	4539.62	211	-2.53	MFW88
		4565.78	174	-2.11	MFW88
	44	4618.63	280	-1.11	MFW88
		4555.02	261	-1.38	MFW88
FeI	43	4045.82	137±5	+0.28	Bla80
	43	4063.60	99±7	+0.07	FMW88
	43	4071.74	82±22	-0.02	Bla80
	152	4187.04	158±39	-0.55	Bla82
	152	4187.80	246±52	-0.55	Bla82
	42	4271.76	134±6	-0.16	Bla80
	71	4282.41	218±8	-0.81	FMW88
	41	4383.55	96±68	+0.20	Bla80
	41	4404.75	183±74	-0.14	Bla80
	68	4494.59	98±6	-1.14	Bla82
	318	4891.50	69±22	-0.14	FMW88
FeII	188	4111.90	162±9	-2.47	Heb83
	28	4122.64	305±31	-3.38	FMW88
	22	4124.79	194±17	-4.20	Bla80
	21	4177.70	296±68	-3.48	Heb83
	28	4178.86	579±11	-2.48	FMW88
	27	4273.32	297±51	-3.34	FMW88
	28	4296.57	376±80	-3.01	FMW88
	27	4303.17	458±13	-2.49	FMW88
	27	4385.38	350±92	-2.57	FMW88
	32	4413.60	203±63	-3.87	Bla80
	27	4416.82	401±88	-2.60	FMW88
	37	4491.40	337±69	-2.70	FMW88
	38	4508.28	444±103	-2.21	FMW88
	37	4515.34	493±101	-2.48	FMW88
	37	4520.23	434±98	-2.60	FMW88
	38	4522.85	451±103	-2.03	FMW88
	38	4541.52	405±106	-3.10	Moi83
	37	4555.89	488±99	-2.29	FMW88
	38	4576.33	368±50	-3.09	Moi83
	37	4582.84	263±61	-3.10	FMW88
	38	4620.51	261±44	-3.28	FMW88
	37	4666.75	286±37	-3.38	Moi83
	43	4731.44	327±36	-3.41	Moi83

Table 11.1: *continued.*

Ion	Mult.	Wavelength	EW (mÅ)	log gf	Ref.
Fe III	4	4419.59	271±44	-2.33	KP75
	4	4395.78	218±53	-2.71	KP75
H I	1	4101.74	545±16	-2.43	<i>e.g.</i> All73
	1	4340.47	661±254	-2.14	<i>e.g.</i> All73
	1	4861.33	726±21	-1.74	<i>e.g.</i> All73
He I	12	4713.14	357±63		
	12	4713.37			
	14	4471.48	594±17		
	14	4471.68			
	16	4120.81	367±71	-1.97	TayOP
	16	4120.99		-1.07	TayOP
	18	4026.19	789±36		
	18	4026.36			
	50	4437.55	249±38	-2.02	TayOP
51	4387.93	489±192			
Mg II	4	4481.13	779	0.57	Wie69
	4	4481.33		0.73	Wie69
	9	4428.00	186	-1.20	Wie69
		4433.99	256	-0.90	Wie69
	10	4390.59	305	-0.53	Wie 69
Ni	5	4223.04	184	-1.09	Wie66
		4214.73	63	-1.45	Wie66
	6	4151.46	175	0.19	Wie66
		4137.63	126	0.06	Wie66
	10	4099.94	147	0.46	Wie66
N II	5	4630.54	239	0.09	Bec89
		4613.87	158	-0.61	Bec89
		4643.09	201	-0.39	Bec89
		4607.15	207	-0.48	Bec89
	12	3995.00	237	0.23	Bec89
	15	4447.03	126	0.24	Bec89
O II	2	4349.43	27	0.06	Bec88
P II	15	4601.97	106	0.74	Wie 69
		4658.12	112	-0.31	Wie 69
S II	8	4779.11	123	-1.65	Wie69
	9	4815.52	380	-0.05	Wie69
	43	4483.42	168	-0.43	Wie69
		4402.86	224	-1.27	Wie69
	44	4162.70	212	0.78	Wie69
		4153.10	196	0.62	Wie69
		4145.10	263	0.44	Wie69
		4213.50	106	-1.30	Wie69
	49	4267.80	281	0.28	Wie69

Table 11.1: *continued.*

Ion	Mult.	Wavelength	EW (mÅ)	log gf	Ref.
Sc II	7	4246.83	209	0.32	MFW88
Si II	3	4130.88	557	0.55	Bec90
Ti II	18	4493.53	127	-2.41	Sav 90
	19	4395.03	296	-0.43	Sav 90
		4443.80	244	-0.70	Sav 90
		4450.49	197	-1.45	Sav 90
	20	4337.92	256	-0.88	Sav 90
		4287.89	183	-1.68	RAS 73
	21	4161.52	100	-2.00	Sav 90
		4184.33	131	-1.44	Sav 90
	31	4468.49	223	-0.60	Sav 90
		4501.27	248	-0.75	Sav 90
	40	4417.72	172	-1.20	Sav 90
		41	4290.22	262	-0.87
			4301.93	175	-1.16
		4307.90	231	-1.04	Sav 90
	50	4563.76	273	-0.94	Sav 90
	51	4399.77	152	-1.27	Sav 90
		4394.06	97	-1.59	Sav 90
82	4571.97	289	-0.52	Sav 90	
94	4316.81	87	-1.52	War 67	
105	4163.64	197	-0.24	Sav 90	
106	4064.35	90	-1.67	War 67	
115	4411.08	163	-0.28	Sav 90	
V II	25	4220.05	57	-0.52	Bie 89
	32	4023.39	134	-0.69	Bie 89

References: All73: Allen (1973); Bec88: Becker & Butler (1988); Bec89: Becker & Butler (1989); Bec90: Becker & Butler (1990); Bla80: Blackwell, Petford, Shallis & Simmons (1980); Bla82: Blackwell, Petford, Shallis & Simmons (1982); FMW88: Fuhr, Martin & Wiese (1988); Heb83: Heber (1983); KP75: Kurucz & Petryeman (1975); MFW88: Martin, Fuhr & Wiese (1988); Moi83: Moity (1983) adjusted according to Gigas (1986); RAS73: Roberts, Andersen & Sørensen (1973); Sav90: Savanov, Huovelin & Tuominen (1990) TayOP: Taylor *et al.* (Opacity Project, private communication); War67: Warner (1967); Wie66: Wiese, Smith & Glennon (1966); Wie69: Wiese, Smith & Miles (1969) .

### 11.3 The Models

All the models used for this analysis were generated by STERNE. In the form used it is a LTE line-blanketed, hydrogen-deficient model atmosphere code. The models are referred to as TttGgg where tt is the temperature of the star in thousands of Kelvin and gg is ten times the logarithm of the surface gravity (c.g.s.).

Initially a coarse grid of models covering a wide range of temperatures and surface gravities was generated with a composition that is close to the expected one. The temperature, gravity and composition was then determined with some accuracy from these models and the observed profiles and equivalent widths. A further set of models were then determined with an improved composition. It is these models (the N02 series) that were used in the analysis detailed below.

These models were then input into SPECTRUM which generates theoretical LTE line profiles. In this treatment the source function includes the scattering integral but does not solve the rate equations to determine the level populations. A Boltzmann distribution is assumed. This treatment is referred to as LTE with scattering (LTE<sub>S</sub>).

Details of the initial model grid are given in Table 11.2.

Table 11.2: The model grid for the fine analysis of  $\nu$  Sgr.

Temperature (K)	log g							
	3.0	2.5	2.0	1.7	1.5	1.3	1.2	1.0
6,000						X		X
7,000						X		X
8,000	X	X	X		X			X
10,000	X	X	X		X			X
11,000	X	X	X		X			X
11,500						X		
11,800	X	X	X		X	X		X
12,000	X	X	X		X			X
12,500						X		
13,000	X	X	X		X	X	X	
14,000	X	X	X		X			
15,000	X	X	X	X				
16,000	X	X	X	X				

## 11.4 Microturbulent and Rotational Velocities

Before attempting to determine the temperature by using a curve of growth analysis or line profile fitting it is necessary to determine both the microturbulent and rotational velocities.

### 11.4.1 Microturbulent velocity

Microturbulence is due to random turbulent motions in the line forming region of the star. Once just used as a fitting factor there now seems to be some definite turbulent velocities in stars although the turbulences determined from model atmospheres are somewhat larger than this.

The effect of this turbulence is to broaden the emergent line profiles and to increase their EW's. Any modelling that requires accurate theoretical EW's, such as temperature determination from a curve of growth analysis, requires a pre-determination of this velocity.

To determine the microturbulent velocity the criterion used is that for the correct value of the turbulent velocity the derived abundance should be independent of the line strength. Difficulties arise as for the best fits (least scatter) the lines need to be on the linear part of the curve of growth (CoG). However the lines are often too strong (especially Fe II and Fe III) and lie on the flat part of the CoG thus increasing the scatter as, for a given observed EW there is a range of abundances that can lead to that EW. Dufton, Durrant & Durrant (1981) indicate that this method gives rise to turbulent velocities that are  $1\text{-}2\text{ km s}^{-1}$  too high for good spectroscopic data.

The model used for this analysis was a T12g15 one that agrees with the gravity determined in Chapter 2 and the temperature from Chapter 8. The exact choice of model is not critical. To obtain the most accurate results models were run with LTE<sub>S</sub> radiative transfer as well as the LTE transfer. The results for  $v_t = 20, 10, 9, 8, 7, 6, 5$  and  $4\text{ km s}^{-1}$  are shown in Figure 11.1. A value of  $v_t = 8 \pm 2\text{ km s}^{-1}$  was judged to fit the data best in good agreement with  $8\text{ km s}^{-1}$  from Mg II lines (Hack & Pasinetti 1963) and  $7.1\text{ km s}^{-1}$  (Leushin & Topil'skaya 1988a).

### 11.4.2 Rotational velocity

Stellar rotation has the effect of broadening the spectral lines of a star but does not affect the EW's of the lines. The broadening of the lines is compensated by a reduction in depth. Such rotation has no effect on a curve of growth analysis but will affect line profile fitting as used, for example, in gravity determination.

From Chapter 2 the radius of the primary was found to be  $60 R_{\odot}$  assuming it is filling it's

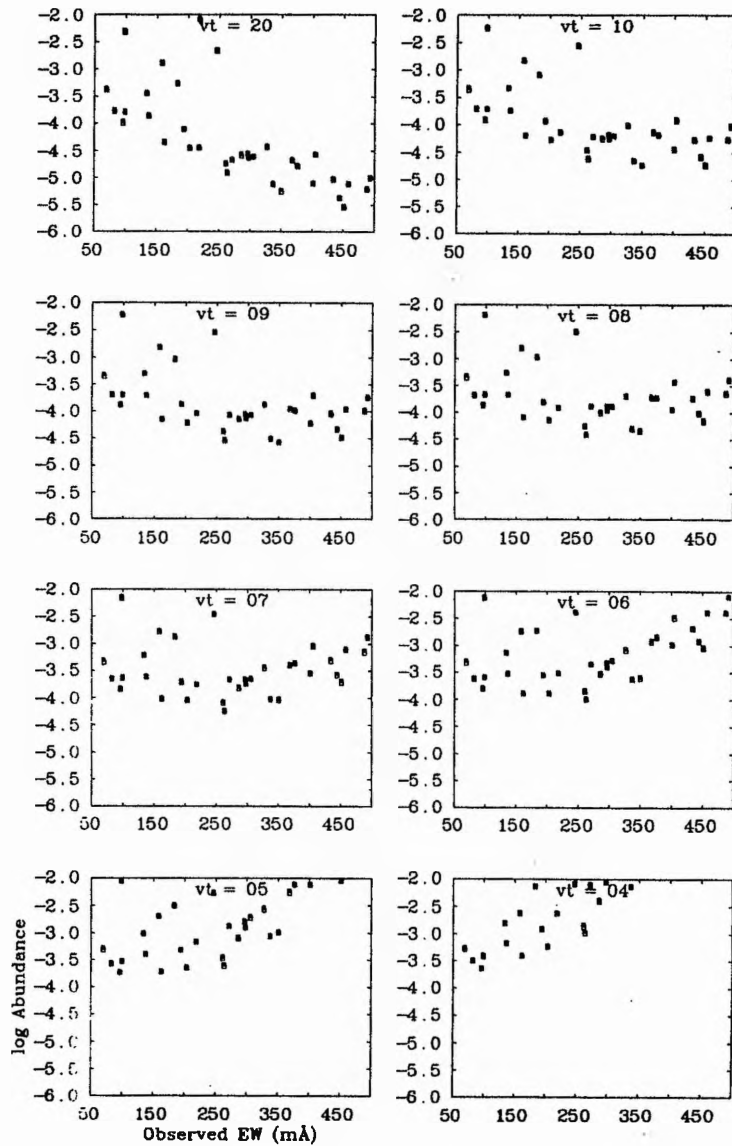


Figure 11.1: Iron abundance vs. equivalent width for  $v$  Sgr to determine the microturbulent velocity. Filled squares are for LTE radiative transfer, open squares for the  $LTE_S$  radiative transfer. A T12G15 model was used.

Roche lobe. Due to the effect of mass transfer synchronising the orbital period (138 days) with the rotational period the rotational velocity is then  $22 \text{ km s}^{-1}$  if the Earth lies in the rotational plane, *i.e.* if the inclination is  $90^\circ$ . From the discussion of the Roche Lobe and eclipse geometry the inclination must be between  $56^\circ$  and  $78^\circ$ . Thus the line of sight velocity,  $v \sin i$ , is between  $18.2$  and  $21.5 \text{ km s}^{-1}$  as determined by the orbital analysis.

To use this value for the atmospheric modelling then the results of this Chapter and Chapter 2 are tied together. An independent confirmation of the rotational velocity would both strengthen the orbital analysis and give extra weight to the results of the atmospheric modelling.

The narrowest Fe II lines are used for the determination of the rotational velocity. Figure 11.2 shows the results for the  $4273 \text{ \AA}$  line; other lines show similar results. The heavy line is the observed Fe II  $4273 \text{ \AA}$  profile while the light lines are theoretical profiles from a  $12,000\text{K}$ ,  $\log g = 1.5$  model. The abundance used for the modelling was chosen to reproduce the observed EW. Rotational velocities from  $0 \text{ km s}^{-1}$  to  $30 \text{ km s}^{-1}$  in steps of  $5 \text{ km s}^{-1}$  are shown with the  $0 \text{ km s}^{-1}$  model having the steepest wings. The line core has an irregular profile due to problems with the modelling. However the line wings are well fitted with a rotational velocity of  $25 \pm 5 \text{ km s}^{-1}$ . Instrumental broadening will only have a small effect and so a value of  $25 \text{ km s}^{-1}$  has been adopted for the future analysis. If the orbital period and rotational period are synchronised then, if the primary is not filling its Roche lobe, a rotational velocity of  $\lesssim 20 \text{ km s}^{-1}$  would be expected. As the determined rotational velocity is larger than this a Roche lobe filling primary is strongly indicated. The observed rotational velocity then constrains the inclination to be  $i > 65^\circ$ .

## 11.5 Temperature Determination

### 11.5.1 Iron lines

Using the Fe I, II and III lines (Table 11.1) an initial determination of the temperature can be made. From a LTE<sub>S</sub> curve of growth analysis a plot of abundance for each line against temperature can be made, a different plot for each assumed gravity. The plots for the Fe lines are given in Figure 11.3.

From these lines a temperature of  $11,000 \pm 1000$  is determined for the  $\log g = 1.0$  model up to  $13,000 \pm 1000$  for the  $\log g = 3.0$  model. The scatter is large and the lines from Fe I and II are almost parallel and do not constrain the temperature well. The two Fe III lines have almost constant abundance irrespective of the temperature or gravity of the models. The results are shown in Table 11.3.

Modelling of the Fe II  $\lambda 4273.32 \text{ \AA}$  line was undertaken. By interpolation, a T12G08 or T13G22 model would fit the depth of the absorption line well. This appears to be a very temper-

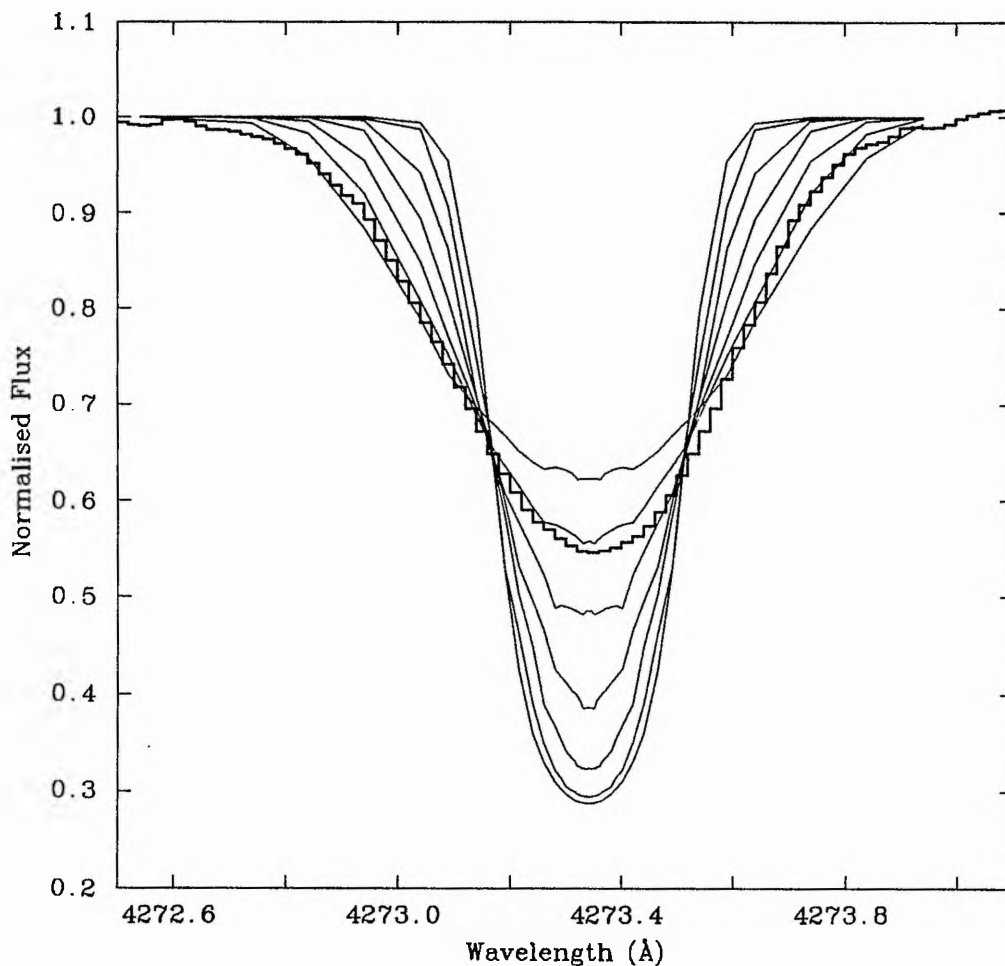
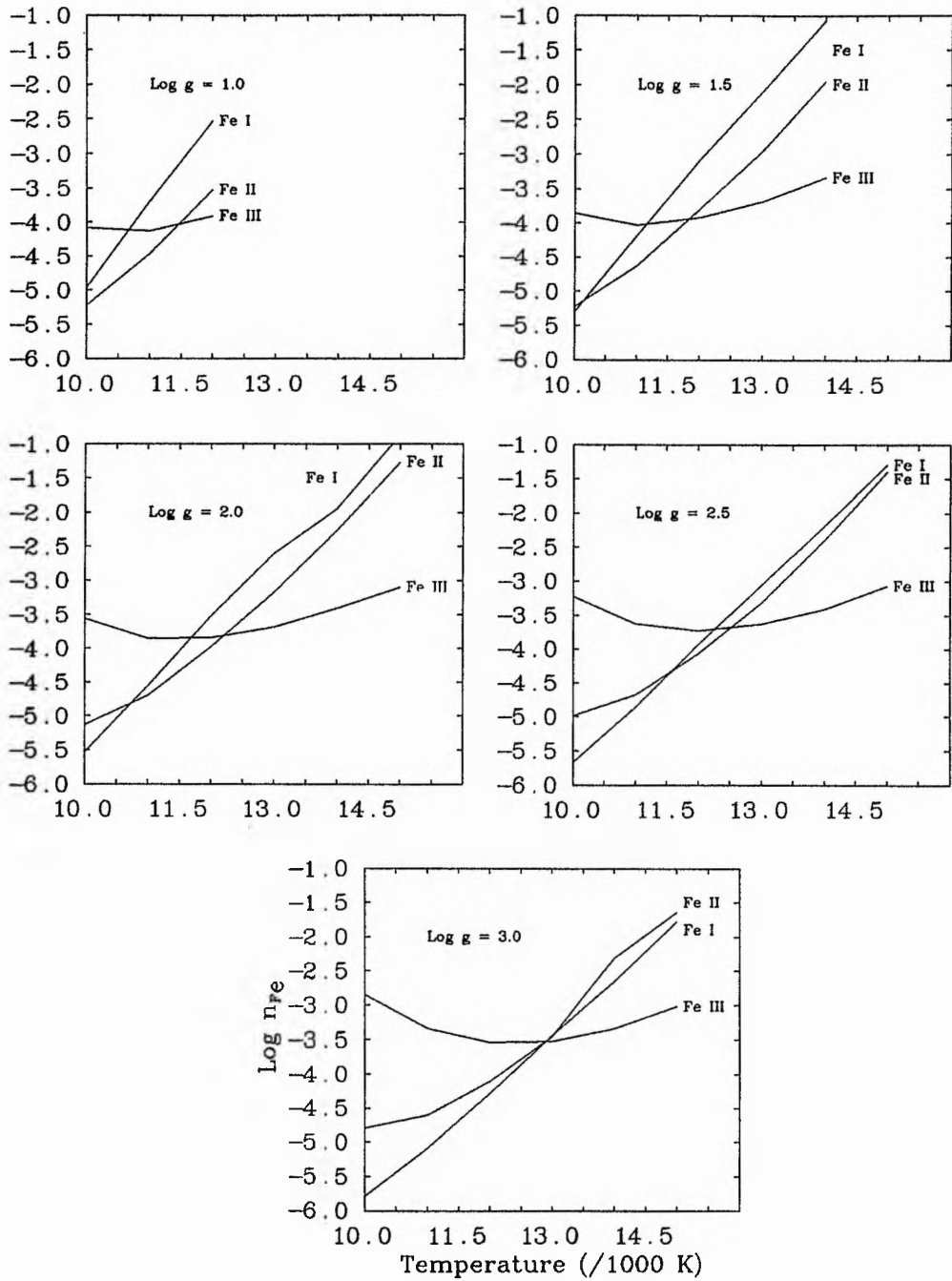


Figure 11.2: Rotational velocity of  $\nu$  Sgr from the Fe II 4273 Å line. The heavy line is the observed profile, light lines from the theoretical model ( $T_{\text{eff}} = 12,000\text{K}$ ,  $\log g = 1.5$ ). Rotational broadening from 0 (deepest profile) to  $30\text{ km s}^{-1}$  in steps of  $5\text{ km s}^{-1}$  has been applied. A rotational velocity of  $25 \pm 5\text{ km s}^{-1}$  is indicated from the fitting of the wings.



**Figure 11.3: Initial temperature determination for  $\nu$  Sgr from a LTE<sub>S</sub> Fe curve of growth analysis. The plotted abundances are the means from 26 (FeI), 11 (FeII) and 2 (FeIII) lines respectively.**

Table 11.3: Temperature determination from Fe and N lines for  $\nu$  Sgr.

Gravity $\log g$	Temperature (K)	
	NI / NII	FeI / FeII / FeIII
1.0	11700 $\pm$ 500	11000 $\pm$ 1000
1.5	12000 $\pm$ 500	11500 $\pm$ 500
2.0	12500 $\pm$ 500	12000 $\pm$ 500
2.5	13000 $\pm$ 500	12500 $\pm$ 500
3.0	13500 $\pm$ 500	13000 $\pm$ 500

ature and gravity sensitive line. Due to the constancy of the determined Fe abundance from the CoG analysis and the saturated nature of the line this effect is due to gravity as the line lies on the steep "saturated" part of the CoG and is less dependent on the elemental abundance.

### 11.5.2 Nitrogen lines

The only other element with two ionisation stages represented in the wavelength range available is nitrogen. The results of a LTE<sub>S</sub> analysis are shown in Figure 11.4. The relationships between abundance and temperature for NI and NII are more steeply inclined to each other than FeI and FeII and should give a more accurate determination of the temperature. The results are shown in Table 11.3.

### 11.5.3 Titanium lines

The TiII lines at 4443.80 Å and 4444.56 Å were modelled, assuming solar abundances. In the spectrum of  $\nu$  Sgr the 4443.80 Å line reaches a depth of 0.61, a depth best fitted by the T12 models. T14 and T16 models produced a line that was hardly visible while a T08 model produces heavily saturated lines. A temperature of 12,000 $\pm$ 1,000K is indicated.

### 11.5.4 UV spectra

High resolution IUE spectra covering 1200 - 2800 Å are available and contain lines of elements in a high ionisation state. These could in principle be combined with the low ionisation state lines observed in the visual to determine the temperature by a CoG analysis.

Due to the effects of line blanketing in the UV it would be extremely difficult to set a continuum level; EW's would be uncertain by at least a factor of 2, probably substantially more, while line identifications and good atomic data for these transitions are scarce. These difficulties

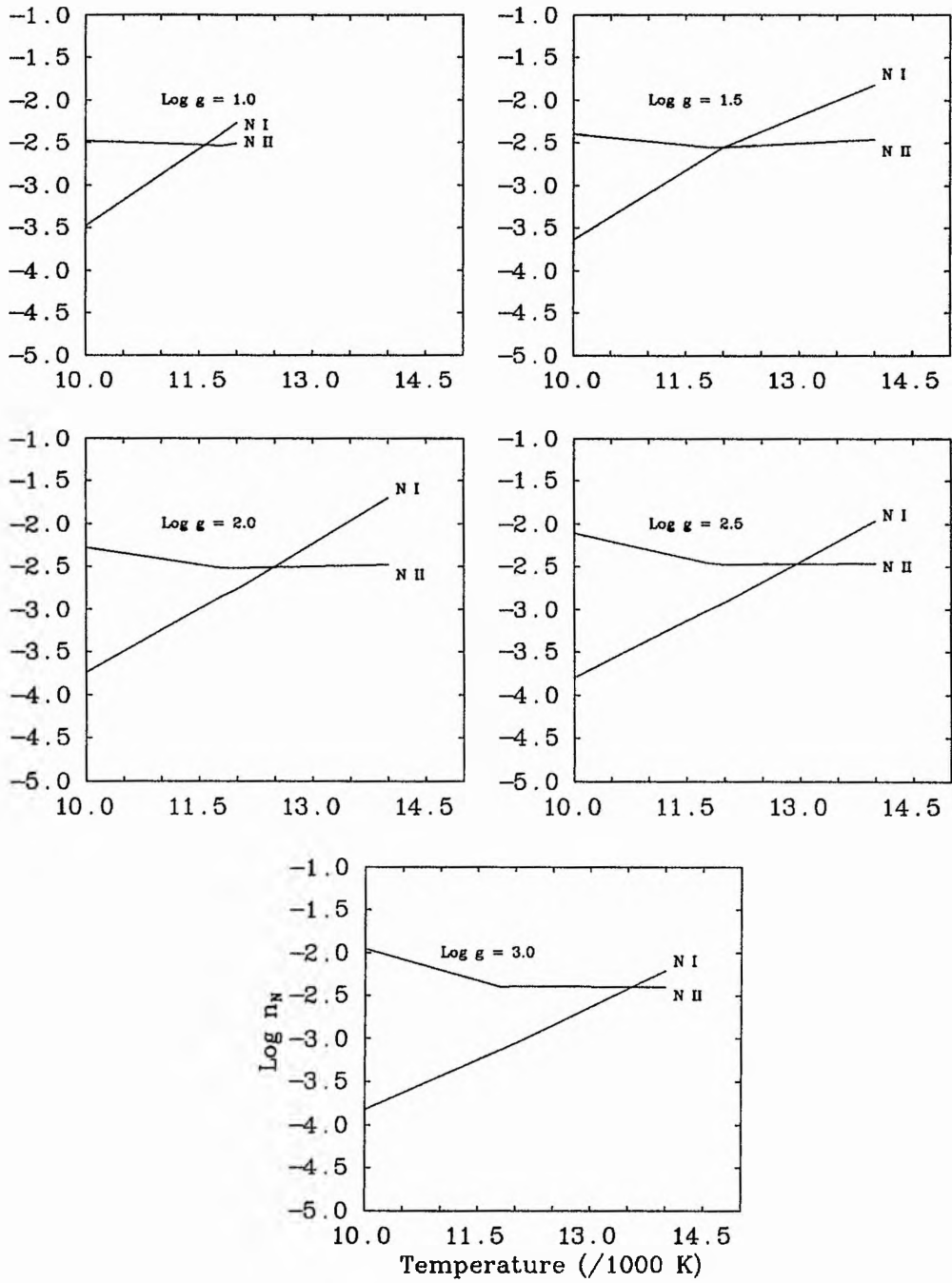


Figure 11.4: Initial temperature determination for  $\nu$  Sgr from a  $\text{LTE}_S$  N curve of growth analysis.

compounded with the poor signal to noise ratio of the IUE spectra with respect to the optical spectrum meant that UV lines were not used at all.

## 11.6 Gravity Determination

The surface gravity of a star can be determined from the shape of the wings of spectral lines; high gravity objects giving rise to broader lines than low gravity objects due to the effects of pressure broadening. As may be expected for  $\nu$  Sgr most of the lines are very sharp. The helium line profiles show the most pronounced wings and these can be used to constrain the gravity. The hydrogen lines may also be used, especially in light of the difficulties experienced with the helium lines.

For all profile fitting the accurate positioning of the continuum is vital; all profiles that were fitted had their continuum re-determined for the greatest accuracy.

### 11.6.1 Helium lines

Figure 11.5 shows theoretical line profiles from models with temperatures between 10,000K and 16,000K. Apart from the hottest models the profile fitting is very poor. The temperature is very different from the  $\sim 12,000$ K determined from all other means including the very accurate flux distribution method.

To explain the temperature discrepancy of these lines a number of possibilities can be excluded.

1. The observed lines cannot come from a hotter component as the *expected* profiles from the primary at 12,000K should be deeper and broader than the observed profiles.
2. A helium abundance below  $\sim 99\%$  cannot be used to explain the discrepancy as the compositional determination gives very small abundances for hydrogen and the metals indicating the remainder must be helium.
3. SPECTRUM cannot be at fault with incorrect internal values of the oscillator strengths and broadening constants as very good results are regularly obtained on other, albeit hotter, objects.

Figure 11.6 shows the same lines with 6 8,000K models each with a different surface gravity between 1.0 and 3.0. The profiles for the 4437 Å and 4121 Å lines indicate a low gravity while the other three lines show almost no dependence of wing profile with gravity. For the other three lines the fit to the wings is very poor the model underestimating the observed flux by up to 20%, a

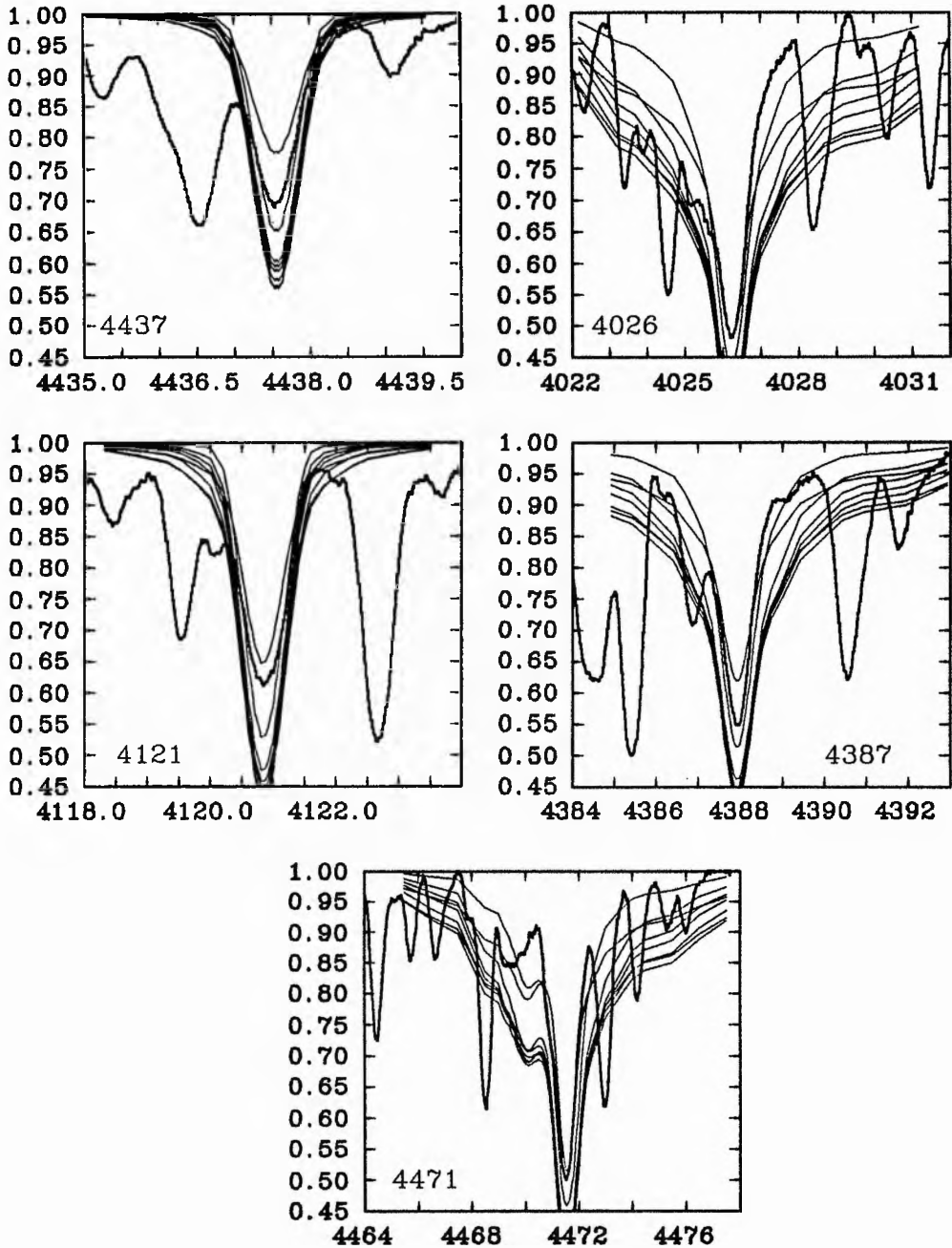


Figure 11.5: Initial gravity determination for  $\nu$  Sgr. The jagged lines are the observed profiles of 5 He I lines. The curves are for the theoretical line profiles, after rotationally broadening by  $25 \text{ km s}^{-1}$ ; one for each model. The uppermost line is for the T16G17 model and the one below that the T15G17 model. The others are T14G15, T13G12, T12G10, T11G10 and T10G10 (lowest line).

discrepancy that cannot be due to continuum placement problems alone. It is possible that NLTE effects are in part responsible for this problem.

Although a low gravity seems to be indicated from two of the He lines the discrepancy with the other lines and the temperature problem for all the lines renders the low gravity value almost worthless on the strength of the helium lines alone.

### 11.6.2 Hydrogen lines

Not as useful as the helium lines the hydrogen line profiles can also be modelled to determine the gravity. Shown in Figure 11.7 are the 4101 Å and 4340 Å lines and profiles from the T10, T12 and T14 models with  $\log g = 1.0$  (greatest central depth) and 3.0. Only a small wavelength region is shown to increase clarity; the continuum was determined over a larger range. For each model a hydrogen abundance was chosen to fit the observed EW.

The 4340 Å and 4101 Å lines show the best observed profiles. The 4340 Å has an excellent blue wing profile while the 4101 Å profile shows good blue and red wings but there is evidence of a contaminant line from the asymmetry in the wings. The shape of the line cores is possibly due to emission. The 4861 Å profile is very poor. Problems with the mask extraction of the echelle data (detailed in Chapter 10) lead to a discontinuity at 4859.5 Å of some 7% in flux (15-20% of the depth of the profile) leading to a poorly determined continuum. As well as the obvious blend in the blue wing the red wing also seems to suffer blending from flux at 0.80 and upwards which lead to an asymmetry in the profile. The surface gravity was not determined from this line.

From Figure 11.7 the 4101 Å line is more sensitive to the model gravity than the 4340 Å line and so was weighted more in the final gravity determination. For a 10,000K model  $\log g = 1.5 \pm 0.5$  was indicated while for the 12,000K and 14,000K models the results were  $1.5 \pm 0.5$  and  $1.0 \pm 0.5$  respectively.

## 11.7 The Final Model

Figure 11.8 shows the results of the temperature and gravity determination on a temperature-gravity diagram. The final determined temperature is  $11,750 \pm 750$ K and for the surface gravity  $\log g = 1.5 \pm 0.5$ . The temperature is in excellent agreement with the flux distribution result of  $11,800 \pm 500$ K while the gravity measurement is in agreement with the value of  $1.43 \pm 0.14$  from the orbital analysis if  $\nu$  Sgr is filling its  $60 R_{\odot}$  Roche lobe.

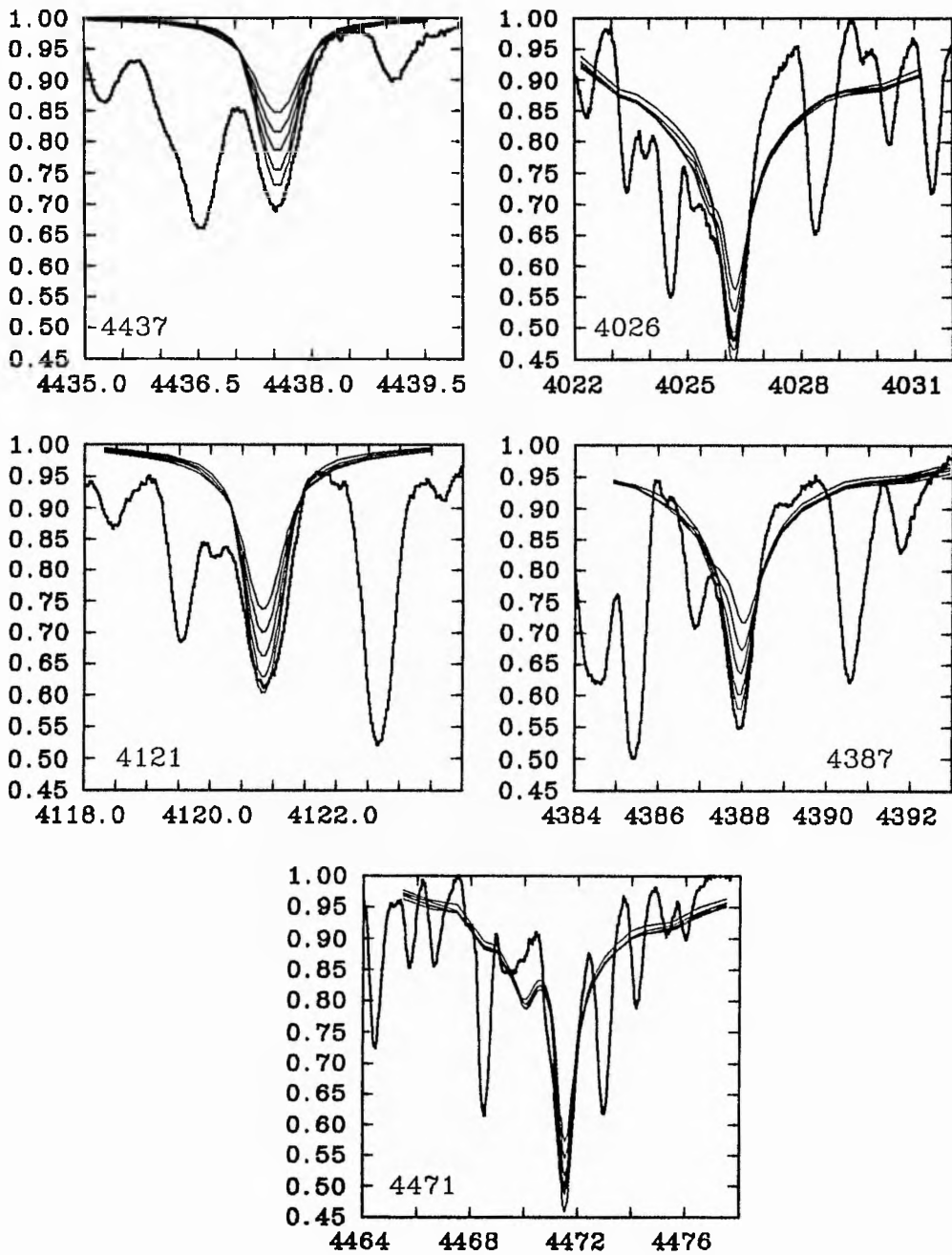


Figure 11.6: Profile fitting the He lines using 8,000K models with  $\log g = 1.0$  (top) to 3.0 (bottom) in steps of 0.5.

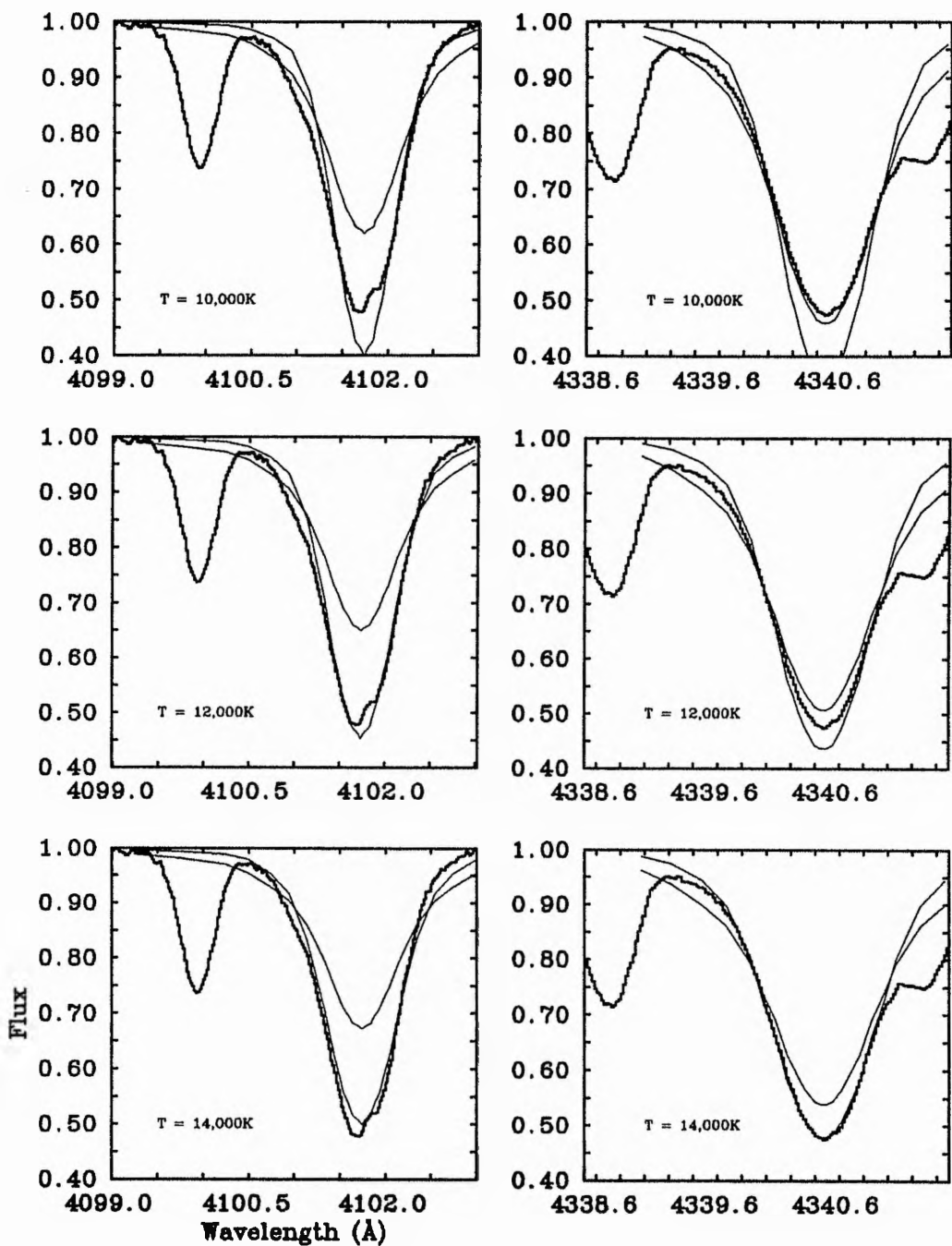


Figure 11.7: Modelling the hydrogen line profiles of  $\nu$  Sgr. The observed lines (heavy) for the 4101 Å (left) and 4340 Å (right) lines are compared to  $\log g = 1.0$  (lowest central depth) and  $\log g = 3.0$  models for temperatures of 10,000K, 12,000K and 14,000K. All the model profiles have been rotationally broadened by  $25 \text{ km s}^{-1}$ .

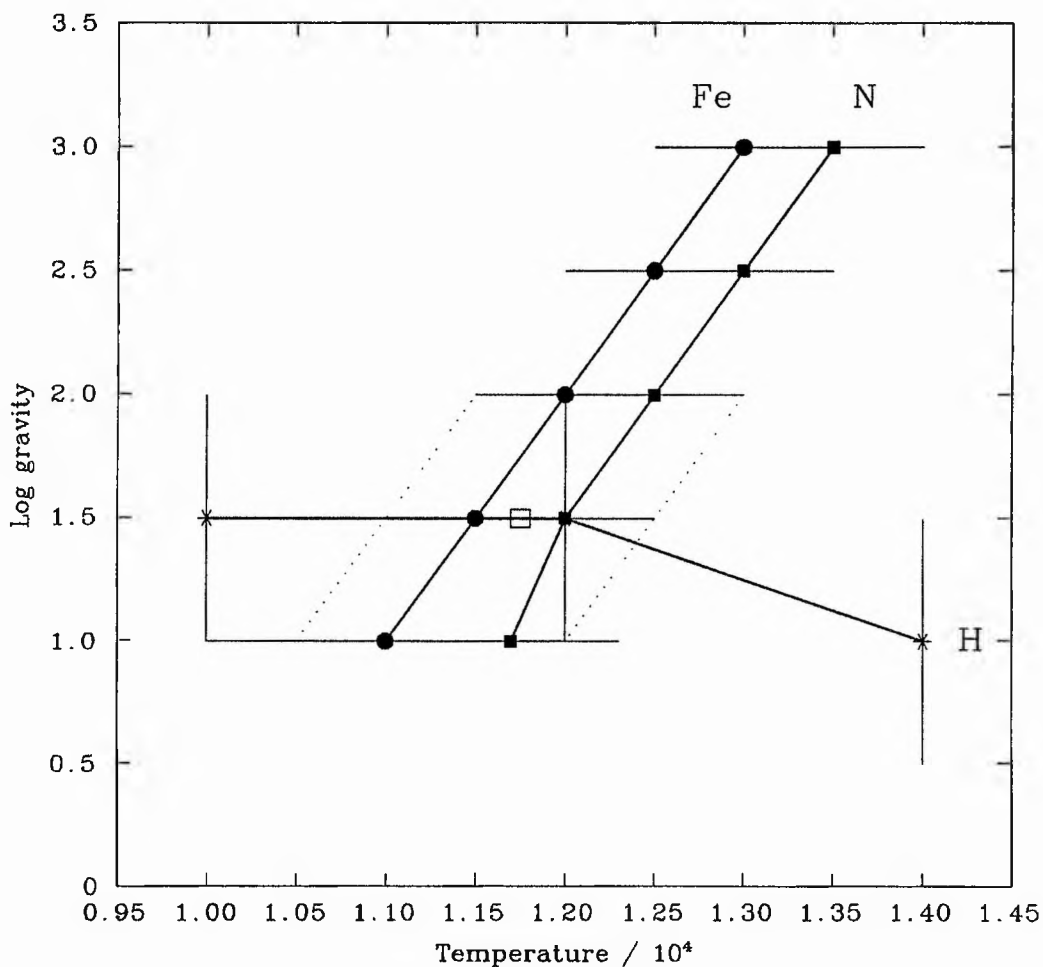


Figure 11.8: The final temperature and gravity determination for  $\nu$  Sgr. The filled symbols are the run of temperature with gravity for NI and NII (squares) and FeI, FeII and FeIII (circles). The stars show the run of gravity with temperature from the 4101 Å and 4340 Å hydrogen lines. The light lines are the error bounds on these results. The open square indicates the final model adopted ( $T_{\text{eff}} = 11,750\text{K}$ ,  $\log g = 1.5$ ) with the dotted line denoting the error box on this result ( $\pm 750\text{K}$ ,  $\pm 0.5$ ).

Table 11.4: The final derived abundances for  $\nu$  Sgr, expressed as log (number fraction), compared to those from the fine analyses of Hack & Pasinetti (1963) (HP63) and Leushin & Topil'skaya (1988b) (LT88). Solar values are given for comparison (Holweger 1979). For this study abundances with no quoted error are from a single line, the exception being helium with an abundance of one minus the sum of the other elements. The Hack & Pasinetti results are relative to a solar iron abundance.

Element	Abundance			
	Solar	This study	HP63	LT88
H	-0.15	-3.76±0.04	-2.3	-3.3
He	-1.15	-0.0013	-0.5	-0.02
C	-3.48	-4.13	-2.9	-2.27±0.13
N	-4.16	-2.74±0.42	-1.9	-1.87±0.07
O	-3.23	-3.22	-4.0	-2.7
Mg	-4.62	-4.32±0.11	-3.2	-4.07±0.07
Si	-4.65	-4.97	-3.9	-4.13±0.07
P	-6.80	-5.93±0.73	-	-4.90±0.20
S	-4.95	-3.89±0.66	-3.4	-4.54±0.04
Ti	-7.27	-6.37±0.32	-7.5	-5.66±0.07
V	-8.24	-6.62±1.08	-8.0	-6.70±0.10
Cr	-6.54	-5.63±0.36	-5.9	-5.16±0.05
Fe	-4.69	-3.78±0.61	-4.5	-3.33±0.10

## 11.8 Final Abundances

Using the values of  $T_{\text{eff}} = 11,800\text{K}$  found from both the fine analysis and the flux distribution and  $\log g = 1.5$ , the final derived abundances were determined. These abundances, expressed as number fractions, are shown in Table 11.4 with those of Hack & Pasinetti (1963) and Leushin & Topil'skaya (1988b) for comparison.

**Hydrogen** At 0.017% the hydrogen abundance determined here is less than from both the other two determinations although the Hack & Pasinetti (1963) result can be discounted (Schönberner & Drilling 1982). Hydrogen is confirmed as a trace element.

**Carbon** At 0.0049% the carbon abundance has been determined to be underabundant (0.65 dex) with respect to the sun, in contrast to both the Hack & Pasinetti and Leushin & Topil'skaya (1988b) results where carbon is overabundant. In the current analysis only one unblended carbon line was identified - C II<sub>6</sub>  $\lambda 4267 \text{ \AA}$  doublet. This line is often out of LTE and is overly strong for the assumed abundance. If this is the case then the low determined abundance will be an upper limit to the actual carbon abundance. Although uncertain, the carbon

abundance must be regarded as subsolar.

**Nitrogen** A nitrogen abundance of 0.18% is indicated from 11 measured lines. Although overabundant by 1.5 dex with respect to the sun this overabundance is less pronounced than that from the other investigators.

**Oxygen** Only one line of oxygen was identified in the available spectrum of  $\nu$  Sgr, the O II<sub>2</sub>  $\lambda$ 4349.43 Å line with an equivalent width of 27 mÅ. The determined abundance of 0.06% is approximately solar and falls between the results of the other investigators.

**Iron** At 0.017% the determined iron abundance is almost one dex overabundant with respect to the sun, in approximate agreement with the results of Leushin & Topil'skaya (1988b).

**Other metals** Of the other metals with determined abundances magnesium and silicon are approximately solar with the other metals (P, S, Ti, V, Cr) about one dex overabundant with respect to the sun.

**Helium** As the most dominant species helium cannot have its abundance determined by a CoG analysis but must be assigned an abundance equal to the remainder after the other abundances have been accounted for. On this basis a helium abundance of 99.7% is assigned. This is higher than that determined by Leushin & Topil'skaya (1988b).

## 11.9 Discussion

The temperature determinations from a number of species, both with CoG analysis and profile fitting, give temperatures that agree well with the final adopted value of  $11,750 \pm 750$  K. The gravity has been less well determined ( $\log g = 1.5 \pm 0.5$ ) due to the inability to use the helium lines for gravity determination. These results are in excellent agreement with the flux distribution analysis ( $11,800 \pm 500$  K) and the determined gravity from the orbital analysis ( $\log g = 1.5 \pm 0.2$ ). The helium line problem has not been solved and no explanation is offered. This problem may also be applicable to the other HDBs and especially LSS4300 that has had its temperature and surface gravity determined from the He I 4471 Å line (Schönberner & Drilling 1984). The determined values of  $T = 14,400$  K and  $\log g = 1.4$  have been confirmed with SPECTRUM. The flux analysis in Chapter 9 gives a temperature of  $12,000 \pm 1,000$  K for LSS4300, some 3,000 K cooler than from modelling the He line. This discrepancy is probably be due to the helium line problem encountered for  $\nu$  Sgr whereby a  $\sim 16,000$  K model would fit the helium lines but all other indicators give  $\sim 12,000$  K.

The abundance analysis confirms that  $\nu$  Sgr is hydrogen-deficient and helium rich indicating that substantial mass loss from the primary has occurred exposing nuclear processed material in the core. The fact that nitrogen is overabundant with respect to the sun indicates that hydrogen

burning via the CNO cycle has occurred in the core. As the carbon abundance is subsolar and the oxygen abundance solar there is no evidence that triple- $\alpha$  processed material has been brought to the surface. The probable evolutionary scenario of case BB mass loss, after core helium exhaustion, with the luminosity being provided by a helium burning shell would indicate that substantial amounts of carbon has been synthesised in the core. Convective dredge-up does not appear to have exposed this material.

The overabundance of nitrogen as evidence for the CNO cycle indicates that the primary component was once more massive than  $\sim 5 M_{\odot}$ . If an initial solar composition is assumed then the total number of CNO nuclei should be conserved if no  $3\alpha$  material has been mixed into the observed surface layers. The total solar CNO abundance is 0.092% while the observed total is  $0.25^{+0.25}_{-0.11}\%$ . This result appears to indicate that the total CNO abundance is twice that of the sun indicating that either some enrichment of the atmosphere by  $3\alpha$  material has taken place or that the main sequence metal content of  $\nu$  Sgr was twice that of the sun. As  $\nu$  Sgr is younger than the sun an initial metal content of twice that of the sun may be expected. Then the observed C and O abundances are less than the initial abundance while nitrogen is overabundant. Then no carbon enrichment is observed and the CNO abundances are explained by the CNO cycle alone. The metals appear to be, on average, one dex overabundant with respect to the sun; a greater overabundance than for the CNO elements.

## 11.10 Summary

*From an atmospheric fine analysis using line-blanketed hydrogen-deficient model atmospheres and improved observational and atomic data the primary component of  $\nu$  Sgr has been determined to have a temperature of  $11,750 \pm 750 K$  and a surface gravity of  $\log g = 1.5 \pm 0.5$ . The temperature is in excellent agreement with that from the flux distribution analysis ( $11,800 \pm 500 K$ ) and the gravity is consistent with a  $3.0 \pm 0.3 M_{\odot}$  star filling a  $\sim 60 R_{\odot}$  Roche lobe ( $\log g = 1.5 \pm 0.2$ ). The determined rotational velocity of  $25 \pm 5 \text{ km s}^{-1}$  also supports this result. Assuming synchronous rotation the orbital inclination can be further constrained to  $i > 65^{\circ}$ .*

*The surface composition has been shown to be extremely hydrogen deficient (0.017% by number) and helium rich (99.7%). Oxygen is solar, carbon subsolar and nitrogen enhanced by a factor of 30 with respect to the sun. There is no evidence for enhancement of the atmosphere by  $3\alpha$  processed material. The high nitrogen abundance indicates the processing of material by the CNO cycle and confirms the high mass of the primary of  $\nu$  Sgr when on the ZAMS. A high metallicity (one dex overabundant) is determined, somewhat higher than the CNO overabundance (0.4 dex).*

*The helium lines cannot be modelled using the final model. For these lines either a  $\sim 16,000 K$  or  $\sim 8,000 K$  model is indicated or an extremely low, unphysical (and unmodelable), surface gravity together with a  $12,000 K$  effective temperature. No explanation is offered for this effect but if it occurs in the LSS4300 then it would explain the difference between the temperature determined from the He I  $4471 \text{ \AA}$  line (Schönberner & Drilling 1984) and from the flux distribution analysis (Chapter 9). From the experience with  $\nu$  Sgr the flux distribution results are more reliable.*

## 11.11 References

- Allen, C.W., 1973. *Astrophysical Quantities*, Third Edition, Athlone Press.
- Becker, S.R. & Butler, K., 1988. *Astr. Astrophys.*, **201**, 232.
- Becker, S.R. & Butler, K., 1989. *Astr. Astrophys.*, **209**, 244.
- Becker, S.R. & Butler, K., 1990. *Astr. Astrophys.*, **235**, 326.
- Blackwell, D.E., Petford, A.D., Shallis, M.J. & Simmons, G.J., 1980. *Mon. Not. R. astr. Soc.*, **191**, 445.
- Blackwell, D.E., Petford, A.D., Shallis, M.J. & Simmons, G.J., 1982. *Mon. Not. R. astr. Soc.*, **199**, 43.
- Dufton, P.L., Durrant, A.C. & Durrant, C.J., 1981. *Astr. Astrophys.*, **97**, 10.
- Fuhr, J.R., Martin, G.A. & Wiese, W.L., 1988. *J. Phys. Chem. Ref. Data*, **17**, Suppl. 4.
- Gigas, D., 1986. *Astr. Astrophys.*, **165**, 170.
- Hack, M. & Pasinetti, L., 1963. *Contr. Oss. astr. Milano-Merate*, **215**, 1.
- Heber, U., 1983. *Astr. Astrophys.*, **118**, 39.
- Holweger, H., 1979. *22<sup>nd</sup> Liege International Astrophys. Symp.*, 117.
- Howarth, I.D. & Murray, J., 1991. *STARLINK User Note 50.11*.
- Kurucz, R.L. & Petryeman, E., 1975. *SAO Special Report*, **362**.
- Leushin, V.V. & Topil'skaya, G.P., 1984. *Astrophysics*, **22**, 74.
- Leushin, V.V. & Topil'skaya, G.P., 1987. *Astrophysics*, **26**, 117.
- Leushin, V.V. & Topil'skaya, G.P., 1988a. *Astrophysics*, **28**, 213.
- Leushin, V.V. & Topil'skaya, G.P., 1988b. *Astrophysics*, **28**, 329.
- Martin, G.A., Fuhr, J.R. & Wiese, W.L., 1988. *J. Phys. Chem. Ref. Data*, **17**, Suppl. 3.
- Moity, J., 1983. *Astr. Astrophys. Suppl.*, **52**, 37.
- Roberts, J.R., Andersen, T. & Sørensen, G., 1973. *Astrophys. J.*, **181**, 567.
- Savanov, I.S., Huovelin, J. & Tuominen, I., 1990. *Astr. Astrophys. Suppl.*, **86**, 531.
- Schönberner, D. & Drilling, J.S., 1982. *Astrophys. J.*, **268**, 225.
- Schönberner, D. & Drilling, J.S., 1984. *Astrophys. J.*, **276**, 229.
- Warner, B., 1967. *Mon. Not. R. astr. Soc.*, **137**, 119.

Wiese, W.L., Smith, M.W. & Glennon, B.M., 1966. *Atomic Transition Probabilities*, NBS, Washington.

Wiese, W.L., Smith, M.W. & Miles, B.M., 1969. *Atomic Transition Probabilities*, NBS, Washington.

# Chapter 12

## Summary & Conclusions

### 12.1 Summary

Summaries of each Chapter are given at the end of that Chapter. Below is a list of those results that are new, as determined in this work.

1. The secondary component of  $\nu$  Sgr has been positively detected for the first time using improved cross-correlation techniques.
2. The velocity semi-amplitude of the secondary component is  $29.7 \pm 1.7 \text{ km s}^{-1}$ .
3. The orbit of the system has been shown to be consistent with a circular one, thus removing the problem of a non-circular orbit in a system that has undergone substantial mass transfer.
4. From the eclipse geometry and rotational velocity the inclination is between  $65^\circ$  and  $78^\circ$ .
5. The masses of the two components are then  $3.0 \pm 0.3 M_\odot$  and  $4.8 \pm 0.5 M_\odot$  for the primary and secondary respectively with an orbital separation of  $230 \pm 20 R_\odot$ .
6. From the observed mass loss and hydrogen emission the primary is expected to fill its Roche lobe and to have a radius of  $60 R_\odot$ . The surface gravity is then  $\log g = 1.5 \pm 0.2$ .
7. The secondary spectrum has been obtained by deconvolution and, although the data are poor, the high excitation lines indicate the secondary is hotter than the primary.
8. Wind line profile fitting used on  $\nu$  Sgr for the first time has determined a mass-loss rate of  $> 2.5 \times 10^{-10} M_\odot \text{ yr}^{-1}$ . The actual mass-loss rate is probably  $\sim 100$  times this, but ionisation fractions could not be determined.
9. The revised orbital parameters constrains the upper limit of the mass loss from  $\nu$  Sgr to be  $1.9 \times 10^{-5} M_\odot \text{ yr}^{-1}$ .

10. Removal of the Lyman- $\alpha$  profile in UV spectra of  $\nu$  Sgr for the first time provides confirmation of the interstellar extinction of  $E_{B-V} = 0.20 \pm 0.05$  as previously determined from the 2,200 Å feature.
11. The flux distribution of  $\nu$  Sgr has been modelled with line-blanketed hydrogen-deficient model atmospheres to determine a temperature of  $11,800 \pm 500$  K and an extinction of  $E_{B-V} = 0.20 \pm 0.05$ .
12. The long standing problem of the flux distribution has mostly been solved using these improved model atmospheres.
13. The distance to  $\nu$  Sgr is  $1400 \pm 300$  pc determined from the flux distribution and the radius of the primary.
14. The flux distribution confirms that the UV flux comes mainly from the primary and that little of the flux is from the secondary as was previously thought.
15. The most accurate high resolution spectrum yet published has been obtained for  $\nu$  Sgr in the range 3980 - 4915 Å with an echelle spectrograph and CCD combination. Over 500 lines have been identified.
16. Using the best available atomic data, hydrogen-deficient line-blanketed model atmospheres and LTE with scattering line formation codes, a fine analysis has been carried out for  $\nu$  Sgr. A temperature of  $11,750 \pm 750$  K confirms the values from the flux distribution and a low gravity ( $\log g = 1.5 \pm 0.5$ ) in agreement with the orbital analysis is found.
17. An analysis of a small number of O stars has indicated that the gradient of the velocity law,  $\beta$ , may increase with decreasing temperature.
18. Two sdO stars, BD +37° 1977 and BD +37° 442, have also had their UV wind line profiles analysed by profile fitting for the first time to obtain mass-loss rates of at least  $10^{-9}$  and  $10^{-10} M_{\odot} \text{ yr}^{-1}$  respectively, although the true mass-loss rates are probably 100 times or so greater.
19. The flux distributions of the three other HDBs (KS Per, LSS 1922 and LSS 4300) have determined higher (KS Per,  $12,500 \pm 500$  K) and lower (LSS 1922,  $12,000 \pm 500$  K; LSS 4300,  $12,000 \pm 1,000$  K) temperatures than previously determined.
20. The extinction of KS Per has been shown to be substantially higher than previously thought at  $0.55 \pm 0.10$ .
21. The flux distributions have shown that for a range of temperatures spanning at least 9,000 - 12,000 K, hydrogen-deficient line-blanketed model atmospheres indicate that stars should have a flux "bump" at  $\sim 2,200$  Å, possibly due to an absorption edge. For such stars flattening the 2,200 Å feature in UV spectra to determine interstellar extinction may lead to a serious underestimate of this value.

As well as these new determinations of parameters there are a number of confirmations of previous results presented, such as the confirmation of the primary velocity curve of  $\nu$  Sgr, the interstellar extinctions of LSS 1922 and LSS 4300, and the mass-loss rates from three EHe stars.

The SEI wind line profile fitting code has been thoroughly tested and applied to both single stars and, with suitable simplifying approximations, to the binary  $\nu$  Sgr. The technique of template sharpening has been discussed, and shown to fail for the Wolf-Rayet binary  $\gamma^2$  Vel, thus helping to confine the type of systems for which this technique will work.

## 12.2 Conclusions

The main conclusion from this work concerns the ultimate fate of the primary component of  $\nu$  Sgr. As detailed in the introduction a powerful case can be put forward for HDBs being progenitors of Type Ib supernovae, the only drawback being their assumed masses.

Delgado & Thomas (1981) determine that for core carbon ignition after case BB mass transfer a star needs a mass of  $2-3 M_{\odot}$  to allow burning through to iron and finally core collapse.

The new results presented here, of the primary component having a mass of  $\sim 3.0 M_{\odot}$ , strongly suggest that it is massive enough to eventually undergo core collapse. The very low hydrogen abundance indicates that substantial mass loss must have occurred and which must have been due to case BB mass transfer. For this to occur the primary component must be ascending the asymptotic giant branch on the way to carbon ignition. Upon carbon ignition the star contracts and mass transfer/loss enters a quiescent phase. The mass loss rate limits determined here are not precise enough to indicate that  $\nu$  Sgr is in such a low mass loss phase. From the surface CNO abundances there is no indication that carbon ignition has occurred yet. With the mass being at the upper end of the range indicated by Delgado & Thomas the indications are that  $\nu$  Sgr will probably undergo a SN Ib event.

The literature on stellar evolution in binary systems with mass loss and transfer is large (*e.g.* Delgado & Thomas 1981; Paczynski 1971; Plavec 1970; Lauterborn 1970; de Greve & Loore 1977; Doom & de Greve 1983; Iben & Tutukov 1985; Habets 1986a,b) but the current status of  $\nu$  Sgr is known and thus all that is required is the mass at which the primary needs to be now to undergo Fe core collapse in the future. To determine the fate of  $\nu$  Sgr a full evolutionary scenario does not need to be modelled, just a knowledge of the current mass, mass-loss rate and the indication that core carbon ignition has occurred, or is about to occur. However, for an understanding of the system as a whole a full evolutionary scenario is required. Although work has been done on binary systems with ZAMS masses in the range expected for  $\nu$  Sgr the periods used are too small - there are no models available for such evolved systems with such long periods.

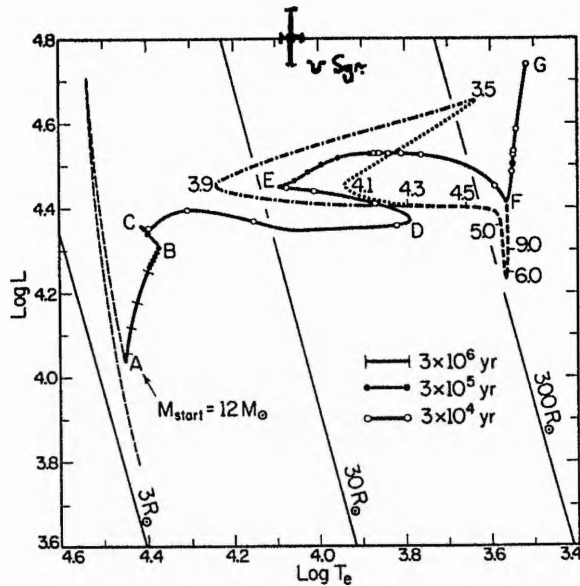


Figure 12.1: The evolution of a binary system with a  $12 M_{\odot}$  primary component. Shown are an evolutionary track for a primary component with a ZAMS mass of  $12 M_{\odot}$ . The solid line is a model for a single star without mass loss, the dotted and dashed lines for the primary component within binary system. The secondary component is not modelled but mass loss is assumed to begin at various points (e.g. the first phase of mass loss occurs at  $R_p \gtrsim 300 R_{\odot}$ ). No separations or secondary masses are used. The current position of the primary component of  $v$  Sgr is indicated. From Iben & Tutukov (1985).

Figure 12.1 shows a binary model for a primary component with a ZAMS mass of  $12 M_{\odot}$  from Iben & Tutukov (1985). The binary aspects are simply treated with mass being removed from the primary when it exceeds an arbitrary radius. The model has no direct relevance to  $v$  Sgr as such but does indicate that the primary component of  $v$  Sgr with  $\log(L/L_{\odot}) = 4.8 \pm 0.05$  and  $\log T_{\text{eff}} = 4.07 \pm 0.03$  is consistent (in theory) with a late stage of evolution, if the primary component were more massive than  $12 M_{\odot}$  when on the ZAMS.

The classification of a type Ib SN is based on

1. They are found near star forming regions and must therefore be massive Population I stars to still be in the vicinity of their birthplace when they explode.
2. No hydrogen is seen in the spectra of Ib events so the progenitors must burn or in some way lose all the hydrogen in them.
3. Helium is seen in large quantities so it must not all be burnt or otherwise lost.
4. The observed radio emission from Ib events indicates they are embedded in circumstellar material, presumably from the progenitor.

5. Type Ib events have similar luminosities to Type II events and lower luminosities than Ia events.

1) is satisfied as a mass of  $\sim 15 M_{\odot}$  is found by Delgado & Thomas (1981) for a progenitor star that undergoes Case BB mass transfer and still has a mass of  $2-3 M_{\odot}$ . Such a massive star will evolve quickly.

2) and 3) are explained by the Case BB hypothesis.

4) arises naturally from the two phases of mass transfer that precede the core collapse.

5) is explained as the mechanism for the Ib event (*i.e.* core collapse following core iron exhaustion) is exactly the mechanism of a Type II event and thus the luminosity would be expected to be similar to Type II events rather than Ia (accretion onto a white dwarf in a binary system pushes the WD mass over the Chandrasekhar mass limit for WD's ( $\sim 1.4 M_{\odot}$ ) causing explosive ignition throughout the WD).

Thus  $\nu$  Sgr (and by extension the other HDBs, if massive enough) naturally explain the phenomena of the Type Ib SN.

From the data amassed in this work it must be concluded that the primary of  $\nu$  Sgr will undergo core Fe collapse, and will be classified as a Type Ib SN, in about 400,000 years time (see discussion in Chapter 2).

The question arises as to what would be the effect of a SN Ib event at  $\sim 1400$ pc. SN Ib events are very similar to SN II events, the most studied of which is SN 1987A. Due to the extra envelope material in the progenitor of SN 1987A compared to  $\nu$  Sgr it may be expected that the  $\nu$  Sgr event would be at least as luminous as SN 1987A. If so, the  $\nu$  Sgr event would have a peak visual magnitude of  $\sim -5$  making it as bright as than the Crab Nebula event (1054A.D.,  $M_{v,peak} = -5$ ) and brighter than Tycho's supernova (1572A.D.,  $M_{v,peak} = -4.0$ ). It would be jointly the third brightest supernova ever recorded after the event of 185A.D. that left the radio remnant G315.4-2.3. The brightest recorded supernova event was in 1006A.D. with  $M_{v,peak} = -9$  that left the radio remnant G327.6+14.5. No effect on the planet was recorded from this event and thus none would be expected from the  $\nu$  Sgr event. As  $\nu$  Sgr is  $\sim 35$  times closer to the Earth than SN 1987A in the LMC all the effects from that event would be multiplied by  $\sim 1,200$  times, *e.g.* some 25,000 neutrino events would be expected to be detected in the IMB and Kamiokande II detectors. The event would not be bright enough to affect astronomical observations, even those requiring the darkest conditions.

## 12.3 Future Work

To follow on from this work the following points need to be addressed.

1. **Photometry.** For the two poorly observed HDBs (LSS 1922, LSS 4300) there is a need for further photometry, especially in the UV and IR to allow the determination of the temperatures more accurately by flux modeling. Multi-colour photometry is also required to determine if eclipses occur for all four of these objects to help constrain their inclinations.
2. **UV Spectroscopy.** For all four known HDBs there is a need for UV spectroscopy to allow the detection of the secondary components of KS Per, LSS 1922 and LSS 4300 and to determine secondary radial velocities and then masses. Spectroscopy is also required to provide better data for a confirmation of the secondary radial velocities for  $\nu$  Sgr presented here. From the wind line profiles in the UV mass-loss rates may be determined for KS Per, LSS 1922 and LSS 4300.
3. **Visual Spectroscopy.** For LSS 1922 and LSS 4300 which do not have reliable orbital periods determined for them visual spectroscopy is required to determine such a period and a primary velocity semi-amplitude.
4. **Fine Analyses.** Visual spectra for the KS Per, LSS 1922 and LSS 4300 need to be obtained and combined with the numerical codes and atomic data used here for  $\nu$  Sgr to determine the temperature, gravity and, especially, surface composition to allow the evolutionary status of these three objects to be determined.
5. **Evolutionary Modeling.** Although Delgado & Thomas (1981) determine that a mass of  $2-3 M_{\odot}$  is sufficient at core carbon ignition to lead to a SN Ib event the rest of their model is poor with regard to the final mass of the secondary and the orbital periods. What is required are evolutionary calculations to determine the initial masses of the two components and their initial separation given that at core carbon ignition the masses are  $3.0 \pm 0.3$  and  $4.8 \pm 0.5 M_{\odot}$  respectively with a period of 138 days.

In short, all the techniques applied to  $\nu$  Sgr in this thesis should be applied to the other three HDBs once the required observational data are available to conclude the determination of all the important parameters about the four known members of this class of objects. New HDBs should be looked for although the surveys appear to be complete (Drilling 1986). The eccentric nature of the orbit of KS Per is a problem that needs to be resolved and the discussion of its origin (given in Chapter 2) needs to be confirmed or rejected.

## 12.4 References

- Delgado, A.J. & Thomas, H.-C., 1981. *Astr. Astrophys.*, **96**, 142.
- de Greve, J.-P. & de Loore, C., 1977. *Astrophys. Space Sci.*, **50**, 75.
- Doom, C. & de Greve, J.-P., 1983. *Astr. Astrophys.*, **120**, 97.
- Drilling, J.S., 1986. In: *Hydrogen-Deficient Stars & Related Objects*, IAU Coll. No. 87, p.9, eds. K. Hunger, D. Schönberner & N.K. Rao, Reidel, Dordrecht, Holland.
- Habets, G.M.H.J., 1986a. *Astr. Astrophys.*, **165**, 95.
- Habets, G.M.H.J., 1986b. *Astr. Astrophys.*, **167**, 61.
- Iben, I. Jr. & Tutukov, A.V., 1985. *Astrophys. J. Suppl.*, **58**, 661.
- Lauterborn, D., 1970. *Astr. Astrophys.*, **7**, 150.
- Paczynski, B., 1971. *Ann. Rev. Astr. Astrophys.*, **9**, 183.
- Plavec, M.J., 1970. *Publs astr. Soc. Pacif.*, **82**, 957.

# Appendix A

## The Lucy Test

When determining the orbit of a spectroscopic binary observational errors may lead to the assignment of a non-zero eccentricity to a star in a circular orbit. Simple tests for spurious eccentricity were devised by Lucy and Sweeney (1971) and by Bassett (1978); the relationships between them being clarified by Lucy (1989).

The first Bassett test ignores some reductions in the number of degrees of freedom and leads to large errors when the number of data points is small. Lucy (1989) provides a more accurate form of the first Bassett test and it is this test that has been used in this work and is described below.

### A.1 The Test

To decide if the eccentricity of a binary star is zero the statistical hypothesis "*the eccentricity is zero*" is tested. If the hypothesis is rejected at the 5% level of significance then the non-zero eccentricity is regarded as significant, otherwise a circular orbit is assigned. With this in mind the Lucy form of the first Bassett test becomes

$$(N - M) \ln \left( \frac{R_c}{R_e} \right) = -2 \ln p \quad (\text{A.1})$$

where

- $N$  = number of observations.  
 $M$  = number of elements of the elliptical orbit  
estimated from the observed data.

- $R_e, R_c$  = weighted sum of the squares of the residuals  
left by the least squares fit on the elliptical and  
circular orbit, respectively.
- $p$  = probability of the hypothesis of a circular orbit.

Thus if the probability,  $p$ , is less than 5% then the eccentric orbit is deemed to be significant and is accepted.

## A.2 Example: $\nu$ Sgr

For the orbital determination of  $\nu$  Sgr, using all the available data, we have 87 data points and are trying to determine 6 orbital elements. Sterne's method was used to determine the parameters of the eccentric and circular orbits yielding summed squared residuals of  $R_c=2163$  and  $R_e = 2026$  ( $\text{km s}^{-1}$ )<sup>2</sup>. The eccentric orbit yields the better fit and the determined eccentricity ( $e=0.051\pm 0.016$ ) has errors that do not include the circular orbit. However applying the Lucy test we find (with  $M=6$  and  $N=87$ )  $p=7\%$ . This is greater than 5% and so the hypothesis of the circular orbit cannot be rejected.

## A.3 References

- Bassett, E.E, 1978. *Observatory*, **98**, 123 .
- Lucy, L.B., 1989. *Observatory*, **109**, 100.
- Lucy, L.B. & Sweeney, M.A., 1971. *Astr. J.*, **76**, 544.

## Appendix B

# Non-Linear Least Squares Fit to an Arbitrary Function

### B.1 Introduction

Often in complex problems it is necessary to find an empirical fit to a function,  $y(x)$ , which is non-linear in its  $m$  free parameters,  $a_j$  (where  $j = 1, m$ ).

A goodness of fit of the calculated function to the observed data,  $\chi^2$ , can be defined by:

$$\chi^2 = \sum_{i=1}^N \left\{ \frac{1}{\sigma_i^2} [y_i - y(x_i)]^2 \right\} \quad (\text{B.1})$$

where

- $\chi^2$  = goodness of fit.
- $N$  = Number of data points to be fitted.
- $y_i$  = Observed data value at the point  $x_i$ .
- $y(x_i)$  = Calculated data value at the point  $x_i$ .
- $\frac{1}{\sigma_i^2}$  = Weight of the  $i^{\text{th}}$  data point.

To obtain the optimum values of  $a_j$ , the value of  $\chi^2$  is minimised with respect to each of the  $m$  free parameters simultaneously. This is achieved by solving  $m$  simultaneous equations each of which consists of the partial derivative of  $\chi^2$ , with respect to one of the free parameters, set to zero. *i.e.*  $m$  equations of the form:

$$\frac{\partial \chi^2}{\partial a_j} = \frac{\partial}{\partial a_j} \sum_{i=1}^N \left\{ \frac{1}{\sigma_i^2} [y_i - y(x_i)]^2 \right\} = 0 \quad j = (1, m) \quad (\text{B.2})$$

The value of  $\chi^2$  for any of set of  $m$  values of the free parameters can be represented by a hypersurface in  $m$ -dimensional hyperspace. This hyperspace must be searched for the global minimum value of  $\chi^2$ , noting that there may be many local minima.

A number of methods of solution are available (Bevington 1969, and references therein) of which the one showing the greatest speed of convergence is a gradient search of the linearised fitting function.

## B.2 Linearisation of the Fitting Function

Applying a 1<sup>st</sup> order Taylor expansion to the fitting function as a function of the free parameters,  $a_j$ , to obtain:

$$y_i \simeq y_0(x_i) + \sum_{j=1}^m \left( \frac{\partial y_0(x_i)}{\partial a_j} \delta a_j \right) \quad i = (1, N) \quad (\text{B.3})$$

This function is then linear in the parameter increments  $\delta a_j$ .  $y_0$  is the initial value (*i.e.* with a fixed set of parameters) of the fitting function.

To determine the derivatives a numerical method is used, being completely general. (If analytic derivatives are available then these could also be used.)

$$\frac{\partial y_0(x_i)}{\partial a_j} \simeq \left[ \frac{y_0(a_j + \Delta a_j) - y_0(a_j - \Delta a_j)}{2\Delta a_j} \right]_i \quad j = (1, m) \quad (\text{B.4})$$

Substituting Equation (B.3) into Equation (B.1), to obtain:

$$\chi^2 = \sum_{i=1}^N \left( \frac{1}{\sigma_i^2} \left\{ y_i - y_0(x_i) - \sum_{j=1}^m \left[ \frac{\partial y_0(x_i)}{\partial a_j} \delta a_j \right] \right\}^2 \right) \quad (\text{B.5})$$

Now, following the least squares procedure,  $\chi^2$  is minimised with respect to the parameter increments,  $\delta a_j$ , by differentiating with respect to these increments and setting the differentials to zero, to obtain  $m$  simultaneous equation of the form:

$$\begin{aligned} \frac{\partial \chi^2}{\partial \delta a_k} &= -2 \sum_{i=1}^N \left\{ \frac{1}{\sigma_i^2} \left( y_i - y_0(x_i) - \sum_{j=1}^m \left[ \frac{\partial y_0(x_i)}{\partial a_j} \delta a_j \right] \right) \right. \\ &\times \left. \left( \frac{\partial y_i}{\partial \delta a_k} - \frac{\partial y_0(x_i)}{\partial \delta a_k} - \sum_{j=1}^m \left[ \frac{\partial}{\partial \delta a_k} \left( \frac{\partial y_0(x_i)}{\partial a_j} \right) \delta a_j + \frac{\partial y_0(x_i)}{\partial a_j} \frac{\partial \delta a_j}{\partial \delta a_k} \right] \right) \right\} \\ &= 0 \quad k = (1, m) \end{aligned} \quad (\text{B.6})$$

The second bracket can be simplified by noting that

$$\frac{\partial y_i}{\partial \delta a_k} = 0 \quad (\text{B.7})$$

as the observed data points do not depend on any of the parameters  $\delta a_k$  (or on *any* parameters), and

$$\frac{\partial}{\partial \delta a_k} \left( \frac{\partial y_0(x_i)}{\partial a_j} \right) = 0 \quad (\text{B.8})$$

as  $y_0$  has no dependence on  $\delta a_k$ , only on  $a_k$ . Also note

$$\frac{\partial y_0(x_i)}{\partial a_j} \frac{\partial \delta a_j}{\partial \delta a_k} \begin{cases} = 0 & j \neq k \\ = \frac{\partial y_0(x_i)}{\partial a_k} & j = k \end{cases} \quad (\text{B.9})$$

Finally obtaining,

$$\begin{aligned} \frac{\partial \chi^2}{\partial \delta a_k} &= -2 \sum_{i=1}^N \left\{ \frac{1}{\sigma_i^2} \left( y_i - y_0(x_i) - \sum_{j=1}^m \left[ \frac{\partial y_0(x_i)}{\partial a_j} \delta a_j \right] \right) \frac{\partial y_0(x_i)}{\partial a_k} \right\} \\ &= 0 \end{aligned} \quad (\text{B.10})$$

$k = (1, m)$

Expanding, and changing the order of summation, to obtain

$$\sum_{i=1}^N \frac{1}{\sigma_i^2} (y_i - y_0(x_i)) \frac{\partial y_0(x_i)}{\partial a_k} = \sum_{i=1}^N \frac{1}{\sigma_i^2} \sum_{j=1}^m \frac{\partial y_0(x_i)}{\partial a_j} \frac{\partial y_0(x_i)}{\partial a_k} \delta a_j \quad (\text{B.11})$$

$k = (1, m)$

The following are then defined

$$\beta_k = \sum_{i=1}^N \frac{1}{\sigma_i^2} (y_i - y_0(x_i)) \frac{\partial y_0(x_i)}{\partial a_k} \quad k = (1, m) \quad (\text{B.12})$$

$$\alpha_{jk} \simeq \sum_{i=1}^N \frac{1}{\sigma_i^2} \frac{\partial y_0(x_i)}{\partial a_j} \frac{\partial y_0(x_i)}{\partial a_k} \quad k = (1, m) \quad (\text{B.13})$$

Then a row matrix,  $\beta$ , can be constructed from the  $\beta_k$ 's and a symmetric matrix,  $\alpha$ , from the  $\alpha_{jk}$ 's.

$$\beta = \left( \beta_1 \quad \beta_2 \quad \cdots \quad \beta_m \right) \quad (\text{B.14})$$

$$\alpha = \begin{pmatrix} \alpha_{11} & \alpha_{12} & \cdots & \alpha_{1m} \\ \alpha_{21} & \alpha_{22} & & \\ \vdots & & \ddots & \\ \alpha_{m1} & & & \alpha_{mm} \end{pmatrix} \quad (\text{B.15})$$

$\alpha$  and  $\beta$  are related by

$$\beta_k = \sum_{j=1}^m \alpha_{jk} \delta a_j \quad (\text{B.16})$$

and

$$\beta = \delta a \alpha \quad (\text{B.17})$$

### B.3 Gradient Search

A procedure for determining the minimum of  $\chi^2$  by linearising the fitting formula will achieve good convergence from points close to the minima but convergence becomes unreliable from points further away from the minimum. However the gradient search method allows good convergence from points far away from the minimum but convergence is slow when the minimum is approached.

Combining the two methods results in a scheme for obtaining the minimum of  $\chi^2$  that behaves like the linearisation method when in the neighbourhood of the solution (and where limitations due to the first order expansion are small) and like the gradient search method at more distant points.

The method given here was devised by Marquardt (1963) and described in Bevington (1969).

The two extremes of the method are the gradient search and the linearisation of the fitting function; the factor  $\lambda$  controls the degree of interpolation between the two extremes. The diagonal terms of the curvature matrix,  $\alpha$ , are increased by a factor of  $(1 + \lambda)$  to create the new curvature matrix  $\alpha'$ . Then

$$\beta = \delta a \alpha' \quad (\text{B.18})$$

$$\alpha'_{jk} = \begin{cases} \alpha_{jk} (1 + \lambda) & j = k \\ \alpha_{jk} & j \neq k \end{cases} \quad (\text{B.19})$$

If  $\lambda$  is large then the diagonal terms of  $\alpha'$  become large and the matrix equation degenerates into  $m$  separate equations (as the cross-terms are small compared to the diagonal terms, cf Equation (B.16)), *i.e.*

$$\beta_k \simeq \sum_{j=1}^m \lambda \delta a_j \alpha_{jk} \quad k = (1, m) \quad (\text{B.20})$$

Conversely, if  $\lambda$  is very small, then the matrix equation becomes the linearisation equation (Equation (B.17)).

To obtain the parameter increments,  $\delta a_j$ , the inverse of the new curvature matrix (*i.e.*  $\epsilon \equiv (\alpha')^{-1}$ , with elements  $\epsilon_{jk}$ ) is taken and used to multiply the matrix equation (B.18),

$$\delta a_j = \beta \epsilon = \sum_{k=1}^m (\beta_k \epsilon_{jk}) \quad (\text{B.21})$$

Using these equations an algorithm can be constructed to solve the non-linear least squares problem. See Figure B.1. Using an initial value of  $\lambda = 0.001$  the algorithm continues until two successive values of  $\chi^2$  lie within 1% of each other.

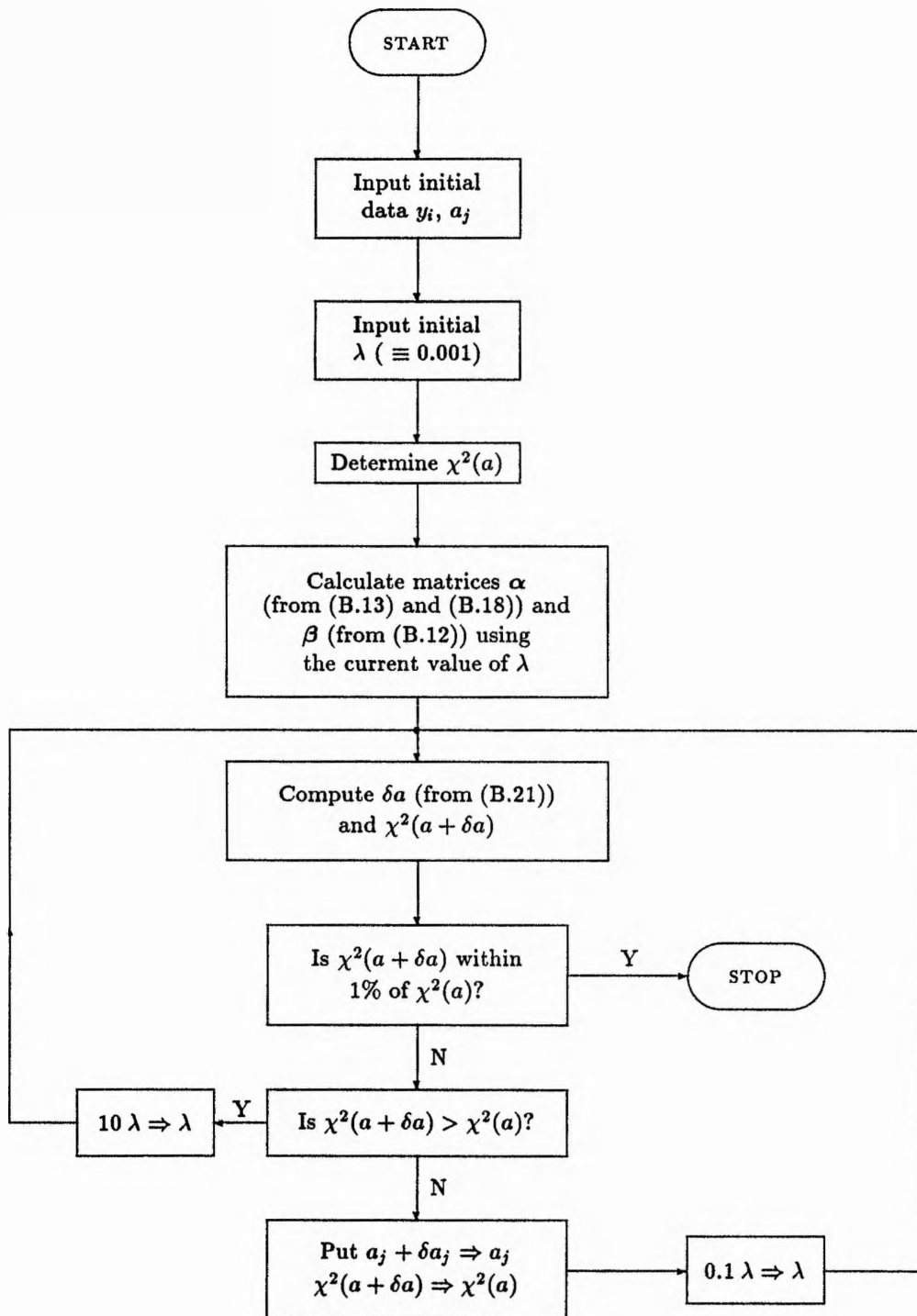


Figure B.1: A flowchart for a non-linear least squares fit to an arbitrary function using a gradient search of the linearised fitting function.

## B.4 Error Determination

As the method described above is non-analytic there is no analytic formula for the error on the parameter fits, however some reasonable approximations can be made and errors determined. See Bevington (1969) for proofs and details.

If one parameter,  $a_j$ , is incremented by an amount  $\Delta a_j$ , and all the other free parameters are optimised to minimise  $\chi^2$ , then  $\chi^2$  would be changed by  $\Delta\chi^2$  where

$$\Delta\chi^2 = \frac{\Delta a_j^2}{\epsilon_{jj}} \quad (\text{B.22})$$

To put reasonable errors on the free parameters,  $a_j$ , two cases can be considered, the relationship between them being self evident.

1. The error in  $a_j$  such that the value of  $\chi^2$  would double if all other parameters were optimised and  $a_j$  changed by  $\Delta a_j$ . This is achieved by replacing  $\Delta\chi^2$  in Equation (B.22) by  $\chi^2$ , so

$$\Delta a_j = \sqrt{\epsilon_{jj} \chi^2} \quad (\text{B.23})$$

This method will give small errors for good fits and large errors for poor fits but has the disadvantage that the error criterion depends on  $\chi^2$ .

2. Alternatively, the value of  $\Delta a_j$  required to alter the value of  $\chi^2$  by 1 can be calculated by putting  $\Delta\chi^2 = 1$  in Equation (B.22).

$$\Delta a_j = \sqrt{\epsilon_{jj}} \quad (\text{B.24})$$

This method is useful as the same error criterion is used for all fits.

## B.5 Weighting

A number of weighting schemes can be implemented, depending on the nature of the data and analysis being performed. Three are described here and are in the codes that implement the theory described above, although others could be used.

In the theory outlined above the weight of an observed data point has been represented by  $\frac{1}{\sigma_i^2}$ . In the program SEILS all data points are input with a value for  $\sigma_i$  although this may not be used depending on the mode of weighting adopted. The variable `mode` is used to describe the weighting adopted and has the following meaning

Thus only `mode = 1` uses the inputted value of  $\sigma_i$ ; the other modes base their weighting on the data value itself or adopt a uniform weighting.

Table B.1: Weighting and MODE of data.

MODE	Weighting
-1	$\frac{1}{\sigma_i^2} = \left  \frac{1}{y_i} \right , (y_i \neq 0)$ $\frac{1}{\sigma_i^2} = 1 (y_i = 0)$
0	$\frac{1}{\sigma_i^2} = 1$
1	$\frac{1}{\sigma_i^2} = \frac{1}{\sigma_i^2}$

## B.6 References

Bevington, P.R., 1969. *Data Reduction and Error Analysis for the Physical Sciences*, McGraw-Hill.

Marquardt, D.W., 1963. *J. Soc. Ind. Appl. Math.*, 11, 431.

## Appendix C

# SEILS - Parameters, Sample Input and Guide

There are three versions of SEILS all of which do much the same thing but require different inputs.

1. SEILS1: The standard least squares version of SEI using both a single velocity law and single optical depth law throughout the wind. Photospheric profiles may only be Gaussian.
2. SEILS2: The same as SEILS1 except that the photospheric profile may be of arbitrary shape and is read in from a data file before execution. SEILS2 was used to model the outer regions of the wind of  $\nu$  Sgr after the inner regions had been determined with SEILS1.
3. SEILS3: A two component optical depth law is used with the cross-over point being specified in the input file. Used for modelling the wind of  $\nu$  Sgr.

SEILS2 and SEILS3 were developed for the analysis of  $\nu$  Sgr only while SEILS1 is a general wind line analysis code for the analysis of single star winds. The following descriptions are about SEILS1 unless otherwise stated. The generic term SEILS is used to refer to all three programs.

### C.1 Input Files

SEILS requires a number of files to be set up before execution. The first one is called SEILS\_DEFAULTS.DAT and contains the values of those parameters that are likely to remain fixed for many runs but may need to be changed for other projects. An example of this file is given in Figure C.1.

Another data file is required for SEILS; an example is given in Figure C.2. This file contains

0.001	$\lambda$	Initial value of the parameter used in the least squares fit. See Appendix B.
0.	$\epsilon_B$	Collisional de-excitation parameter.
0.	$\epsilon_R$	Collisional de-excitation parameter.
1.	$a_T$	Parameter governing the radial behaviour of the Planck Function in the wind.
1.	$\left(\frac{B_\nu}{T_c}\right)_0$	Planck Function in the wind.
1.	MODE	Weighting scheme for the data points. (Table B.1)
1	BFLAG	Determines if the optical depth law with the $\frac{1}{\beta}$ term is used (BFLAG = 1) or not (0).

Figure C.1: A sample SEILS\_DEFAULTS.DAT file.

all the data required for a fit plus values of those parameters that are likely to need changing more frequently than those in the SEILS\_DEFAULTS.DAT file.

*S/D* An integer denoting whether a singlet (1) or doublet (2) line is to be fitted.

$w_0$  The normalised photospheric velocity.

$w_{HI}, w_{LO}$  The upper and lower values of the normalised velocity outside of which the optical depth is zero. ( $w_{HI} \equiv w_1$ )

IGMAX The number of points within the turbulent profile. 15 is usual unless  $w_g > 0.3$  in which case use 31. IGMAX must be an odd number.

$x_{I/O}$  The point, in units of stellar radii at which the Inner Region optical depth parameters ( $\alpha_1, \alpha_2$ ) change to the Outer Region ones ( $\alpha_3, \alpha_4$ ). SEILS3 only.

$N$  The number of data points that have been selected from the original spectrum.

$\lambda_B, \lambda_R$  The shorter and longer rest wavelengths of the doublet to be fitted, or the wavelength of the singlet line to be fitted.

$D_i, i = 1, N$   $N$  sets of data triplets in the form of the wavelength, flux value and weight of the data point.

$\beta, \dots, v_\infty$  Data pairs for the free parameters in the fit; 6 for SEILS1 and SEILS2, 8 for SEILS3. The first number is the initial value for the parameter while the second number is the amount to either side that the program looks when calculating the derivative of the fit with respect to the parameter. Only for  $\alpha_1, \alpha_2, \alpha_3$  and  $\alpha_4$  can  $\Delta$  be larger than the initial value. If  $\Delta$  for a given parameter is fixed to be zero then that parameter is fixed at its initial value and will not be allowed to vary in the subsequent fit. The optical depth of the red component ( $T_R$ ) is not a free parameter; it is assumed to be one half of the optical depth of the blue component.

Figure C.2: A SEILS data file.

1		$S/D$
0.01		$w_0$
0.0 1.0		$w_{LO}, w_{HI}$
15		IGMAX
80		$x_{I/O}$ SEILS3 only
20		$N$
1548.19 1550.76 <sup>†</sup>		$\lambda_B, \lambda_R$
1533.04 1.000 1		$D_1$
1542.02 0.998 1		$D_2$
⋮		
1555.35 1.000 1		$D_N$
0.7 0.1		$\beta$
0.1 0.5		$\alpha_1$
0.1 0.5		$\alpha_2$
0.1 0.05		$w_g$
5.0 2.0		$T_B$
700 200		$v_\infty$
0.5 0.1		$\alpha_3$ SEILS3 only.
0.5 0.1		$\alpha_4$ SEILS3 only.
1.61 0.4		$A_{phot_B}, w_{phot_B}$
1.61 <sup>†</sup> 0.4 <sup>†</sup>		$A_{phot_R}, w_{phot_R}$
-3.0 3.0 0.1		PRSTART, PREND, PRSTEP
'text...' <sup>‡</sup>		Header text.

<sup>†</sup> Must be included when fitting slaglet lines, but the value is ignored.

<sup>‡</sup> Optional.

This is true for resonance doublet lines. However for some lines (*e.g.* the C II doublet)  $T_R = 2T_B$ . This feature can be invoked within SEILS by setting  $T_B$  to be negative in the input file. Within SEILS  $T_B$  is set to the absolute value of this quantity and  $T_R$  to be twice this.

$A_{phot_B}, A_{phot_R}$  The depths of the photospheric line components, if present. The depth is related to the normalised flux by  $A_{phot} = -\ln(flux)$ .

$w_{phot_B}, w_{phot_R}$  The widths of the photospheric lines in terms of the terminal velocity of the wind.

PRSTART, PREND, PRSTEP The interval, in normalised velocity units, between which the final profiles are determined. PRSTEP determines the coarseness of this final profile.

**Header text** This (optional) single line of text will be printed at the top of the output file. It allows the contents of the output file to be easily identified *etc.*

Finally, a .COM file is required when running SEILS in batch, an example is given in Figure C.3. Input, output and photospheric profile (SEILS2 only) file names need to be specified. If no photospheric file is required (*i.e.* the standard Gaussian photospheric lines are to be used rather than inputting an arbitrary profile) then the first three letters of the photospheric file name should be "NUL".

```
$ set default user2:[scratch.asrrd.stars]
$ run seils
star.in
star.out
line.phot
$ rename seils_phot.sp0 star_phot.sp0
$ rename seils_wind.sp0 star_wind.sp0
```

Figure C.3: A sample .COM file for running SEILS in batch.

The "standard input" values for the parameters given in Table C.1. These standard inputs were not always used, being varied, usually only slightly, if necessary.

## C.2 Output Files

SEILS gives four output files per run. The first is SEILS\_OUT.DAT and gives the same information as the SEISOUT3.DAT and SEIDOUT3.DAT files that are output from the SEISING3 and SEIDOUT3 programs (*i.e.* the turbulent profile, source functions and final profile). SEILS also outputs two DIPSO files, one of the total wind line profile (SEILS\_WIND.DAT), the other (SEILS\_PHOT.DAT) the photospheric profile used. They are determined using the values found by SEILS after the least squares solution has been found. The final output file, the name of which is specified in the .COM

Table C.1: "Standard inputs" for a SEILS data file. The terminal velocity initial value is chosen to be close to the expected value. For the determination of O star winds (Chapter 5) a value of  $2500 \text{ km s}^{-1}$  with a  $\Delta$  of  $500 \text{ km s}^{-1}$  was used. For the EHe and HDB stars (Chapters 6 and 7) values of  $750$  and  $100 \text{ km s}^{-1}$  were used.  $\alpha_3$  and  $\alpha_4$  are required for SEILS3 only.

Param.	Value	$\Delta$
$\beta$	0.7	0.1
$\alpha_1$	0.1	2.
$\alpha_2$	0.1	2.
$w_g$	0.10	0.05
$T_B$	10.0	5.0
$v_\infty$	variable	
$\alpha_3$	0.1	2.
$\alpha_4$	0.1	2.

file contains the results of the least squares solution. An example of the output file is given in Figure C.4.

Text...

-----  
DEFAULTS: FLAMDA EPSOB EPSOR AT BICO MODE BFLAG  
          0.001  0.0  0.0  1.0  1.0  1  0  
-----

DOUBLET:     1548.19  1552.34

VELOCITIES: PHOTOSPHERIC:  0.01  
              LOW:           0.00  
              HIGH:          1.00  
IGMAX:                      15

-----  
DATA POINTS        20  
PHOT LINES (B) :       1.61  0.400  
PHOT LINES (R) :       1.61  0.400  
-----

PARAM	INITIAL	FINAL	ERROR
BETA	0.700	0.732	0.165
Vinf	570.	641.	249.
Wg	0.100	0.103	0.003
ALPHA1	0.100	0.768	1.142
ALPHA2	0.100	-0.243	2.305
T(B)	5.000	7.451	0.862

-----  
SEP:     0.840     0.793  
AFTER  3 CALLS, CHISQR (FINAL) =  1.26025  
CONVERGED

Figure C.4: A sample output file from SEILS for a doublet line. For a singlet line the output file is very similar. For SEILS2 the name of the input photospheric file is given. For SEILS3 details of the Inner/Outer Region point and the results for  $\alpha_3$  and  $\alpha_4$  are also given.

# Appendix D

## Checklist for Wind Line Analysis

A system of steps can be given for the good determination of wind lines. These are guidelines and some lines may need special attention.

1. Careful determination of the continuum is the most important step and consists of a number of individual steps.
  - (a) Re-binning. If the spectrum shows much noise (*e.g.* a single IUE spectrum) then re-binning allows a more accurate determination of the flux levels without sacrificing the independence of the wavelength-flux data points. Re-binning to  $0.2 \text{ \AA}$  is usually sufficient.
  - (b) Flux zero point determination. Due to the occasional poor extraction of IUE spectra the lowest flux recorded will be sub-zero. This is most noticeable in the Lyman- $\alpha$  line at  $1215 \text{ \AA}$  which is usually massively saturated. The lowest part of this profile should be set at zero flux.
  - (c) Remove the general slope of the continuum, if necessary, by looking at the slope of the continuum over a few hundred Angstroms.
  - (d) Remove any contribution from interstellar Lyman- $\alpha$ , if dealing with the NV doublet.
  - (e) Select the actual level of the continuum through the wind line by considering the flux going into the line. Set the continuum level to be 90-95% of the peaks in this small range of spectrum.
2. Select the data points carefully, with more points in regions of importance such as the blue edge of the line.
3. Select values for photospheric line depths and widths;
  - (a) Use values from published results.

- (b) Use a model atmosphere program to determine the photospheric lines. This procedure requires knowledge of
    - i. Atomic data such as oscillator strengths, electron damping constants and collisional cross-sections. These may only be poorly known for highly excited lines in the UV.
    - ii. The temperature and surface composition of the star need to be known. In studies of peculiar stars (*e.g.* Hydrogen-deficient stars) these facts may only be poorly known.
    - iii. NLTE model atmospheres may need to be used; these are not always available especially when combined with studies of highly excited lines in peculiar stars.
  - (c) From studies of similar objects make an initial estimate of the line depths and widths. After a solution is obtained the depths and widths can be altered if these parameters are being treated as ways of improving the fit rather than as true physical parameters.
4. Determine an initial solution, for all lines of a given star, using SEILS with a standard input file, with initial photospheric lines.
  5. Determine values for  $v_\infty$ ,  $\beta$  and  $w_g$  by looking at all the lines of a given star, noting
    - (a) The doublet lines are more sensitive to parameter changes than the singlet lines, so weight the doublet results more.
    - (b) The singlet lines are not resonance lines so the extent of the blue edge may not be equal to the terminal velocity, *i.e.*  $w_1$  may not equal 1. However in the standard input file  $w_1$  is set to 1. Thus the initial results for singlet lines should be rerun with  $w_1 < 1$  if necessary to get a better fit.
  6. Error values can be used to indicate the goodness of fit. A small error on a parameter means that varying the parameter slightly will have a large effect on the goodness of fit. A large error indicates that the value of the parameter is not so critical.
  7. Having selected  $v_\infty$ ,  $\beta$  and  $w_g$ , re-determine the other parameters using SEILS with another standard input file for all lines of a given star.
  8. Adjust the values of  $v_\infty$ ,  $\beta$ ,  $w_g$  and the photospheric components, if necessary, and re-determine all the parameters. Repeat this step as necessary.

## Appendix E

# Echelle Reduction - A Worked Example

One of the problems with echelle reduction is that few people have done it and the information required to do it is sparse. A manual is available for the FIGARO routines but this is not complete and is in some case misleading especially in the values given as examples. When reducing the AAO/UCLES data for  $\nu$  Sgr much effort was put into finding a scheme that would work. The results of this effort are given here in the form of a worked example that has been proven in the reduction of AAO/UCLES data. The image frame consisted of a 1024x1024 pixel images (Thompson chip) covering the 27 orders 116 - 142 (blue). This corresponded to a wavelength coverage of approx. 3980-4910 Å. These values will have to be modified for other formats and wavelength coverage but the reduction scheme outlined here should still be valid. All inputs have been described together with the inputs used for this reduction. This should allow batch jobs to be written to reduce many similar frames. Here the interactive reduction need only be done once and then the results from this (*e.g.* the mask frame from ECHMASK and the arc wavelength calibration data from ECHARC) used for the succeeding frames. This is possible as the AAO/UCLES system is very stable; the orders lie on the same place on the CCD in succeeding frames.

1) Obtain the data (this is generally the hardest part). The following are required.

1. Bias frame(s)
2. Flat field (*i.e.* continuum source) frame(s).
3. Arc spectrum frame (only one required).
4. Object frame(s).

2) Determine a final bias frame from the set of individual bias frames. The readout time is short and thus cosmic ray events should be at a minimum. However as bias subtraction is an important step the bias frames should be free from such events. If three or more bias frames are available then they should be median filtered to remove the cosmic ray events. Median filtering finds the median value of each pixel from the values of that pixel in each of the individual frames. This will ignore very large values that occur because of cosmic ray events. It will not counteract effects such as hot pixels that effect the same pixel on each frame.

Generate a file `BIAS.LIST` with the filenames of all the bias frames

SYNTAX: \$ MEDSKY FILES, OUTput  
FILES = Name of file containing the list of frames  
OUTput = Filename of the resulting image.

*e.g.* \$ MEDSKY BIAS.LIST, BIAS.DST

3) Subtract the median bias frame from each of the object and flat field frames.

SYNTAX: \$ ISUB IMage, IMAGE1, OUTput  
IMage = First frame (ie object or flat field frame)  
IMAGE1 = The second frame (ie median bias frame)  
OUTput = The output filename

*e.g.* \$ ISUB UPS\_SGR1, BIAS, UPS\_SGR\_BIAS1  
\$ ISUB FLAT1, BIAS, FLAT\_BIAS1

4) Now determine a median filtered flat field image, using MEDSKY again with `FLAT.LIST` containing a list of the (bias subtracted) flat field image names.

*e.g.* \$ MEDSKY FLAT.LIST, FLAT.DST

5) Determine a final object frame. Using MEDSKY here will remove cosmic ray events but will not increase the signal to noise ratio as the series of object frames are not added together. A direct summation of the bias subtracted object frames is needed, but (later) cosmic ray events need to be flagged and ignored. Use `IADD`.

SYNTAX: \$ IADD IMAge, IMAGE1, OUTput  
IMAge = First frame.  
IMAGE1 = Second frame.  
OUTput = The output filename

*e.g.* \$ ISUB UPS\_SGR\_BIAS1, UPS\_SGR\_BIAS2, UPS  
\$ IADD UPS, UPS\_SGR\_BIAS3, UPS  
... etc

We now have a summed object frame (UPS), and a median bias subtracted flat field frame (FLAT) along with the unmodified arc frame (ARC).

6) For the correct analysis on the CCD echelle data the frames from the CCD need to be rotated and flipped to get them in the correct orientation (wavelength increasing left to right and order number increasing bottom to top). Use ROTATE and IREVY

SYNTAX: \$ ROTATE IMAge, OUTput  
IMAge = Frame to be rotated.  
OUTput = The output filename.

SYNTAX: \$ IREVY IMAge, OUTput  
IMAge = Frame to be flipped.  
OUTput = The output filename.

*e.g.* \$ ROTATE UPS, UPS\_ROT  
\$ IREVY UPS\_ROT, UPS  
\$ ROTATE FLAT, FLAT\_ROT  
\$ IREVY FLAT\_ROT, FLAT  
\$ ROTATE ARC, ARC\_ROT  
\$ IREVY ARC\_ROT, ARC

7) The object image now needs to be corrected for the blaze function by division by the flat field frame. Use IDIV.

SYNTAX: \$ IDIV IMAge, IMAGE1, OUTput

IMage = First frame.  
IMAGE1 = Second frame.  
OUTput = The output filename

*e.g.* \$ IDIV UPS, FLAT, UPS

8) The orders on the image frame are not horizontal; to allow further processing the positions of the orders must be determined. As the AAO echelle spectrograph is extremely stable the positions of the orders can be found on the flat field frame. This avoids problems when trying to track orders that have absorption lines in them. First display the image on an image display unit (that has been assigned, *e.g.* \$ IKON XAA0, Y).

SYNTAX: \$ IMAGE IMage, YStart, YEnd, XStart, XEnd, AUtoscale, OPTimize,  
          XPlaces, YPlaces, ASpect, ERASE

IMage = Frame to be displayed.

YStart = First Y pixel.

YEnd = Final Y pixel.

XStart = First X pixel.

XEnd = Final X pixel.

Autoscale = Automatically scale the image so it all fits on the screen?

OPTimize = Amount of histogram optimization.

XPlaces = Number of sub-displays across the screen in X.

YPlaces = Number of sub-displays across the screen in Y.

ASpect = Maintain correct aspect ratio?

ERASE = Erase the screen before display?

*e.g.* \$ IMAGE FLAT, 1, 1024, 1, 1024, YES, 0, 1, 1, YES, YES

Now determine the center of each order interactively by using ICUR and the mouse/cursors. Set the vertical line to the center of the image then in turn set the horizontal line on each order with the point where the lines cross being in the center of the order. In the case of the UPS image there were 27 orders. Press Q when finished.

SYNTAX: \$ ICUR

Now use SDIST to track the orders automatically and display the results on top of the displayed image. The values in the example were found to work best on the AAO images. A low value of COLumns was found to work best on the continuum source frame. The trace mode is arbitrary for fitting a continuum source but Gaussian works best for an image frame. For the width of the spectra in pixels a large value of 30 was used; this being about twice the actual half width. However smaller values were not so successful. For the degree of polynomial to use in fitting the orders the smallest value possible should be used. Large values tend to produce very poor results at the ends of orders. When using UCLES there is very little distortion and the orders are generally straight but not horizontal. A polynomial of degree one gave good results. These results can be shown either on an image device or on a graphics terminal.

SYNTAX: \$ SDIST IMage, COLumns, TRace, Width, MAXdeg, Display, SOft

Image = Filename of image to be analysed.

COLumns = Number of columns to average to get peaks.

TRace = Trace mode - G(aussian), C(enter of gravity), E(dge).

Width = Half width of spectra in pixels.

MAXdeg = Maximum degree of polynomial to use.

Display = Use image display to show results.

SOft = Display results on graphics device.

*e.g.* \$ SDIST FLAT, 3, C, 30, 1, YES, NO

If many orders are not tracked or many are not tracked from end to end then repeat the ICUR step with more care. Probably not all of the orders will be tracked from end to end; if this is only true for a few orders then edit the SDIST.DAT file. This contains the coefficients of the polynomials used to fit the orders. For those that don't go from end to end change the limits to 1 and 1024 (in this case). In the case of orders that are not found examine the polynomial coefficients in the previous few orders. A pattern should be obvious as the orders are almost straight but the inclination changes slightly for each order. Determine the likely polynomial coefficients and enter these in the SDIST.DAT file. To display the results use ODIST, the displayed orders should be well tracked; if this is not so then edit the SDIST.DAT file some more.

9) Now a mask needs to be created showing where the orders are. The program CDIST does not work and the "new-ECHARC" program has not been written. Thus the optimum extraction of orders cannot be performed. The mask extraction method is only slightly worse. Use ECHMASK to create the mask. The lowest order number needs to be known - this may be on the log sheet. Failing this it can be found from looking at the ARC spectrum and identifying orders from the arc line present. In this case 116 was the lowest order (the first to be fitted). ECHMASK allows the

sky/star periscope to be fitted and sky and object to be extracted separately. This is not required with the AAO/UCLES data and most of the input connected with this can be set to zero (see example).

**SYNTAX:** \$ ECHMASK COFile, PERIScope, OBJwidth, OBJOffset, S1Width,  
MStart, MDelta, MASK

COFile = The name of the file with the SDIST coefficients.

PERIScope = Is the star/sky periscope fitted.

OBJWidth = No. of rows of object to extract per order.

OBJOffset = Offset of order centre from object center.

S1Width = Number of rows of region 1 sky to extract.

MStart = Number of the first order fitted.

MDelta = Order number increases or decreases (+1/-1) after the first.

MASK = Name of the output mask file.

*e.g.* \$ ECHMASK SDIST, NO, 8, 0, 0, 116, +1, MASK

10) Using this mask the object and arc frames must have their orders extracted using MASKEXT. The value of SUBord should always be one when the periscope is not fitted and the object only needs extracting. The final result is a "collapsed echellogram" with one row for each order.

**SYNTAX:** \$ MASKEXT IMage, MAsk, MLow, MHigh, SUBord, OUTput

IMage = Filename of the image to have its orders extracted.

MAsk = Name of the mask file created with ECHMASK.

MLow = Lowest order number to be extracted.

MHigh = Highest order number to be extracted.

SUBord = SUBorder to extract.

OUTput = Output filename.

*e.g.* \$ MASKEXT UPS, MASK, 116, 142, 1, UPSE

\$ MASKEXT ARC, MASK, 116, 142, 1, ARCE

11) The arc image must now be wavelength calibrated. Display the original ARC spectrum and using a booklet of arc line identifications for each order (*e.g.* ESO Scientific Report No. 6, July 1987. eds. S. D'Odorico, M. Ghigo and D. Ponz) and identify lines in the top and bottom orders and for an order in the middle. The type of arc spectrum used was a Thorium-Argon (THAR)

one.

SYNTAX: \$ ECHARC IMage, ARctype, PREvious, INTeractive, ORDers,  
ORDERfit, Sigma, DOWaves

IMage = Filename of the arc image to analyse.

ARctype = Type of arc used.

PREvious = Use arc lines from a previous fit.

INTeractive = The number of orders to fit interactively.

ORDers = The order numbers to fit.

ORDERfit = Polynomial order for first fit.

Sigma = Arc line half-width in pixels.

DOWaves = Write wavelength information to a separate file.

*e.g.* \$ ECHARC ARCE, THAR, N, 3, (116,133,142), 3, 3, No

This displays each order of the three indicated and asks for identifications to be made. The default setting is to only show the first 200 pixels of the order so change this to display the whole order (press L and follow the prompts). After identifying the lines in each of the three orders continue and the program will automatically identify many lines in all of the orders.

12) Now copy the wavelength information contained in the ARCE image to the UPSE image.

SYNTAX: \$ XCOPY SPectrum, ARc, OUTput  
SPectrum = File requiring wavelength calibration.  
ARc = File containing wavelength calibration.  
OUTput = Resulting wavelength calibrated file.

*e.g.* \$ XCOPY UPSE,ARCE,UPSL

13) The object frame now needs to be re-binned using SCRUNCH. The beginning and end wavelengths need to be known (EXAM will do this) and the number of bins (and thus the bin width) need to be decided.

SYNTAX: \$ SCRUNCH SPectrum, LOg, WStart, WEnd, BIns, Mean, Quad,  
OUTput  
SPectrum = Spectrum to be scrunched.

LOg = Bin to logarithmic wavelength bins.  
WStart = Wavelength of centre of first bin.  
WEnd = Wavelength increment per bin.  
BIns = Number of bins.  
Mean = Conserve mean value.  
Quad = Use quadratic interpolation for data.  
OUTput = Output filename.

*e.g.* \$ SCRUNCH UPSL, No, 3940, 0.02, 49000, No, Yes, UPSLS

14) Finally the calibrated and re-binned orders are merged into a complete spectrum. No second image is required so type a space at the prompt. In the overlap region of two orders the signal should be roughly equal. However if the blaze function has not been totally removed by the flatfielding process then this may not be the case. Here if the weaker component is less than 4 times the strength of the stronger one it is ignored, otherwise a mean value is taken.

SYNTAX: \$ ECHMERGE IMage, IMAGE2, Box, CUToff, OUTput  
IMage = Image to be merged.  
IMAGE2 = Name of second image.  
Box = Size of box for median filter.  
CUToff = Max ratio of data to allow contribution by the weaker.  
OUTput = Name of resulting spectrum.

*e.g.* \$ ECHMERGE UPSLS, , 7, 4, UPS\_FINAL

15) The spectrum should now be displayed with SPLOT. In all probability not all of the blaze function has been removed. If this is true then EXTRACT each order separately from the image UPSLS and written out in a set of x,y values using ALASOUT. Using WDIPSO to write the data in SP0 format will not work in this case as each order now consists of 49000 data points covering the whole spectral range (3940 to 4920 in this case). The data values are zero for all parts of this range that do not lie in the original order being extracted. So edit the output spectra files deleting all the zero values (a simple FORTRAN program can be written to aid in this). Then in DIPSO read in the spectra (ALASRD) and then write them out in SP0 format (SP0WR). Then, still in DIPSO, determine the continuum with CREGS and divide the original spectrum by this continuum. This will normalise the spectra but will have removed the residual blaze function. The individual corrected spectra can be merged in DIPSO.

## Appendix F

# Individual Line Fits for the O Stars, Extreme Helium Stars and $v$ Sgr

### F.1 O Stars

The individual fits are shown in Figure F.1 and the fit parameters tabulated in Table F.1. Notes on the final selection of parameters are given below. The final parameters are given in Table 5.3 and shown in Figure 5.1.

**HD 14947.** There are only two wind lines for this star, CIV and SiIV, both of which are well fitted individually. The model lines show increased flux to the red side of the observed emission peak and the SiIV line also shows increased model flux to the redward side of both absorption components.

Values of the three parameters  $\beta, w_g$  and  $v_\infty$  are very close for both lines. The final adopted value of  $\beta$  is an average values while those of  $w_g$  and  $v_\infty$  are closer to the CIV than SiIV values as the quality of the overall fit is marginally better for CIV.

**HD 24912.** Three lines of which the CIV and NV fits are very good. The NIV profile is good in the absorption region but very poor in the emission region. This is probably due to a numerical problem where the “best fit” is a combination of a good fit to one part of the profile and a very poor fit to another part rather than a “reasonable” fit to the whole profile. The NIV parameters were not used in the determination of the final parameters.

The final values for  $w_g$  and  $v_\infty$  were from the CIV profile which had a slightly better fit than the NV profile although the parameters were very close.  $\beta$  was a weighted average of the CIV and NV values with the CIV values being given a higher weighting.

**HD 30614.** Three lines with CIV and SiIV being excellent and NV very good. This excellence of fit is shown in the parameter values; the values of  $\beta, w_g$  and  $v_\infty$  are very close for all three lines. Straight averages were taken for the final values of all three parameters.

**HD 37043.** Three lines of variable quality. The CIV is good, NV fair and CIII poor. Final values of  $w_g$  and  $v_\infty$  are from the CIV line with  $\beta$  an average of CIV and NV as the fits to the emission peaks (strongly determined by  $\beta$ ) are equally good for these two lines. CIII was ignored.

**HD 41650.** Three lines with CIV good, NIV and NV reasonable. Good agreement on  $\beta$  for all three lines so a straight average taken.  $v_\infty$  was average to find a final value while for  $w_g$  a low values from the agreement of CIV and NIV was adopted.

**$\zeta$  Puppis.** There are 4 lines with CIV and SiIV very good; NIV and NV only fair.  $\beta$  is taken from the CIV fit,  $v_\infty$  from a average of the three line values excluding NIV. Good agreement on  $w_g$  leads to a straight average for the final adopted value.

Table F.1: Individual fits for 6 O stars.

Star	Ion	$\beta$	$v_{\infty}$	$w_g$	$\alpha_1$	$\alpha_2$	$T_B$	$A_{phot_B}$	$w_{phot_B}$
HD14947 O5 If+	CIV	1.28	2110	0.133	0.05	-0.65	9.84	3.6	0.04
		0.15	110	0.015	0.44	0.43	3.64		
	SiIV	1.04	2030	0.141	-1.04	-0.77	4.33	0.0	0.00
		0.03	30	0.005	0.09	0.10	0.30		
HD24912 O7.5 IIIaf	CIV	0.84	2200	0.246	0.14	-0.10	5.56	0.0	0.00
		0.77	310	0.097	0.25	0.98	3.98		
	NV	1.28	2290	0.220	0.62	0.51	9.24	0.0	0.00
		3.84	1180	0.354	3.39	3.24	26.37		
	NIV	0.44	2680	0.000	-1.64	-0.45	1.65	0.9	0.04
		0.82	180	0.053	0.82	0.50	0.28		
HD30614 O9.5 Ia	CIV	1.17	1430	0.205	-0.30	-0.48	12.26	0.0	0.00
		0.83	120	0.026	0.42	0.46	4.25		
	NV	1.91	1770	0.014	1.69	1.11	9.71	0.0	0.00
		2.68	425	0.085	2.43	1.88	6.72		
	SiIV	2.39	1320	0.159	-1.10	-1.18	8.57	0.0	0.00
		0.75	30	0.008	0.27	0.14	1.36		
HD37043 O9 III	CIV	0.59	2490	0.005	-0.38	0.58	2.40	2.0	0.15
		0.23	70	0.087	0.14	0.20	0.26		
	NV	1.95	4580	0.014	-0.93	1.19	3.94	0.8	0.08
		0.34	320	0.005	0.14	0.14	0.55		
	CIII	0.16	1380	0.149	-2.84	-1.77	1.26	3.5	0.09
		0.01	20	0.004	0.08	0.12	0.17		
HD41650 O5 VI	CIV	0.71	3010	0.032	-0.64	-0.22	3.08	2.0	0.07
		0.41	120	0.016	0.32	0.32	0.70		
	NV	0.81	2930	0.413	-0.81	0.19	5.79	2.0	0.03
		0.14	120	0.010	0.02	0.17	0.73		
	NIV	0.76	3410	0.036	-0.93	-1.00	0.21	0.8	0.04
		0.07	130	0.010	0.17	0.22	0.02		
HD66811 $\zeta$ Puppis O4 Iaf	CIV	0.94	2420	0.099	0.13	-0.23	7.87	0.0	0.00
		1.13	850	0.117	2.06	2.70	18.7		
	NV	1.76	2140	0.114	-1.80	-1.60	11.25	0.7	0.10
		0.04	11.2	0.001	0.03	0.04	0.42		
	NIV	0.68	1720	0.070	-0.71	0.44	2.30	0.0	0.00
		0.88	1000	0.135	1.30	2.30	2.70		
	SiIV	0.41	2260	0.108	0.60	-0.04	1.65	1.0	0.10
		1.42	1200	0.242	3.47	2.89	2.27		

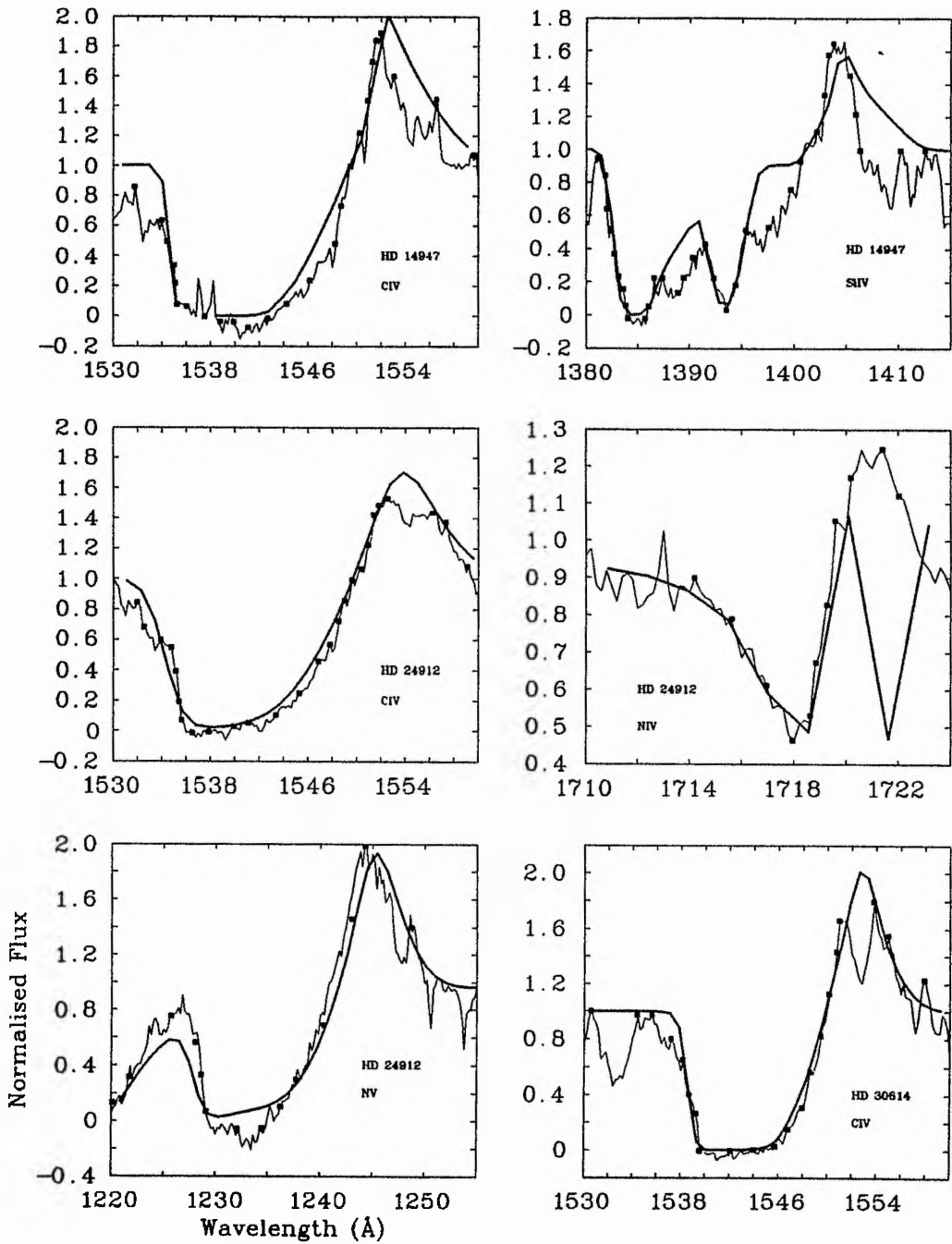


Figure F.1: Initial profiles for the 6 O stars using the  $\beta$ -independent optical depth law.

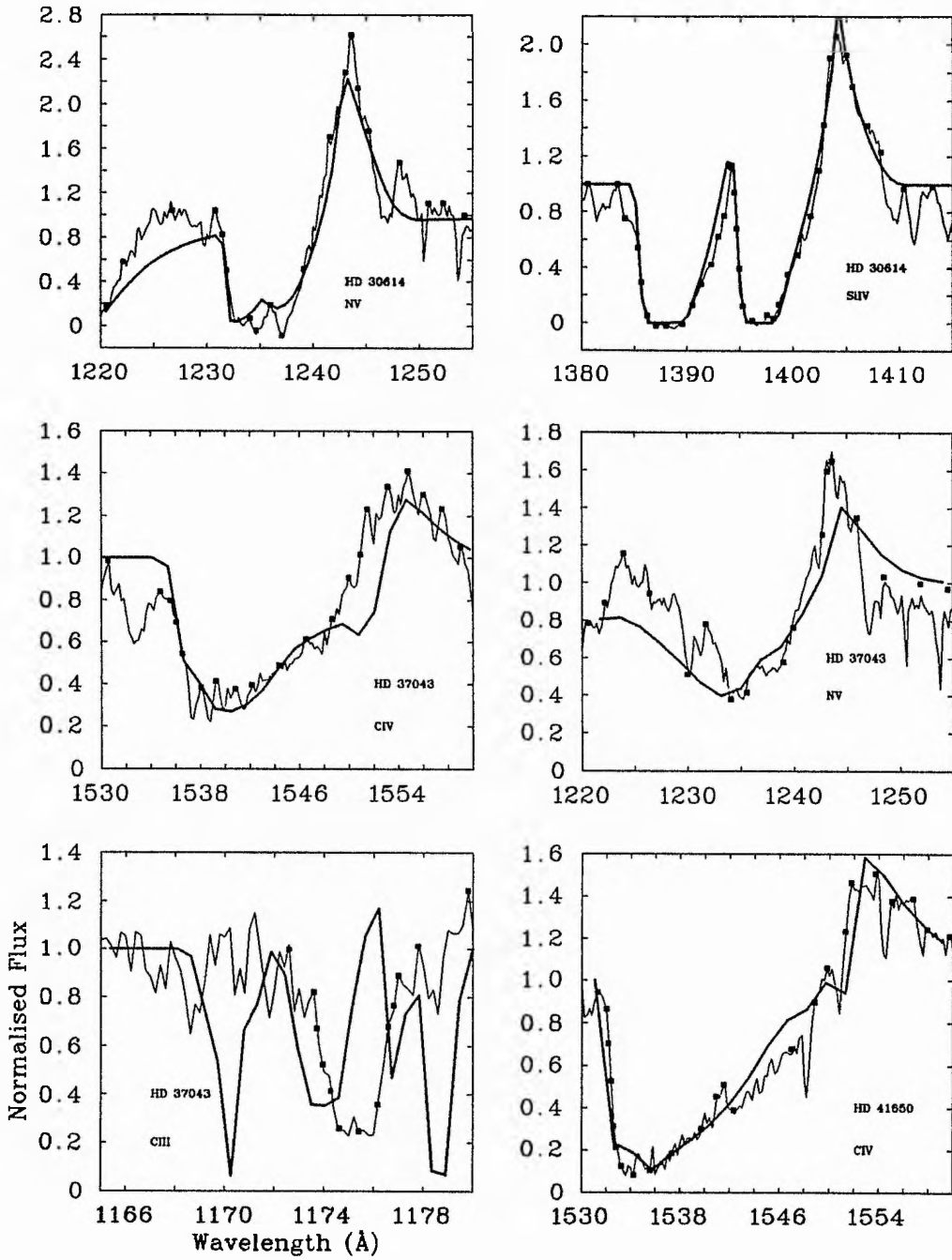


Figure F.1: *continued.*

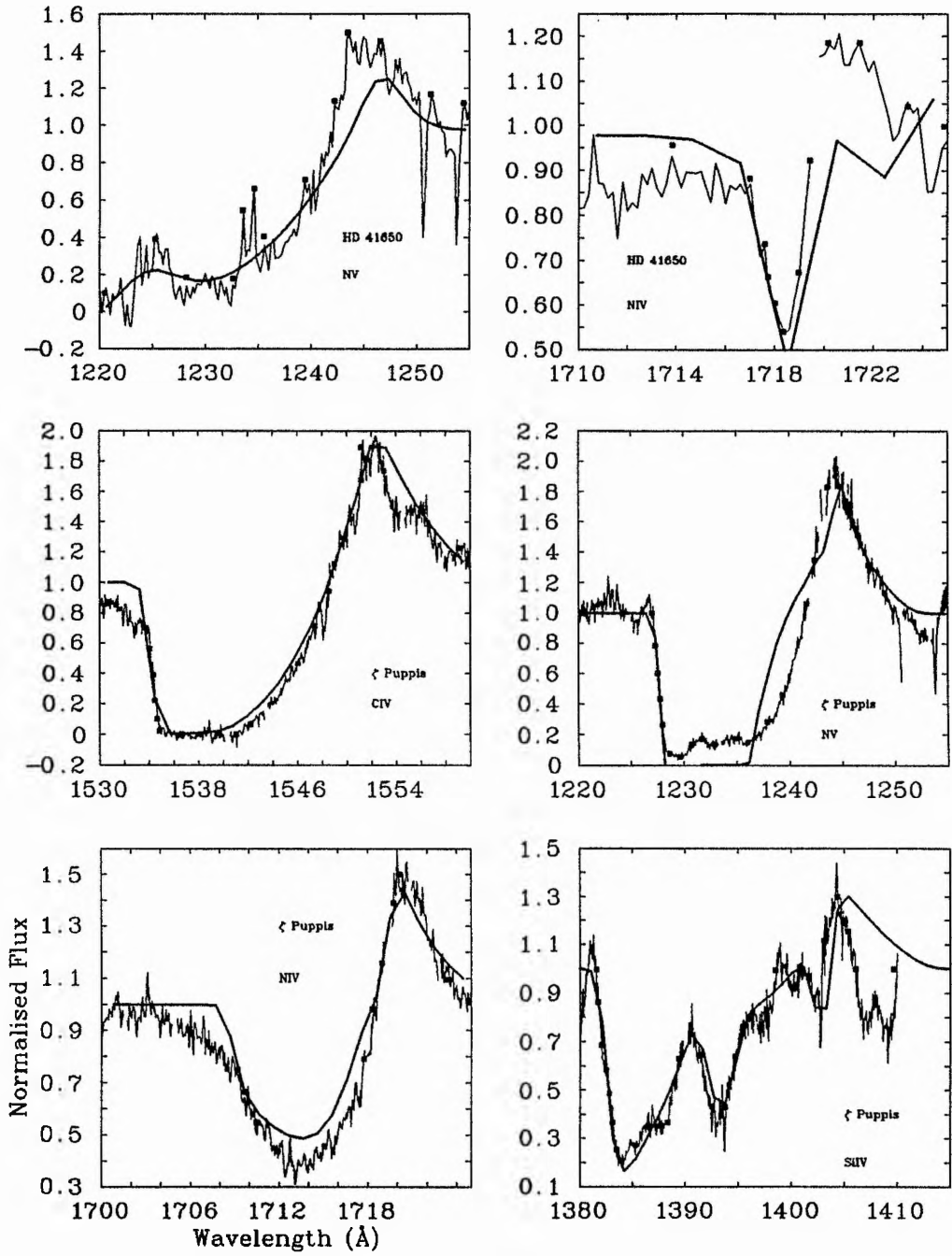


Figure F.1: *continued.*

## F.2 Extreme Helium Stars

### F.2.1 Notes on final parameter selection: $\beta$ -dependent

The individual fits are shown in Figure F.2 and the fit parameters tabulated in Table F.2. Notes on the final selection of parameters are given below. The final parameters are given in Table 6.4 and shown in Figure 6.1.

**BD -9° 4395.** Three lines; CIV and SiIV fairly good with CIII very poor. The large emission peak of CIV is not fitted. Both CIV and SiIV have a well defined terminal and turbulent velocity so a straight average was used to determine the final values of these parameters.  $\beta$  is less well defined, a compromise value of 1.0 was used based mainly of the CIV result but modified for the lower SiIV value.

**HD 160641.** 4 lines. NV and SiIV good fits with CII and CIV less so.  $v_\infty$  from the good terminal velocity of SiIV lowered slightly to account for the NV value.  $w_g$  from the good agreements between the CIV, NV and SiIV lines.  $\beta$  from the NV profile which has the lowest uncertainty and falls within the error bounds of the CIV and SiIV fit values.

**BD +37° 1977.** Good CIV and NV profiles with a poor NIV. The good fits to the CIV and NV emission peaks leads to the retention of their low values of  $\beta$  for the final fit.  $w_g$  retained from CIV and  $v_\infty$  from CIV and NV with the latter value increase due to the lower adopted turbulent velocity.

**BD +37° 442.** Good CIV and NIV lines, poor NV.  $\beta$ ,  $w_g$  and  $v_\infty$  all retained from the CIV fit.

Table F.2: Individual fits for the EHe stars using the  $\beta$ -dependent optical depth law. BD +10° 2179 is not shown in this table as it only has one line capable of being modelled. The fit for this line is given in Table 6.4. Errors are in small type.

Star	Ion	$\beta$	$v_\infty$	$w_g$	$\alpha_1$	$\alpha_2$	$T_B$
BD -9° 4395	C IV	1.19	460	0.236	0.23	-0.77	11.75
		0.99	20	0.020	0.96	0.13	3.77
	Si IV	0.30	330	0.645	-1.15	-0.24	38.36
		0.48	140	0.257	1.90	1.56	152.62
	C II	4.14	320	0.423	6.60	3.39	6.11
		49.6	80	0.165	6.47	2.97	7.61
HD160641	C II	0.86	390	0.113	-3.11	-1.66	63.9
		2.71	400	0.236	1.99	2.81	7.41
	C IV	5.29	670	0.266	-1.47	-0.72	22.60
		44.55	180	0.088	2.15	1.94	41.47
	N V	3.56	470	0.228	-1.81	-1.49	0.37
		0.01	0	0.000	0.01	0.00	0.00
	Si IV	34.04	670	0.219	1.73	0.94	8.66
		287	160	0.107	1.71	1.71	7.50
BD +37° 1977	C IV	0.17	1930	0.059	2.97	4.81	75.2
		0.64	510	0.326	39.32	21.43	687.99
	N IV	0.06	1120	0.173	-0.88	-0.42	0.07
		0.79	3220	1.899	8.01	27.57	1.02
	N V	0.16	1260	0.553	14.82	1.44	3.88
		0.81	710	0.588	100.85	17.85	6.08
BD +37° 442	C IV	0.99	2220	0.030	0.80	1.13	4.51
		1.01	260	0.225	1.36	0.66	4.94
	N IV	0.33	1840	0.007	-1.01	0.63	0.71
		2.64	3741	0.126	2.96	8.98	2.25
	N V	1.28	3030	0.033	2.18	1.91	13.20
		0.99	970	0.338	11.36	6.29	34.64

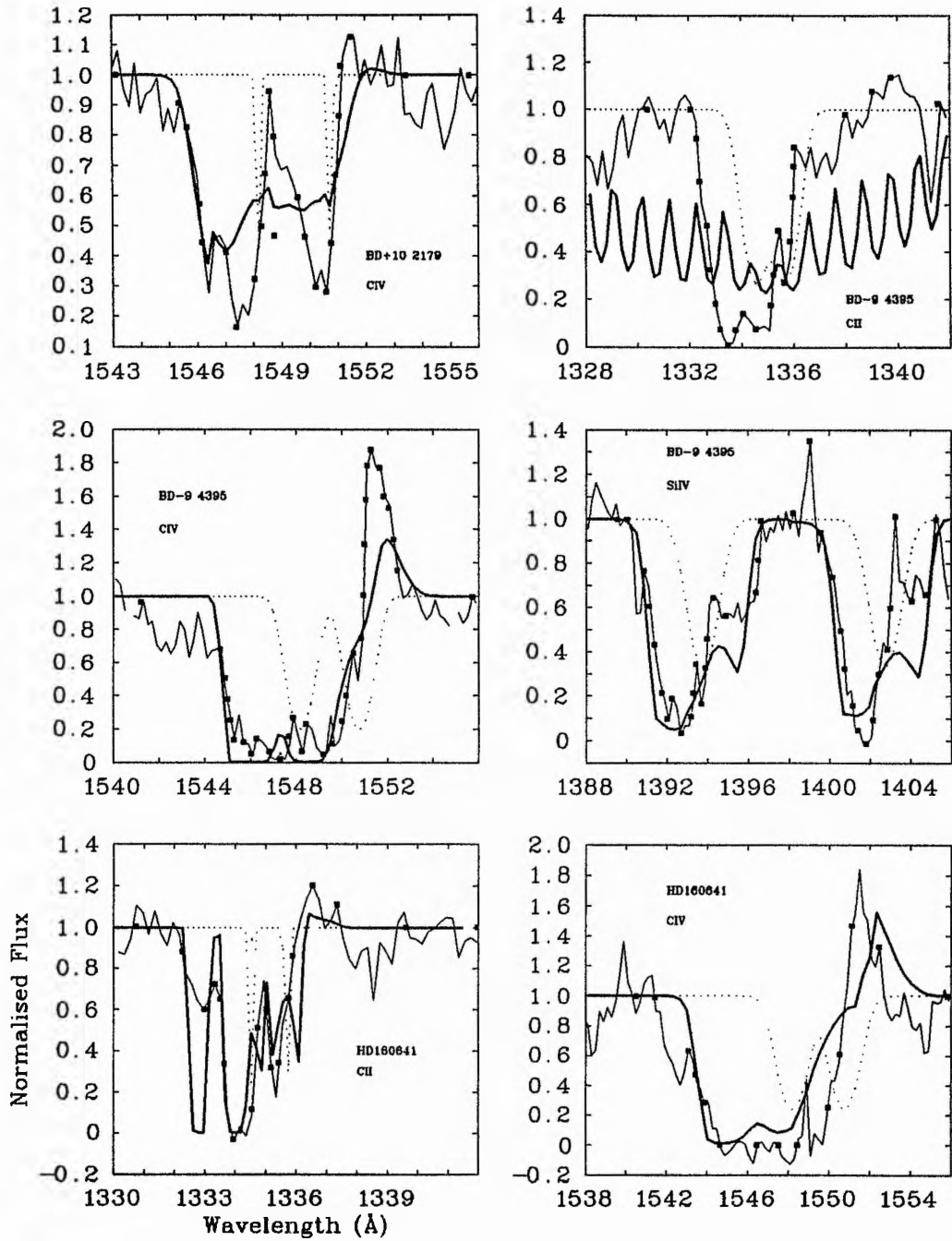


Figure F.2: Initial profiles for the EHe stars using the  $\beta$ -dependent optical depth law. The heavy lines are the fitted profiles, the dotted lines the photospheric profiles.

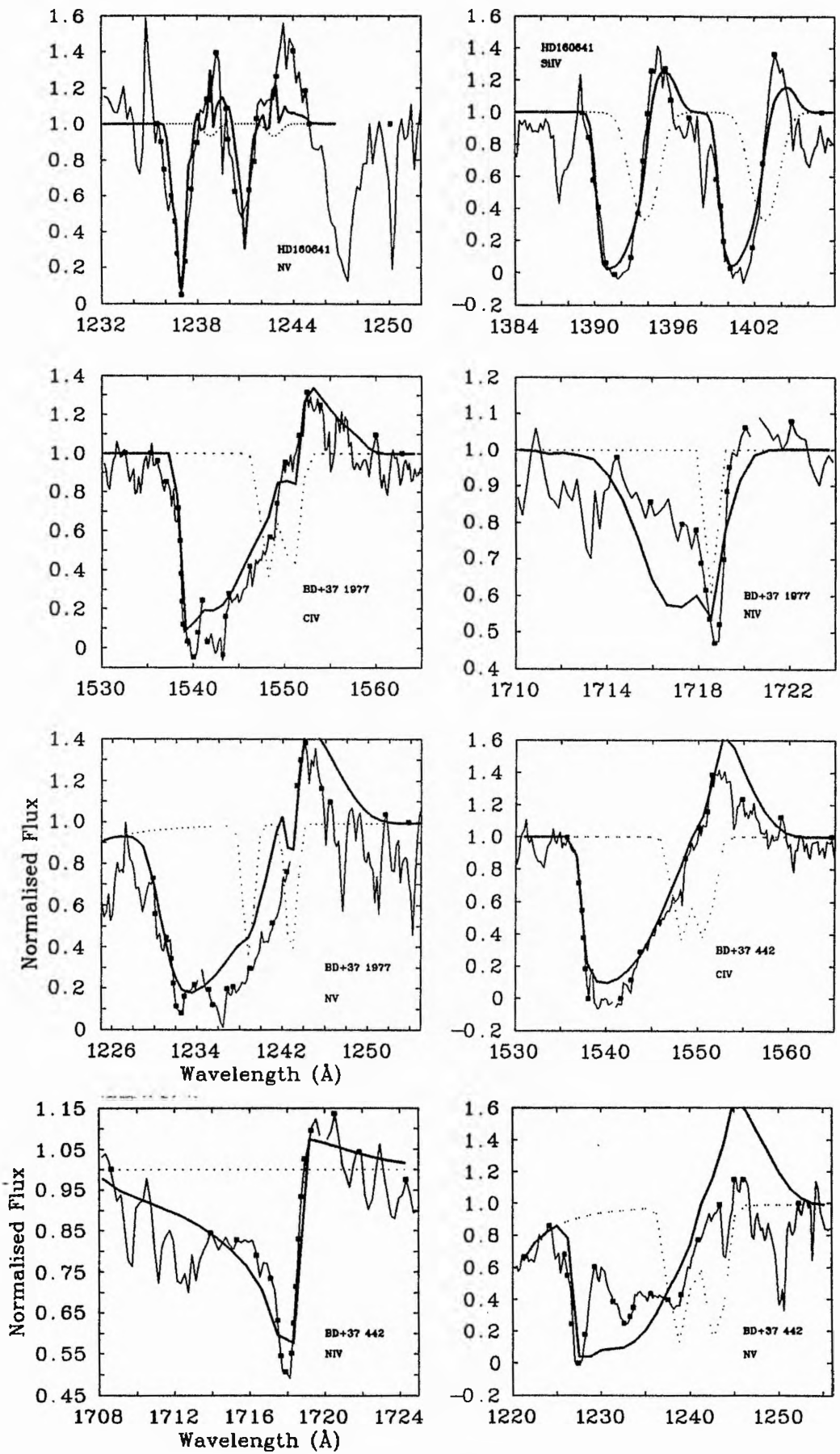


Figure F.2: *continued.*

## F.2.2 Notes on final parameter selection: $\beta$ -independent

The individual fits are shown in Figure F.3 and the fit parameters tabulated in Table F.3. Notes on the final selection of parameters are given below. The final parameters are given in Table 6.5 and shown in Figure 6.2.

**BD -9° 4395.** All three fits are very good. The high value of  $\beta$  from CIV and Si IV is retained as a weighted average.  $v_{\infty}$  is set slightly higher than the CIV value as the fit is not so good.  $w_g$  retains the CIV value.

**HD 160641.** Good fits for Si IV and NV, poorer fits for C II and CIV.  $\beta$  from a straight average of all four lines.  $v_{\infty}$  and  $w_g$  from an average of the CIV, NV and Si IV fits.

**BD +37° 1977.** Very good fit for CIV, fair for NIV and poor for NV. Final parameters are all retained from the CIV fit.

**BD +37° 442.** Very good CIV fit, good fits for NV, NIV. Final parameters are all retained from the CIV fit.

Table F.3: Individual fits for the EHe stars using the  $\beta$ -independent optical depth law. BD +10° 2179 is not shown in this table as it only has one line capable of being modelled. The fit for this line is given in Table 6.5. Errors are in small type.

Star	Ion	$\beta$	$v_\infty$	$w_g$	$\alpha_1$	$\alpha_2$	$T_B$
BD -9° 4395	C II	2.54	340	0.414	2.74	1.70	13.50
		35.	390	1.023	17.9	9.20	163
	C IV	16.8	400	0.261	0.82	-0.91	4.06
		11.6	20	0.020	1.77	0.19	1.1
	Si IV	8.79	690	0.112	-0.59	1.42	57.1
		10.8	160	0.130	1.40	1.08	75
HD160641	C II	1.96	300	0.388	-2.85	-1.72	1.7
		0.01	00	0.000	0.00	0.00	0.01
	C IV	5.20	480	0.361	-1.51	-1.78	2.39
		0.03	10	0.000	0.01	0.00	0.01
	N V	2.05	520	0.309	0.18	-0.67	0.51
		3.6	100	0.193	1.68	0.81	0.36
	Si IV	3.42	450	0.346	-1.68	-1.49	3.74
		2.94	60	0.071	1.06	0.93	5.15
BD +37° 1977	C IV	0.09	1730	0.072	0.66	0.05	9.4
		0.28	290	0.13	2.96	1.86	28.0
	N IV	0.54	4460	0.046	-0.78	1.47	0.04
		10.2	16430	0.239	5.67	42.0	0.39
	N V	0.09	1170	0.606	18.66	0.73	1.08
		0.03	30	0.035	3.21	0.07	0.06
BD +37° 442	C IV	0.98	2240	0.020	0.78	1.33	5.92
		2.77	1650	0.416	17.7	9.34	34.1
	N IV	0.38	1620	0.001	-0.82	0.68	0.52
		0.25	1040	0.038	0.45	2.27	0.38
	N V	0.22	2230	0.165	-0.17	0.80	3.05
		0.00	10	0.001	0.01	0.01	0.02

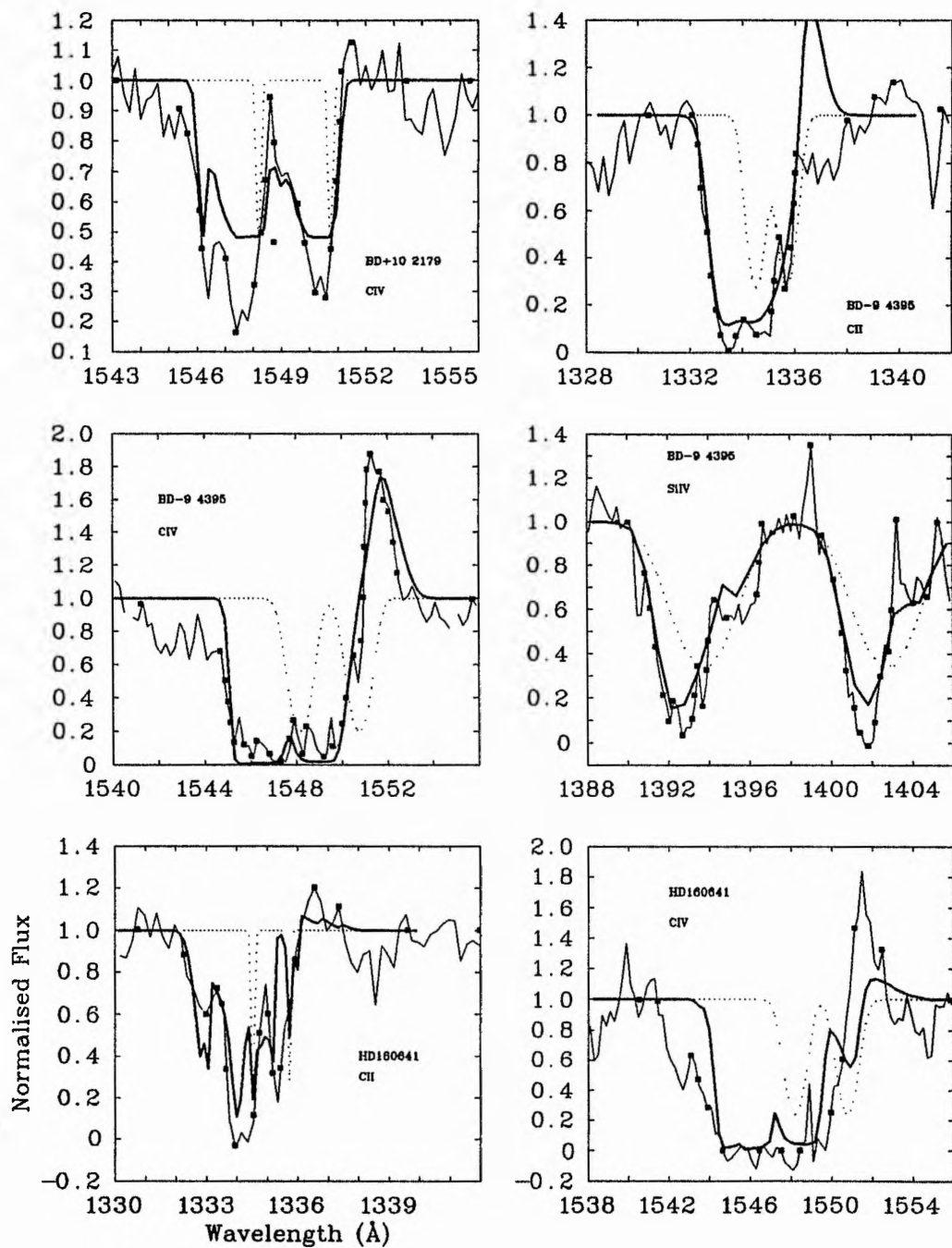


Figure F.3: Initial profiles for the EHe stars using the  $\beta$ -independent optical depth law. The heavy lines are the fitted profiles, the dotted lines the photospheric profiles.

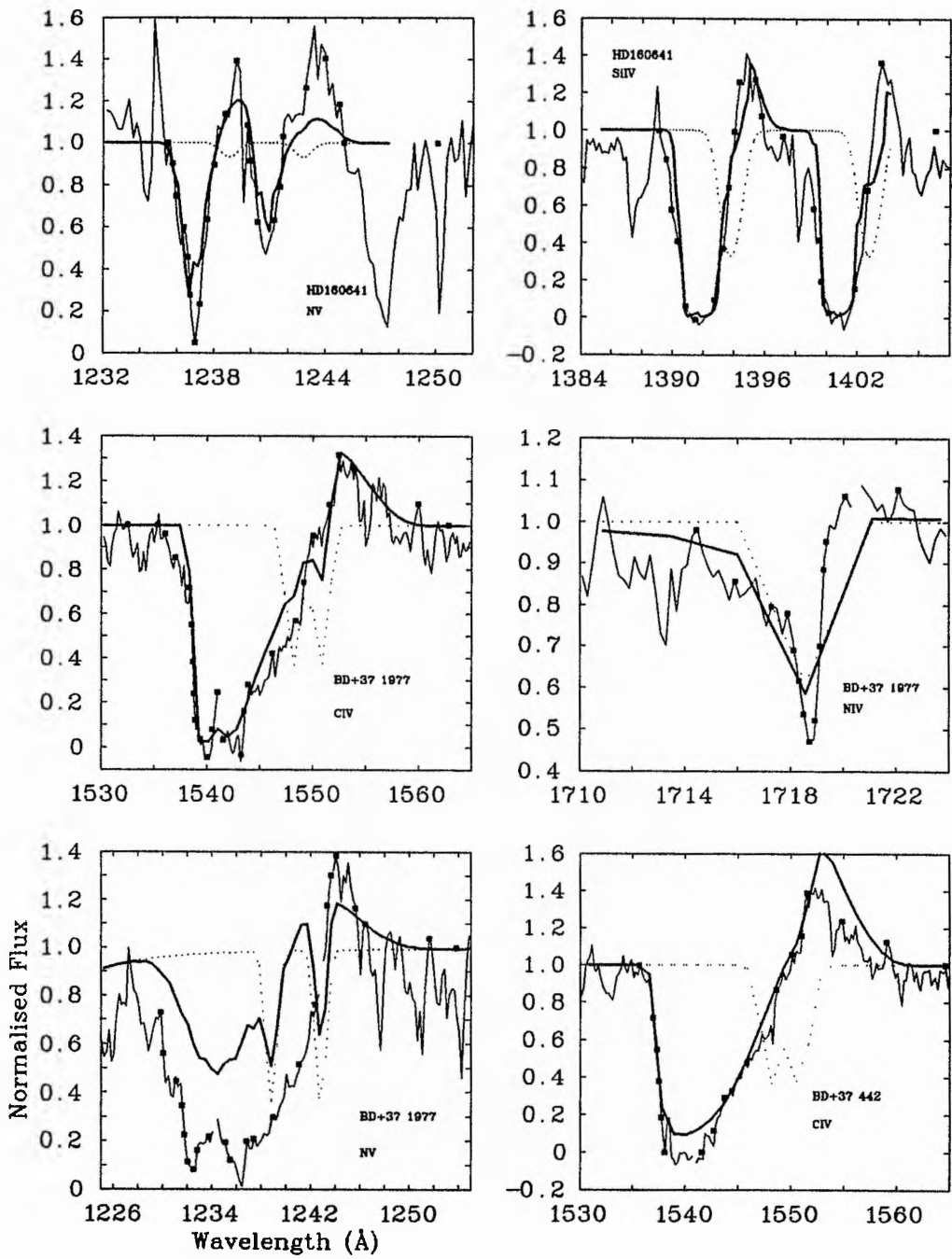


Figure F.3: *continued.*

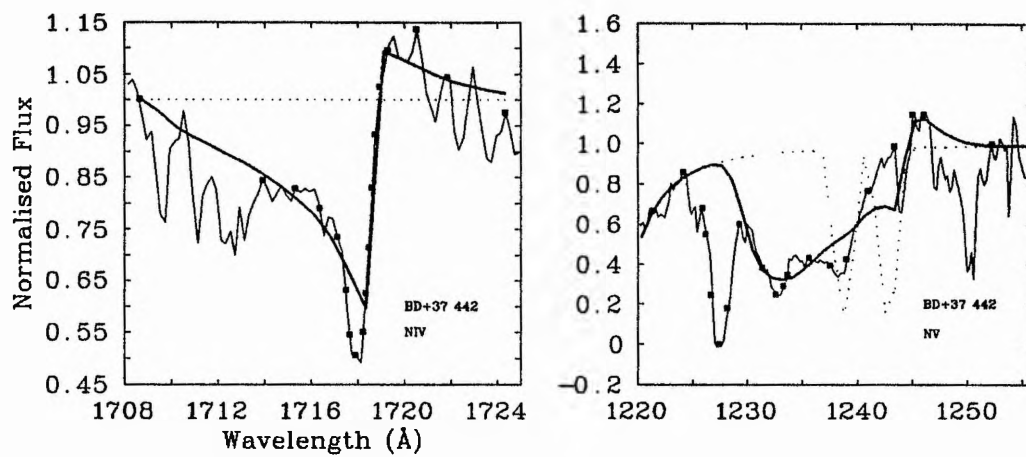


Figure F.3: *continued.*

### F.2.3 Notes on final parameter selection: $\beta = 1.0$

The individual fits are shown in Figure F.4 and the fit parameters tabulated in Table F.4. Notes on the final selection of parameters are given below. The final parameters are given in Table 6.6 and shown in Figure 6.3.

**BD -9° 4395.** Good profiles for CII and SiIV, fair for CIV with the emission peak not well fitted.  $v_\infty$  from the excellent fit to the blue edge of CII,  $w_g$  from CIV.

**HD 160641.** NV and SiIV very good with CII and CIV fair.  $v_\infty$  from the average of the values for CIV, NV and SiIV,  $w_g$  from NV.

**BD +37° 1977.** CIV and NV very good with NIV good.  $v_\infty$  from CIV,  $w_g$  from a weighted mean of CIV and NV.

**BD +37° 442.** CIV, NV and NIV all very good.  $v_\infty$  and  $w_g$  from the good blue edge fit for CIV.

## F.3 $\nu$ Sgr

The initial results for the binary modelling of the winds of  $\nu$  Sgr using the modified optical depth law are given in Table F.5 with the profiles shown in Figure F.5.

The optical depth law coefficients  $\alpha_1$  and  $\alpha_2$  correspond to the Inner Region ( $r < 240 R_\odot$ ) while  $\alpha_3$  and  $\alpha_4$  correspond to the Outer Region ( $r > 240 R_\odot$ ).

A value of  $\pm 10.0$  and an error of  $\pm 9.0$  indicates that the value of  $\alpha$  lies outside  $\pm 10$  the sign of the value indicating in which direction the result lies. The values of  $\alpha$  had these constraints imposed on them to avoid very large (positive or negative) values occurring if that parameter were unimportant but causing SEILS to fail by causing subsequent computations to exceed the capacity of the computer.

Table F.4: Individual fits for the EHe stars using the  $\beta$ -independent optical depth law and  $\beta$  fixed at 1.0. BD +10° 2179 is not shown in this table as it only has one line capable of being modelled. The fit for this line is given in Table 6.6. Errors are in small type.

Star	Ion	$\beta$	$v_\infty$	$w_g$	$\alpha_1$	$\alpha_2$	$T_B$
BD -9° 4395	C II	1.00	320	0.494	0.96	0.308	3.48
			<small>230</small>	<small>0.723</small>	<small>4.69</small>	<small>5.87</small>	<small>10.2</small>
	C IV	1.00	370	0.294	0.81	-1.09	11.63
			<small>20</small>	<small>0.018</small>	<small>1.01</small>	<small>0.26</small>	<small>3.6</small>
	Si IV	1.00	400	0.220	-0.45	-0.18	20.0
			<small>20</small>	<small>0.039</small>	<small>0.41</small>	<small>0.43</small>	<small>10.5</small>
HD160641	C II	1.00	190	0.667	0.128	-0.51	1.4
			<small>10</small>	<small>0.029</small>	<small>0.10</small>	<small>0.02</small>	<small>0.12</small>
	C IV	1.00	560	0.327	-1.15	-1.12	13.6
			<small>60</small>	<small>0.027</small>	<small>0.21</small>	<small>0.37</small>	<small>0.2</small>
	N V	1.00	510	0.291	0.99	-0.53	0.69
			<small>10</small>	<small>0.009</small>	<small>0.08</small>	<small>0.03</small>	<small>0.02</small>
Si IV	1.00	430	0.387	0.35	-0.94	2.73	
		<small>10</small>	<small>0.013</small>	<small>0.22</small>	<small>0.16</small>	<small>0.30</small>	
BD +37° 1977	C IV	1.00	1840	0.123	-0.72	0.00	5.85
			<small>230</small>	<small>0.153</small>	<small>0.47</small>	<small>0.39</small>	<small>4.8</small>
	N IV	1.00	940	0.341	-4.19	-2.33	0.16
			<small>70</small>	<small>0.017</small>	<small>0.36</small>	<small>0.12</small>	<small>0.03</small>
	N V	1.00	1240	0.487	0.04	-0.79	1.56
			<small>90</small>	<small>0.055</small>	<small>0.69</small>	<small>0.09</small>	<small>0.36</small>
BD +37° 442	C IV	1.00	2340	0.006	1.73	3.18	24.40
			<small>990</small>	<small>0.325</small>	<small>21.35</small>	<small>7.15</small>	<small>227</small>
	N IV	1.00	4310	0.004	-1.71	0.82	0.36
			<small>12000</small>	<small>0.019</small>	<small>5.08</small>	<small>43.1</small>	<small>1.45</small>
	N V	1.00	1700	0.599	-1.56	0.04	2.90
			<small>850</small>	<small>0.218</small>	<small>0.40</small>	<small>0.39</small>	<small>1.07</small>

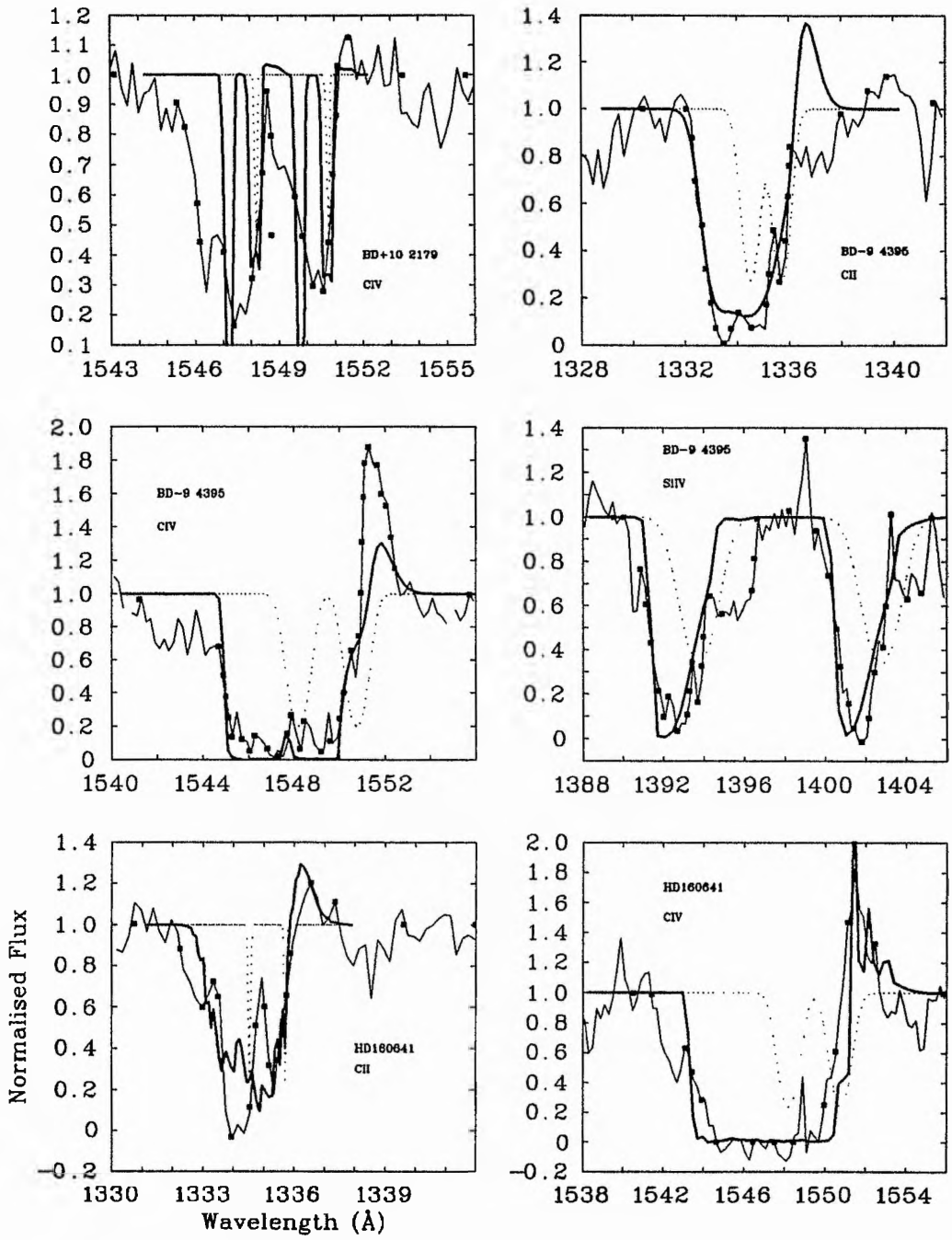


**Figure F.4:** Initial profiles for the EHe stars with  $\beta$  fixed at 1.0. The heavy lines are the fitted profiles, the dotted lines the photospheric profiles.

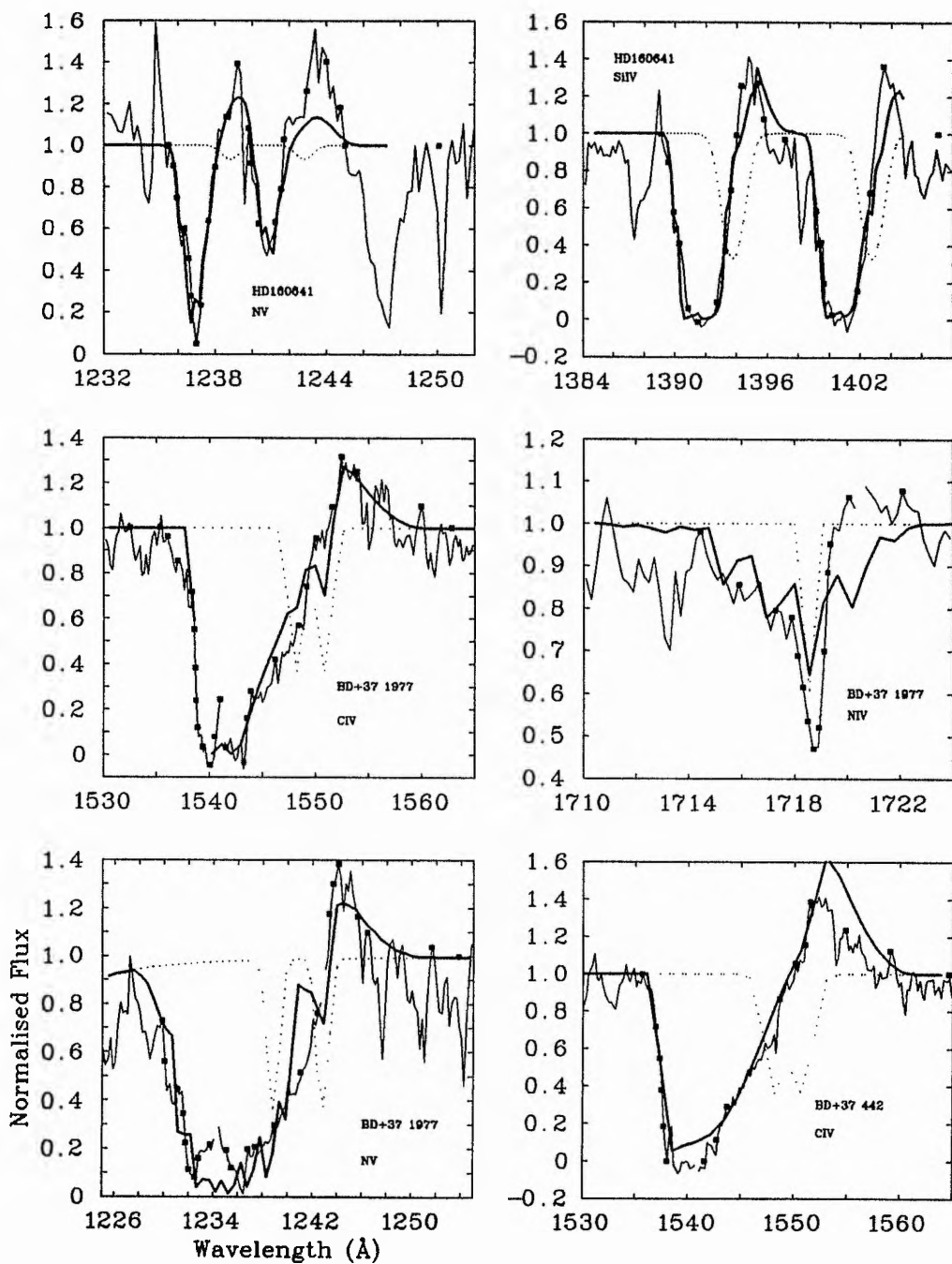


Figure F.4: *continued.*

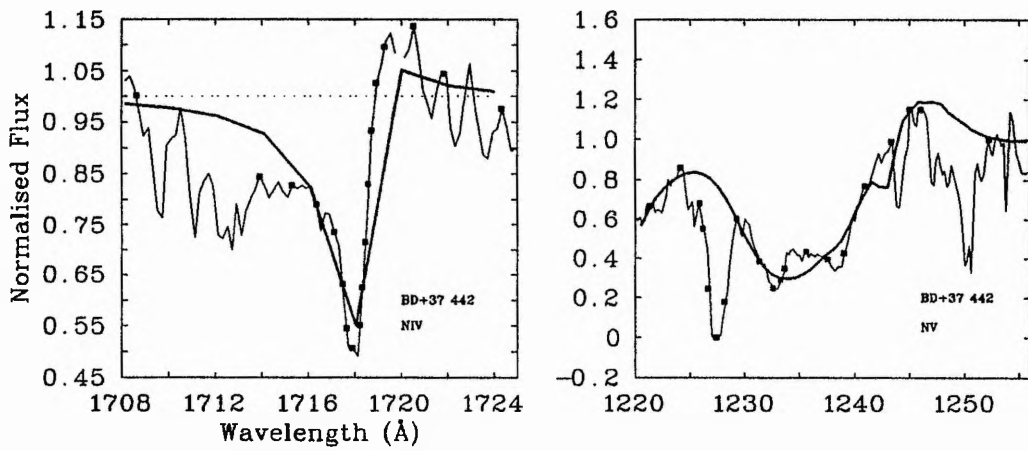


Figure F.4: *continued.*

Table F.5: Individual fits for  $\nu$  Sgr using the modified optical depth law approximation with  $\beta$  both free and fixed at 1.0. The  $\beta$ -dependent optical depth law was used and results are shown for both the primary ( $x = 4$ ) and the secondary ( $x = 80$ ) models. Errors are in small type.

Model	Ion	$\beta$	$v_\infty$	$w_g$	$\alpha_1$	$\alpha_2$	$\alpha_3$	$\alpha_4$	$T_B$
Primary ( $x = 4$ ) $\beta$ free	CII	0.03	285	0.61	0.03	-0.74	10.0	-0.50	3.19
		0.09	86	0.08	0.50	8.63	9.0	0.14	1.64
	CIV	2.08	148	0.45	-2.33	5.46	1.14	-5.13	6.28
		12.04	466	0.94	13.70	27.91	150.87	8.01	21.44
	NV	0.42	427	0.57	0.27	10.0	3.65	0.02	11.84
		0.16	30	0.09	0.34	9.0	19.08	0.15	3.89
	SiIV	0.02	207	0.26	-0.03	10.0	10.0	-0.61	10.69
		0.06	8	0.02	0.33	9.0	9.0	0.08	6.19
Primary ( $x = 4$ ) $\beta = 1$	CII	1.0	278	.94	1.11	9.60	9.74	1.35	7.63
		151	0.50	0.83	10.97	15.92	0.82	8.51	
	CIV	1.0	297	0.51	-2.35	7.19	10.0	-1.98	5.95
		6	0.01	0.03	14.48	9.0	0.03	1.20	
	NV	1.0	655	0.24	-3.27	-9.98	10.0	-1.97	5.57
		12	0.01	0.15	0.76	9.0	0.14	0.61	
	SiIV	1.0	457	0.24	-6.46	10.0	10.0	-4.53	69.01
		61	0.04	0.01	9.0	9.0	0.00	123.4	
Secondary ( $x = 80$ ) $\beta$ free	CII	0.54	328	0.79	0.14	-0.30	-10.0	3.59	3.43
		0.49	61	0.20	0.68	0.64	-9.0	0.68	1.45
	CIV	0.18	369	0.85	-0.34	-0.98	-10.0	-0.15	7.62
		0.44	127	0.32	1.00	2.35	9.0	0.89	6.07
	NV	0.07	419	0.55	-0.25	-0.87	10.0	-0.35	12.27
		0.34	84	0.16	0.91	2.11	9.0	0.35	13.81
	SiIV	0.10	451	0.53	-0.75	-1.28	-10.0	-0.56	6.88
		0.11	22	0.04	0.20	0.61	9.0	0.10	2.15
Secondary ( $x = 80$ ) $\beta = 1$	CII	1.0	323	0.98	0.39	-0.26	-10.0	4.90	2.96
		63	0.13	0.86	0.97	-9.0	-9.0	1.07	
	CIV	1.0	474	0.48	-0.86	6.05	10.0	-0.49	2.41
		83	0.07	0.22	4.62	9.0	0.12	0.78	
	NV	1.0	437	0.30	-2.30	10.0	2.87	-1.38	24.48
		9	0.01	0.13	9.0	74.61	0.07	3.61	
	SiIV	1.0	713	0.07	-6.85	-0.30	10.0	-1.46	18.80
		430	0.72	11.43	6.00	9.0	3.64	33.38	

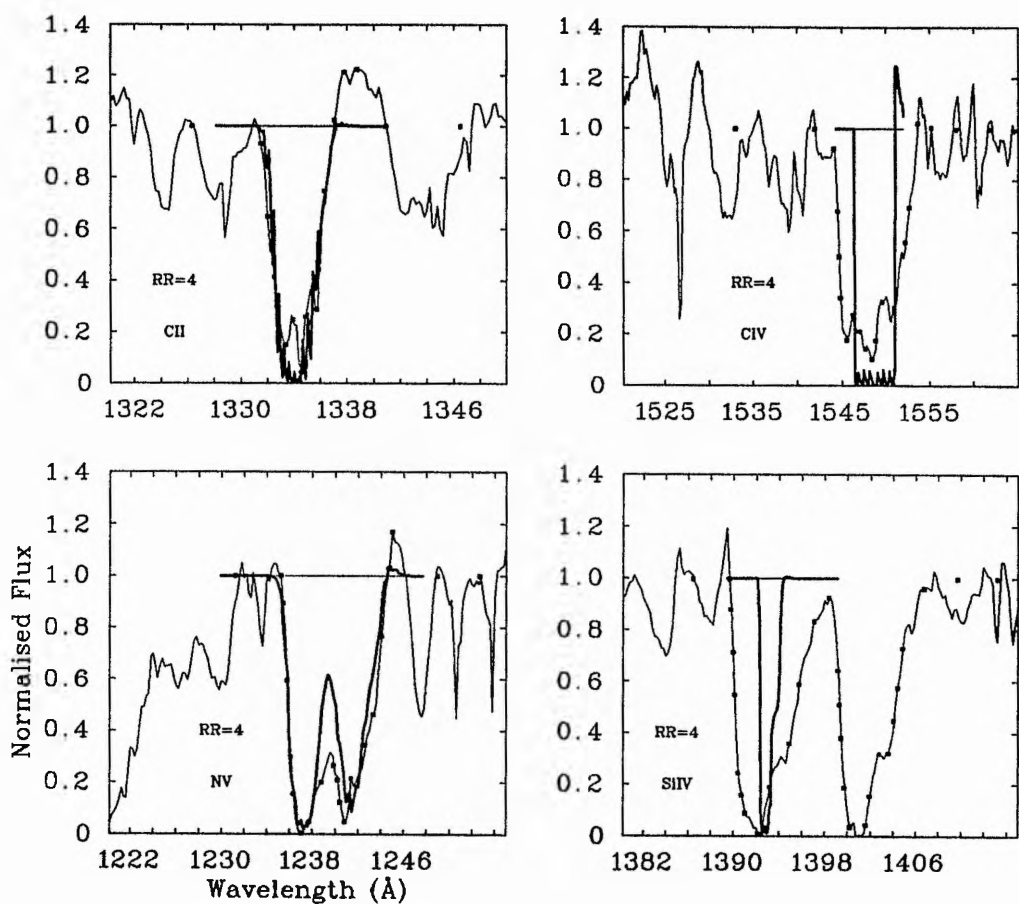


Figure F.5: Initial wind line profiles for  $\nu$  Sgr modelled as a binary star with the modified optical depth law. The heavy lines are the final profiles, the dotted lines the photospheric profiles. This page: Primary approximation ( $x = 4$ ) with  $\beta$  free.

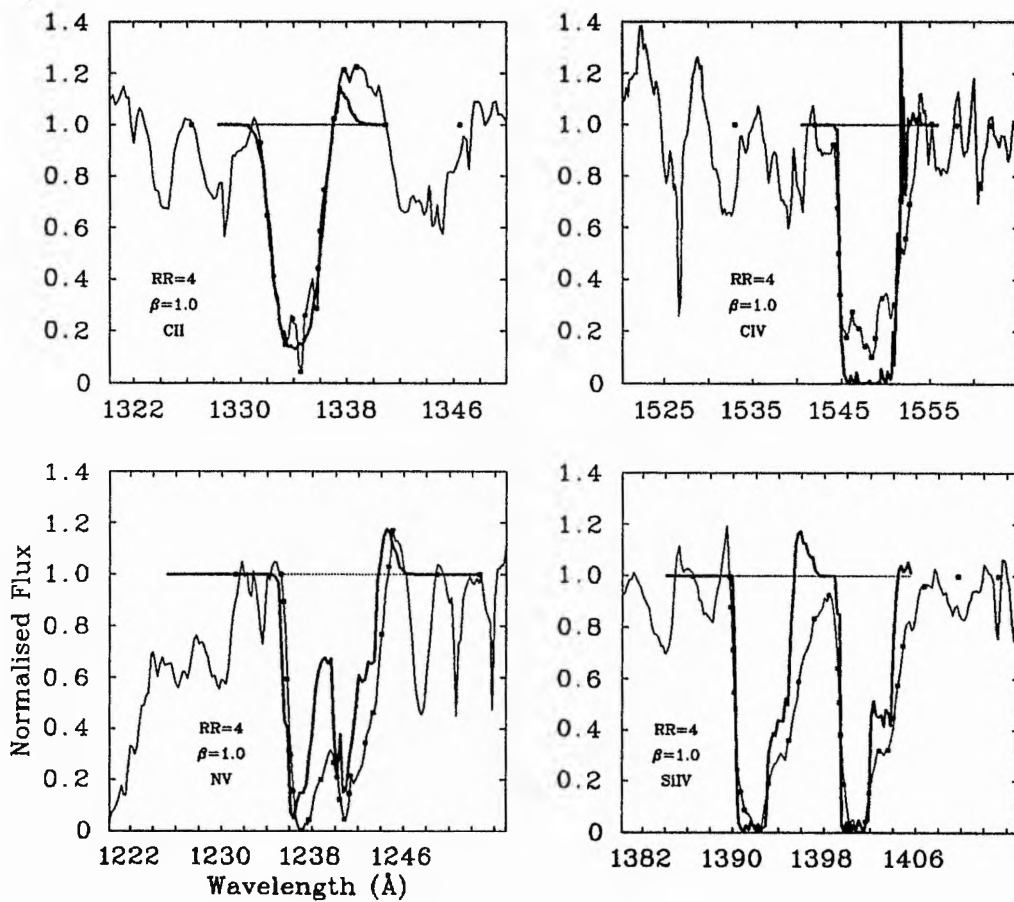


Figure F.5: *continued.* Primary approximation ( $x = 4$ ) with  $\beta = 1$ .

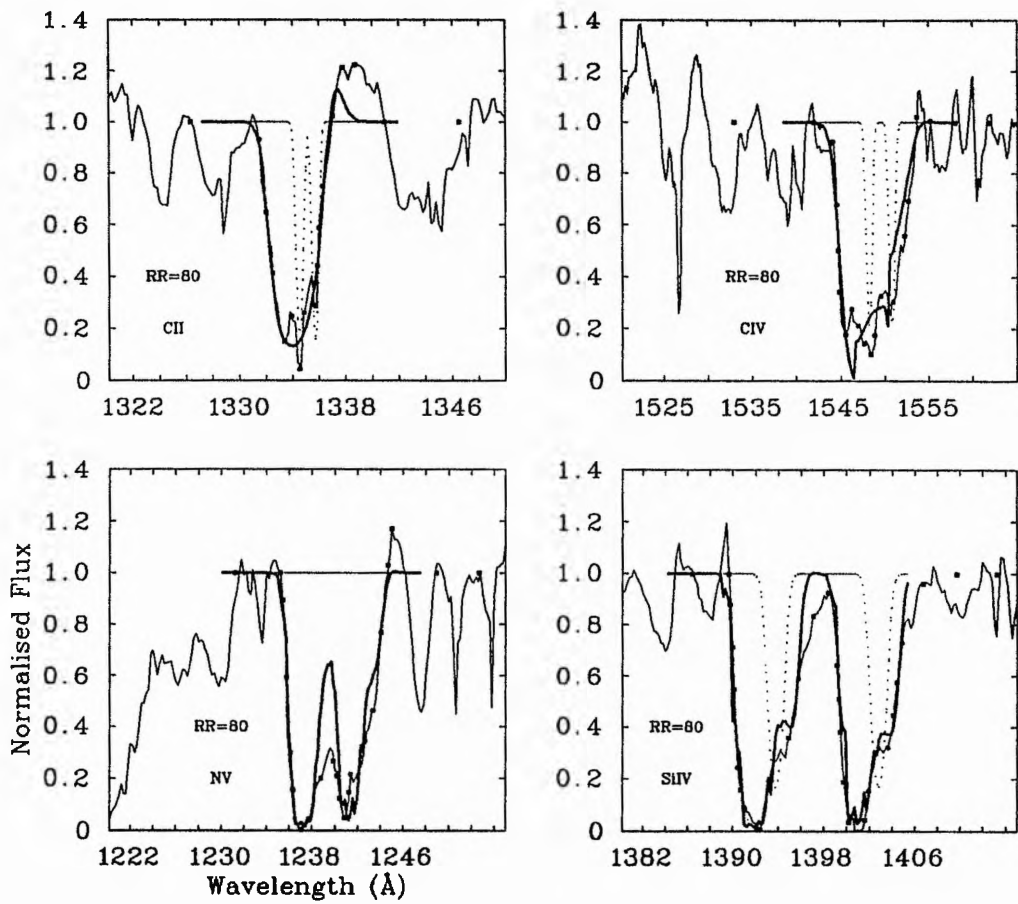


Figure F.5: *continued*. Secondary approximation ( $x = 80$ ) with  $\beta$  free.

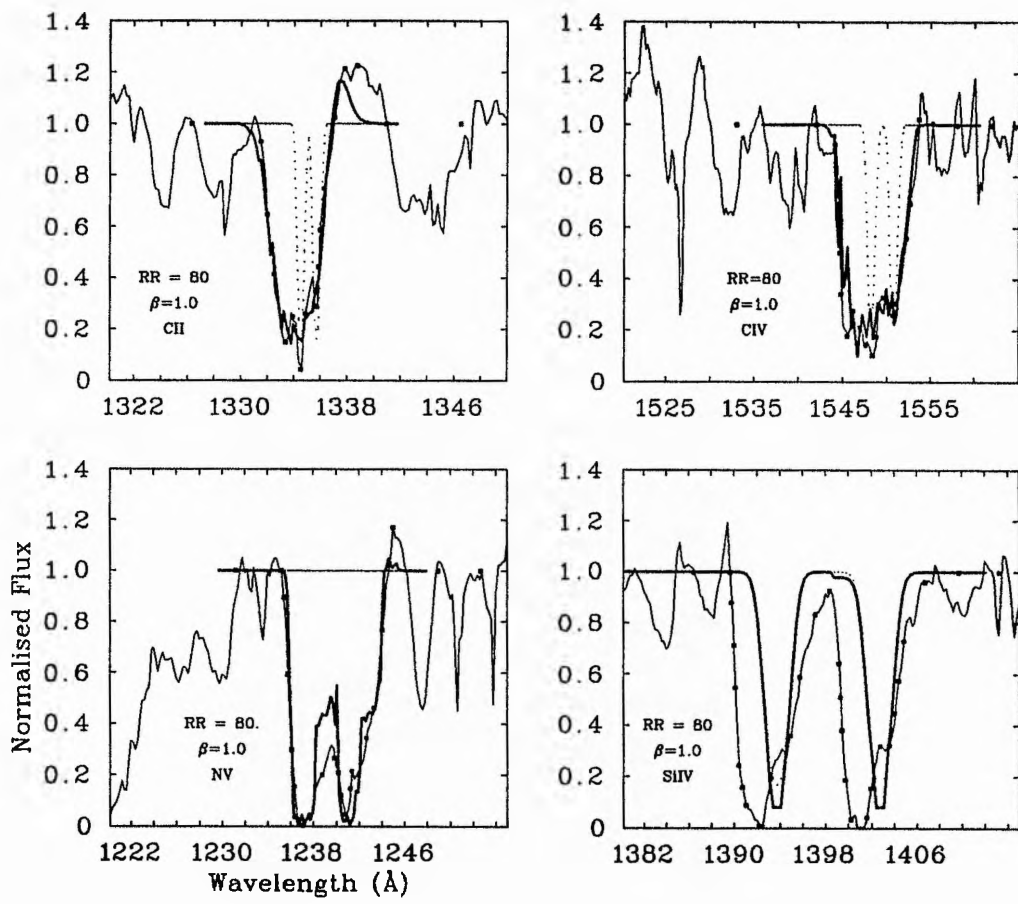


Figure F.5: *continued*. Secondary approximation ( $x = 80$ ) with  $\beta = 1$ .

## Appendix G

# The Principles of a Spectroscopic Fine Analysis

A spectroscopic fine analysis is a long process although not intrinsically difficult. The algorithm below shows the main steps where a hydrogen-deficient star is assumed. Figure G.1 gives some schematic examples of the individual steps.

1. **Spectrum Reduction.** Using the methods given in Chapter 10 or similar obtain a normalised spectrum.
2. **Equivalent Widths.** Using the reduced spectrum measure the equivalent widths of those lines that are not too severely blended. As many lines as possible should be measured especially those used for the temperature determination (*e.g.* Fe I, II and III) and those of the major compositional components (*e.g.* H, He, C, N and O).
3. **Model Atmospheres.** Calculate a grid of helium-rich, line-blanketed model atmospheres (*e.g.* using STERNE). The range of the grid should encompass the expected temperature and gravity; the initial composition comes from the literature, a similar object or a good guess. The values are not too critical as these are just initial models.
4. **Curves of Growth.** For each model in the grid ...
  - (a) For each ion considered...
    - i. For each line of the ion...
      - A. For each of a range of element abundances determine a theoretical equivalent width.
      - B. Combine these EW's to form a curve of growth.

C. Using the measured EW for the line read off from the curve of growth the derived abundance for that element. (Figure G.1a).

**5. Temperature Determination.** For each assumed value of the gravity plot a graph of derived elemental abundance vs temperature.

- (a) For each line of each ion used for the temperature determination (*e.g.* Fe) for each model in the temperature grid plot the value of the derived elemental abundance against the model temperature. Join the points for a given line.
- (b) Determine the crossover point between the series of lines for different ions. From this crossover point read off the derived surface temperature and the elemental abundance (for the assumed gravity). (Figure G.1b where only the mean lines for FeI and II have been drawn for clarity).

**6. Gravity Determination.** For each value of temperature in the model grid...

- (a) Determine theoretical line profiles for each gravity sensitive line (*e.g.* He) using NLTE codes if possible.
- (b) Broaden the theoretical profiles for the effect of rotation, if applicable.
- (c) Compare the theoretical profiles with the observed profiles to determine a best fit gravity for each assumed temperature using all the profiles. (Figure G.1c shows one profile).

**7. Gravity and Temperature Determination.**

- (a) Plot a graph of gravity against temperature.
- (b) For each gravity in the model grid plot the determined temperature (step 5) against this gravity. Join the points.
- (c) For each temperature in the model grid plot the determined gravity (step 6) against this temperature. Join the points.
- (d) From where these lines cross the determined temperature and gravity can be read off. (Figure G.1d).

**8. Calculate New Abundances.**

- (a) Using the determined  $T_{\text{eff}}$ ,  $\log g$  and the measured equivalent widths, determine the new abundances.
- (b) Using these abundances, run a new grid of models and repeat the analysis from step 3 onwards.
- (c) Continue until the newly determined values of temperature, gravity and abundances agree with those that were used in the models; *i.e.* until convergence is achieved.

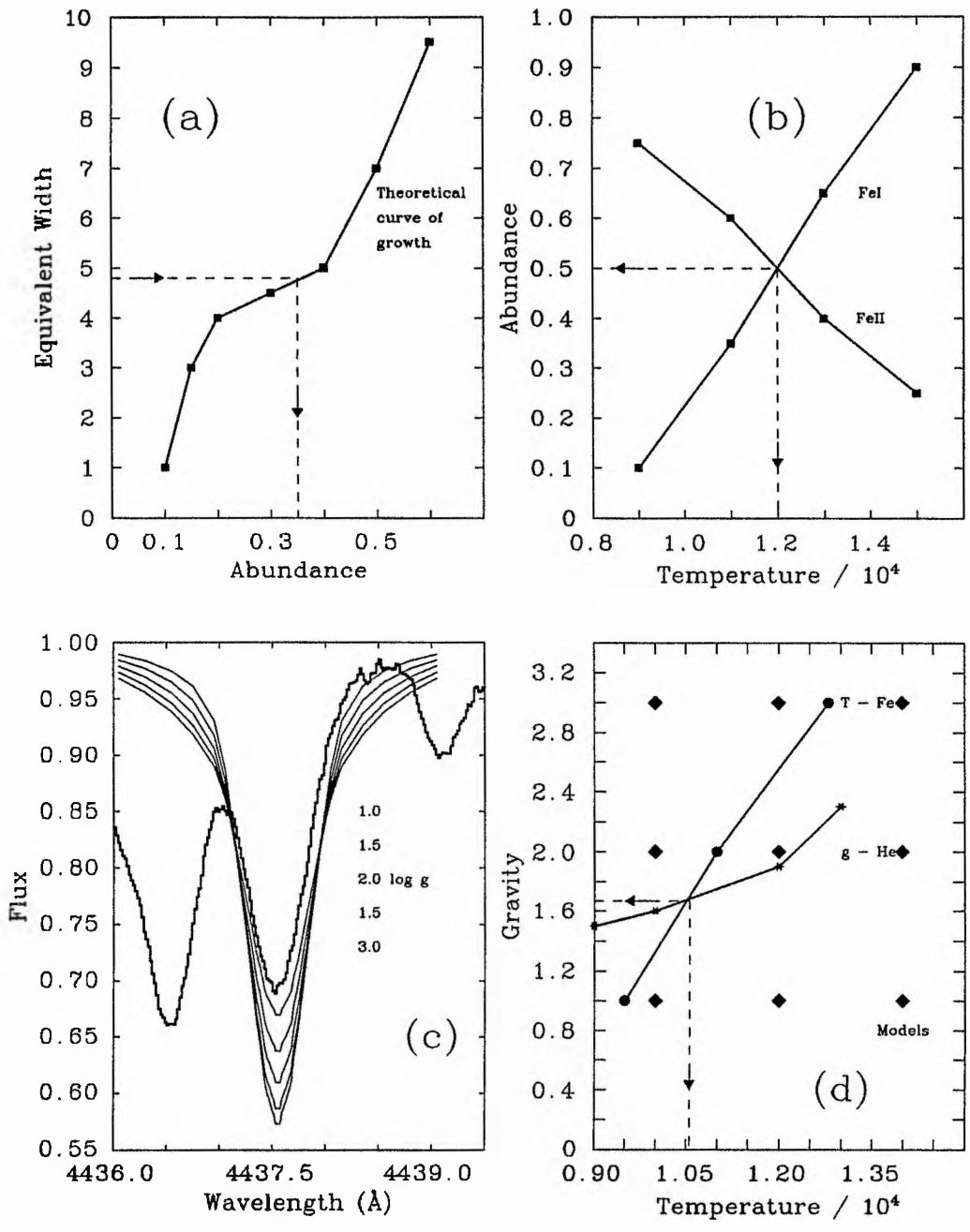


**Figure G.1:** Schematic fine analysis results showing the determination of an elemental abundance from the measured EW of a single line of a single ion (a). Combining many such results into a single abundance for each ion for each model in the grid allows the temperature and abundance to be determined (b). Gravity is determined by looking at many line profiles and their theoretical equivalents to determine a gravity for a given model temperature (c). Finally the temperature and gravity results are combined to find the actual temperature and gravity of the star (d).

## Appendix H

# Atomic Data and Multiplet Lists for $\nu$ Sgr, 3980-4915 Å

Table H.1: Multiplet lists and Atomic data for  $\nu$  Sgr, 3980-4915 Å.  $\chi_l$  and  $\chi_u$  are the lower and upper energy levels of the transition respectively, in eV.

Ion	Mult.	$\lambda$ (Å)	$\chi_l$	$\chi_u$	log g /	Ref.
Al II	2	4663.03	10.55	13.20	-0.30	Wie 69
Ba II	1	4554.03	0.00	2.71	0.93	The 89
Cl I	14	4371.39	7.68	10.52	-2.08	Heb 83
C II	6	4267.27	17.97	20.66	0.56	Van 87
	6	4267.02	17.97	20.66	0.73	Van 87
Ca I	23	4585.87	2.51	5.21	-0.45	The 89
	23	4581.40	2.51	5.21	-0.58	The 89
	23	4576.86	2.51	5.21	-0.87	The 89
Ca II	17	4109.83	7.48	10.49	-0.74	Wie 69
	17	4097.12	7.47	10.49	-1.00	Wie 69
	17	4110.33	7.48	10.49	-1.71	Wie 69
Cr II	18	4111.01	3.09	6.09		
	18	4172.60	3.09	6.05		
	18	4217.07	3.09	6.02	-3.29	The 89
	18	4113.24	3.09	6.09	-2.74	MFW 88
	18	4171.92	3.09	6.05		
	18	4218.77	3.09	6.02		
	18	4112.59	3.09	6.09		
	18	4170.58	3.09	6.05		
	19	4030.28	3.09	6.16		
	19	4063.94	3.09	6.13		
	19	4053.45	3.09	6.14		
	19	4075.63	3.09	6.12		
	19	4061.77	3.09	6.13		
	19	4054.11	3.09	6.14	-2.59	MFW 88
	19	4076.87	3.09	6.12		
	19	4087.63	3.09	6.11	-3.22	MFW 88
	19	4081.97	3.09	6.14		
	19	4077.50	3.09	6.12		
	19	4088.90	3.09	6.11		
	26	4179.43	3.81	6.76		
	26	4111.02	3.74	6.74		
	26	4072.66	3.70	6.73		
	26	4207.35	3.81	6.74		
	26	4132.41	3.74	6.75		
	26	4086.14	3.70	6.72		
	26	4229.81	3.81	6.73	-2.61	Kar 75
	30	4824.13	3.85	6.41	-1.22	MFW 88
	30	4848.24	3.85	6.39	-1.44	MFW 88
	30	4864.32	3.84	6.38		
	30	4876.41	3.84	6.37	-1.46	MFW 88
30	4860.20	3.85	6.39			
30	4876.48	3.85	6.38			
30	4864.57	3.84	6.37	-2.08	MFW 88	
30	4812.35	3.85	6.41	-1.80	MFW 88	

Table H.1: *continued*

Ion	Mult.	$\lambda$ (Å)	$\chi_i$	$\chi_e$	$\log gf$	Ref.
Cr II	30	4836.22	3.84	6.39	-2.25	MPW 88
	30	4856.19	3.84	6.38	-2.26	MPW 88
	31	4242.38	3.85	6.76		
	31	4261.92	3.85	6.74	-1.93	Kur 75
	31	4278.57	3.84	6.73	-2.12	Kur 75
	31	4284.21	3.84	6.72		
	31	4233.28	3.85	6.76		
	31	4252.62	3.84	6.74		
	31	4269.28	3.84	6.73		
	31	4224.09	3.84	6.76		
	31	4246.41	3.84	6.74		
	39	4539.62	4.02	6.74	-2.53	MPW 88
	39	4565.78	4.02	6.73	-2.11	MPW 88
	44	4858.66	4.06	6.76	-0.66	MPW 88
	44	4866.22	4.08	6.74	-0.63	MPW 88
	44	4616.83	4.06	6.73	-1.11	MPW 88
	44	4634.11	4.05	6.72	-1.24	MPW 88
	44	4558.02	4.05	6.76	-1.38	MPW 88
	44	4592.09	4.06	6.74	-1.22	MPW 88
	44	4616.64	4.05	6.73	-1.29	MPW 88
	44	4558.83	4.06	6.76		
	44	4589.89	4.05	6.74	-2.26	MPW 88
	161	4195.41	5.50	8.24		
	161	4278.10	5.51	8.19		
	162	4145.77	5.50	8.27		
	162	4224.65	5.51	8.23		
	162	4209.02	5.50	8.23		
	162	4161.05	5.51	8.27		
	164	4089.49	5.50	8.31		
	165	4081.21	5.50	8.32		
	166	4082.50	5.50	8.32		
	166	4098.44	5.51	8.32		
	166	4002.48	5.50	8.38		
	166	4017.96	5.51	8.38		
	179	4341.09	5.65	8.49		
	179	4362.93	5.64	8.47		
	179	4374.61	5.65	8.47		
	180	4204.83	5.65	8.58		
	180	4199.02	5.64	8.58		
	180	4209.64	5.65	8.58		
	180	4222.00	5.64	8.56		
	180	4232.96	5.65	8.56		
	181	4127.08	5.65	8.64		
	181	4170.86	5.64	8.60		
181	4181.50	5.65	8.60			
181	4116.66	5.64	8.64			
182	4048.02	5.65	8.69			
182	4056.07	5.64	8.66			
182	4066.16	5.65	8.66			
183	4012.50	5.64	8.71			
183	4022.36	5.65	8.71			
190	4901.63	6.46	8.98			
190	4912.49	6.46	8.97			
191	4465.78	6.48	9.22			
191	4511.82	6.46	9.19			
191	4516.56	6.46	9.19			
192	4256.16	6.46	9.36			
192	4268.93	6.46	9.35			
193	4070.90	6.46	9.49			
193	4049.14	6.46	9.50			
193	4067.05	6.46	9.49			
194	4038.03	6.46	9.52			
194	4003.33	6.46	9.54			
194	4007.04	6.46	9.54			
200	4867.60	6.66	9.20			
Fe I	41	4383.58	1.48	4.29	0.20	Bla 80
	41	4404.75	1.55	4.35	-0.14	Bla 80
	41	4413.13	1.60	4.40	-0.62	Bla 80
	41	4294.13	1.48	4.35	-0.97	BKK 91
	41	4337.08	1.55	4.40	-1.70	Bla 80
	41	4567.91	1.60	4.43	-2.65	FMW 88
	41	4229.78	1.48	4.40	-3.43	Bla 80
	41	4291.47	1.55	4.43		
	42	4271.76	1.48	4.37	-0.16	Bla 80
	42	4307.91	1.55	4.42	-0.06	MCS
	42	4328.77	1.60	4.45	-0.01	FMW 88
	42	4202.03	1.48	4.42	-0.71	Bla 80
	42	4280.79	1.55	4.45	-0.71	FMW 88
	42	4147.67	1.48	4.45	-2.10	Bla 80
	43	4045.82	1.48	4.53	0.28	Bla 80
	43	4083.60	1.55	4.59	0.07	FMW 88
	43	4071.74	1.60	4.63	-0.02	Bla 80
	43	4005.25	1.55	4.63	-0.61	Bla 80
	43	4143.87	1.55	4.33	-0.46	MCS
	43	4132.01	1.60	4.59	-0.65	FMW 88
	68	4528.62	2.17	4.89	-1.48	Bla 82
	68	4494.59	2.19	4.93	-1.14	Bla 82
	68	4482.26	2.21	4.97		
	68	4459.12	2.17	4.93	-1.28	Bla 82
	68	4442.34	2.19	4.97	-1.25	Bla 82
	68	4447.72	2.21	4.99	-1.34	Bla 82
	68	4407.71	2.17	4.97	-1.92	FMW 88
	68	4406.42	2.19	4.99	-1.77	FMW 88
	68	4430.62	2.21	5.00	-1.66	Bla 82
	71	4282.41	2.17	5.05	-0.81	FMW 88
	71	4318.09	2.19	5.05	-0.94	MCS
	71	4352.74	2.21	5.05	-1.23	MCS
152	4280.48	2.39	5.29	-0.02	FMW 88	
152	4235.94	2.41	5.36	-0.34	Bla 82	
152	4222.22	2.44	5.36	-0.97	Bla 82	

Table H.1: *continued*

Ion	Mult.	$\lambda$ (Å)	$\chi_i$	$\chi_u$	$\log g_f$	Ref.	
Fe I	152	4210.35	2.47	5.40	-0.87	FMW 88	
	152	4198.31	2.39	5.33	-0.72	Bla 82	
	152	4187.80	2.41	5.36	-0.55	Bla 82	
	152	4187.04	2.44	5.39	-0.55	Bla 82	
	152	4191.44	2.46	5.40			
	152	4299.24	2.41	5.29	-0.46	MCS	
	152	4271.16	2.44	5.33	-0.35	Bla 82	
	152	4250.13	2.46	5.36	-0.41	Bla 82	
	152	4233.61	2.47	5.39	-0.60	Bla 82	
	278	3997.39	2.72	5.80	-0.39	FMW 88	
	278	4021.87	2.75	5.82	-0.66	FMW 88	
	318	4891.50	2.84	5.36	-0.14	FMW 88	
	318	4871.32	2.85	5.39	-0.41	FMW 88	
	318	4859.75	2.86	5.40	-0.65	FMW 88	
	318	4890.76	2.86	5.39	-0.45	FMW 88	
	318	4872.14	2.87	5.40	-0.60	FMW 88	
	318	4903.32	2.87	5.39	-1.08	FMW 88	
	318	4878.22	2.87	5.40	-1.01	FMW 88	
	822	4199.10	3.03	5.97	0.25	FMW 88	
	693	4227.43	3.32	6.24	0.18	MCS	
	693	4247.43	3.35	6.26	-0.23	FMW 88	
	693	4238.82	3.36	6.29	-0.28	FMW 88	
	693	4225.46	3.40	6.32	-0.50	FMW 88	
	693	4217.55	3.42	6.34	-0.51	FMW 88	
	693	4195.34	3.32	6.26			
	693	4194.27	3.35	6.29			
	693	4196.22	3.38	6.32	-0.74	FMW 88	
	693	4194.66	3.40	6.34	-0.76	FMW 88	
	693	4147.34	3.32	6.29			
	693	4156.46	3.35	6.32			
	693	4169.78	3.38	6.34	-1.01	FMW 88	
	726	4137.00	3.40	6.38	-0.54	FMW 88	
	800	4219.35	3.56	6.48	0.12	FMW 88	
	Fe II	21	4177.70	2.53	5.59	-3.48	Heb 83
		21	4258.35	2.63	5.53		
		21	4119.53	2.53	5.53	-4.17	Heb 83
		21	4211.80	2.63	5.56		
		21	4075.95	2.53	5.56	-3.38	FMW 88
		21	4183.20	2.63	5.58		
		22	4124.79	2.53	5.52	-4.20	Bla 80
22		4205.48	2.63	5.57			
22		4070.03	2.53	5.57	-4.33	Heb 83	
22		4164.66	2.63	5.59			
22		4035.54	2.53	5.59			
25		4670.17	2.57	5.21	-4.22	Bla 80	
25		4871.27	2.69	5.23			
25		4648.93	2.57	5.23			
25		4855.54	2.69	5.23			
25		4634.60	2.57	5.23			
25		4846.47	2.69	5.24			
26		4580.06	2.57	5.27			
26		4665.80	2.69	5.34			
26		4713.18	2.77	5.39			
26		4461.43	2.57	5.34			
26		4583.09	2.69	5.39			
26		4386.57	2.57	5.39			
27		4233.17	2.57	5.49	-2.00	FMW 88	
27		4351.76	2.69	5.53	-2.10	FMW 88	
27		4416.82	2.77	5.56	-2.60	FMW 88	
27		4173.45	2.57	5.53	-2.18	FMW 88	
27		4303.17	2.69	5.56	-2.49	FMW 88	
27		4365.38	2.77	5.58	-2.37	FMW 88	
27		4128.74	2.57	5.56	-3.77	FMW 88	
27		4273.32	2.69	5.58	-3.34	FMW 88	
28		4178.86	2.57	5.52	-2.48	FMW 88	
28		4296.57	2.69	5.57	-3.01	FMW 88	
28		4369.40	2.77	5.59	-3.67	FMW 88	
28		4122.64	2.57	5.57	-3.38	FMW 88	
28		4288.16	2.69	5.59	-3.40	FMW 88	
28		4087.27	2.57	5.59	-4.71	FMW 88	
29		4002.07	2.77	5.85			
30		4825.71	2.62	5.18			
30		4833.21	2.65	5.20	-4.78	FMW 88	
30		4840.00	2.66	5.21	-4.90	FMW 88	
30		4847.61	2.68	5.23			
30		4867.73	2.65	5.18			
30		4868.82	2.66	5.20			
30		4870.71	2.68	5.21			
30		4903.85	2.66	5.18			
30		4899.90	2.68	5.20			
32	4384.33	2.65	5.46	-3.50	FMW 88		
32	4314.29	2.66	5.52	-3.07	Heb 83		
32	4278.13	2.68	5.57	-3.68	Heb 83		
32	4413.60	2.66	5.48	-3.78	Bla 80		
32	4338.70	2.68	5.52				
32	4439.13	2.68	5.46				
33	4372.22	2.66	5.49				
33	4332.88	2.68	5.53				
33	4397.27	2.68	5.49				
36	4893.70	2.82	5.34	-4.45	FMW 88		
37	4629.34	2.79	5.46	-2.37	FMW 88		
37	4855.89	2.82	5.52	-2.29	FMW 88		
37	4515.34	2.83	5.57	-2.48	FMW 88		
37	4491.40	2.84	5.59	-2.70	FMW 88		
37	4820.23	2.79	5.52	-2.60	FMW 88		
37	4489.19	2.82	5.57	-2.97	FMW 88		
37	4472.92	2.83	5.59	-3.43	FMW 88		
37	4665.75	2.82	5.46	-3.33	FMW 88		
37	4582.64	2.83	5.52	-3.10	FMW 88		
37	4534.17	2.84	5.57	-3.47	FMW 88		

Table H.1: *continued*

Ion	Mult.	$\lambda$ (Å)	$x_j$	$x_u$	$\log gf$	Ref.
FeII	38	4543.63	2.79	5.49	-2.03	Moi 83
	38	4549.47	2.82	5.53	-1.75	FMW 88
	38	4522.63	2.83	5.56	-2.03	FMW 88
	38	4808.28	2.84	5.58	-2.21	FMW 88
	38	4620.51	2.82	5.49	-3.28	FMW 88
	38	4576.33	2.83	5.53	-3.09	Moi 83
	38	4541.52	2.84	5.56	-3.10	Moi 83
	38	4644.23	2.83	5.49		
	38	4593.68	2.84	5.53		
	39	4136.40	2.82	5.80	-4.02	Heb 83
	39	4084.75	2.83	5.85		
	39	4064.75	2.84	5.88		
	39	4160.62	2.83	5.80		
	39	4104.18	2.84	5.85		
	43	4731.44	2.88	5.49	-3.41	Moi 83
	43	4636.97	2.88	5.53	-3.81	Bla 80
	43	4601.34	2.88	5.56		
	44	4663.70	2.88	5.52	-3.73	Heb 83
	44	4720.15	3.18	5.60	-4.75	FMW 88
	44	4884.92	3.32	5.85		
	44	4627.66	3.18	5.85		
	44	4831.11	3.32	5.88		
	44	4577.78	3.18	5.68		
	126	4046.61	4.48	7.53		
	126	4012.47	4.46	7.54		
	126	4032.95	4.48	7.54		
	127	4024.55	4.46	7.54	-2.46	FMW 88
	127	4004.15	4.46	7.54		
	151	4031.46	4.71	7.77		
	161	4084.58	4.72	7.74		
	171	4526.58	5.54	8.27		
	171	4474.19	5.55	8.30		
	171	4529.56	5.55	8.27		
	172	4048.83	5.54	8.59	-1.91	Heb 83
	172	4044.01	5.55	8.60	-2.37	Heb 83
	172	4041.64	5.54	8.60		
	172	4031.21	5.55	8.59		
	187	4446.25	5.93	8.71		
	188	4111.90	5.93	8.93	-2.47	Heb 83
	188	4069.68	5.89	8.92		
	188	4131.17	5.93	8.92		
	188	4081.42	5.89	8.91		
	188	4143.07	5.93	8.91		
	189	4061.79	5.93	8.97	-2.50	Heb 83
	189	4007.72	5.89	8.96		
190	4002.85	5.93	9.01			
190	3996.36	5.93	9.02			
212	4037.46	7.24	10.28			
213	4354.36	7.62	10.43			
213	4507.20	7.74	10.48			
219	4598.53	7.77	10.45			
219	4628.62	7.81	10.46			
219	4631.90	7.83	10.50			
219	4628.33	7.85	10.31			
219	4652.28	7.85	10.30			
220	4313.03	7.77	10.63			
220	4319.72	7.61	10.67			
220	4321.34	7.83	10.69			
220	4318.22	7.63	10.70			
FeIII	4	4419.59	8.21	11.00	-2.33	Kur 75
	4	4382.31	8.21	11.03		
	4	4363.56	8.22	11.05		
	4	4371.10	8.21	11.03		
	4	4352.70	8.21	11.05		
	4	4430.95	8.21	11.00	-2.69	Kur 75
	4	4395.78	8.22	11.03	-2.71	Kur 75
HI	1	4861.33	10.15	12.89	-1.74	e.g. All 73
	1	4340.47	10.15	13.00	-2.14	e.g. All 73
	1	4101.74	10.15	13.16	-2.43	e.g. All 73
HeI	12	4713.14	20.87	23.49	-1.07	Tey OP
	12	4713.37	20.87	23.49	-1.99	Tey OP
	14	4471.44	20.87	23.63		
	14	4471.69	20.87	23.63		
	16	4120.61	20.87	23.87	-1.53	Tey OP
	16	4120.99	20.87	23.87	-2.43	Tey OP
	18	4026.19	20.87	23.94		
	18	4026.36	20.87	23.94		
	50	4437.55	21.13	23.91	-2.02	Tey OP
	61	4387.93	21.13	23.94		
	82	4188.67	21.13	24.09	-2.32	Tey OP
	83	4143.76	21.13	24.11		
	84	4023.69	21.13	24.19		
85	4009.27	21.13	24.21			
MgI	11	4702.98	4.33	6.93	-0.58	Wie 69
MgII	4	4481.13	8.83	11.58	0.57	Wie 69
	4	4481.33	8.83	11.58	0.73	Wie 69
	9	4433.98	9.95	12.74	-0.90	Wie 69
	9	4428.00	9.95	12.74	-1.20	Wie 69
	10	4390.59	9.96	12.77	-0.53	Wie 69
	10	4384.64	9.95	12.77	-0.78	Wie 69
	18	4739.59	11.82	14.12	-0.42	Kur 75
	19	4436.48	11.82	14.30		
	20	4242.47	11.82	14.43		
	21	4109.54	11.82	14.52		
	22	4013.60	11.82	14.59		
	25	4651.10	11.58	14.12		
26	4534.26	11.58	14.30			
27	4331.93	11.58	14.43	-0.68	Kur 75	
28	4193.44	11.58	14.52			
29	4093.90	11.58	14.59			

Table H.1: *continued*

Ion	Mult.	$\lambda$ (Å)	$\chi_i$	$\chi_u$	log gf	Ref.
Mn II	2	4085.87	1.77	4.79		
	2	4174.31	1.80	4.76		
	2	4238.79	1.82	4.74		
	2	4328.14	1.77	4.76		
	2	4205.37	1.80	4.74		
	2	4328.87	1.80	4.79		
	2	4207.23	1.82	4.76		
	2	4280.47	1.84	4.74		
	3	4753.73	5.37	7.97		
	3	4764.70	5.37	7.98		
	3	4738.29	5.36	7.98		
	3	4730.38	5.35	7.96		
	3	4727.90	5.35	7.96		
	6	4343.99	5.37	8.21		
	6	4326.76	5.37	8.23		
	6	4322.25	5.36	8.23		
	6	4283.77	5.35	8.23		
	6	4284.43	5.35	8.23		
	6	4325.10	5.37	8.23		
	6	4345.60	5.37	8.21		
6	4300.20	5.36	8.23			
7	4206.38	5.37	8.31			
7	4259.20	5.37	8.27			
7	4253.02	5.36	8.26			
7	4244.26	5.35	8.26			
Ni I	5	4223.04	10.29	13.21	-1.09	Wie 66
	5	4230.35	10.29	13.21	-1.45	Wie 66
	5	4224.74	10.29	13.21	-1.49	Wie 66
	5	4214.73	10.29	13.21	-1.45	Wie 66
	5	4215.92	10.28	13.21	-1.49	Wie 66
	6	4151.46	10.29	13.26	0.19	Wie 66
	6	4143.42	10.29	13.26	0.11	Wie 66
	6	4137.63	10.28	13.26	0.06	Wie 66
	10	4109.98	10.64	13.65	0.83	Wie 66
	10	4099.94	10.63	13.64	0.46	Wie 66
	10	4114.20	10.64	13.64	0.09	Wie 66
00	4492.40	0.00	0.00			
00	4356.48	0.00	0.00			
00	4317.70	0.00	0.00			
Ni II	1	4895.20	17.80	20.32		
	8	4630.54	18.40	21.07	0.09	Bec 89
	8	4613.87	18.39	21.06	-0.61	Bec 89
	8	4643.09	18.40	21.06	-0.39	Bec 89
	8	4621.39	18.39	21.06	-0.48	Bec 89
	8	4601.48	18.39	21.07	-0.39	Bec 89
	8	4607.15	18.38	21.06	-0.48	Bec 89
	12	3995.00	18.42	21.51	0.23	Bec 89
	13	4447.03	20.32	23.10	0.24	Bec 89
	16	4375.00	20.32	23.14		
	20	4805.27	20.56	23.15	-0.14	Bec 89
	20	4788.13	20.56	23.14	-0.39	Bec 89
	20	4779.71	20.56	23.14	-0.58	Bec 89
	20	4610.29	20.58	23.14	-1.04	Bec 89
	20	4793.66	20.56	23.14	-1.05	Bec 89
	20	4781.17	20.56	23.15	-1.04	Bec 89
	20	4774.22	20.56	23.14	-1.05	Bec 89
	33	4227.75	21.81	24.43	-0.09	Bec 89
	39	4041.32	23.04	26.10	0.83	Bec 89
	39	4043.84	23.03	26.08	0.71	Bec 89
	39	4033.09	23.02	26.08	0.60	Bec 89
	39	4057.00	23.04	26.08	-0.46	Bec 89
	39	4044.75	23.03	26.08	-0.46	Bec 89
	40	4026.08	23.03	26.10		
	48	4241.79	23.15	26.06	0.73	Bec 89
	48	4237.05	23.14	26.05	0.57	Bec 89
	48	4236.86	23.14	26.05	0.40	Bec 89
	48	4236.98	23.14	26.05	0.57	Bec 89
Ni II	9	4362.10	4.01	6.84	-2.71	Kur 75
	9	4244.80	4.01	6.82		
	10	4384.60	4.01	6.83		
	10	4192.07	4.01	6.96		
	11	4067.06	4.01	7.05	-0.59	Heb 83
	11	4071.00	4.01	7.05		
12	4018.50	4.01	7.09	-1.25	Heb 83	
O II	2	4349.43	22.90	25.74	0.06	Bec 88
	2	4336.87	22.88	25.73	-0.78	Bec 88
	2	4325.78	22.87	25.72	-1.13	Bec 88
	2	4366.89	22.90	25.73	-0.28	Bec 88
	2	4345.56	22.88	25.72	-0.34	Bec 88
	2	4319.63	22.88	25.74	-0.37	Bec 88
	2	4317.14	22.87	25.73	-0.37	Bec 88
P II	15	4601.97	12.80	15.48	0.74	Wie 69
	15	4588.04	12.76	15.45	0.58	Wie 69
	15	4589.86	12.76	15.48	0.42	Wie 69
	15	4658.12	12.80	15.45	-0.31	Wie 69
	15	4621.70	12.76	15.43	-0.31	Wie 69
15	4698.16	12.76	15.43	-1.65	Wie 69	
S II	8	4779.11	13.61	16.20	-1.65	Wie 69
	8	4804.12	13.61	16.13	-3.09	Wie 69
	8	4681.32	13.56	16.20	-2.23	Wie 69
	8	4742.20	13.53	16.13	-2.78	Wie 69
	9	4815.82	13.61	16.18	-0.05	Wie 69
	9	4716.23	13.58	16.18	-0.52	Wie 69
	9	4656.74	13.53	16.18	-0.81	Wie 69
	10	4193.81	13.56	16.45		
	15	4885.63	13.94	16.47	-0.74	Wie 69
	32	4431.02	14.59	17.37		
	36	4668.58	14.73	17.37		
36	4648.17	14.72	17.38			
40	4524.95	15.00	17.73	0.08	Wie 69	

Table H.1: continued

Ion	Mult.	$\lambda$ (Å)	$\chi_i$	$\chi_u$	$\log gf$	Ref.
S II	40	4552.38	15.00	17.71	-0.10	Wie 69
	40	4524.64	15.00	17.73	-0.94	Wie 69
	43	4463.58	15.84	18.64	-0.02	Wie 69
	43	4483.42	15.83	18.58	-0.43	Wie 69
	43	4486.66	15.80	18.55	-0.40	Wie 69
	43	4391.84	15.83	18.64	-0.56	Wie 69
	43	4432.41	15.40	18.56	-0.46	Wie 69
	43	4456.43	15.78	18.55	-0.56	Wie 69
	43	4342.84	15.80	18.64	-1.52	Wie 69
	43	4402.86	15.78	18.56	-1.27	Wie 69
	44	4102.70	15.88	18.84	0.78	Wie 69
	44	4153.10	15.83	18.80	0.62	Wie 69
	44	4145.10	15.80	18.78	0.44	Wie 69
	44	4142.29	15.78	18.76	0.24	Wie 69
	44	4217.23	15.88	18.80	-0.15	Wie 69
	44	4189.71	15.83	18.78	-0.04	Wie 69
	44	4168.41	15.80	18.75	-0.18	Wie 69
	44	4255.01	15.88	18.78	-1.45	Wie 69
	44	4213.50	15.83	18.76	-1.30	Wie 69
	45	4028.79	15.88	18.94	-0.00	Wie 69
	45	3990.94	15.83	18.92	-0.30	Wie 69
	45	4080.11	15.88	18.92	-0.78	Wie 69
	45	4003.89	15.83	18.91	-0.69	Wie 69
	46	4792.02	16.07	18.64	-0.12	Wie 69
	46	4838.88	16.03	18.58	-0.99	Wie 69
	46	4883.73	16.02	18.55	-1.19	Wie 69
	46	4901.30	16.07	18.58	-0.46	Wie 69
	46	4900.47	16.03	18.55	-0.49	Wie 69
	46	4729.48	16.03	18.64	-0.49	Wie 69
	46	4819.60	16.02	18.56	-0.50	Wie 69
	47	4590.80	16.07	18.75		
	47	4533.30	16.03	18.75		
	47	4818.90	16.02	18.75		
	48	4552.39	16.07	18.78		
	48	4495.90	16.03	18.76		
	48	4506.00	16.02	18.76		
	49	4294.43	16.07	18.94	0.56	Wie 69
	49	4267.80	16.03	18.92	0.28	Wie 69
	49	4269.76	16.02	18.91	-0.12	Wie 69
	49	4318.68	16.07	18.92	-0.08	Wie 69
	49	4282.63	16.03	18.91	-0.01	Wie 69
	49	4278.34	16.02	18.91	-0.12	Wie 69
	49	4333.84	16.07	18.91	-1.03	Wie 69
	49	4291.45	16.03	18.91	-0.81	Wie 69
	59	4032.81	16.18	19.24	0.24	Wie 69
	59	3998.79	16.18	19.26	0.05	Wie 69
	64	4189.72	17.32	20.27	0.19	Wie 69
	64	4165.11	17.31	20.27	0.06	Wie 69
	64	4180.70	17.32	20.27	-1.24	Wie 69
	64	4174.04	17.31	20.37	-1.24	Wie 69
66	4258.18	17.37	20.27	0.52	Wie 69	
66	4287.42	17.38	20.27	0.36	Wie 69	
66	4249.92	17.37	20.27	-0.79	Wie 69	
00	4624.11	0.00	0.00			
00	4591.05	0.00	0.00			
00	4561.88	0.00	0.00			
00	4549.54	0.00	0.00			
00	4464.43	0.00	0.00			
00	4185.95	0.00	0.00			
00	4174.30	0.00	0.00			
Sc II	7	4246.83	0.31	3.22	0.32	MPW 88
	14	4374.46	0.62	3.44	-0.44	MPW 88
	14	4400.36	0.60	3.41		
	14	4415.56	0.59	3.39		
	14	4420.67	0.62	3.41		
	14	4431.37	0.60	3.39		
	14	4354.61	0.60	3.44		
	14	4384.61	0.59	3.41		
	15	4314.08	0.62	3.48	-0.10	MPW 88
	15	4320.75	0.60	3.46	-0.26	MPW 88
	15	4325.01	0.59	3.45	-0.44	MPW 88
	15	4294.77	0.60	3.48		
	15	4305.72	0.59	3.46		
15	4279.93	0.59	3.48			
16	4008.50	0.60	3.68			
S III	3	4130.68	9.80	12.78	0.53	Bec 90
	3	4128.05	9.79	12.78	0.37	Bec 90
	00	4889.28	0.00	0.00		
	00	4198.17	0.00	0.00		
	00	4190.74	0.00	0.00		
	00	4076.78	0.00	0.00		
	00	4078.48	0.00	0.00		
Sr II	1	4077.71	0.00	3.03		
	1	4218.82	0.00	2.93		
Ti III	17	4762.77	1.08	3.67	-2.71	MPW 88
	17	4798.54	1.08	3.65	-2.43	MPW 88
	17	4806.33	1.08	3.65		
	18	4449.18	1.08	3.64	-1.84	War 67
	18	4483.53	1.08	3.62	-2.41	Sav 90
	18	4500.32	1.08	3.62		
	18	4518.30	1.08	3.61		
	18	4525.21	1.08	3.61		
	19	4395.03	1.08	3.69	-0.43	Sav 90
	19	4443.80	1.08	3.65	-0.70	Sav 90
	19	4480.49	1.08	3.65	-1.45	Sav 90
	20	4294.10	1.08	3.95	-0.88	Sav 90
	20	4337.92	1.08	3.92	-0.88	Sav 90
20	4344.29	1.08	3.92	-1.86	Sav 90	
20	4287.69	1.08	3.95	-2.02	MPW 88	

Table H.1: *continued*

Ion	Mult.	$\lambda$ (Å)	$\chi_i$	$\chi_w$	$\log g_f$	Ref.
Ti II	21	4161.52	1.08	4.05	-2.00	Sav 90
	21	4167.67	1.08	4.04		
	21	4173.54	1.08	4.04	-1.59	War 67
	21	4184.33	1.08	4.02	-1.44	War 67
	21	4190.29	1.08	4.02	-2.01	War 67
	21	4195.64	1.08	4.02		
	31	4468.49	1.13	3.89	-0.60	Sav 90
	31	4501.27	1.11	3.85	-0.75	Sav 90
	31	4444.56	1.11	3.89	-2.20	Sav 90
	32	4341.37	1.11	3.95	-2.05	Sav 90
	40	4441.73	1.18	3.95	-2.41	MPW 88
	40	4470.66	1.16	3.92	-2.00	Sav 90
	40	4495.46	1.18	3.92		
	40	4417.72	1.16	3.95	-1.20	Sav 90
	40	4464.46	1.16	3.92	-1.78	Sav 90
	41	4300.05	1.18	4.05	-0.55	Sav 90
	41	4280.22	1.16	4.04	-0.87	Sav 90
	41	4301.93	1.16	4.02	-1.16	Sav 90
	41	4312.86	1.18	4.04	-1.16	Sav 90
	41	4307.90	1.16	4.02	-1.04	Sav 90
	41	4314.98	1.16	4.02	-1.13	Sav 90
	41	4330.71	1.18	4.02	-2.04	Sav 90
	41	4320.97	1.16	4.02	-1.87	Sav 90
	48	4764.54	1.23	3.82		
	48	4763.84	1.22	3.81		
	48	4792.39	1.23	3.81		
	50	4333.97	1.23	3.93	-0.66	Sav 90
	50	4363.76	1.22	3.92	-0.94	Sav 90
	50	4369.96	1.23	3.92	-1.75	Sav 90
	51	4399.77	1.23	4.04	-1.27	Sav 90
	51	4394.06	1.22	4.02	-1.59	Sav 90
	51	4418.34	1.23	4.02	-1.47	Sav 90
	51	4407.68	1.22	4.02	-2.47	Sav 90
	51	4432.09	1.23	4.02	-2.07	Sav 90
	62	4549.62	1.68	4.29	-0.43	Sav 90
	62	4571.97	1.56	4.26	-0.52	Sav 90
	62	4529.47	1.56	4.29	-1.93	Sav 90
	87	4028.33	1.88	4.95	-1.12	Sav 90
	87	4053.81	1.88	4.93	-1.29	Sav 90
	87	4029.64	1.88	4.95		
	92	4805.11	2.05	4.82	-1.05	Sav 90
	92	4779.99	2.04	4.62	-1.38	Sav 90
	93	4374.83	2.05	4.87	-1.49	Sav 90
	93	4400.63	2.04	4.84		
	93	4421.95	2.05	4.84	-1.43	Sav 90
	94	4360.83	2.05	4.89	-1.81	Sav 90
	94	4316.81	2.04	4.90	-1.52	MPW 88
	94	4337.33	2.05	4.90	-2.08	War 67
	94	4330.26	2.04	4.89	-1.51	MPW 88
	104	4367.66	2.58	5.40	-1.22	Sav 90
	104	4384.86	2.59	5.40	-1.11	Sav 90
	104	4375.35	2.58	5.40	-1.93	Sav 90
	105	4163.64	2.58	5.54	-0.24	Sav 90
	105	4171.90	2.59	5.54	-0.41	Sav 90
	105	4174.09	2.59	5.54	-1.14	Sav 90
	106	4064.35	2.59	5.62	-1.67	War 67
	114	4911.21	3.11	5.82	-0.79	Sav 90
114	4874.03	3.08	5.61	-0.99	Sav 90	
114	4835.93	3.08	5.62			
115	4488.32	3.11	5.86	-0.68	Sav 90	
115	4411.08	3.08	5.88	-0.82	Sav 90	
115	4456.63	3.11	5.86	-1.51	War 67	
VII	9	3997.13	1.47	4.56	-1.23	Bie 69
	9	4036.78	1.47	4.53	-1.59	Bie 69
	9	4002.94	1.42	4.50	-1.45	Bie 69
	9	4087.03	1.47	4.50	-2.46	Bie 69
	14	4086.27	1.57	4.61	-2.42	Bie 69
	14	4075.66	1.58	4.59		
	18	4236.82	1.68	4.59		
	18	4254.41	1.67	4.57	-1.66	Bie 69
	18	4260.75	1.67	4.58		
	28	4202.38	1.70	4.63	-1.52	Bie 69
	28	4174.39	1.68	4.63	-1.57	Bie 69
	28	4190.40	1.67	4.61		
	28	4204.20	1.70	4.63	-2.45	MPW 88
	28	4208.05	1.68	4.61		
	28	4209.74	1.67	4.60		
	28	4231.17	1.70	4.61		
	28	4226.51	1.68	4.60	-2.65	MPW 88
	28	4220.05	1.67	4.59	-2.97	RAS 73
	32	4008.71	1.81	4.89	-0.52	Bie 69
	32	4023.39	1.80	4.86	-0.69	Bie 69
	32	4038.63	1.79	4.84	-0.77	Bie 69
	32	4039.57	1.81	4.86	-2.40	Bie 69
	32	4051.06	1.80	4.84		
	32	3949.60	1.80	4.89	-2.00	Bie 69
	32	4008.17	1.79	4.86	-2.07	Bie 69
	37	4183.44	2.04	4.99	-1.11	Bie 69
	37	4205.08	2.03	4.94	-1.30	Bie 69
	37	4228.29	2.02	4.94	-1.44	Bie 69
	37	4164.02	2.03	4.99		
	37	4190.69	2.02	4.96		
	37	4150.08	2.02	4.99		
	56	4528.51	2.27	4.99	-1.10	Bie 69
56	4564.59	2.26	4.96	-1.39	Bie 69	
56	4600.19	2.26	4.94	-1.52	Bie 69	
56	4577.13	2.27	4.96			
56	4605.35	2.26	4.94			
56	4618.12	2.27	4.94			
Zr II	30	3991.14	0.78	3.85		

Table H.1: *continued*

ion	Mult.	$\lambda$ (Å)	$x_l$	$x_w$	$\log gf$	Ref.
Zr II	30	4045.63	0.71	3.76		
	30	4110.05	0.76	3.76		
	41	4149.22	0.80	3.77		
	41	4208.99	0.71	3.64		
	41	4339.58	0.80	3.64		
	41	4029.68	0.71	3.77		

References: All 73: Allen (1973). Bec 88: Becker & Butler (1988). Bec 89: Becker & Butler (1989). Bec 90: Becker & Butler (1990).  
 Bie 89: Biedmont et al. (1989). Bia 80: Blackwell, Pettford, Shallis & Simmons (1980). Bia 82: Blackwell, Pettford, Shallis & Simmons (1982).  
 BrK 74: Bridges & Kornblith (1974) corrected by Blackwell, Pettford & Shallis (1982). FMW 88: Fuhr, Martin & Wiese (1988). GIF 89: Giridhar & Ferro (1989). GuK 81: Gurtovenko & Kostik (1981). KP 75: Kurucz & Petryman (1975). MFW 88: Martin, Fuhr & Wiese (1988).  
 Moi 83: Moity (1983) corrected by Gigas (1986). RAS73a: Roberts, Andersen & Sørensen (1973a). RAS73b: Roberts, Andersen & Sørensen (1973b). Sav 90: Savanov, Huovelin & Tuomina (1990). Tay OP: Taylor et al. (private communication). War 67: Warner (1967). Wie 66: Wiese, Smith & Glennon (1966). Wie 69: Wiese, Smith & Miles (1969). Yan 87: Yan, Taylor & Seaton (1987).

## H.1 References

- Allen, C.W., 1973. *Astrophysical Quantities*, Third Edition, Athlone Press.
- Becker, S.R. & Butler, K., 1988. *Astr. Astrophys.*, **201**, 232.
- Becker, S.R. & Butler, K., 1989. *Astr. Astrophys.*, **209**, 244.
- Becker, S.R. & Butler, K., 1990. *Astr. Astrophys.*, **235**, 326.
- Biémont, E., Grevesse, N., Faires, L.M., Marsden, G., Lawler, J.E. & Whaling, W., 1989. *Astr. Astrophys.*, **209**, 391.
- Blackwell, D.E., Petford, A.D., Shallis, M.J. & Simmons, G.J., 1980. *Mon. Not. R. astr. Soc.*, **191**, 445.
- Blackwell, D.E., Petford, A.D., Shallis, M.J. & Simmons, G.J., 1982. *Mon. Not. R. astr. Soc.*, **199**, 43.
- Blackwell, D.E., Petford, A.D. & Simmons, G.J., 1982. *Mon. Not. R. astr. Soc.*, **201**, 595.
- Bridges, J.M. & Kornblith, R.L., 1974. *Astrophys. J.*, **192**, 793.
- Fuhr, J.R., Martin, G.A. & Wiese, W.L., 1988. *J. Phys. Chem. Ref. Data*, **17**, Suppl. 4.
- Gigas, D., 1986. *Astr. Astrophys.*, **165**, 170.
- Giridhar, S. & Ferro, A.A., 1989. *J. Astrophys. astr.*, **10**, 47.
- Gurtovenko, E.A. & Kostik, R.I., 1981. *Astr. Astrophys. Suppl.*, **46**, 239.
- Kurucz, R.L. & Petryeman, E., 1975. *SAO Special Report*, **362**.
- Martin, G.A., Fuhr, J.R. & Wiese, W.L., 1988. *J. Phys. Chem. Ref. Data*, **17**, Suppl. 3.
- Meggers, W.F., Corliss, C.H. & Seribner, B.R., . *NBS Monograph*, **145**, 1.
- Moity, J., 1983. *Astr. Astrophys. Suppl.*, **52**, 37.
- Roberts, J.R., Andersen, T. & Sørensen, G., 1973a. *Astrophys. J.*, **181**, 567.
- Roberts, J.R., Andersen, T. & Sørensen, G., 1973b. *Astrophys. J.*, **181**, 587.
- Savanov, I.S., Huovelin, J. & Tuominen, I., 1990. *Astr. Astrophys. Suppl.*, **86**, 531.
- Taylor, K.T. *et al.* , Opacity Project. Private communication
- Warner, B., 1967. *Mem. R. astr. Soc.*, **70**, 165.
- Wiese, W.L., Smith, M.W. & Glennon, , 1966. *Atomic Transition Probabilities*, NBS, Washington.

Wiese, W.L., Smith, M.W. & Miles, B.M., 1969. *Atomic Transition Probabilities*, NBS, Washington.

Yan, Y., Taylor, K.T. & Seaton, M.J., 1987. *J. Phys. B*, **20**, 6399.